

OFFICE OF CIVILIAN RADIOACTIVE WASTE MANAGEMENT

SCIENTIFIC ANALYSIS COVER SHEET

1. QA: QA
 Page: 1
 Of: 384

NEL
 9/6/02
 388

2. Scientific Analyses Title
 Geotechnical Data for a Potential Waste Handling Building and for Ground Motion Analyses for the Yucca (see Block 11)

3. DI (including Revision Number)
 ANL-MGR-GE-000003 Rev 00

4. Total Attachments
 17

5. Attachment Numbers - Number of pages in each
 I-98, II-10, III-12, IV-14, V-16, VI-6, VII-66, VIII-26, IX-70, X-8, XI-8 (continued in Block 11)

	Print Name	Signature	Date
6. Originator	M.J. Luebbers, I.G. Wong, R. Lung	<i>Michael Luebbers</i> <i>Ivan Wong by Michael Luebbers</i>	07-23-02 07-23-02
7. Checker	D. Kicker, N. Biggar	<i>D. Kicker</i> <i>N. Biggar</i>	8/2/02 7/25/02
8. QER	K. Gilkerson	<i>K. Gilkerson</i> <i>Kenneth McFall</i>	8/5/2002 8/6/02
9. Responsible Manager/Lead	C. Howard	<i>Cliff Howard</i>	9-6-02 8-6-02
10. Responsible Manager	T. Doering	<i>T. Doering</i>	9-6-02

11. Remarks
 Block 2: The complete title of this Scientific Analysis is: Geotechnical Data for a Potential Waste Handling Building and for Ground Motion Analyses for the Yucca Mountain Site Characterization Project.

Block 5 (continued): XII-64, XIII-12, XIV-16, XV-64, XVI-10, XVII-34, XVIII-8

NEL
 9/6/02

Technical Contact/Department: Cliff Howard

Revision History

12. Revision/ICN No.	13. Description of Revision/Change
00	initial issue

INTENTIONALLY LEFT BLANK

CONTENTS

	Page
ACRONYMS AND ABBREVIATIONS	19
1. PURPOSE	23
1.1 PURPOSE.....	23
1.2 LIMITATIONS.....	23
2. QUALITY ASSURANCE	25
3. USE OF SOFTWARE.....	26
4. INPUTS	27
4.1 DATA AND PARAMETERS	27
4.2 CRITERIA	29
4.3 CODES AND STANDARDS.....	29
5. ASSUMPTIONS	30
6. SCIENTIFIC ANALYSIS DISCUSSION	32
6.1 OVERVIEW	32
6.2 DATA ACQUIRED AT WHB AREA	33
6.2.1 Overview	33
6.2.2 Boreholes.....	34
6.2.3 Revision of RF#13 Borehole Log.....	38
6.2.4 Test Pits	39
6.2.5 Downhole Seismic Velocity Surveys	41
6.2.6 Suspension Seismic Surveys	83
6.2.7 SASW Surveys	102
6.2.8 Borehole Wireline Geophysical Surveys.....	161
6.2.9 Geotechnical Laboratory Static Testing	164
6.2.10 Geotechnical Laboratory Dynamic Testing.....	170
6.3 DATA ACQUIRED IN THE ESF MAIN DRIFT.....	229
6.3.1 Overview	229
6.3.2 SASW Surveys	229
6.3.3 Geotechnical Laboratory Dynamic Testing.....	231
6.4 DATA ACQUIRED AT THE CREST OF YUCCA MOUNTAIN	240
6.4.1 Overview	240
6.4.2 SASW Surveys	240
6.4.3 Downhole Seismic Surveys.....	293
6.5 DATA ACQUIRED FOR BORROW MATERIAL.....	308
6.5.1 Overview	308
6.5.2 Geotechnical Laboratory Static Testing	308
6.5.3 Geotechnical Laboratory Dynamic Testing.....	317
6.6 GEOLOGIC CONDITIONS.....	324
6.6.1 Regional Geologic and Topographic Conditions	324

CONTENTS (Continued)

	Page
6.6.2	Subsurface Geologic Conditions326
6.6.3	Groundwater Conditions341
6.7	EVALUATION OF SEISMIC VELOCITY DATA FROM WHB AREA 342
6.7.1	Shear-Wave Velocities Determined by Various Seismic Methods at Other Sites342
6.7.2	Comparison of Shear-Wave Velocities from Borehole Seismic Methods ...348
6.8	PREVIOUS DATA 358
6.8.1	Overview358
6.8.2	Previous Geotechnical Testing on Core Samples.....359
6.8.3	Alluvium.....366
7.	CONCLUSION 370
7.1	SUMMARY 370
7.2	RESTRICTIONS 371
7.3	UNCERTAINTIES AND LIMITATIONS..... 371
7.3.1	Sufficiency of Geotechnical Data for Fran Ridge Borrow Area371
7.3.2	Sufficiency of Seismic Data for Emplacement Area.....371
7.3.3	Sufficiency of Seismic Data in the WHB Area372
7.3.4	Lithographic Unit Identification and Accuracy of Contacts372
7.3.5	Strike and Dip of Bedding.....372
7.3.6	Fault Locations373
7.3.7	Dynamic Properties at High Shear Strain.....373
7.3.8	Uncertainty Concerning Borrow Area.....373
8.	INPUTS AND REFERENCES 374
8.1	DOCUMENTS CITED..... 374
8.2	STANDARDS AND PROCEDURES..... 380
8.3	SOURCE DATA, LISTED BY DATA TRACKING NUMBER (DTN)..... 382
8.4	SOFTWARE CODES 387
9.	ATTACHMENTS 388
ATTACHMENT I –	LOGS OF BOREHOLES RF#14 TO RF#29 I-1
ATTACHMENT II –	REVISED LOG OF BOREHOLE RF#13..... II-1
ATTACHMENT III –	LOGS OF TEST PITS TP-WHB-1 TO TP-WHB-4 III-1
ATTACHMENT IV –	PHOTOMOSAIC MAPS OF TEST PITS TP-WHB-1 TO TP-WHB-4 IV-1
ATTACHMENT V –	DOWNHOLE SEISMIC VELOCITY PLOTS (REDPATH) – WHB AREA..... V-1

CONTENTS (Continued)

	Page
ATTACHMENT VI – DOWNHOLE SEISMIC VELOCITY PLOTS (GEOVISION) – WHB AREA	VI-1
ATTACHMENT VII – SUSPENSION SEISMIC INTERVAL VELOCITY RESULTS.....	VII-1
ATTACHMENT VIII – SUSPENSION SEISMIC ACCUMULATED VELOCITY RESULTS.....	VIII-1
ATTACHMENT IX – SASW VELOCITY PLOTS – WHB AREA	IX-1
ATTACHMENT X – BOREHOLE GEOPHYSICAL SURVEYS.....	X-1
ATTACHMENT XI – GEOTECHNICAL LABORATORY STATIC TESTING – WHB AREA	XI-1
ATTACHMENT XII – GEOTECHNICAL LABORATORY DYNAMIC TESTING – WHB AREA	XII-1
ATTACHMENT XIII – SASW VELOCITY PLOTS – ESF	XIII-1
ATTACHMENT XIV – GEOTECHNICAL LABORATORY DYNAMIC TESTING – ESF	XIV-1
ATTACHMENT XV – SASW VELOCITY PLOTS –YUCCA MOUNTAIN CREST	XV-1
ATTACHMENT XVI – DOWNHOLE SEISMIC VELOCITY PLOTS – YUCCA MOUNTAIN CREST.....	XVI-1
ATTACHMENT XVII – GEOTECHNICAL LABORATORY DYNAMIC TESTING – FRAN RIDGE BORROW AREA.....	XVII-1
ATTACHMENT XVIII – GLOSSARY	XVIII-1

INTENTIONALLY LEFT BLANK

FIGURES

	Page
1. Definition of WHB Area	31
2. Locations of Boreholes and Test Pits Completed in 1998 and 2000 in the WHB Area	36
3. Locations of Downhole Measurements in Boreholes at the WHB Site Characterization Area.....	42
4. Borehole RF#13 Compression- and Shear-Wave Velocities from Downhole Measurements and Generalized Lithology.....	53
5. Borehole RF#14 Compression- and Shear-Wave Velocities from Downhole Measurements and Generalized Lithology.....	54
6. Borehole RF#15 Compression- and Shear-Wave Velocities from Downhole Measurements and Generalized Lithology.....	55
7. Borehole RF#16 Compression- and Shear-Wave Velocities from Downhole Measurements and Generalized Lithology.....	56
8. Borehole RF#17 Compression- and Shear-Wave Velocities from Downhole Measurements and Generalized Lithology.....	57
9. Borehole RF#18 Compression- and Shear-Wave Velocities from Downhole Measurements and Generalized Lithology.....	58
10. Borehole RF#19 Compression- and Shear-Wave Velocities from Downhole Measurements and Generalized Lithology.....	59
11. Borehole RF#20 Compression- and Shear-Wave Velocities from Downhole Measurements and Generalized Lithology.....	60
12. Borehole RF#21 Compression- and Shear-Wave Velocities from Downhole Measurements and Generalized Lithology.....	61
13. Borehole RF#22 Compression- and Shear-Wave Velocities from Downhole Measurements and Generalized Lithology.....	62
14. Borehole RF#23 Compression- and Shear-Wave Velocities from Downhole Measurements and Generalized Lithology.....	63
15. Borehole RF#24 Compression- and Shear-Wave Velocities from Downhole Measurements and Generalized Lithology.....	64
16. Borehole RF#25 Compression- and Shear-Wave Velocities from Downhole Measurements and Generalized Lithology.....	65
17. Borehole RF#26 Compression- and Shear-Wave Velocities from Downhole Measurements and Generalized Lithology.....	66
18. Borehole RF#28 Compression- and Shear-Wave Velocities from Downhole Measurements and Generalized Lithology.....	67
19. Borehole RF#29 Compression- and Shear-Wave Velocities from Downhole Measurements and Generalized Lithology.....	68
20. Shear-Wave Velocities from Downhole Measurements in the WHB Area	70
21. Compression-Wave Velocities from Downhole Measurements in the WHB Area	71
22. Statistical Analyses of Shear-Wave Velocities from Downhole Measurements in the WHB Area.....	73

FIGURES (Continued)

		Page
23.	Statistical Analyses of Compression-Wave Velocities from Downhole Measurements in the WHB Area.....	74
24.	Statistical Analyses of Shear-Wave Velocities from Downhole Measurements in the WHB Area (Without RF#13 and RF#15).....	75
25.	Statistical Analyses of Shear-Wave Velocities from Downhole Measurements in the WHB Area, Uplifted Side of the Exile Hill Fault Splay	76
26.	Statistical Analyses of Shear-Wave Velocities from Downhole Measurements in the WHB Area, Downthrown Side of the Exile Hill Fault Splay.....	77
27.	Comparison of Downhole Shear-Wave Velocities Across the Exile Hill Fault Splay.....	78
28.	Poisson’s Ratios from Downhole Measurements in the WHB Area.....	79
29.	Schematic Diagram of OYO P-S Logging Equipment.....	84
30.	Shear-Wave Velocity by Depth Interval from Receiver-to-Receiver Interval Suspension Surveys in WHB Area.....	89
31.	Shear-Wave Velocity by Depth Interval from Source-to-Receiver Interval Suspension Surveys in WHB Area.....	90
32.	Statistical Values of Shear-Wave Velocity by Lithostratigraphic Unit from Receiver-to-Receiver Interval Suspension Surveys in WHB Area	91
33.	Statistical Values of Shear-Wave Velocity by Lithostratigraphic Unit from Source-to-Receiver Interval Suspension Surveys in WHB Area.....	92
34.	Compression-Wave Velocity by Depth Interval from Source-to-Receiver Interval Suspension Surveys in WHB Area.....	94
35.	Statistical Values of Compression-Wave Velocity by Lithostratigraphic Unit from Source-to-Receiver Interval Suspension Surveys in WHB Area	95
36.	Poisson’s Ratio by Depth Interval from Source-to-Receiver Interval Suspension Surveys in WHB Area.....	97
37.	Statistical Values of Poisson’s Ratio by Lithostratigraphic Unit for Poisson’s Ratio from Source-to-Receiver Interval Suspension Surveys in WHB Area	98
38.	Shear-Wave Velocities from Linear Fits to Suspension Seismic Time Data.....	99
39.	Compression-Wave Velocities from Linear Fits to Suspension Seismic Time Data.....	100
40.	Poisson’s Ratio from Linear Fits to Suspension Seismic Time Data.....	101
41.	Illustration of Surface Waves with Different Wavelengths Sampling Different Materials in a Layered System which Results in Dispersion in Wave Velocities.....	103
42.	Schematic Diagram of the Generalized Equipment Arrangement Used for SASW Measurements.....	104
43.	Locations of SASW Lines at the WHB Site Characterization Area	105
44.	Common Receivers-Midpoint Geometry Often Used in SASW Surveys.....	106
45.	Using the Sledgehammer Source at SASW-23	107
46.	SASW Survey Set-Up Using the Bulldozer as a Wave Source.....	107
47.	Bulldozer Source in Operation at SASW-32.....	108
48.	Cross-Power Spectrum and Coherence Function Measured at SASW-24 from 50-ft Receiver Spacing.....	110

FIGURES (Continued)

		Page
49.	Cross-Power Spectrum and Coherence Function Measured at SASW-24 from 50-ft Receiver Spacing Shown with Masking Applied to Near-Field and Low Coherence Regions of the Phase Plot.....	111
50.	Individual Dispersion Curve Created from 50-ft Receiver Spacing at SASW-24.....	112
51.	Composite Experimental Dispersion Curve Created from All Receiver Spacings at SASW-24.....	112
52.	Theoretical Dispersion Curve Fit to the Experimental Dispersion Curve at SASW-24.....	114
53.	Final Shear-Wave Velocity Profiles Determined at SASW-24.....	114
54.	Shear-Wave Velocity Profile from SASW-1 and Generalized Lithology from RF#13.....	115
55.	Shear-Wave Velocity Profile from SASW-2 and Generalized Lithology from RF#21.....	116
56.	Shear-Wave Velocity Profile from SASW-3.....	117
57.	Shear-Wave Velocity Profile from SASW-4 and Generalized Lithology from RF#26.....	118
58.	Shear-Wave Velocity Profile from SASW-5.....	119
59.	Shear-Wave Velocity Profile from SASW-6.....	120
60.	Shear-Wave Velocity Profile from SASW-7.....	121
61.	Shear-Wave Velocity Profile from SASW-8 and Generalized Lithology from RF#28.....	122
62.	Shear-Wave Velocity Profile from SASW-9.....	123
63.	Shear-Wave Velocity Profile from SASW-10+37 and Generalized Lithology from RF#15.....	124
64.	Shear-Wave Velocity Profile from SASW-11.....	125
65.	Shear-Wave Velocity Profile from SASW-12.....	126
66.	Shear-Wave Velocity Profile from SASW-13.....	127
67.	Shear-Wave Velocity Profile from SASW-14.....	128
68.	Shear-Wave Velocity Profile from SASW-15.....	129
69.	Shear-Wave Velocity Profile from SASW-16.....	130
70.	Shear-Wave Velocity Profile form SASW-17.....	131
71.	Shear-Wave Velocity Profile from SASW-18.....	132
72.	Shear-Wave Velocity Profile from SASW-19.....	133
73.	Shear-Wave Velocity Profile from SASW-20.....	134
74.	Shear-Wave Velocity Profile from SASW-21.....	135
75.	Shear-Wave Velocity Profile from SASW-22.....	136
76.	Shear-Wave Velocity Profile from SASW-23 and Generalized Lithology from RF#22.....	137
77.	Shear-Wave Velocity Profile from SASW-24.....	138
78.	Shear-Wave Velocity Profile from SASW-25.....	139
79.	Shear-Wave Velocity Profile from SASW-26.....	140
80.	Shear-Wave Velocity Profile from SASW-27.....	141
81.	Shear-Wave Velocity Profile from SASW-28.....	142

FIGURES (Continued)

		Page
82.	Shear-Wave Velocity Profile from SASW-29 and Generalized Lithology from RF#16	143
83.	Shear-Wave Velocity Profile from SASW-30	144
84.	Shear-Wave Velocity Profile from SASW-31	145
85.	Shear-Wave Velocity Profile from SASW-32+35 and Generalized Lithology from RF#23	146
86.	Shear-Wave Velocity Profile from SASW-33	147
87.	Shear-Wave Velocity Profile from SASW-34+36 and Generalized Lithology from RF#17	148
88.	Shear-Wave Velocity Profile from SASW D-12	149
89.	Shear-Wave Velocities from SASW Measurements in the WHB Area.....	150
90.	Shear-Wave Velocities from SASW Measurements at Sites Outside of WHB Pad Area	152
91.	Statistical Analyses of Shear-Wave Velocities from SASW Measurements in the WHB Area.....	153
92.	Shear-Wave Velocities from SASW Measurements in the WHB Area (Area 1)	154
93.	Shear-Wave Velocities from SASW Measurements in the WHB Area (Area 2)	155
94.	Shear-Wave Velocities from SASW Measurements in the WHB Area (Area 3)	156
95.	Comparison of Shear-Wave Velocities from SASW Measurements by Area	157
96.	Statistical Analyses of Shear-Wave Velocities from SASW Measurements in the WHB Area, Downthrown Side of the Exile Hill Fault Splay.....	158
97.	Statistical Analyses of Shear-Wave Velocities from SASW Measurements in the WHB Area, Uprthrown Side of the Exile Hill Fault Splay	159
98.	Comparison of SASW Shear-Wave Velocities Across the Exile Hill Fault Splay	160
99.	Schematic Diagram of Dual-Detector Formation Density Logging Device	163
100.	"Spine and Ribs" Plot Used To Compute Bulk Density And Density Correction From Dual Detector Density Tools	163
101.	Density from gamma-gamma Logging as a Function of Depth and Lithostratigraphic Unit	168
102.	Particle-Size Distribution Curves for TP-WHB-1 to TP-WHB-4.....	174
103.	Idealized Fixed-Free RCTS Equipment	175
104.	(a) Simplified Diagram of a Fixed-Free Resonant Column Test and (b) an Associated Frequency Response Curve.....	176
105.	(a) Configuration of a Torsional Shear Test and (b) Evaluation of Shear Modulus (G) and Material Damping Ratio (D).....	177
106.	Calibration Curves of Equipment-Generated Damping for Drive Plate #4	179
107.	Calibration Curves of Equipment-Generated Damping for Drive Plate #5	180
108.	Shearing Strain in RCTS Specimen Column	182
109.	Determination of Material Damping Ratio from the Free-Vibration Decay Curve Using Metal Specimen	184
110.	Determination of Material Damping from the Half-Power Bandwidth Method Using a Metal Specimen	185
111.	Determination of Shear Modulus and Damping Ratio in the Torsional Shear Test.....	187

FIGURES (Continued)

	Page
112. Specimens UTA-23-A to 23-J	193
113. UTA-20 Group: Specimens 20-A, 20-B, 20-C, and 20-D are from the WHB Boreholes. Specimens 20-F, 20-G, 20-I, 20-J, and 20-L are from the ESF (Section 6.3.3)	194
114. Specimens UTA-23-Q, UTA-23-R, UTA-23-S, and UTA-23-T, which were Cored from Larger Test Specimens	195
115. Variation in Normalized Small-Strain Shear Modulus with Normalized Confining Pressure of Group 1 Intact Tuff Specimens	200
116. Variation in Normalized Small-Strain Shear Modulus with Normalized Confining Pressure of Group 2 Intact Tuff Specimens	201
117. Variation in Normalized Small-Strain Shear Modulus with Normalized Confining Pressure of Group 3 Intact Tuff Specimens	202
118. Variation of Shear-Wave Velocity Measured in the Laboratory at In-Situ Mean Total Stress with Dry Unit Weight of Intact Tuff Specimens	203
119. Variation of Shear-Wave Velocity Measured in the Laboratory at In-Situ Mean Total Stress with Total Unit Weight of Intact Tuff Specimens.....	204
120. Variation in Small-Strain Material Damping Ratio with Normalized Confining Pressure of Group 1 Intact Tuff Specimens	205
121. Variation in Small-Strain Material Damping Ratio with Normalized Confining Pressure of Group 2 Intact Tuff Specimens	206
122. Variation in Small-Strain Material Damping Ratio with Normalized Confining Pressure of Group 3 Intact Tuff Specimens	207
123. Variation in Shear Modulus with Shearing Strain of Group 1 Intact Tuff Specimens.....	208
124. Variation in Shear Modulus with Shearing Strain of Group 2 Intact Tuff Specimens.....	209
125. Variation in Shear Modulus with Shearing Strain of Group 3 Intact Tuff Specimens.....	210
126. Variation in Normalized Shear Modulus with Shearing Strain of Group 1 Intact Tuff Specimens.....	211
127. Variation in Normalized Shear Modulus with Shearing Strain of Group 2 Intact Tuff Specimens.....	212
128. Variation in Normalized Shear Modulus with Shearing Strain of Group 3 Intact Tuff Specimens.....	213
129. Variation in Material Damping Ratio with Shearing Strain of Group 1 Intact Tuff Specimens.....	214
130. Variation in Material Damping Ratio with Shearing Strain of Group 2 Intact Tuff Specimens.....	215
131. Variation in Material Damping Ratio with Shearing Strain of Group 3 Intact Tuff Specimens.....	216
132. Resonant Column and Torsional Shear Results for Tpcpmn	217
133. Resonant Column and Torsional Shear Results for Tpcpul	218
134. Resonant Column Shear Results for Tpcrn	219
135. Torsional Shear Results for Tpcrn.....	220
136. Resonant Column and Torsional Shear Results for Tпки.....	221

FIGURES (Continued)

	Page
137. Resonant Column and Torsional Shear Results for Tiva Canyon Tuff from 1999 Study and This Study.....	222
138. Resonant Column and Torsional Shear Results for Tpki from 1999 Study and This Study	223
139. Variation in Small-Strain Shear Modulus with Isotropic Confining Pressure of Reconstituted Quaternary Alluvium Specimen.....	224
140. Variation in Small-Strain Material Damping Ratio with Isotropic Confining Pressure of Reconstituted Quaternary Alluvium Specimen.....	225
141. Variation in Shear Modulus with Shearing Strain of Reconstituted Quaternary Alluvium Specimen.....	226
142. Variation in Normalized Shear Modulus with Shearing Strain of Reconstituted Quaternary Alluvium Specimen.....	227
143. Variation in Material Damping Ratio with Shearing Strain of Reconstituted Quaternary Alluvium Specimen.....	228
144. Locations of SASW Surveys in the ESF	230
145. Shear-Wave Velocity Profiles from SASW T-1	232
146. Shear-Wave Velocity Profile from SASW T-2.....	233
147. Shear-Wave Velocity Profile from SASW T-3.....	234
148. Shear-Wave Velocity Profile from SASW T-4.....	235
149. Shear-Wave Velocity Profile from SASW T-5.....	236
150. Shear-Wave Velocity Profiles from SASW Measurements in ESF.....	237
151. Statistical Analyses of Shear-Wave Velocity Profiles from SASW Measurements in ESF 238	
152. Variation in Normalized Small-Strain Shear Modulus with Normalized Confining Pressure of Intact Tuff Specimens from the ESF.....	241
153. Variation in Small-Strain Material Damping Ratio with Normalized Confining Pressure of Intact Tuff Specimens from the ESF.....	242
154. Variation in Shear Modulus with Shearing Strain of Intact Tuff Specimens from the ESF 243	
155. Variation in Normalized Shear Modulus with Shearing Strain of Intact Tuff Specimens from the ESF	244
156. Variation in Material Damping Ratio with Shearing Strain of Intact Tuff Specimens from the ESF	245
157. Locations of Boreholes Used for Vertical Seismic Profiling Surveys and SASW Surveys at Yucca Mountain.	246
158. Photograph of Vibroseis Truck in Operation on the Crest of Yucca Mountain.....	248
159. Photograph of SASW Survey Going Downslope with the Vibroseis Truck Being Readied for Use as the Source.....	248
160. Cross-Power Spectrum and Coherence Function Measured at Site D-2 from the 400-ft Receiver Spacing.....	250
161. Shear-Wave Velocity Profile from SASW C-1.....	251
162. Shear-Wave Velocity Profiles from SASW C-2	252
163. Shear-Wave Velocity Profile from SASW C-3.....	253

FIGURES (Continued)

	Page
164. Shear-Wave Velocity Profile from SASW C-4.....	254
165. Shear-Wave Velocity Profile from SASW C-5.....	255
166. Shear-Wave Velocity Profiles from SASW C-6.....	256
167. Shear-Wave Velocity Profile from SASW C-7.....	257
168. Shear-Wave Velocity Profile from SASW D-1.....	258
169. Shear-Wave Velocity Profile from SASW D-2.....	259
170. Shear-Wave Velocity Profile from SASW D-3.....	260
171. Shear-Wave Velocity Profile from SASW D-4.....	261
172. Shear-Wave Velocity Profile from SASW D-5.....	262
173. Shear-Wave Velocity Profiles from SASW D-6.....	263
174. Shear-Wave Velocity Profile from SASW D-7.....	264
175. Shear-Wave Velocity Profile from SASW D-8.....	265
176. Shear-Wave Velocity Profile from SASW D-9.....	266
177. Shear-Wave Velocity Profile from SASW D-10.....	267
178. Shear-Wave Velocity Profiles from SASW D-11.....	268
179. Shear-Wave Velocity Profile from SASW S-1.....	269
180. Shear-Wave Velocity Profile from SASW S-2.....	270
181. Shear-Wave Velocity Profile from SASW S-3.....	271
182. Shear-Wave Velocity Profile from SASW S-4.....	272
183. Shear-Wave Velocity Profile from SASW S-5.....	273
184. Shear-Wave Velocity Profile from SASW S-6.....	274
185. Shear-Wave Velocity Profile from SASW S-7.....	275
186. Shear-Wave Velocity Profile from SASW S-8.....	276
187. Shear-Wave Velocity Profile from SASW S-9.....	277
188. Shear-Wave Velocity Profile from SASW S-10.....	278
189. Shear-Wave Velocity Profile from SASW S-11.....	279
190. Shear-Wave Velocity Profile from SASW S-12.....	280
191. Shear-Wave Velocity Profiles from SASW R Measurements.....	281
192. Shear-Wave Velocity Profiles from SASW Measurements on Top of Yucca Mountain.....	282
193. Statistical Analyses of Shear-Wave Velocity Profiles from SASW Measurements on Top of Yucca Mountain.....	283
194. Shear-Wave Velocity Profiles from SASW Measurements Parallel to the Crest of Yucca Mountain.....	285
195. Shear-Wave Velocity Profiles from SASW Measurements Perpendicular to the Crest of Yucca Mountain.....	286
196. Comparison of Mean Shear-Wave Velocity Profiles from SASW Measurements Relative to the Orientation to the Crest of Yucca Mountain.....	287
197. Shear-Wave Velocity Profiles Off the Crest of Yucca Mountain.....	288
198. Shear-Wave Velocity Profiles from SASW D-1, D-2, and D-3.....	289
199. Shear-Wave Velocity Profiles from SASW D-4, D-5, and D-6.....	290
200. Shear-Wave Velocity Profiles from SASW D-7 and S-12.....	291

FIGURES (Continued)

	Page
201. Experimental Dispersion Curve Recorded at D-11 showing the Variability in Surface Wave Velocity at Shallow Depths	292
202. Boreholes on or Near the Crest of Yucca Mountain Where Downhole Velocity and VSP Measurements Were Performed.....	294
203. UZ-N27 Shear-Wave Velocities from Downhole Measurements and Generalized Lithology	298
204. UZ-N33 Shear-Wave Velocities from Downhole Measurements and Generalized Lithology	299
205. UZ-N46 Shear-Wave Velocities from Downhole Measurements and Generalized Lithology	300
206. UZ-N64 Shear-Wave Velocities from Downhole Measurements and Generalized Lithology	301
207. UZ-N66 Shear-Wave Velocities from Downhole Measurements and Generalized Lithology	302
208. UZ-N71 Shear-Wave Velocities from Downhole Measurements and Generalized Lithology	303
209. UZ-N75 Shear-Wave Velocities from Downhole Measurements and Generalized Lithology	304
210. UZ-N94 Shear-Wave Velocities from Downhole Measurements and Generalized Lithology	305
211. Shear-Wave Velocities from Downhole Measurements at Crest of Yucca Mountain.....	306
212. Statistical Analyses of Shear-Wave Velocities from Downhole Measurements at Crest of Yucca Mountain	307
213. Location of Fran Ridge Borrow Samples.....	309
214. Particle-Size Distributions – Fran Ridge Borrow Area Composite Sample.....	311
215. Compaction Test Results – Fran Ridge Borrow Area Composite Sample.....	312
216. Results of Isotropically Consolidated Drained Triaxial Compression Tests - Fran Ridge Borrow Area Composite Sample	315
217. Mohr Circles at Peak Deviator Stress for Isotropically Consolidated Drained Triaxial Compression Tests - Fran Ridge Borrow Area Composite Sample	316
218. Variation in Small-Strain Shear Modulus with Isotropic Confining Pressure of Reconstituted Specimens from the Fran Ridge Borrow Area	319
219. Variation in Small-Strain Material Damping Ratio with Isotropic Confining Pressure of Reconstituted Specimens from the Fran Ridge Borrow Area	320
220. Variation in Shear Modulus with Shearing Strain of Reconstituted Specimens from the Fran Ridge Borrow Area	321
221. Variation in Normalized Shear Modulus with Shearing Strain of Reconstituted Specimens from the Fran Ridge Borrow Area	322
222. Variation in Material Damping Ratio with Shearing Strain of Reconstituted Specimens from the Fran Ridge Borrow Area	323
223. Generalized Geologic Map of the WHB Area, including Exile Hill.....	325
224. Locations of Cross Sections and Interpreted Faults through the WHB Area.....	327
225. WHB Area Geologic Cross Section A-A', Looking South.....	328

FIGURES (Continued)

	Page
226. WHB Area Geologic Cross Section B-B', Looking West	329
227. WHB Area Geologic Cross Section C-C', Looking West	330
228. WHB Area Geologic Cross Section D-D', Looking South.....	331
229. WHB Area Geologic Cross Section E-E', Looking South.....	332
230. WHB Area Geologic Cross Section F-F', Looking West	333
231. WHB Area Geologic Cross Section G-G', Looking Northwest.....	334
232. Elevation Contours for Top-of-Bedrock	335
233. Generalized Lithostratigraphic Column Showing the Stratigraphic Interval Considered in this Scientific Analysis.....	337
234. Amplification Ratio Comparing Shear-Wave Velocity from Downhole and Suspension Logging Surveys	351
235. Comparison of Density from gamma-gamma Surveys, RCTS tests and Previous Laboratory Data.....	367
236. Total Density of Alluvium	369

INTENTIONALLY LEFT BLANK

TABLES

		Page
1.	Computer Software Used for This Scientific Analysis.....	26
2.	Summary of Input Data Used in This Scientific Analysis.....	27
3.	WHB Area Borehole Locations, Total Depth and Drilling Method.....	37
4.	WHB Area Boreholes with Contact Depths and Total Depths in Feet.....	38
5.	Revised Contact Depths and Total Depths in Feet in Borehole RF#13.....	39
6.	Summary of In-Place Density Tests and Relative Density.....	40
7.	Boreholes Used for Downhole Surveys at WHB Area.....	42
8.	WHB Area Downhole Shear-Wave Velocities.....	48
9.	WHB Area Downhole Compression-Wave Velocities.....	51
10.	Poisson's Ratios from Downhole Measurements in the WHB Area.....	80
11.	Extent of Suspension Seismic Logging in 2000.....	87
12.	Statistical Summary of Density Measurements by Lithostratigraphic Unit.....	165
13.	Summary of Laboratory Tests on Material Excavated for In-Situ Density Tests.....	172
14.	Initial Properties of Intact Tuff Specimens with a Dry Unit Weight Between 133 pcf and 147 pcf from WHB Boreholes (Group 1).....	191
15.	Initial Properties of Intact Tuff Specimens with a Dry Unit Weight between 117 pcf and 132 pcf from WHB Boreholes (Group 2).....	191
16.	Initial Properties of Intact Tuff Specimens with a Dry Unit Weight between 78 pcf and 94 pcf from WHB Boreholes (Group 3).....	192
17.	Initial Properties of Reconstituted Alluvial Specimen.....	196
18.	Confining Pressures at Which RCTS Tests were Performed on Intact Tuff and Reconstituted Qal Specimens from WHB Boreholes.....	196
19.	Fixed-Free, Small-Strain RCTS Test Results of Group 1 Intact Tuff Specimens at Estimated In-Situ Stress State.....	197
20.	Fixed-Free, Small-Strain RCTS Test Results of Group 2 Intact Tuff Specimens at Estimated In-Situ Stress State.....	198
21.	Fixed-Free, Small-Strain RCTS Test Results of Group 3 Intact Tuff Specimens at Estimated In-Situ Stress State.....	198
22.	Fixed-Free, Small-Strain RCTS Test Results of Reconstituted Quaternary Alluvial Specimen.....	198
23.	Initial Properties of Intact Tuff Specimens from the ESF.....	239
24.	Confining Pressures at which RCTS Tests Were Performed on the Intact Tuff Specimens from the ESF.....	239
25.	Boreholes Used for Downhole Surveys at Crest of Yucca Mountain.....	293
26.	Downhole Shear-Wave Velocities at Crest of Yucca Mountain.....	297
27.	Tests Performed in Denver, CO, on a Composite Sample of Fran Ridge Materials.....	310
28.	Summary of Isotropically Consolidated, Drained Triaxial Compression Tests Performed on Laboratory-Compacted Specimens of the Fran Ridge Borrow Area Composite Sample.....	314
29.	Initial Properties of Reconstituted Specimens of the Fran Ridge Borrow Material.....	318
30.	Confining Pressures at which RCTS Tests Were Performed on the Fran Ridge Borrow Material.....	318
31.	Comparison of Downhole Seismic, Suspension Seismic and SASW Methods.....	344

TABLES (Continued)

	Page
32. Seismic Methods Used at EPRI Comparison Sites	345
33. Depths in Feet to Tops of Selected Lithostratigraphic Units by Borehole	361
34. Statistics by Lithostratigraphic Unit	363
35. Porosity, Void Ratio, and Saturation Water Content by Lithostratigraphic Unit	365
36. Moist and Dry Density Results for Borehole RF#13	365

ACRONYMS, ABBREVIATIONS AND SYMBOLS

ACC	Accession Number
API	American Petroleum Institute
ASTM	American Society for Testing and Materials
bgs	below ground surface
cm	centimeter, centimeters
CRWMS	Civilian Radioactive Waste Management System
DTN	Data Tracking Number
Eq.	equation
ESF	Exploratory Studies Facility
f	frequency in Hertz (cycles per sec)
ft	foot, feet (unit of measurement)
ft/s	feet per second
ft/sec	feet per second
g	gram, grams
g/cm^3	grams per cubic centimeter
GM	silty gravel or silty gravel with sand
G_{max}	low-strain (maximum) shear modulus
GP	poorly graded gravel or poorly graded gravel with sand
GP-GM	poorly graded gravel with silt or poorly graded gravel with silt and sand
GR	gamma ray
GW	well-graded gravel or well-graded gravel with sand
GW-GM	well-graded gravel with silt or well-graded gravel with silt and sand
Hz	hertz
in.	inch
kPa	kilopascals (i.e., thousand newtons per square meter, or about 20.886 lbs/ft ²)
ksf	kips-force per square foot
lbs	pounds (either pounds-force or pounds-mass)
lbs/ft ²	pounds-force per square foot
lb/ft ³	pounds-force per cubic foot
lbm/ft ³	pounds-mass per cubic foot
lbs/ft ³	pounds per cubic foot (either pounds-force or pounds-mass)
M&O	Management and Operating Contractor
MPa	megapascal (i.e., million newtons per square meter, or about 20,886 lbs/ft ²)
ms	millisecond
msec	millisecond

ACRONYMS, ABBREVIATIONS AND SYMBOLS (Continued)

pcf	pounds per cubic foot (either pounds-force or pounds-mass)
pp	pages
psi	pounds-force per square inch
“Q”	“quality”
QA	quality assurance
Qal	Quaternary alluvium
QAP	Quality Administrative Procedure
QTac	undifferentiated Quaternary/Tertiary alluvium and colluvium
RC	relative compaction
RC	resonant column
RCTS	resonant column and torsional shear
Rev	revision
RQD	Rock Quality Designator or Rock Quality Designation
s	second
SASW	spectral analysis of surface waves
sec	second
SM	silty sand or silty sand with gravel
SMF	Sample Management Facility
SP	poorly graded sand or poorly graded sand with gravel
SP-SM	poorly graded sand with silt or poorly graded sand with silt and gravel
SW	well-graded sand or well-graded sand with gravel
SW-SM	well-graded sand with silt or well-graded sand with silt and gravel
SSD	saturated surface dry
TIC	Technical Information Center
Tpc	Tiva Canyon Tuff
TDMS	Technical Data Management System
Tmbt1	pre-Rainier Mesa Tuff bedded tuff
Tmr	Rainier Mesa Tuff of the Timber Mountain Group
Tpbt4	pre-Tiva Canyon Tuff bedded tuff
Tpbt5	pre-Tuff unit “x” bedded tuffs (also known as post-Tiva Canyon Tuff bedded tuff)
Tpcpl1	Tiva Canyon Tuff: crystal-poor member, lower lithophysal zone
Tpcpln	Tiva Canyon Tuff: crystal-poor member, lower nonlithophysal zone
Tpcpmn	Tiva Canyon Tuff: crystal-poor member, middle nonlithophysal zone
Tpcpul	Tiva Canyon Tuff: crystal-poor member, upper lithophysal zone
Tpcpun	Tiva Canyon Tuff: crystal-poor member, upper non-lithophysal zone
Tpcpv	Tiva Canyon Tuff: crystal-poor member, vitric zone
Tpcpv1	Tiva Canyon Tuff: crystal-poor member, vitric zone, nonwelded to partially welded subzone
Tpcpv2	Tiva Canyon Tuff: crystal- poor member, vitric zone, moderately welded subzone
Tpcpv3	Tiva Canyon Tuff: crystal- poor member, vitric zone, densely welded subzone

ACRONYMS, ABBREVIATIONS AND SYMBOLS (Continued)

Tpcr	Strictly, the Tiva Canyon Tuff: crystal-rich member
Tpcrl	Strictly, the Tiva Canyon Tuff: crystal-rich member, lithophysal zone
Tpcrn	Strictly, the Tiva Canyon Tuff: crystal-rich member, nonlithophysal zone, but in this report it includes Tpcrv, Tpcrl, and Tpcrn and is synonymous with Tpcr
Tpcrv	Tiva Canyon Tuff: crystal-rich member, vitric zone
Tpcrv1	Tiva Canyon Tuff: crystal-rich member, vitric zone, vitrophyre subzone
Tpcrv2	Tiva Canyon Tuff: crystal-rich member, vitric zone, moderately welded subzone
Tpcrv3	Tiva Canyon Tuff: crystal-rich member, vitric zone, non to partially welded subzone
Tpki	Tuff unit "x"
TS	torsional shear
U.S.	United States
USBR	U.S. Bureau of Reclamation
USCS	Unified Soil Classification System
USGS	U.S. Geological Survey
UTA	University of Texas, Austin
UTACED	University of Texas at Austin, Civil Engineering Department
VSP	vertical seismic profiling
v_p	compression-wave seismic velocity
V_R	Raleigh-wave phase velocity
vs.	versus
v_s	shear-wave seismic velocity
WHB	Waste Handling Building
YMP	Yucca Mountain Site Characterization Project

INTENTIONALLY LEFT BLANK

1. PURPOSE

1.1 PURPOSE

The purpose of this scientific analysis is to compile and provide basic interpretation of data acquired during 2000 and 2001 for use in evaluating ground motions for the Yucca Mountain Site Characterization Project (YMP) and in developing recommendations for foundations for a proposed Waste Handling Building (WHB) at the North Portal. This scientific analysis has been prepared under *Technical Work Plan for: Testing and Monitoring*, TWP-MGR-MD-000018 (BSC 2001).

This scientific analysis documents the acquisition of geological, geophysical, and geotechnical data to support engineering calculations for a potential Waste Handling Building and ground motion analyses for the repository. It also documents basic interpretations of the acquired data and presents a geologic interpretation with seven cross sections based on both the data reported herein and previously acquired data.

This work supports work package P4D1226TH2 “Surface Facility Characterization,” the planning for which is documented in TWP-MGR-MD-000018 (BSC 2001). This scientific analysis supports the task of preparing a report that summarizes the acquisition of geological, geophysical, and geotechnical data for use in evaluating ground motions and in developing recommendations for foundations for the WHB. This task was accomplished by compiling the relevant data acquired or developed for evaluating ground motions and/or for developing recommendations for the WHB foundations, compiling other data from previous investigations that could be useful for these purposes, and performing some basic comparisons of the shear-wave velocity, compression-wave velocity, Poisson’s ratio, and total density data when data were available from more than one method or source.

1.2 LIMITATIONS

This scientific analysis is intended to characterize the WHB Area to a level suitable to support License Application (see Section 5 for the definition and extent of the WHB Area). The locations of individual structures and the site grading plan were unknown at the time the work described herein was performed. The data in this scientific analysis provide a general characterization of the site subsurface conditions and of the potential engineered fill material to support License Application. When the locations of individual structures and the site grading plan become known, the data and interpretations in this report should be reviewed to evaluate whether any changes are required.

With regards to the development of seismic design ground motions, there are areas within the WHB Area and the currently proposed emplacement area where no velocity measurements have been made. This lack of sampling, however, can be adequately accounted for by incorporating a greater degree of variability in the velocity profiles used in the ground motion calculations. In particular, there are areas outside of the existing pad in the northern part of the WHB Area where no measurements were taken based on the assumption that all structures would be sited in the current pad area. Once the locations of individual structures are finalized, some confirmatory shallow boreholes and velocity measurements may be required.

At the time the field investigations were being carried out, the size and areal extent of the proposed emplacement area was being re-evaluated. The emplacement area may be larger in size and extend farther to the north and east (Board et al. 2002, Figure 3-1) than does the area investigated and described in this report. Thus, the velocity data collected to date do not sample some of these areas. Also, velocity surveys were limited in their depth penetration beneath the crest of Yucca Mountain. Measurements are lacking in the depth range of about 700 to 1000 feet.

Finally, the dynamic laboratory measurements of material properties were limited to strains of about 0.1% in this study due to equipment limitations and because the emphasis was placed on the preclosure seismic design (hazard levels defined at annual exceedance probabilities of 10^{-3} and 10^{-4}). The strains associated with ground motions at annual exceedance probabilities of 10^{-6} or lower for postclosure performance assessment may approach 1%, and data are lacking at these higher strains.

2. QUALITY ASSURANCE

The activities documented in this scientific analysis were evaluated in accordance with procedure AP-2.21Q, *Quality Determinations and Planning for Scientific, Engineering, and Regulatory Compliance Activities*, and they were determined to be subject to the Yucca Mountain quality assurance program. This evaluation is documented in the technical work plan (BSC 2001, Attachment I).

The control of the electronic management of data for this document included:

- Backing-up on tape of all project electronic files twice daily, with tapes being sent every Wednesday to an offsite storage location.
- All electronic data transfers were checked for alteration using a file-size comparison, using a zip file format, using a Project-approved file comparison software (signature generation and compare routine), or visually comparing the electronic file with a printed copy from the Technical Data Management System (TDMS).
- Write-protecting files before including them in a scientific notebook or other permanent record.
- Backing-up of all unique physical records and storing the backup in a dual location.
- Saving any intermediate analysis records required to understand how acquired data were processed/analyzed.

This scientific analysis does not directly impact engineering, construction, or operational tasks associated with the Q-list items and as discussed in AP-2.22Q, *Classification Criteria and Maintenance of the Monitored Geologic Repository Q-List*. It does provide data and analyses pertinent to the subsequent design of the waste handling facilities and emplacement drifts, which are classified as Quality Level 1, and other safety-related structures, systems, and components. This scientific analysis does not report on natural barriers that are included in the Q-List (YMP 2001) as items important to waste isolation.

3. USE OF SOFTWARE

The computer programs used in developing the parameter values in this scientific analysis are listed in Table 1:

Table 1. Computer Software Used for This Scientific Analysis

Software Name	Software Tracking No.	Computer Type
Microsoft Word, ver. 97 SR-2 and 2000	Exempted by Section 2.1.1 of AP-SI.1Q*	IBM PC-compatible
Microsoft Excel, ver. 97 SR-2 and 2000	Exempted by Section 2.1.1 of AP-SI.1Q	IBM PC-compatible
AutoCAD, version Release 14	Exempted by Section 2.1.2 of AP-SI.1Q	IBM PC-compatible
CorelDraw version 10	Exempted by Section 2.1.2 of AP-SI.1Q	IBM PC-compatible
Adobe Acrobat versions 4 and 5	Exempted by Section 2.1.2 of AP-SI.1Q	IBM PC-compatible
gINT, version 4.16	Used solely for graphic representation	IBM PC-compatible
Grapher versions 2.02 and 3.02	Used solely for graphic representation	IBM PC-compatible
WinSASW, version 1.23	10588-1.23-00	IBM PC-compatible
RCTEST, version 2.1	Integral to testing equipment/not modified	IBM PC-compatible
TSTEST, version 3.1	Integral to testing equipment/not modified	IBM PC-compatible

* AP-SI.1Q, *Software Management*

In accordance with Section 2.1.1 of AP-SI.1Q, Microsoft Word versions 97 SR-2 and 2000 and Microsoft Excel versions 97 SR-2 and 2000 are exempted software products.

In accordance with Section 2.1.2 of AP-SI.1Q, AutoCAD version Release 14, CorelDraw version 10, and Adobe Acrobat versions 4 and 5 are exempted software products.

WinSASW version 1.23 was used in accordance with AP-SI.1Q. The program was obtained from Configuration Management, was appropriate for its intended use, and was used only within its range of validation. The program was run on a Dell Dimension Desktop or a Dell Latitude Laptop Computer with a Windows 98 operating system. The computers are located at the Geoengineering Department in Austin, Texas. Inputs were collected with a .dat extension and produced files with .exd, .prf, and .thd extensions (experimental dispersion curves, final shear wave velocity profile records, and theoretical dispersion curves). An electronic copy of all data is included in Scientific Notebook SN-M&O-SCI-040-V1 (Wong 2002a, Appendix 38). The outputs are shown in Figures 50-98, 145-151, 157, 160-201, and in Attachments IX, XIII, and XV.

RCTEST version 2.1 and TSTEST version 3.1, referred to in Section 6.2.10.2, are integral to the measuring and testing equipment and are also exempted software, per Section 2.1.4 of AP-SI.1Q.

4. INPUTS

4.1 DATA AND PARAMETERS

The input data used and considered in this scientific analysis are summarized in Table 2. The Q-status of each of these inputs is provided in the electronic Document Input Reference System.

Table 2. Summary of Input Data Used in This Scientific Analysis

Description	DTN or Reference
Survey data	
Locations of Test Pits TP-WHB-1 to -4	MO0012GSC00405.000
Ground survey elevations along Sections A-A' to F-F'	MO0008GSC00286.000
Point features of YMP boreholes	MO0101COV00396.000*
Fran Ridge Borrow Area – survey locations for samples	MO0112GSC01170.000
Data related to boreholes and test pits in the WHB Area that were acquired as part of the current work	
Sample Management Facility logs of boreholes RF#14 through RF#26, RF#28, and RF#29	MO0101SEPBLOG.000
Logs of boreholes RF#13 through RF#26, RF#28, and RF#29	GS020383114233.003
Logs and photographic maps of Test Pits TP-WHB-1 to TP-WHB-4	GS020383114233.001
Data related to geophysical surveys in the WHB Area that were acquired/developed as part of the current work	
Downhole seismic v_s and v_p profiles, RF#13 (1998 survey)	MO020498DNHOLE.000
Downhole seismic v_s and v_p profiles, RF#13 to #16, #18 to 26, #28, #29	MO0111DVDWHBSC.001
Downhole seismic time picks, RF#13 to #16, #18 to 26, #28, #29	MO0202WHBTMPKS.000
Downhole seismic v_s and v_p profiles, RF#13 and #17	MO0110DVBBOREH.000
Downhole seismic interpreted travel times, RF#13 and #17	MO0202DWAVEATD.000
Suspension seismic data, RF#13 (1998 survey)	MO0204SEISDWHB.001
Suspension seismic data, RF#14 to #26, #28, #29	MO0204SEPBSWHB.001
v_s , v_p and Poisson's ratio profiles from suspension seismic surveys at boreholes RF#14 to #26, #28 and #29	MO0204SEPFDSSS.000
v_s profiles from a suspension seismic survey at borehole RF#13	MO0204SEPSWSSS.000
v_s profiles for SASW lines SASW-1 to SASW-37	MO0110SASWWHBS.000
Borehole geophysical data (caliper, gamma-gamma density)	MO0112GPLOGWHB.001
Statistical analysis of gamma-gamma density by lithostratigraphic unit	MO0204SEPGAMDM.000
Statistics for v_s , v_p , and Poisson's ratio from suspension seismic surveys by depth interval	MO02045FTDSUSP.001
Statistics for bulk density values for bedrock units	MO0204DENBROCK.000
Plots of average shear-wave velocity versus depth and quarter-wavelength amplification ratio versus frequency at boreholes UE-25 RF#14 to UE-25 RF#19 and UE-25 RF#29	MO0205SWDQRTWF.000
Profiles of Poisson's ratio from downhole seismic surveys	MO0205SEPPRDSV.000
Statistics for v_s , v_p and Poisson's ratio from suspension seismic surveys by lithostratigraphic unit	MO0204SUSPSEIS.001

Table 2. Summary of Input Data Used in This Scientific Analysis (continued)

Description	DTN or ACC
Data related to laboratory testing of samples from the WHB Area that were acquired/developed as part of the current work	
Results of static laboratory tests on Fran Ridge composite sample	MO0203EBSCTCTS.016
Results of static laboratory tests on Fran Ridge composite sample	MO0206EBSFRBLT.018*
Results of static laboratory tests on WHB test pit samples	GS020483114233.004, GS020783114233.005
Results of dynamic laboratory tests on core and reconstituted alluvium samples from WHB Area and on Fran Ridge composite sample	MO0203DHRSSWHB.001
Data that were acquired/developed as part of the current work but are not related geographically to the WHB Area	
Downhole seismic v_s and v_p profiles at crest of Yucca Mountain	MO0202DVDWHBSC.002
v_s profiles for SASW lines S-1 to S-12 and D-1 to D-12 (includes one line near the WHB Area)	MO0110SASWVDYM.000
v_s profiles for SASW lines C-1 to C-7 from the top of Yucca Mountain	MO0203SEPSASWD.000
v_s profiles for SASW lines R-1 to R-3 (rock sites on Yucca Mountain) and T-1 to T-5 (in the ESF)	MO0206SASWROCK.000
Results of dynamic laboratory tests on core	MO0203DHRSSWHB.001
Data that were not acquired/developed as part of the current work	
Stratigraphic nomenclature	Buesch et al. 1996*
Strikes and dips of contacts - geologic map of the Drainage Channel and North Portal	GS940408314224.004
Bedrock Geologic Map of the Yucca Mountain Area	GS980608314221.002
Depths of lithostratigraphic contacts in borehole UE-25 NRG#2 , #2a, #2b, and #3 and USW NRG-6	GS940308314211.009
Depths of lithostratigraphic contacts in borehole USW NRG-7/7A	GS940708314211.032
Depths of lithostratigraphic contacts in borehole USW SD-9	GS941108314211.052
Depths of lithostratigraphic contacts in borehole USW SD-12	GS940908314211.045
Depths of lithostratigraphic contacts in borehole UE-25 UZ-N27	GS940208314211.004
Depths of lithostratigraphic contacts in borehole UE-25 UZ-N33	GS940208314211.006
Depths of lithostratigraphic contacts in borehole UE-25 UZ-N64	Craig (1997)*
Graphical Lithologic Log of Borehole UE-25-RF#3	GS931008314211.036
Logs of boreholes UE-25 RF-#3b, #9, #10, and #11	SNSAND90249100.000 (See Assumption 6)
Downhole seismic v_s and v_p arrival times, RF#13 (1998 survey)	MO0001SEPRADSD.000
In-place ring density data for alluvium	GS920983114220.001
In-place density data for alluvium from drive-tube samples - RF#3b	SNSAND85081500.000*
In-place density data for alluvium from sand cone and nuclear methods in Test Pit SFS-3	Ho et al. 1986*
Results of dynamic laboratory tests on samples from borehole RF#13	MO9905LABDYNRS.000
Laboratory test results from NRG and SD boreholes	SNL02030193001.001 to .024, .026 & .027, SNL01A05059301.005
Groundwater elevations	GS000508312332.001
Velocity profile used in previous analysis	MO98PRECLOSURE.000*
Data developed from previous data	
Mean values of rock properties by lithostratigraphic unit	MO0204SEPSOILP.000
Statistical summary of rock properties by lithostratigraphic unit	MO0202GEOSOILP.000

Note: v_s means shear-wave seismic velocity and v_p means compression-wave seismic velocity.

* indicates the reference was used for corroboration or reference purposes only.

Many of these data sets were acquired or developed to support the geotechnical investigation for the WHB or the ground motion analyses for the YMP. Such data sets that were acquired or developed for this work are deemed appropriate for the purposes of this scientific analysis. Some data sets that were used were the product of previous work. The investigators used the data that were known to them and that were judged to be appropriate and applicable to the analyses of the geotechnical character of soils and bedrock in the WHB Area.

4.2 CRITERIA

This report complies with Subparts of 10 CFR 63 pertaining to the characterization of the Yucca Mountain site (Subpart B, Section 63.15) and the compilation of information regarding materials of construction of the geologic repository operations area, in support of the License Application (Section 63.21 [c][2]).

4.3 CODES AND STANDARDS

No codes or standards were used in the analyses developed in this report.

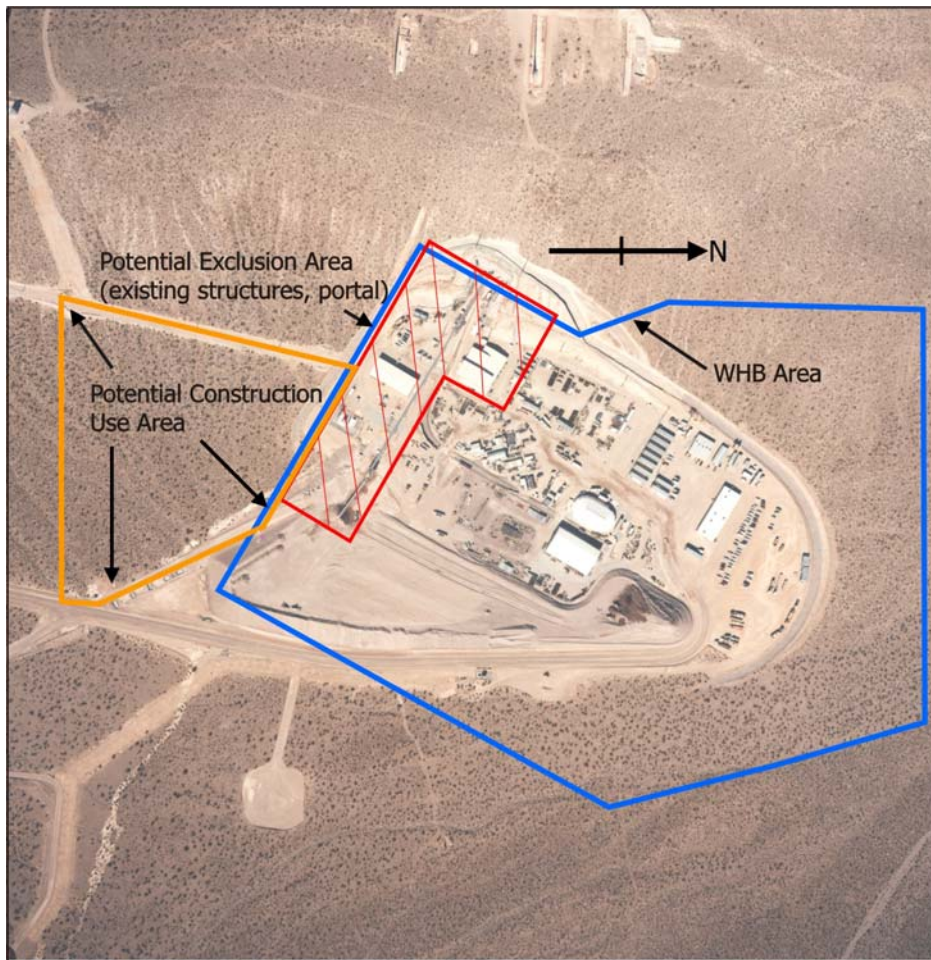
5. ASSUMPTIONS

The following assumptions have been used in this scientific analysis. The assumptions do not need further confirmation for the Analysis presented herein, unless specifically addressed below.

1. Throughout this scientific analysis it is assumed that the WHB will be located within the area bounded by the blue heptagon on Figure 1. This area is referred to in this scientific analysis as the **WHB Area**. This assumption is consistent with the summary of the site layout contained in the *Monitored Geologic Repository Site Layout System Description Document* (CRWMS M&O 1999a).
2. In Section 6.6 of this scientific analysis, the geologic interpretations of subsurface conditions are based on data collected from the WHB area, but some interpretations are guided by lithostratigraphic and structural bounding conditions from outside the WHB area. These bounding conditions include trends in the thickness of lithostratigraphic units, general orientation (strike and dip) of lithostratigraphic units, and the type of faults. The main assumptions are that (1) the thickness of lithostratigraphic units remain relatively constant (or vary systematically) across the WHB area, (2) the lithostratigraphic sequence is northeast striking and southeast dipping, and (3) the lithostratigraphic sequence has been structurally disrupted by northerly trending, steeply dipping, (mostly) normal faults. These assumptions reflect the findings provided in previous borehole log reports (Geslin et al., 1995) and reports and maps summarizing the geology in the area and along the north ramp (Buesch et al., 1994; Beason et al., 1996; Barr et al., 1996; Day et al., 1998).
3. The proposed emplacement area shown on Figure 157 represents the base case repository layout that was considered as part of site recommendation evaluations (DOE 2001, Section 2.3.1.1). This layout accommodates 70,000 metric tonnes of heavy metal under a higher-temperature operating mode. This footprint was assumed to be the area to be evaluated and thus was the focus of geotechnical investigations to characterize the emplacement block. More recently, ideas concerning the repository layout have evolved with the objectives of reducing uncertainties in a License Application and supporting a flexible design with respect to repository temperature, waste types, and receipt rates (Board et al. 2002, p. vii). Board et al. (2002, Figure 4-5 and 5-4) suggest a repository footprint that includes much of the base case footprint used for site recommendation evaluations and changes the footprint to include area to the east. The geotechnical investigations described in this report provide only a sparse coverage of the eastern, lower block component of the new suggested footprint.
4. It is assumed that the alluvium logged in borehole UE-25 RF#21 between about 70 and 115 feet (DTN: GS020383114233.003) is in fact bedrock. The unit weight of the alluvium measured by the gamma-gamma survey between depths of about 70 and 115 feet below ground surface (bgs) in borehole UE-25 RF#21 is anomalously low (compare densities of the alluvium below 70 feet in RF#21 on Figure 101 with the typical density of alluvium on Figure 101 and in Table 12). This low density could be explained by misidentification of the fine drill cuttings from borehole UE-25 RF#21, which was not otherwise sampled. In addition, an examination of the cross-section on Figure 232 supports a 70 foot bedrock depth. For this scientific analysis it is assumed that the drill cuttings in borehole UE-25 RF#21 were

misidentified and that the material from about 70 to 115 feet below ground surface is actually bedrock. This assumption is used in Section 6.6.

5. Calculation of the quarter-wavelength amplification ratio for suspension results (Section 6.7.2) requires making an assumption about the part of the profile above the shallowest data. In this report, the suspension profile is assumed to be the same as the downhole profile at shallow depths where there are no suspension data. This assumption is considered reasonable given that both methods are measuring the shear-wave velocity of the subsurface materials and have been found to give reasonably similar results (Section 6.7.1). This assumption causes the ratio to equal unity at the highest frequency (shallowest depth). The quarter-wavelength amplification ratio is used only as one means of understanding the results from various sources and as such this assumption does not require verification.



Note: Base photograph is YMP Photograph #BN8811_50

Figure 1. Definition of WHB Area

6. It is assumed that the locations of boreholes UE-25 RF#3, #9, #10, and #11, provided in DTN: MO0101COV00396.000, are sufficiently accurate for this report. It is also assumed that the geologic contacts for the boreholes RF#9, #10, and #11, provided in DTN: SNSAND90249100.000, are also sufficiently accurate for this report. The thickness

and sequence of the lithostratigraphic units identified in the boreholes are consistent with those observed in more recent boreholes described in Attachment I. The boreholes, used in Section 6.6, only have to be approximately located to support the conclusions in this report.

6. SCIENTIFIC ANALYSIS DISCUSSION

6.1 OVERVIEW

Section 6 presents data that were acquired and parameters that were developed for use in preliminary geotechnical analyses for the WHB and in ground motion analyses for the WHB and the repository. Field and geotechnical laboratory data were acquired for three distinct geographic areas: the WHB Area (as defined in Section 5), the North Ramp of the Exploratory Studies Facility (ESF), and the crest of Yucca Mountain. In addition, geotechnical laboratory data were acquired for a composite sample of material from the Fran Ridge Borrow Area.

Data that were acquired in 2000 and 2001 within the WHB Area are summarized in Section 6.2 and consist of:

- Geologic data from fifteen new boreholes. The new boreholes are designated UE-25 RF#14 through UE-25 RF#29^{1,2}.
- Shear-wave and compression-wave arrival times from downhole seismic surveys at boreholes RF#14 through RF#29.
- Shear wave-and compression-wave arrival times from downhole seismic surveys at existing borehole RF#13.
- Shear-wave and compression-wave travel times from suspension seismic surveys at boreholes RF#14 through RF#29.
- Caliper and gamma-gamma wireline surveys in boreholes RF#16, RF#18, RF#20, RF#21, RF#22, RF#24, and RF#28.
- Shear-wave velocity profiles from spectral analysis of surface waves (SASW) surveys SASW-1 to SASW-36 and D-12.
- Geologic data, photographs and in-place density measurements in the alluvium encountered in test pits TP-WHB-1 to TP-WHB-4.
- Maximum density, minimum density, specific gravity, particle-size distribution, in-place density, natural water content, and relative density corresponding to in-place density tests that were performed in test pits.

¹ The new boreholes were all advanced in Area UE-25 of the Nevada Test Site. For brevity, the UE-25 preface will be omitted in this report. The UE-25 preface will also be omitted from existing boreholes UE-25 RF#3, #9, #10, #11 and #13.

² Note that Borehole RF#27 was abandoned after setting a surface casing in favor of advancing a borehole at a different location, which is designated RF#29. Thus, when reference is made to RF#13 through RF#29 or RF#14 through RF#29, the reader should recall that there will be no data associated with RF#27.

- Resonant column and torsional shear (RCTS) test results for samples of tuff, alluvium and engineered fill (includes density; water content; shear-wave velocity, and shear modulus and material damping ratio as a function of shear strain and confining pressure).

Data that were acquired in 2000 and 2001 along the North Ramp and Main Drift of the ESF are summarized in Section 6.3 and consist of:

- Shear-wave velocity profiles from SASW surveys T-1 to T-5.
- RCTS test results for samples of bedrock taken in the ESF North Ramp.
- Crosshole seismic surveys were attempted but did not yield useable results (Wong 2001, page 19).

Data that were acquired in 2000 and 2001 at or near the crest of Yucca Mountain are summarized in Section 6.4 and consist of:

- SASW surveys C-1 to C-7, S-1 to S-12, D-1 to D-11, and R-1 to R-3.
- Downhole seismic surveys using existing boreholes.

Geotechnical laboratory data that were acquired in 2000 and 2001 on a composite sample from the Fran Ridge Borrow Area are summarized in Section 6.5 and consist of:

- Maximum and minimum density
- Compaction characteristics (maximum dry density and optimum water content)
- Specific gravity
- Particle-size distribution
- Static drained shear strength
- RCTS test results (includes same types of data as for WHB Area test).

The remainder of Section 6 presents analysis and discussions of the data as follows:

- Section 6.6 - Geologic conditions at the WHB Area
- Section 6.7 - Evaluation of seismic velocity data
- Section 6.8 - Previous data.

6.2 DATA ACQUIRED AT WHB AREA

6.2.1 Overview

Section 6.2 summarizes the results of the explorations and tests performed in 2000 and 2001 in the WHB Area for the WHB. The type of exploration or test and the scientific analysis section where the results are presented are as follows:

- 6.2.2 - Boreholes RF#14 through RF#29
- 6.2.3 - Revision of RF#13 borehole log
- 6.2.4 - Test pits TP-WHB-1 through TP-WHB-4
- 6.2.5 - Downhole seismic surveys in boreholes RF#13 through RF#29
- 6.2.6 - Suspension seismic surveys in boreholes RF#13 through RF#29

- 6.2.7 - SASW surveys SASW-1 through SASW-37 and D-12
- 6.2.8 - Borehole caliper and gamma-gamma in boreholes RF#16, 18, 20, 21, 22, 24, 28
- 6.2.9 - Geotechnical laboratory static testing
- 6.2.10 - Geotechnical laboratory dynamic testing.

6.2.2 Boreholes

Exploratory drilling in the WHB Area began in June 2000 and concluded in November 2000 at the locations shown on Figure 2. The drilling program was developed to gain an understanding of the subsurface geologic conditions and provide access for downhole geophysical methods. Fifteen new boreholes were drilled, seven “deep” boreholes and eight “shallow” boreholes. The borehole depths were selected with the objective that deep boreholes would extend 100 feet into bedrock with a shear-wave velocity of at least 5,000 ft/s and shallow boreholes would extend 50 feet into the densely welded Tiva Canyon Tuff. Because the shear-wave velocity in the deep boreholes would not be known until after the holes had been drilled and cased, the depths at which 5,000 ft/s rock would be found in each borehole were estimated based on the downhole results from borehole RF#13 as about 20 to 30 feet into the Tiva Canyon Tuff crystal-poor middle nonlithophysal zone (Tpcpmn).

Of the seven deep boreholes, four were advanced by continuous PQ (3.35 inch) and HQ (2.5 inch) diamond-bit core from the ground surface. The other three deep boreholes and the eight shallow boreholes were advanced by the mud-rotary method. Geologic data acquired in the boreholes included depth bgs of lithostratigraphic subunit contacts; depth bgs and dip of faults and other structural features; rock hardness, welding, and fracture density; percent core recovery, and Rock Quality Designation (RQD). Refer to Table 3 for specific locations and depths of these borings and to Table 4 for lithostratigraphic contacts. Detailed geologic borehole logs are included in Attachment I.

Given the difficulty of collecting useful information regarding geotechnical properties in alluvial material with a significant gravel and cobble content, it was elected to core through the alluvium in the four core boreholes. This method allowed collection of representative, though disturbed, samples of the alluvium and a better understanding of the nature of caliche cementation in the alluvial material. Due to budgetary constraints, the other boreholes could not be cored.

All fifteen boreholes were reamed to 8.5 inches in diameter (nominal) and cased with PVC to allow various geophysical surveys to be conducted. Refer to Section 6.2.5 through 6.2.7 for detailed descriptions of geophysical surveys and analysis. All boreholes are plotted on detailed geologic cross sections along with a discussion of the area’s geology in Section 6.6.2.

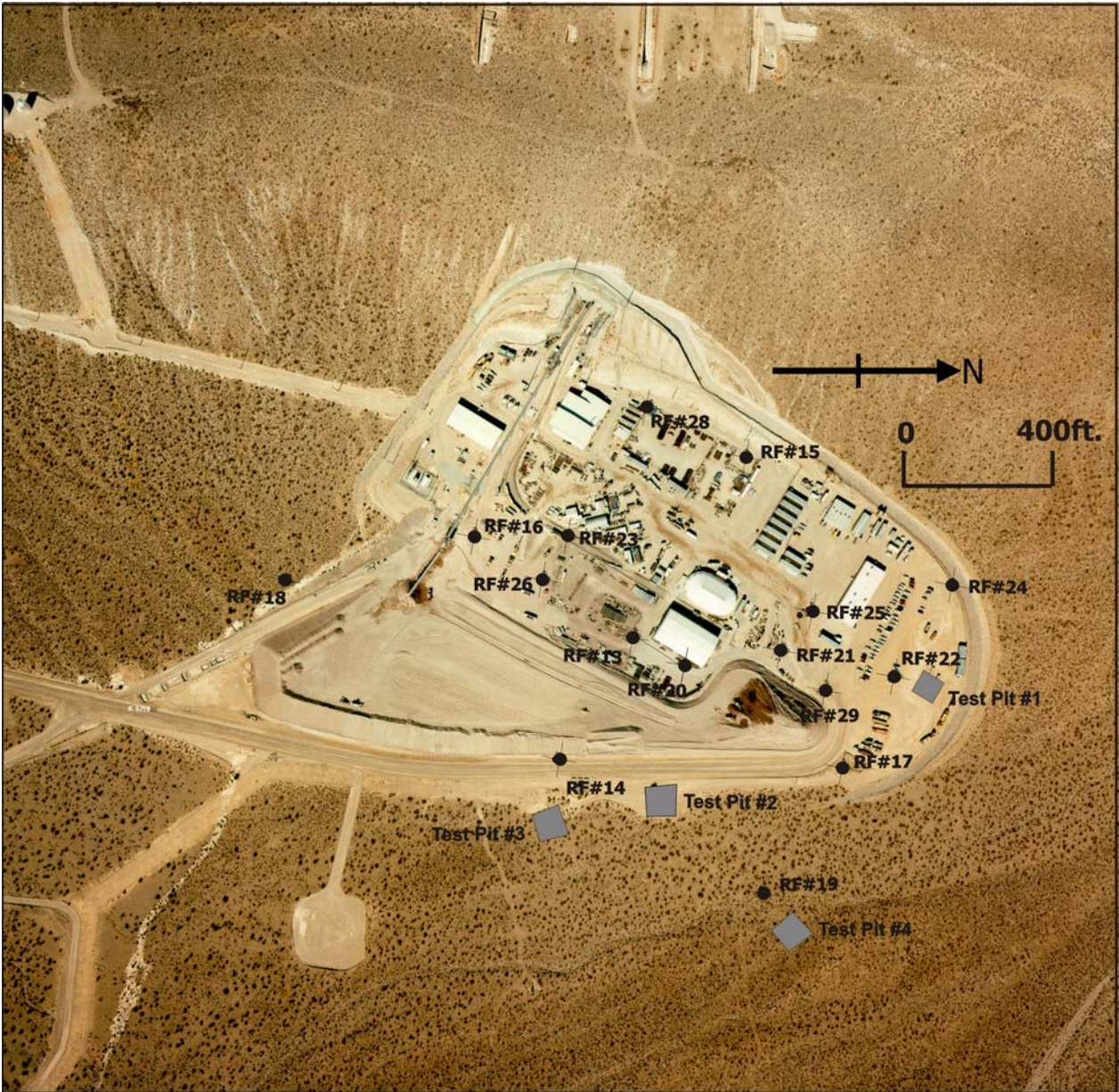
For the purposes of this report several factors noted on the borehole logs should be considered:

- The Miocene-age lithostratigraphic units penetrated by the boreholes in the WHB area include the section from the nonwelded tuffaceous pre-Rainer Mesa bedded tuffs (Tmbt1) to the crystal-poor, densely welded, crystallized, nonlithophysal zone of the Tiva Canyon Tuff (Tpcpln). The lithostratigraphic units in this section have distinctive characteristics (crystal, pumice, and lithic fragments (or clasts), grain size distributions, bedding characteristics, amount of welding and lithophysae, and type of crystallization)

that enable identification of the unit and the bounding contacts. The type of contacts include those formed from depositional, welding, and crystallization processes, and these contacts can be sharp or gradational. Sharp contacts such as depositional contacts in the bedded tuffs can be identified to 0.1 ft. Relatively sharp but gradational contacts such as the moderately to densely welded subzone contact in the crystal-rich Tiva Canyon Tuff (Tpcrv2-Tpcrv1) and the vitric to crystallized contact in the Tiva Canyon Tuff (Tpcrv1-Tpcrn) can be identified to 1 ft. For gradational contacts, even though the features are gradational across 3 to 10 ft, the criteria for identification of the contact typically permits identification within a few feet.

- The estimated accuracy of the lithostratigraphic contacts relative to the designated contact depth is plus or minus 1 ft in cored boreholes and plus or minus 5 ft in the mud-rotary boreholes. Overall, the uncertainty in the accuracy of lithostratigraphic contacts in a borehole is a function of the (1) type of contact (depositional, welding, or crystallization, and sharp versus gradational), (2) drilling and sample collection techniques, (3) availability and type of geophysical logs from the borehole, (4) amount of geophysical logs from that same interval in cored boreholes, and (5) previously collected information about the contact and the character of the lithostratigraphic unit on either side of the contact. In cored boreholes, a well-defined depositional contact can be identified to an accuracy of 0.1 foot, whereas a gradational contact can have an uncertainty of 3 to 10 feet. In cored boreholes, if some of the rock that is cored is not recovered, the uncertainty in the contact is proportional to the amount of nonrecovered core. For a mud-rotary borehole, the sample interval is 5 ft; therefore, the minimum accuracy is plus or minus 5 feet, even for sharp depositional contacts. Based on the drilling and sample collection technique, some contacts (especially gradational ones) are difficult to resolve to less than 30 ft; however, the uncertainty might be reduced to about 5 to 15 feet with geophysical logs from the borehole. The resolution of contacts can further be minimized with information available for the contact from nearby cored boreholes and use of the thickness trends for the units above and below the contact. After evaluating all the available information from the borehole, adjacent boreholes, and “regional” trends in thickness and structure of the lithostratigraphic units, the contacts listed in table 4 have typical accuracy of plus or minus 5 ft.
- The densely welded pyroclastic flow deposits of Yucca Mountain contain zones within the flows that are characterized by having an abundance of lithophysae. Lithophysal zones occur where vapor concentrations in the densely welded part of ignimbrites form lithophysal cavities (Ross and Smith 1961, pg. 37 to 38). Lithophysae generally have gray rims composed of vapor phase minerals about 1 to 3 mm thick. The WHB drilling encountered the upper and lower lithophysal zone of the Tiva Canyon Tuff (Tpcpul and Tpcpll, respectively). Depending on the size and continuity of the lithophysae, the lithophysae can be difficult to drill because the void space can reduce the core to rubble and create a loss of circulation during drilling. Also, while casing operations are taking place, these voids can require a greater amount of grout to set casing.
- During the drilling program several zones of what has been termed fracture fill material were identified in some of the core holes. Several explanations for these zones have been put forth, the most likely being that these zones represent open paleo-fractures that

were subsequently infilled with detrital volcanic material consisting primarily of clay and fine-grained sediment (see borehole logs in Attachment I for detailed descriptions of fracture fill zones).



DTNS: GS020383114233.001, GS020383114233.003

Note: Borehole RF#13 completed in 1998. All other boreholes completed in 2000. Base photo is YMP Photo #BN8811_50.

Figure 2. Locations of Boreholes and Test Pits Completed in 1998 and 2000 in the WHB Area

Table 3. WHB Area Borehole Locations, Total Depth and Drilling Method

Designation	Northing	Easting	Elevation (ft.)	Total Depth (ft)	Drilling Method
RF#14	N765,309	E571,065	3651.5	550.0	Core
RF#15	N765,774	E570,225	3681.0	330.0	Core
RF#16	N765,056	E570,473	3672.0	452.8	Core
RF#17	N766,076	E571,042	3672.4	667.8	Core
RF#18	N764,522	E570,627	3640.3	493.6	Mud Rotary
RF#19	N765,880	E571,384	3661.8	645.2	Mud Rotary
RF#20	N765,637	E570,797	3671.3	160.0	Mud Rotary
RF#21	N765,899	E570,739	3673.0	192.2	Mud Rotary
RF#22	N766,206	E570,793	3679.2	540.6	Mud Rotary/core
RF#23	N765,311	E570,465	3674.0	159.1	Mud Rotary
RF#24	N766,344	E570,542	3684.5	268.0	Mud Rotary
RF#25	N765,968	E570,626	3676.5	159.0	Mud Rotary
RF#26	N765,248	E570,580	3670.8	264.9	Mud Rotary
RF#28	N765,510	E570,105	3680.6	99.8	Mud Rotary
RF#29	N766,018	E570,836	3672.7	430.0	Mud Rotary

DTN: GS020383114233.003

Note: DTN: GS020383114233.003 has some minor internal inconsistencies, as follows: RF#24: Log page 1 says at the top that total depth is 268.0 feet and at the bottom that total depth is 267.9 feet. RF#26: Log page 1 says at top that total depth is 264.9 feet and at bottom that total depth is 265.0 feet. RF#28: log page 1 says at the top that total depth is 100.0 feet and at the bottom that total depth is 99.8 feet. The values used herein are based on a review of the data.

Table 4. WHB Area Boreholes with Contact Depths and Total Depths in Feet

Borehole	Fill	Qal	Tmbt1	Tpki	Tpbt5	Tpcrn	Tpcpul	Tpcpmn	Tpcpll	Tpcpln	Total Depth (ft)
RF#14 (core)		0.0		101.8	192.5	203.4	275.0	395.0	443.7	455.6	550.0
RF#15 (core)	0.0					6.5	78.0	196.0	242.4	256.6	330.0
RF#16 (core)	0.0	22.4		75.7	133.2	137.8	222.0	360.0	403.0	422.5	452.8
RF#17 (core)		0.0	92.4	287.2	348.4	368.9	478.0	587.3	637.6	653.2	667.8
RF#18 (cuttings)		0	60	65		204	292	425	470		493.6
RF#19 (cuttings)		0	120	280	410	420	510	635			645.2
RF#20 (cuttings)	0	28			98	102	127				160.0
RF#21 (cuttings)	0	5				115 ⁽⁵⁾	165				192.2
RF#22 (cuttings/core)		0	80	318	415	438	530				540.6
RF#23 (cuttings)	0	12		76	92	95					159.1
RF#24 (cuttings)	0	10				30	110	230			268.0
RF#25 (cuttings)	0	10				70	125				159.0
RF#26 (cuttings)	0	14		85	204	211					264.9
RF#28 (cuttings)	0	5				15	70				99.8
RF#29 (cuttings)		0	85	280	370	380					430.0

DTN: GS020383114233.003

- Notes:
1. Lithostratigraphic units are identified on Figure 233 and detailed lithostratigraphic descriptions are provided in Attachment I. Note that Tpcrn includes Tpcrv, Tpcrl and Tpcrn.
 2. Contacts are given as the depths in feet to the tops of the units. Contact depths are given to 0.1 feet in core borings (RF#14 to RF#17) and to 1 foot in mud rotary borings (RF#18 to RF#29).
 3. A blank cell means that the unit was not encountered.
 4. DTN: GS020383114233.003 has some minor internal inconsistencies, as follows: RF#17 - log page 1 says the base of the alluvium is at 96.1 feet, while log page 2 says the top of Tmbt1 (i.e., base of the alluvium) is at 92.4 feet. RF#22 - log page 1 says the base of Tpcrn is at 530.5 feet, while log page 2 says the top of Tpcpul (i.e., base of Tpcrn) is at 530.0 feet. The values used herein are based on a review of the data. Also, see note in Table 3.
 5. See Assumption 4, Section 5 for a discussion of an alternative interpretation of the RF#21 borehole log.

6.2.3 Revision of RF#13 Borehole Log

Borehole RF#13 was originally drilled in October 1998 at the location shown on Figure 2. ODEX drilling methods with a Modified California and Pitcher Tube samplers were used to a depth of 98.0 feet. The remainder of the borehole was drilled with continuous wireline core to a total depth of 350.1 feet (DTN: GS020383114233.003). The log of borehole RF#13 was revised (DTN: GS020383114233.003) for this program in order to have engineering properties and shear-wave velocity added to the log. During the process of creating final SMF geologic logs for the current program, borehole RF#13 core was reexamined. In 1998, the borehole was logged with a repeated section of Tiva Canyon Tuff crystal-poor middle nonlithophysal zone (Tpcpmn) at the bottom of the hole due to faulting. With further drilling data, project geologists now accept that the zone in question is Tpcpln instead of the Tpcpmn, which is supported by the cored boreholes in the current program. The changes in the stratigraphic contacts were added to the revised log and are reflected in Table 5. For the purposes of this report, the new log is a combination of engineering properties, shear-wave velocities, and revised geology and is presented in Attachment II.

Table 5. Revised Contact Depths and Total Depths in Feet in Borehole RF#13

Borehole	Fill	Qal	Tmbt1	Tpki	Tpbt 5	Tpcrn	Tpcpu I	Tpcpmn	Tpcpll	Tpcplin	Total Depth
RF#13 (cored)	0.0	12.5		98.0	164.4	169.3	219.1	231.5	286.7	300.9	350.1

DTN: GS020383114233.003

Notes: Contacts are given as the depths in feet to the tops of the units.
A blank cell means that the unit was not encountered.

6.2.4 Test Pits

Beginning in July 2000, four test pits were excavated to study and analyze soil properties in the WHB Area. The test pits, designated TP-WHB-1 through -4, were located as shown on Figure 2. The test pits were dug to approximately 19-ft depth bgs, with side slopes formed by a series of 5 benches with vertical sides and horizontal benches (approximately 4-foot depth to each level), yielding an overall average slope of about 2:1 (horizontal to vertical) for slope stability. The pits were of a square configuration, approximately 75 feet on a side (at ground surface), with one of the four side slopes being excavated out to provide a ramp to the bottom of the pit. The limits of the test pits were surveyed (DTN: MO0012GSC00405.000). All test pits were sprayed with water during excavation to control dust; as a result, the measured water contents are not representative of field conditions.

The alluvium in the three exposed walls of each test pit were mapped and logged according to the Unified Soil Classification System (USCS) using USBR 5005-86, *Procedure for Determining Unified Soil Classification (Visual Method)*. The results of mapping are shown on the test pit logs in Attachment III and on the Photomosaic Test Pit Maps in Attachment IV.

Six 6-foot ring density tests, and sixteen 20-inch sand cone density tests were performed within the test pit excavations. Twenty-inch sand cone tests were performed in accordance with USBR 7205-89, *Procedure for Determining Unit Weight of Soils In-Place by the Sand-Cone Method*, in soils containing 20 percent or less particles retained on the 1-1/2-inch (37.5-mm) sieve. Six-ft ring density tests were performed using USBR 7221-89, *Procedure for Determining Unit Weight of Soils In-Place by the Water Replacement Method in a Test Pit*, where there was greater than 20 percent of the particles retained (on a weight basis) on the 1-1/2-inch (37.5-mm) sieve. Samples were collected and sent to a geotechnical laboratory in Denver for classification and property tests. The results of laboratory tests are discussed in Section 6.2.9.

The results of the in-place density tests are summarized in Table 6. Table 6 also gives the relative density, which is based in part on the laboratory data discussed in Section 6.2.9. USCS group classifications indicated on Table 6 are based on laboratory classifications (USBR 5000-86, *Procedure for Determining Unified Soil Classification (Laboratory Method)*) and not the field classifications discussed below.

There is not much variation in the materials encountered in the test pits. The field classifications indicate that all the material is coarse-grained, mainly poorly graded gravel (GP) or silty gravel (GM) with varying percentages of sand, cobbles, and boulders. When the percent of fines was estimated visually at 10 percent, a dual classification was given, i.e., (GP-GM), also with varying percentages of sand, cobbles, and boulders. There was also a thin layer (zero- to two-feet thick)

of silty sand (SM) with varying percentages of gravel and cobbles at the surface of test pit TP-WHB-4.

Seven soil units were mapped and field-classified within test pit TP-WHB-1, as shown on the photographs in Attachment IV. The USCS group names for the mapped units are poorly graded gravel (GP), poorly graded gravel with silt (GP-GM), and silty gravel (GM). The units have varying percentages of sand, cobbles, and boulders. The lowest measured dry density value, from a 20-inch sand cone density test at 12.3-foot depth, was 105.3 lbm/ft³, and the highest measured dry density value, from 6-foot ring density tests at both 4- and 12-foot depths, was 110.5 lbm/ft³.

Five soil units were mapped and field-classified within test pit TP-WHB-2, as shown on the photographs in Attachment IV. Four of the units are poorly graded gravel with silt (GP-GM) with varying percentages of sand, cobbles and boulders, and one unit is silty gravel (GM) with sand, cobbles, and boulders. The lowest measured dry density, from a 20-inch sand cone density test at 16-foot depth, was 104.0 lbm/ft³, and the highest measured dry density value, from a 6-foot ring density test at 12-foot depth, was 114.0 lbm/ft³.

Table 6. Summary of In-Place Density Tests and Relative Density

Test Pit No. ⁽¹⁾	Sample Depth feet	Sample No. 65A- ⁽²⁾	USCS Group Symbol ⁽³⁾	Volume of Test Hole ft ³	Total Mass of Test Material ⁽⁴⁾ pounds	In-Place Wet Density lbm/ft ³	Water Content, %		In Place Dry Density lbm/ft ³	Relative Density %
							Minus No. 4 Sieve	Plus No. 4 Sieve		
1	4	606	GW-GM	14.67	1712	116.7	7.9	4.4	110.5	74 ⁽⁵⁾
1	12	607	GW-GM	20.93	2436.3	116.4	7.5	4.0	110.5	74 ⁽⁵⁾
1	12	614	GP-GM	1.4908	164.6	110.4	4.4	3.3	106.3	41
1	12.3	615	SP-SM	1.0959	121.0	110.4	5.6	3.9	105.3	48
1	20	608	GP	23.38	2642.8	113.0	4.8	3.9	108.4	55 ⁽⁵⁾
2	8	616	GP	22.77	2774.4	121.8	10.6	5.9	113.4	86 ⁽⁵⁾
2	12	620	GP-GM	21.42	2582.2	120.6	5.8 ⁽⁶⁾	5.8 ⁽⁶⁾	114.0	68 ⁽⁵⁾
2	16	624	GW-GM	0.7455	86.3	115.8	8.7	6.3	107.9	70
2	16	625	SW-SM	0.7942	88.3	111.2	7.4	6.1	104.0	54
2	16	626	SP-SM	0.791	88.5	111.9	5.3	3.9	106.8	81
2	19	628	GW	0.640	74.7	116.7	9.6	6.9	108.0	66
3	8	617	GP-GM	1.0949	116.9	106.8	3.5	2.3	103.7	51
3	8	618	GP-GM	0.9901	100.7	101.7	4.4	3.6	97.9	25
3	8	619	GP-GM	0.8609	91.2	105.9	5.1	3.0	102.4	65
3	12	621	GP	0.8598	100.9	117.4	8.9	6.3	109.7	84
3	12	622	GP	0.6396	70.5	110.2	6.9	4.2	105.1	90
3	12	623	GP-GM	0.7857	93.5	119.0	4.1	3.0	115.1	72
3	19	629	GW-GM	0.677	75.0	110.8	16.0	7.7	100.3	120
4	4	627	GW	22.00	2583.7	117.4	6.7 ⁽⁶⁾	6.7 ⁽⁶⁾	110.1	75 ⁽⁵⁾
4	8	631	GP-GM	0.8048	87.0	108.1	6.9	5.0	102.0	36
4	12	632	GP	0.8704	99.5	114.3	8.0	4.7	107.7	80
4	16	633	GW-GM	0.7413	86.3	116.4	8.0	6.6	108.5	72

DTN: GS020483114233.004

Notes:

- (1) The complete test pit designation is preceded by TP-WHB-
- (2) Laboratory Sample Index Number
- (3) For explanation of USCS soil group symbols, see Glossary and USBR 5000-86
- (4) Tests with a total mass greater than 200 pounds were performed by the water replacement method and tests with a total mass less than 200 pounds were performed by the sand-cone (20-inch) method
- (5) Relative density of minus 3-inch control fraction
- (6) Water content of total sample (all particle sizes)

Seven soil units were mapped and field-classified within test pit TP-WHB-3, as shown on the photographs in Attachment IV. The USCS group names for the mapped units are poorly graded gravel (GP), poorly graded gravel with silt (GP-GM), and silty gravel (GM). The units have varying percentages of sand, cobbles, and boulders. The lowest measured dry density value, from a 20-inch sand cone density test at 8-foot depth, was 97.9 lbm/ft³, and the highest measured dry density value, from a 20-inch sand cone at 12-foot depth, was 115.1 lbm/ft³.

Five soil units were mapped and field-classified within test pit TP-WHB-4, as shown on the photographs in Attachment IV. Four of the mapped units are poorly graded gravel with silt (GP-GM) with varying percentages of sand, cobbles, and boulders. The fifth unit is a thin (zero-to two-foot thick) surface layer of silty sand (SM) with gravel and cobbles that covered a portion of the test pit site. The lowest measured dry density value, from a 20-inch sand cone density test at 8-foot depth, was 102.0 lbm/ft³, and the highest measured dry density value, from a 6-ft ring density test at 4-foot depth, was 110.1 lbm/ft³.

After completion of mapping and mapping review, the test pits were backfilled with non-engineered fill. During the construction of facilities in the WHB Area, the surveyed locations of the tests pits (as well as of older test pits excavated at the site) should be used to identify on the construction drawings areas that need to be re-excavated and backfilled with engineered fill.

6.2.5 Downhole Seismic Velocity Surveys

This section describes the collection, analyses, and estimates of shear- and compression-wave velocities in 16 boreholes at the WHB site through the use of downhole seismic velocity surveys. Procedures and equipment used to acquire the data by means of the standard downhole technique are described. The work was performed by Bruce Redpath of Redpath Geophysics and Rob Steller of GEOVision, Inc. (GEOVision). Redpath Geophysics performed surveys in all boreholes except RF#17. GEOVision surveyed borehole RF#17 as well as borehole RF#13. The latter was performed to compare the results of two independent surveys in the same borehole (Section 6.2.5.3). Downhole measurements were also conducted by URS Corporation in 1998 in borehole RF#13 (CRWMS M&O 1999b, Section 4.3 and Appendix N). All procedures and relevant calibration information are documented in Scientific Notebooks SN-M&O-SCI-030-V1 (Wong 2002b) for the Redpath Geophysics surveys and SN-M&O-SCI-025-V1 (Luebbbers 2002c) for the GEOVision surveys. These notebooks also contain the data collected, data reduction, and data interpretation, which were compiled as the work progressed.

The fieldwork for these investigations was performed from October to December 2000. Surveys were performed in the boreholes listed in Table 7. Borehole locations are shown on Figure 3.

Table 7. Boreholes Used for Downhole Surveys at WHB Area

Borehole	Elevation Above MSL (ft)	Depth of Survey (ft)
RF#13	3671.1	345
RF#14	3651.5	520
RF#15	3681.0	200
RF#16	3672.0	445
RF#17	3672.4	620
RF#18	3640.3	485
RF#19	3661.8	640
RF#20	3671.3	155
RF#21	3673.0	185
RF#22	3679.2	505
RF#23	3674.0	155
RF#24	3684.5	260
RF#25	3676.5	155
RF#26	3670.8	260
RF#28	3680.6	96
RF#29	3672.7	405

DTNs: GS020383114233.003, MO0111DWDWHBSC.001, MO0110DVBBOREH.000

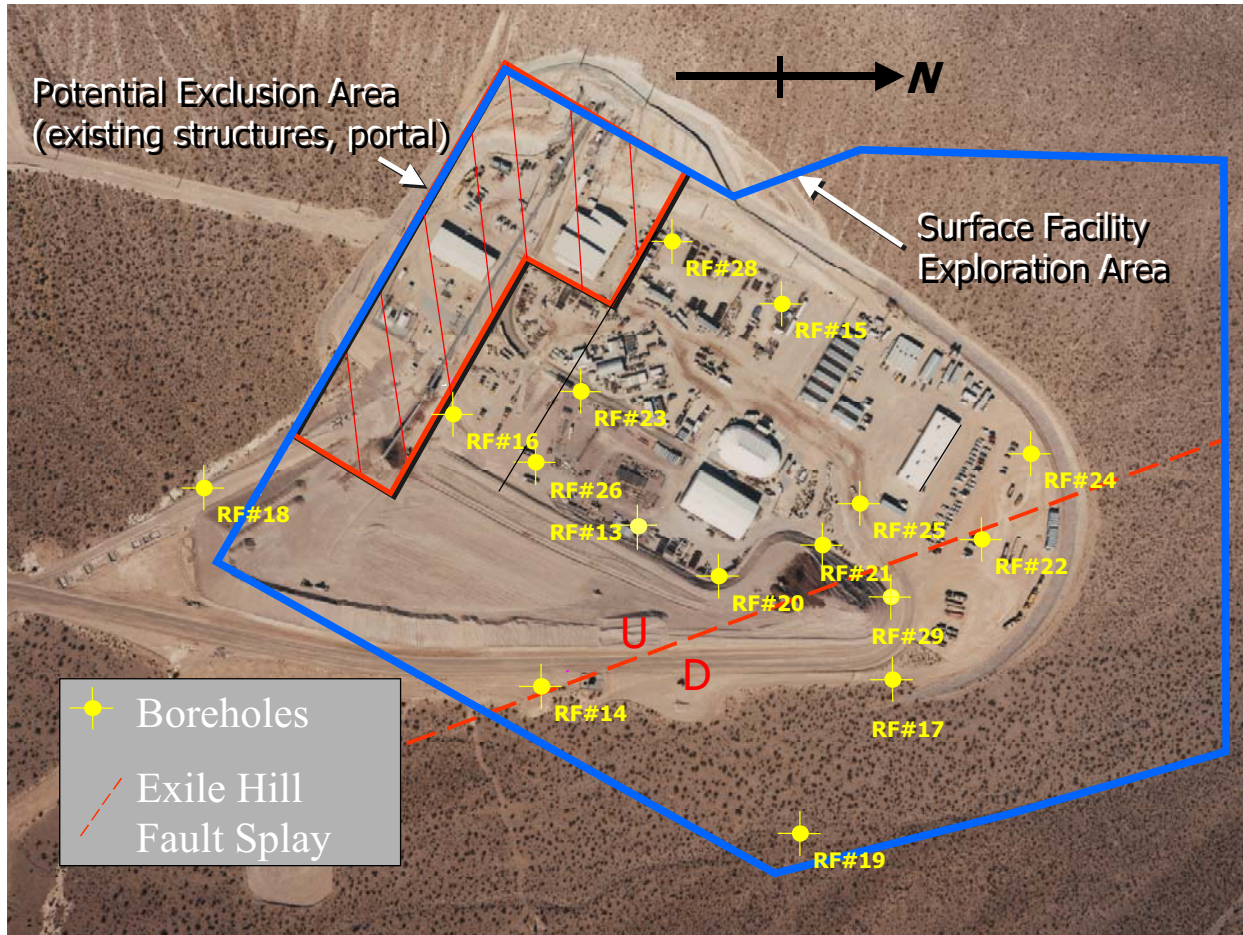


Figure 3. Locations of Downhole Measurements in Boreholes at the WHB Site Characterization Area

6.2.5.1 Procedures and Equipment

The conventional downhole survey method was used in which travel times of signals from an impulsive source of energy at the surface are measured to various depths in the borehole. The corresponding plot of travel time vs. depth is then converted to velocity vs. depth by computing slopes of the interpreted major straight-line segments of the plotted data.

All of the holes were cased with 4-inch PVC pipe grouted in place. The water inside the casing in each hole (holes were filled for suspension seismic surveys; Section 6.2.6) was pumped out prior to performing the downhole velocity surveys. Although the downhole geophone assemblies are designed to operate under water, the holes were pumped dry to avoid any chance of tube waves interfering with the shear-wave signals. (A tube wave is a pressure pulse that propagates nearly unattenuated down the fluid in a borehole at a velocity close to that of the shear wave in the surrounding material.)

The procedures followed by Redpath Geophysics and GEOVision are similar. Because Redpath Geophysics performed the vast majority of the surveys, Redpath Geophysics procedures are described first, followed by any differences pertaining to GEOVision. A vehicle-on-a-beam traction source located about 10 ft from the collar of the hole was used to generate shear waves. The source consisted of a 7-ft-long, 6 x 6 inch wood beam with steel end caps, the beam being held in firm contact with the ground by driving the front wheels of a vehicle onto it. Horizontal blows to the ends of the beam with a sledgehammer generated shear-wave pulses. Shear-wave signals with 'positive' and 'negative' polarities were generated by striking each end of the beam in sequence. The 'positive' and 'negative' shear waves are, ideally, mirror images of each other and, viewed as a pair, greatly assist in identifying the shear wave. The sledgehammer had an impact sensor attached to the handle near the head that started the timing process in the recording instrument upon impact with the beam. Where site conditions permitted, the beam was aligned at an azimuth of 340°. Compression-wave signals were generated by vertical hammer blows to a steel striker plate on the ground, also located close to the collar of the hole.

The downhole sensor for the Redpath Geophysics velocity surveys was a Model BHG-3 geophone manufactured by Geostuff of Saratoga, California. The sensor package contained an orthogonal array of three geophones, mounted on a gearhead-motor assembly, and a fluxgate compass. A servo-circuit linked the compass to the motor for the geophone array so that the horizontal geophones maintained a constant, pre-determined azimuth at each measurement point. This allowed one of the two horizontal geophone elements to stay aligned with the shear-wave source as the sensor package was raised or lowered in the hole. This capability ensures that the detected shear-wave signal was recorded at its maximum amplitudes. The BHG-3 was mechanically locked in the hole casing with a motor-actuated clamping spring operated from the control box at the surface.

GEOVision also used a variable-azimuth downhole sensor package. Their locking was accomplished using a pneumatic bladder system. They also placed vertical and horizontal geophones in the soil near the center of the traction plank, near the borehole collar to record reference waveforms to verify consistent triggering from each hammer blow.

Redpath Geophysics recorded signals with a Geometrics R24 'Strataview' digital seismograph. The R24 was configured to record 24 1024-sample channels of data, sampling at a rate of 125 or 250 microseconds, depending on the hole depth. In the downhole surveys, the data were collected channel-by-channel until 24 channels had been recorded or until the survey was complete, at which time the signals were transferred to a hard disk drive and printed on the R24's internal printer for field examination. The raw signals on disk can be filtered and processed on playback and prior to printing. The data were ultimately stored in SEG-2 binary format on 3½-inch disks.

GEOVision used an OYO Model 170 Digital Logging Recorder. The Model 170 recorder had six channels (two simultaneous recording channels), each with a 12-bit 1024-sample record. The recorded data were displayed on a cathode ray tube display and on paper tape output as six channels with a common time scale. Data and all system parameters were stored on 3.5-inch floppy diskettes for further processing. Review of the displayed data on the cathode ray tube or paper tape allowed the operator to set the gains, filters, sample rate, and summing (or stacking) number in order to optimize the quality of the data before recording to floppy diskette.

The procedure was to lower the BHG-3 to the bottom of the hole and expand the clamping spring so that the BHG-3 could be pulled up the hole and still hold its position in the hole (azimuth). Travel times were then measured from the bottom up at 5-ft intervals to a depth of 100 ft, and at 3-ft intervals from there to the surface. Exceptions to this procedure were made at boreholes RF#14 and RF#19, in which measurements were made at 10-ft intervals below 480 and 490 ft, respectively. In some of the deep holes, data were acquired in two phases, first from 400 ft up to the surface and then from 400 ft downwards. Because of the weight of the cable attached to the BHG-3, it is difficult for one person to pull more than 400 ft of cable up the hole between each measurement point. Depths were measured using marking on the calibrated cable.

In GEOVision's procedure, the cable travels over a 1-m circumference measuring wheel with a rotary encoder coupled to the measuring head, whose output was automatically recorded with each set of data. Depth information was verified at each measurement location with a mechanical counter was well.

Careful attention was given to the polarity of the shear-wave signals. Prior to beginning a survey, one of the two horizontal geophones inside the BHG-3 was aligned with the shear-wave beam. The system was always configured so that at each measurement point, the first blow to the beam would produce a shear wave for which the initial deflection of the trace on the seismograph record was upwards, *i.e.*, towards the top of the paper record. At each measurement point, the same end of the beam was always struck first and the resulting signal recorded on an odd-numbered channel. The signal from the blow to the other end of the beam was then recorded on the adjacent even-numbered channel. A compression-wave signal was recorded next (while still at the same depth) and a switch box directed that signal to a separate block of channels allocated to compression wave measurements. Because each measurement point consists of two shear-wave signals and one compression-wave signal, a total of 8 measurement points comprise a 24-channel record; channels 1 through 16 are shear waves and channels 17-through 24 are compression waves. The ability to keep careful track of the polarity of the shear-wave signals proved to be important in the interpretation of the data acquired in these surveys.

The R24 seismograph has the capability of ‘stacking’ or linearly adding multiple signals. More than one hammer blow for each signal is almost always required at the deeper measurement points in order to increase the signal-to-noise ratio or to clearly develop the shear-wave amidst interfering arrivals. As many as 5 blows to each end of the plank were sometimes required.

It was initially thought that some degree of horizontal shear-wave anisotropy might be present at the WHB site, *i.e.*, that the shear-wave velocity might be a function of the direction of polarization of the signals. For this reason, an experiment was performed in borehole RF#25 in which two orthogonal shear-wave sources (340° and 250°) were set up at equal distances from the collar of the hole. Prior to starting the survey, the ‘longitudinal’ geophone in the BHG-3 was aligned with the 340° source and, consequently, the ‘transverse’ geophone was aligned with the second source. As mentioned above, the first blow to each shear-wave beam produced an initial upward deflection of the seismograph trace. At each measurement point, shear waves from both sources were recorded before the BHG-3 was raised to the next measurement point. A special switchbox was used which routed the signals from one shear-wave source to channels 1 through 8, signals from the second source were directed to channels 9 through 16, and the compression-wave signals were sent to channels 21 through 24; channels 17 through 20 were not used. Four measurement points comprised a complete record. In this manner, a direct visual comparison of arrival times from the two shear-wave sources could be made at each measurement point. Significant anisotropy was not present; differences in the shear-wave travel times from the two sources at each depth were generally less than 1 millisecond (ms), and no further experiments of this nature were performed.

6.2.5.2 Analysis

Complete sets of the shear- and compression-wave signals are contained in the scientific notebooks (Wong 2002b; Luebbers 2002c). The source offset and the frequency of the low-pass filters used for playback are shown on each set of records.

Redpath Geophysics

As stated previously, the horizontal geophones in the BHG-3 maintained a constant azimuth during each survey and, therefore, the polarity of the recorded shear-wave signal was always consistent with the direction of the hammer blow. A blow to the first end of the beam always resulted in an initial upward deflection of the seismograph trace. Some filtering was applied to all of the signals during playback from the hard disk. The signals acquired in the velocity surveys were transferred to the hard drive without any filtering; filtering was used only during playback to the R24’s internal printer. The filtering was accomplished by using the digital filters built into the R24’s operating system. The R24 filters used for processing these records were either 100-, 200- or 400-Hz low-pass.

The degree of filtering varied from hole to hole and depended upon the amount of interference present. For example, it appears that shear-wave signals arriving at the BHG-3 transducer in portions of borehole RF#15 may have traveled by different paths, *i.e.*, multiple and overlapping signals were present. In this specific instance, the least amount of filtering was used (400 Hz) to allow tracking the ‘predominant’ shear wave from the top of the hole to the bottom. A contrasting example is borehole RF#22 where more filtering (100 Hz) was judged necessary

because of weak signals near the bottom of the hole and because of noise from nearby drilling operations. Only one filter setting was used for the shear waves in any given borehole. A 400-Hz low-pass filtering was used for all the compression-waves signals.

Generally, Redpath Geophysics did not use the time of the onset or ‘first break’ of the shear wave to calculate the travel time. The onset of the pulse may be reasonably clear at shallow depths, but becomes vague or completely obscured as the depth increases. For this reason, picking the time of the first peak (and of the first trough of the corresponding reverse-polarity blow) was the preferred approach in measuring the travel time of the shear wave. In most boreholes in the WHB Area, even the first peak/trough becomes too ambiguous at depth to time accurately and reliably, and it was necessary to use the maximum trough (which immediately follows the first peak) and its corresponding first peak (which immediately follows the first trough of the reverse polarity blow) to determine the travel time. In every case, the average time of a peak and its corresponding trough (reverse polarity) was used. The average time of the first peak and its corresponding first trough was used only for boreholes RF#25 and RF#28. The time of the first peak of the compression wave was always used as its travel time.

Because the energy source, whether compression or shear, is offset horizontally from the collar of the hole, the travel times were adjusted at shallow depths for this offset. The adjustment is intended to convert the actual travel time along the slant path from source to receiver to the equivalent time required to travel vertically from the surface down to the receiver. The offset is adjusted according to equation 1 (Wong 2002b, Attachment B, p. 5):

$$t_{\text{vertical}} = \Delta t + \Delta t_o + \left[(t_{\text{peak}} - \Delta t - \Delta t_o) \right] \cos(\Theta) \quad (\text{Eq. 1})$$

where t_{vertical} is the time that is plotted against the depth to the measurement point, t_{peak} is the time of the selected peak (or average of peak and corresponding trough), Δt is the time difference between the onset of the signal and the selected peak (and corresponding trough) for signals recorded at shallow depths, Δt_o is the time shift of the onset of the signal due to filtering, and Θ is the angle between the slant path and vertical. This shift is easily measured at shallow depths by comparing the times of onset of unfiltered and filtered signals in each hole. In practice, the value of $\cos\Theta$ is computed from the source offset, s , and the depth to the transducer, d , so that the above equation becomes (Wong 2002b, Attachment B, p. 5):

$$t_{\text{vertical}} = \Delta t + \Delta t_o + \left[(t_{\text{peak}} - \Delta t - \Delta t_o) \right] \frac{d}{\sqrt{d^2 + s^2}} \quad (\text{Eq. 2})$$

The cosine adjustment is required to a depth equal to approximately 10 times the offset distance. As shown above, it was applied to the travel times in these surveys until the difference between the raw and the corrected time was only 0.1 ms.

Small-scale plots of shear- and compression-wave times vs. depth are shown in Attachment V. It must be emphasized that the determination of the reported velocities was performed on the large-scale hand-drawn plots that are attached to the scientific notebook (Wong 2002b) describing these surveys.

In general, the quality of the raw data was good to excellent. It is noted on the time vs. depth plots (Attachment V) that there is some scatter of the data points about their respective trend lines over portions of some boreholes. The scatter is most probably attributable to the complex geology at the WHB site. The scatter is not due to insufficient signal amplitudes, to noise from extraneous sources, nor to some systemic flaw in the recording instrumentation or procedures. In many cases, an examination of the shear-wave records suggests that signals are arriving at the transducer from more than one pathway. This may also be happening in the case of compression waves, but this cannot be discerned by looking at the recorded signals. The degree of scatter is not large in absolute terms, typically a departure of only 1 to 2 ms from the overall trend line of the data points; in extreme cases, the departure was as high as 4 ms. However, because of the relatively high velocities present at the site, even small variations in travel times can be significant.

There is always some judgement involved when assigning travel-time data points to a layer. Often the change of slope of the data points is not especially pronounced when crossing a boundary between velocity zones, and the exact depth of the boundary becomes somewhat uncertain due to the inherent scatter in the data. Least-squares calculations of slopes were applied in many cases, but it was also necessary to use judgement in many cases where it appeared that scatter precluded meaningful statistical calculations.

The best overall signal quality was observed in borehole RF#19, despite the fact that this was the deepest hole surveyed in this report. Only two hammer blows were required to produce a clear and unambiguous shear wave at a depth of 640 ft, and multiple or overlapping shear waves were not evident. The scatter in arrival times was typically less than 1 ms.

GEOVision Analysis

Compression-wave first arrivals were picked on the vertical downhole receiver using the computer program PSLOG by OYO Corporation. First arrivals were also picked on the vertical surface receiver records for timing corrections. During picking of shear-wave arrivals, the horizontal records were studied to verify the presence of clear shear-wave pulses, as indicated by the presence of opposite polarity pulses on each pair of horizontal records. Ideally, the shear-wave signals from the 'normal' and 'reverse' hammer blows are very nearly inverted images of each other. In practice, particularly near the surface, waveforms are contaminated by cultural noise and converted compression-wave signals. Zero phase shift Digital FFT - IFFT lowpass filtering was used to remove unwanted high frequency noise from the shear-wave signal.

Shear-wave first arrivals were picked on both the horizontal normal (HN) and horizontal reverse (HR) polarity downhole receiver records. Similar to the compression wave, first arrivals were also picked on the horizontal surface receivers for timing corrections. The first arrival data were imported into Microsoft Excel for data processing. Compression- and shear-wave first arrival data from normal and reverse polarity records were then averaged. Both compression and shear-wave first arrival data were then adjusted for source-offset by multiplying each arrival time by the cosine of the angle between the slant path and the vertical. Because of the use of first breaks and filtering that does not introduce phase shift, Eq. 3 was used (Luebbbers 2002c, Attachment 2):

$$t_{\text{vertical}} = t_{\text{break}} \frac{d}{\sqrt{d^2 + s^2}} \quad (\text{Eq. 3})$$

where t_{break} is the time of the first break and the other symbols are as defined for equations 1 and 2.

Corrected compression- and shear-wave first-arrival times were then plotted versus receiver depth for each borehole. A piece-wise linear regression curve fit was then performed on the travel time curves to determine the different velocity zones present in the formation surrounding the borehole (Attachments V and VI). The analysis was performed graphically by an experienced geophysicist. Once a satisfactory fit was obtained, the slope of each segment of the linear curve fit was then calculated using Excel's curve fitting function to provide the average compression- and shear-wave velocity of that segment of the soil column.

6.2.5.3 Results

The final values of shear-wave velocity (v_s) and compression-wave velocity (v_p) are listed in Tables 8 and 9, respectively. Figures 4 to 19 are velocity-depth plots for shear wave and compression wave, often referred to as shear-wave velocity profiles and compression-wave velocity profiles, respectively. Note there is a maximum of 45-ft difference in the ground surface elevation between the 16 boreholes (Table 7). Also shown is the generalized lithology

Table 8. WHB Area Downhole Shear-Wave Velocities

RF#13 (all boreholes surveyed by Redpath Geophysics unless otherwise indicated)	Depth Range (ft)	Velocity (ft/s)
	3 - 10	750
	10 - 25	1355
	25 - 80	2030
	80 - 230	2740
	230 - 345	5,800 ±
RF#13 (GEOVision)	Depth Range (ft)	Velocity (ft/s)
	0 - 15	1,090
	15 - 36	1,960
	36 - 99	2,490
	99 - 215	2810
	215 - 345	6490
RF#14	Depth Range (ft)	Velocity (ft/s)
	3 - 15	1240
	15 - 38	1700
	38 - 114	2375
	114 - 165	3390
	165 - 305	2640
	305 - 520	5000 ±
RF#15	Depth Range (ft)	Velocity (ft/s)
	3 - 38	1935
	38 - 122	2700 ±
	122 - 230	3380
	230 - 320	5900

Table 8. WHB Downhole Shear-Wave Velocities (continued)

RF#16	Depth Range (ft)	Velocity (ft/s)	
	3 - 15	655	
	15 - 24	1130	
	24 - 50	1640	
	50 - 296	2800	
	296 - 376	3540	
RF#17 (GEOVision)	Depth Range (ft)	Velocity (ft/s)	
	0 - 15	1210	
	15 - 30	1880	
	30 - 100	2490	
	100 - 400	3160	
	400 - 500	3890	
RF#18	Depth Range (ft)	Velocity (ft/s)	
	3 - 24	1435	
	24 - 48	1670	
	48 - 78	2900	
	78 - 220	3860	
	220 - 250	2400	
RF#19	Depth Range (ft)	Velocity (ft/s)	
	3 - 18	1285	
	18 - 39	1810	
	39 - 96	2305	
	96 - 282	2740	
	282 - 550	3780	
RF#20	Depth Range (ft)	Velocity (ft/s)	
	3 - 24	1200	
	24 - 70	2020	
	70 - 155	2800 ±	
	RF#21	Depth Range (ft)	Velocity (ft/s)
		3 - 20	1310
20 - 84		1930	
84 - 185		2500 ±	
RF#22	Depth Range (ft)	Velocity (ft/s)	
	3 - 21	1465	
	21 - 83	2200	
	83 - 175	3540	
	175 - 192	1400	
RF#23	Depth Range (ft)	Velocity (ft/s)	
	3 - 9	690	
	9 - 21	1565	
	21 - 72	2100	
	72 - 110	2865	
RF#24	Depth Range (ft)	Velocity (ft/s)	
	3 - 18	1195	
	18 - 33	1535	
	33 - 260	2070	

Table 8. WHB Downhole Shear-Wave Velocities (continued)

RF#25	Depth Range (ft)	Velocity (ft/s)
	3 - 37	1645
	37 - 86	2940
	86 - 155	2100
RF# 26	Depth Range (ft)	Velocity (ft/s)
	3 - 12	425
	12 - 46	1745
	46 - 95	2550
	95 - 260	3780
RF#28	Depth Range (ft)	Velocity (ft/s)
	3 - 10	1305
	10 - 39	1980
	39 - 95	3300
RF#29	Depth Range (ft)	Velocity (ft/s)
	3 - 33	1660
	33-75	2170
	75-138	2560
	138-230	3320
	230 -405	3800

DTNS: MO0111DVDWHBSC.001, MO0110DVBBOREH.000

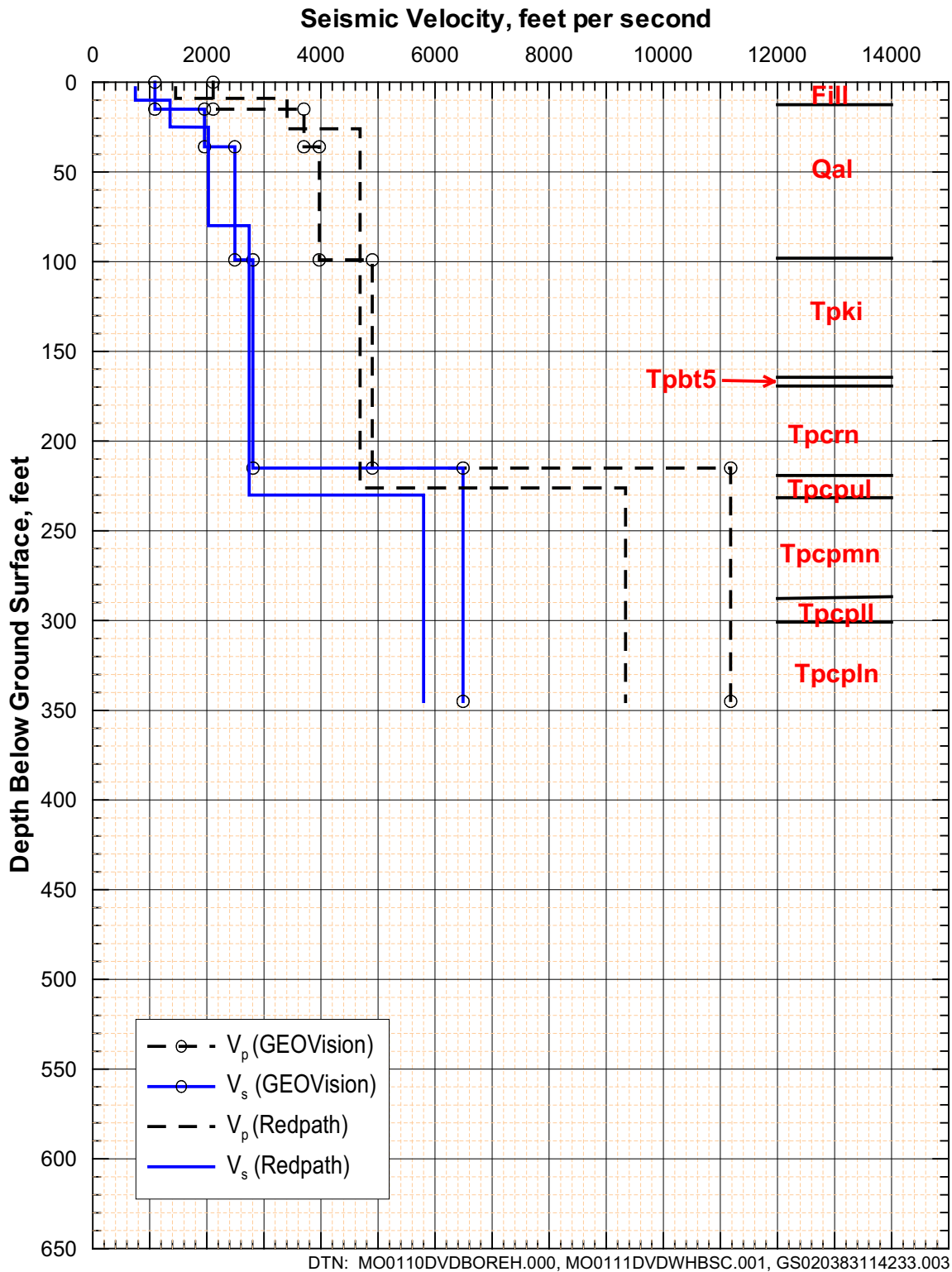
Table 9. WHB Area Downhole Compression-Wave Velocities

RF#13 (all boreholes surveyed by Redpath Geophysics unless otherwise indicated)	Depth Range (ft)	Velocity (ft/s)
	3 - 9	1455
	9 - 26	3405
	26 - 226	4685
	226 - 345	9335
RF#13 (GEOVision)	Depth Range (ft)	Velocity (ft/s)
	0 - 15	2110
	15 - 36	3700
	36 - 99	3970
	99 - 215	4900
215 - 345	11,180	
RF#14	Depth Range (ft)	Velocity (ft/s)
	6 - 12	2530
	12 - 38	3805
	38 - 110	4300
	110 - 304	5900
	304 - 420	7500
420 - 520	11,000	
RF#15	Depth Range (ft)	Velocity (ft/s)
	3 - 18	3215
	18 - 39	3815
	38 - 133	4600 ±
	133 - 210	9850
210 - 320	14,000 ±	
RF#16	Depth Range (ft)	Velocity (ft/s)
	3 - 15	1590
	15 - 50	3075
	50 - 280	4850
	280 - 376	6600 ±
376 - 445	10,000 ±	
RF#17 (GEOVision)	Depth Range (ft)	Velocity (ft/s)
	0 - 15	2510
	15 - 30	4160
	30 - 100	4060
	100 - 400	5580
	400 - 500	7190
500 - 620	10,210	
RF#18	Depth Range (ft)	Velocity (ft/s)
	3 - 48	3305
	48 - 78	4600
	78 - 290	5850
	290 - 390	7200
390 - 485	8300 ±	
RF#19	Depth Range (ft)	Velocity (ft/s)
	3 - 9	1710
	9 - 39	3440
	39 - 104	3950
	104 - 294	5000
294 - 640	6350	

Table 9. Downhole Compression Wave Velocities (concluded)

RF#20	Depth Range (ft)	Velocity (ft/s)
	3 - 13	1935
	13 - 70	3540
	70 - 155	4320
RF#21	Depth Range (ft)	Velocity (ft/s)
	3-57	2845
	57 -120	3900
	120-185	4850
RF#22	Depth Range (ft)	Velocity (ft/s)
	3 - 24	2445
	24 - 87	4185
	87 - 505	5560
RF#23	Depth Range (ft)	Velocity (ft/s)
	3 - 18	2000
	18 - 72	3765
	72 - 120	4700
	120 - 155	5500
RF#24	Depth Range (ft)	Velocity (ft/s)
	3 - 12	1425
	12 - 33	2785
	33 - 260	4960
RF#25	Depth Range (ft)	Velocity (ft/s)
	3 - 41	2710
	41 - 86	4840
	86 - 105	3400
	105 - 155	4800 ±
RF#26	Depth Range (ft)	Velocity (ft/s)
	3 - 10	840
	10 - 95	4115
	95 - 140	7030
	140 - 260	5750
RF#28	Depth Range (ft)	Velocity (ft/s)
	3 - 39	3995
	39 - 96	5640
RF#29	Depth Range (ft)	Velocity (ft/s)
	3 - 33	2875
	33 - 75	3675
	75 - 135	4500
	135 - 405	6040

DTN: MO0111DVDWHBSC.001, MO0110DVBBOREH.000



Note: Stratigraphic units are identified on Figure 233 and detailed lithostratigraphic descriptions are provided in Attachment I. Note that Tpcrn includes Tpcrv, Tpcl and Tpcrn.

Figure 4. Borehole RF#13 Compression- and Shear-Wave Velocities from Downhole Measurements and Generalized Lithology

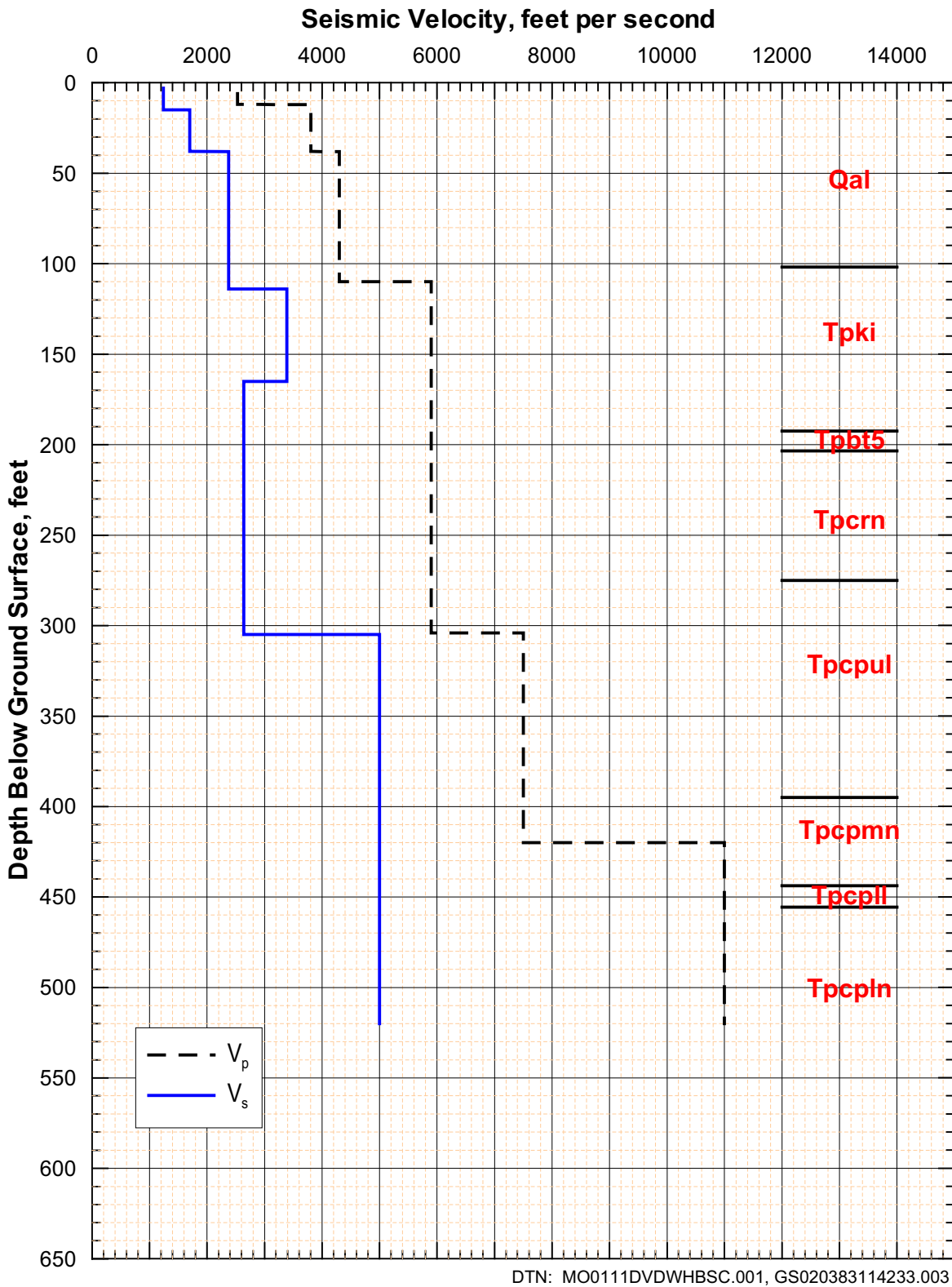
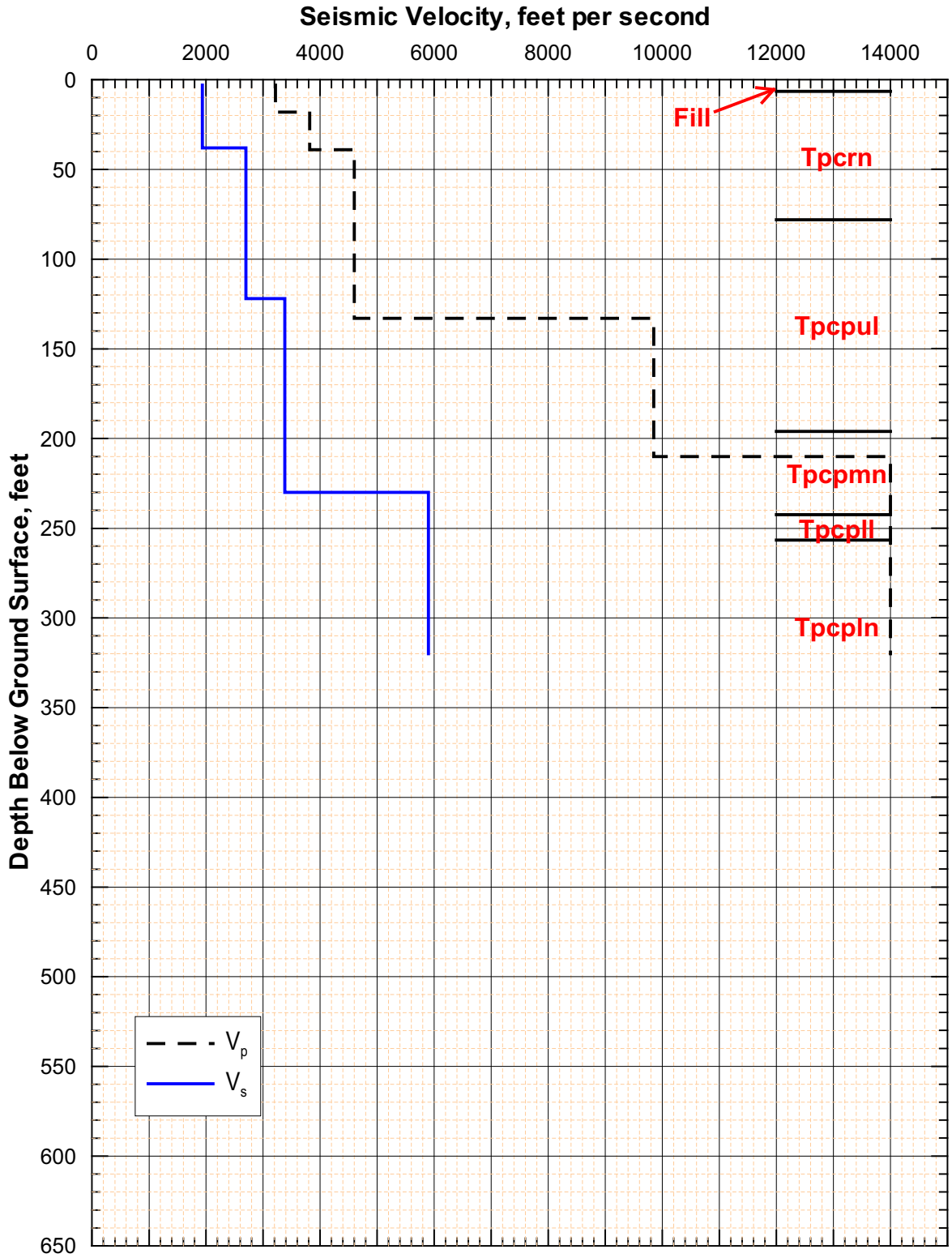


Figure 5. Borehole RF#14 Compression- and Shear-Wave Velocities from Downhole Measurements and Generalized Lithology



DTN: MO0111DVDWHBSC.001, GS020383114233.003

Figure 6. Borehole RF#15 Compression- and Shear-Wave Velocities from Downhole Measurements and Generalized Lithology

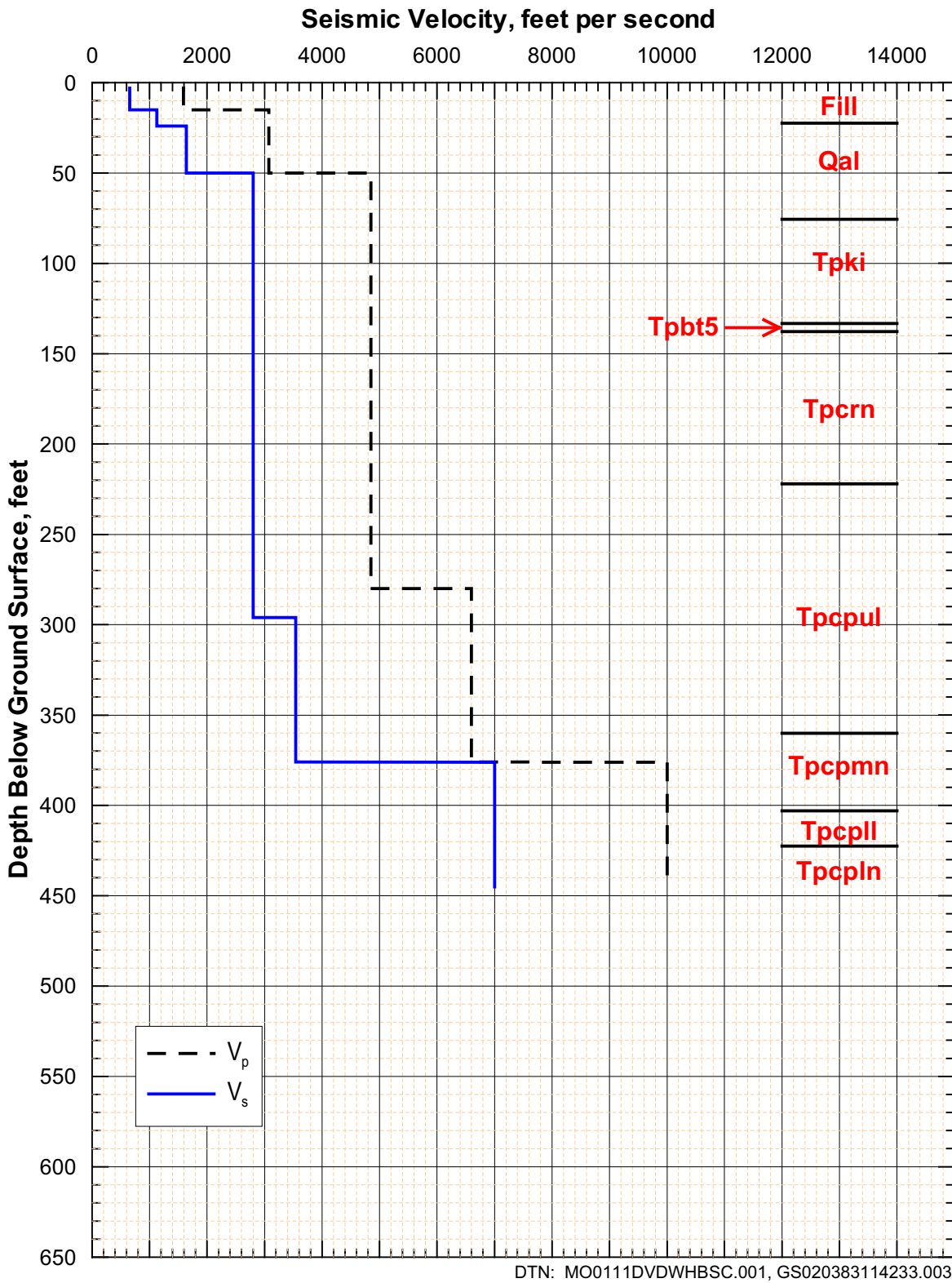


Figure 7. Borehole RF#16 Compression- and Shear-Wave Velocities from Downhole Measurements and Generalized Lithology

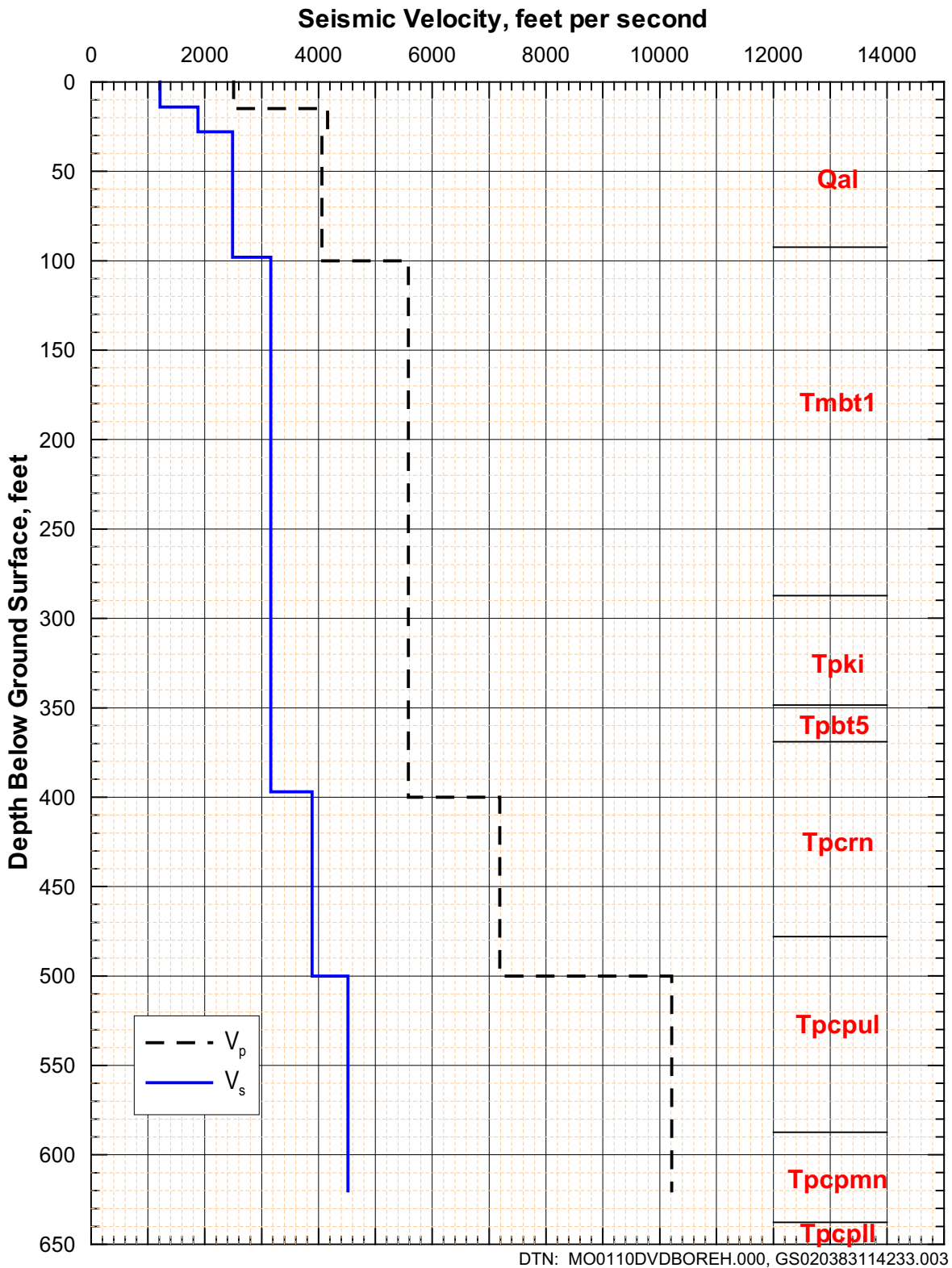


Figure 8. Borehole RF#17 Compression- and Shear-Wave Velocities from Downhole Measurements and Generalized Lithology

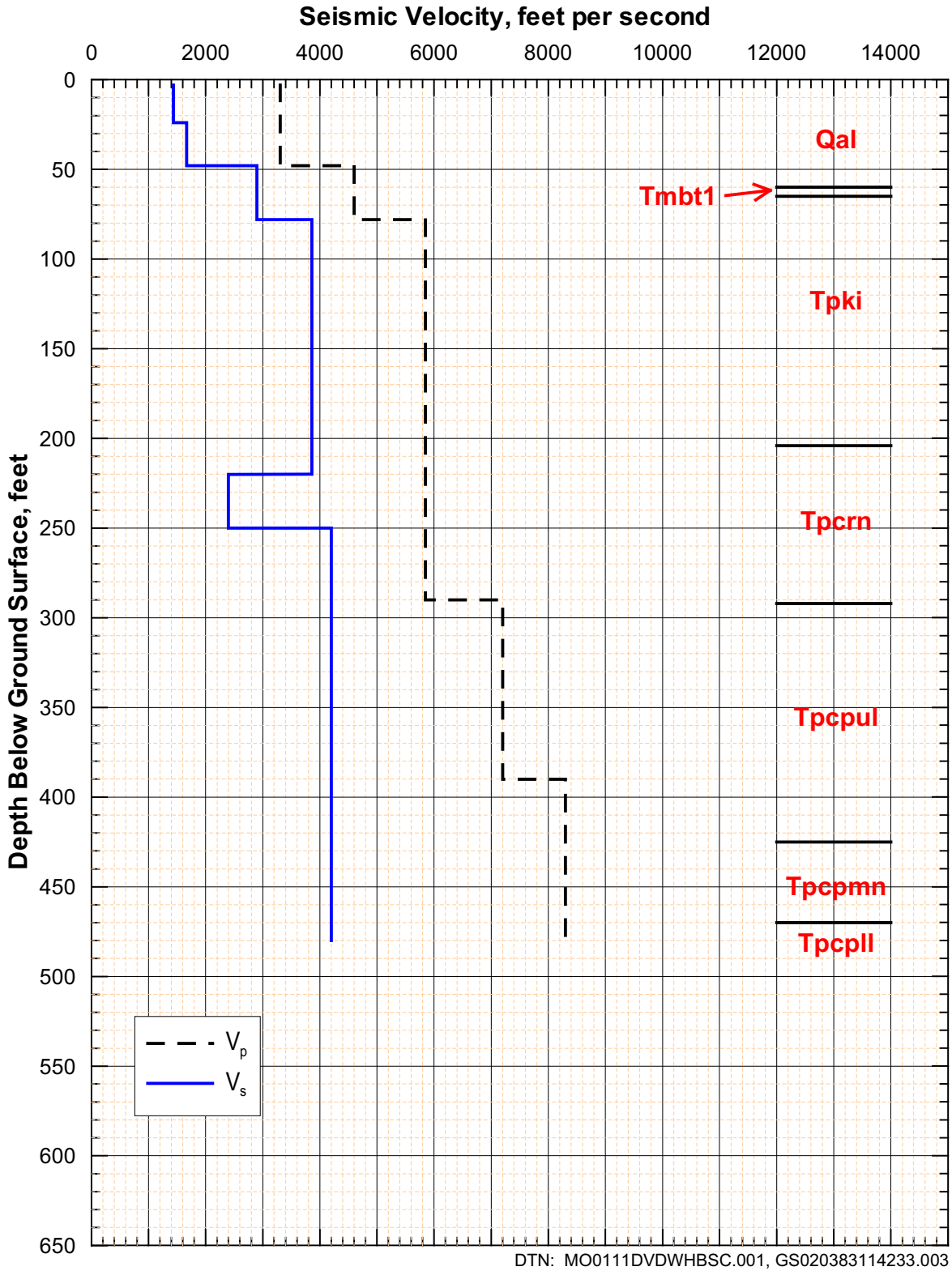


Figure 9. Borehole RF#18 Compression- and Shear-Wave Velocities from Downhole Measurements and Generalized Lithology

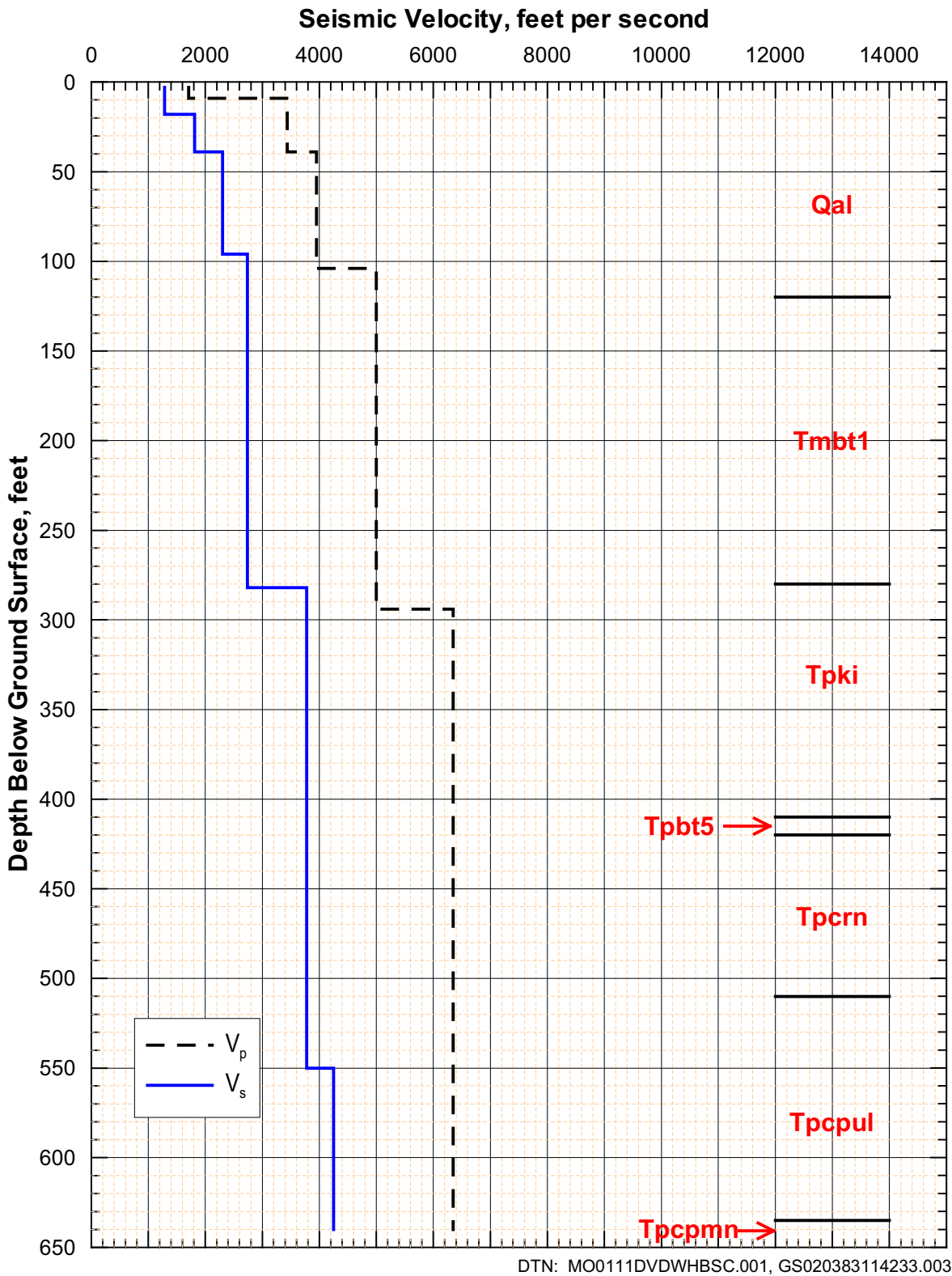
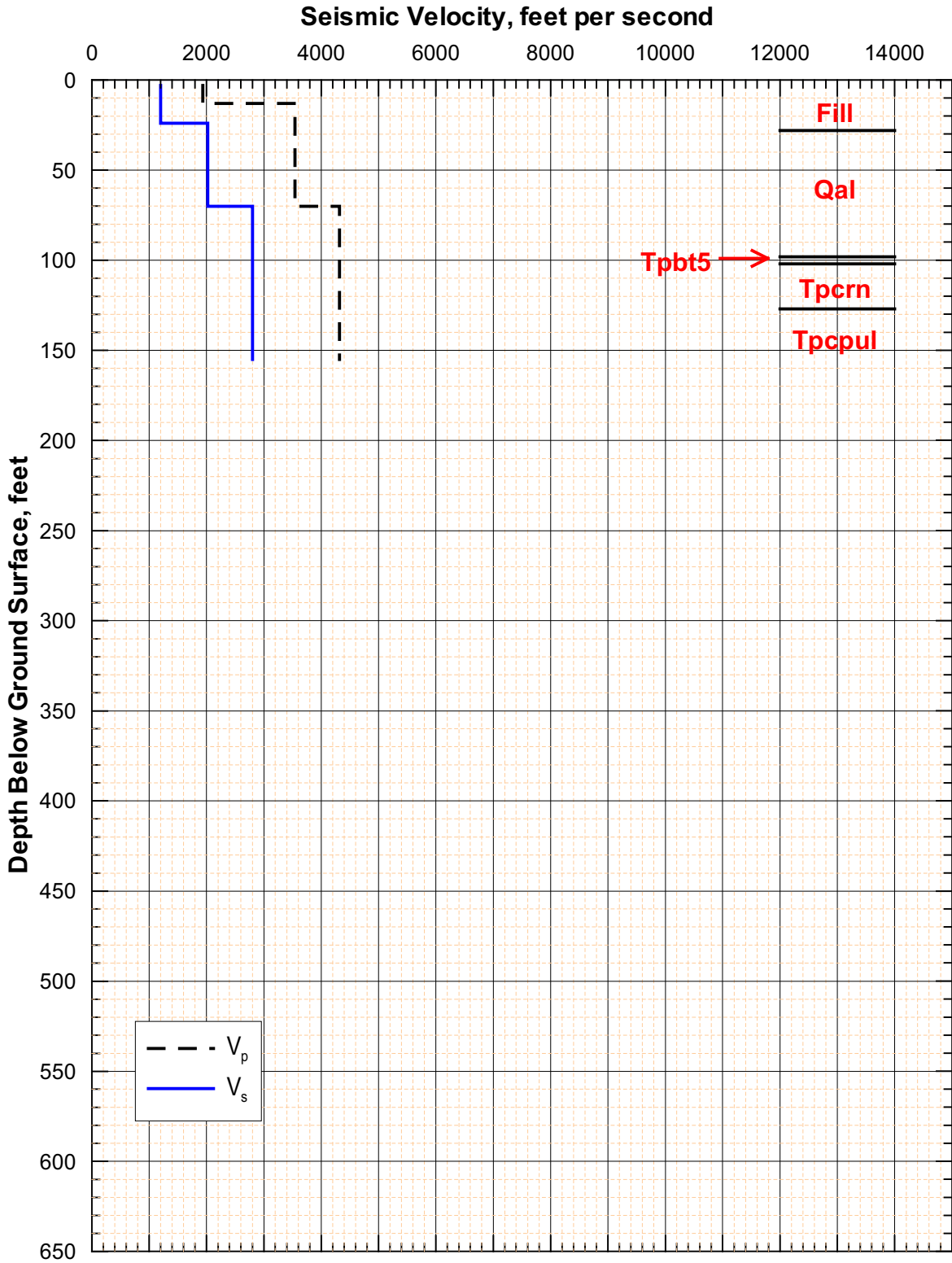
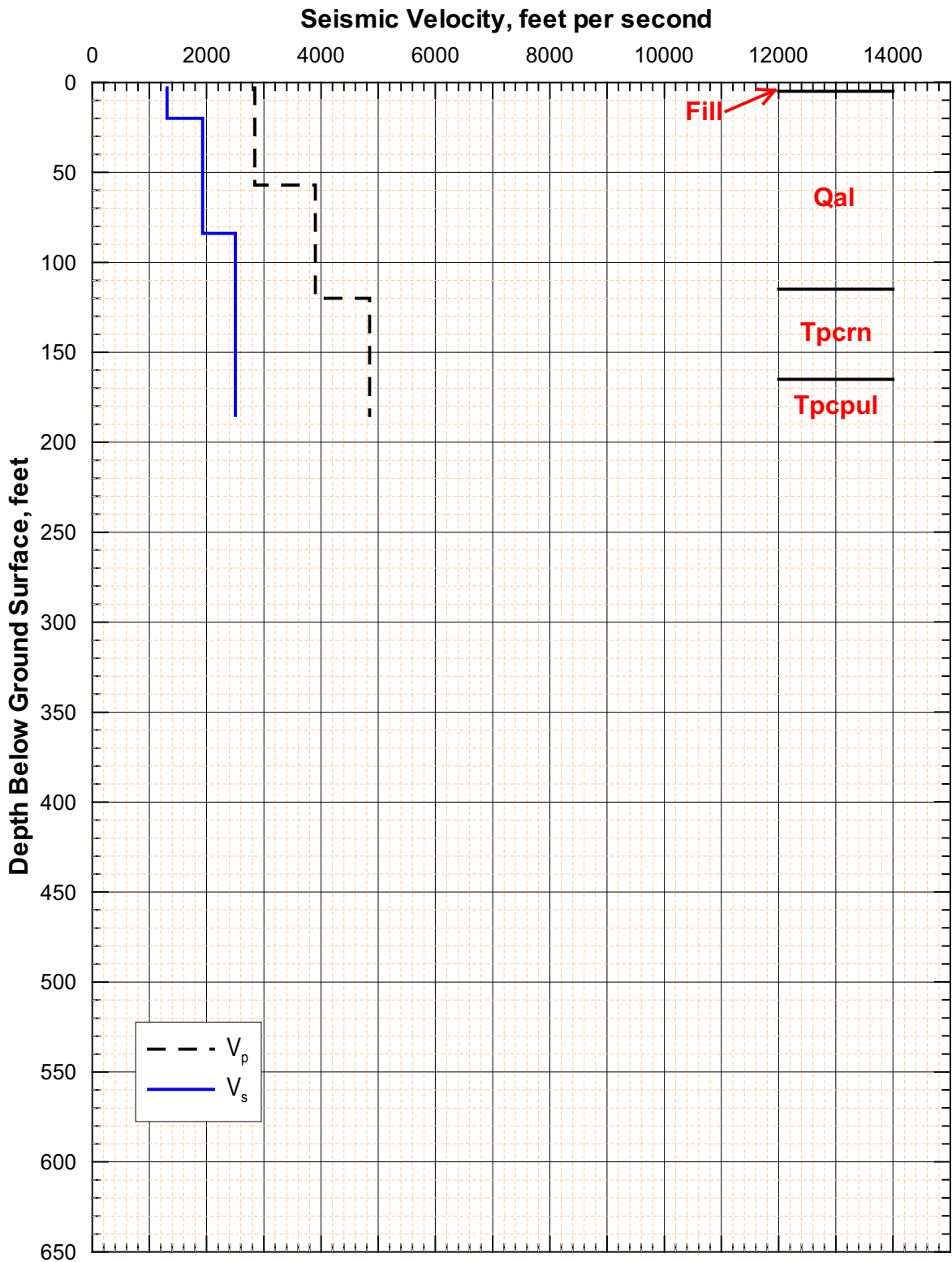


Figure 10. Borehole RF#19 Compression- and Shear-Wave Velocities from Downhole Measurements and Generalized Lithology



DTN: MO0111DVDWHBSC.001, GS020383114233.003

Figure 11. Borehole RF#20 Compression- and Shear-Wave Velocities from Downhole Measurements and Generalized Lithology



DTN: MO0111DVDWHBSC.001, GS020383114233.003

Note: In Assumption 4, Section 5, the contact between the Qal and Tpcrn is assumed to be at a depth of 70 feet. This figure follows the geologic logs in Attachment I.

Figure 12. Borehole RF#21 Compression- and Shear-Wave Velocities from Downhole Measurements and Generalized Lithology

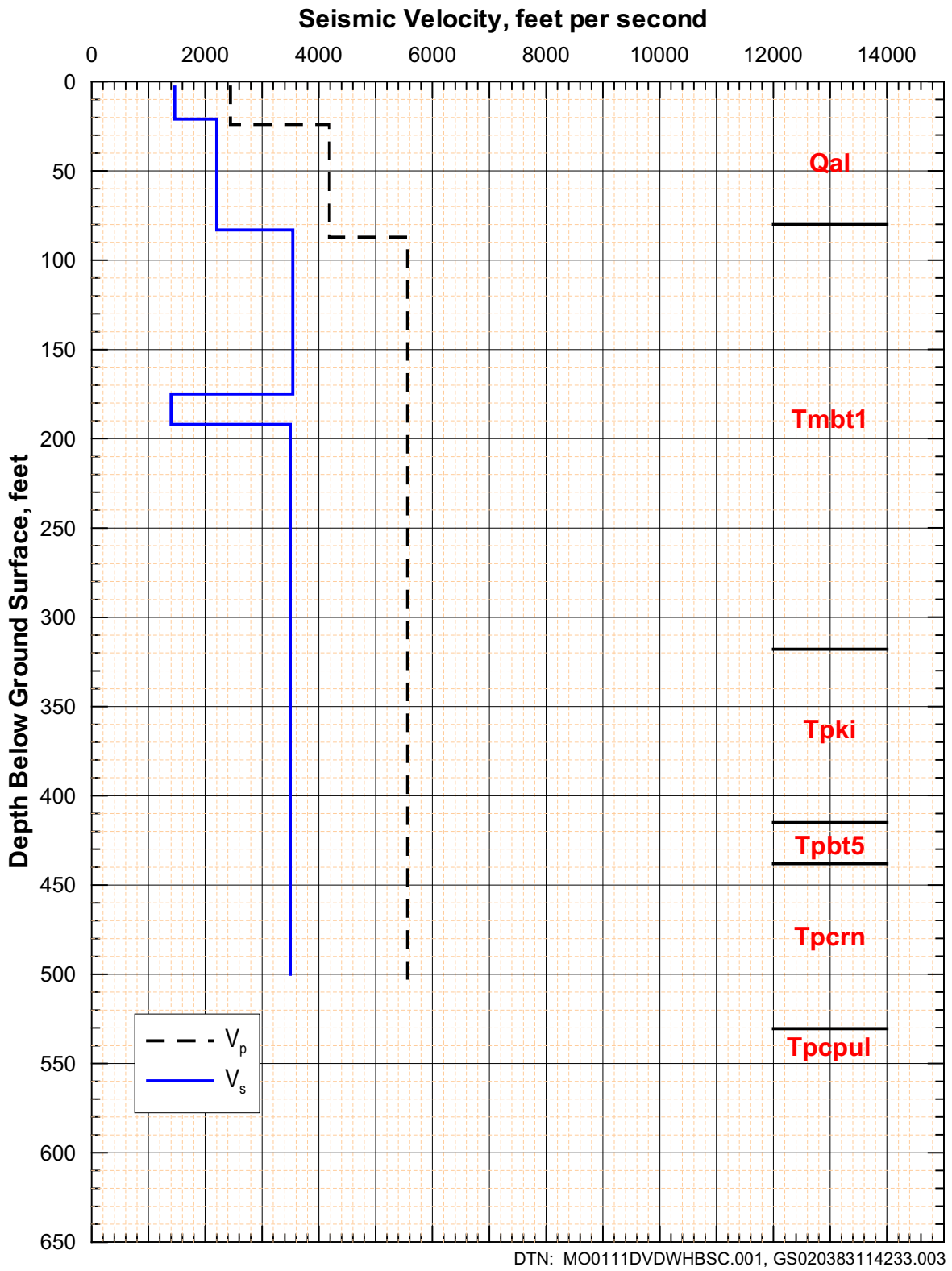


Figure 13. Borehole RF#22 Compression- and Shear-Wave Velocities from Downhole Measurements and Generalized Lithology

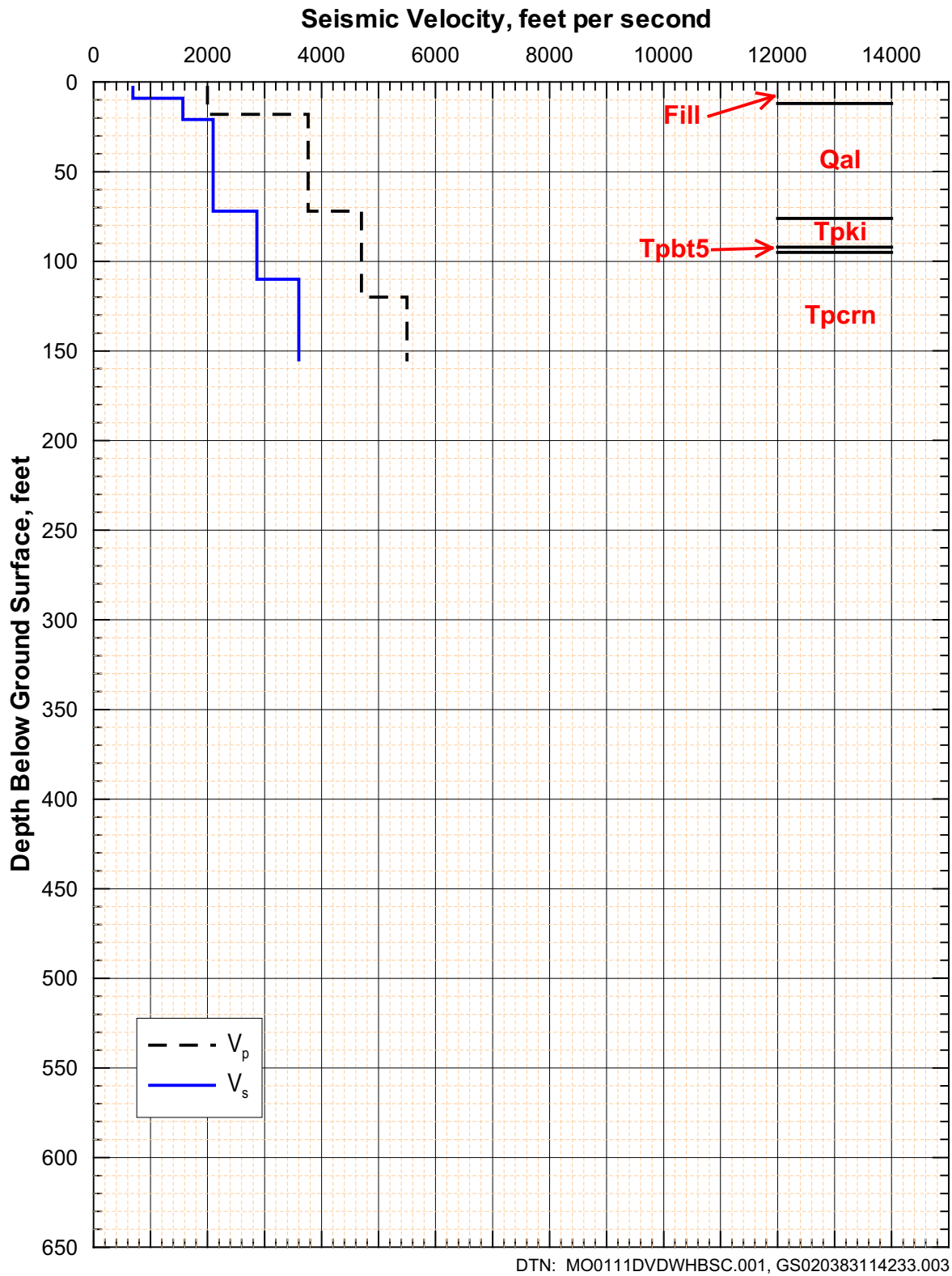
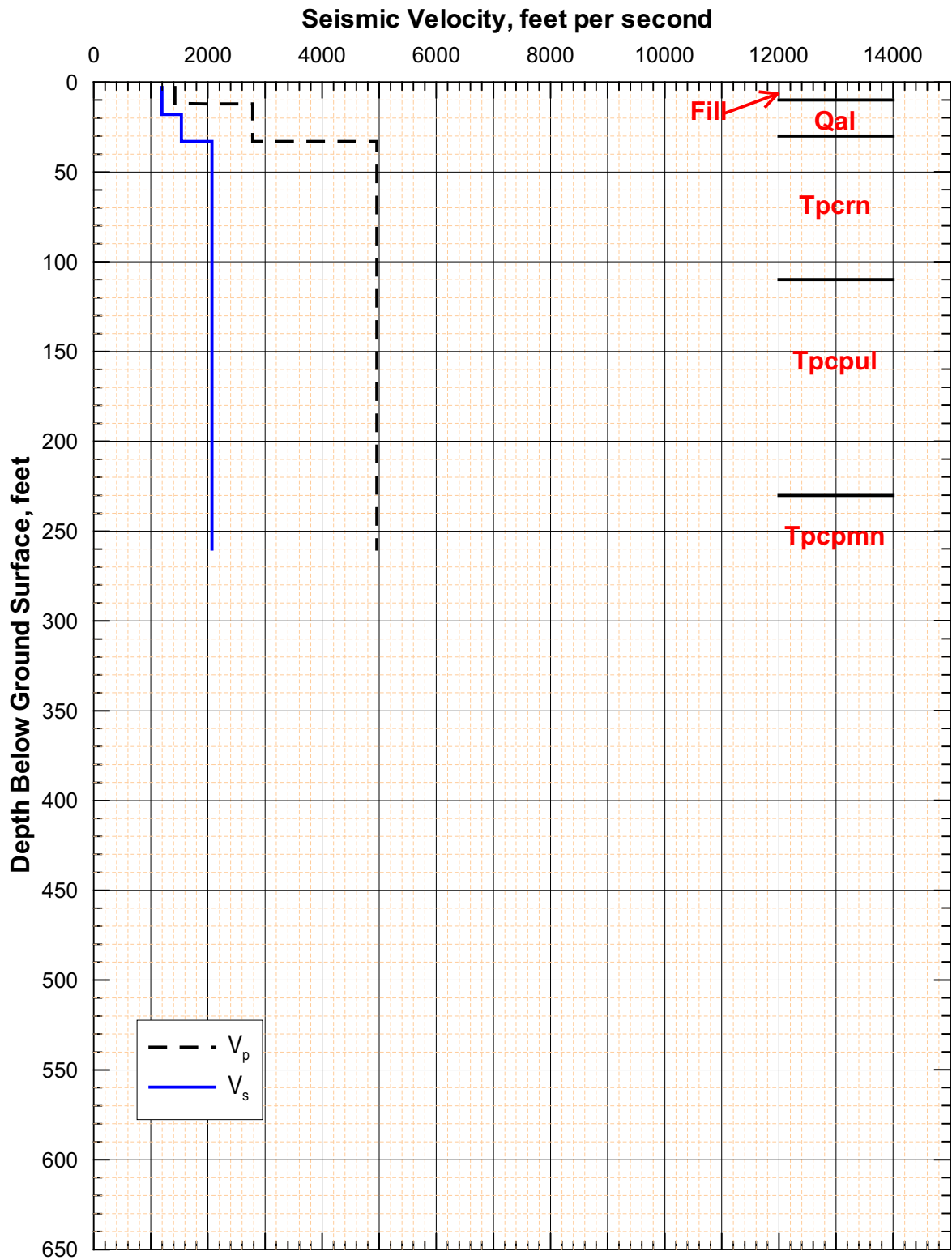


Figure 14. Borehole RF#23 Compression- and Shear-Wave Velocities from Downhole Measurements and Generalized Lithology



DTN: MO0111DVDWHBSC.001, GS020383114233.003

Figure 15. Borehole RF#24 Compression- and Shear-Wave Velocities from Downhole Measurements and Generalized Lithology

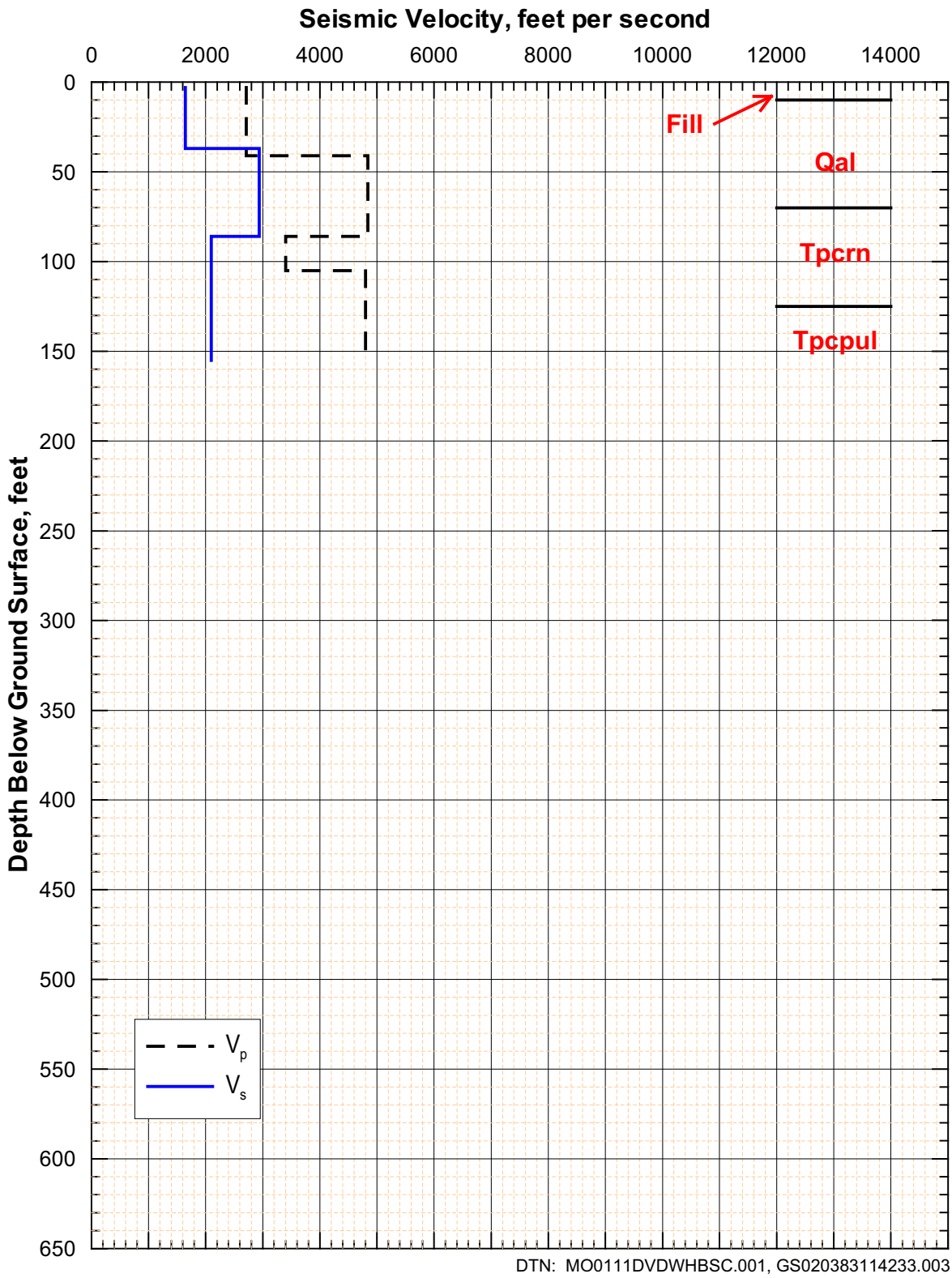


Figure 16. Borehole RF#25 Compression- and Shear-Wave Velocities from Downhole Measurements and Generalized Lithology

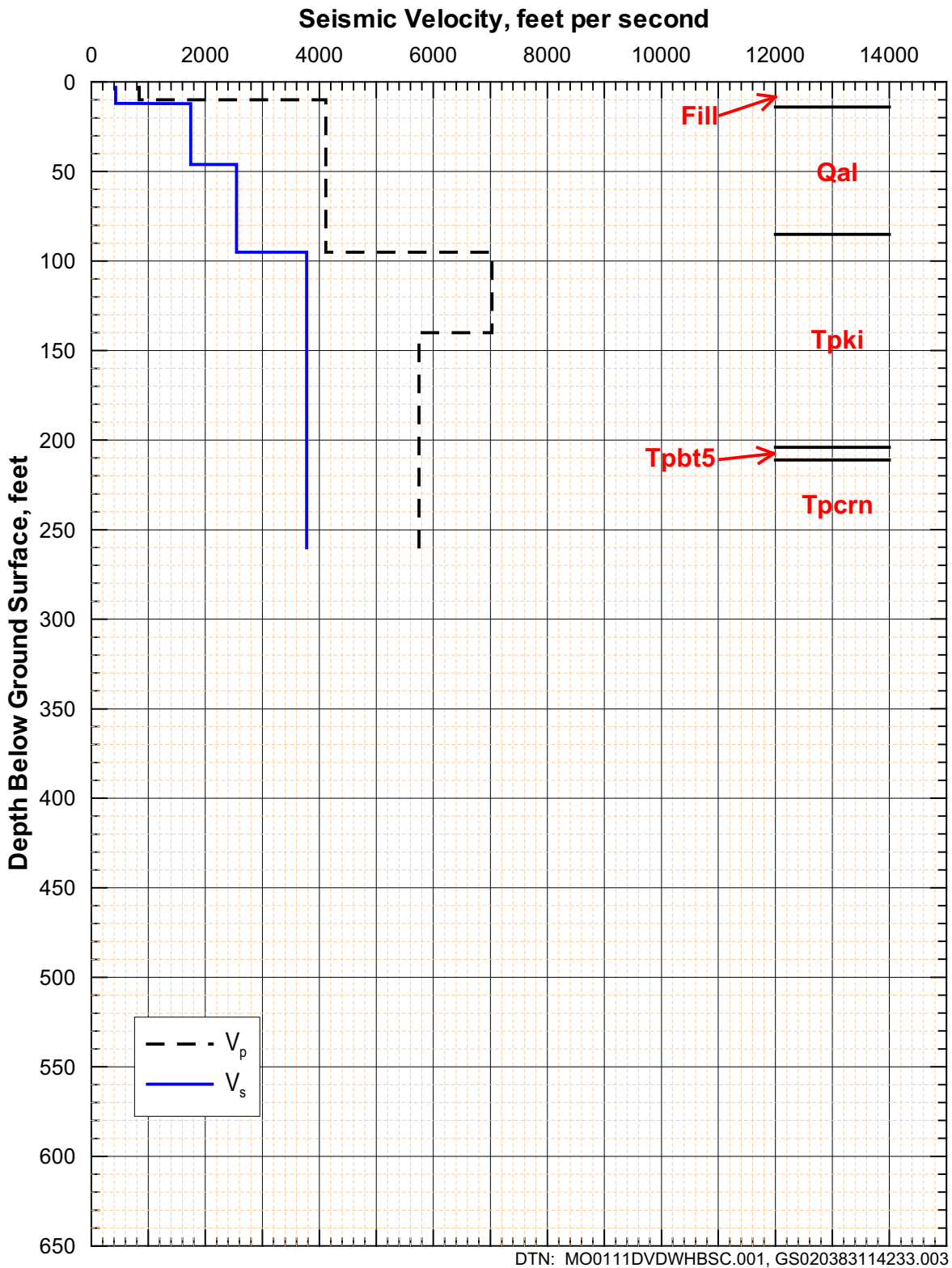
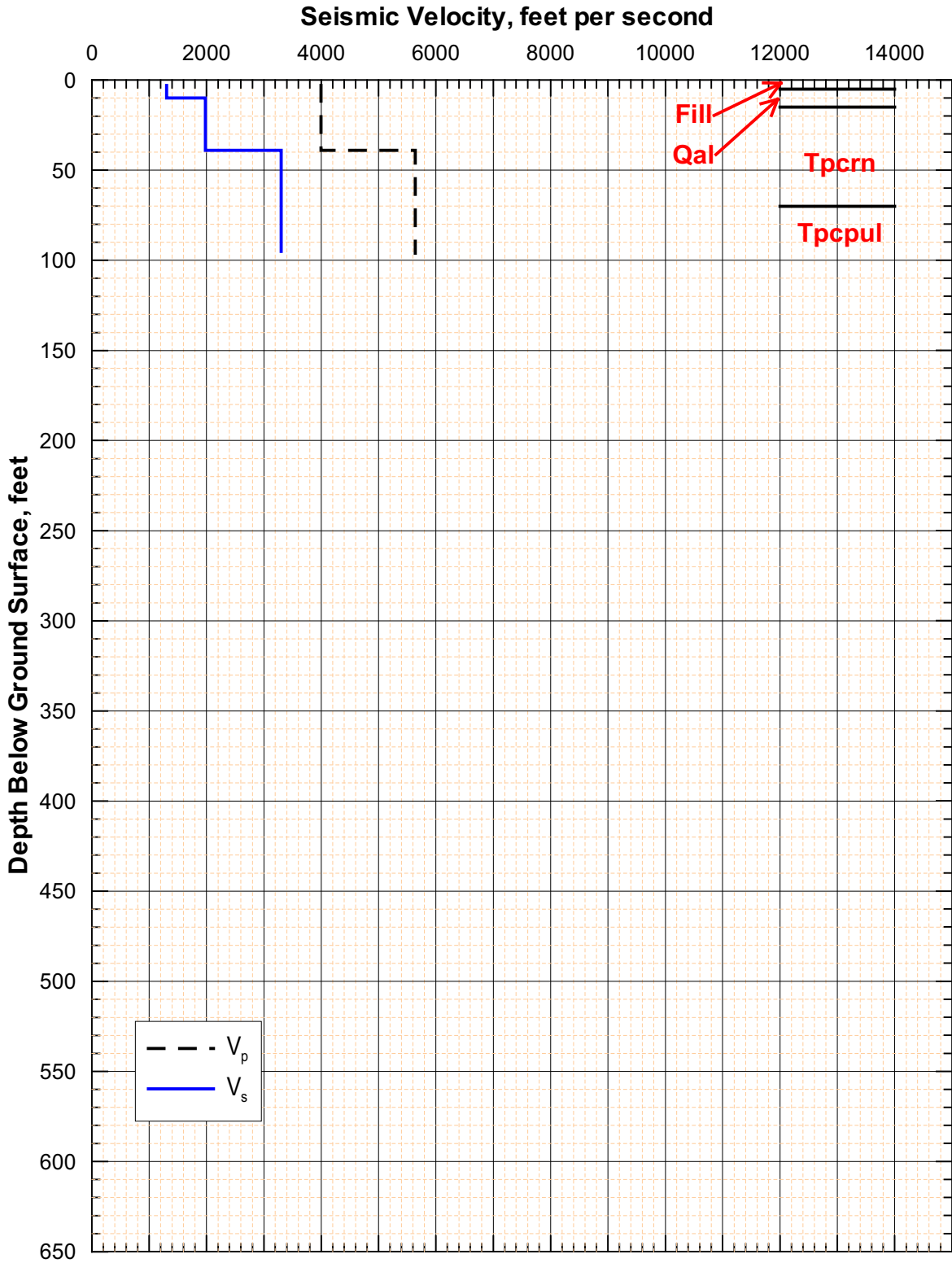


Figure 17. Borehole RF#26 Compression- and Shear-Wave Velocities from Downhole Measurements and Generalized Lithology



DTN: MO0111DVDWHBSC.001, GS020383114233.003

Figure 18. Borehole RF#28 Compression- and Shear-Wave Velocities from Downhole Measurements and Generalized Lithology

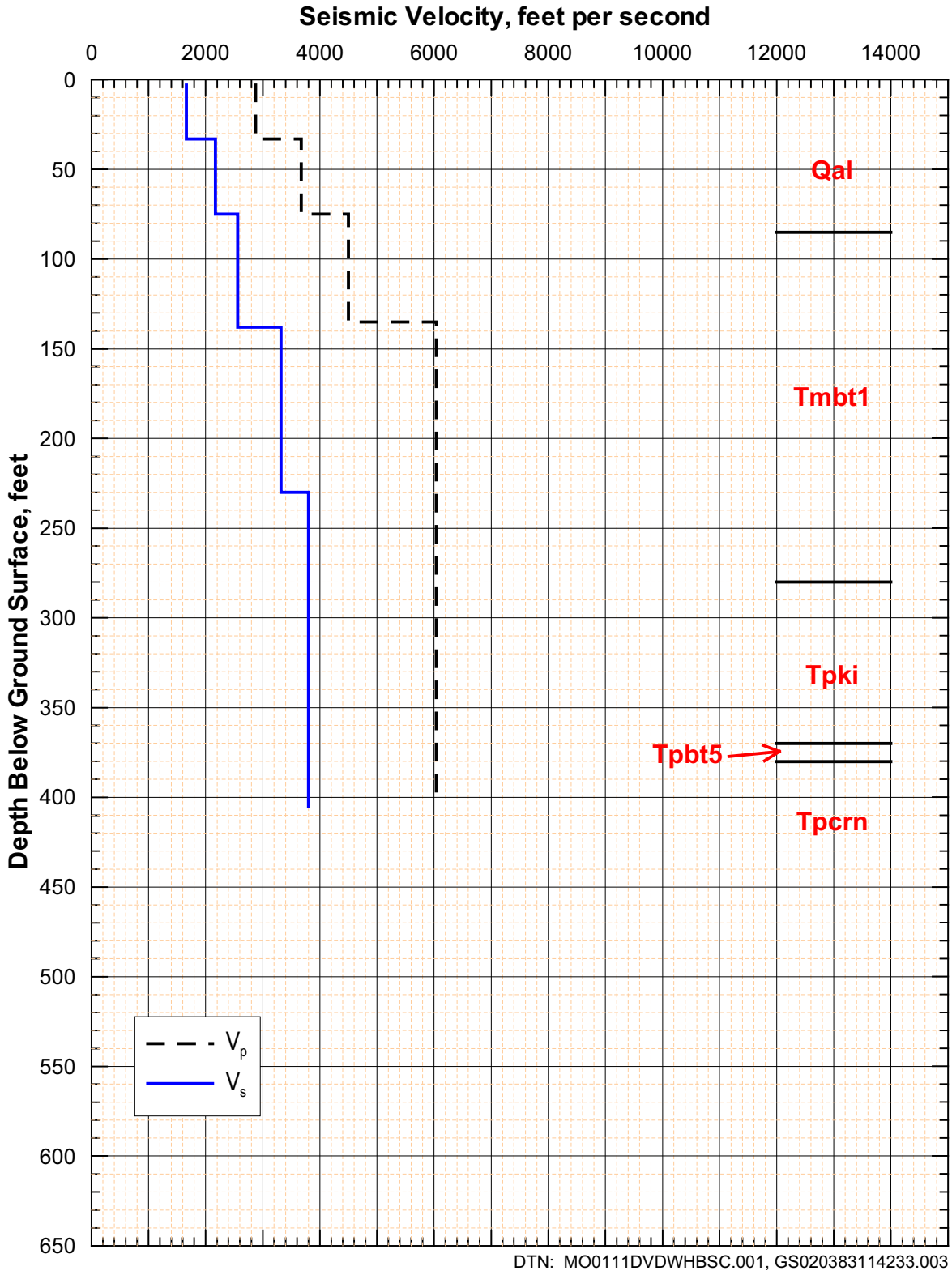


Figure 19. Borehole RF#29 Compression- and Shear-Wave Velocities from Downhole Measurements and Generalized Lithology

taken from the borehole logs (Tables 4 and 5). A discussion of the correlation of the velocity layers with the lithology is discussed in Section 6.7.

Examination and comparison of the tabulated values of shear- and compression-wave velocities reveals that the depths to the interfaces between layers based on the respective velocities are not always coincident, *i.e.*, the shear- and compression-wave boundaries may not agree. This may be due to the possibility that the shear- and compression-wave signals do not always follow the same path from source to receiver.

The presence of multiple signal pathways is suggested in GEOVision's compression-wave data from borehole RF#13 between 215 to 230 ft, which result in trend lines that do not "connect" at the correct depth (Figure VI-1). It can be observed that there are four data points from 215 to 225 ft that have very nearly the same arrival times. These data points depart from the trend line by a maximum of approximately 3 ms, compared to the typical difference, which is on the order of 0.5 ms.

There is an apparent low-shear-wave-velocity zone in borehole RF#22 from a depth of 175 to 192 ft, but there is no corresponding decrease in the compression-wave velocity over this depth range (Figure 13). This anomaly suggests that the low shear-wave velocity may be an artifact of different travel paths that in turn, is probably a manifestation of the complex geology associated with the graben in which the borehole is located, as discussed in Section 6.6.2.

Figure 4 compares the velocities obtained by Redpath Geophysics and GEOVision in borehole RF#13. The shear-wave velocities are similar for much of the hole. The differences in depths to the major velocity changes are in general agreement. Likewise, the compression-wave velocity profiles are similar except the velocity contrast at about 220 to 230 ft depth is much stronger based on the Redpath Geophysics data and interpretations. The contrasts in both shear- and compression-wave velocities were also observed in the downhole measurements of borehole RF#13 conducted in 1998 (DTN: MO0001SEPRADSD.000; CRWMS M&O 1999b, Appendix N) (see also Figures VII-1 and VIII-1, introduced in Section 6.2.6).

On Figures 20 and 21, the velocities for all holes are shown. Overall, the shear-wave velocities increase with depth in the top 100 ft. The variability in velocities spans a range of $\pm 1,000$ ft/s except at the velocity contrasts observed in boreholes RF#13 and RF#15 at a depth of about 230 ft, at 305 ft in borehole RF#14, and 375 ft in borehole RF#16 (Figure 20). Similar trends are observed in the compression-wave profiles (Figure 21). Variability is smaller for the compression-wave velocities except for the strong contrasts observed in some of the boreholes, *e.g.*, at a depth of 130 and 210 ft in borehole RF#15.

The nature of the sharp velocity contrasts is perplexing. At borehole RF#13, the step in both compression- and shear-wave velocities appears to coincide with the top of the unit Tpcpul (upper lithophysal) or Tpcpmn (middle non-lithophysal) (Figure 4). However, the borehole RF#15 profile shows a sharp increase in the compression-wave velocity and small increase in the shear-wave velocity occurring in the middle of Tpcpul (Figure 6). Borehole RF#14 shows a compression-wave velocity contrast the middle of Tpcpmn but no such contrast is observed in shear-wave velocity (Figure 5). A contrast also is observed within Tpcpmn in borehole RF#16 (Figure 7).

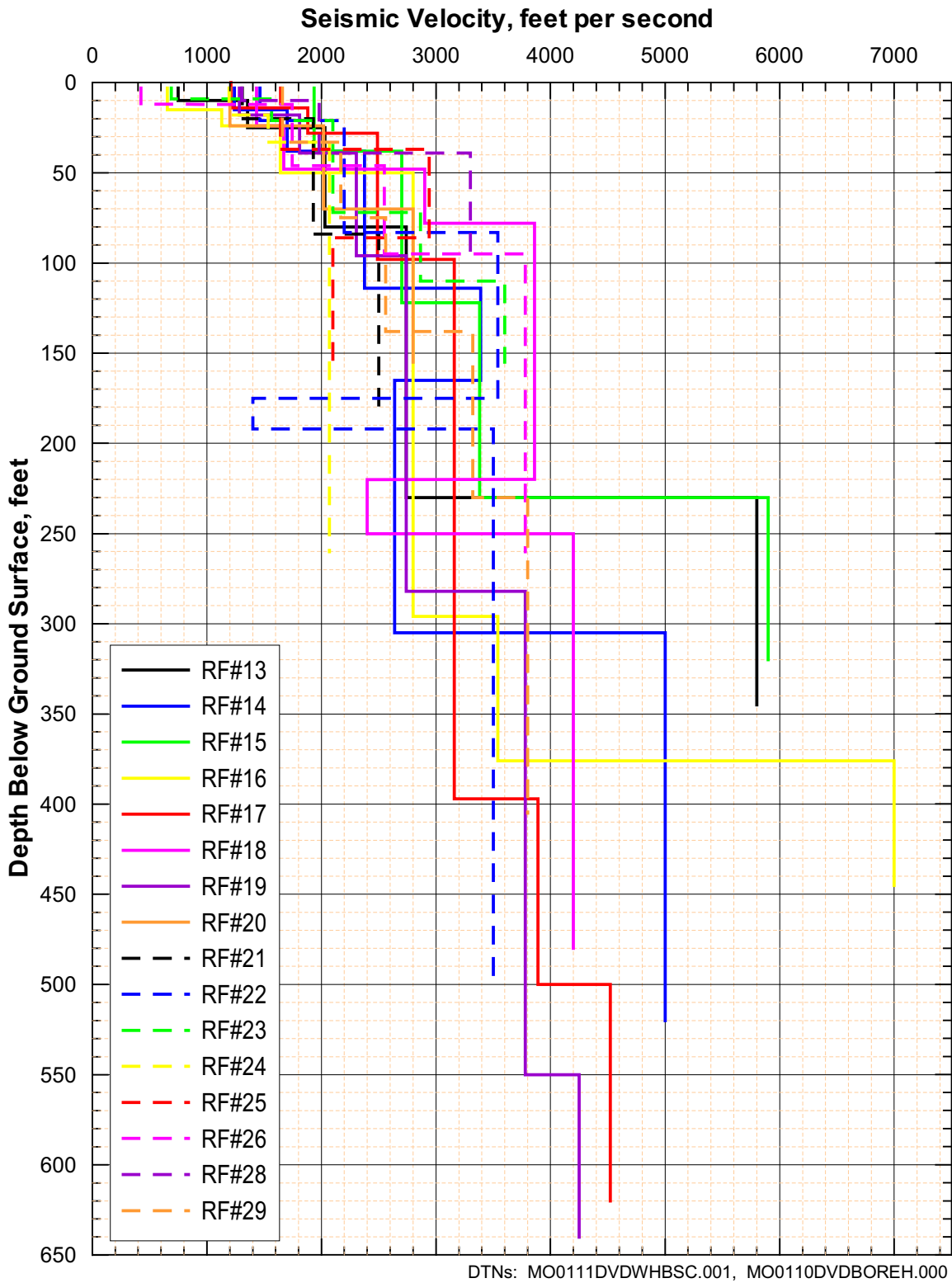


Figure 20. Shear-Wave Velocities from Downhole Measurements in the WHB Area

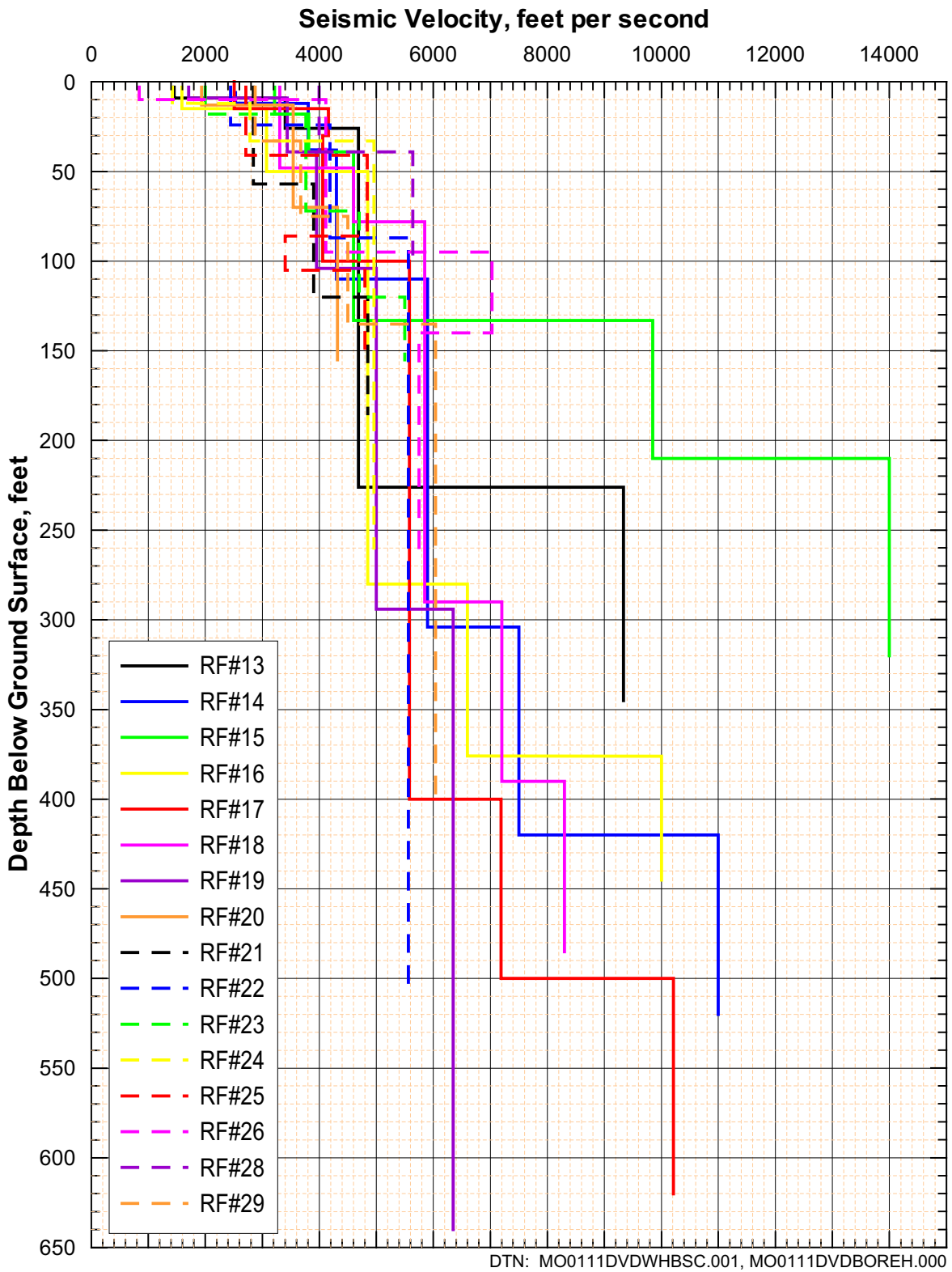


Figure 21. Compression-Wave Velocities from Downhole Measurements in the WHB Area

The nature of the sharp velocity contrasts is perplexing. At borehole RF#13, the step in both compression- and shear-wave velocities appears to coincide with the top of the Tpcpul (upper lithophysal) or Tpcpmn (middle non-lithophysal) unit (Figure 4). However, the borehole RF#15 profile shows a sharp increase in the compression-wave velocity and small increase in the shear-wave velocity occurring in the middle of the Tpcpul (Figure 6). Borehole RF#14 shows a compression-wave velocity contrast the middle of the Tpcpmn, but no such contrast is observed in shear-wave velocity (Figure 5). A contrast, also within the Tpcpmn, is observed in borehole RF#16 (Figure 7).

Figures 22 and 23 show the calculated mean, median, and mean plus and minus one standard deviation (σ) velocity profiles at the WHB. Also shown is the WHB shear-wave velocity profile that was based on borehole RF#13 and used in the preliminary seismic design ground motion calculations in 1999 (Luebbers 2000, page 207). The 1999 WHB shear-wave velocity profile is generally within the \pm one standard deviation profiles except at and below the 245 ft-deep velocity contrast. If mean and median profiles are calculated for the shear-wave velocity profiles without the borehole RF#13 and RF#15 data, the variability decreases significantly at depths of 250 to 350 feet but the mean and median profiles do not differ significantly from those based on all of the boreholes (Figures 22 and 24).

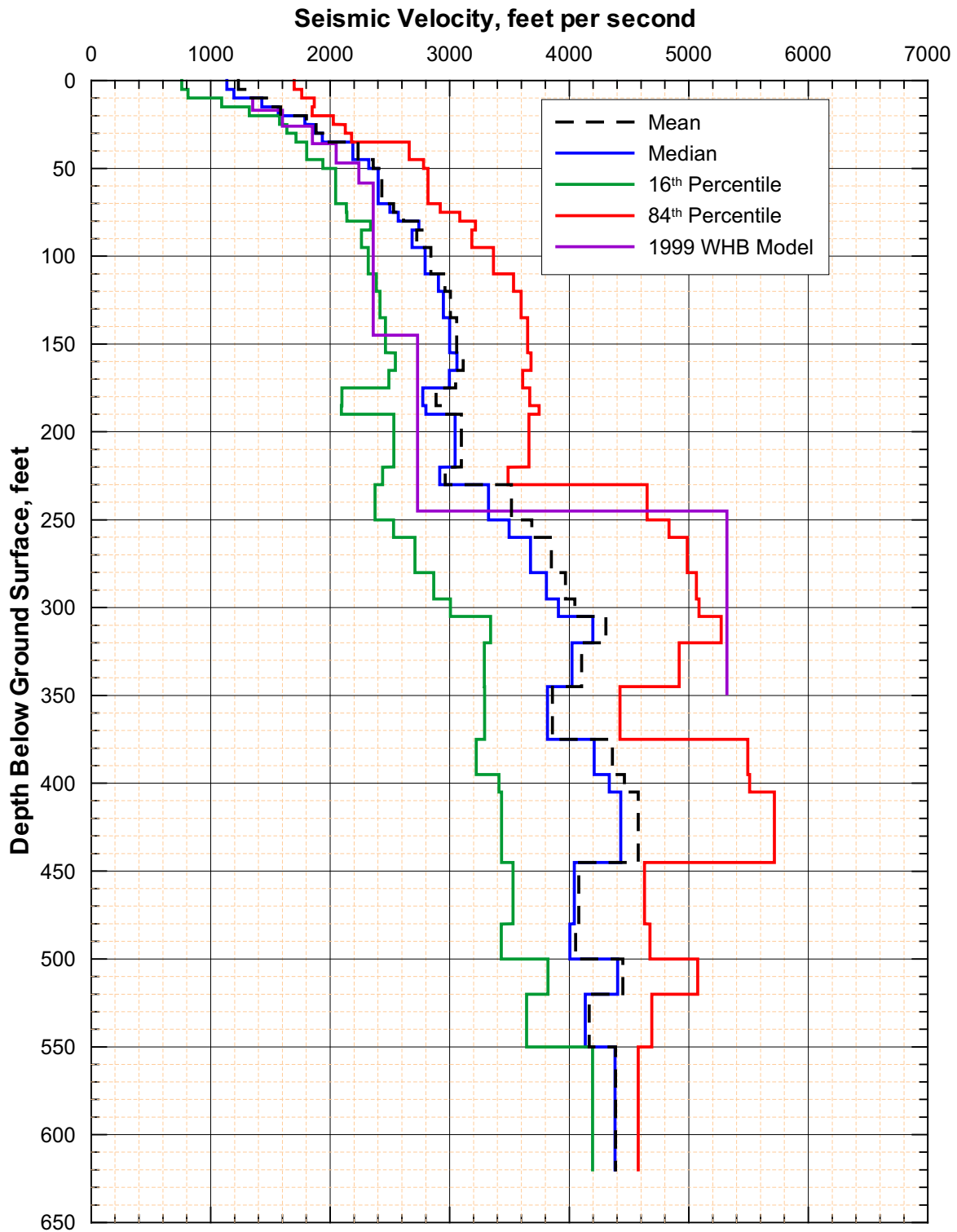
A significant structural feature at the WHB is a north-northwest-striking normal fault in the northeast corner of the pad (Section 6.6.2), referred to on Figure 3 as the Exile Hill fault splay. Because there is a maximum amount of throw of about 300 ft on the fault, the mean, median, and mean plus and minus one standard deviation velocity profiles on the upthrown and downthrown sides of the fault were computed and compared on Figures 25 to 27. Boreholes on the downthrown side were RF#14, 17, 19, 22, and 29 (Figure 3). Comparison of the median profiles indicates differences in velocities consistent with the existence of a fault between the two sets of velocity profiles. At a depth of about 230 ft, the shear-wave velocities increase significantly on the upthrown side (Figure 27). This increase corresponds to the sharp velocity contrasts observed in boreholes RF#13 to 16, all located on the upthrown side.

Where both shear-wave and compression-wave velocity are known for the same depth interval, the value of Poisson's ratio, ν , can be calculated using the equation from the theory of elasticity for homogeneous, isotropic elastic materials:

$$\nu = (R^2 - 2) / [2(R^2 - 1)] \quad (\text{Eq. 4})$$

where $R = v_p/v_s$ (Wilson et al. 1978, page 1019). Note that this relationship between R and ν is such that for v_p/v_s less than about 0.4 (which would include the velocity ratios typically measured in dry soils), a relatively small error in R leads to a large error in ν (Wilson et al. 1978, pages 1020-21).

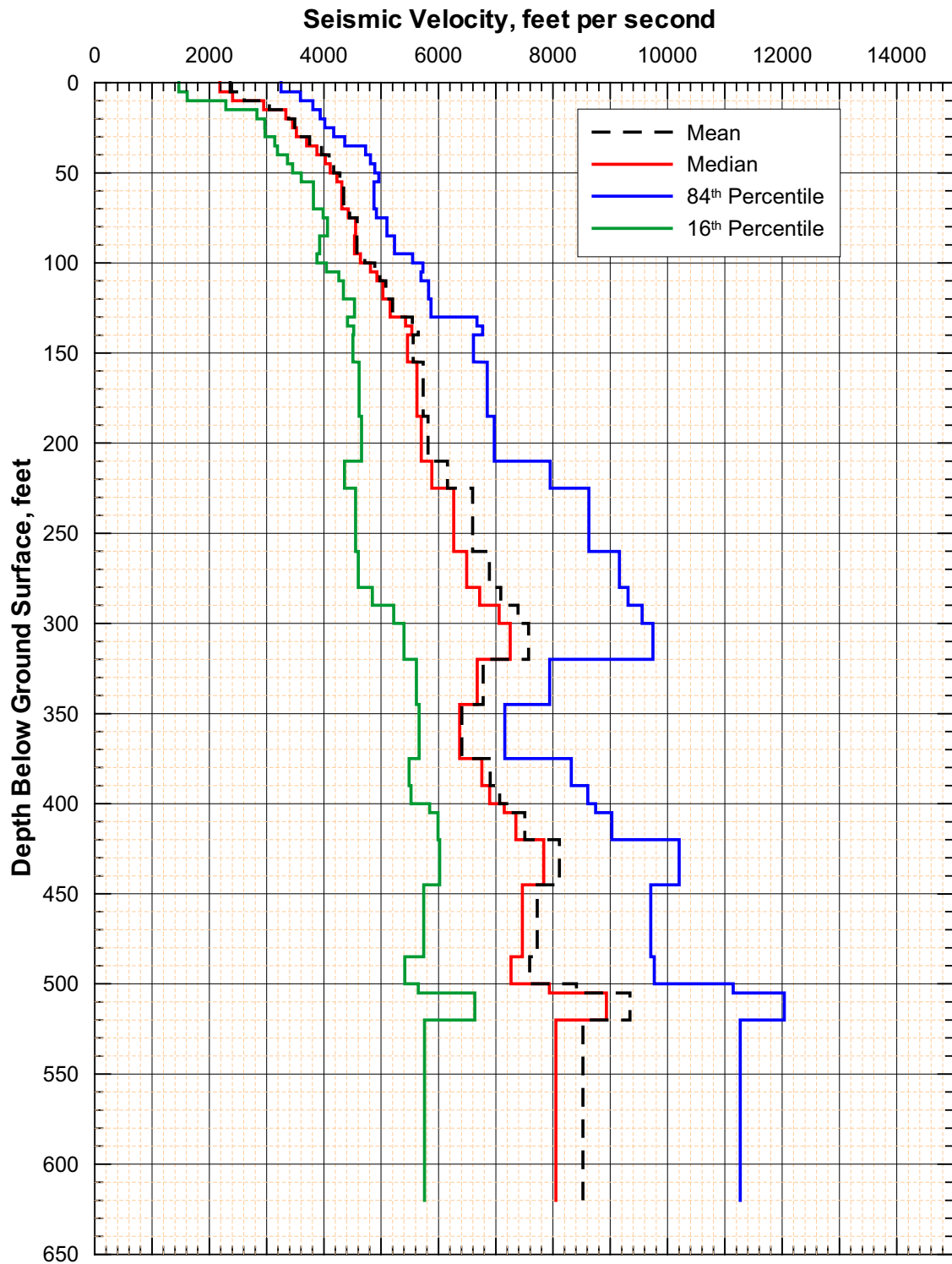
Table 10 and Figure 28 show the calculated values of Poisson's ratios. In general, a range of values from 0.15 to 0.40, typical of most geologic materials, is indicated for most of the velocity layers. Negative values (boreholes RF#18, 19, 23, and 24) indicate that the compression-wave velocities may be low relative to the shear-wave velocity. This phenomenon has been observed at other sites at very shallow depths with no plausible physical basis.



Source: For 1999 WHB Model is Luebbers (2000, page 207)

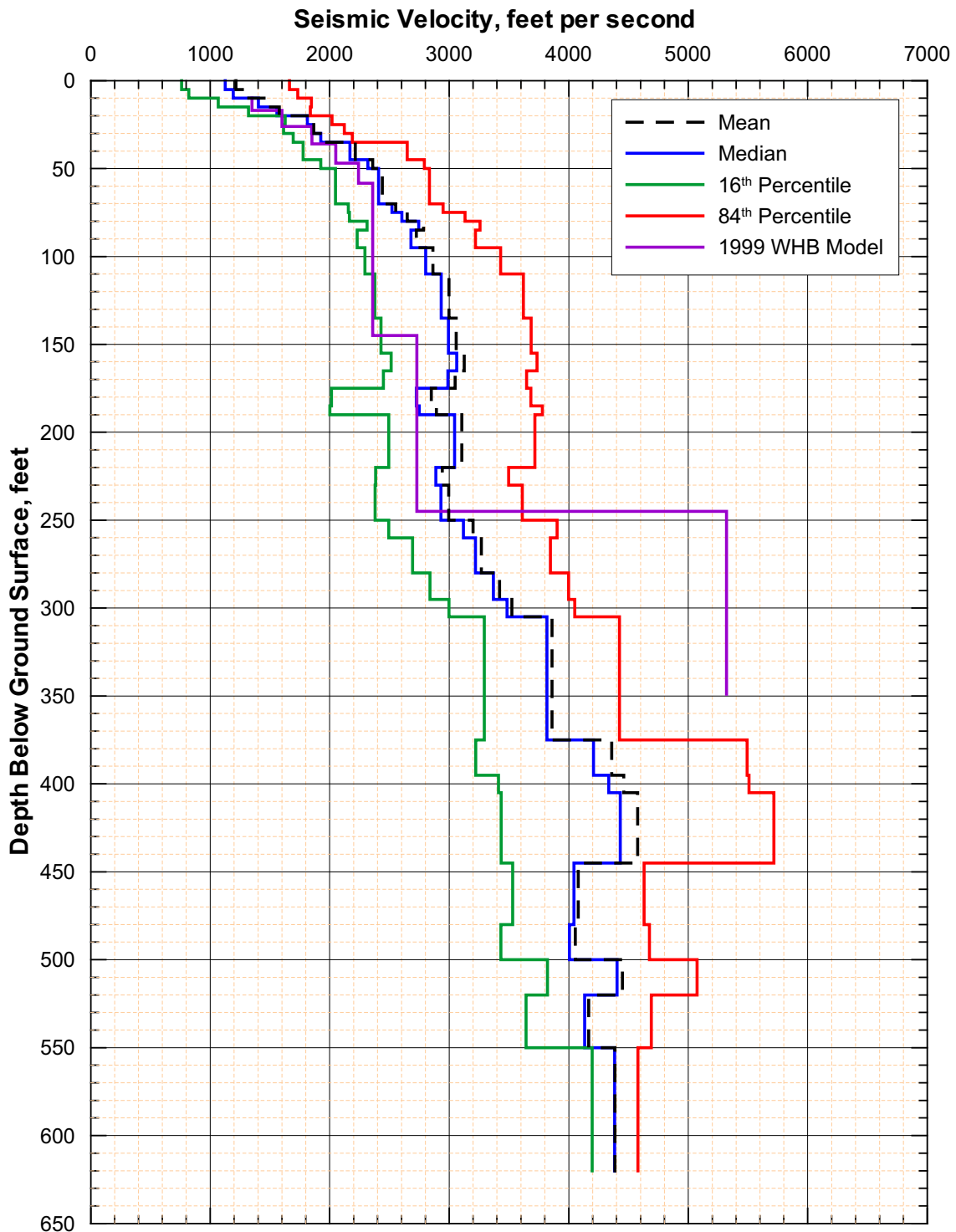
Note: These statistics have been calculated for illustrative purposes only. Final statistics calculated for use in the forthcoming scientific analysis entitled *Development of Seismic Design Input Ground Motions for a Geologic Repository at Yucca Mountain* will be submitted to the TDMS.

Figure 22. Statistical Analyses of Shear-Wave Velocities from Downhole Measurements in the WHB Area



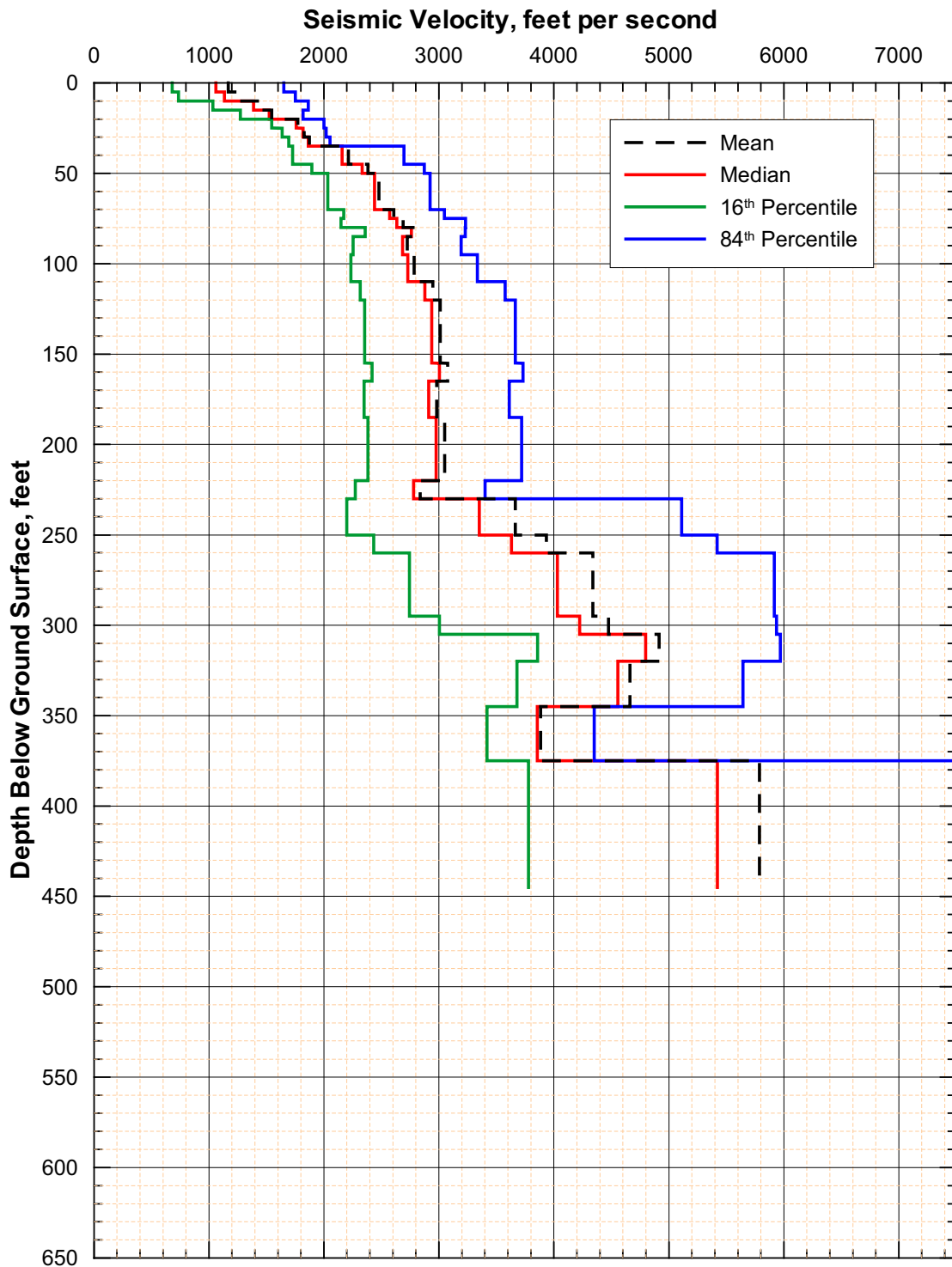
Note: These statistics have been calculated for illustrative purposes only. Final statistics calculated for use in the forthcoming scientific analysis entitled *Development of Seismic Design Input Ground Motions for a Geologic Repository at Yucca Mountain* will be submitted to the TDMS.

Figure 23. Statistical Analyses of Compression-Wave Velocities from Downhole Measurements in the WHB Area



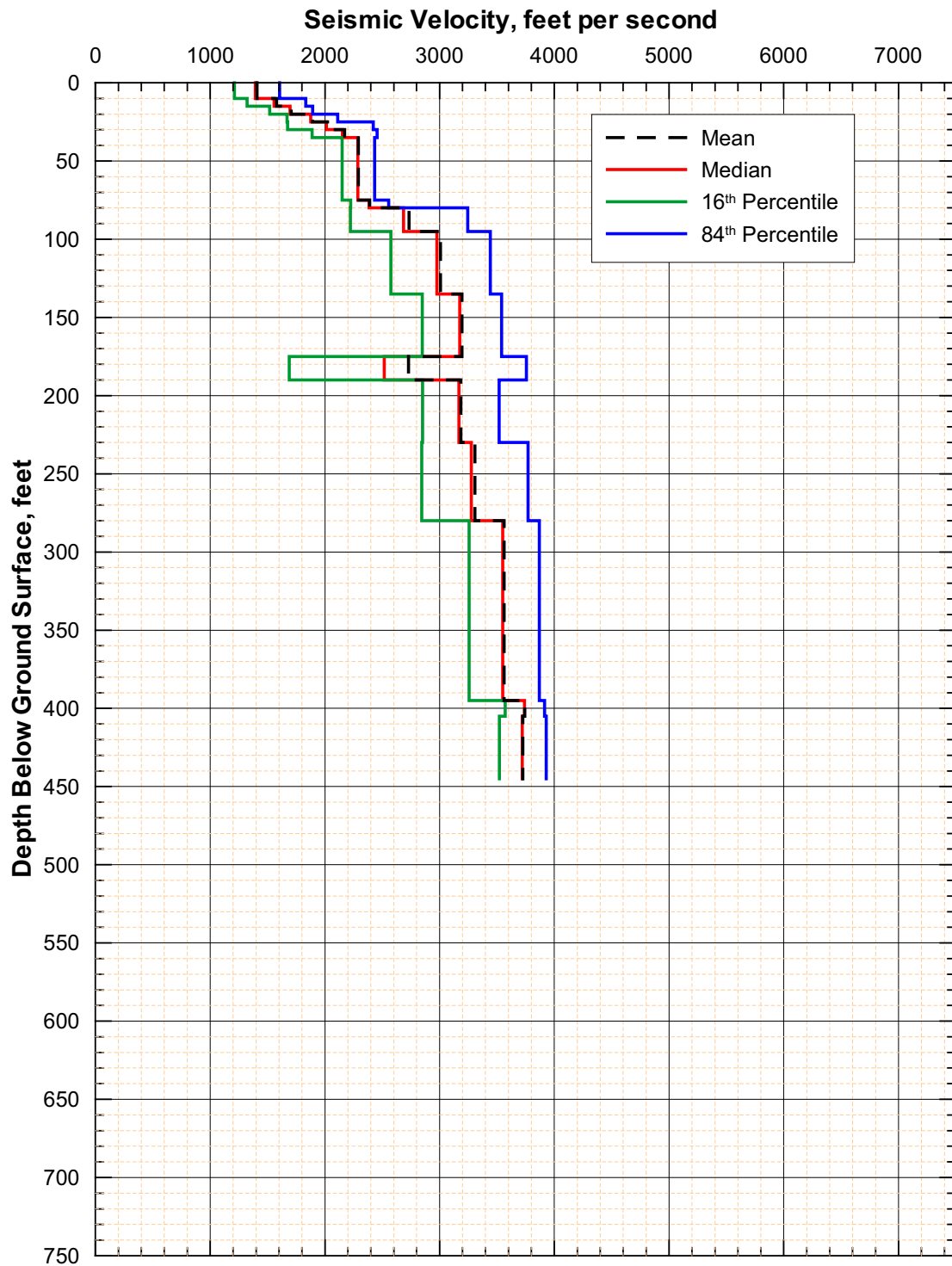
Note: These statistics have been calculated for illustrative purposes only. Final statistics calculated for use in the forthcoming scientific analysis entitled *Development of Seismic Design Input Ground Motions for a Geologic Repository at Yucca Mountain* will be submitted to the TDMS.

Figure 24. Statistical Analyses of Shear-Wave Velocities from Downhole Measurements in the WHB Area (Without RF#13 and RF#15)



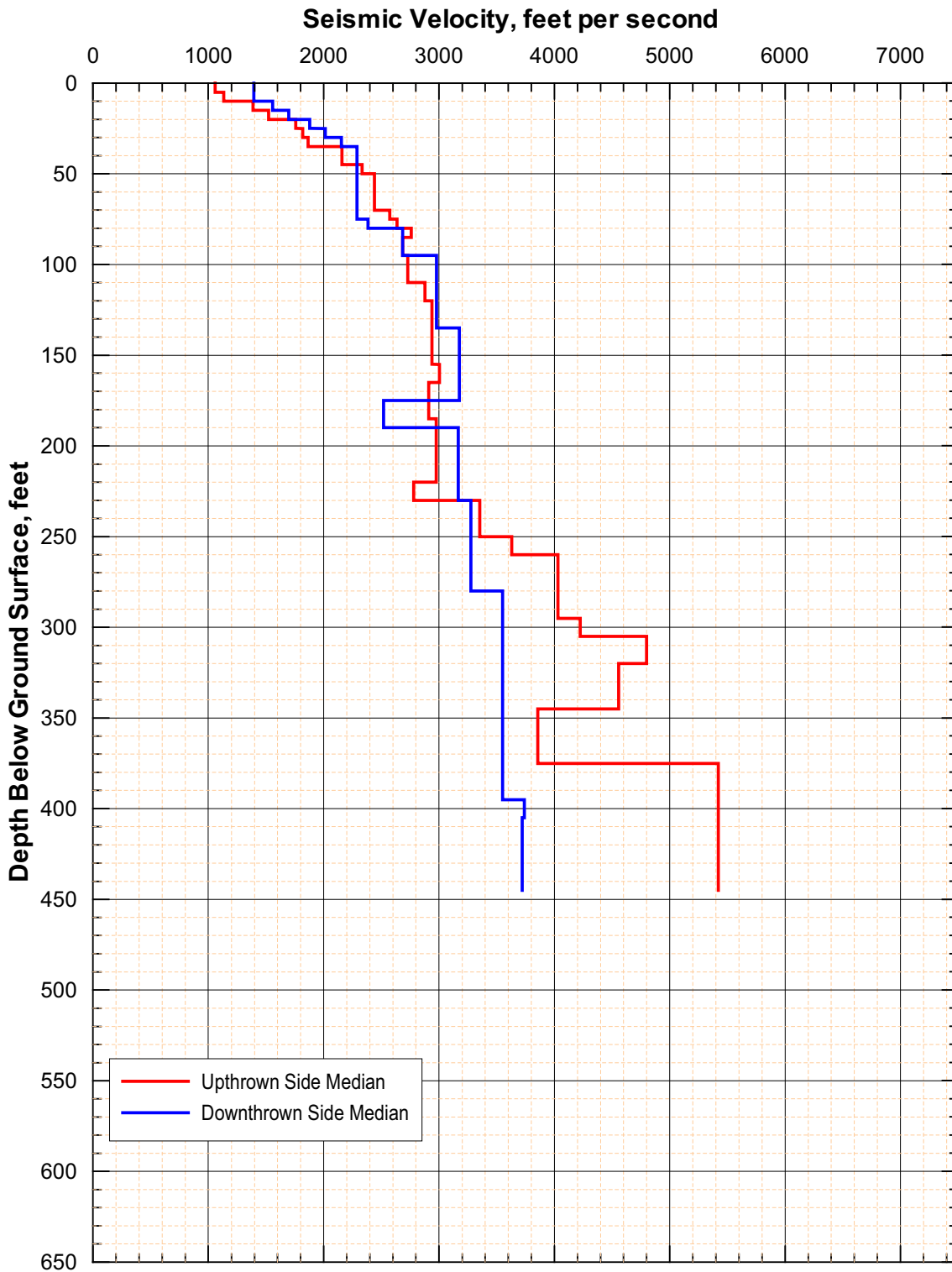
Note: These statistics have been calculated for illustrative purposes only. Final statistics calculated for use in the forthcoming scientific analysis entitled *Development of Seismic Design Input Ground Motions for a Geologic Repository at Yucca Mountain* will be submitted to the TDMS.

Figure 25. Statistical Analyses of Shear-Wave Velocities from Downhole Measurements in the WHB Area, Uphrown Side of the Exile Hill Fault Splay



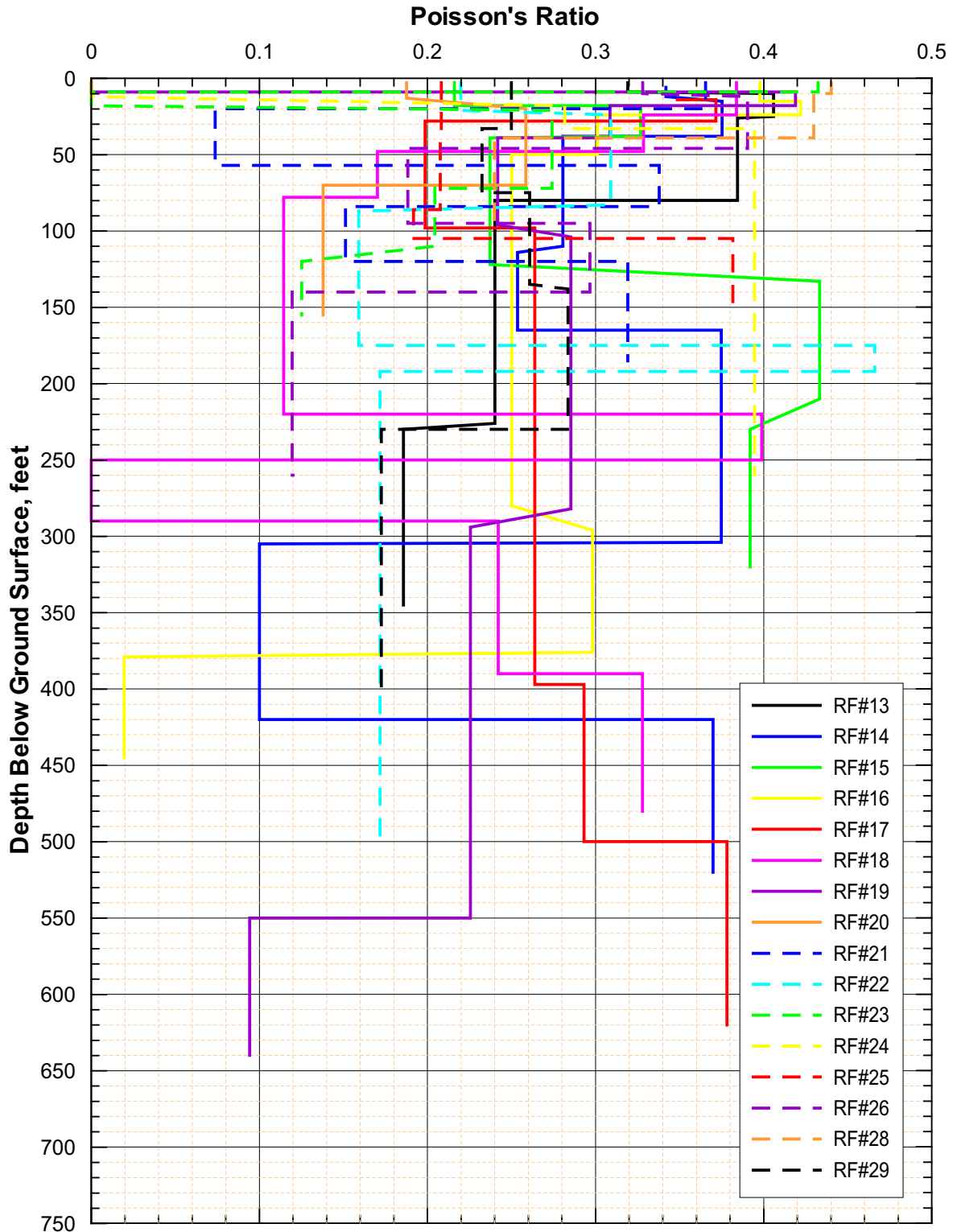
Note: These statistics have been calculated for illustrative purposes only. Final statistics calculated for use in the forthcoming scientific analysis entitled *Development of Seismic Design Input Ground Motions for a Geologic Repository at Yucca Mountain* will be submitted to the TDMS.

Figure 26. Statistical Analyses of Shear-Wave Velocities from Downhole Measurements in the WHB Area, Downthrown Side of the Exile Hill Fault Splay



Note: These statistics have been calculated for illustrative purposes only. Final statistics calculated for use in the forthcoming scientific analysis entitled *Development of Seismic Design Input Ground Motions for a Geologic Repository at Yucca Mountain* will be submitted to the TDMS.

Figure 27. Comparison of Downhole Shear-Wave Velocities Across the Exile Hill Fault Splay



Note: These Poisson's ratios have been calculated for illustrative purposes only. Final values of Poisson's ratio calculated for use in the forthcoming scientific analysis entitled *Development of Seismic Design Input Ground Motions for a Geologic Repository at Yucca Mountain* will be submitted to the TDMS.

Figure 28. Poisson's Ratios from Downhole Measurements in the WHB Area

Table 10. Poisson's Ratios from Downhole Measurements in the WHB Area

RF#13 (all boreholes surveyed by Redpath Geophysics unless otherwise indicated)	Depth Range (ft)	Poisson's Ratio
	3 - 9	0.32
	10 - 25	0.41
	26 - 80	0.38
	80 - 226	0.24
	230 - 345	0.19
RF#13 (Geovision)	Depth Range (ft)	Poisson's Ratio
	0 - 15	0.32
	15 - 36	0.30
	36 - 99	0.18
	99 - 215	0.25
	215 - 345	0.25
RF#14	Depth Range (ft)	Poisson's Ratio
	6 - 12	0.34
	15 - 38	0.38
	38 - 110	0.28
	114 - 165	0.25
	165 - 304	0.37
	305 - 420	0.10
	420 - 520	0.37
RF#15	Depth Range (ft)	Poisson's Ratio
	3 - 18	0.22
	18 - 38	0.33
	39 - 122	0.24
	133 - 210	0.43
	230 - 320	0.39
RF#16	Depth Range (ft)	Poisson's Ratio
	3 - 15	0.40
	15 - 24	0.42
	24 - 50	0.30
	50 - 280	0.25
	296 - 376	0.30
	376 - 445	0.02
RF#17 (Geovision)	Depth Range (ft)	Poisson's Ratio
	0 - 15	0.35
	15 - 30	0.37
	30 - 100	0.20
	100 - 400	0.26
	400 - 500	0.29
	500 - 620	0.38
RF#18	Depth Range (ft)	Poisson's Ratio
	3 - 24	0.38
	24 - 48	0.33
	48 - 78	0.17
	78 - 220	0.11
	220 - 250	0.40
	250 - 290	-0.03
	290 - 390	0.24
	390 - 480	0.33

Table 10. Poisson's Ratios Poisson's Ratios from Downhole Measurements in the WHB Area (continued)

RF#19	Depth Range (ft)	Poisson's Ratio
	3 - 9	-0.15
	9 - 18	0.42
	18 - 39	0.31
	39 - 96	0.24
	104 - 282	0.29
	294 - 550	0.23
550 - 640	0.09	
RF#20	Depth Range (ft)	Poisson's Ratio
	3 - 13	0.19
	20 - 70	0.26
70 - 155	0.14	
RF#21	Depth Range (ft)	Poisson's Ratio
	3 - 20	0.37
	20 - 57	0.07
	57 - 84	0.34
	84 - 120	0.15
120 - 185	0.32	
RF#22	Depth Range (ft)	Poisson's Ratio
	3 - 21	0.22
	24 - 83	0.31
	87 - 175	0.16
	175 - 192	0.47
192 - 500	0.17	
RF#23	Depth Range (ft)	Poisson's Ratio
	3 - 9	0.43
	9 - 18	-0.29
	21 - 72	0.27
	72 - 110	0.20
120 - 155	0.13	
RF#24	Depth Range (ft)	Poisson's Ratio
	3 - 12	-0.68
	18 - 33	0.28
33 - 260	0.39	
RF#25	Depth Range (ft)	Poisson's Ratio
	3 - 37	0.21
	41 - 86	0.21
	86 - 105	0.19
105 - 155	0.38	
RF#26	Depth Range (ft)	Poisson's Ratio
	3 - 10	0.33
	12 - 46	0.39
	46 - 95	0.19
	95 - 140	0.30
140 - 260	0.12	

Table 10. Poisson's Ratios from Downhole Measurements in the WHB Area (concluded)

RF#28	Depth Range (ft)	Poisson's Ratio
	3 - 10	0.44
	10 - 39	0.43
	39 - 95	0.24
RF#29	Depth Range (ft)	Poisson's Ratio
	3 - 33	0.25
	33 - 75	0.23
	75 - 135	0.26
	138 - 230	0.28
	230 - 405	0.17

Note: Poisson's ratios have been calculated for illustrative purposes only. Final Poisson's ratios calculated for use in the forthcoming scientific analysis entitled *Development of Seismic Design Input Ground Motions for a Geologic Repository at Yucca Mountain* will be submitted to the TDMS.

6.2.6 Suspension Seismic Surveys

6.2.6.1 Introduction

Suspension seismic P-S logging at boreholes RF#14 through #29 was conducted from September 17 to 19 and December 5 to 12, 2000 using an OYO Model 170 P-S suspension logging system. In addition, suspension seismic logging was conducted at borehole RF#13 located in the center of the potential WHB footprint on December 15, 1998 using similar equipment and methods. Although logged before the current phase of site exploration, the borehole RF#13 results are presented herein due to their particular relevance to this scientific analysis. The locations of boreholes RF#13 through RF#29 are shown on Figure 3.

6.2.6.2 Equipment

As shown on Figure 29, the suspension system included a downhole tool, consisting of an energy source, isolation tubes and two biaxial geophone receivers; an OYO Model 170 digital data recorder for recording the seismic waves arriving at the two geophones; and a hoisting/depth measurement system.

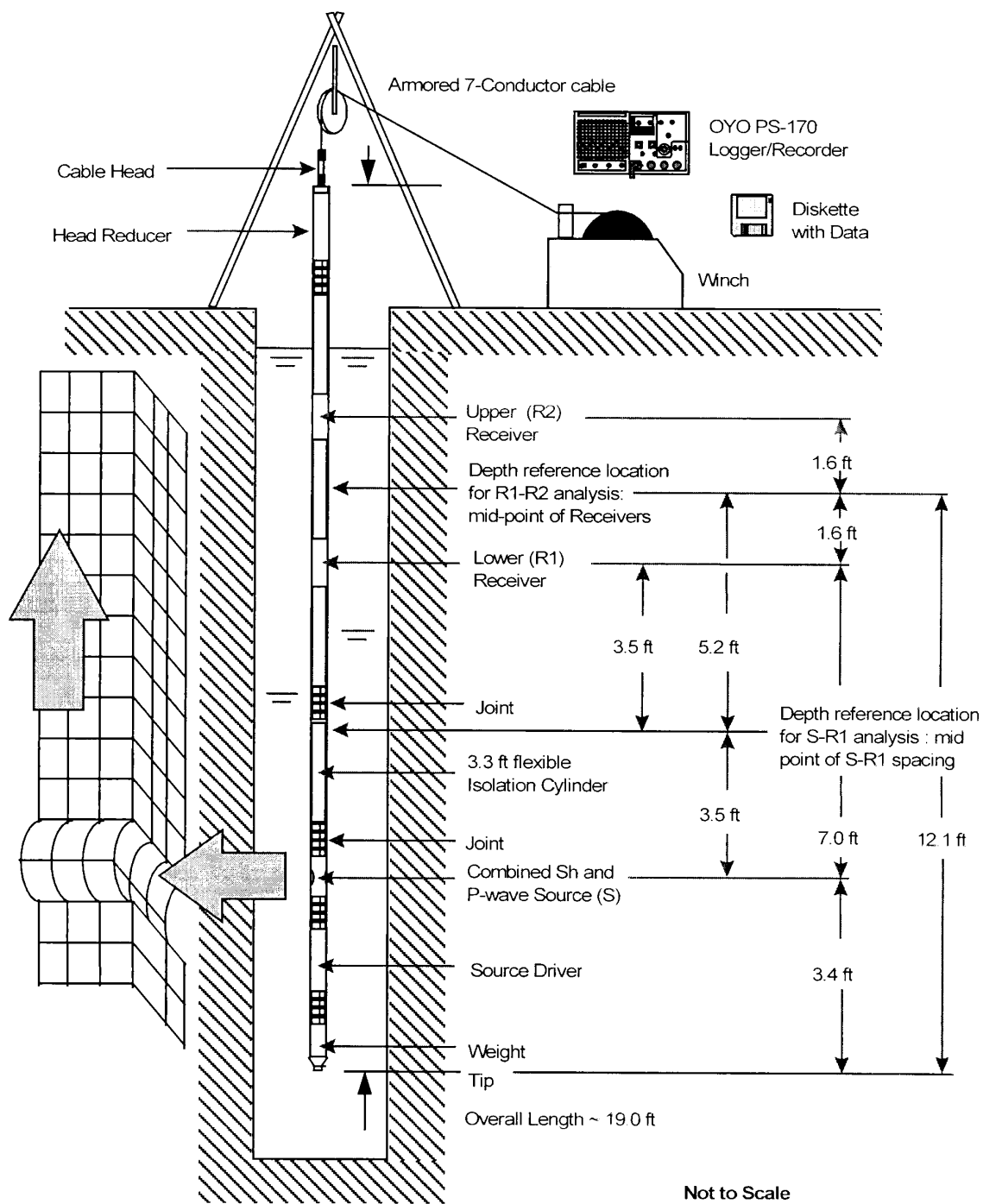
The distance from the energy source, which was mounted near the bottom of the tool, to the near (lower) receiver was approximately 7.11 to 7.17 feet, except it was approximately 3.74 feet at borehole RF#16. The distance between receivers was approximately 3.33 to 3.36 feet.

The energy source is a solenoid whose activation causes a “hammer” to strike the tool casing, producing an impulsive pressure wave in the borehole liquid.³ This pressure wave transmits energy to the borehole wall, producing both P and S waves that travel through the geologic formation. The dominant S-wave frequencies are typically 500 to 2,000 hertz and the P-wave frequencies, 1,000 to 3,000 hertz. The wave field can be treated as a point source in an infinite medium since the wavelength is sufficiently longer than the borehole diameter. As the P and S waves arrive near each geophone, they couple through the borehole liquid to the geophones. Flexible rubber tubes are incorporated in the tool casing to attenuate and filter wave propagation along the tool.

Each biaxial geophone included one vertical sensor and one horizontal sensor. The geophones are mounted in the downhole tool at an elevation higher than the source.

The OYO Model 170 recorder has six channels, two of which can record simultaneously. Each channel records 1024 12-bit samples at equal time intervals. The record length can be set at 5, 10, 20, 50 or 100 milliseconds. The recorded data was displayed on a cathode ray tube display, which allows the operator to adjust the gains, filters, delay time, pulse length (energy), and sample rate to improve the quality of the data before final recording of the data. In addition, the recorder allows the operator to sum up to eight sampling sequences to improve the signal-to-noise ratio. Before moving on to the next measurement depth, the final record was printed on paper tape with a common time scale and was stored on a floppy diskette for further processing.

³ Suspension seismic measurements can only be performed below the level to which the borehole is filled with a liquid such as water or drilling mud.



Source: Luebbers (2002b, page 18 of Attachment 4)

Note: The dimensions shown are typical dimensions and will vary with the specific equipment used for a particular survey. The dimensions have been converted from meters to feet.

Figure 29. Schematic Diagram of OYO P-S Logging Equipment

6.2.6.3 Procedures

To conduct the survey, the borehole⁴ was filled with water and the suspension tool was lowered to the bottom of the casing by a winch and armored cable containing the data leads. The cable moved across a digital wheel assembly that recorded the movement of the cable and hence the depth of the tool.

Logging was conducted from lower elevations to higher ones, with velocity measurements being made at 0.5-meter (1.64-foot) intervals (occasional variations occurred). At each measurement depth the seismic energy source was actuated three times: (1) the source is activated in one direction (arbitrarily called the “normal” direction), producing dominantly horizontal shear with some vertical compression, and the waves are recorded on the horizontal geophones; (2) the source is activated in the opposite direction (referred to as the “reverse” direction), again producing dominantly horizontal shear with some vertical compression, and the waves are again recorded on the horizontal geophones; and (3) the source is again activated in the normal direction and the waves are recorded on the vertical geophones. The data logger began the record at the time the signal was transmitted to the actuator to cause the hammer to strike.

Upon completion of the measurements in each borehole and with the probe at zero depth, the operator checked that the digital depth readout indicated that the probe was at zero depth.

6.2.6.4 Data Evaluation and Results

The suspension data were analyzed by picking arrival times for both the compression wave and the shear wave at appropriate sensors. The compression wave was normally picked as the first break on the vertical sensors. The shear waves were identified by comparing the records for the normal source actuation and the reverse source actuation and noting a reversal in the waveform. The travel time to the peak of the first shear wave cycle was then picked; this point could be identified more accurately than the first break due to the continued signal from the compression wave and noise.

In some cases an arrival could not be identified with confidence on one or more of the sensors and this is reflected by a gap in the data. Most of the data where a pick was not made involves the compression wave. In general, the suspension seismic method has difficulty in recording compression waves above the water table, and all the logging reported herein was performed above the water table. There were also a significant number of measurement locations where a shear wave could be identified on the near receiver recording, but not on the far one. This is caused by loss of signal strength due to spatial spreading and material damping. Material damping can be affected by the type of material and by the type and extent of discontinuities in the medium, such as fractures, lithophysae, joints, and faults.

The OYO Model 170 suspension seismic logger system enables measurement of seismic velocity in two ways. Generally, the usual method is to calculate the velocity based on the difference in wave travel times from the source to the far and near receivers and the known distance between the receivers. The second method is to calculate the velocity based on the wave travel time from

⁴ RF#22 was not cased at the time of suspension seismic logging. In all other boreholes a casing had been grouted in place before the geophysical survey.

the source to the near receiver and the known distance between the source and near receiver. The advantages of the receiver-to-receiver method are:

- The receiver-to-receiver is normally more accurate because the picks are made from the peak of the arrival waveform. The analyst picks the arrival waveform and software is used to find the peaks.
- For the typical setup, and for the results reviewed herein, receiver-to-receiver data has higher resolution because the distance between receivers is usually less than one-half the distance between the source and near receiver. Thus, the receiver-to-receiver data is better suited to identifying thin layers of notably high or low velocity, but gives the appearance of having more scatter.
- In the source-to-near receiver analysis the “normal” and “reverse” travel times were averaged, which reduces errors due to differences in source actuation pulses. In the receiver-to-receiver analysis, only the normal travel times were interpreted.
- Source-to-receiver travel times are subject to a source delay, nominally 4 milliseconds, whose variation could introduce some degree of error. In the receiver-to-receiver method the delay times cancel out, eliminating one potential source of error.
- The source-to-near receiver data are more subject to “picking” errors because the picks are based on the analyst’s choice of first motion rather than detection of the peak by software. The effect of these errors on velocity is reduced, however, by the longer travel path and hence longer travel time.
- Because of the geometric arrangement of the source and the two receivers, the receiver-to-receiver survey usually extends to a depth about 5 feet closer to the ground surface than the source-to-near receiver survey.

The advantages of the source-to-near receiver method are:

- For the typical setup, and for the results reviewed herein, source-to-near receiver data has lower resolution because the distance from source to the near receiver is usually more than twice the distance between the receivers. Thus, the source-to-near receiver data should appear to have less variability (scatter) than the receiver-to-receiver data. Although less suited to identifying thin layers of notably high or low velocity, the source-to-near receiver velocities may be more appropriate for ground motion analysis because the velocity is measured over a longer interval.
- Because of the geometric arrangement of the source and the two receivers, the source-to-near receiver survey usually extends to a depth about 5 feet greater than the receiver-to-receiver survey.

Considering these points, the receiver-to-receiver results are usually considered the “primary” results and the source-to-near receiver results are used as a quality control check on the receiver-to-receiver results. Despite the general preference for receiver-to-receiver data on principle, in practice, more, and sometimes much more, of the receiver-to-receiver is missing and, primarily

for that reason, the decision was made to accept the source-to-near receiver results as being primary. Thus, on the boring logs in Attachment I, the source-to-near receiver suspension results are shown.

The reason why more receiver-to-receiver data are missing than source-to-receiver data is that the seismic waves must travel farther to reach the far receiver than to reach the near receiver and the farther the waves travel from the source, the more their amplitude is attenuated by spatial and material damping. In general, the ability to recognize the compression wave arrival at the far receiver was lost more frequently than the ability to recognize the shear wave arrival. The energy loss is higher in more fractured bedrock relative to less fractured bedrock.

The raw and filtered waveforms are reported in Scientific Notebooks SN-M&O-SCI-024-V1 (Luebbers 2002a) and SN-M&O-SCI-024-V2 (Luebbers 2002b). The interpreted arrival times and interval velocities are reported in DTN: MO0204SEPBSWHB.001. A similar suspension seismic survey of borehole RF#13 performed in 1998 is described in CRWMS M&O (1999b, Section 4.4) and the interpreted arrival times and interval velocities are reported in DTN: MO0204SEISDWHB.001. Based on an assessment of data quality, some inconsistencies were recognized in the data collected at shallow depths (generally to 25-foot depth, but as deep as 77 feet in borehole RF#25) and thus these data are ignored. The data that were collected and interpreted but ultimately ignored are summarized by depth (i.e., depth bgs to the midpoint between the two receivers) in Table 11.

Table 11. Extent of Suspension Seismic Logging in 2000

Borehole No. and Casing Condition	Data Collected	Depth of Logging	Depth of Data to be ignored
RF#14 Cased	12/9/00	543.3 ft	surface to 44.30 ft bgs
RF#15 Cased	12/5/00	316.9 ft	surface to 19.69 ft bgs
RF#16 Cased	12/12/00	446.4 ft	surface to 22.97 ft bgs
RF#17 Cased	12/11/00	648.3 ft	surface to 47.60 ft bgs
RF#18 Cased	12/12/00	484.3 ft	surface to 27.90 ft bgs
RF#19 Cased	12/7/00	638.5 ft	surface to 27.90 ft bgs
RF#20 Cased	12/7/00	151.2 ft	surface to 14.80 ft bgs
RF#21 Cased	12/7/00	184.0 ft	surface to 13.12 ft bgs
RF#22 Uncased	9/19/00	393.7 ft	Data OK
RF#23 Cased	12/7/00	151.2 ft	Data OK
RF#24 Cased	12/6/00	262.1 ft	surface to 23.00 ft bgs
RF#25 Cased	12/3/00	151.2 ft	surface to 77.10 ft bgs
RF#26 Cased	9/17/00	256.2 ft	surface to 13.12 ft bgs
RF#28 Cased	12/6/00	93.8 ft	surface to 22.97 ft bgs
RF#29 Cased	12/7/00	402.2 ft	surface to 19.69 ft bgs

Source: Page 12 of Luebbers (2002b, Attachment 4)

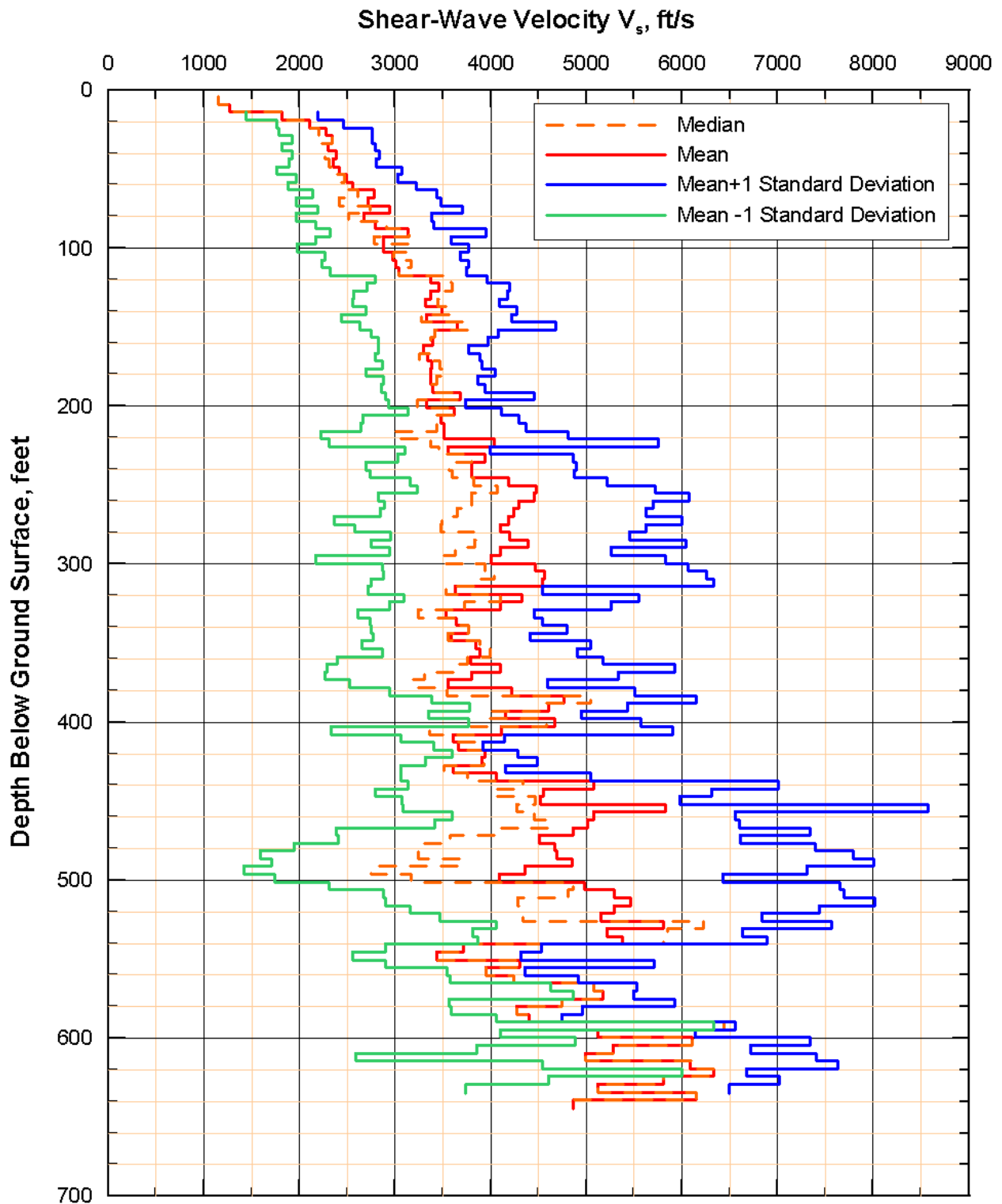
Notes: (1) The depth of logging is based on midpoint between source and the near receiver. (2) In the "Depth of Data to be Ignored" column, the use of the term surface is not intended to indicate that measurements were performed from borehole bottom to a depth of zero feet bgs, but rather that no data was retained from the ground surface to the stated lower limit.

The results of suspension seismic surveys are usually presented as plots of interval velocities versus depth. The velocity across the interval between the two receivers was calculated by dividing the fixed distance between the two biaxial receivers (approximately 3.3 feet) by the difference in travel times from the source to the respective receiver. The velocity across the interval between the source and the near receiver was calculated in a similar fashion by dividing the fixed distance between the source and the near receiver (approximately 7 feet) by the difference in travel time from the source to the near receiver. The travel time from the source to the near receiver was adjusted for the delay between the time the signal is given for the test to begin and the time the seismic wave is actually initiated. This adjustment to the source-to-receiver travel time does not need to be made to the receiver-to-receiver travel time because it is the difference between two source-to-receiver travel times and thus automatically adjusts for the factors involved.

Figures VII-1 to VII-16 present plots of suspension seismic shear-wave interval velocities versus depth bgs for each of boreholes RF#13 to RF#29.⁵ For boreholes RF#14 to RF#29, two shear-wave velocity plots are presented, one based on the receiver-to-receiver travel time difference, and the other based on the source-to-near receiver travel time difference. The receiver-to-receiver velocity is plotted against the average of the depths bgs of the two receivers, while the source-to-near receiver velocity is plotted against the average of the depths bgs of the source and the near receiver. The shear-wave velocities derived from the downhole seismic measurements (discussed in Section 6.2.5) at the same borehole and the SASW velocity profile(s) for a survey located near the borehole (discussed in Section 6.2.7) are also shown for reference. For the downhole profiles, see DTNs: MO0111DVDWHBSC.001, MO0110DVDBOREH.000 and MO020498DNHOLE.000; and for the SASW profiles, see DTN: MO0110SASWWHBS.000.

The shear-wave interval velocity data from boreholes RF#13 to RF#29 were examined statistically in two ways. First, the data acquired at 0.5-meter intervals were divided into 1.5-meter (4.92 feet) sets and the mean, median, mean plus one standard deviation and mean minus one standard deviation was calculated for each set. The 1.5-meter depth increment was chosen to be similar to the 5-foot increment used for the downhole statistics discussed in Section 6.2.5.3. The results of this analysis are shown on Figures 30 (receiver-to-receiver) and 31 (source-to-receiver). The data were also divided according to lithostratigraphic unit and the same statistical parameters were calculated. The median, mean plus one standard deviation and mean minus one standard deviation are shown on Figures 32 (receiver-to-receiver) and 33 (source-to-receiver). Values of mean, median, standard deviation, and coefficient of variation and count (number of measurements in the data set) by lithostratigraphic unit are summarized in Tables VII-1 (receiver-to-receiver) and VII-2 (source-to-receiver). To facilitate comparisons, Figures VII-49 and VII-50 shows a plot of the averaged v_s for individual boreholes versus depth, together with the mean and mean \pm one standard deviation for the entire data set. The number of profiles included in the statistical analysis at each depth interval is indicated in the bar graph along the right edge of the plot. At shallow and deeper depths, few profiles are available to be included in the statistical analysis, and the statistical values may not be meaningful.

⁵ Throughout Attachments VII and VIII, the surveys performed by Redpath Geophysics are referred to as the 2000-1 surveys, the surveys performed by GEOVision Inc. (RF#13 and RF#17) are referred to as the 2000-2 surveys, and the survey performed by URS Corporation (RF#13) is referred to as the 1998 survey.



DTN: MO02045FTDSUSP.001

Figure 30. Shear-Wave Velocity by Depth Interval from Receiver-to-Receiver Interval Suspension Surveys in WHB Area

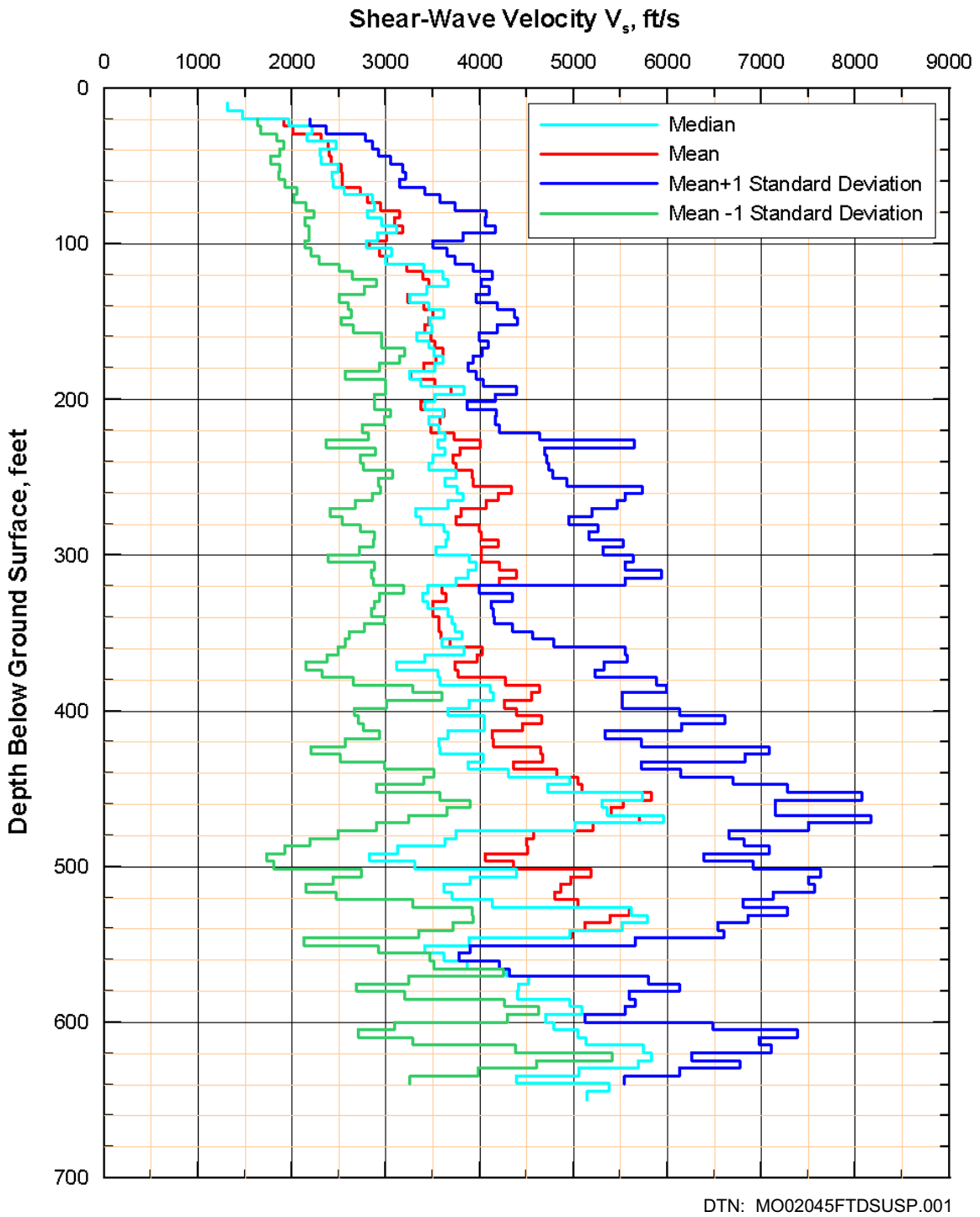
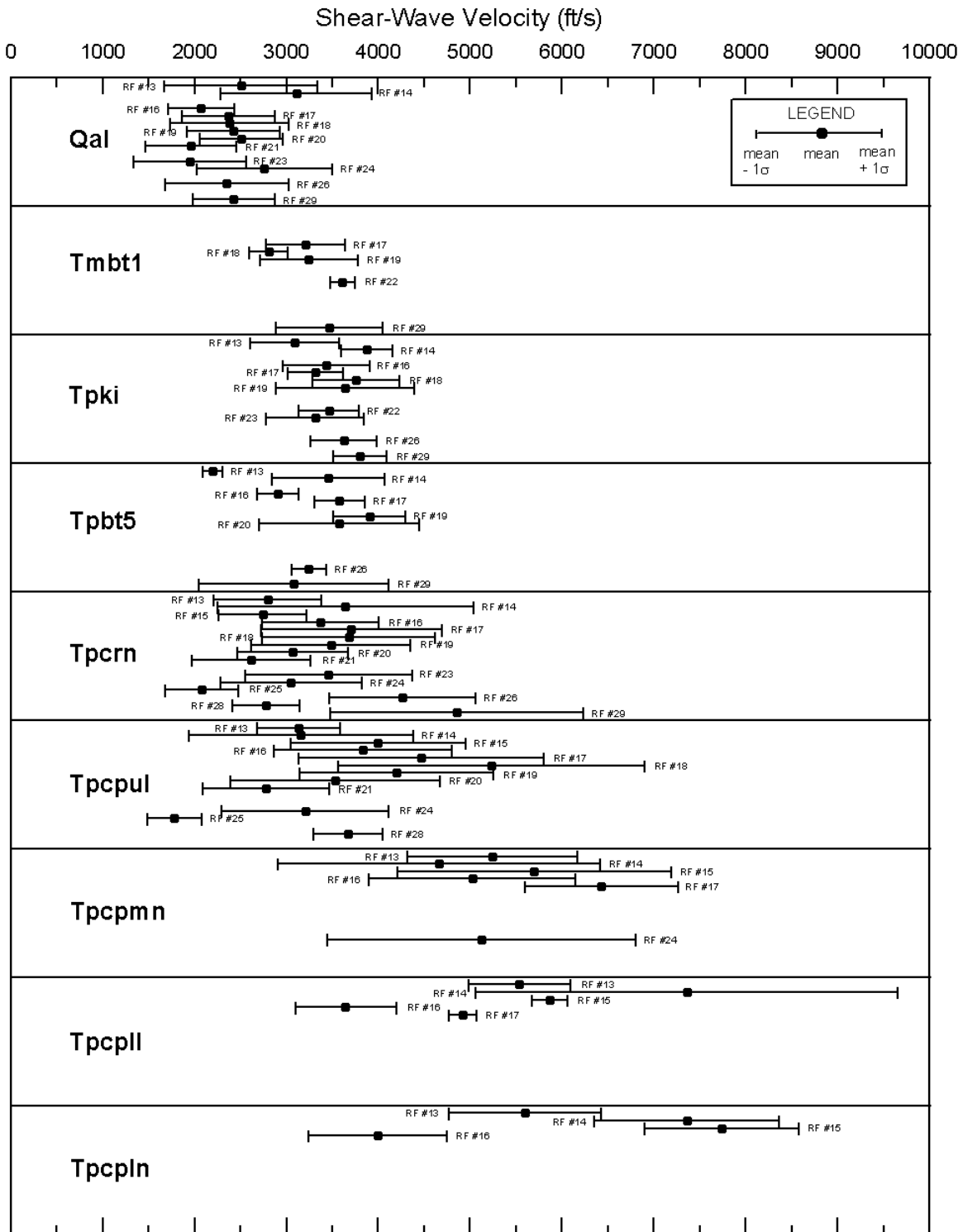


Figure 31. Shear-Wave Velocity by Depth Interval from Source-to-Receiver Interval Suspension Surveys in WHB Area



DTN: MO0204SUSPSEIS.001

Figure 32. Statistical Values of Shear-Wave Velocity by Lithostratigraphic Unit from Receiver-to-Receiver Interval Suspension Surveys in WHB Area

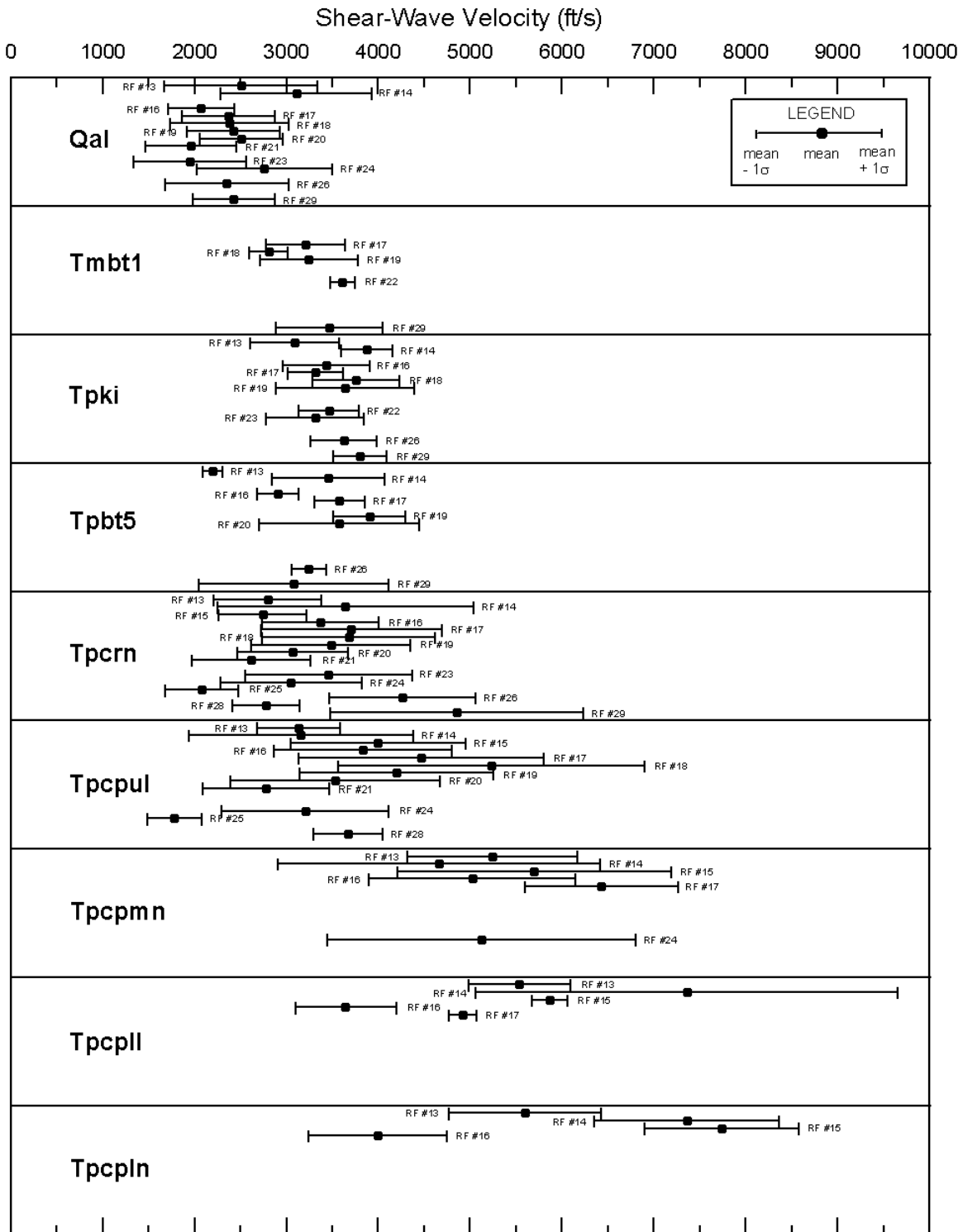


Figure 33. Statistical Values of Shear-Wave Velocity by Lithostratigraphic Unit from Source-to-Receiver Interval Suspension Surveys in WHB Area

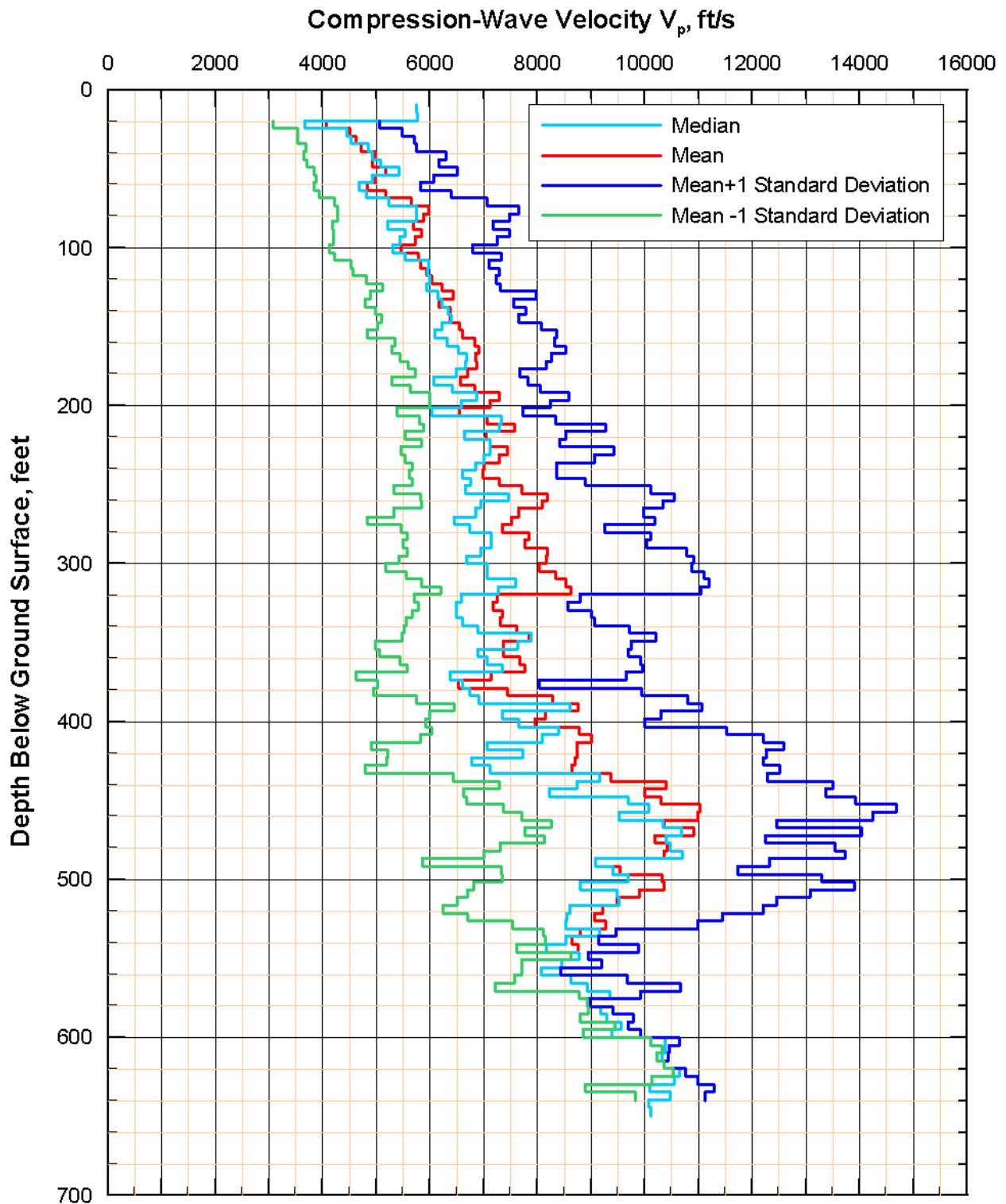
As mentioned in Section 6.2.2, it was estimated prior to drilling the deep boreholes that a shear-wave velocity of 5,000 ft/s rock would be found, based on the downhole results from borehole RF#13, at about 20 to 30 feet into the Tiva Canyon Tuff crystal-poor middle nonlithophysal zone (Tpcpmn). As can be seen from Figures 32 and 33, the mean value of shear-wave velocity is generally above 5,000 ft/s in the Tpcpmn and older zones. Where the shear-wave velocity is less than 5,000 ft/s in the Tpcpmn and older zones, the rock is generally highly fractured or the borehole passed through a zone of fracture fill (see Section 6.6.2 for a discussion of fracture fill). This observation suggests that an improved correlation (lower standard deviation) could be obtained if the velocity statistics were calculated as a function of both lithostratigraphic unit and fracture frequency or RQD. However, such knowledge would seem to have little practical import because the distribution of fractures in the rock is not known.

Figures VII-17 through VII-32 present plots of suspension seismic compression-wave interval velocities versus depth bgs for each of boreholes RF#13 to RF#29.⁶ For each borehole two compression-wave velocity plots are presented, one based on the receiver-to-receiver travel time difference, and the other based on the source-to-near receiver travel time difference. The receiver-to-receiver velocity is plotted against the average depth bgs of the two receivers, while the source-to-near receiver velocity is plotted against the average of the depths bgs of the source and the near receiver. The compression-wave velocities derived from the downhole seismic measurements at the same borehole are also shown for reference.

The compression-wave interval velocity data from boreholes RF#14 to RF#29 were examined statistically in the same way as the shear-wave interval velocity data except that only the source-to-receiver data were considered. Receiver-to-receiver data were not considered because much of the data could not be interpreted and because compression-wave velocity is a less important parameter than shear-wave velocity. The statistics by depth interval and by lithostratigraphic unit are shown on Figures 34 and 35, respectively. Table VII-3 summarizes values of mean, median, standard deviation, and coefficient of variation and count by lithostratigraphic unit. To facilitate comparisons, Figure VII-51 shows a plot of the averaged v_p for individual boreholes versus depth, together with the mean and mean \pm one standard deviation for the entire data set. The number of profiles included in the statistical analysis at each depth interval is indicated in the bar graph along the right edge of the plot. At deeper depths, as well as at very shallow depths, few profiles are available to be included in the statistical analysis, and the statistical values may not be meaningful.

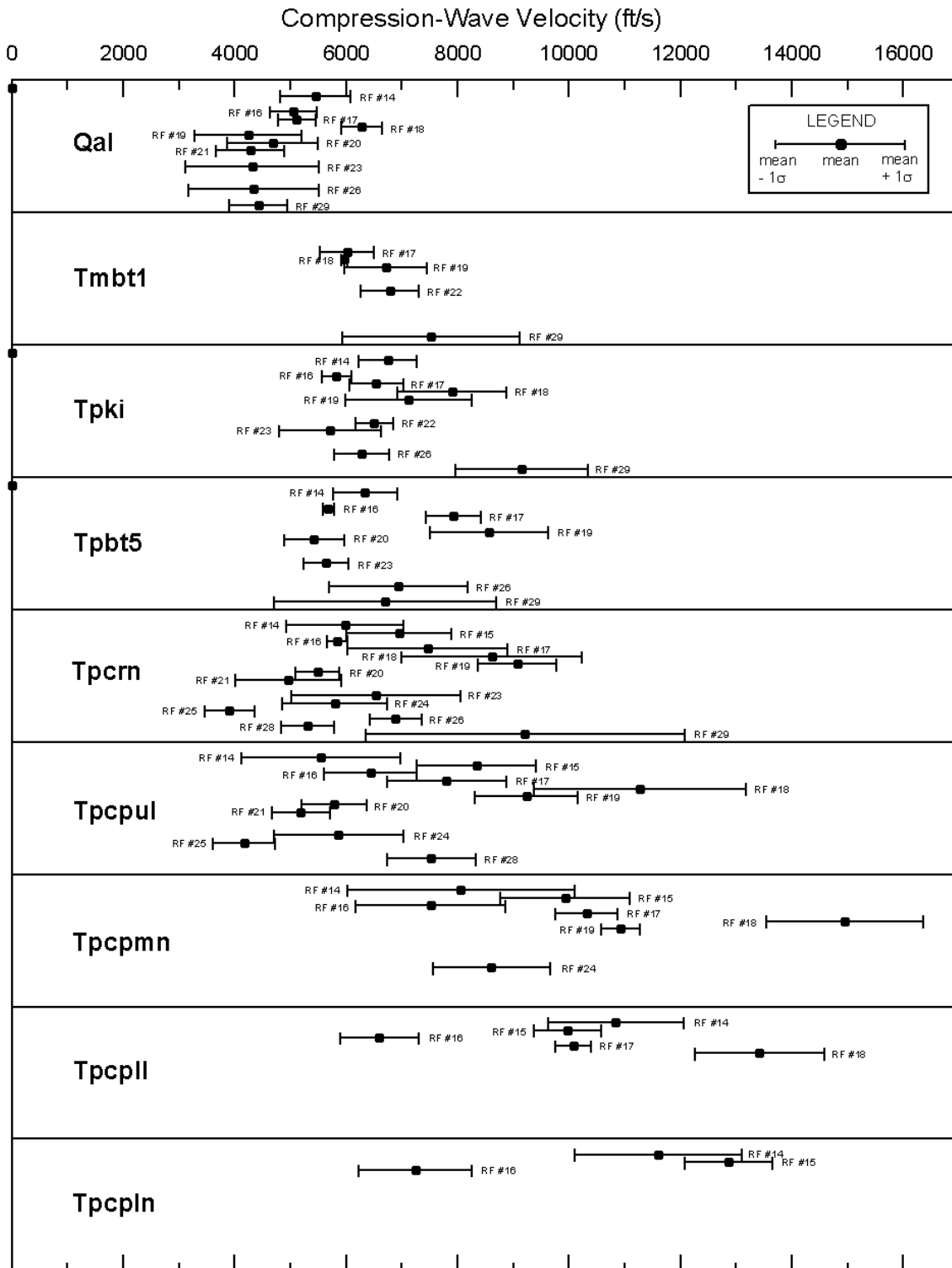
Where both shear-wave and compression-wave velocities are known for the same depth interval, the value of Poisson's ratio was calculated using equation 4 from the theory of elasticity for homogeneous, isotropic elastic materials. Figures VII-33 through VII-48 present plots of Poisson's ratio versus depth bgs derived from the shear- and compression-wave interval velocities measured at each of boreholes RF#13 to RF#29.

⁶ Note that for borehole RF#13, there are no compression-wave suspension seismic velocity results. However, as will be discussed in Section 6.7.2, velocity and Poisson's ratio results from other methods are presented on the figures in Attachments VII and VIII. Consequently, for consistency of presentation, Figures VII-17 and VII-33 for RF#13 are presented even though they contain no suspension seismic data.



DTN: MO02045FTDSUSP.001

Figure 34. Compression-Wave Velocity by Depth Interval from Source-to-Receiver Interval Suspension Surveys in WHB Area



DTN: MO0204SUSPSEIS.001

Figure 35. Statistical Values of Compression-Wave Velocity by Lithostratigraphic Unit from Source-to-Receiver Interval Suspension Surveys in WHB Area

The Poisson's ratio data from boreholes RF#14 to RF#29 were examined statistically in the same way as the shear- and compression-wave interval velocity data. Again, only source-to-receiver data was considered. Figures 36 and 37 show statistics by depth interval and by lithostratigraphic unit, respectively. Table VII-4 summarizes values of mean, median, standard deviation, and coefficient of variation and count by lithostratigraphic unit. To facilitate comparisons, Figure VII-52 shows a plot of Poisson's ratio calculated from the average values of v_s and v_p for individual boreholes versus depth, together with the mean and mean \pm one standard deviation for the entire data set. The number of profiles included in the statistical analysis at each depth interval is indicated in the bar graph along the right edge of the plot. At deeper depths, as well as at very shallow depths, few profiles are available to be included in the statistical analysis, and the statistical values may not be meaningful.

For this scientific analysis, the shear-wave travel times for each suspension seismic interval were accumulated to construct a plot of accumulated shear-wave arrival times versus depth bgs. This plot is the same in form as the adjusted shear-wave travel time versus depth plot from a downhole seismic survey. However, it should be noted that in the suspension method, the seismic waves are constrained to travelling in the relatively limited volume of material in the immediate vicinity of the direct path between the source and the receivers, while in the downhole method a greater potential exists for the seismic waves to deviate from a straight-line path from source to receiver. Plots of these results are presented as Figures VIII-1 through VIII-16.⁷ The downhole adjusted travel times are also plotted for comparison, which is discussed in Section 6.7. As was discussed in Section 6.2.5 relative to the downhole seismic travel time versus depth bgs data, the results plotted on Figures VIII-1 through VIII-16 were evaluated by fitting straight lines to the data in depth intervals where the data suggested a zone of relatively constant velocity when viewed on a macroscale. The seismic velocity was then computed as the first derivative of depth with respect to time and noted on the appropriate figure. All of the resultant shear-wave velocities are plotted on Figure 38. These velocities are referred to as "linear approximations" herein and are also plotted on the graphs in Attachment VII.

Compression-wave arrival times were also accumulated with depth bgs and are shown on Figures VIII-1 through VIII-16. Linear functions were fitted to the accumulated arrival time plots and average compression-wave velocities were computed (DTNs: MO0204SEPFSSS.000, MO0204SEPSWSSS.000). All of the resultant shear-wave velocities are plotted on Figure 39.

Poisson's ratio was calculated from the average shear-wave velocities and average compression-wave velocities on Figures 38 and 39. The resultant values of Poisson's ratio are plotted on Figure 40 for all the surveys as well as on each of Figures VII-33 through -48.

⁷ Note that the travel time from ground surface to the suspension result at the shallowest depth is unknown and must be assigned arbitrarily. Because the travel time from ground surface to the shallowest suspension result is unknown, velocity cannot be assessed in this interval using the suspension results. In some cases, the records of measurements could not be interpreted and these create a gap in the accumulated travel time plot. In general, the downhole results were used to assign a travel time to the shallowest measurement and to shallowest measurement after a gap in the data. Other approaches could be taken, but this approach facilitates comparison of the suspension seismic and downhole seismic data. Note that these assigned travel time values only move the curve laterally on the graph and do not affect the shape or slope of the curve, which means they do not affect the interpreted velocity.

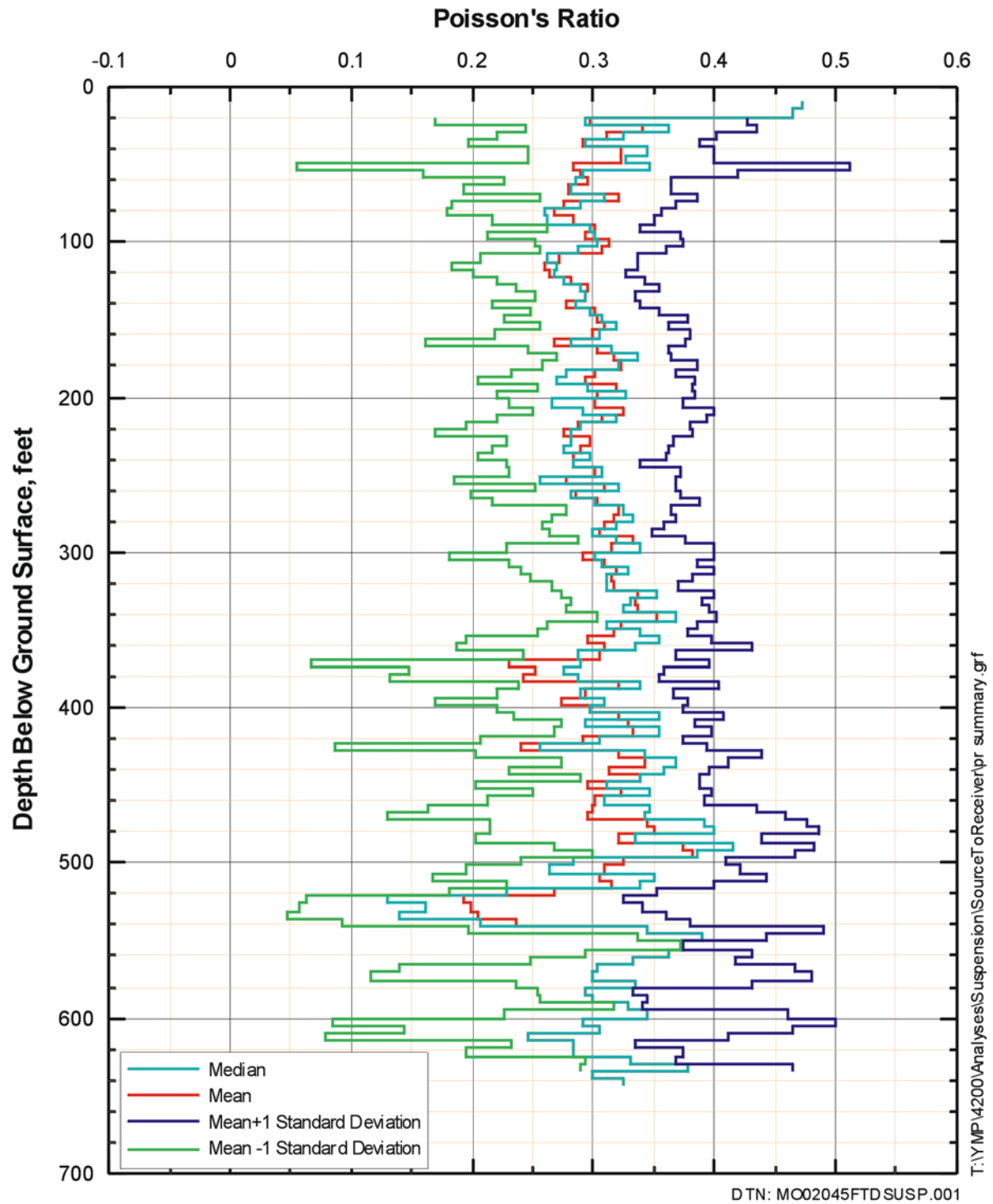


Figure 36. Poisson's Ratio by Depth Interval from Source-to-Receiver Interval Suspension Surveys in WHB Area

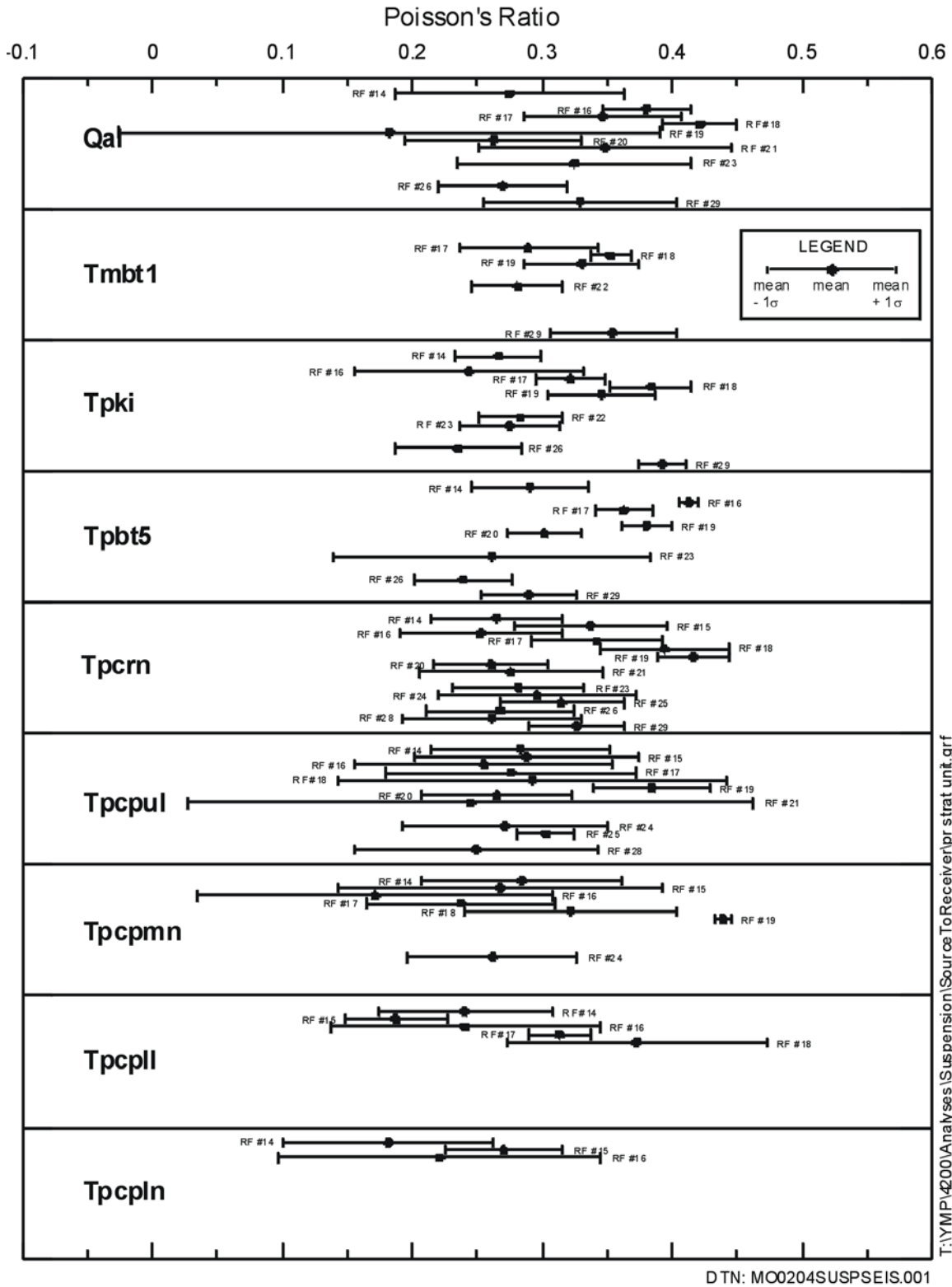


Figure 37. Statistical Values of Poisson's Ratio by Lithostratigraphic Unit for Poisson's Ratio from Source-to-Receiver Interval Suspension Surveys in WHB Area

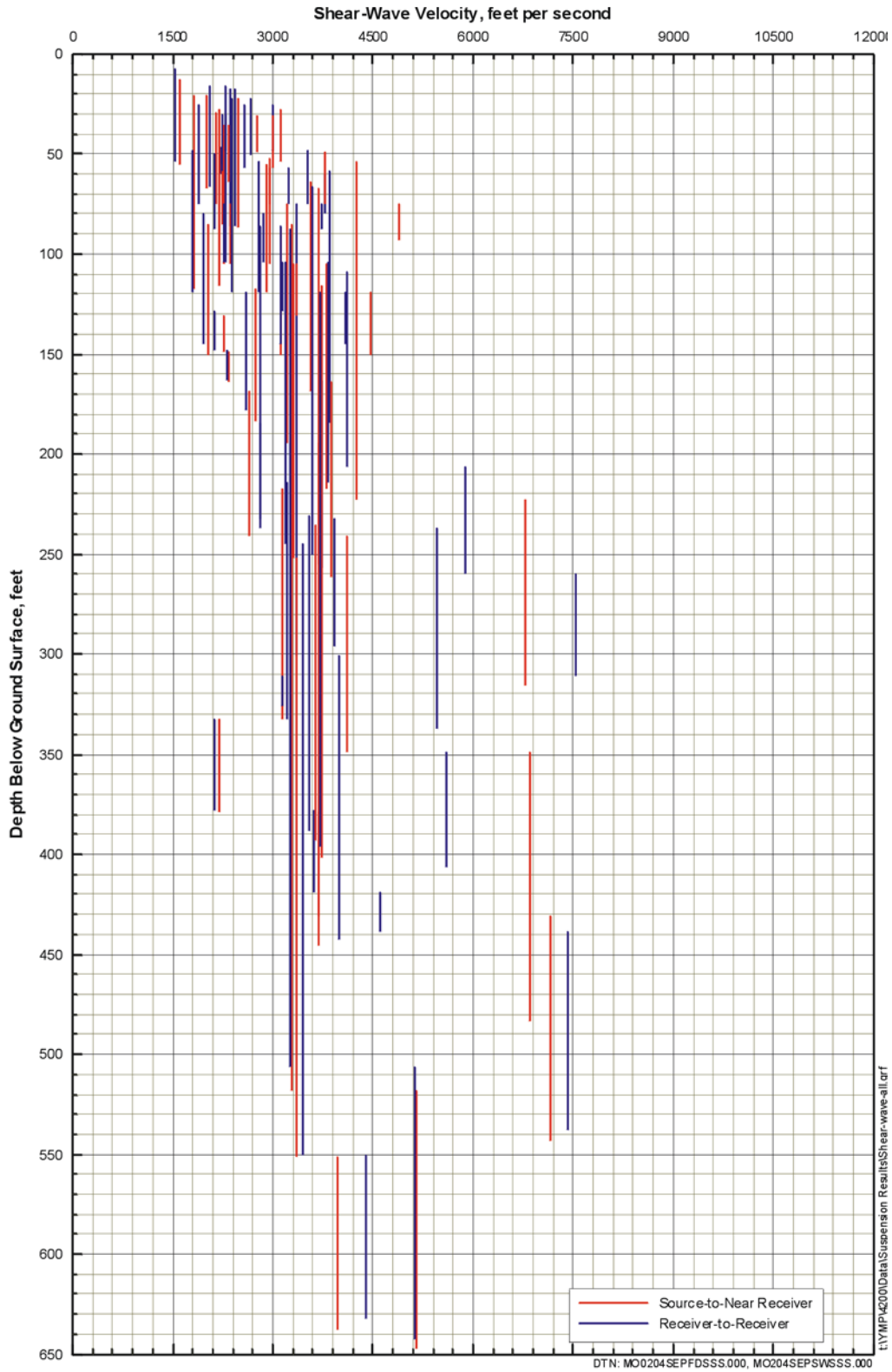


Figure 38. Shear-Wave Velocities from Linear Fits to Suspension Seismic Time Data

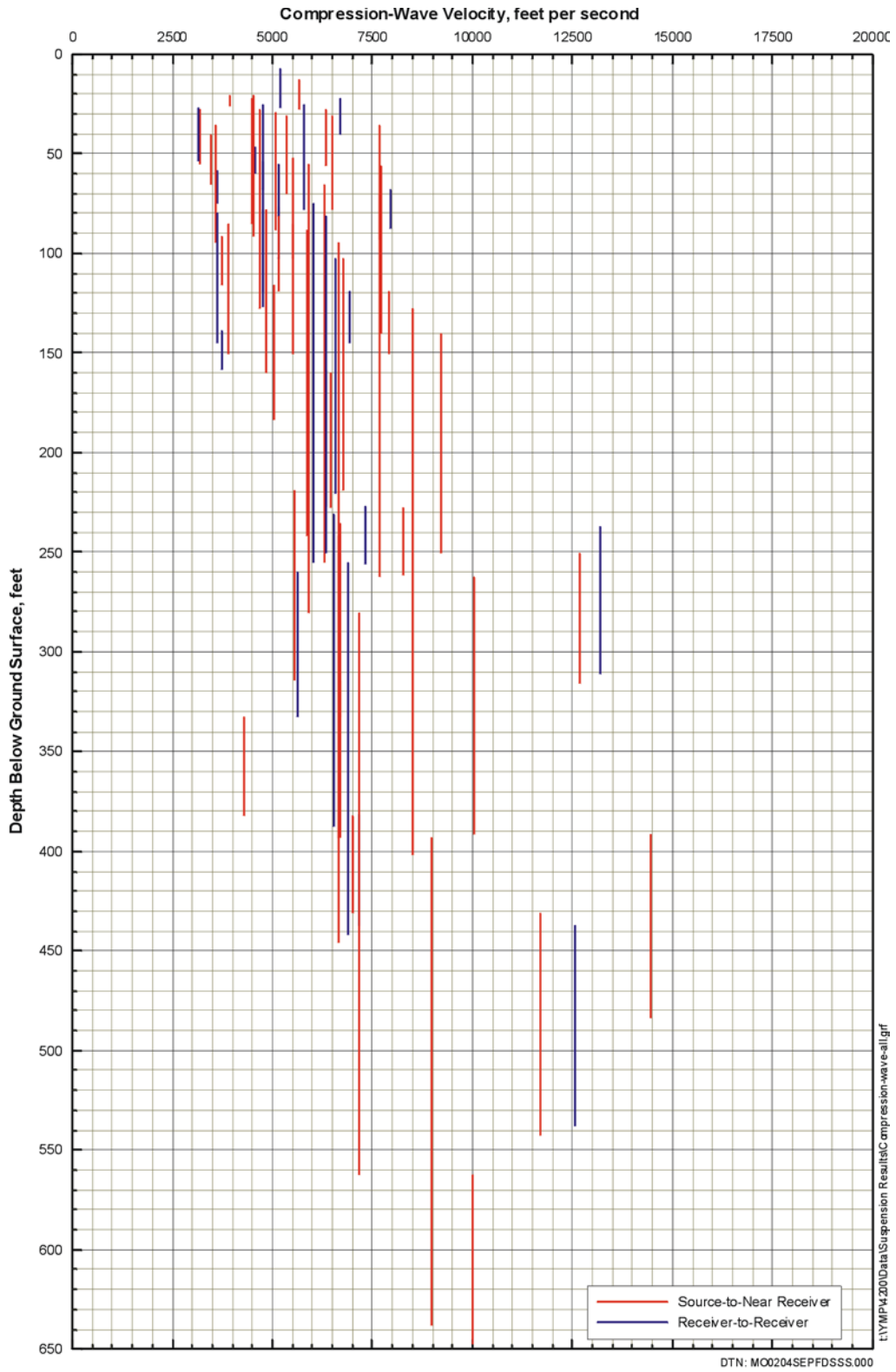


Figure 39. Compression-Wave Velocities from Linear Fits to Suspension Seismic Time Data

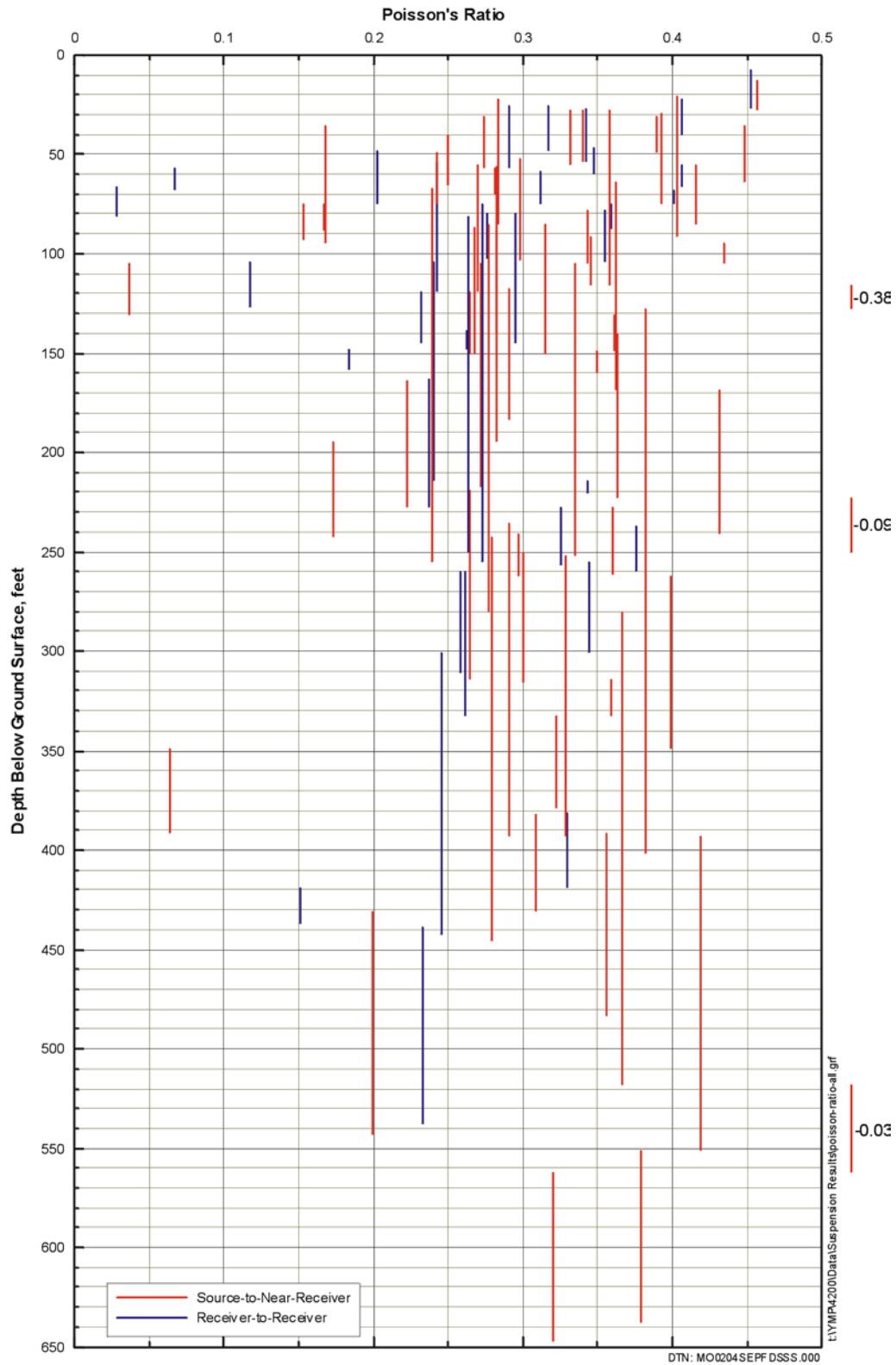


Figure 40. Poisson's Ratio from Linear Fits to Suspension Seismic Time Data

Although natural soil and rock deposits are not homogeneous, isotropic or elastic, at shear strain levels less than about 10^{-4} to 10^{-6} (depending on the particular material), earth materials appear to behave elastically, which is sometimes referred to as pseudo-elastic behavior. Seismic geophysical methods typically involve strain levels less than this threshold strain value, and are considered to reflect behavior in the pseudo-elastic range. Thus, it is generally expected that the v_s and v_p interpreted at a given location (depth and borehole) will yield a value of Poisson's ratio in the range 0.00 to 0.50 associated with homogeneous, isotropic, elastic materials.

As shown on Figures 40 and VII-33 through -48, the values of Poisson's ratio derived from the interval velocities occasionally lie outside the range 0.00 to 0.50 associated with homogeneous, isotropic, elastic materials. All of the values outside the range 0.00 to 0.50 are negative, which means $v_p < \sqrt{2} v_s$, and most are between 0.00 and -0.10. However, the total number of values outside the range 0.00 to 0.50 is only a small fraction of the total number of values, which indicates that overall the velocities yield reasonable values of Poisson's ratio. As for the values of Poisson's ratio derived from the layer-average velocities, there are some intervals, generally short, where Poisson's ratio falls outside the range 0.00 to 0.50. Again, the values are always negative. These values are in every case the result of selecting different layer boundaries for the v_s and v_p profiles and can be ignored.

6.2.7 SASW Surveys

SASW surveys were performed at the proposed site of the WHB in the summers 2000 and 2001 by a team from the University of Texas at Austin (UTA) led by Dr. Kenneth H. Stokoe, II. The majority of the SASW surveys were performed from 24 July through 6 August 2000. Three additional sites were tested on 16 September 2000. A single survey, D-12, was performed in July 2001. This work was performed and documented through the use of Scientific Notebooks SN-M&O-SCI-022-V1 (Wong 2002c) and SN-M&O-SCI-040-V1 (Wong 2002a).

The objective of these investigations was to estimate the shear-wave velocity structure to a depth of approximately 150 ft at closely-spaced intervals on and near the proposed footprint of the WHB Area. A total of 35 shear-wave velocity profiles were developed. This section describes the SASW measurements, analysis procedures and the results.

6.2.7.1 Methodology

The SASW methodology is a non-destructive and non-intrusive seismic method. It utilizes the dispersive nature of Rayleigh-type surface waves propagating through a layered material to estimate the shear-wave velocity profile of the material (Stokoe, Wright et al. 1994). In this context, dispersion arises when surface-wave velocity varies with wavelength or frequency. Dispersion in surface-wave velocity arises from changing stiffness properties of the soil and rock layers with depth. This phenomenon is illustrated on Figure 41 for a multi-layered solid. A high-frequency surface wave, which propagates with a short wavelength, only stresses material near the exposed surface and thus only samples the properties of the shallow, near-surface material (Figure 41b). A lower-frequency surface wave, which has a longer wavelength, stresses material to a greater depth and thus samples the properties of both shallower and deeper materials (Figure 41c). Spectral analysis is used to separate the waves by frequency and wavelength to determine the experimental ("field") dispersion curve for the site. An analytical

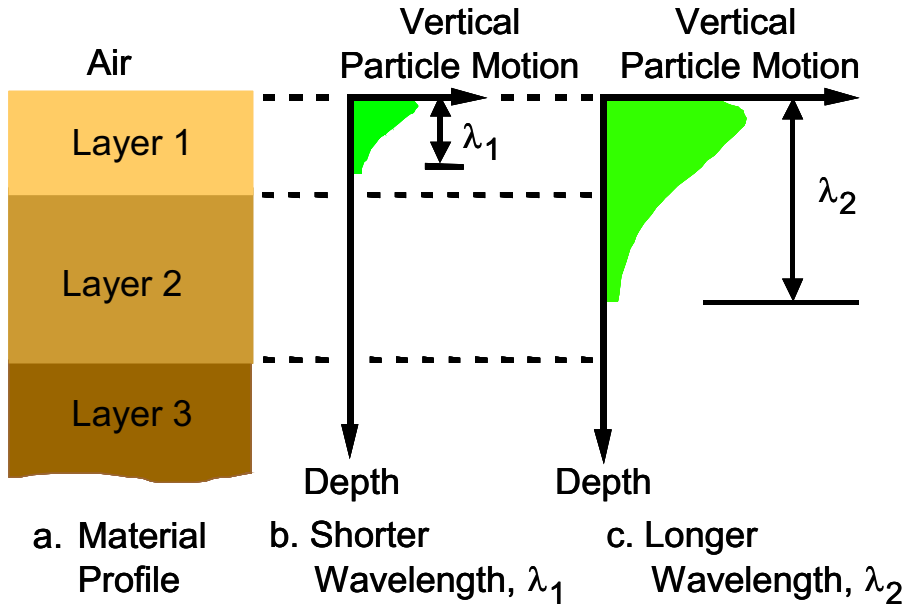


Figure 41. Illustration of Surface Waves with Different Wavelengths Sampling Different Materials in a Layered System which Results in Dispersion in Wave Velocities

theoretically match the field dispersion curve with a one-dimensional layered system of varying layer stiffnesses and thicknesses (Joh 1996). The one-dimensional shear-wave velocity profile that generates a dispersion curve which matches the field dispersion curve is presented as the profile at the site.

SASW measurements involve generating surface waves at one point on the ground surface and recording them as they pass by two or more locations. All measurement points are arranged along a single radial path from the source. Successively longer spacings between the receivers and between the source and first receiver are typically used to measure progressively longer wavelengths. This general configuration for one source/receiver set-up is illustrated on Figure 42. The distance between the source and first receiver (d) is kept equal to the distance between receivers. Measurements are performed with several (typically 7 or more) sets of source-receiver spacings. Phase plots from surface wave propagation between the receivers are recorded for each receiver spacing. From each phase plot, the phase velocity of the surface wave can be calculated at each frequency from (Joh 1996, p. 20):

$$V_R = f \cdot \frac{360}{\phi} \cdot d \quad (\text{Eq. 5})$$

where V_R is the phase velocity in ft/s or m/s, f is the frequency in Hertz (cycles per sec), ϕ is the phase angle in degrees (at frequency f), and d is the distance between the receivers in the same length units as used to represent V_R . From this calculation, a plot of phase velocity versus frequency, called an individual dispersion curve, is generated.

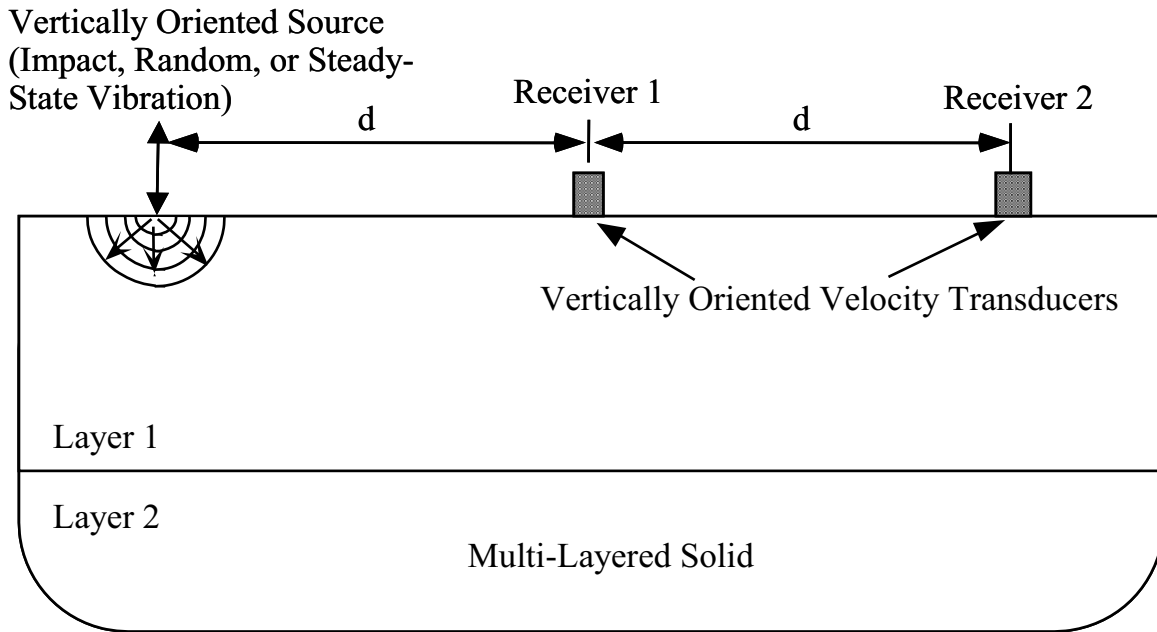


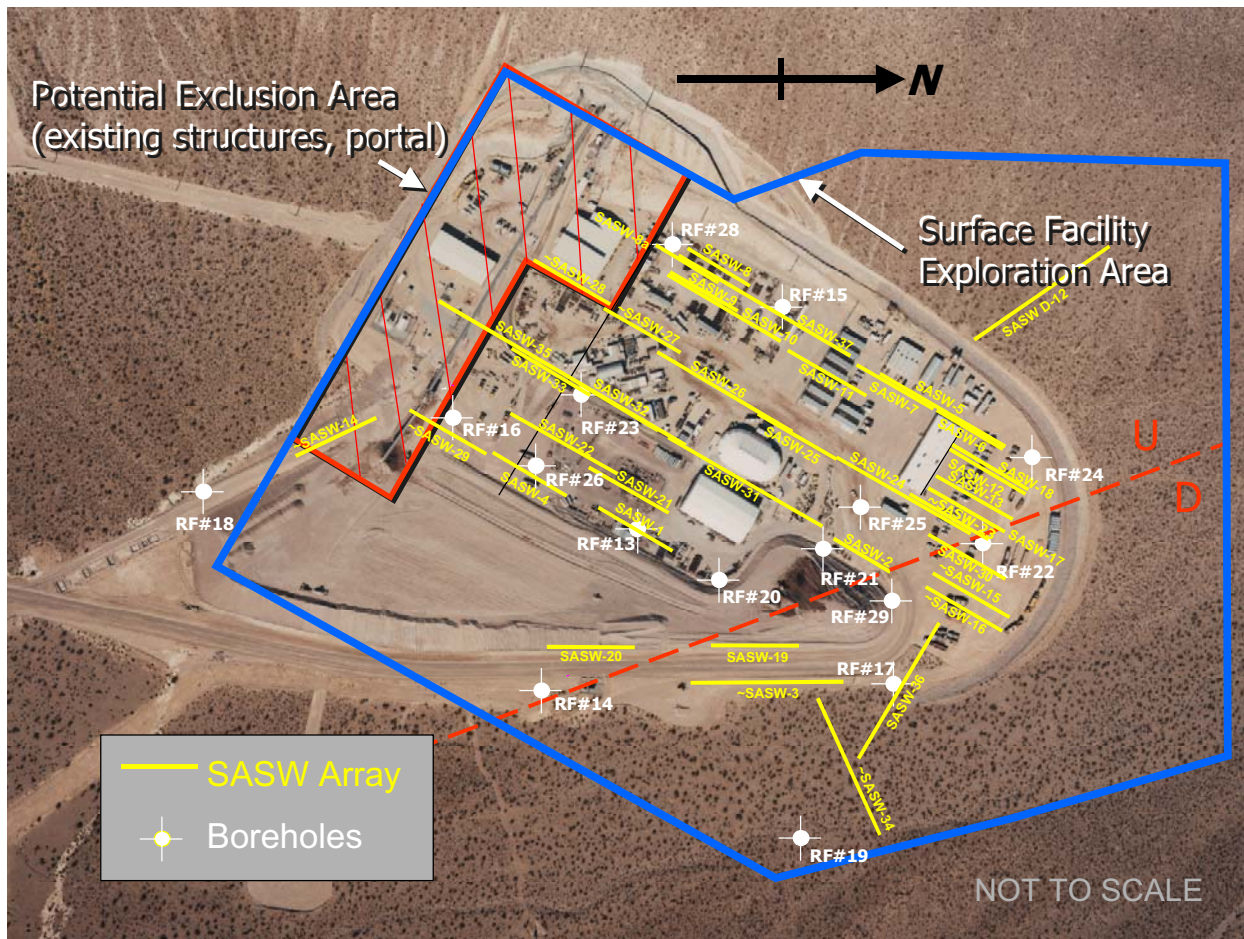
Figure 42. Schematic Diagram of the Generalized Equipment Arrangement Used for SASW Measurements

This procedure is repeated for all source-receiver spacings used at the site and typically involves significant overlapping in the dispersion data between adjacent receiver sets. The individual dispersion curves from all receiver spacings are combined into a single composite dispersion curve called the experimental or field dispersion curve. Once the composite dispersion curve is generated for the site, an iterative forward modeling procedure is used to create a theoretical dispersion curve to match this experimental curve (Joh 1996). The stiffness profile that provides the best match to the experimental dispersion curve is presented as the shear-wave velocity profile at the site.

6.2.7.2 Approach

A total of 40 SASW surveys were performed in the area of the proposed WHB. Their locations are shown on Figure 43. The lengths of the lines are drawn approximately equal to the maximum receiver spacing along SASW survey. To the extent possible, at least one line was laid out near every borehole to allow comparison of the SASW results with the downhole velocity measurements. The majority of the surveys were laid out approximately along strike of the bedding at the WHB to minimize possible 2- and 3-dimensional variations in the velocity structure. A single survey, D-12, was performed across a lower portion of Exile Hill (Figure 43).

Five of the surveys were combined with other adjacent surveys (SASW-8a+8; SASW-9a+9; SASW-10+37, SASW-32+35, and SASW-34+36) resulting in 35 experimental dispersion curves. A total of 35 shear-wave velocity profiles was thus generated within the WHB Area. The locations of these arrays referenced to other landmarks are presented in the Supplement Records of the Scientific Notebook SN-M&O-SCI-022-V1 (Wong 2002c, Appendices 1-34).



Note: The dashed line is the Exile Hill fault splay.

Figure 43. Locations of SASW Lines at the WHB Site Characterization Area

6.2.7.2.1 Equipment and Measurement Procedures

The basic configuration of the source and receivers used in each survey is illustrated on Figure 42. Vertical-component velocity transducers were used as receivers. The majority of the tests were conducted with Mark Products Model L-4C seismometers, which have a natural frequency of 1 Hz. Key characteristics of these receivers are: 1) they have significant output over the measurement frequency range of 2 to 300 Hz; 2) they are matched so that any differences in phase are negligible over the measurement frequency range; 3) they couple well to the ground; and 4) the coupling is similar for each receiver. These 1-Hz seismometers have outputs in excess of 10 volts/(in/sec) and phase shifts between receivers of less than 3.6 degrees for frequencies from 2 to 300 Hz. All equipment calibrations and procedures are presented in Scientific Notebook SN-M&O-SCI-022-V1 (Wong 2002c, Appendix 39).

The preferred arrangement of the receivers for each SASW survey is called a common receivers-midpoint geometry. This arrangement is illustrated on Figure 44. In this arrangement, the two receivers are located equidistant from an imaginary centerline of the survey, which is kept fixed. Due to limited space and numerous physical obstacles at the WHB site, it was not possible in many cases to use the common midpoint geometry. In these situations, a common source

location was employed where the source location was kept constant and the receivers were moved away from the source. Additionally, at each spacing, SASW measurements are ideally performed with the source located first on one end of the survey and then repeated with the source moved to the opposite end of the survey (termed forward and reverse directions). If sound data are recorded in both directions, the cross-power spectra can be combined to eliminate any differences in receiver phase shifts or receiver coupling. Space limitations and numerous obstacles at the WHB limited the ability to perform forward and reverse testing at all spacings. Therefore, in some situations only one direction was recorded. Performing the survey in only one direction had an insignificant effect on the results because the receivers had already been shown to be well matched, and any differences in receiver-to-ground coupling were insignificant.

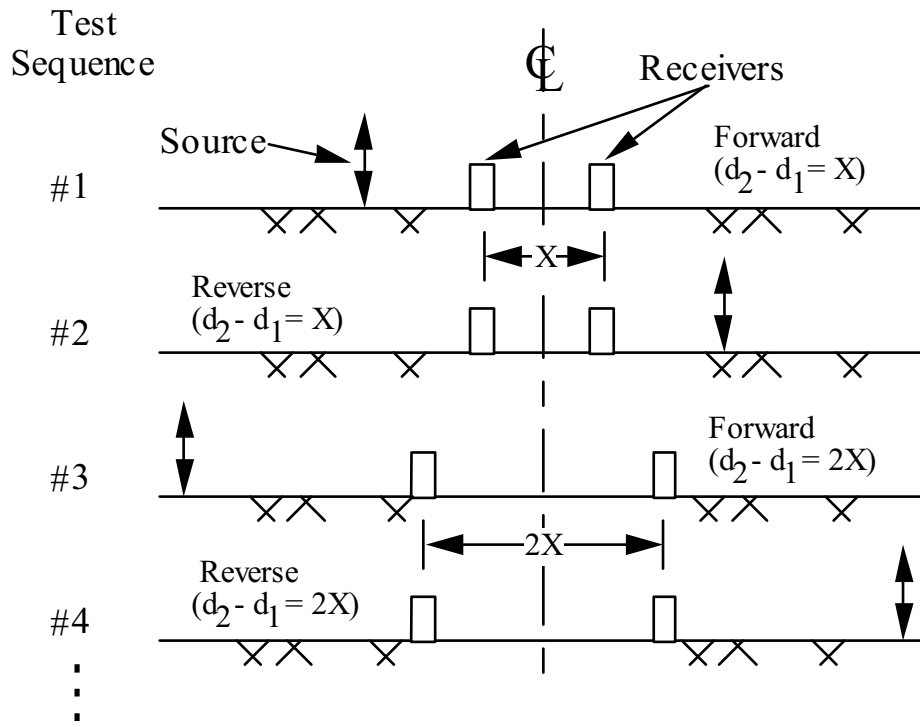


Figure 44. Common Receivers-Midpoint Geometry Often Used in SASW Surveys

Surveys were performed at a series of increasing spacings. Distances between receivers of 3, 6, 12, 25, 50, 100, and 200 ft were typically used to evaluate velocity profiles to depths on the order of 150 ft. The exact receiver spacings used at each site can be found on the data sheets presented in the Supplemental Records to Scientific Notebooks SN-M&O-SCI-022-V1 (Wong 2002c) and SN-M&O-SCI-040-V1 (Wong 2002a). The number and progression of receiver spacings resulted in extensive overlapping of individual dispersion curves used to develop the composite field curve which enhanced the reliability of the measurements.

Several types of sources were used to generate energy over the required frequency ranges. At the shortest receiver spacings (typically 3 and 6 ft), a hand-held geology hammer was used to impact the ground. At larger receiver spacings (typically 12 and 25 ft), a sledgehammer was employed (Figure 45). For receiver spacings equal to and greater than 25 ft, a bulldozer was

used by operating it back and forth over a distance of several meters. This arrangement with the bulldozer as the source is shown on Figures 46 and 47. Generally, when the bulldozer was used, measurements were performed in only the forward direction due to the limitations mentioned previously.



Figure 45. Using the Sledgehammer Source at SASW-23

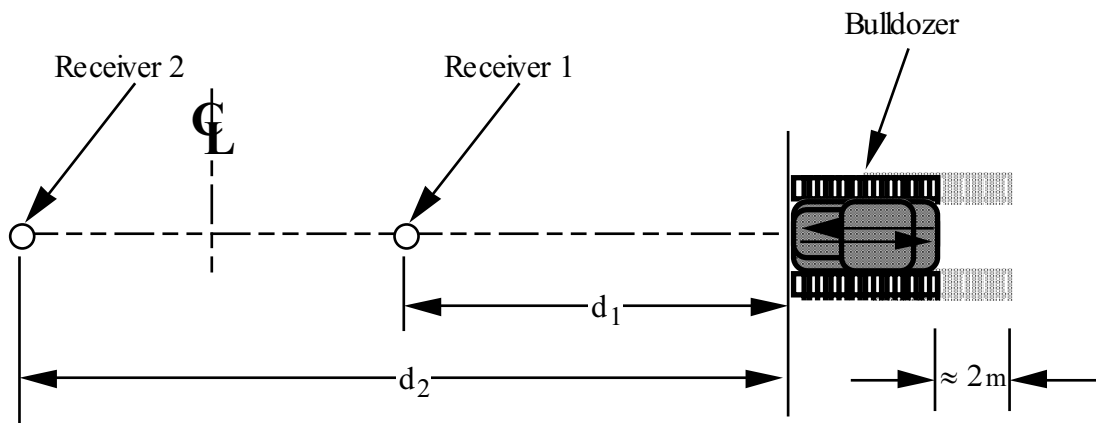


Figure 46. SASW Survey Set-Up Using the Bulldozer as a Wave Source



Figure 47. Bulldozer Source in Operation at SASW-32

At three sites (SASW-35, 36, and 37), deep profiling was performed using a Vibroseis truck as the source of the surface wave energy. As with the bulldozer, surveys were performed only in one direction with this large source. At one of these sites, receiver spacings up to 650 ft were used, generating dispersion curves with a maximum wavelength on the order of 1,000 ft. The dispersion curves from these deep surveys were combined with the shallower dispersion curves from nearby sites (SASW-10+37, 32+35, and 34+36).

The recording device used in the SASW surveys was a Hewlett-Packard 3562A Dynamic Signal Analyzer. The dynamic signal analyzer was used to collect the time records and to perform calculations in the frequency domain so that the relative phase of the cross-power spectrum (discussed below) was reviewed at each receiver spacing. This process also allowed the operator to subjectively evaluate the data being collected in the field to assure consistency with the expected Rayleigh wave propagation in a layered halfspace.

6.2.7.2.2 Calculations

The dynamic signal analyzer was used to measure time-domain records ($x[t]$ and $y[t]$) from the two receivers at each receiver spacing. These time records were then transformed into the frequency domain ($X[f]$ and $Y[f]$) and used to calculate the power spectra (G_{XX} and G_{YY}), the cross spectrum (G_{XY}), and the coherence function (γ^2). Expressions for these quantities are (Joh 1996, p. 32):

$$G_{xx} = X^*(f) \cdot X(f) \quad (\text{Eq. 6})$$

$$G_{YY} = Y^*(f) \cdot Y(f) \quad (\text{Eq. 7})$$

$$G_{XY} = X^*(f) \cdot Y(f) \quad (\text{Eq. 8})$$

$$\phi(f) = \arctan \left[\frac{\text{Im}(G_{XY})}{\text{Re}(G_{XY})} \right] \quad (\text{Eq. 9})$$

$$\gamma^2(f) = \frac{|G_{XY}(f)|^2}{G_{XX}(f) \cdot G_{YY}(f)} \quad (\text{Eq. 10})$$

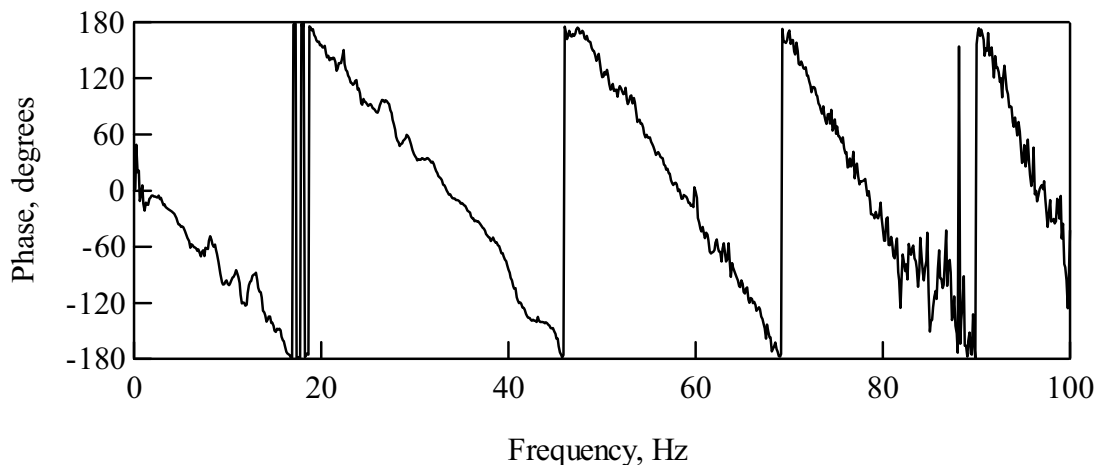
where $G_{XY}(f) = \frac{1}{N} \sum_{i=1}^N X^*(f) \cdot Y_i(f)$ is the cross-power spectrum from coherent signal averaging, (*) represents the complex conjugate of the quantity, Im is the imaginary part of the expression, Re is the real part of the expression, and $\phi(f)$ is the relative phase of the cross-power spectrum.

The relative phase of the cross spectrum $\phi(f)$ is the key spectral quantity in SASW measurements. The coherence function of averaged measurements is also important as an indicator of the quality of the measurement over the monitored frequency range. Low values of coherence indicate a possible decrease in data quality. Typically, 3 to 5 time-domain records were averaged in the determination of the spectral functions when impact sources were used. However, when the bulldozer was used as the source at the larger spacings, 10 to 20 averages were typically taken. The relative phase of the cross spectrum, simply called the phase hereafter, represents the phase difference of the motion at the two receivers. One set of spectral functions was measured for each receiver spacing and measurement direction. All of the phase plots that were used in the interpretation of the data are presented in the Supplemental Records to Scientific Notebooks SN-M&O-SCI-022-V1 (Wong 2002c) and SN-M&O-SCI-040-V1 (Wong 2002a).

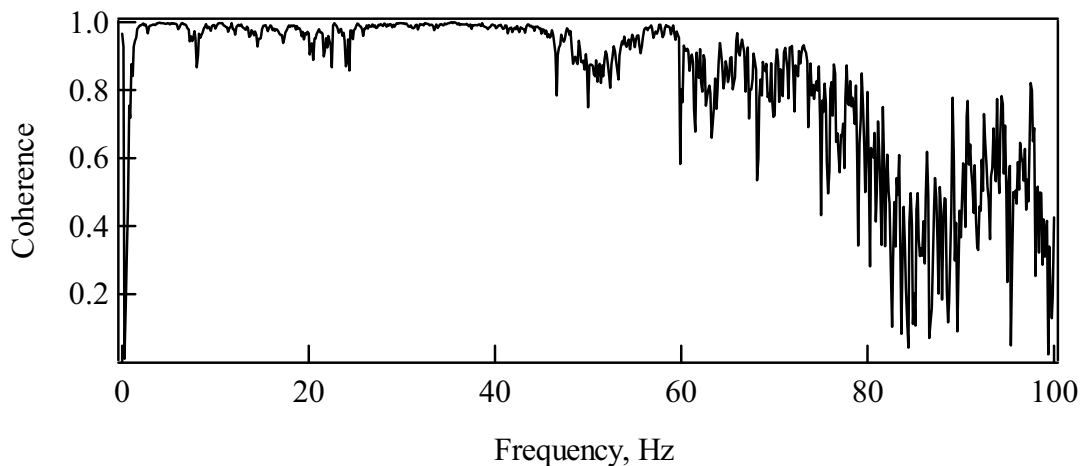
As an example, the wrapped phase spectrum and coherence function from one receiver spacing are shown in Figure 48. These data were collected from the 50-ft receiver spacing recorded at SASW-24.

6.2.7.2.3 Data Reduction and Forward Modeling Procedures

The data collected in the field in the form of phase plots and coherence functions were transferred from the field disks to a laptop computer, as discussed in the Supplemental Records to Scientific Notebook SN-M&O-SCI-022-V1 (Wong 2002c, Appendix 37, pages 327-368). The data were then reduced and interpreted using the program WinSASW, developed by Joh (1996). For each receiver spacing, the phase plot and coherence function were loaded into WinSASW. A masking procedure was performed to manually eliminate portions of the data with poor signal quality or portions of the data contaminated by the near-field noise.



a. Cross-Power Spectrum

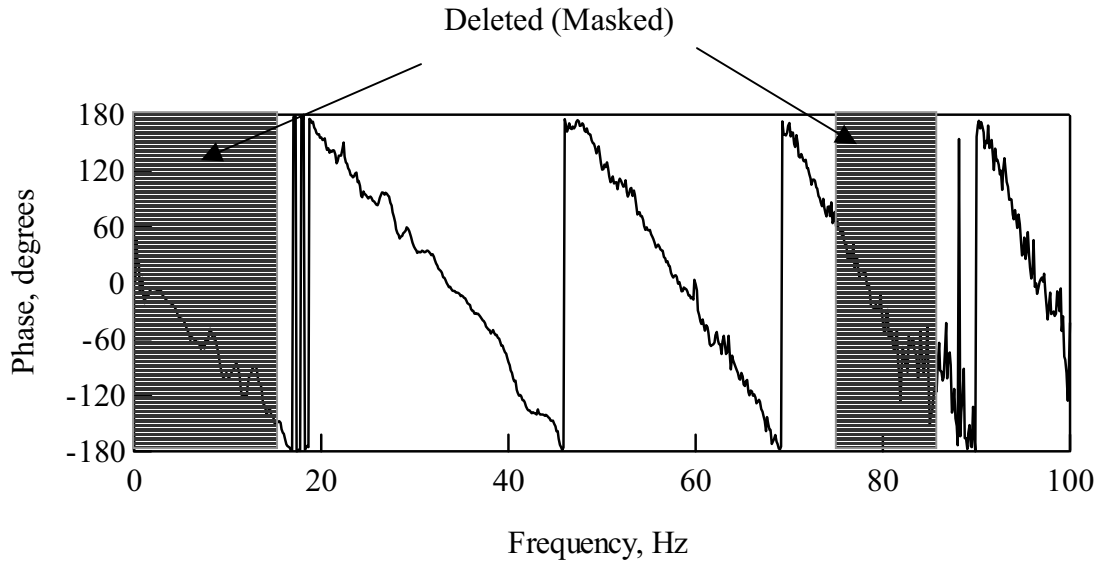


b. Coherence Function

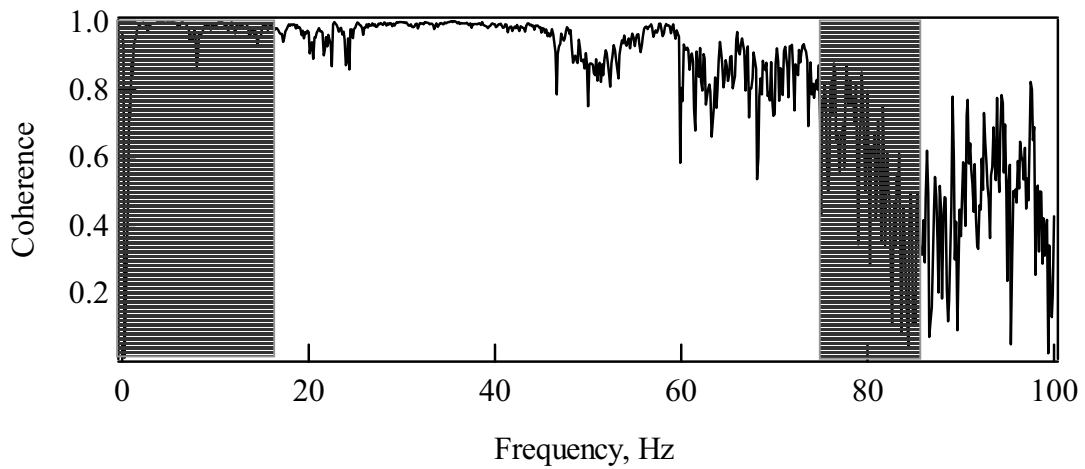
Source: Wong (2002c, Appendix 39, page 437)

Figure 48. Cross-Power Spectrum and Coherence Function Measured at SASW-24 from 50-ft Receiver Spacing

Figure 49 shows the masking applied to the phase plot collected at SASW-24. The masking of every phase plot used in the data analysis at each site is presented in the Supplemental Records to Scientific Notebooks SN-M&O-SCI-022-V1 (Wong 2002c) and SN-M&O-SCI-040-V1 (Wong 2002a). The program uses the masking information to unwrap the phase plot and calculate the dispersion curve using equation 5. Figure 50 shows the individual dispersion curve created from the masking of the phase plot shown on Figure 49. This process was repeated for all receiver spacings resulting in an experimental dispersion curve covering a wide range of wavelengths (typically 1 to 300 ft). Figure 51 shows the composite experimental dispersion curve created at SASW-24.



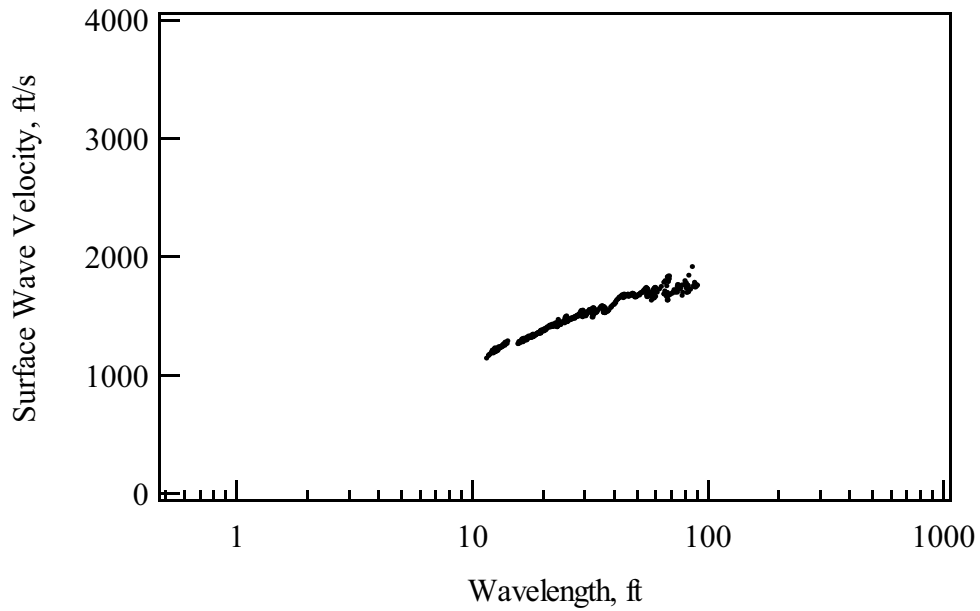
a. Cross-Power Spectrum



b. Coherence Function

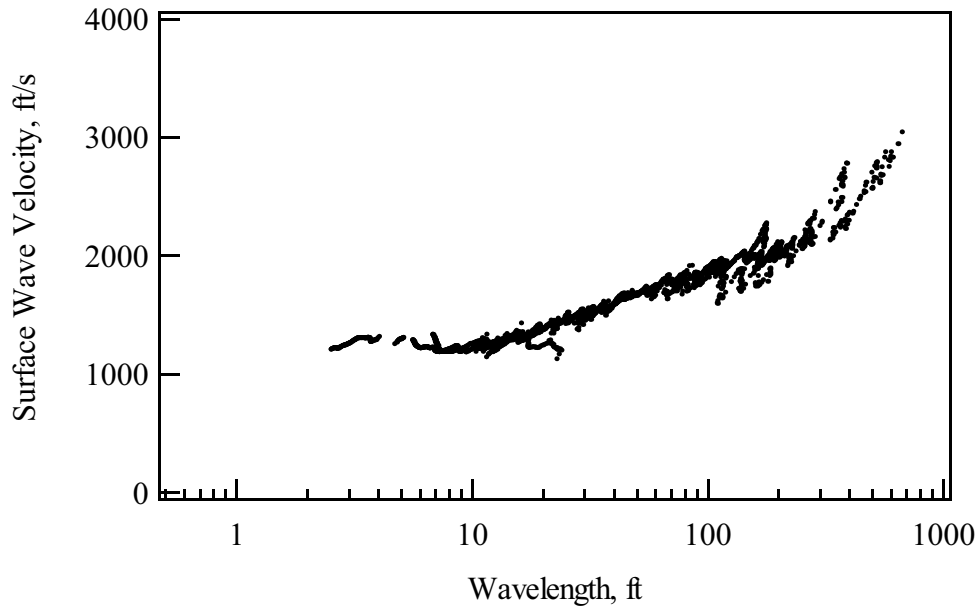
Source: Wong (2002c, Appendix 39, page 438)

Figure 49. Cross-Power Spectrum and Coherence Function Measured at SASW-24 from 50-ft Receiver Spacing Shown with Masking Applied to Near-Field and Low Coherence Regions of the Phase Plot



DTN: MO0110SASWWHBS.000

Figure 50. Individual Dispersion Curve Created from 50-ft Receiver Spacing at SASW-24



Source: Wong (2002c, Appendix 39, page 439)

Figure 51. Composite Experimental Dispersion Curve Created from All Receiver Spacings at SASW-24

The next step in the data reduction procedure was the creation of the theoretical dispersion curve. The program WinSASW was also used for this purpose. WinSASW uses an algorithm based on a stiffness matrix approach to generate a theoretical dispersion curve for a given shear-wave velocity profile (Kausel and Roesset 1981). The theoretical dispersion curve that is generated can be either the first-mode Rayleigh-wave solution (termed 2D approach) or a complete solution that includes all modes and all other body-wave arrivals (termed 3D approach). For these analyses, the more accurate 3D approach was employed. An initial shear-wave velocity profile was estimated based on the characteristics of the measured experimental dispersion curve. The theoretical dispersion curve was generated and compared to the experimental curve. The shear-wave velocities and layer thicknesses were iteratively changed until an acceptable fit to the experimental curve is achieved. Figure 52 shows the final fit to the composite experimental dispersion curve for SASW-24, and Figure 53 shows the final shear-wave velocity profile.

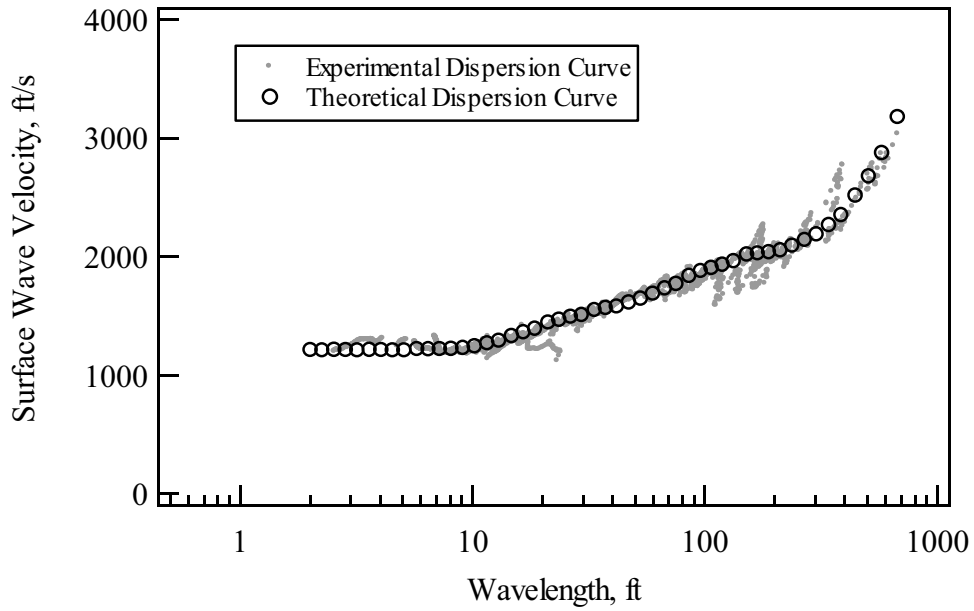
The theoretical and experimental dispersion curves generated at every site are presented in Attachment IX except for D-12. The D-12 survey was performed as part of the 2001 survey (Section 6.4). For the theoretical analysis, several factors must be considered. First, the density and Poisson's ratio of the material must be estimated. A value of Poisson's ratio of 0.25 was assigned to all materials (Figure 28). When no water table is present, as was the case here, low values of Poisson's ratio (< 0.4) have only a minor influence on the calculated dispersion curve (Brown 1998, Section 7.3.2). The values of unit weight were estimated based on values determined in the laboratory (Section 6.2.10). Thus, a density of 120 lbs/ft³ was assigned to material with a shear-wave velocity less than 3,000 ft/s, 80 lbs/ft³ for material between 3,000 and 5,000 ft/s, and 145 lbs/ft³ for material with a shear-wave velocity equal to or greater than 5,000 ft/s. Relative changes in density with depth affect the dispersion curve, but again the effect on the final shear-wave velocity profile is minor. Therefore, precise knowledge of these values is not required.

Secondly, the theoretical dispersion curve can be generated using different configurations of receiver locations. For these analysis, the theoretical dispersion curve was calculated using a source-to-receiver-1 spacing of two wavelengths and a source-to-receiver-2 spacing of four wavelengths. These receiver locations represent far-field motions. Past studies have shown that the range in wavelengths collected in the SASW surveys do not differ significantly from the far-field motions (Foinquinos Mera 1991; Roesset et al. 1991).

Lastly, the final shear-wave velocity profile was presented to a depth of approximately 0.5 times the maximum wavelength in the experimental dispersion curve. This cutoff depth is based on the fact that most of the particle motion occurs at depths less than one-half of the wavelength, as shown on Figure 41. Experience has shown this to be an acceptable cut-off depth for shear-wave velocity profiles (Brown 1998, Section 7.5).

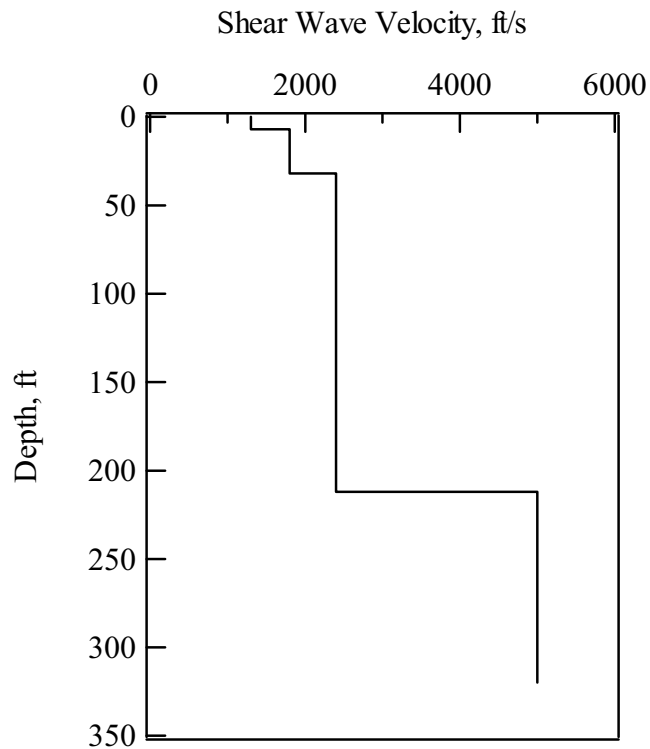
6.2.7.3 Results

All final shear-wave velocity profiles are shown in Figures 54 to 88 and values are listed in Attachment IX.. All 35 shear-wave velocity profiles estimated from the SASW surveys are shown on Figure 89 (except for D-12). For selected profiles, the generalized lithology from the nearest borehole (Figure 43) is also shown. A total of 20 profiles extend to depths of 150 ft or greater. Shear-wave velocity profiles to depths of 300 feet or greater were generated along five



Source: Wong (2002c, Appendix 39, page 440)

Figure 52. Theoretical Dispersion Curve Fit to the Experimental Dispersion Curve at SASW-24



Source: Wong (2002c, Appendix 39, page 440)

Figure 53. Final Shear-Wave Velocity Profiles Determined at SASW-24

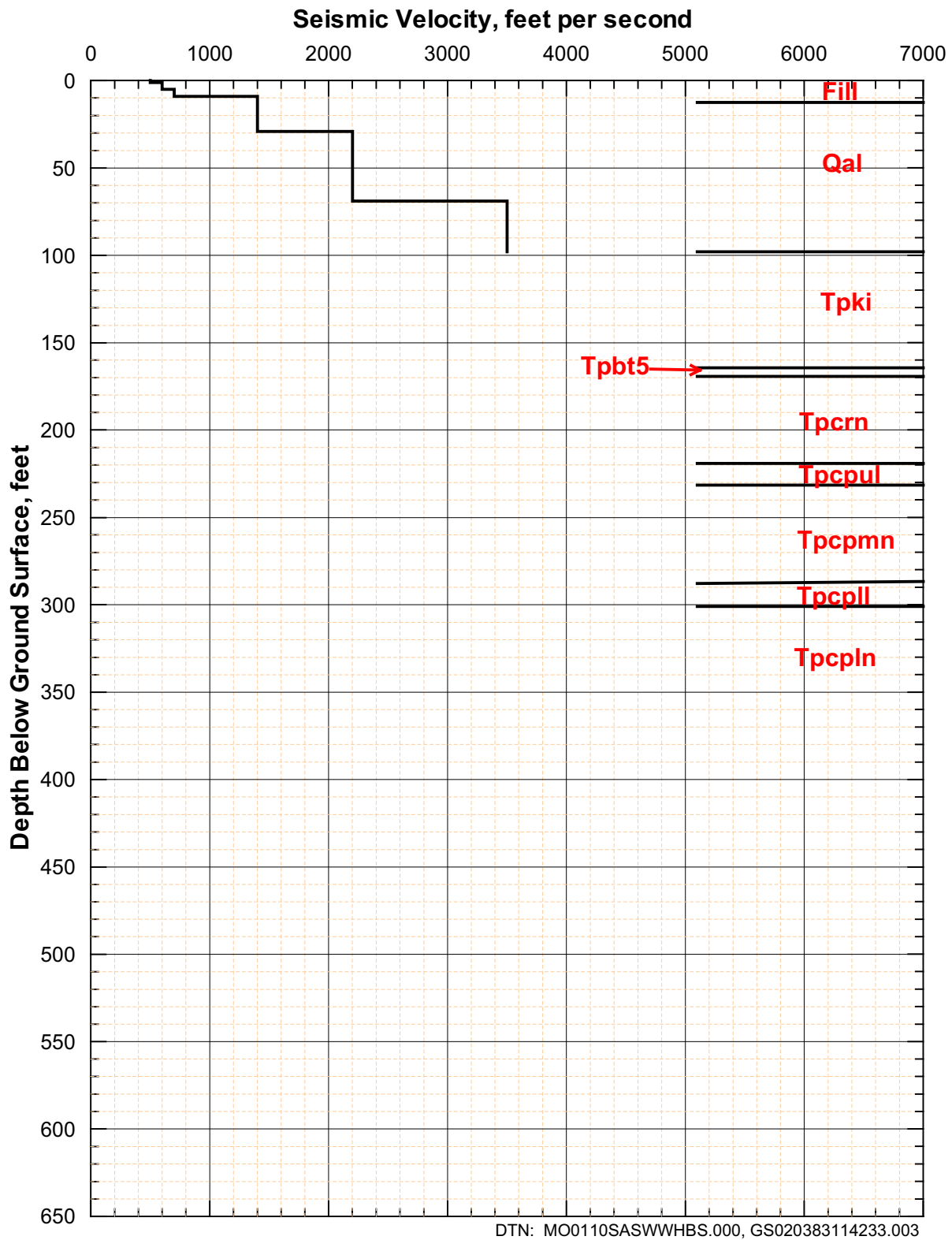


Figure 54. Shear-Wave Velocity Profile from SASW-1 and Generalized Lithology from RF#13

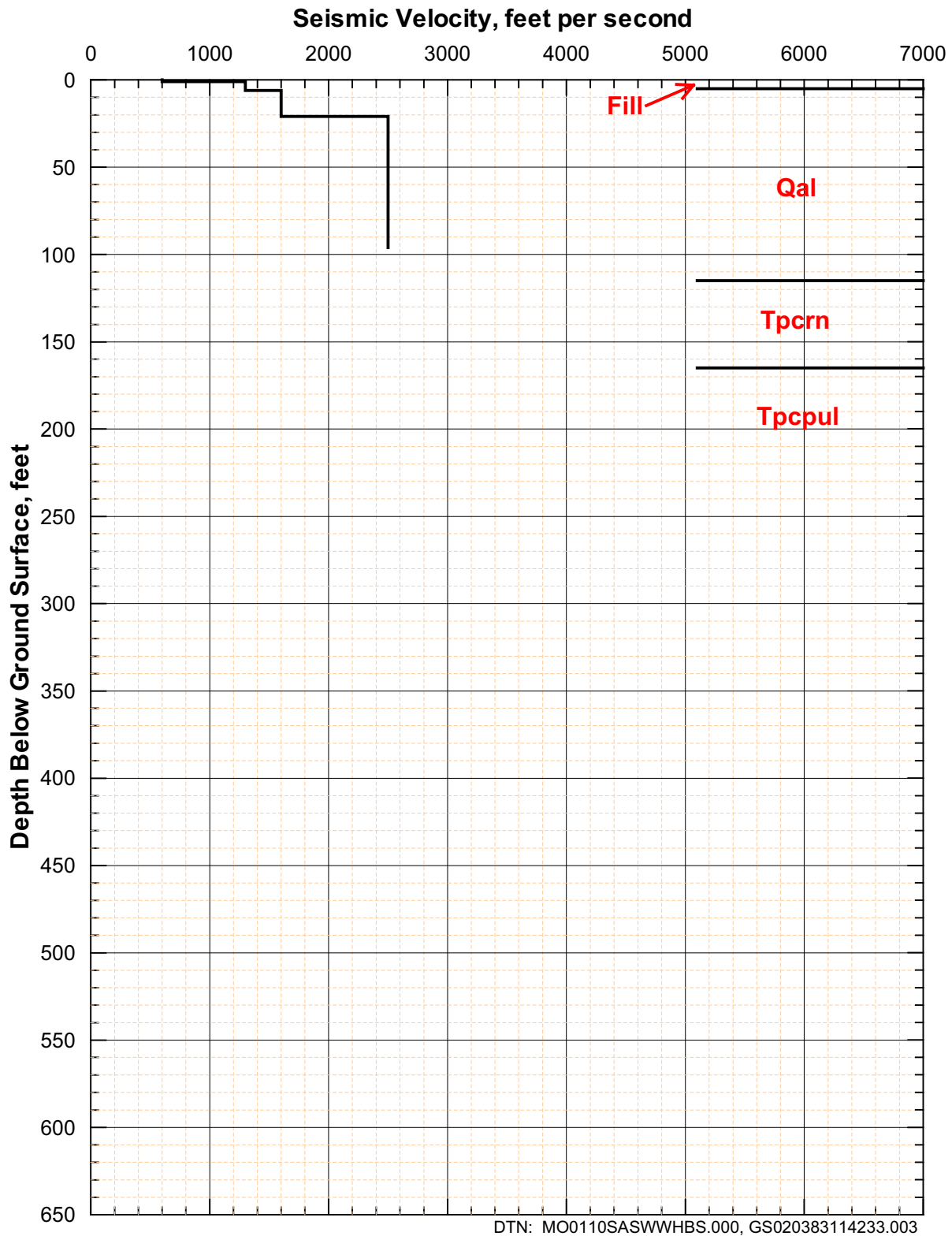
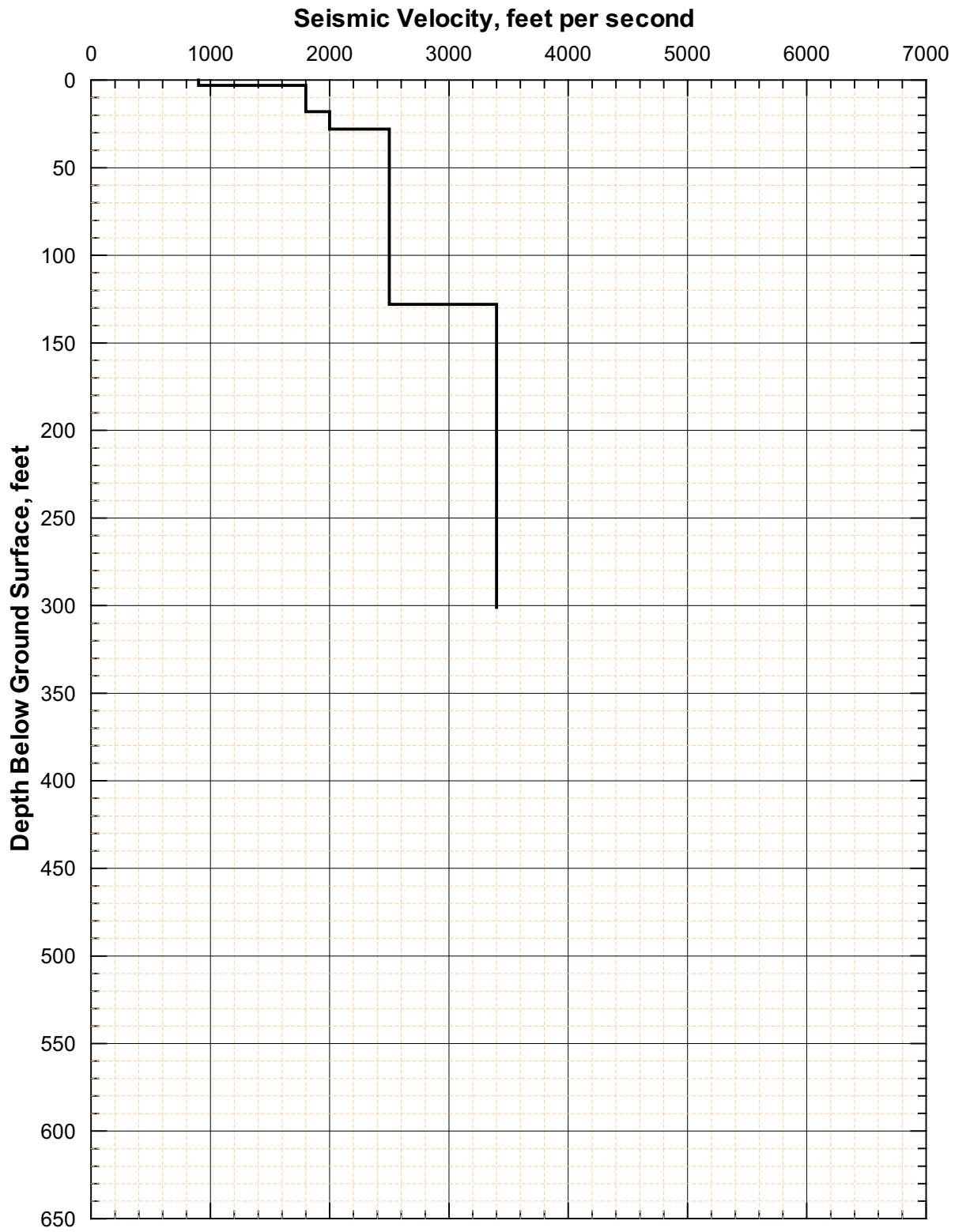


Figure 55. Shear-Wave Velocity Profile from SASW-2 and Generalized Lithology from RF#21



DTN: MO0110SASWWHBS.000

Figure 56. Shear-Wave Velocity Profile from SASW-3

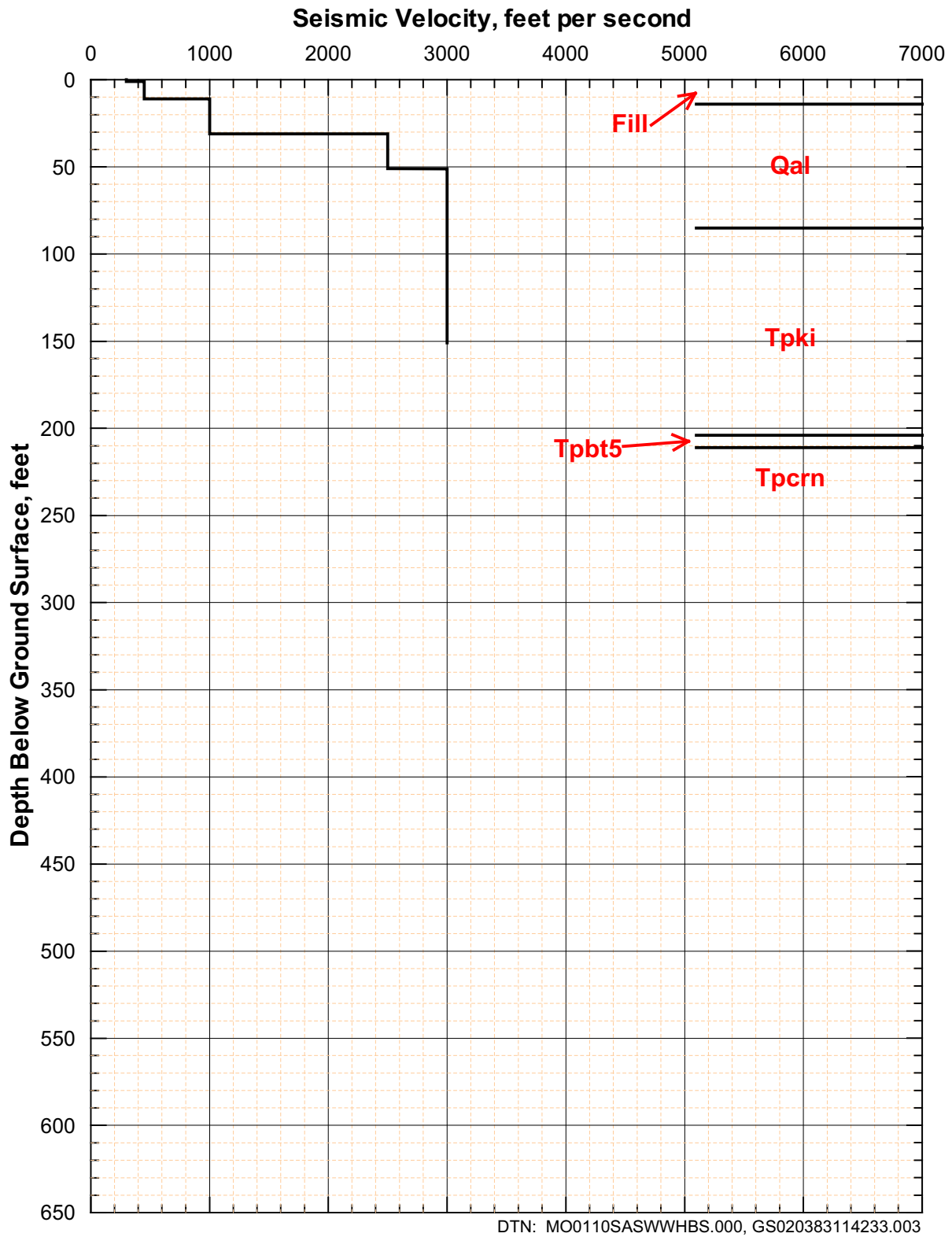


Figure 57. Shear-Wave Velocity Profile from SASW-4 and Generalized Lithology from RF#26

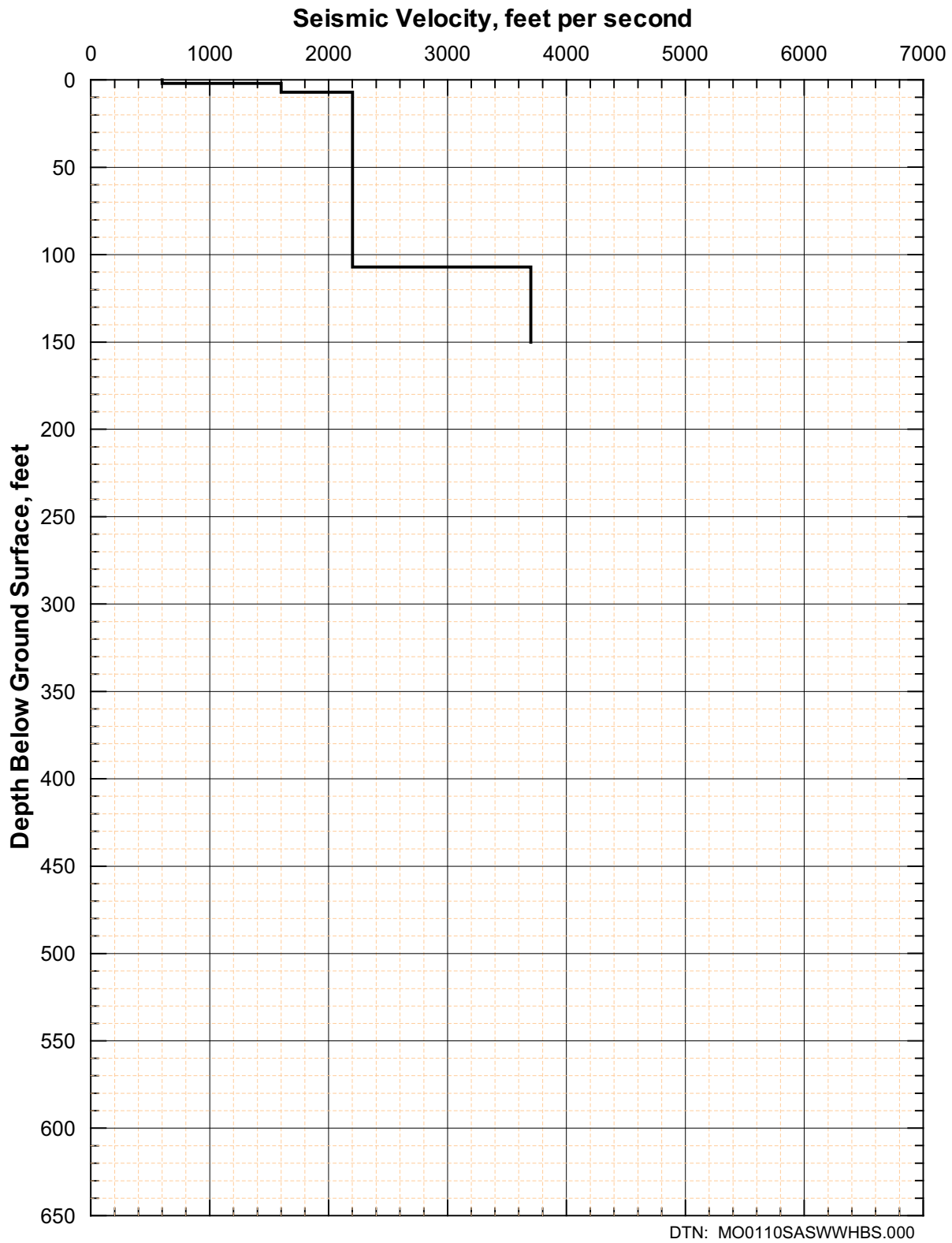


Figure 58. Shear-Wave Velocity Profile from SASW-5

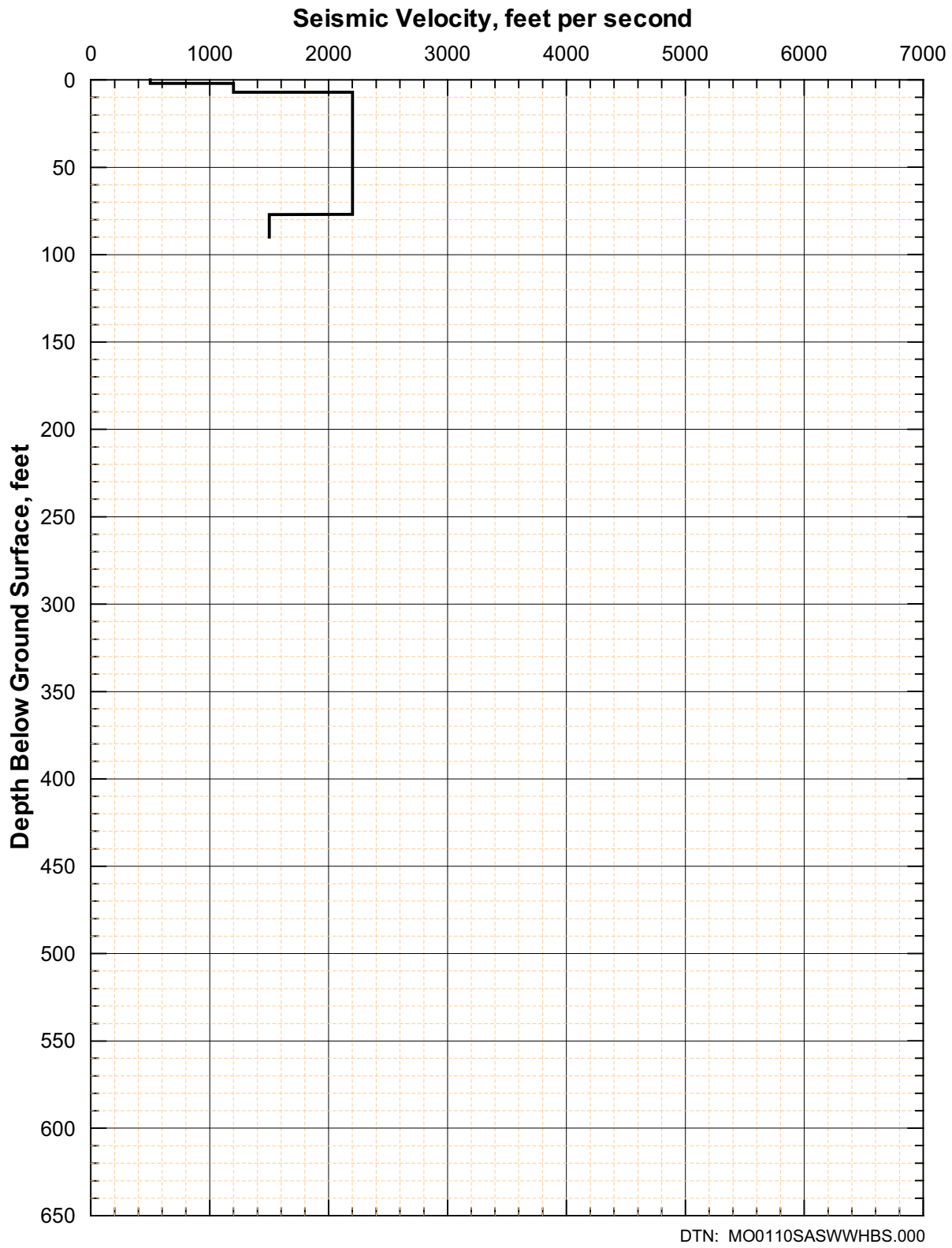


Figure 59. Shear-Wave Velocity Profile from SASW-6

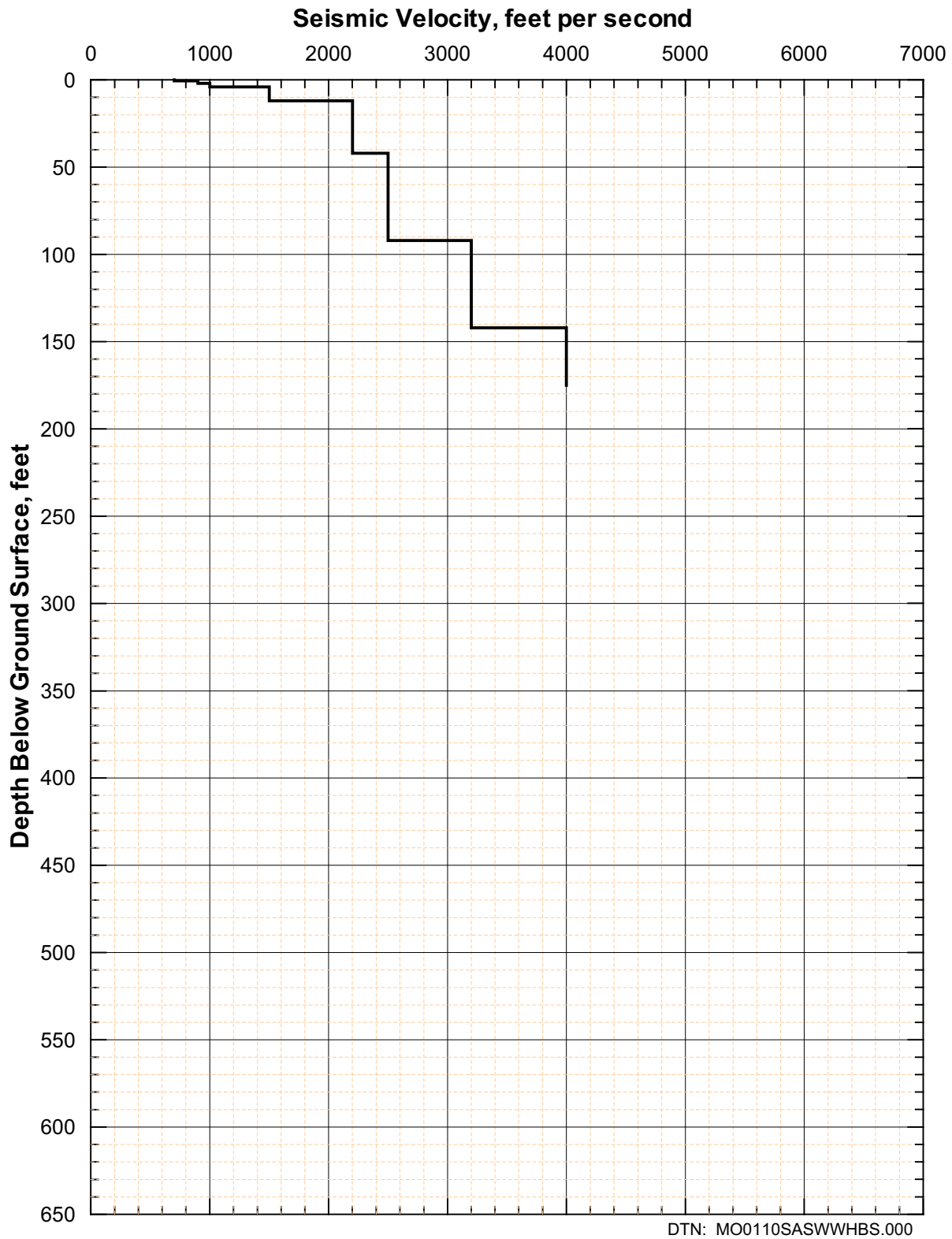


Figure 60. Shear-Wave Velocity Profile from SASW-7

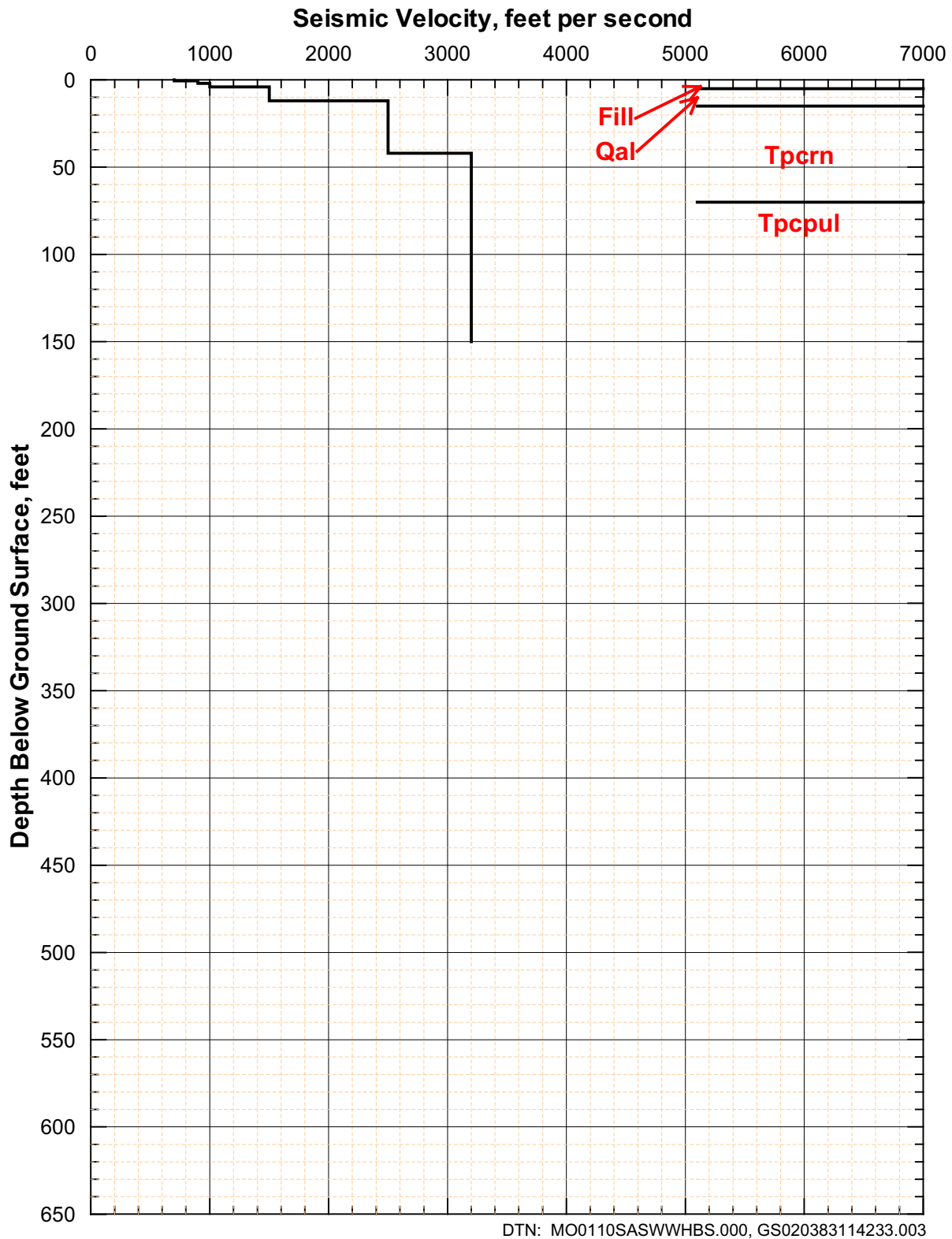


Figure 61. Shear-Wave Velocity Profile from SASW-8 and Generalized Lithology from RF#28

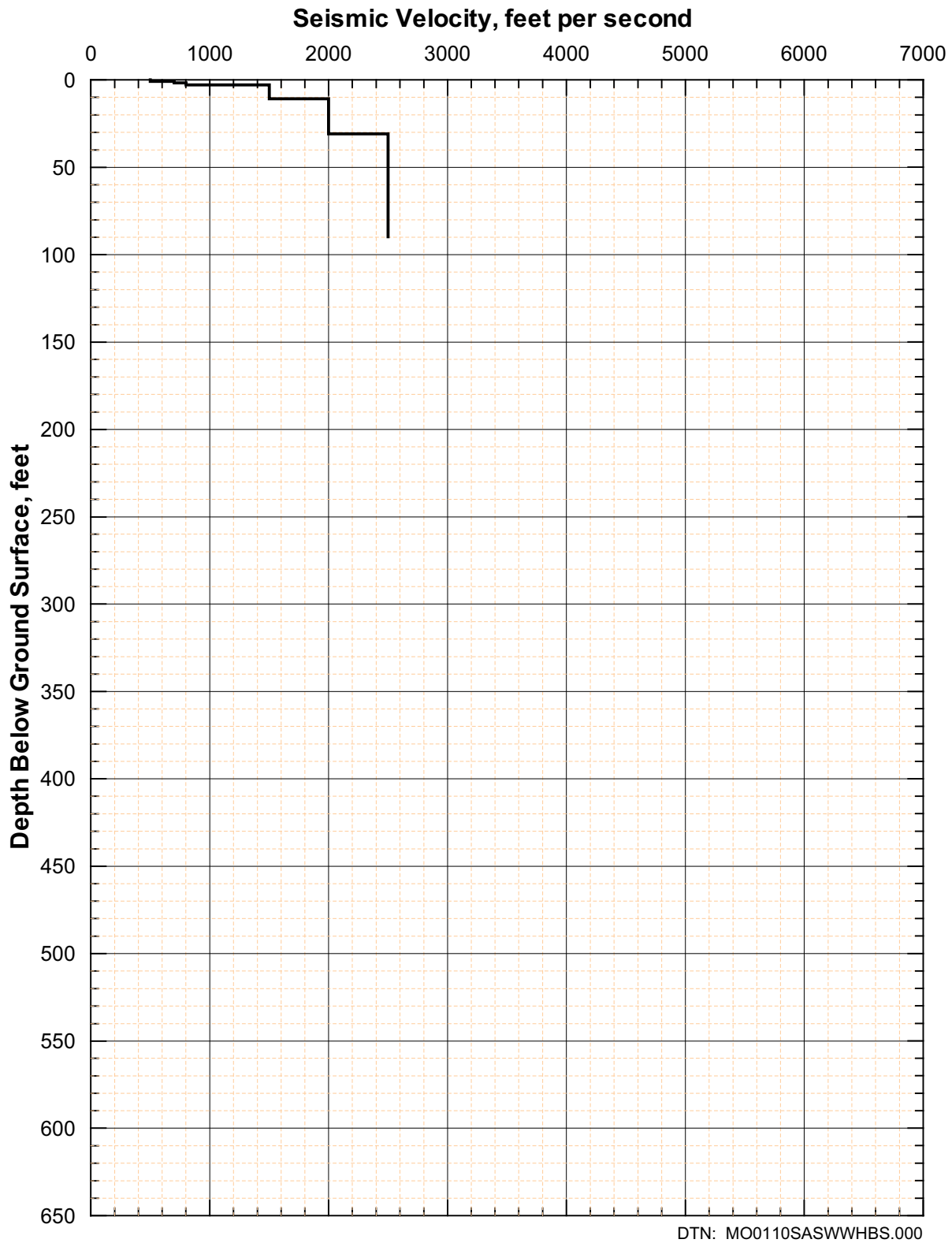


Figure 62. Shear-Wave Velocity Profile from SASW-9

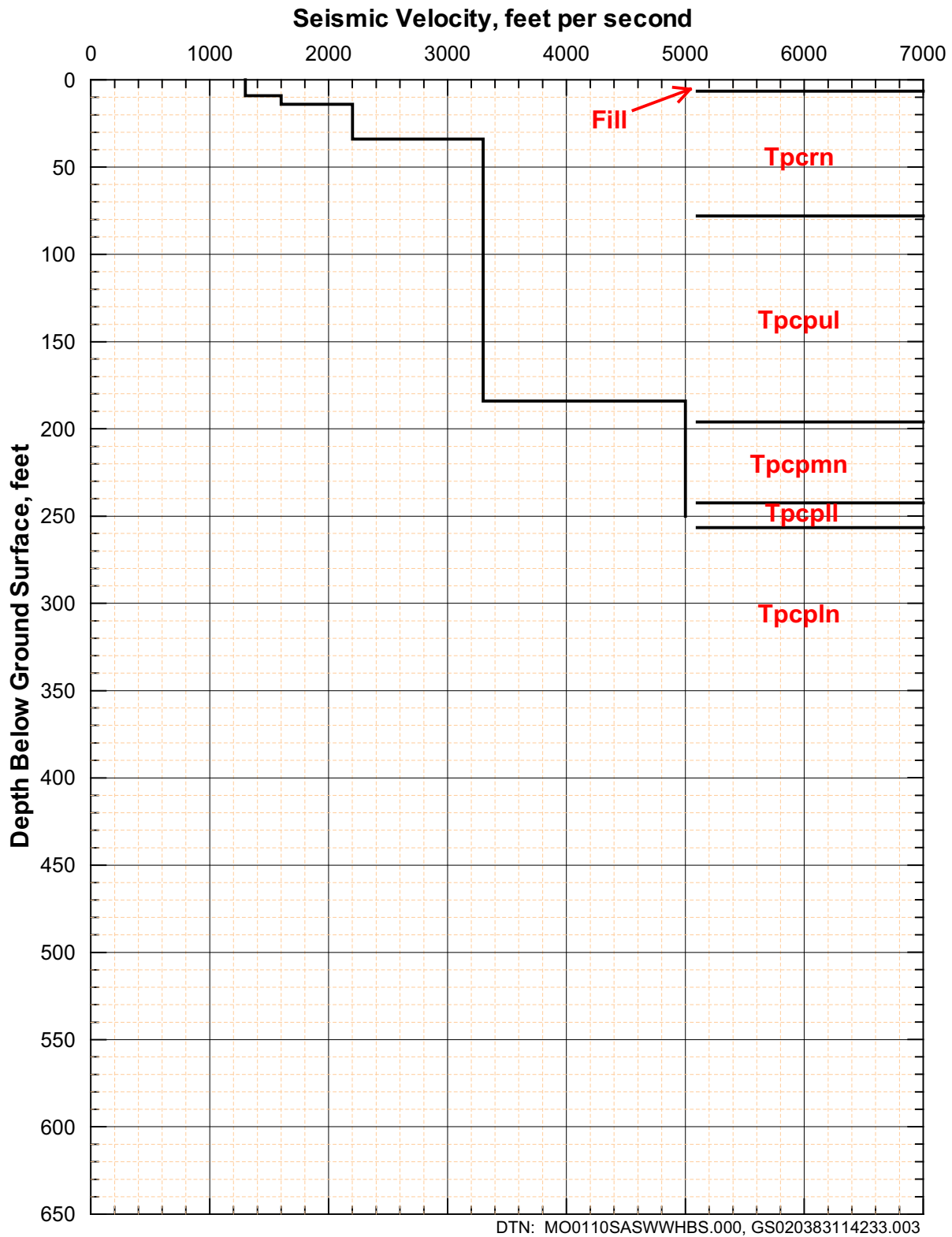


Figure 63. Shear-Wave Velocity Profile from SASW-10+37 and Generalized Lithology from RF#15

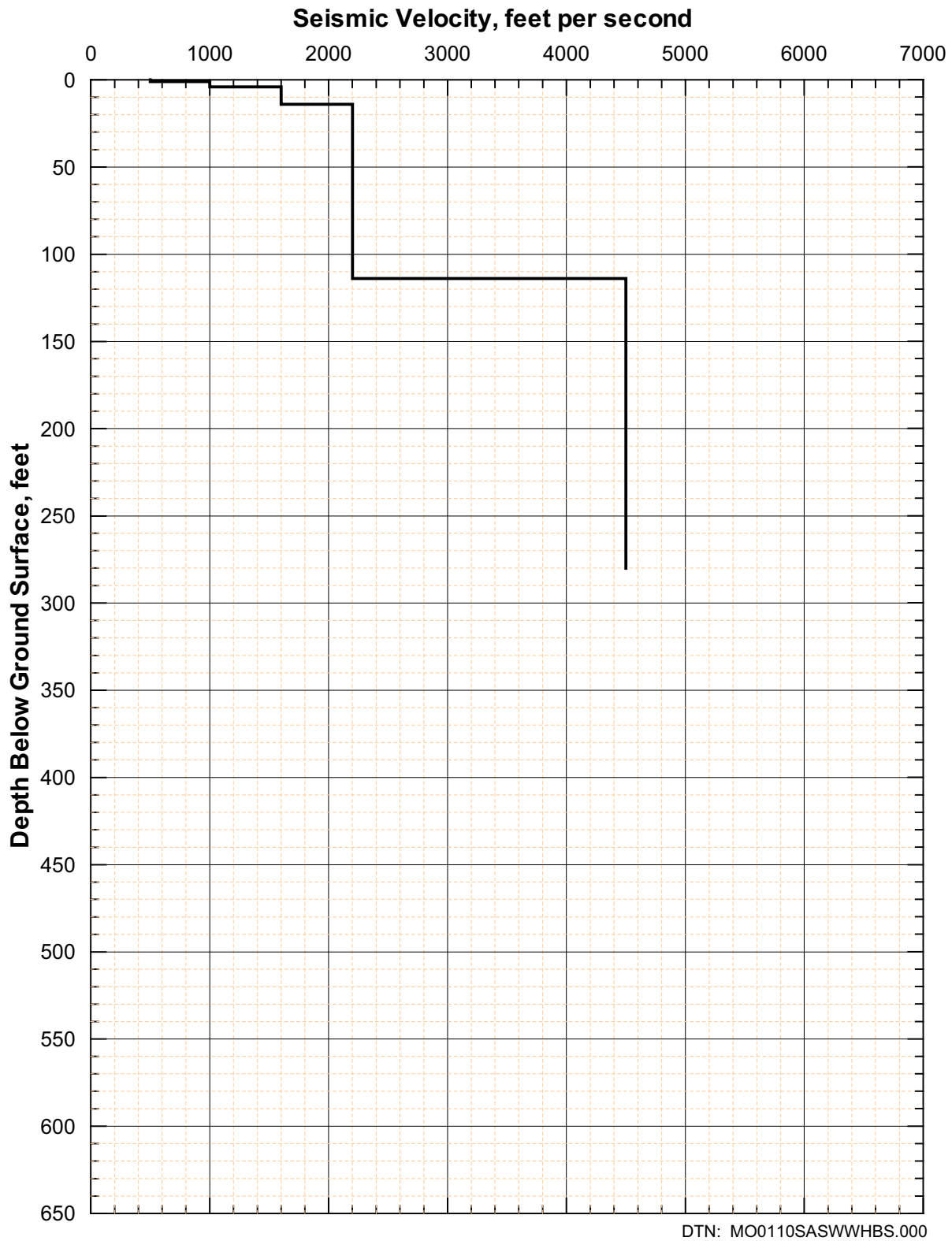


Figure 64. Shear-Wave Velocity Profile from SASW-11

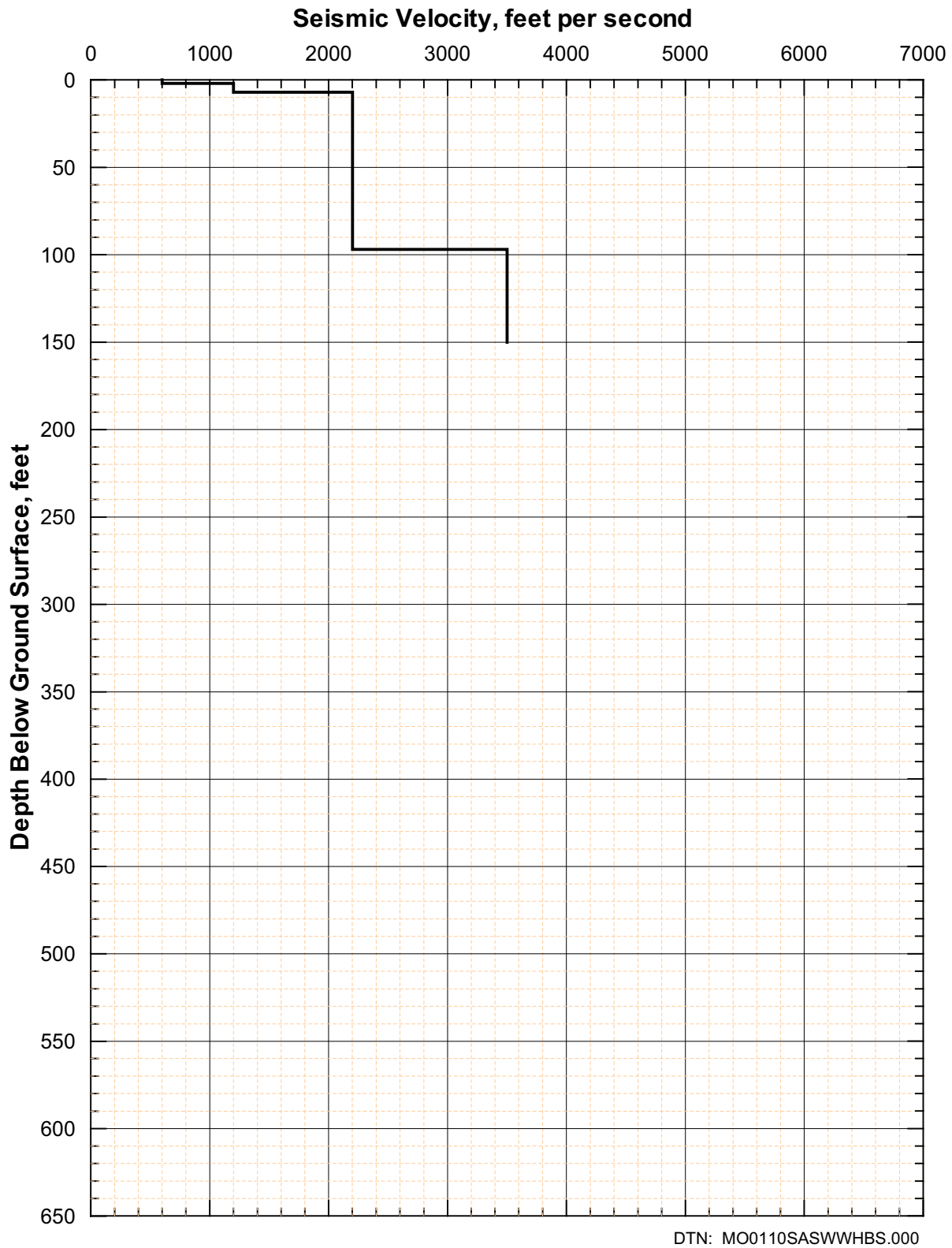


Figure 65. Shear-Wave Velocity Profile from SASW-12

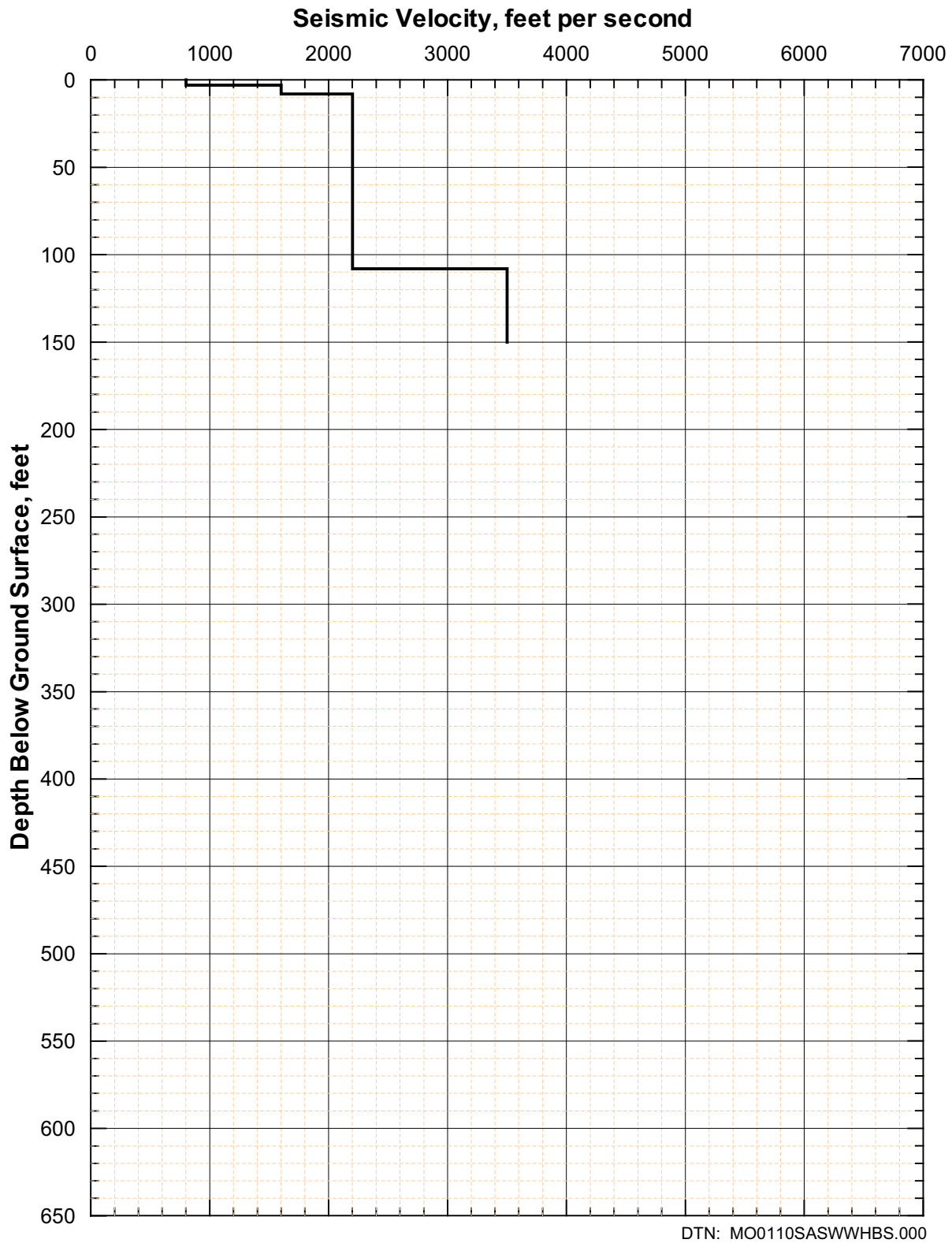


Figure 66. Shear-Wave Velocity Profile from SASW-13

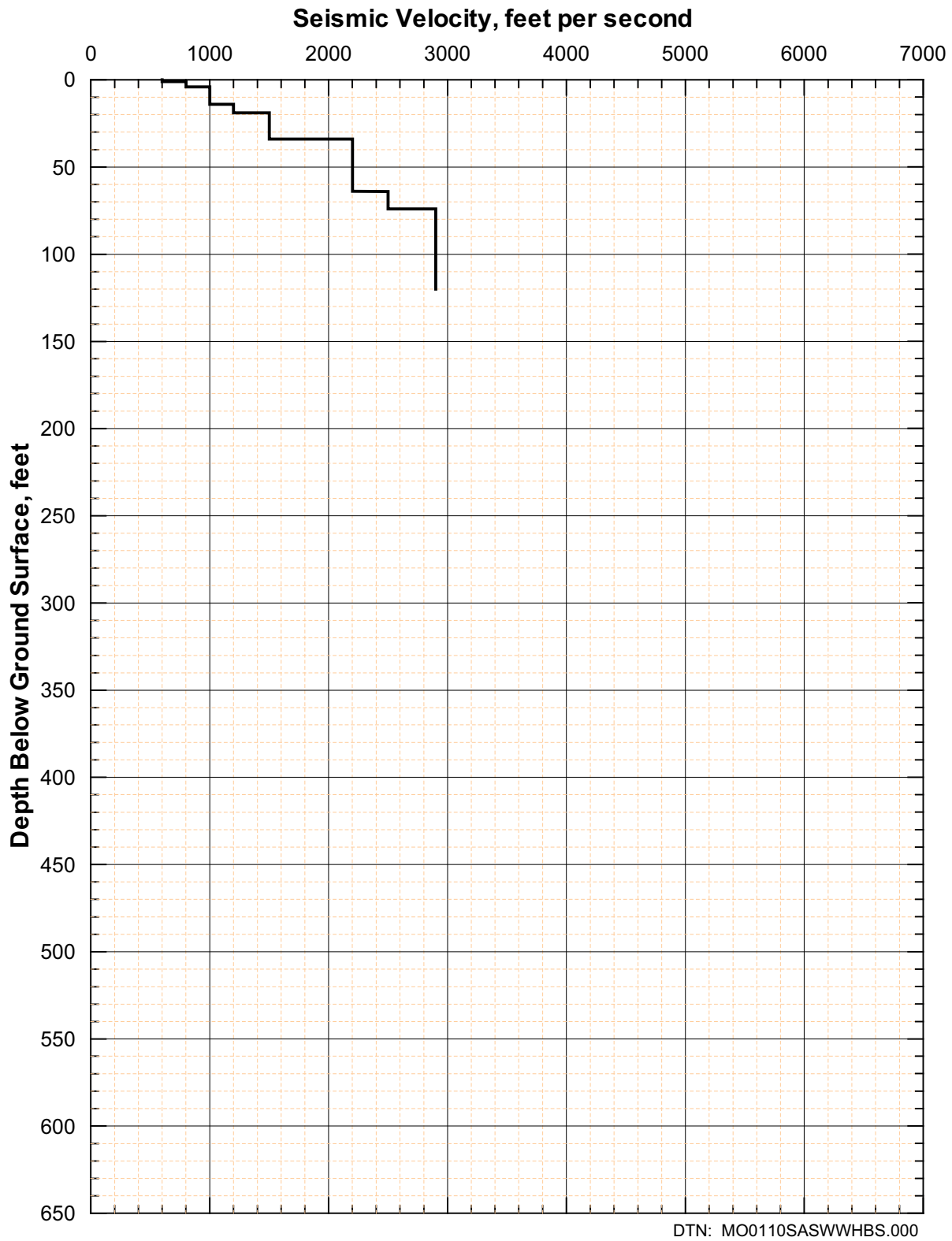


Figure 67. Shear-Wave Velocity Profile from SASW-14

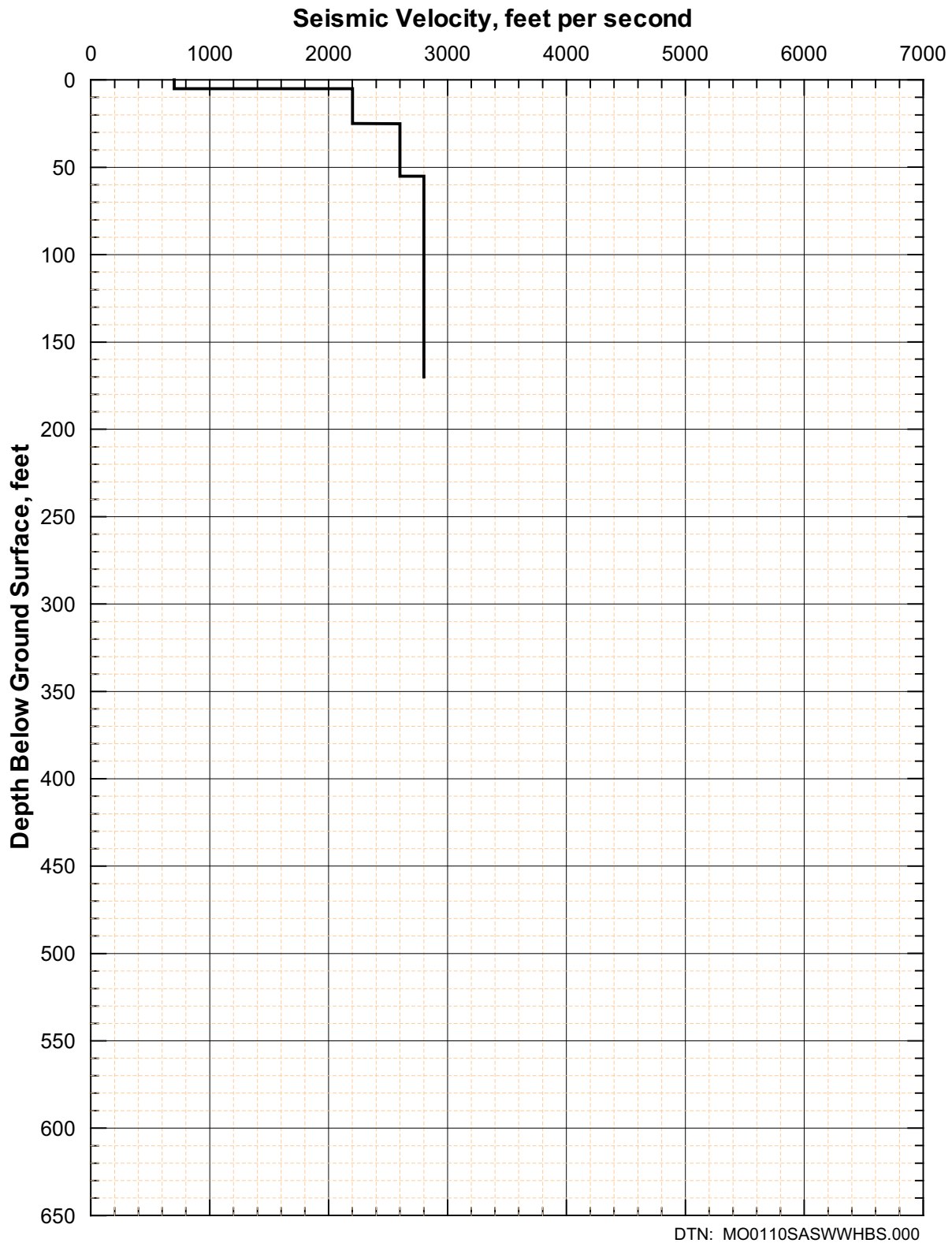


Figure 68. Shear-Wave Velocity Profile from SASW-15

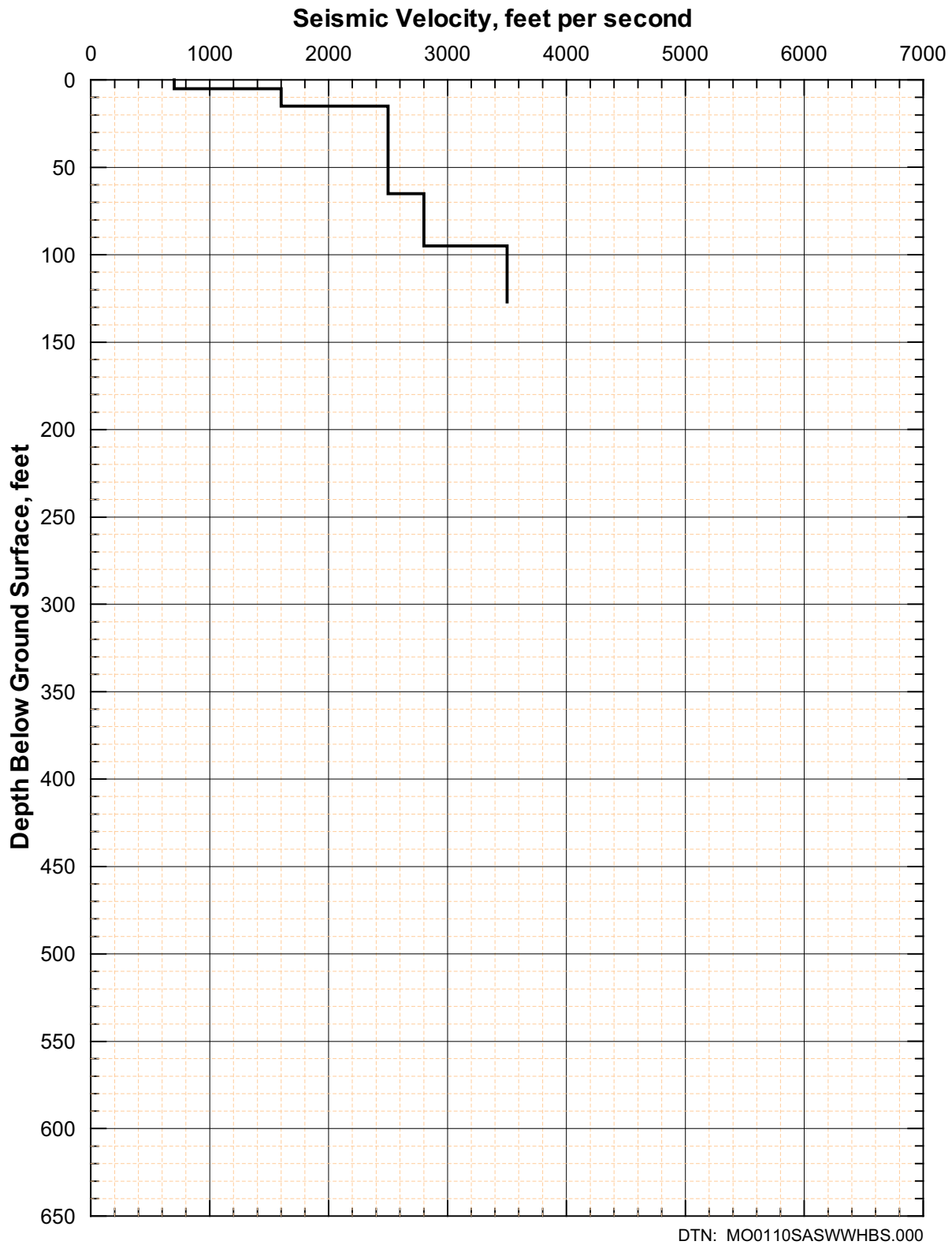


Figure 69. Shear-Wave Velocity Profile from SASW-16

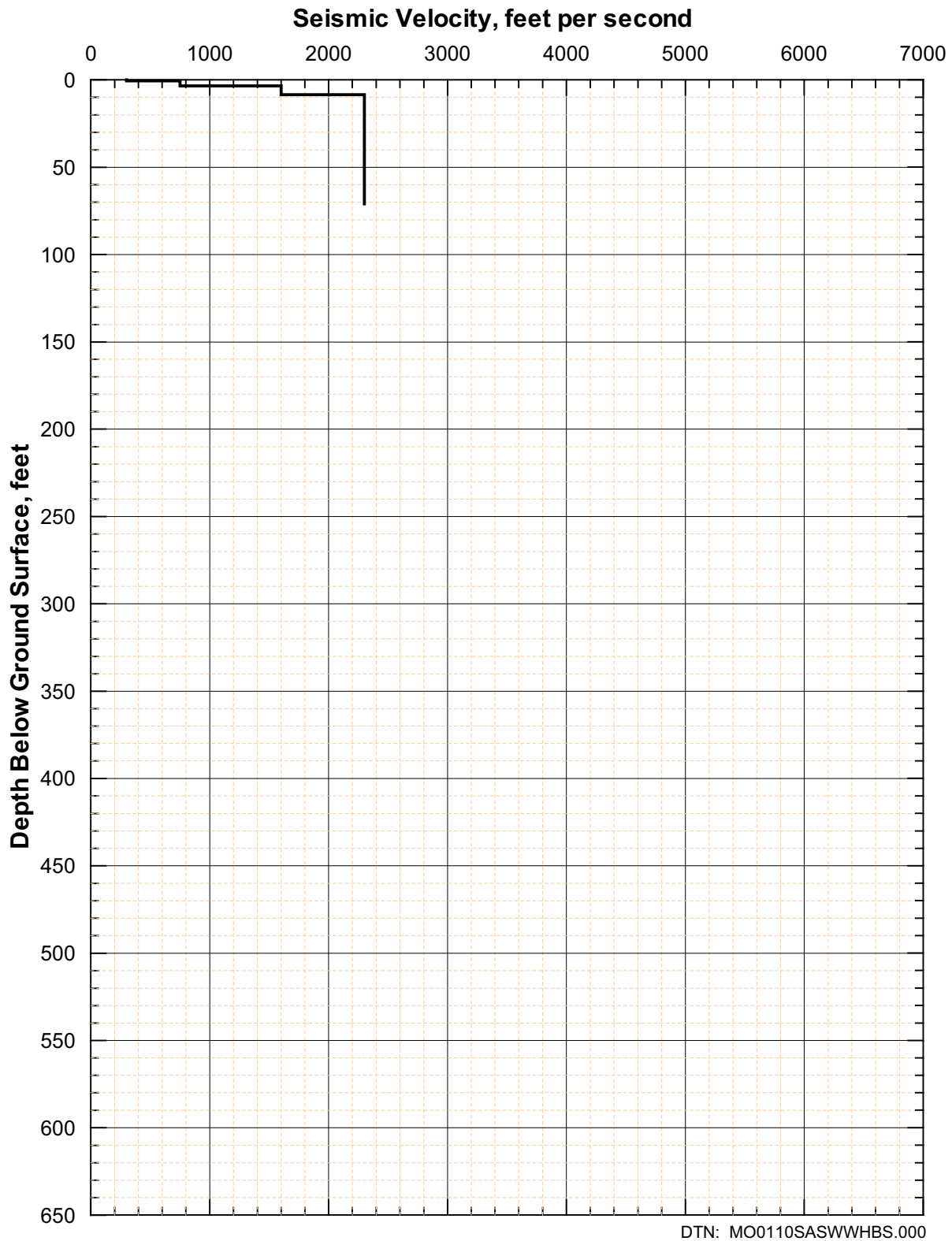


Figure 70. Shear-Wave Velocity Profile form SASW-17

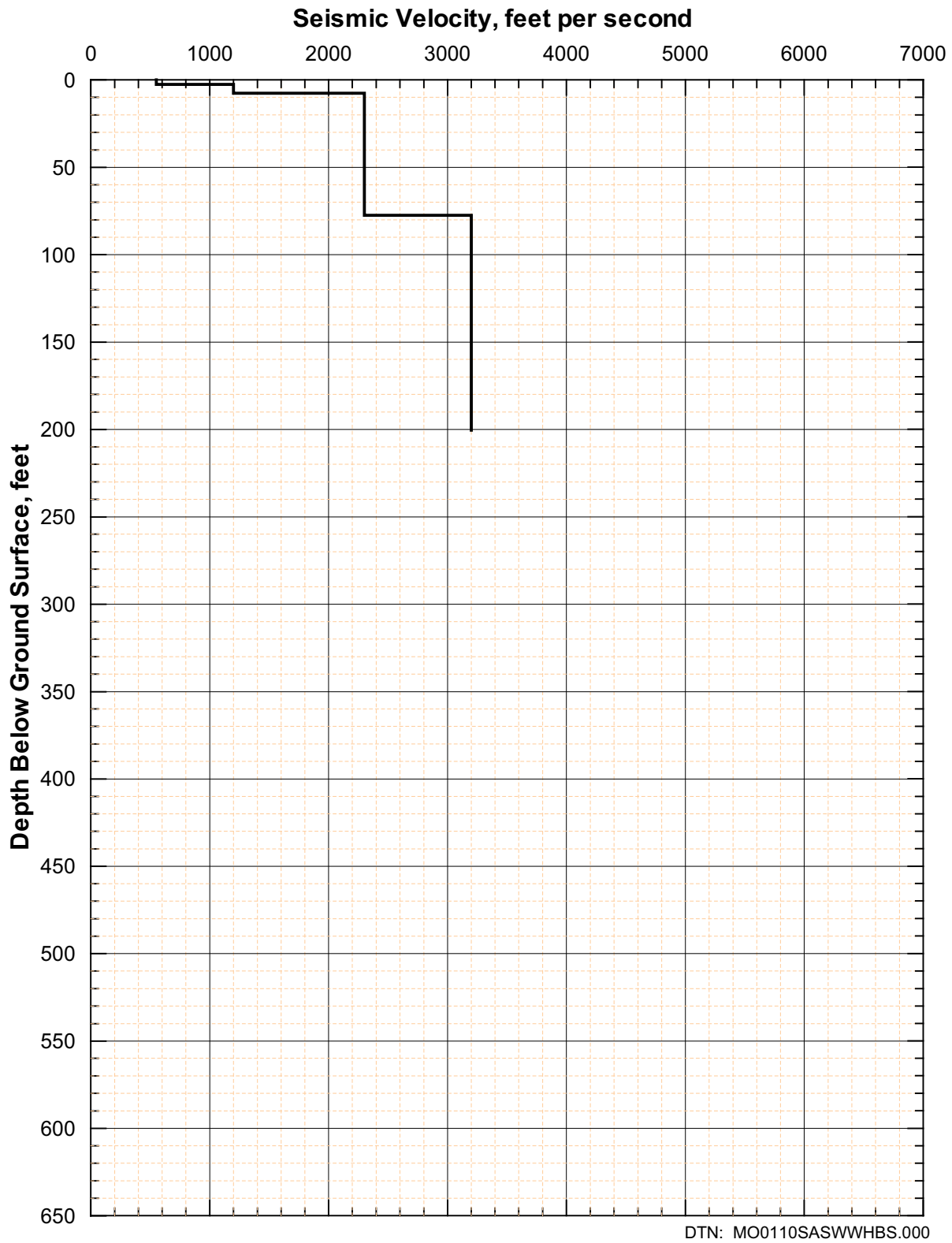


Figure 71. Shear-Wave Velocity Profile from SASW-18

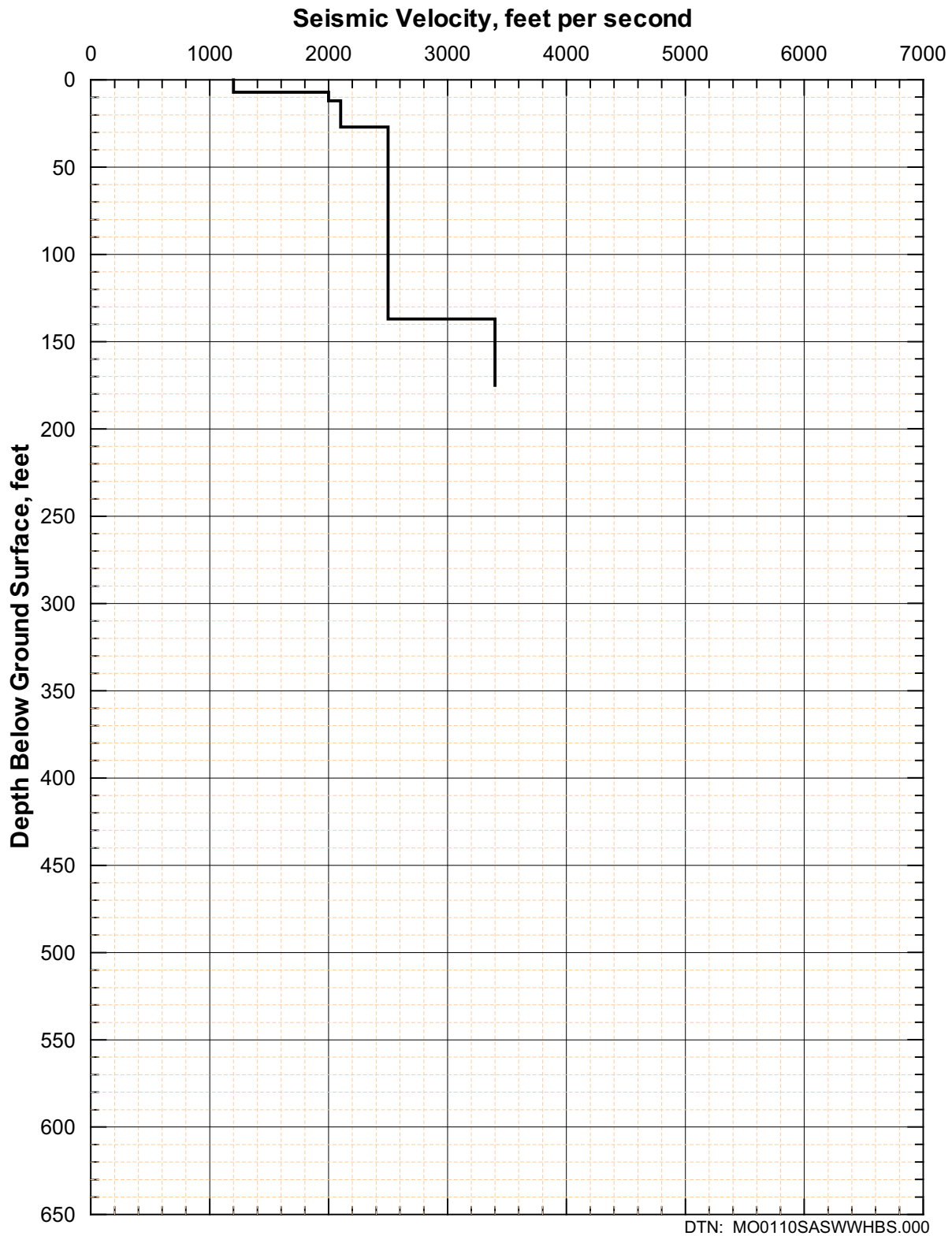


Figure 72. Shear-Wave Velocity Profile from SASW-19

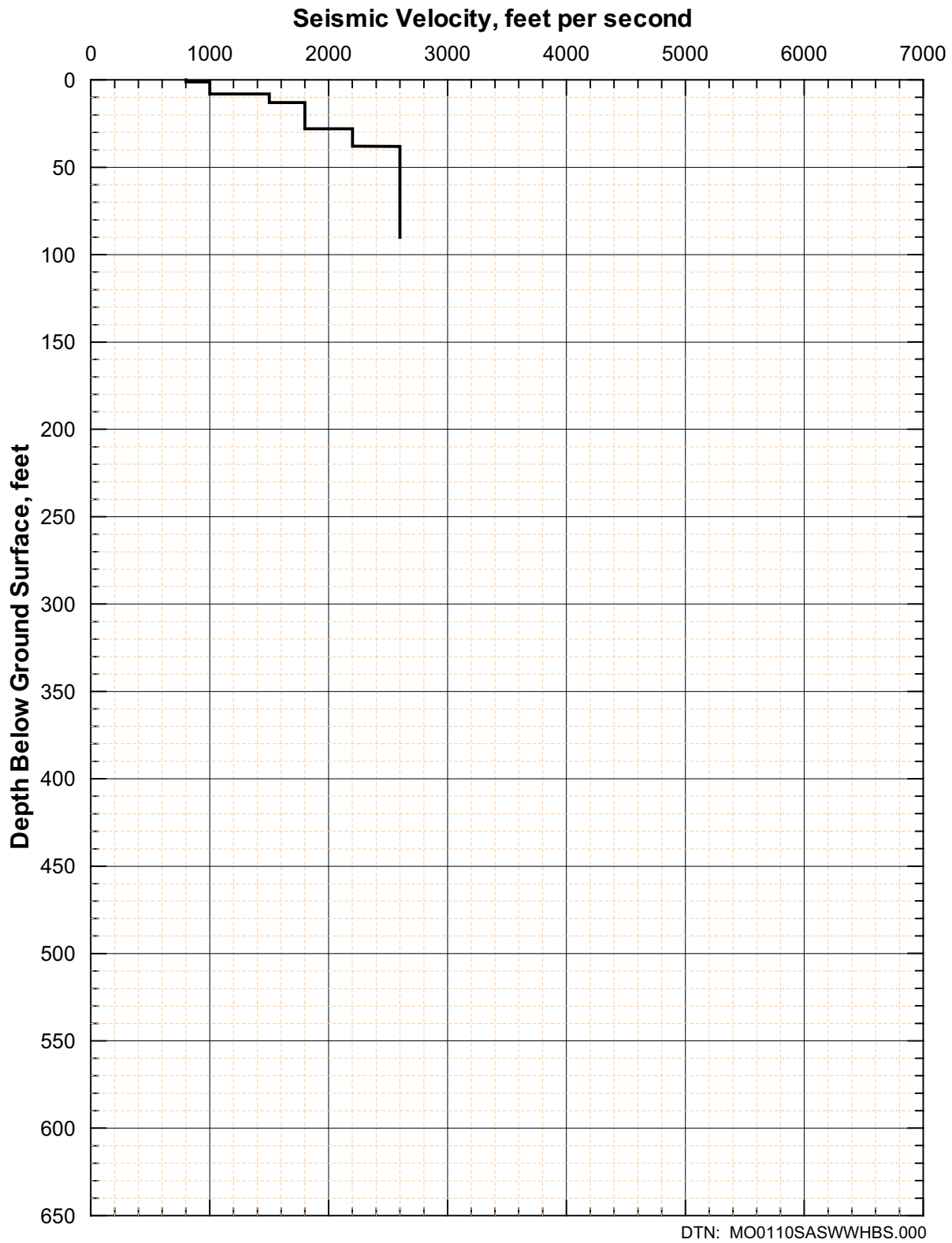


Figure 73. Shear-Wave Velocity Profile from SASW-20

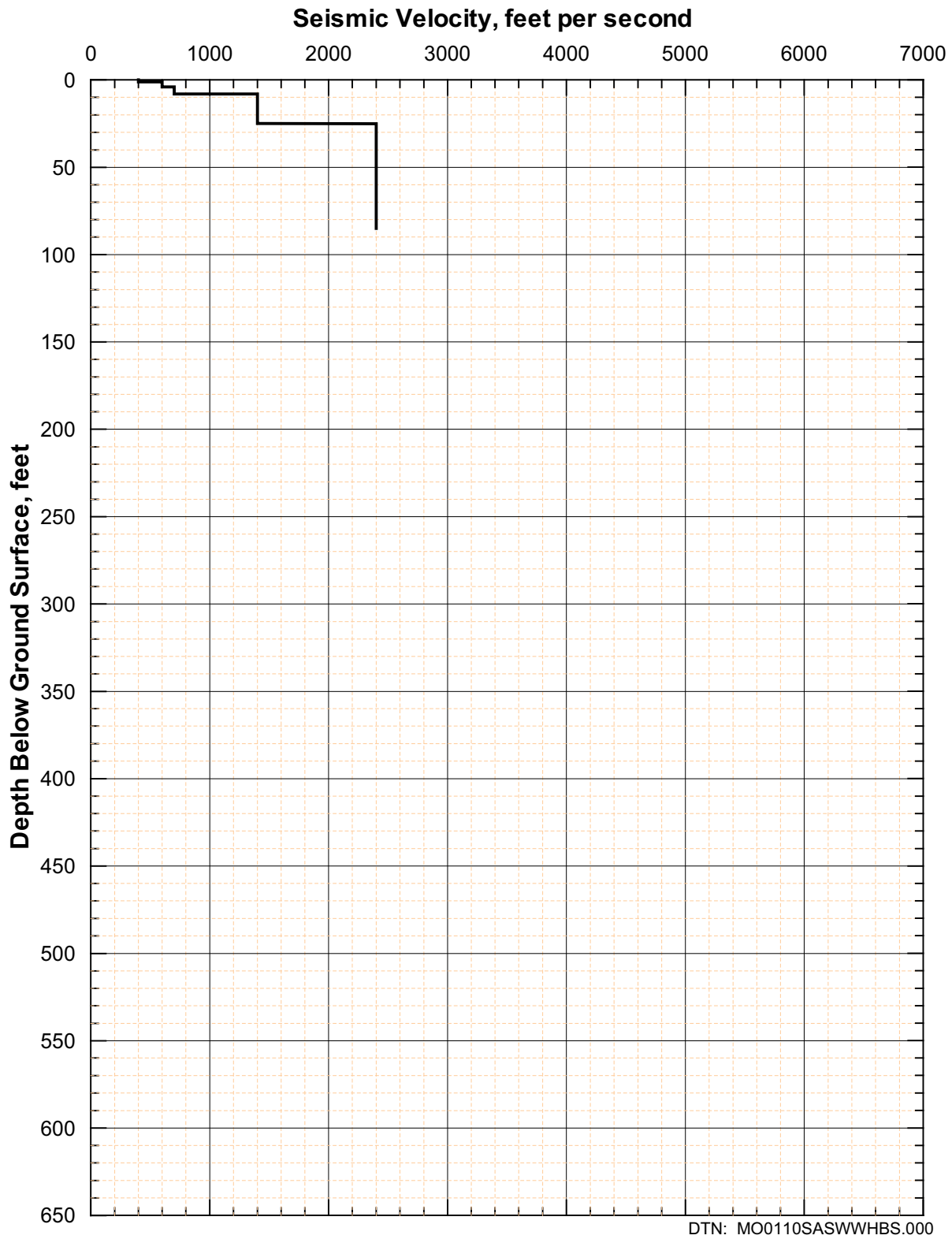


Figure 74. Shear-Wave Velocity Profile from SASW-21

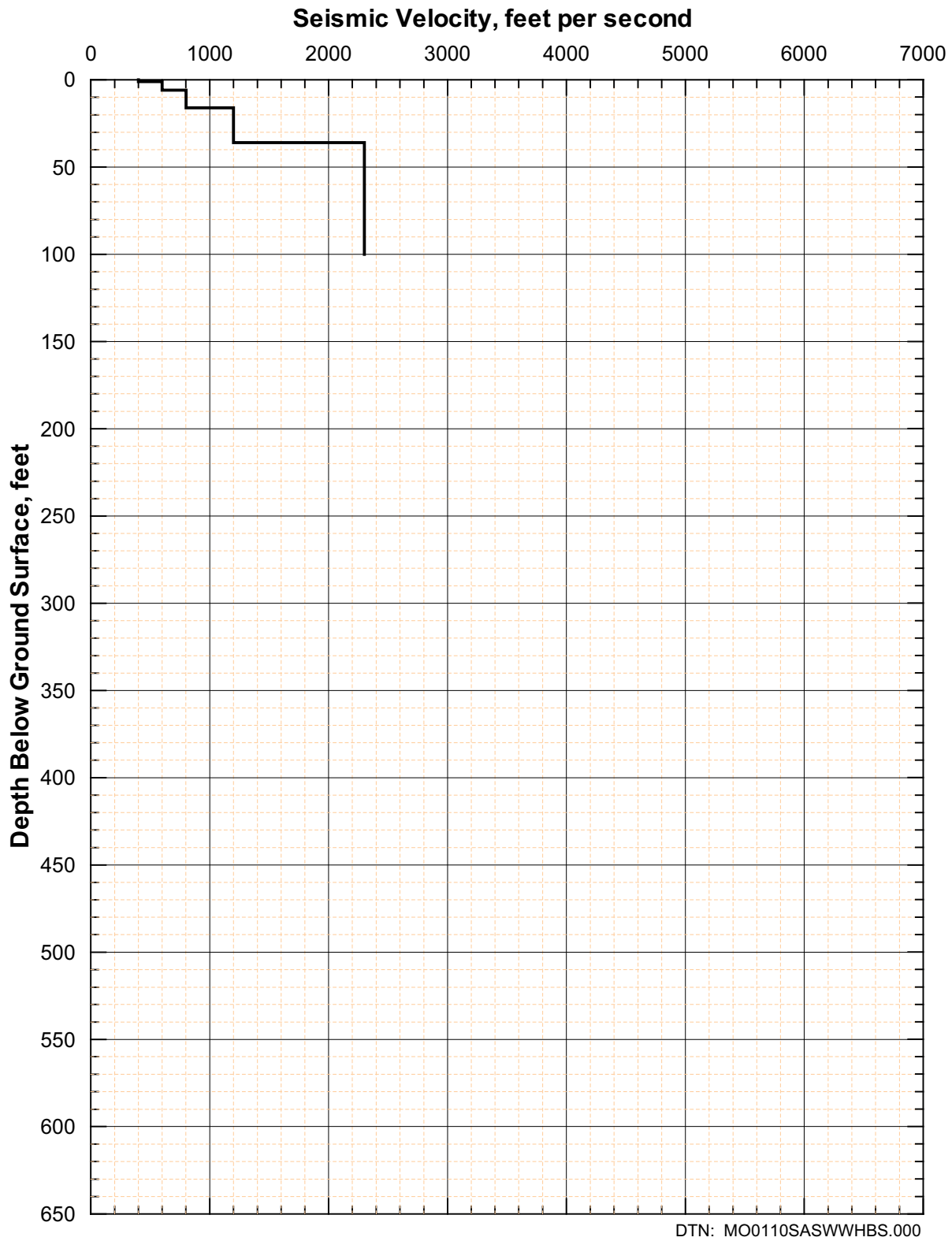


Figure 75. Shear-Wave Velocity Profile from SASW-22

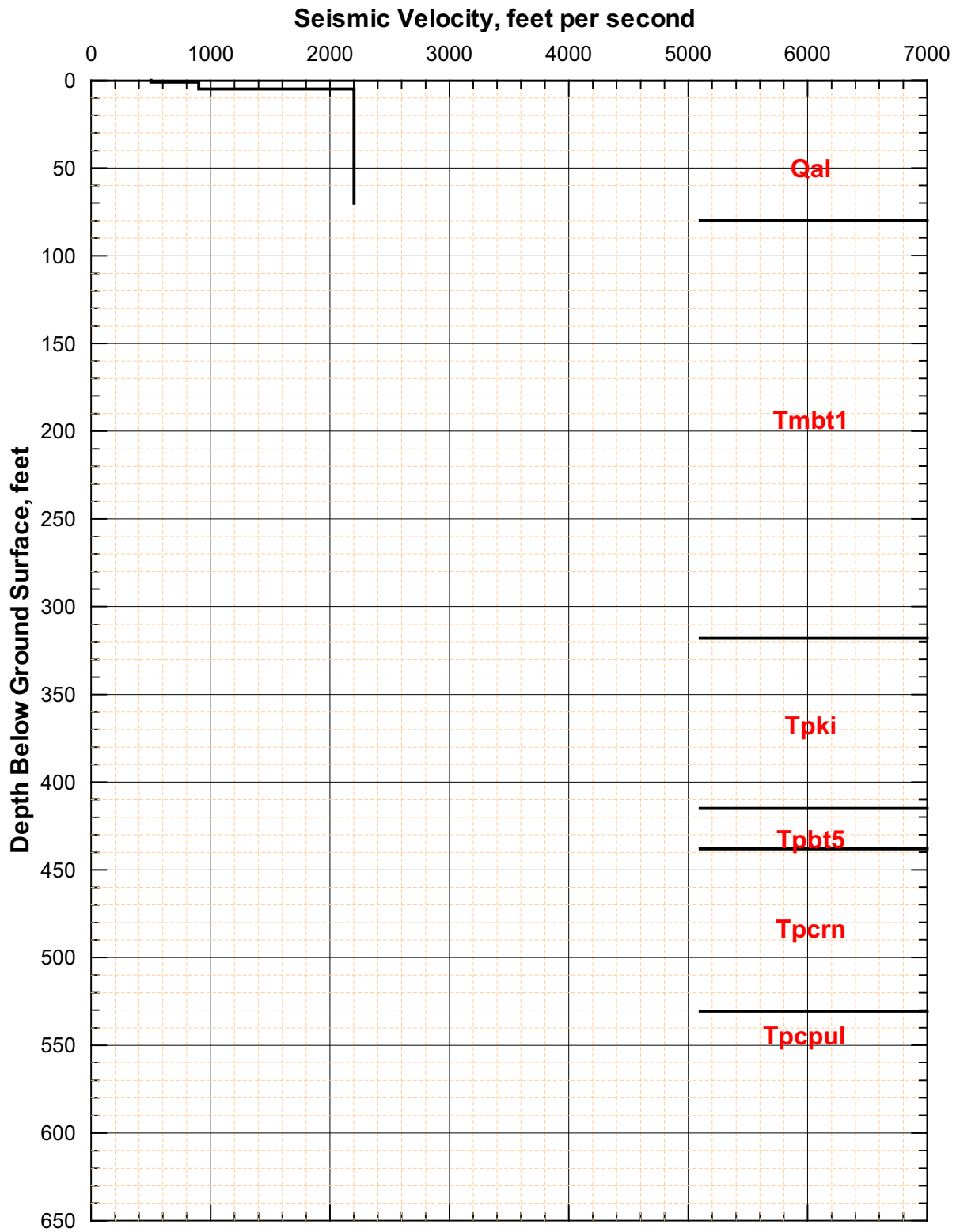


Figure 76. Shear-Wave Velocity Profile from SASW-23 and Generalized Lithology from RF#22

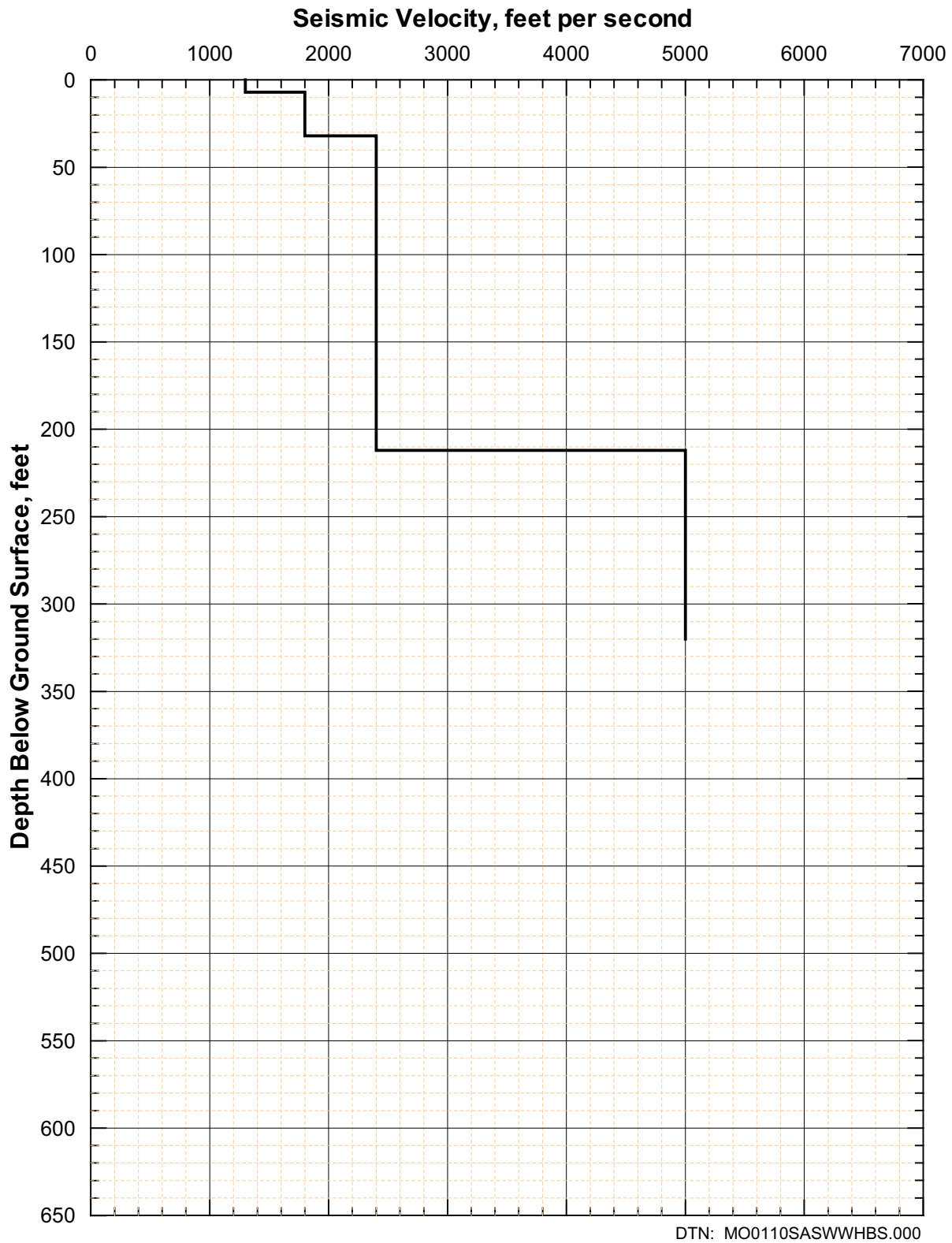


Figure 77. Shear-Wave Velocity Profile from SASW-24

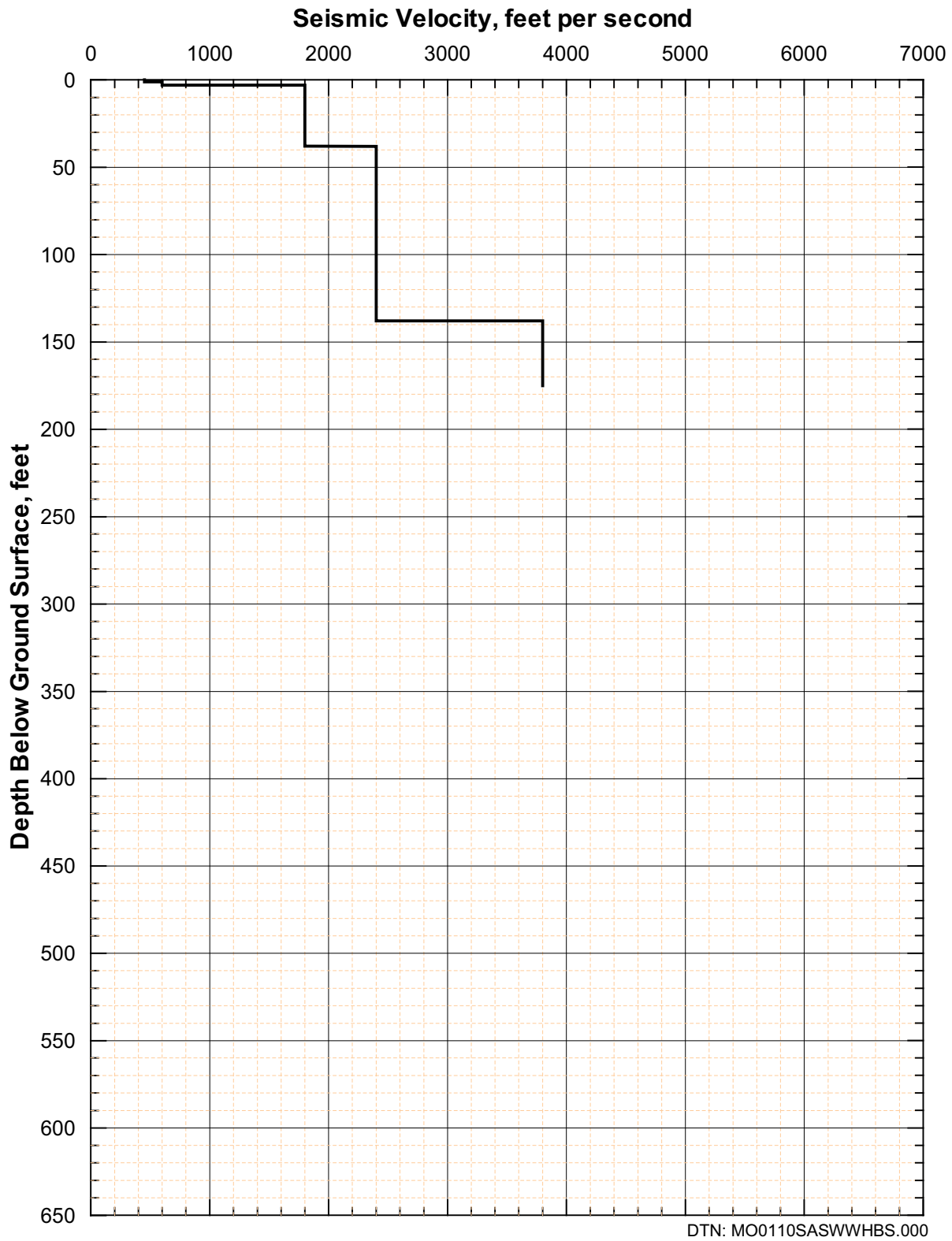


Figure 78. Shear-Wave Velocity Profile from SASW-25

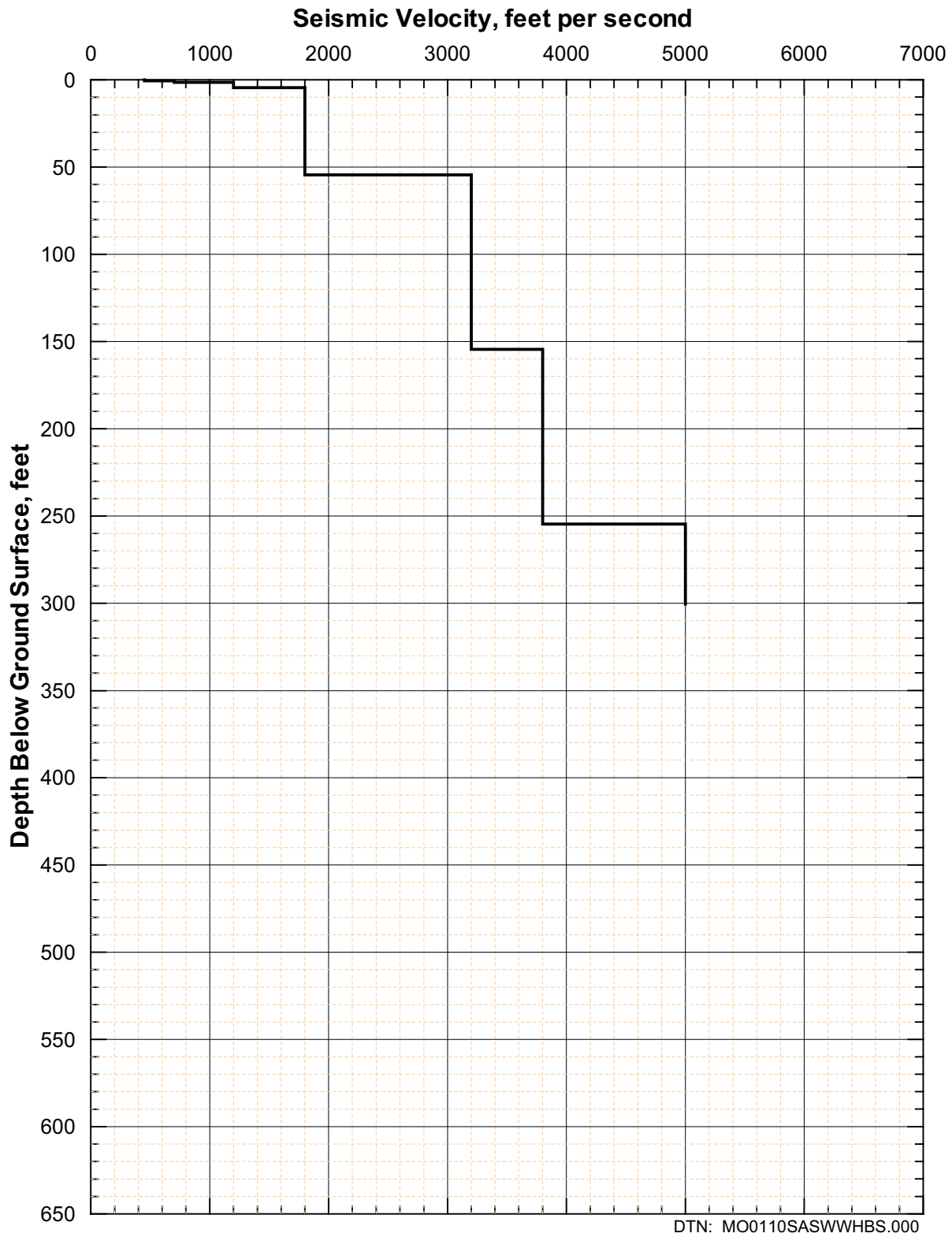


Figure 79. Shear-Wave Velocity Profile from SASW-26

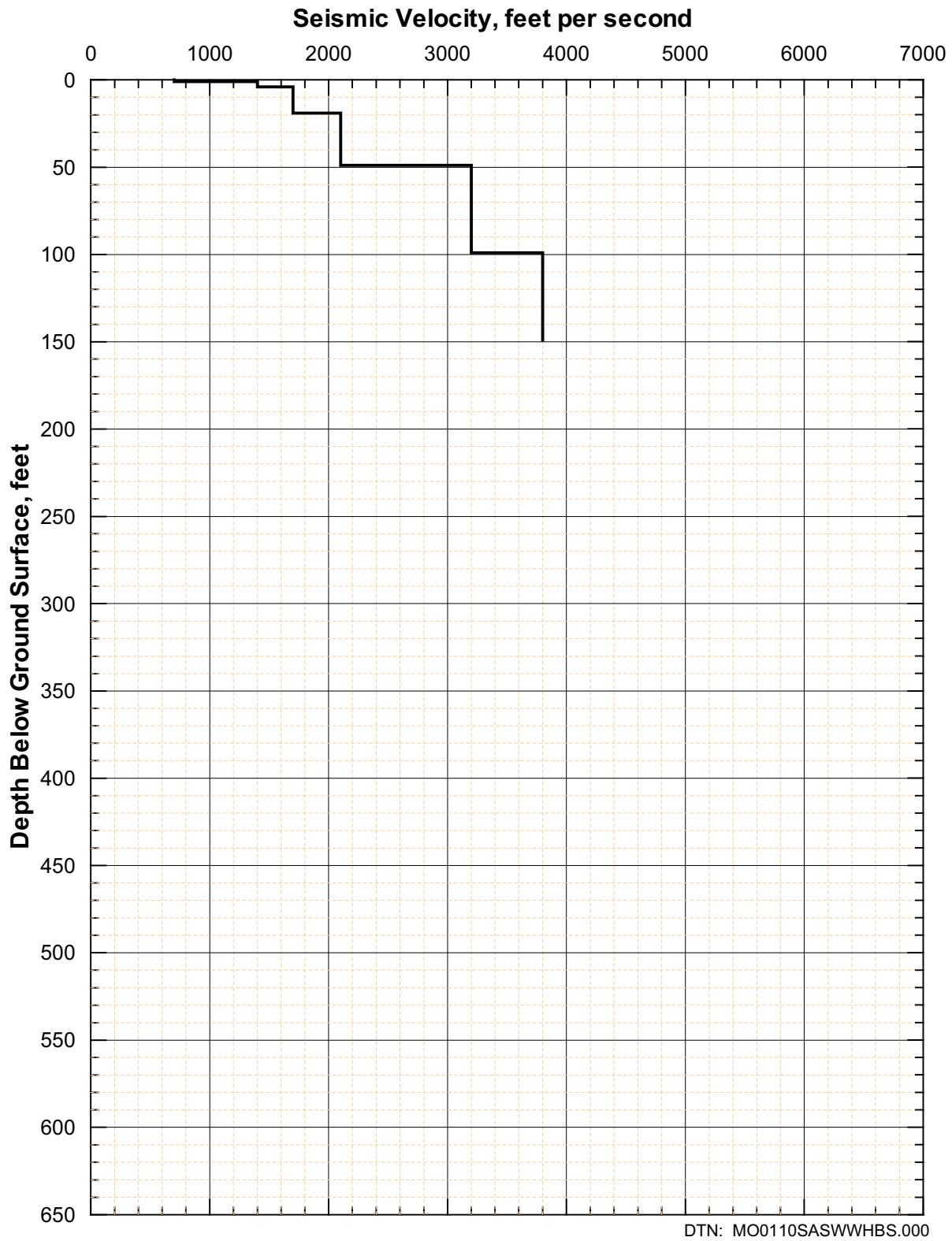


Figure 80. Shear-Wave Velocity Profile from SASW-27

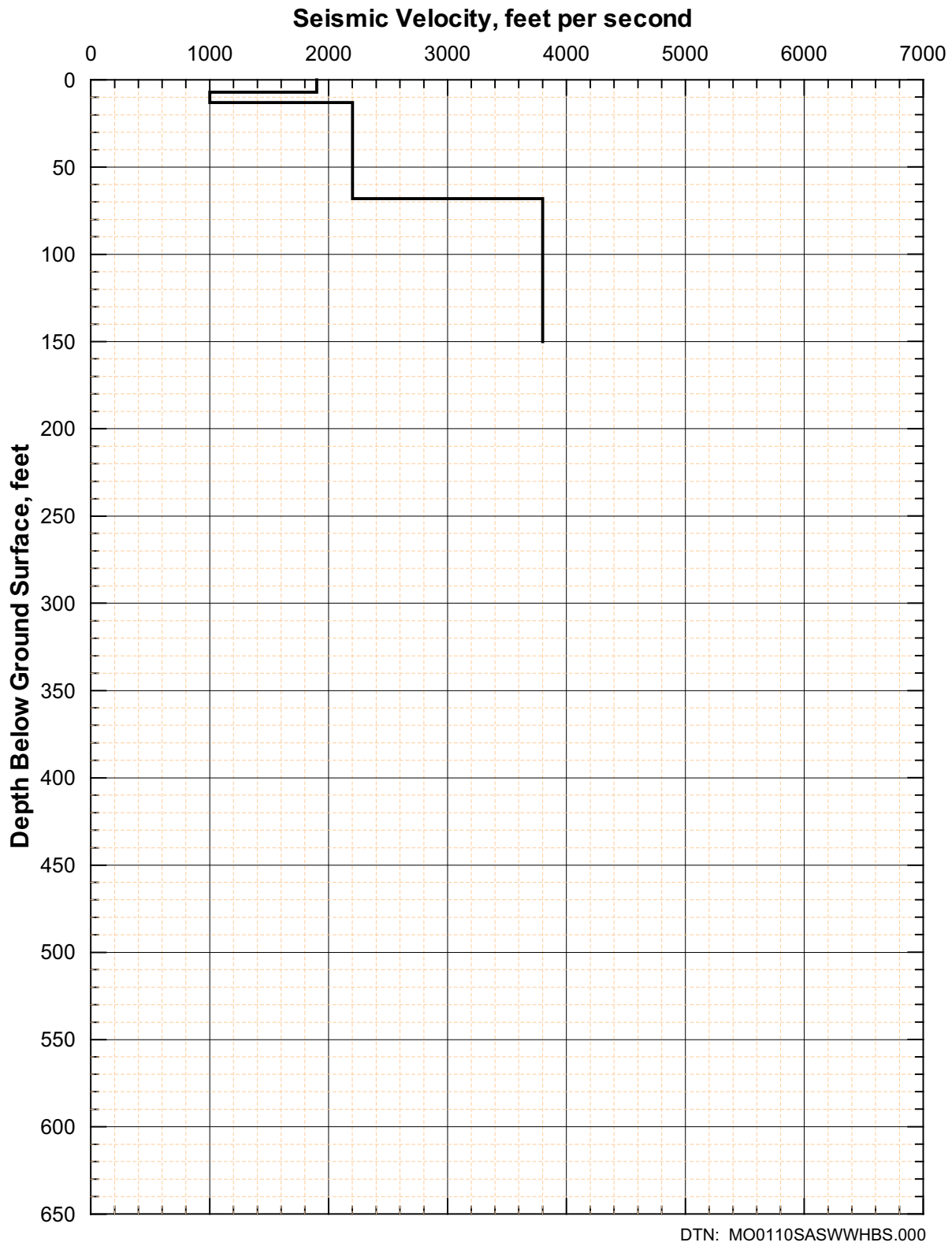


Figure 81. Shear-Wave Velocity Profile from SASW-28

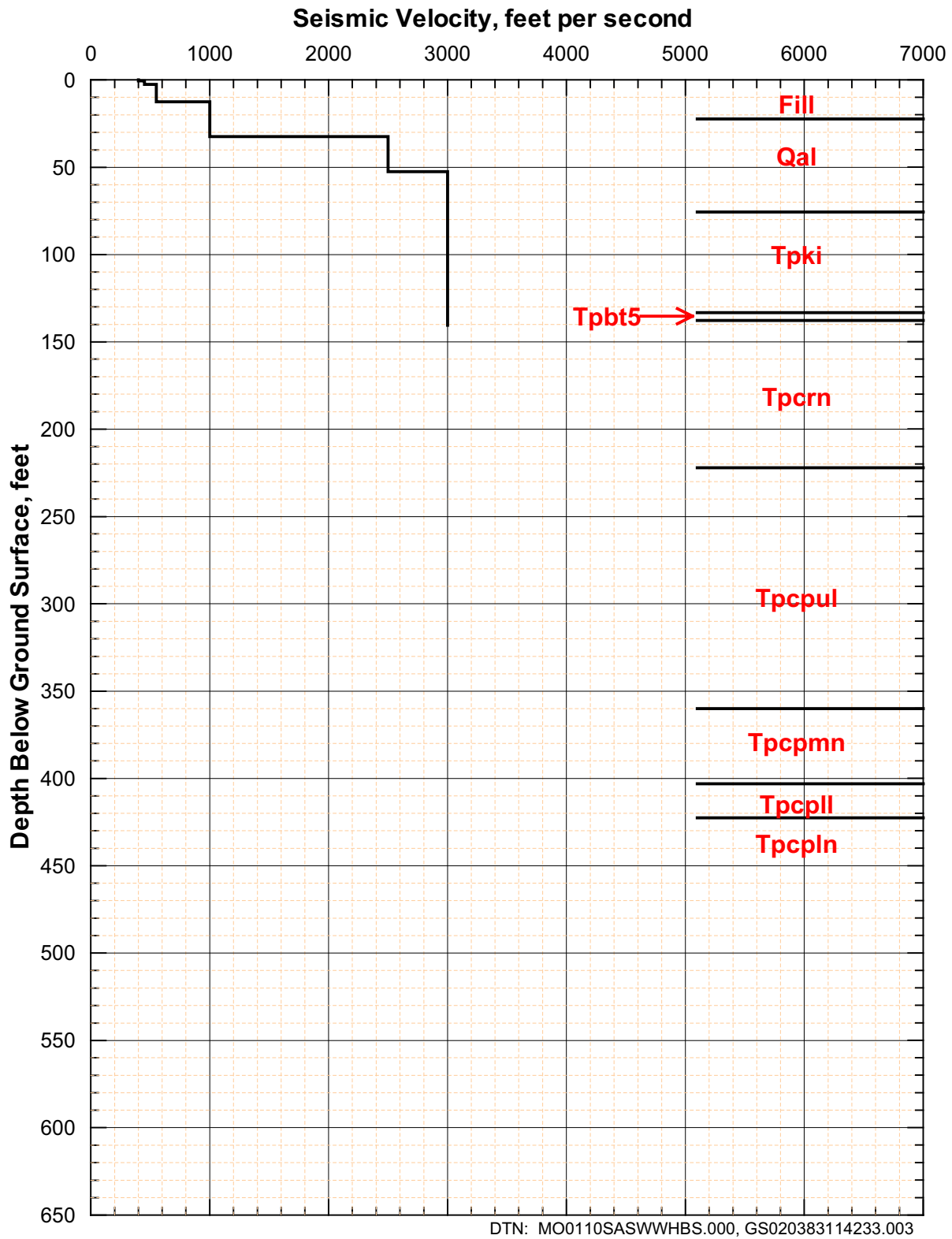


Figure 82. Shear-Wave Velocity Profile from SASW-29 and Generalized Lithology from RF#16

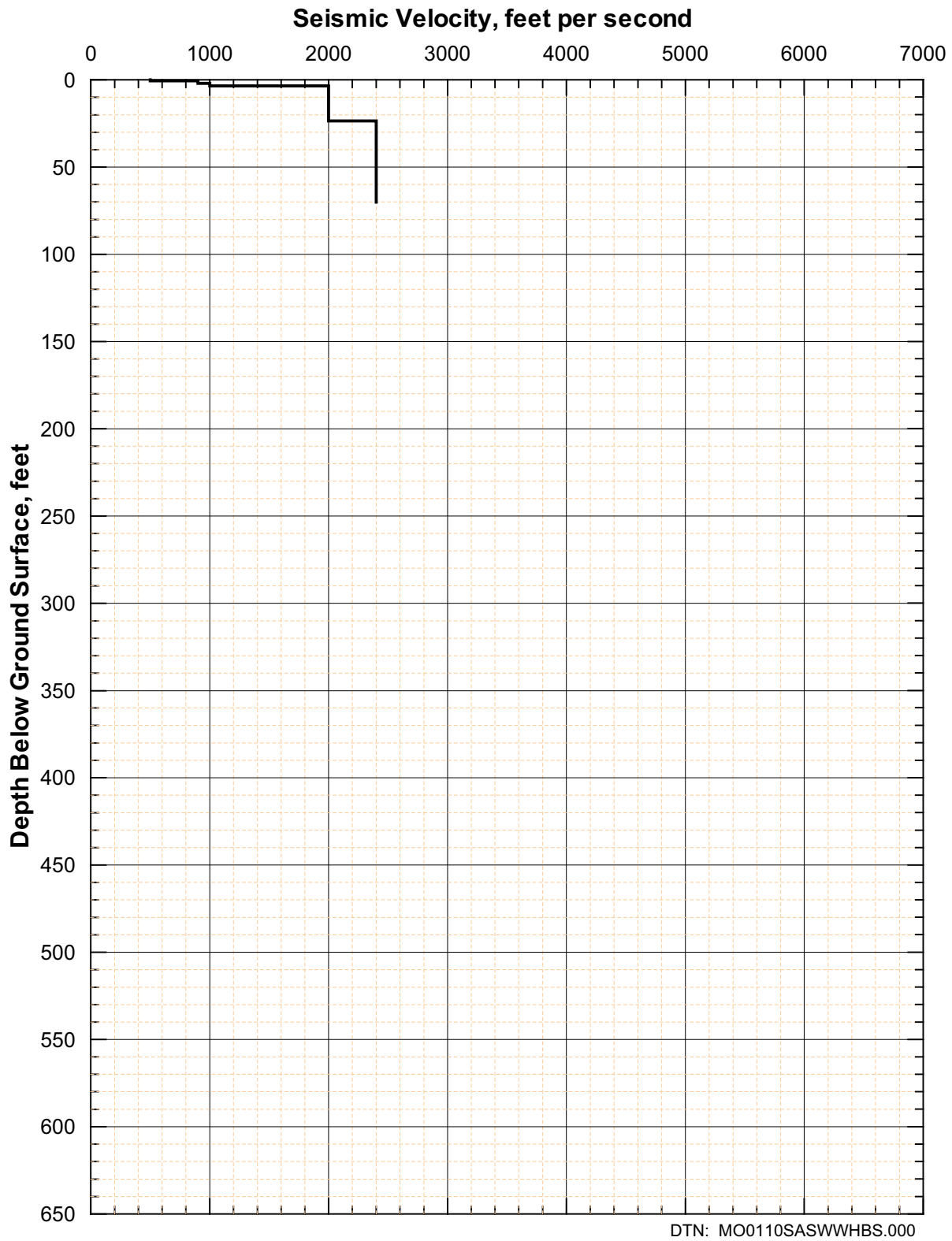


Figure 83. Shear-Wave Velocity Profile from SASW-30

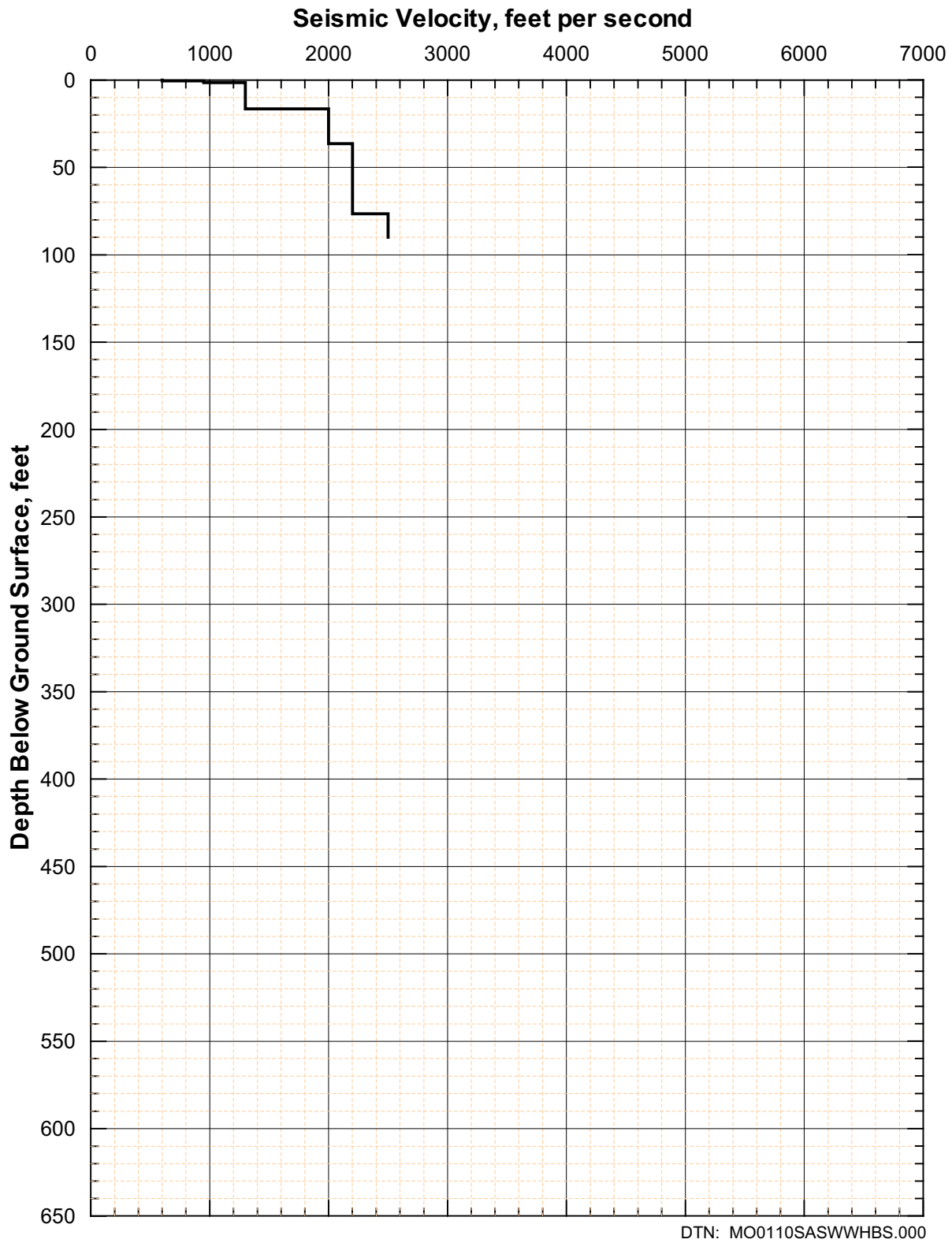


Figure 84. Shear-Wave Velocity Profile from SASW-31

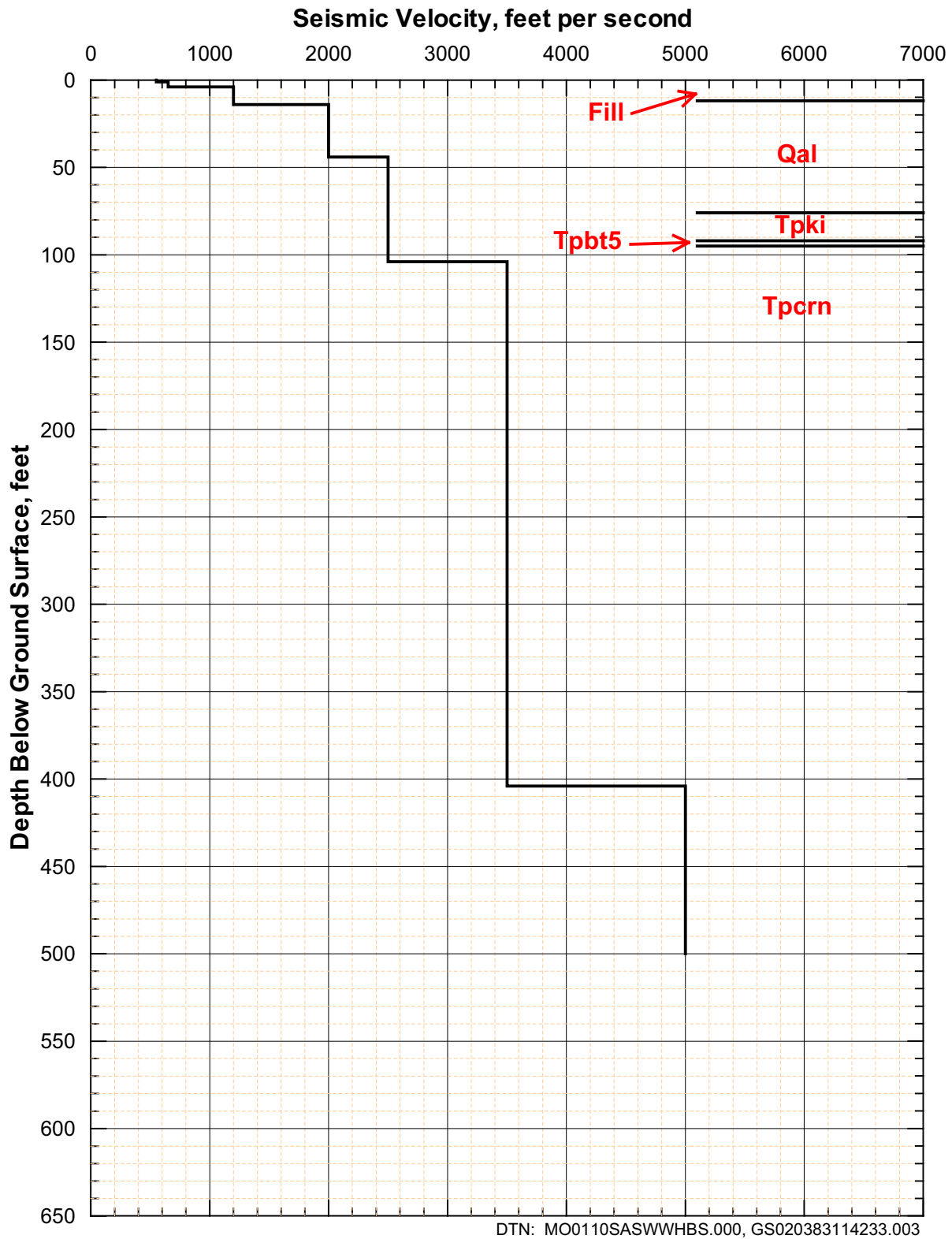
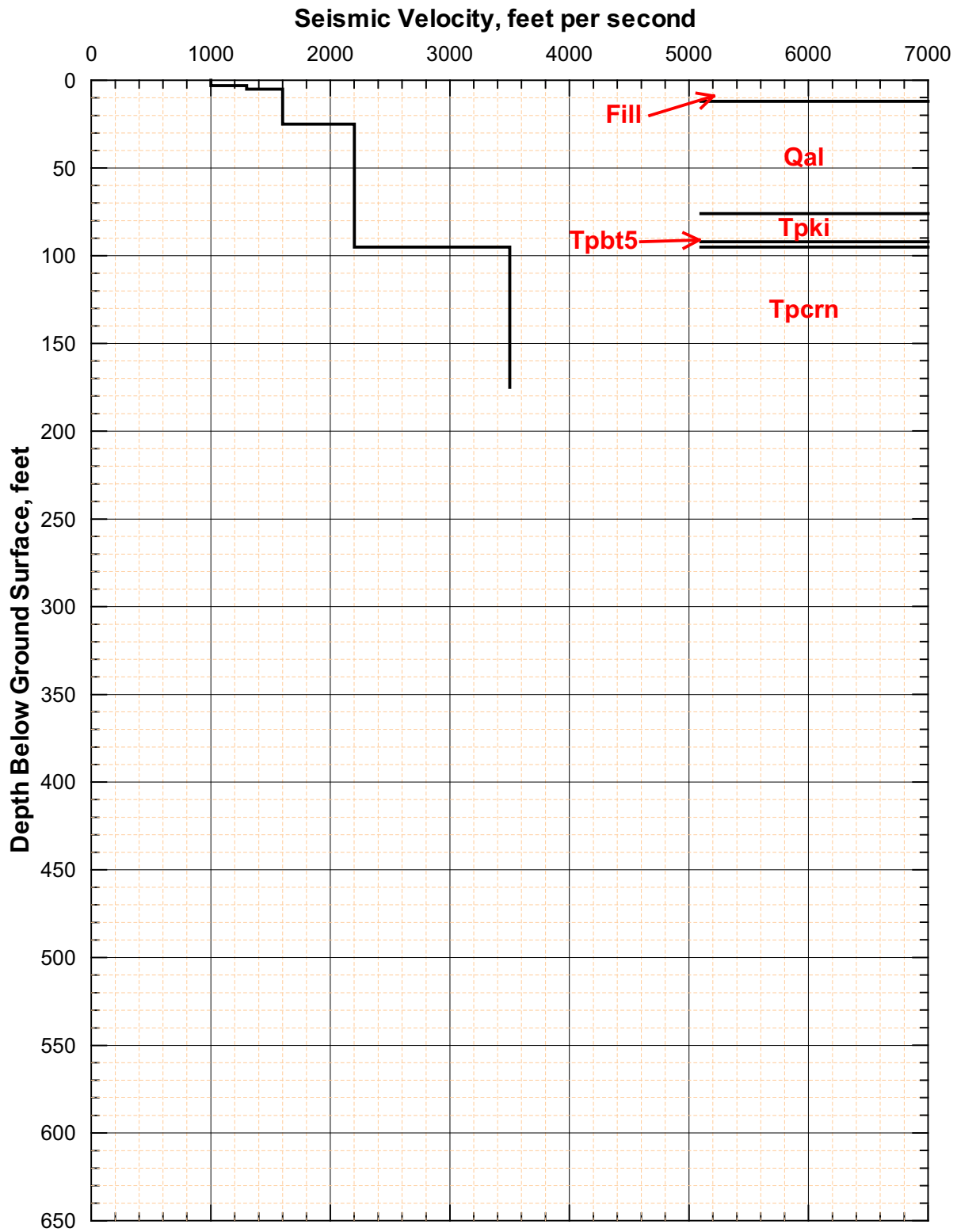


Figure 85. Shear-Wave Velocity Profile from SASW-32+35 and Generalized Lithology from RF#23



DTN: MO0110SASWWHBS.000, GS020383114233.003

Figure 86. Shear-Wave Velocity Profile from SASW-33

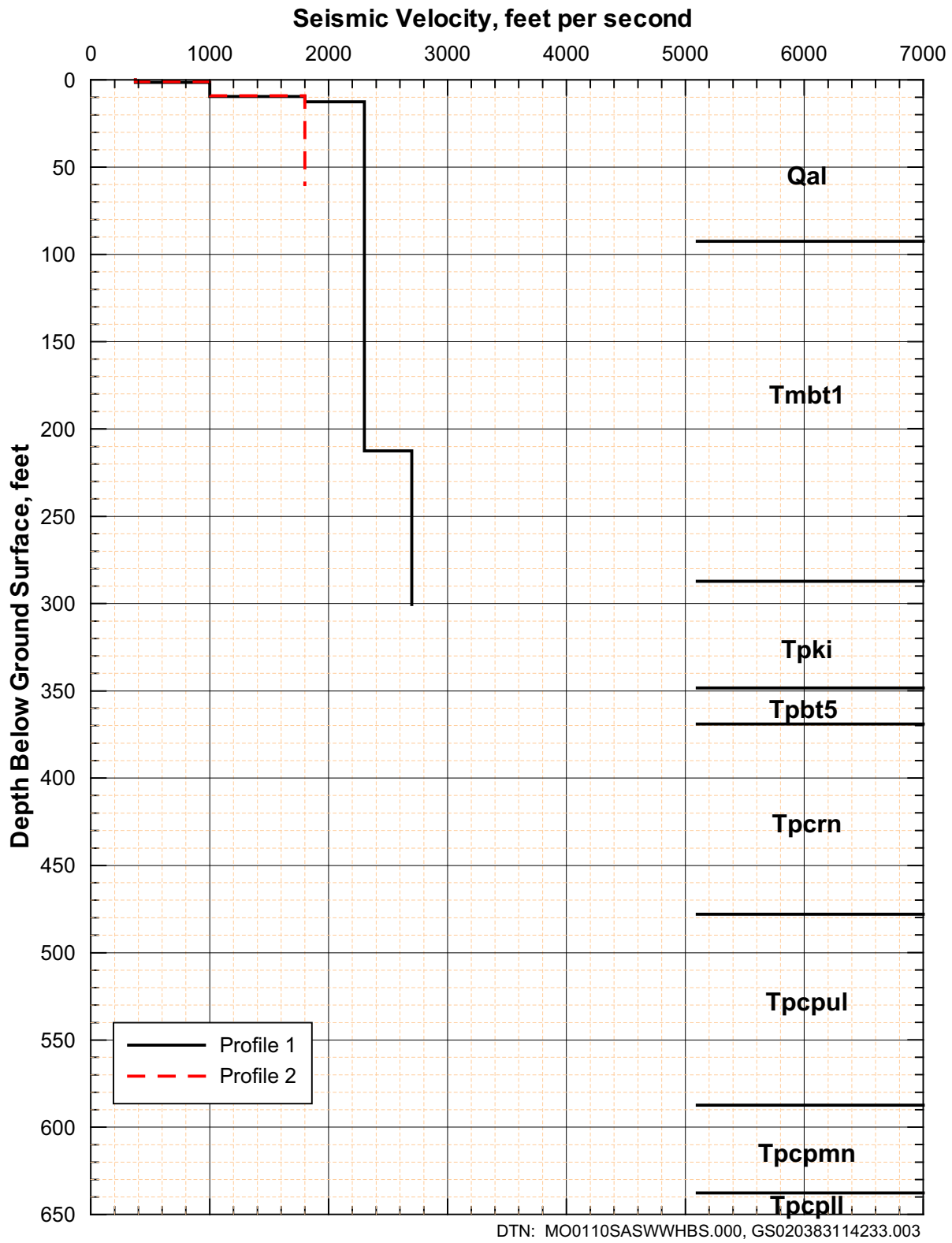


Figure 87. Shear-Wave Velocity Profile from SASW-34+36 and Generalized Lithology from RF#17

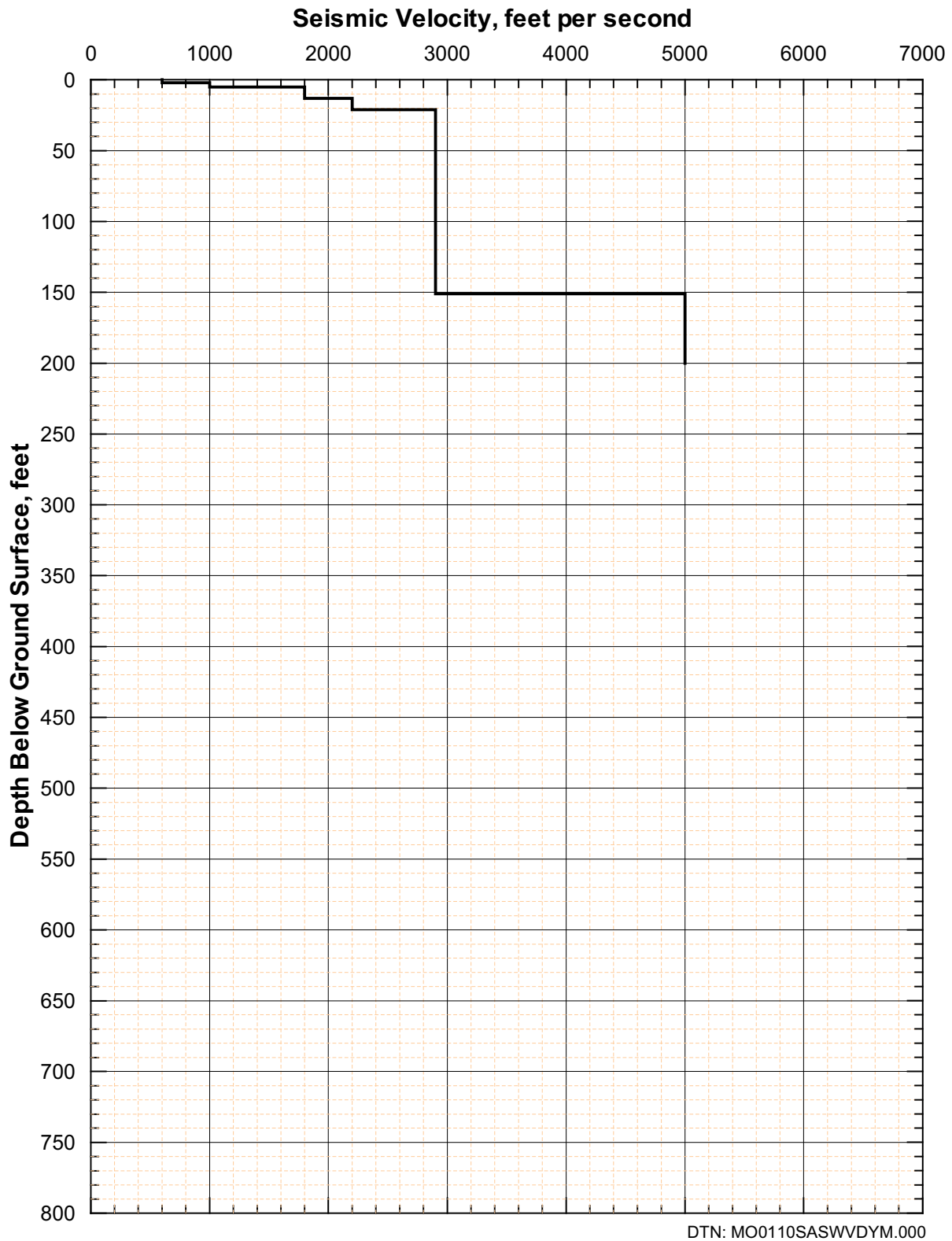


Figure 88. Shear-Wave Velocity Profile from D-12

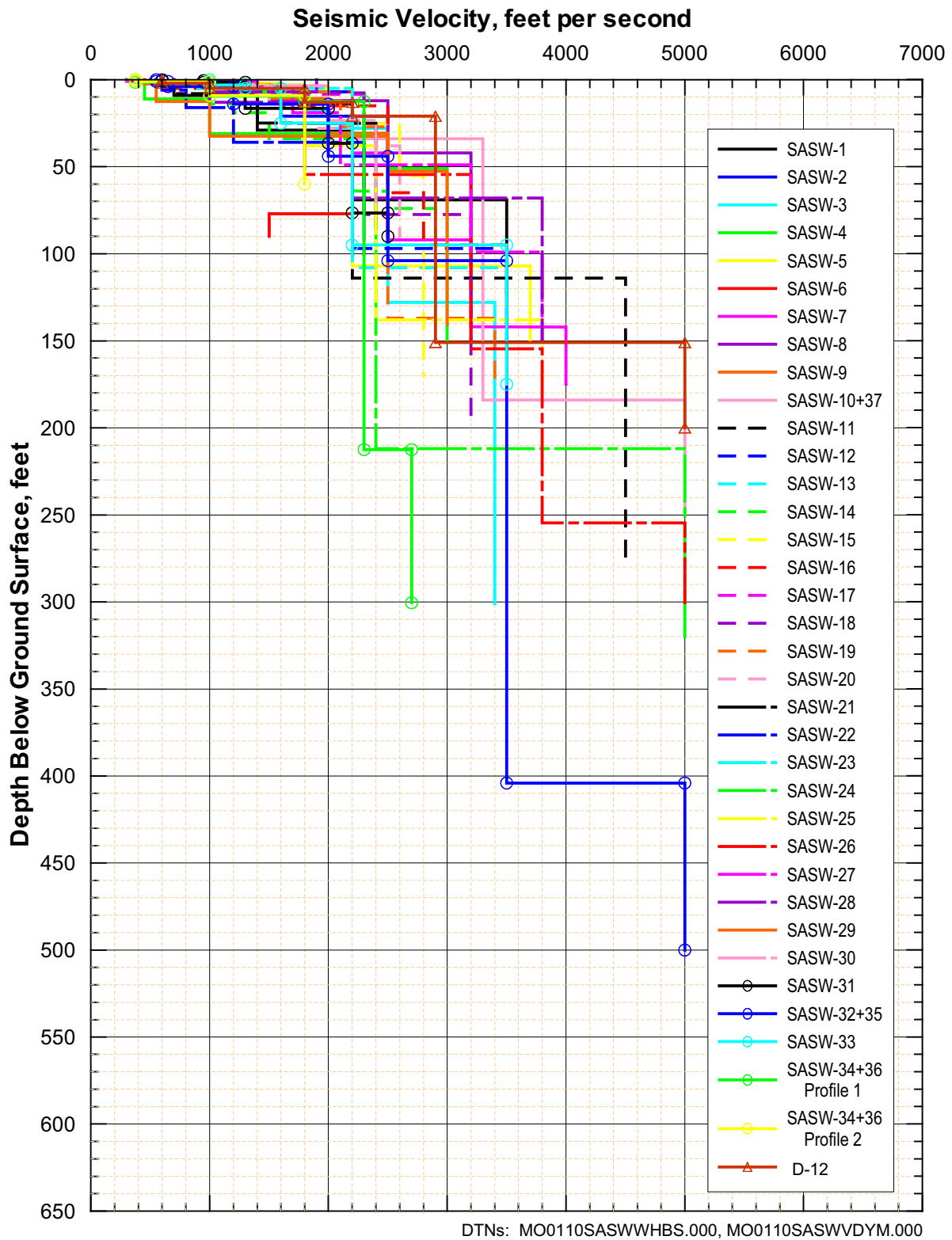


Figure 89. Shear-Wave Velocities from SASW Measurements in the WHB Area

of the surveys (SASW-3, 24, 26, 32+35, and 34+36). The profile for D-12 on Exile Hill is shown on Figure 88. Five profiles (SASW-3, 14, 19, 20, and 34+36) are located off the North Portal pad area and these profiles are shown on Figure 90. For SASW 34+36, the experimental dispersion curve had a portion (from wavelengths of about 30 to 120 ft) where the individual dispersion curves did not overlap. This indicates some lateral changes in velocity. In this wavelength range, there are really two paths for the theoretical dispersion curve to follow and thus, to a depth of about 60 ft, there are two possible profiles. Since the SASW technique is limited to a 1-D model, the two profiles are presented to indicate that there is lateral variability along the extent of the receiver array (Figure 87).

With the exception of SASW 34+36, the five profiles located off the North Portal pad area appear similar to the profiles in the main WHB area (Figures 89 and 90). Most of the profiles start with shear-wave velocities near the surface of less than 1000 ft/s and quickly increase to velocities of 2,500 to 4,000 ft/s at depth. Figure 91 presents the mean, median, and mean \pm one standard deviation profiles for all the profiles.

The shear-wave velocity profile for D-12 shows what appears to be a thin 20 ft-thick soil and/or weathered rock over subunits, probably Tpcrn and Tpcpl, of the Tiva Canyon Tuff.

To examine the possible variability in shear-wave velocity profiles throughout the WHB area, average profiles were calculated for three different areas around the pad. Area 1 is located around boreholes RF#16, RF#26, and RF#13 and includes SASW-1, 4, 21, 22, and 29. Figure 92 shows the five individual profiles and the mean profile in Area 1. Area 2 is located around boreholes RF#28 and RF#15 and includes SASW-8, 9, 10+37 and 11. Figure 93 shows the four profiles and the mean profile determined in this area. Lastly, Area 3 is located around boreholes RF#24 and RF#22 and includes SASW-6, 12, 13, 17, 18, 23, and 30. Figure 94 shows the individual profiles and the mean profile determined in Area 3.

The mean profiles from Areas 1, 2, and 3 are plotted together on Figure 95. They do not differ greatly at depths below 40 ft. Area 3 exhibits slightly slower shear-wave velocities at depths of 60 to 95 ft. In the top 40 ft, however, the mean profile in Area 1 is significantly slower than those in Areas 2 and 3, possibly due to the greater thickness of Qal.

As was done for the downhole velocity profiles (Section 6.2.5.3), the mean and plus and minus one standard deviation SASW velocity profiles on the downthrown and upthrown sides of the Exile Hill fault splay in the northeast corner of the WHB site (discussed in Section 6.6.2) are computed (Figures 96 and 97) and compared (Figure 98). SASW-3, 15, 16, 19, 30, 34, and 36 were located on the downthrown side of the fault (Figure 43). The remaining surveys were on the upthrown side. The comparison shows that the shear-wave velocities on the upthrown side of the fault become increasingly higher than the velocities on the downthrown side at depths below about 100 ft (Figure 98). This pattern is very consistent with the stratigraphic cross sections presented in Section 6.6.2, which indicate that to either side of the projected fault plane there is about 100 feet of alluvium. Below the alluvium, slower velocity bedded tuffs and Tuff unit "x" on the downthrown side abut, over a vertical distance of 200 to 300 ft, higher velocity Tiva Canyon Tuff on the upthrown side.

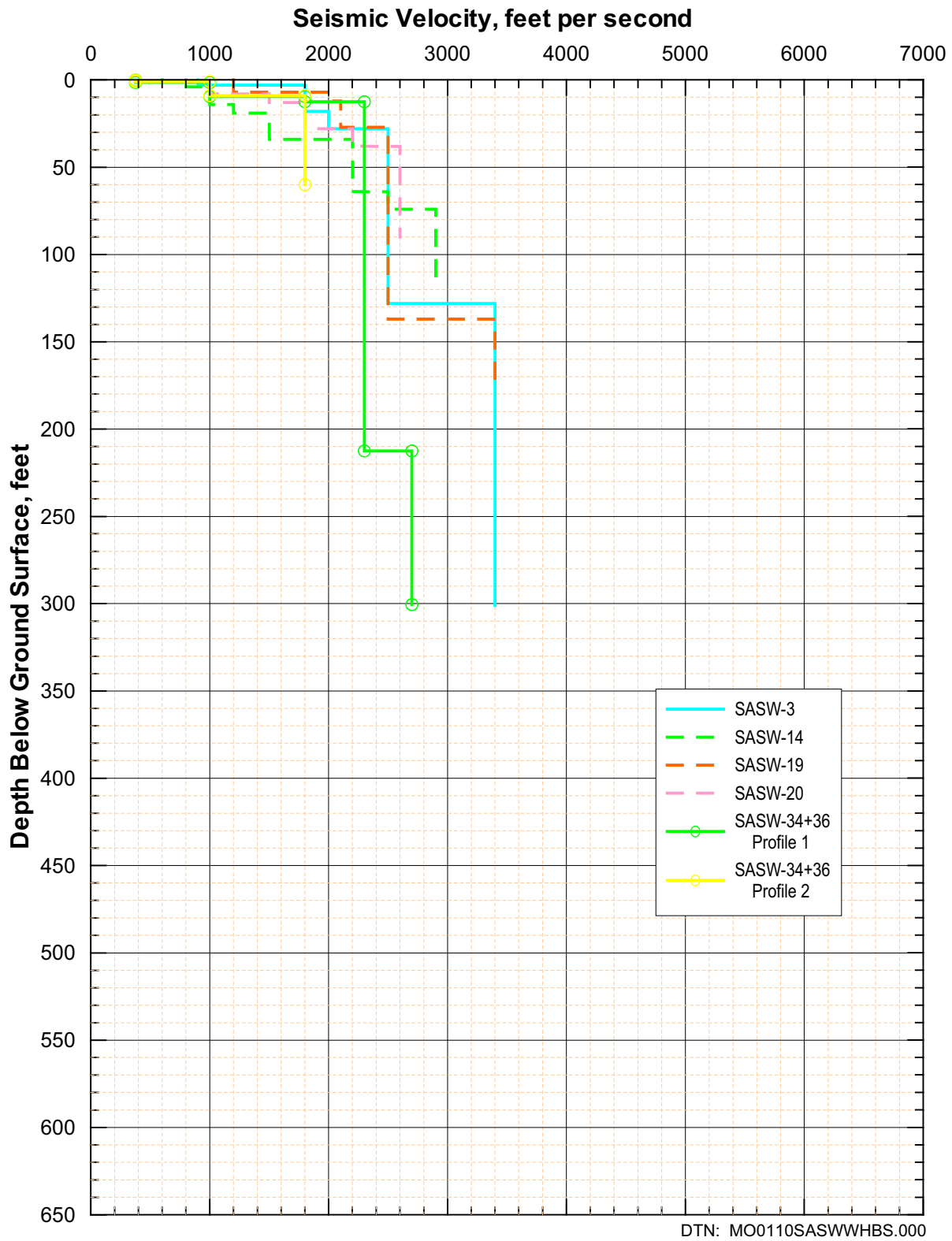
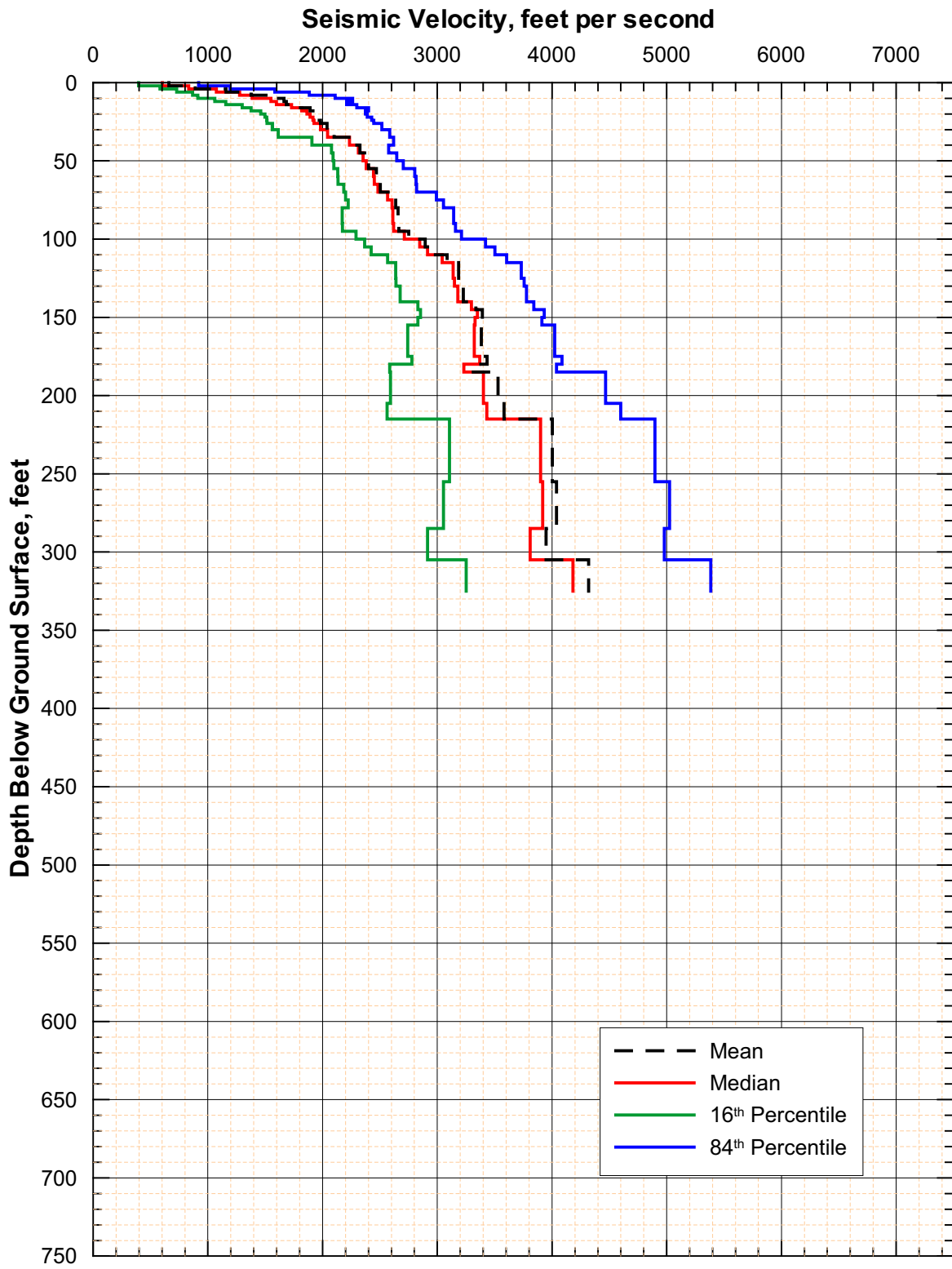


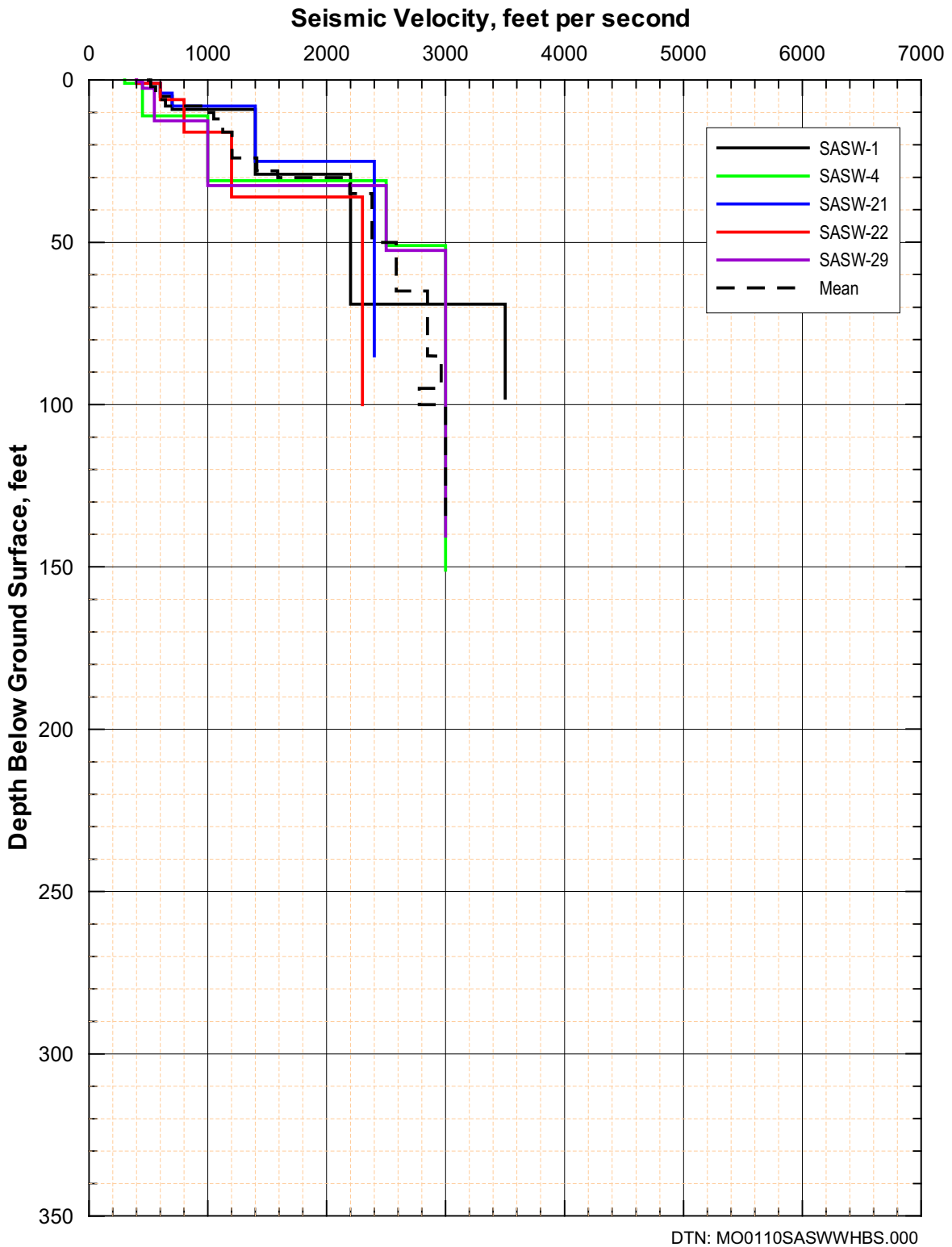
Figure 90. Shear-Wave Velocities from SASW Measurements at Sites Outside of WHB Pad Area



DTN TBD

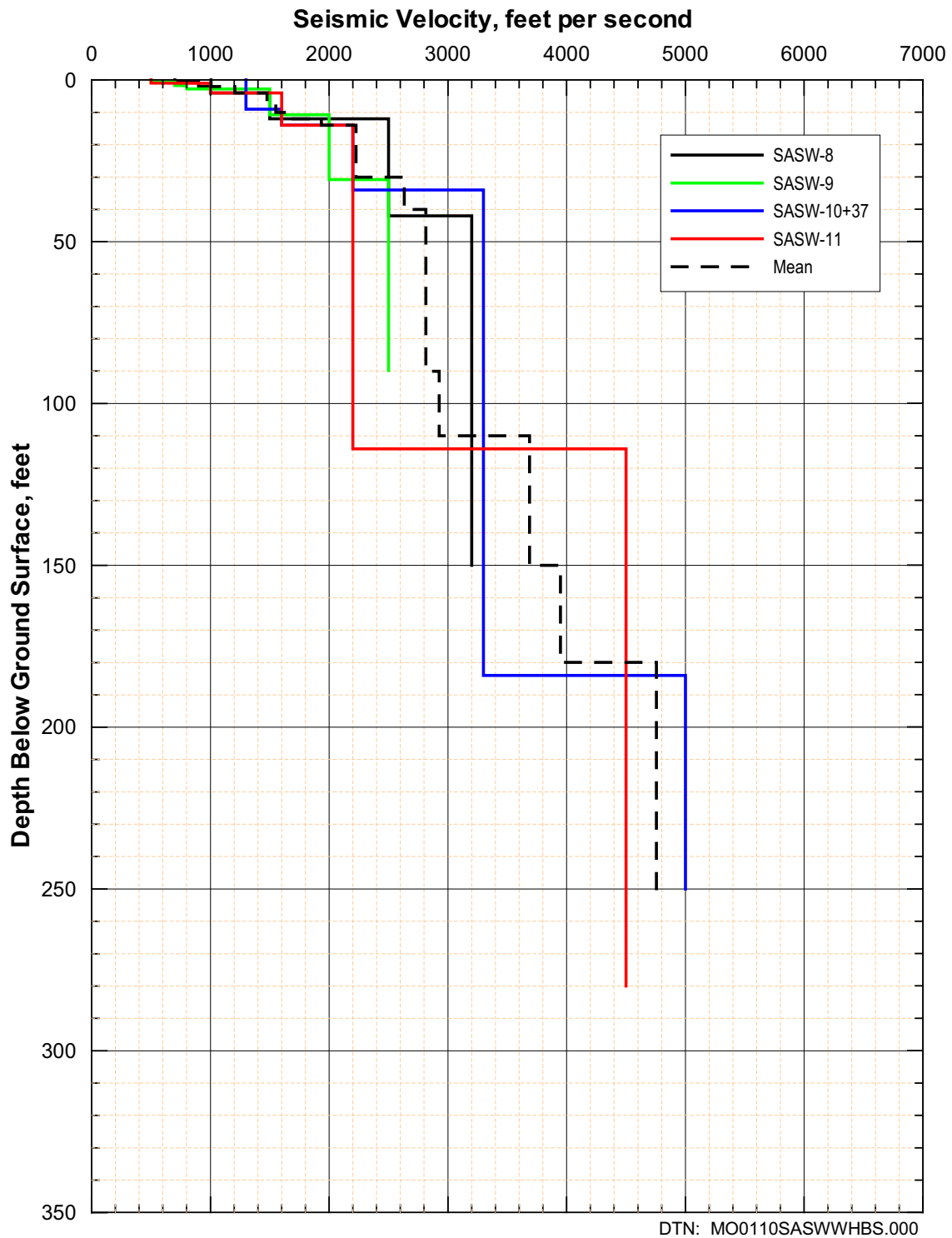
Note: These statistics have been calculated for illustrative purposes only. Final statistics calculated for use in the forthcoming scientific analysis entitled *Development of Seismic Design Input Ground Motions for a Geologic Repository at Yucca Mountain* will be submitted to the TDMS.

Figure 91. Statistical Analyses of Shear-Wave Velocities from SASW Measurements in the WHB Area



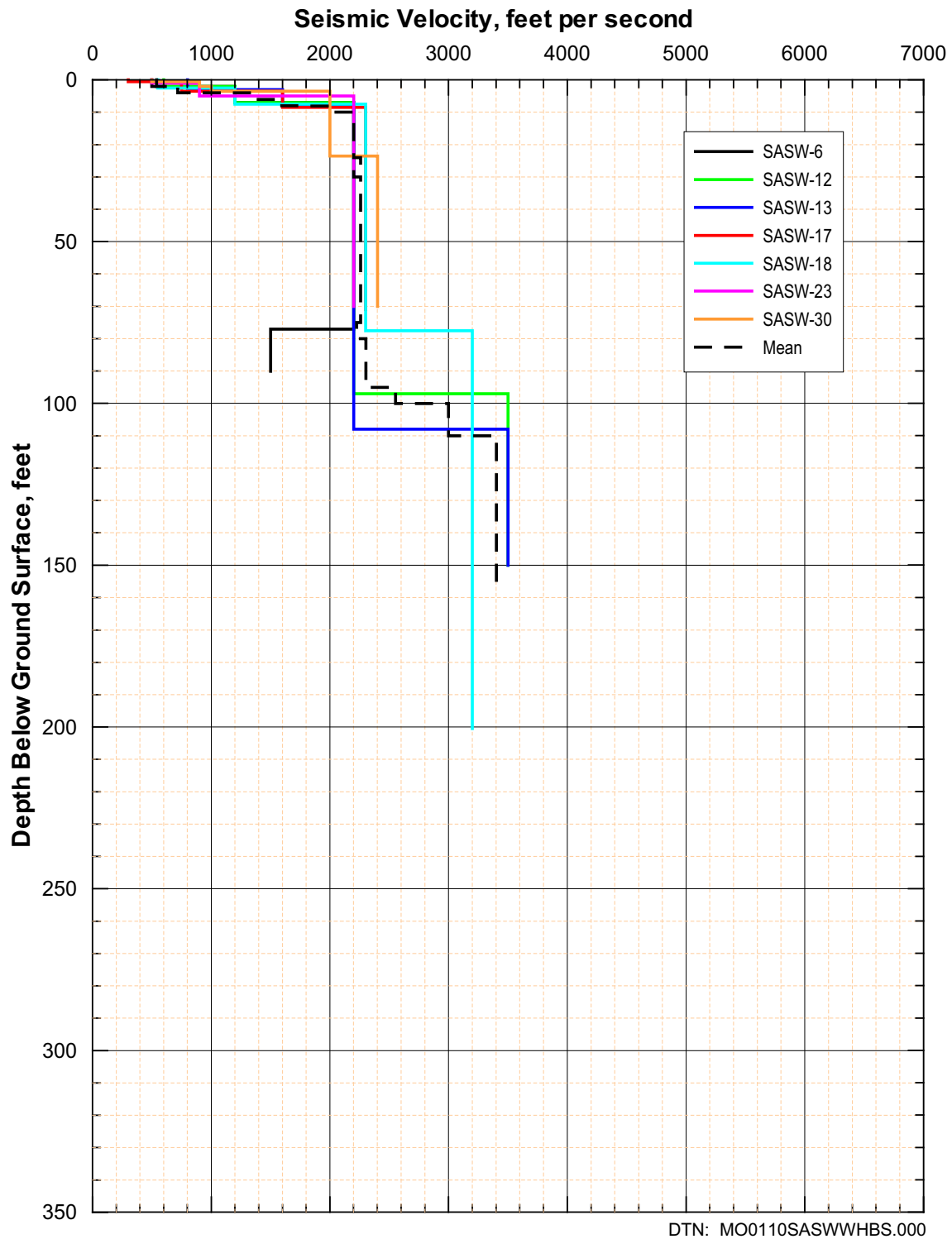
Note: This mean profile has been calculated for illustrative purposes only. Final statistics calculated for use in the forthcoming scientific analysis entitled *Development of Seismic Design Input Ground Motions for a Geologic Repository at Yucca Mountain* will be submitted to the TDMS.

Figure 92. Shear-Wave Velocities from SASW Measurements in the WHB Area (Area 1)



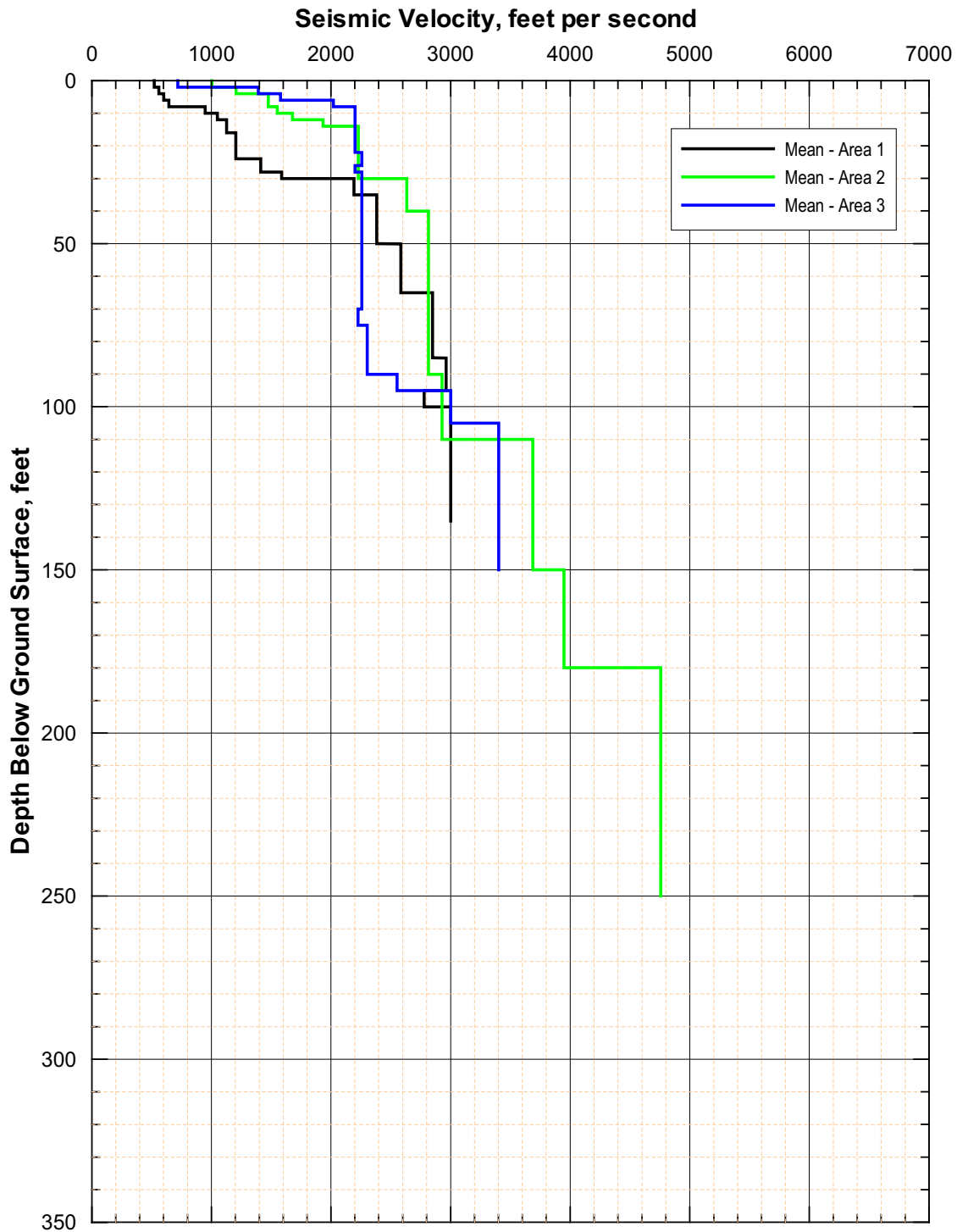
Note: This mean profile has been calculated for illustrative purposes only. Final statistics calculated for use in the forthcoming scientific analysis entitled *Development of Seismic Design Input Ground Motions for a Geologic Repository at Yucca Mountain* will be submitted to the TDMS.

Figure 93. Shear-Wave Velocities from SASW Measurements in the WHB Area (Area 2)



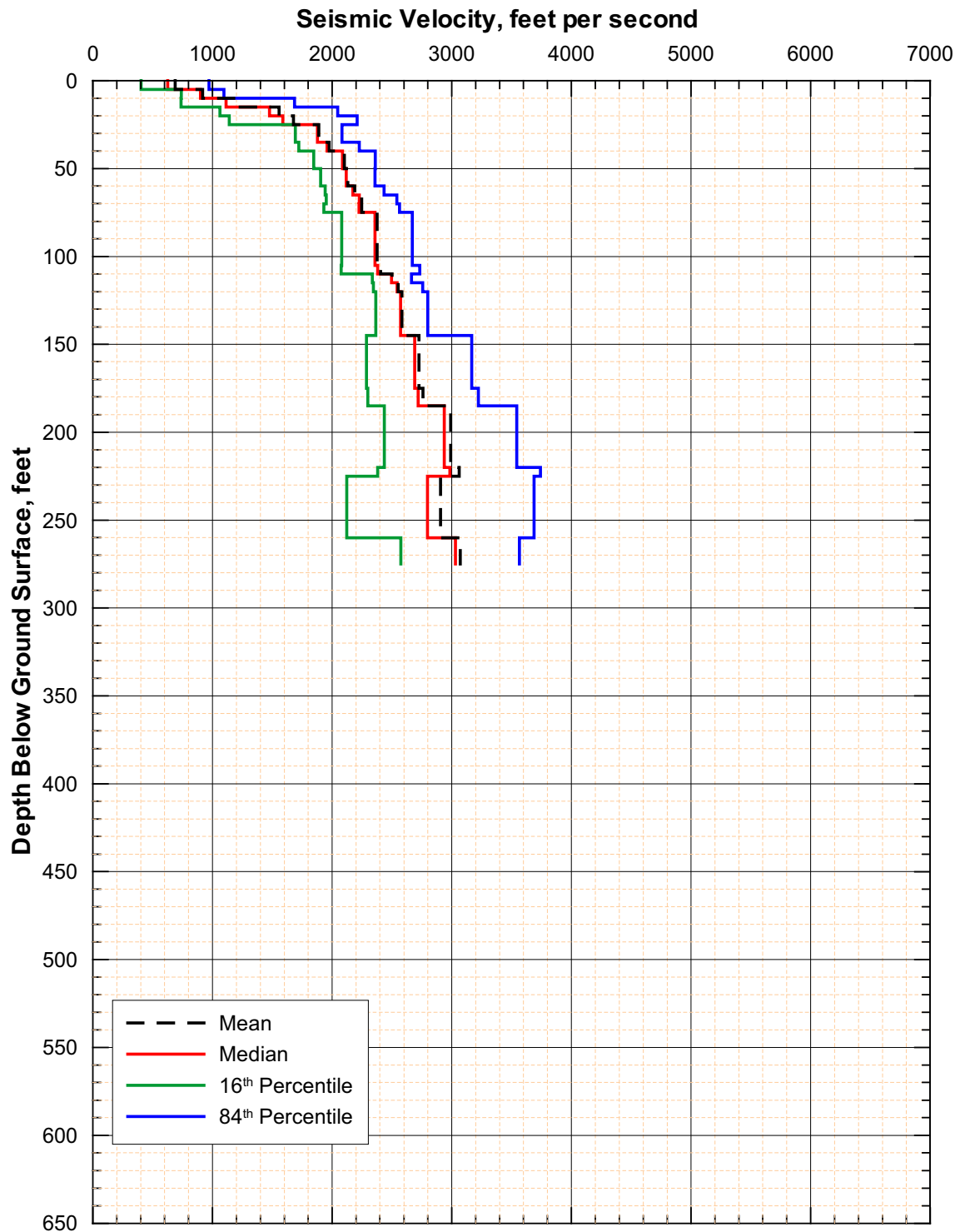
Note: This mean profile has been calculated for illustrative purposes only. Final statistics calculated for use in the forthcoming scientific analysis entitled *Development of Seismic Design Input Ground Motions for a Geologic Repository at Yucca Mountain* will be submitted to the TDMS.

Figure 94. Shear-Wave Velocities from SASW Measurements in the WHB Area (Area 3)



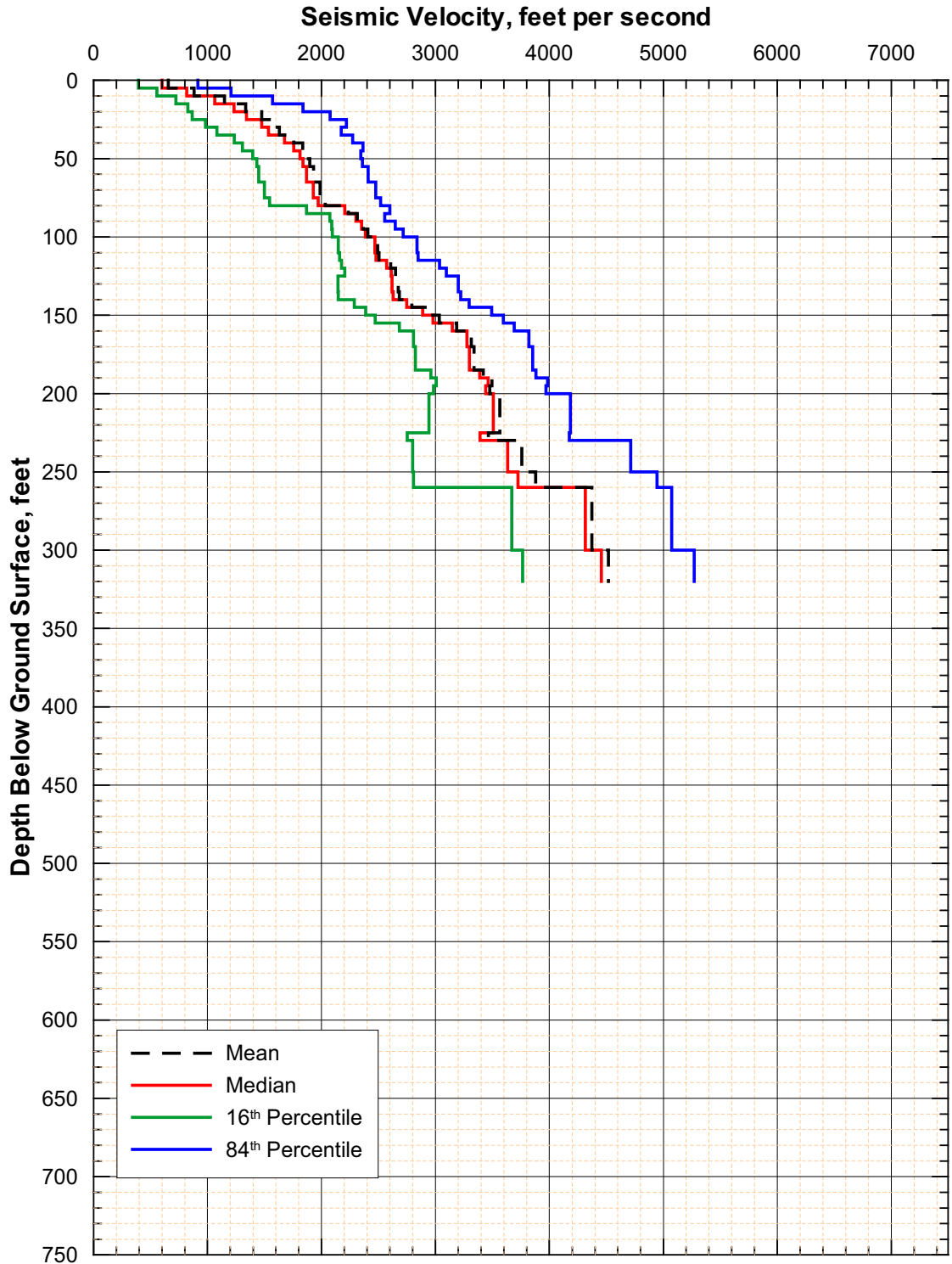
Note: These mean profiles have been calculated for illustrative purposes only. Final statistics calculated for use in the forthcoming scientific analysis entitled *Development of Seismic Design Input Ground Motions for a Geologic Repository at Yucca Mountain* will be submitted to the TDMS.

Figure 95. Comparison of Shear-Wave Velocities from SASW Measurements by Area



Note: These statistics have been calculated for illustrative purposes only. Final statistics calculated for use in the forthcoming scientific analysis entitled *Development of Seismic Design Input Ground Motions for a Geologic Repository at Yucca Mountain* will be submitted to the TDMS.

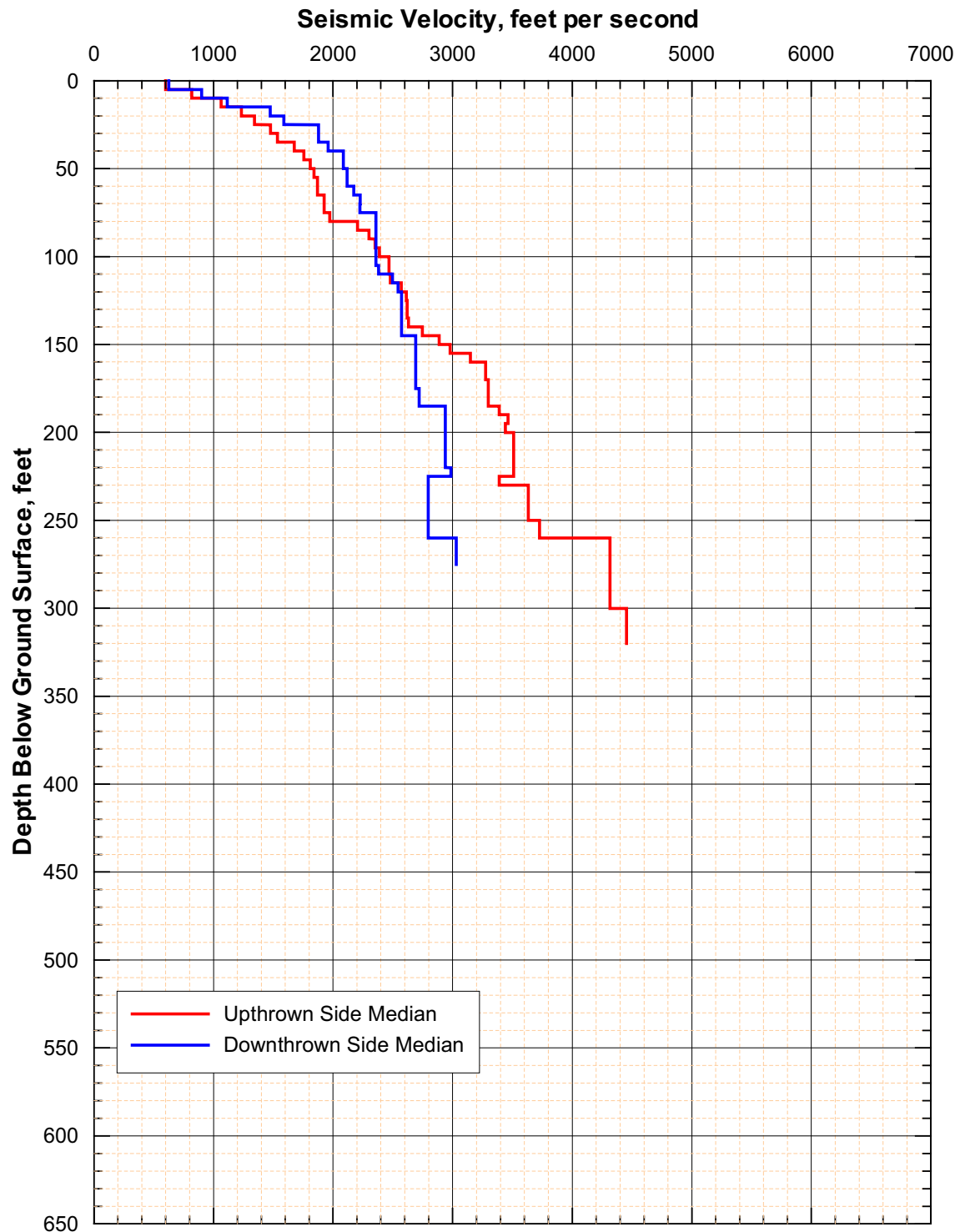
Figure 96. Statistical Analyses of Shear-Wave Velocities from SASW Measurements in the WHB Area, Downthrown Side of the Exile Hill Fault Splay



DTN TBD

Note: These statistics have been calculated for illustrative purposes only. Final statistics calculated for use in the forthcoming scientific analysis entitled *Development of Seismic Design Input Ground Motions for a Geologic Repository at Yucca Mountain* will be submitted to the TDMS.

Figure 97. Statistical Analyses of Shear-Wave Velocities from SASW Measurements in the WHB Area, Uprhown Side of the Exile Hill Fault Splay



DTN TBD

Note: These mean profiles have been calculated for illustrative purposes only. Final statistics calculated for use in the forthcoming scientific analysis entitled *Development of Seismic Design Input Ground Motions for a Geologic Repository at Yucca Mountain* will be submitted to the TDMS.

Figure 98. Comparison of SASW Shear-Wave Velocities Across the Exile Hill Fault Splay

In considering the SASW results, three possible limitations of the methodology should be noted. First, the theoretical model used to determine the shear-wave velocity profile at a site is a one-dimensional layered model. Any lateral variations in shear-wave velocity and layer thickness beneath the extent of the receiver array (hence uniform horizontal layers) are averaged. Therefore, the profile that is presented represents a 1-D layered model that fits the measured dispersion data. It should be noted that lateral variability can be observed qualitatively from mismatches in the individual experimental dispersion curves from adjacent receiver spacings.

Secondly, successful implementation of the SASW method requires that multiple receiver spacings be used at one site. This poses some difficulty when creating a single theoretical dispersion curve to match the experimental dispersion curve. Because the actual receiver spacing is not used, the theoretical dispersion curve is calculated based on the receivers being located 2λ and 4λ (λ is wavelength) from the source. Past studies have shown that these values of receiver spacing do not greatly affect the final shear-wave velocity profile determined at most sites (Joh 1996).

Finally, it is also important to note that as the wavelength used in the SASW methodology increases, and hence as the depth of penetration increases, the surface wave propagates through a greater volume of material. The resolution of the SASW method (ability to detect changes in velocity and thickness at depth) decreases as the wavelength increases. Therefore, the resolution is best near the surface and lowest at the greatest depths in the profile. For these analyses, the shear-wave velocity profiles are presented to a maximum depth of approximately 0.5 times the longest wavelength recorded in the field. The maximum profile depth is based on the fact that most of the surface wave particle motion is occurring at depths less than 0.5 times the longest wavelength. The step-wise shear-wave model used in the SASW analysis reflects the general trend in the shear-wave velocities to this depth (0.5 times the longest wavelength). For the SASW surveys near the WHB, the shear-wave profile is well resolved to depths within the range of approximately 75 to 125 ft. At greater depths, the trend in the shear-wave velocity profile is accurately reflected, but the absolute depths and relative changes in shear-wave velocities at interfaces are less well resolved.

6.2.8 Borehole Wireline Geophysical Surveys

Caliper and gamma-gamma wireline surveys were performed by Schlumberger Limited in boreholes RF#16, RF#18, RF#20, RF#21, RF#22, RF#24 and RF#28. These seven boreholes were the ones that were available for logging at the time when the subcontractor was mobilized to the site. The locations of these boreholes are shown on Figure 2 in Section 6.2.2. The processes established in AP-SIII.5Q, *Yucca Mountain Site Characterization Project Field Verification of Geophysical Operations*, and AP-SIII.6Q, *Geophysical Logging Programs for Surface-Based Testing Program Boreholes*, were followed for both the caliper and gamma-gamma wireline surveys. The main purpose in performing the caliper measurements was to quantitatively assess the extent of erosion of the borehole walls by the drilling fluid, as this was found to be a factor affecting data acquired from borehole RF#13 (see Section 6.7.2 for a discussion of the erosion in borehole RF#13 and the potential effects of that on the suspension seismic results). The main purpose of performing the gamma-gamma measurements was to evaluate the density of the subsurface materials. It was also hoped that the density values would help with identification of the lithostratigraphic units.

The caliper surveys utilized a four-arm caliper, yielding borehole diameter measurements in two orthogonal directions. One pair of arms usually aligns itself with the major axis of an elliptical borehole, and the other with the minor axis (Schlumberger Educational Services 1987, page 42). The caliper logs indicate divergences between the borehole dimensions and the drill bit size, which may reflect rock fractures or erosion of the borehole walls by the drilling fluid. However, borehole ellipticity can result from other factors, including directional drilling, deviated borehole, drilling at an acute angle to bedding, and an oriented pore structure (Schlumberger Educational Services 1987, page 42).

The gamma-gamma density measurement involves emitting a known number of gamma rays from a radioactive source and counting the number of gamma rays arriving at a detector. After leaving the source, the gamma rays collide with electrons in the material surrounding the borehole, causing the gamma rays to lose some of their energy before continuing in a different direction. The percentage of gamma rays arriving at the detector is related to the density of electrons in the formation (electrons per cubic centimeter) and thus to the formation bulk density.

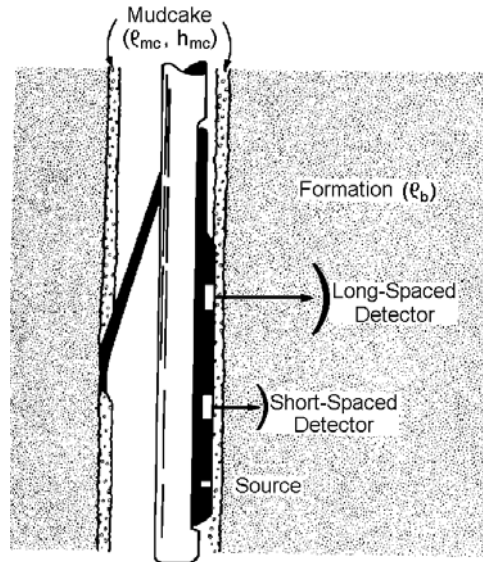
The boreholes were advanced using drilling mud to support the opening. To minimize the effect of the mudcake on the borehole walls, the source and detectors were mounted on a skid and shielded. The shielded openings were pressed against the borehole walls by an eccentricing arm. The force applied by the arm and the plow-shaped design of the skid help the skid to cut through soft mudcakes.

Any mud or mudcake remaining between the source and the formation or between the detectors and the formation affect the gamma rays and must be taken into account. In the dual-detector Formation Density Logging Device (FDLD) shown on Figure 99, mudcake compensation is effected by the use of two detectors with different source-detector spacing and hence different depths of formation penetration. The acquisition software uses data from both detectors to compute a bulk density value (ρ_b) and the correction ($\Delta\rho$). This process is illustrated in the “spine and ribs” charts on Figure 100.

Figure 100 provides the overall concept of the dual-detector correction process using what is referred to as the “spine and ribs” method. The t_{mc} is the mudcake thickness, ρ_b is the bulk density of the formation, ρ_{mc} is the actual bulk density of the mudcake and ρ_{mc}^+ is the apparent density of the mudcake. While the design of the tool removes the influence of electron density from the measurement of bulk density of the formation, the same is not true for the mudcake density. The apparent density of the mudcake, ρ_{mc}^+ , combines the influence of both the bulk density of the mudcake and the electron density.

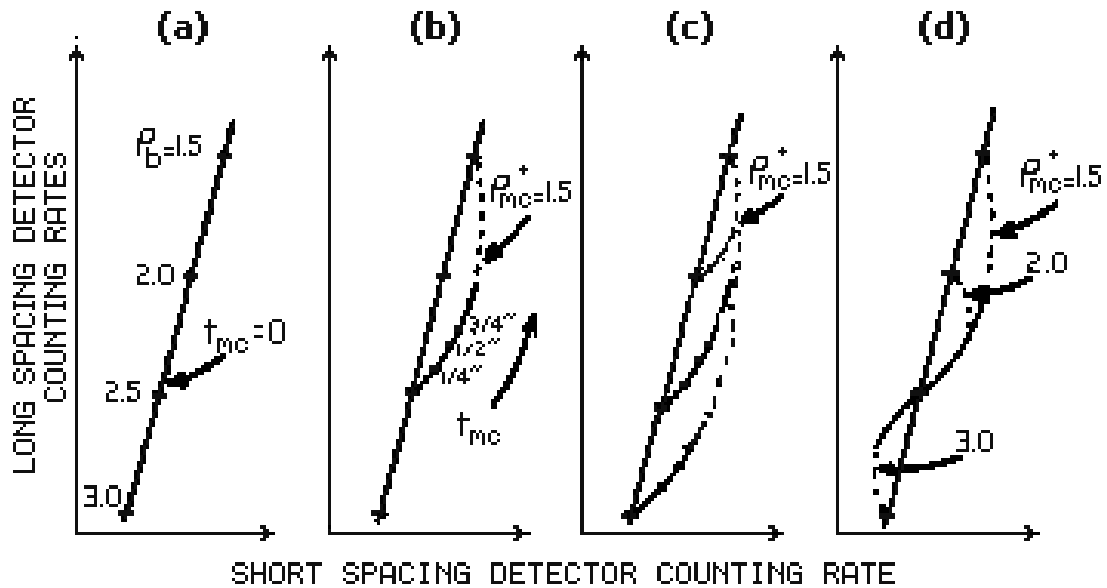
The “spine” is shown in (a) where mudcake thickness is zero and the detector responses are only a function of variations in the formation density.

In (b), for a constant ρ_{mc}^+ (=1.5 gm/cc) and a constant ρ_b (=2.5 gm/cc), the departure from the true bulk density, resulting from increasing mudcake thickness, follows a line that leads to, at infinite mudcake thickness, 1.5 gm/cc.



Source: Wahl et al. (1964, page 1411)

Figure 99. Schematic Diagram of Dual-Detector Formation Density Logging Device



Source: Wahl et al. (1964, page 1413)

Figure 100. "Spine and Ribs" Plot Used To Compute Bulk Density And Density Correction From Dual Detector Density Tools

In (c), ρ_{mc}^+ is constant at 1.5 gm/cc while both t_{mc} and ρ_b are varied. The three curved lines emanating from bulk density values of 2.0 gm/cc, 2.5 gm/cc, and 3.0 gm/cc represent increasing t_{mc} . Once again, when the mudcake thickness becomes infinite, all three ρ_b values converge at the bulk density value of the mudcake.

In (d), varying thickness of three different values of ρ_{mc}^+ (1.5 gm/cc, 2.0 gm/cc, and 3.0 gm/cc) are superimposed on a formation having $\rho_b=2.5$ gm/cc. When ρ_{mc}^+ is greater than ρ_b the mudcake curve falls down and to the left of the “spine”. This indicates that mudcake curves exist on both sides of the “rib” and can be corrected in the same manner. When the mudcake curves are cut off at the point they begin to separate, the “ribs” of the plot become apparent.

The result is that for each value of ρ_b , all mudcake curves leaving one side of the “spine” can be described, for the normal ranges of mudcake thickness, by a single algorithm. This means that, by proper tool design, the correct formation density can be determined by the counting rates of the two detectors.

The above discussion was developed to describe the compensation routine used with the early borehole compensated density tools. The modern density tools still use a dual-detector system along with the “spine and ribs” correction. For moderate borehole rugosity or mudcake, the slope of the line passing through the value for the correct bulk density and the density measured from each detector is virtually the same for the usual densities and thicknesses of intervening materials separating the detectors and the formation wall. This provides a means for estimating the amount of correction to be added to or subtracted from the measured response from the long-spacing detector.

DTN: MO0112GPLOGWHB.001 summarizes the results of the borehole geophysical surveys in tabular format, and these data are shown on the figures in Attachment X. Table 12 and Figure 101 summarize the data. Figure 101 plots the total density as a function of depth bgs, and identifies the lithostratigraphic unit and borehole with different symbol colors and symbol shapes, respectively. With all boreholes considered together, little trend of density with depth can be discerned. However, if the data from borehole RF#22, located north of the Exile Hill fault splay, are considered separately from the data from boreholes located southwest of the Exile Hill fault splay, a trend of increasing density with depth can be observed in the data from southwest of the Exile Hill fault splay. Another can be observed between density and lithostratigraphic unit. Table 12 summarizes the mean and coefficient of variation of the total density values by lithostratigraphic unit.

6.2.9 Geotechnical Laboratory Static Testing

As discussed in Section 6.2.4, four test pits, WHB-1 through -4, were excavated in the WHB area. In-situ density tests were performed in each of the test pits, as described in Section 6.2.4. Most of the material from those tests was placed in lined canvas sacks, but a part of the material excavated in each 6-foot ring test and all material from 20-inch sand cone density tests was placed in sealed plastic buckets to help preserve the specimen’s as-tested water content. The samples were shipped to a geotechnical laboratory in Denver, CO, where additional tests were performed in order to classify the material according to the USCS (see USBR 5000-86) and to determine the in-place relative density.

Table 12. Statistical Summary of Density Measurements by Lithostratigraphic Unit

Unit (Symbol)	RF#16	RF#18	RF#20	RF#21	RF#22	RF#24	RF#28	All
Fill	Data Interval, ft	9-22	11.0-28.0	--	--	--	--	98.26
	Minimum, lbm/ft ³	98.26	109.75	--	--	--	--	131.29
	Maximum, lbm/ft ³	131.29	124.11	--	--	--	--	115.37
	Mean, lbm/ft ³	112.09	117.91	--	--	--	--	7.26
Standard Deviation, lbm/ft ³	9.50	3.24	35					62
Count	27							
Gal	Data Interval, ft	22.5-75.5	28.5-97.5	(see Note 2) 7.0-115.0	7.0-80.0	10.0-30.0	5.0-15.0	80.91
	Minimum, lbm/ft ³	105.75	110.37	80.91	104.50	113.24	93.89	129.41
	Maximum, lbm/ft ³	129.29	126.73	123.42	129.41	122.30	127.79	115.71
	Mean, lbm/ft ³	114.13	118.71	111.24	119.51	118.20	110.12	7.14
Standard Deviation, lbm/ft ³	4.51	3.61	9.51	3.80	2.70	8.76	21	778
Count	107	106	139	217	147	41		
Tmbt1	Data Interval, ft	--	--	--	80.5-318.0	--	--	96.51
	Minimum, lbm/ft ³	--	60.0-64.5	109.44	96.51	130.35	130.35	109.83
	Maximum, lbm/ft ³	--	125.29	117.13	109.67	5.32	5.42	5.42
	Mean, lbm/ft ³	--	5.62	10	476			486
Standard Deviation, lbm/ft ³	--							
Count								
Tpki	Data Interval, ft	76-133	65.0-204.0	--	318.5-409.5	--	--	86.03
	Minimum, lbm/ft ³	86.46	86.03	--	98.51	115.18	115.18	98.26
	Maximum, lbm/ft ³	111.18	113.43	--	102.76	2.52	183	5.69
	Mean, lbm/ft ³	95.08	96.63	--	2.52	183		577
Standard Deviation, lbm/ft ³	7.48	4.43	279					
Count	115							

F:\M\MP4200\data\schlumberger

Table 12. Statistical Summary of Density Measurements by Lithostratigraphic Unit (Continued)

Unit (Symbol)	RF#16	RF#18	RF#20	RF#21	RF#22	RF#24	RF#28	All
Tpbt5	Data Interval, ft	133.5-137.5	98.0-102.0	--	--	--	--	85.09
	Minimum, lbm/ft ³	85.09	119.36	--	--	--	--	123.67
	Maximum, lbm/ft ³	113.62	123.67	--	--	--	--	111.71
	Mean, lbm/ft ³	102.00	121.43	--	--	--	--	12.92
	Standard Deviation, lbm/ft ³	11.84	1.51	--	--	--	--	18
Count	9	9	9	9	9	9	9	18
Tpcrn (see Note 1)	Data Interval, ft	138.0-222.0	204.5-292.0	102.5-118.0	115.5-155.0	30.5-110.0	15.5-70.0	87.34
	Minimum, lbm/ft ³	87.34	95.08	96.45	87.34	97.26	106.13	144.08
	Maximum, lbm/ft ³	138.28	138.59	132.10	125.17	129.98	144.08	116.87
	Mean, lbm/ft ³	115.16	119.52	109.16	113.24	115.77	121.75	9.90
	Standard Deviation, lbm/ft ³	10.09	8.78	12.38	10.89	6.41	10.70	727
Count	169	176	32	80	160	110	110	727
Tpcpun	Data Interval, ft	222.5-255.5	292.5-325.0	--	--	110.5-140.0	70.5-80.0	116.87
	Minimum, lbm/ft ³	119.61	116.87	--	--	139.34	133.03	144.15
	Maximum, lbm/ft ³	138.53	144.15	--	--	111.31	142.65	131.74
	Mean, lbm/ft ³	131.75	133.94	--	--	127.41	137.45	6.70
	Standard Deviation, lbm/ft ³	4.30	6.76	--	--	7.19	3.18	213
Count	67	66	--	--	60	20	20	213
Tpcpul	Data Interval, ft	256.0-360.0	325.5-424.5	--	--	140.5-178.0	80.5-88.0	111.85
	Minimum, lbm/ft ³	111.87	114.87	--	--	111.85	128.48	146.96
	Maximum, lbm/ft ³	136.65	146.96	--	--	129.98	135.91	129.69
	Mean, lbm/ft ³	127.61	134.75	--	--	121.44	132.97	7.45
	Standard Deviation, lbm/ft ³	4.74	7.07	--	--	4.81	2.24	500
Count	209	199	--	--	76	16	16	500

T:\M\420\data\schlumberger

Table 12. Statistical Summary of Density Measurements by Lithostratigraphic Unit (Continued)

Unit (Symbol)	RF#16	RF#18	RF#20	RF#21	RF#22	RF#24	RF#28	All
Tpcpmn	Data Interval, ft	360.5-402.5	425.0-469.5	--	--	--	--	124.73
	Minimum, lbm/ft ³	124.73	144.77	--	--	--	--	148.52
	Maximum, lbm/ft ³	148.52	148.14	--	--	--	--	144.96
	Mean, lbm/ft ³	143.35	146.48	--	--	--	--	3.34
	Standard Deviation, lbm/ft ³	4.17	0.74	--	--	--	--	175
Count	85	90						
Tpcpil	Data Interval, ft	403.0-422.0	470.0-479.0	--	--	--	--	126.17
	Minimum, lbm/ft ³	126.17	136.59	--	--	--	--	146.83
	Maximum, lbm/ft ³	138.90	146.83	--	--	--	--	135.69
	Mean, lbm/ft ³	131.78	143.72	--	--	--	--	6.46
	Standard Deviation, lbm/ft ³	3.30	2.83	--	--	--	--	58
Count	39	19						
Tpcpln	Data Interval, ft	422.5-440.0	--	--	--	--	--	125.61
	Minimum, lbm/ft ³	125.61	--	--	--	--	--	145.21
	Maximum, lbm/ft ³	145.21	--	--	--	--	--	132.29
	Mean, lbm/ft ³	132.29	--	--	--	--	--	4.90
	Standard Deviation, lbm/ft ³	4.90	--	--	--	--	--	36
Count	36							

T:\MYP4200\data\schlumberger

DTN: MO0204SEPGAMD.M.000

Notes: (1) Tpcrn includes Tpcrv, Tpcrl and Tpcrn.

(2) Assumption 4 (Section 5) was not considered in the statistics for data from borehole RF#21.

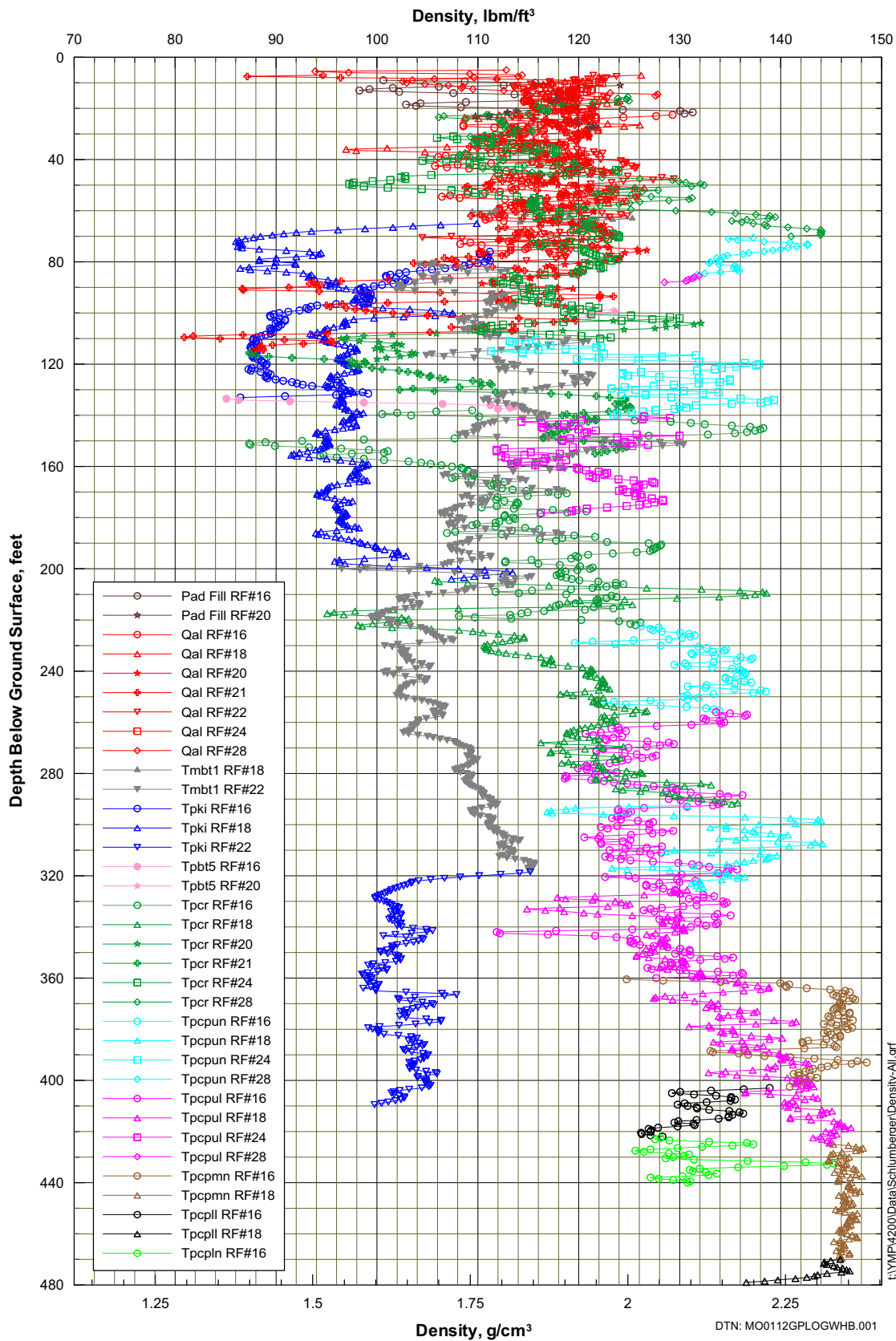


Figure 101. Density from gamma-gamma Logging as a Function of Depth and Lithostratigraphic Unit

INTENTIONALLY LEFT BLANK

The following tests were performed on each sample:

- Particle-size distribution per USBR 5325-89, *Procedure for Performing Gradation Analysis of Gravel Size Fraction of Soils*; USBR 5330-89, *Procedure for Performing Gradation Analysis of Fines and Sand Size Fraction of Soils, Including Hydrometer Analysis*; and USBR 5335-89, *Procedure for Performing Gradation Analysis of Soils Without Hydrometer – Wet Sieve*.
- Water content per USBR 5300-89, *Procedure for Determining Moisture Content of Soil and Rock by the Oven Method*.
- Maximum and minimum index unit weights of the particles passing the 3-inch sieve per USBR 5525-89, *Procedure for Determining the Minimum Index Unit Weight of Cohesionless Soils*, and USBR 5530-89, *Procedure for Determining the Maximum Index Unit Weight of Cohesionless Soils*.
- Specific gravity of the particles passing the 4.75 mm (No. 4) sieve per USBR 5320-89, *Procedure for Determining Specific Gravity of Soils (volume method)*.
- Specific gravity of the particles retained on the 4.75 mm (No. 4) sieve per USBR 5320-89 (suspension method).
- Liquid limit and plastic limit (Atterberg limits) per USBR 5350-89, *Procedure for Determining the Liquid Limit of Soils by the One-Point Method*, and USBR 5360-89, *Procedure for Determining the Plastic Limit and Plasticity Index of Soils*.

The test results are summarized in Table 13, and Figure 102 shows plots of the particle-size distribution results. Attachment XI shows the particle-size distribution data on multiple plots (maximum 5 results per plot).

6.2.10 Geotechnical Laboratory Dynamic Testing

Laboratory tests using combined resonant column and torsional shear (RCTS) equipment were performed to evaluate the dynamic properties of tuff and alluvium from the WHB Area. The tuff and alluvial specimens were from boreholes RF#14, RF#15, RF#16, and RF#17. The core specimens were selected to represent the various tuff units and the range of physical properties. The results from the dynamic testing of 19 specimens are presented in this section. A detailed description of this testing and the apparatus used is contained in Scientific Notebook SN-M&O-SCI-033-V1 (Wong 2002e).

6.2.10.1 Test Procedures

The RCTS equipment has been developed at the University of Texas at Austin Civil Engineering Department (UTACED) over the past two decades (Lodde 1982; Kim 1991). The equipment is of the fixed-free type, with the bottom of the specimen fixed and torsional excitation applied to the top. Both resonant column and torsional shear tests can be performed in a sequential series on the same specimen over a shearing-strain range from about $10^{-4}\%$ to slightly more than $10^{-1}\%$. The primary difference between the two types of tests is the excitation frequency. In the resonant column test, frequencies above 20 Hz are required and the inertia of the specimen and drive system must be known to analyze the measurements. Slow cyclic loading involving frequencies generally below 10 Hz is performed in the torsional shear test and inertia does not enter into the data analysis.

RCTS Equipment

The RCTS apparatus can be idealized as a fixed-free system (Figure 103). The bottom end of the specimen is fixed against rotation at the base pedestal, and the top end of the specimen is connected to the driving system. The driving system, which consists of a top cap and drive plate, can rotate freely to excite the specimen in cyclic torsion.

A simplified diagram of a fixed-free resonant column test is shown in Figure 104a. The basic operational principle is to vibrate the cylindrical specimen in first-mode torsional motion. Harmonic torsional excitation is applied to the top of the specimen over a range in frequencies, and the variation of the acceleration amplitude of the specimen with frequency is obtained (Figure 104b). Once first-mode resonance is established, measurements of the resonant frequency and amplitude of vibration are made. These measurements are then combined with equipment characteristics and specimen size to calculate shear-wave velocity and shear modulus based on elastic wave propagation. Material damping is determined either from the width of the frequency response curve or from the free-vibration decay curve.

The torsional shear test is another method of determining shear modulus and material damping using the same RCTS equipment but operating it in a different manner. The simplified configuration of the torsional shear test is shown on Figure 105a. A cyclic torsional force with a given frequency, generally below 10 Hz, is applied at the top of the specimen. Instead of determining the resonant frequency, the stress-strain hysteresis loop is determined from measuring the torque-twist response of the specimen. Proximitors are used to measure the angle of twist while the voltage applied to the coil is calibrated to yield torque. Shear modulus is calculated from the slope of a line through the end points of the hysteresis loop, and material damping is obtained from the area of the hysteresis loop, as shown on Figure 105b.

The RCTS apparatus used in this study has three advantages. First, both resonant column and torsional shear tests can be performed with the same set-up simply by changing (outside the apparatus) the frequency of the forcing function. Variability due to preparing "identical" samples is eliminated so that both test results can be compared effectively. Second, the torsional shear test can be performed over a shearing-strain range between $5 \times 10^{-4}\%$ and about $10^{-1}\%$, depending upon specimen stiffness. Common types of torsional shear tests, which generate torque by a mechanical motor outside of the confining chamber, are usually performed at strains above 0.01% because of system compliance. However, the RCTS apparatus used in this study generates torque with an electrical coil-magnet system inside the confining chamber, thus eliminating the problem with an external motor. The torsional shear test can be performed at the same low-strain amplitudes as the resonant column test, and results between torsional shear and resonant column testing can be easily compared over a wide range of strains. Third, the loading frequency in the torsional shear test can be changed easily from 0.01 to 10 Hz. Therefore, the effect of frequency on deformational characteristics can be conveniently investigated using this apparatus.

Table 13. Summary of Laboratory Tests on Material Excavated for In-Situ Density Tests

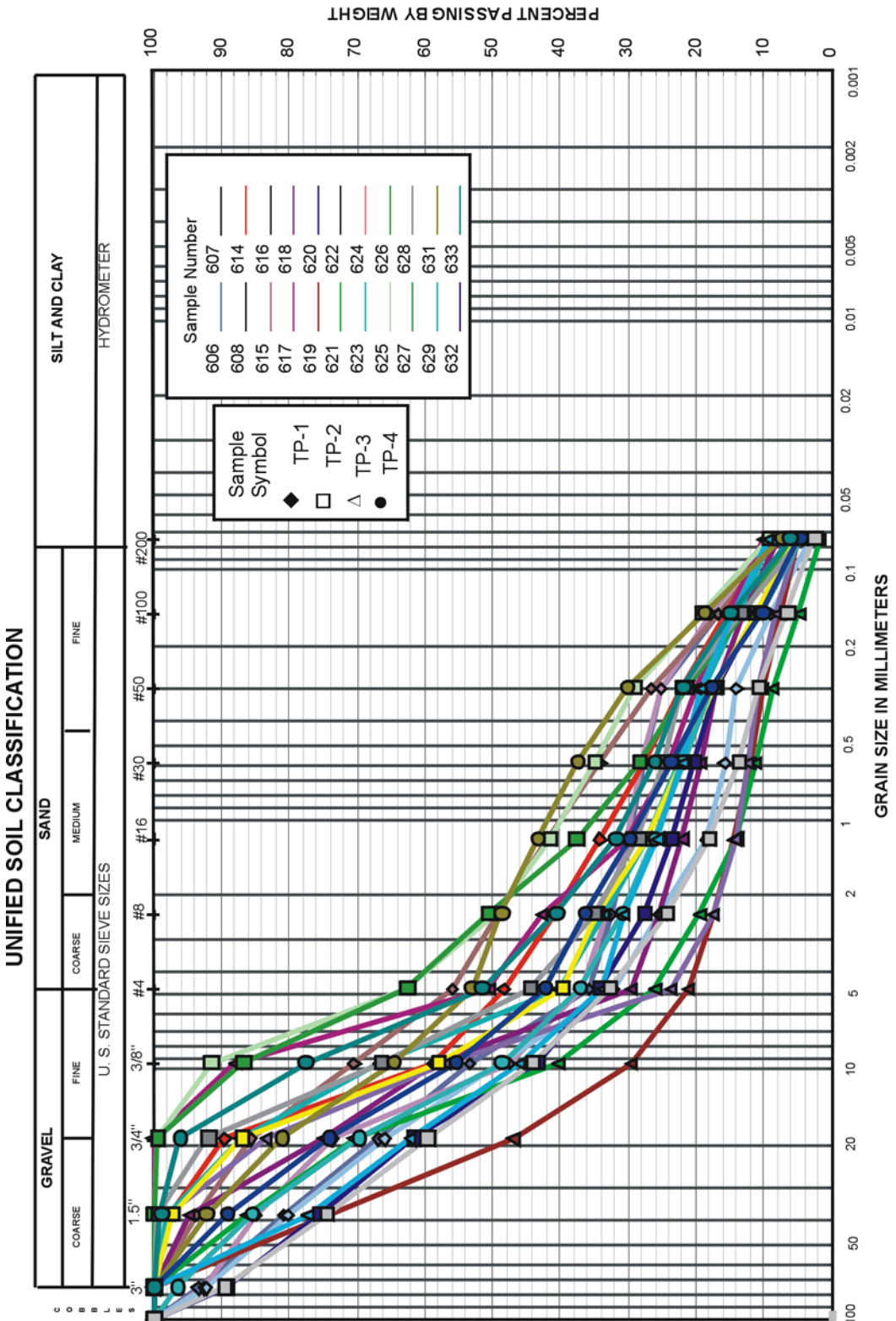
Test Pit No. (1)	Depth feet	Sample No. 65A (2)	USCS Group Symbol	Specific Gravity						Absorption, %			Water Content, %			Particle-Size Distribution				Index Density for Relative Density (6)				
				Plus No. 4 to minus 3" Sieve Fraction		Plus 3-inch Sieve Fraction		Bulk	Oven Dry	Apparent	SSD	Bulk	Oven Dry	No. 4 to 3" sieve Fraction	Plus 3" Fraction	Minus No. 4 sieve %	Plus No. 4 sieve %	Cobbles %	Gravel %	Sand %	Fines (4) %	% Finer than 5 microns	Maximum lbs/ft ³	Minimum lbs/ft ³
				Apparent	SSD	Oven Dry	Apparent																	
1	4	606	GW-GM	2.50	2.40	2.20	2.05	2.18	2.27	2.18	7.1	3.8	4.8	7.9	4.4	6.6	57.7	27.7	8.0	3.0	115.8	92.5		
1	12	607	GW-GM	2.48	2.48	2.28	2.15	2.11	2.21	2.11	6.0	4.8	7.5	4.0	7.5	7.5	55.5	27.9	9.1	3.3	117.6	92.4		
1	12	614	GP-GM	2.52	2.43	2.28	2.17	-	-	-	5.1	-	5.1	4.4	3.3	0	51.7	39.1	9.2	4.4	127.4	95.5		
1	12.3	615	SP-SM	2.55	2.42	2.21	2.06	-	-	-	7.4	-	7.4	5.6	3.9	0	44.2	47.8	8.0	4.9	122.6	93.0		
1	20	608	GP	2.52	2.47	2.29	2.15	2.40	2.27	2.18	6.0	4.2	4.8	3.9	7.8	60.1	28.8	3.3	1.4	120.2	93.8			
2	8	616	GP	2.51	2.41	2.22	2.07	2.38	2.29	2.22	6.9	2.9	10.6	5.91	2.6	57.0	30.1	2.6	2.3	115.4	89.4			
2	12	620	GP-GM	2.50	2.47	2.26	2.12	2.30	2.18	2.09	6.7	4.3	5.8 (7)	8.7	6.3	0	55.3	28.7	5.4	1.9	119.6	98.2		
2	16	624	GW-GM	2.52	2.48	2.27	2.13	-	-	-	6.7	-	6.7	8.7	6.3	0	60.3	33.9	5.8	4.5	116.4	92.0		
2	16	625	SW-SM	2.55	2.50	2.28	2.14	-	-	-	6.8	-	6.8	7.4	6.1	0	37.2	53.6	9.2	8.0	115.1	93.5		
2	16	626	SP-SM	2.48	2.51	2.29	2.14	-	-	-	6.9	-	6.9	5.3	3.9	0	37.3	56.8	5.9	5.1	112.8	87.5		
2	19	628	GW	2.51	2.51	2.26	2.10	-	-	-	7.8	-	7.8	9.6	6.9	0	55.4	40.1	4.5	4.5	118.6	91.9		
3	8	617	GP-GM	2.56	2.49	2.28	2.15	-	-	-	6.4	-	6.4	3.5	2.3	0	49.4	40.6	10.0	7.7	121.5	90.0		
3	8	618	GP-GM	2.54	2.46	2.27	2.13	-	-	-	6.2	-	6.2	4.4	3.6	0	70.4	21.7	7.9	3.6	116.6	92.9		
3	8	619	GP-GM	2.54	2.42	2.24	2.12	-	-	-	5.9	-	5.9	5.1	3.0	0	79.0	16.0	5.0	2.5	112.3	88.0		
3	12	621	GP	2.50	2.45	2.27	2.15	-	-	-	5.8	-	5.8	8.9	6.3	0	73.9	24.5	1.6	1.5	113.8	92.3		
3	12	622	GP	2.54	2.49	2.30	2.17	-	-	-	5.9	-	5.9	6.9	4.2	0	76.3	18.8	4.9	2.9	108.2	84.4		
3	12	623	GP-GM	2.54	2.48	2.29	2.16	-	-	-	6.0	-	6.0	4.1	3.0	0	59.7	31.3	9.0	4.3	125.3	94.9		
3	19	629 (3)	GW-GM	2.53	2.44	2.26	2.13	-	-	-	6.0	-	6.0	16.0	7.7	0	66.2	24.5	9.3	6.3	96.9	83.3		
4	4	627	GW	2.48	2.48	2.28	2.14	2.40	2.28	2.20	6.4	3.7	6.7 (7)	6.7 (7)	6.7 (7)	3.5	58.8	33.0	4.7	1.2	118.1	88.8		
4	8	631	GP-GM	2.50	2.50	2.25	2.08	-	-	-	8.1	-	8.1	6.9	5.0	0	46.9	45.6	7.5	4.5	124.9	92.6		
4	12	632	GP	2.47	2.46	2.23	2.07	-	-	-	7.6	-	7.6	8.0	4.7	0	57.7	37.5	4.8	3.4	112.9	91.5		
4	16	633	GW-GM	2.50	2.51	2.26	2.10	-	-	-	7.9	-	7.9	8.0	6.6	0	48.4	45.4	6.2	4.2	117.5	90.7		

DTN: GS020483114233.004

NOTES:

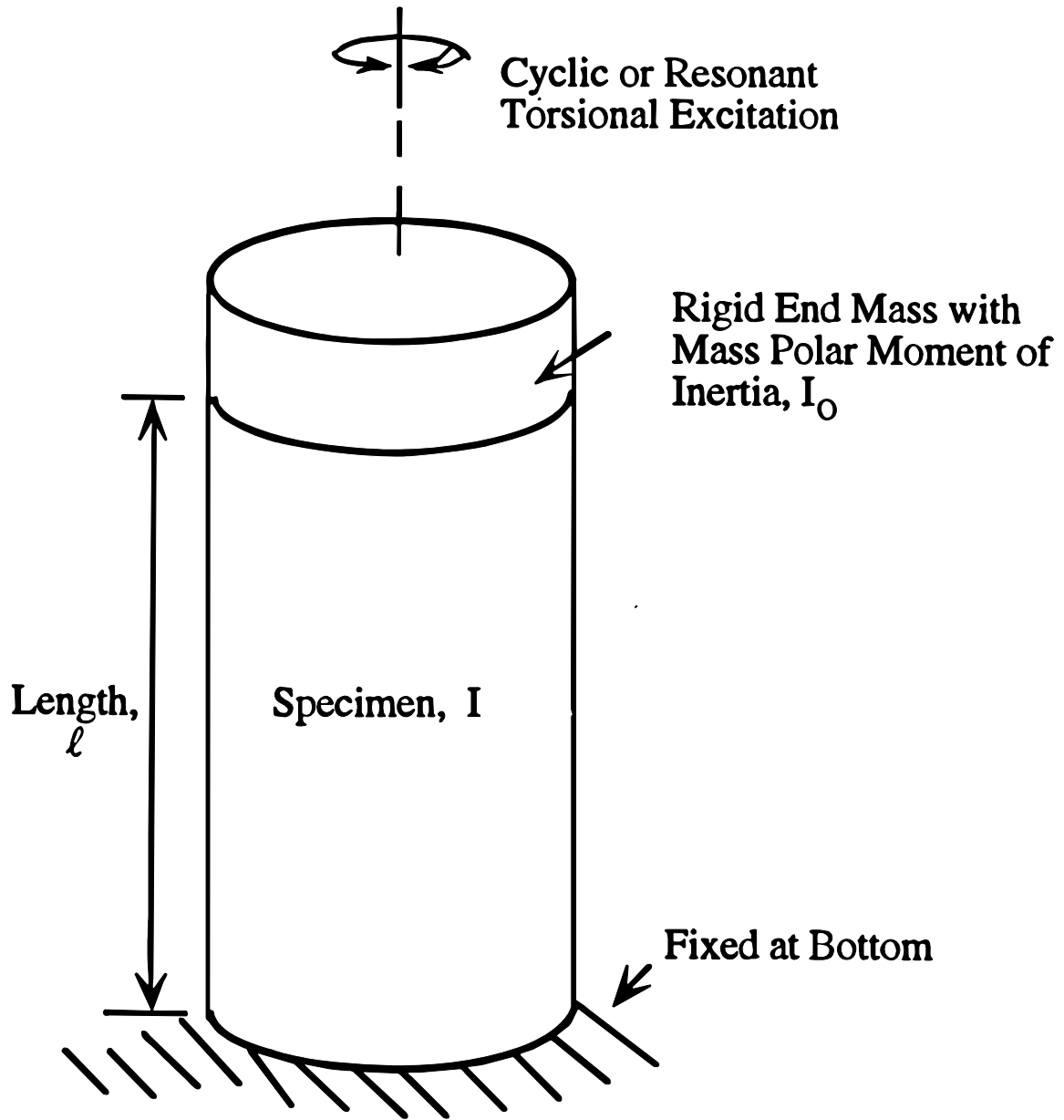
- (1) The complete test pit designation is preceded by TP-WHB-
- (2) Laboratory Sample Index Number
- (3) Sample 629 has a liquid limit of 32, a plastic limit of 6 and a plasticity index of 6. All other samples were non-plastic.
- (4) Fines means particles passing the No. 200 sieve (silt and clay).
- (5) - in a cell means the parameter was not measured.
- (6) Minus 3-inch material.
- (7) Total water content.

INTENTIONALLY LEFT BLANK



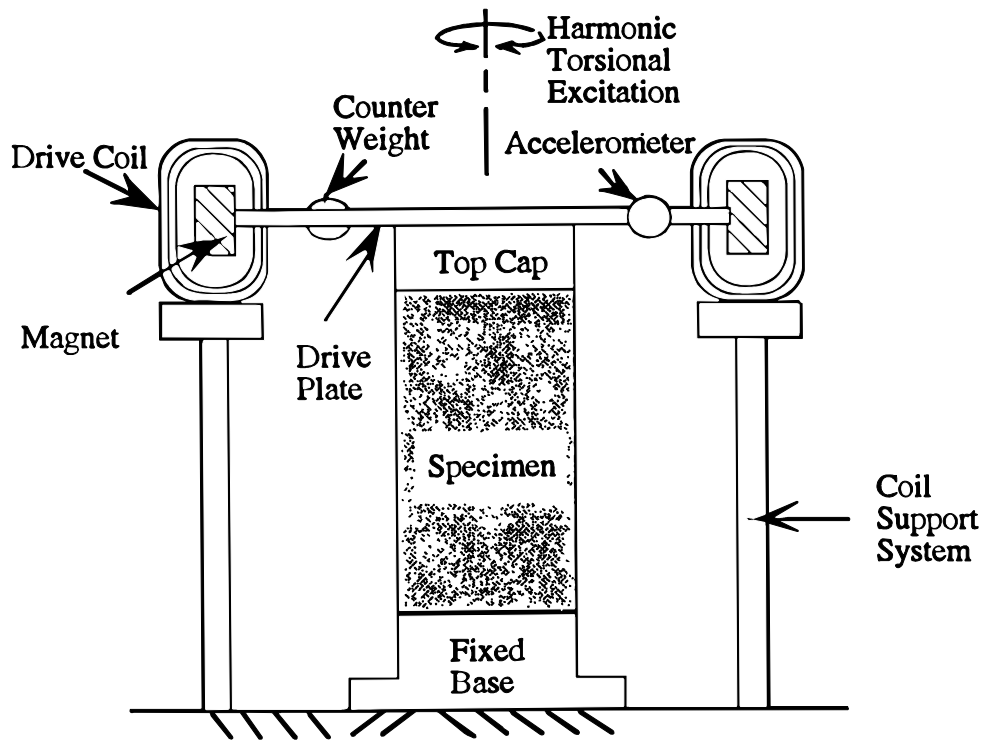
DTN: GS020783114233.005

Figure 102. Particle-Size Distribution Curves for TP-WHB-1 to TP-WHB-4

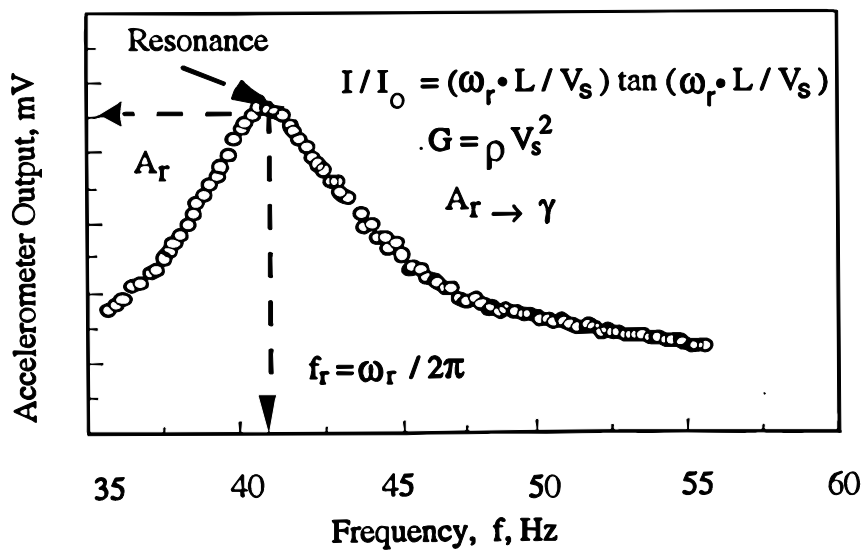


Source: PBRCTS-1 Rev 4 (page 2)

Figure 103. Idealized Fixed-Free RCTS Equipment



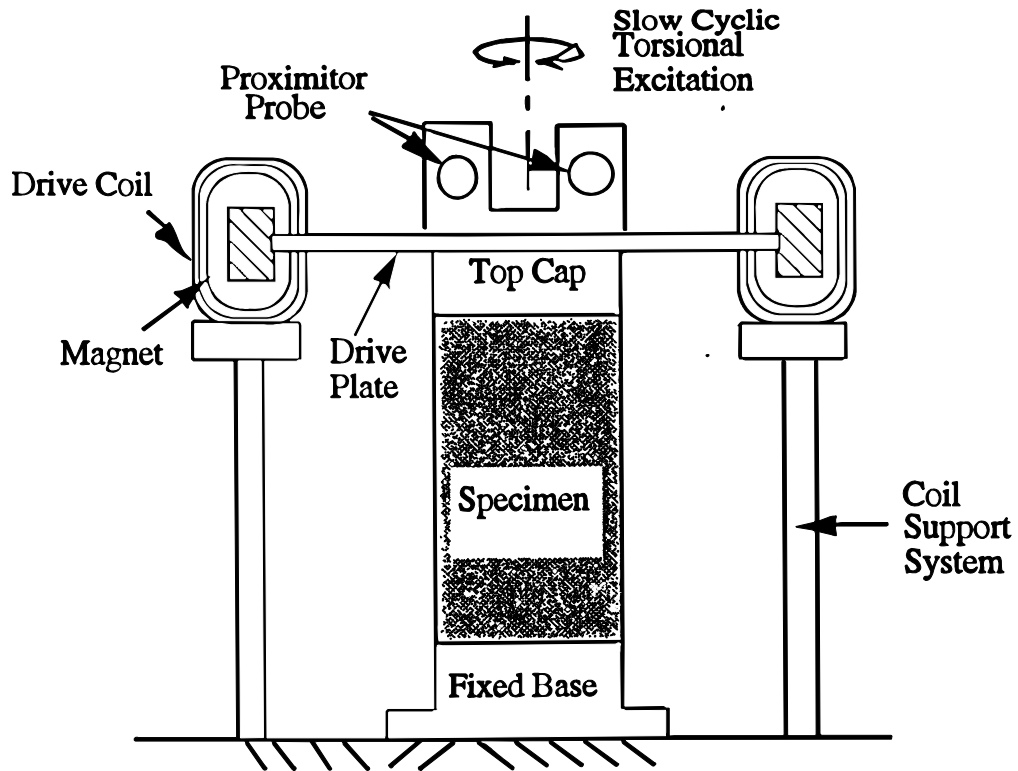
a) Specimen in the Resonant Column Apparatus
(Confinement Chamber Not Shown)



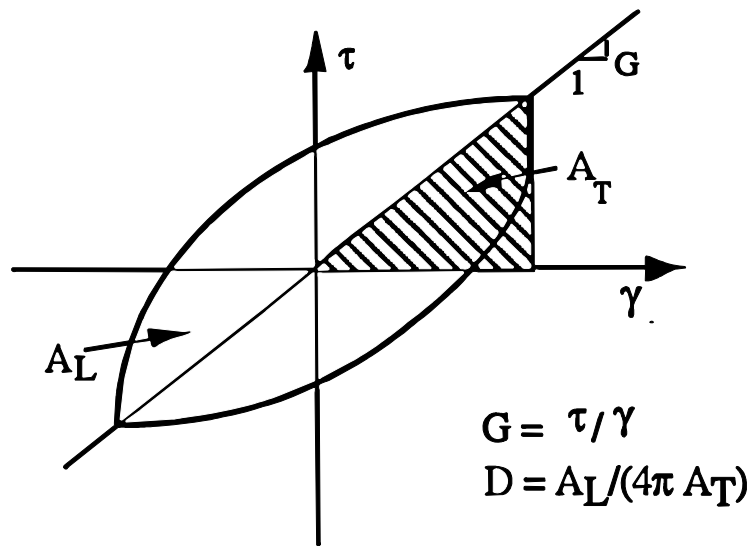
b) Typical Frequency Response Curve

Source: PBRCTS-1 Rev 4 (page 4)

Figure 104. (a) Simplified Diagram of a Fixed-Free Resonant Column Test and (b) an Associated Frequency Response Curve



a) Specimen in the Torsional Shear Test Apparatus (Confinement Chamber Not Shown)



b) Measurement of Shear Modulus and Damping Ratio

Source: PBRCTS-1 Rev 4 (page 5)

Figure 105. (a) Configuration of a Torsional Shear Test and (b) Evaluation of Shear Modulus (G) and Material Damping Ratio (D)

Method of Analysis in the Resonant Column Test

The resonant column test is based on the one-dimensional wave equation derived from the theory of elasticity. The shear modulus is obtained by measuring the first-mode resonant frequency while material damping is evaluated from either the free-vibration decay curve or the width of the frequency response curve using viscous damping principles.

Shear Modulus

The governing equation of motion for the fixed-free torsional resonant column test is (PBRCTS-1, Rev 4, page 12):

$$\frac{\sum I}{I_o} = \frac{\omega_n \ell}{V_s} \tan\left(\frac{\omega_n \ell}{V_s}\right) \quad (\text{Eq. 11})$$

where $\sum I = I_s + I_m + \dots$

I_s = mass moment of inertia of specimens,

I_m = mass moment of inertia of membrane,

I_o = mass moment of inertia of rigid end mass at the top of the specimen,

ℓ = length of the specimen,

V_s = shear-wave velocity of the specimen, and

ω_n = undamped natural circular frequency of the system.

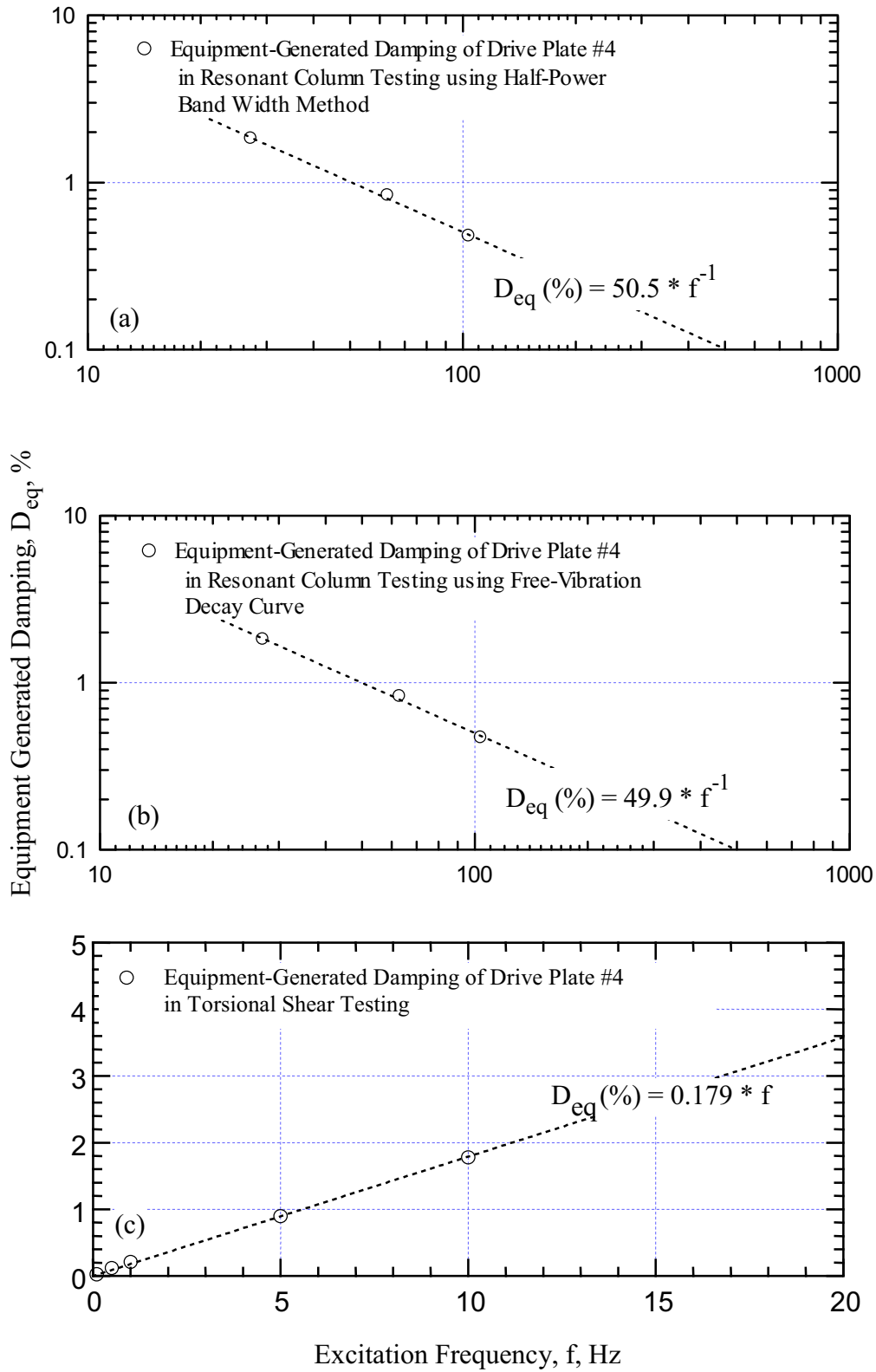
The value of I_o is known from the calibration of the drive plates (Figures 106 and 107). Two individual drive plates (UTACED Number 4 and 5) were used during the testing program. The values of I_s and ℓ are easily determined from the specimen size and weight. Once the first-mode resonant frequency is determined, the shear-wave velocity can be calculated by solving Eq. 11 for ω_n with the resonant circular frequency, ω_r , equal to ω_n .

As noted above and shown on Figure 104b, the resonant circular frequency, ω_r , is measured instead of the undamped natural frequency, ω_n , and ω_r is used to calculate shear-wave velocity. If the damping in the system is zero, ω_n and ω_r are equal. The relationship between ω_r and ω_n is (PBRCTS-1 Rev 4, page 12):

$$\omega_r = \omega_n \sqrt{1 - 2D^2} \quad (\text{Eq. 12})$$

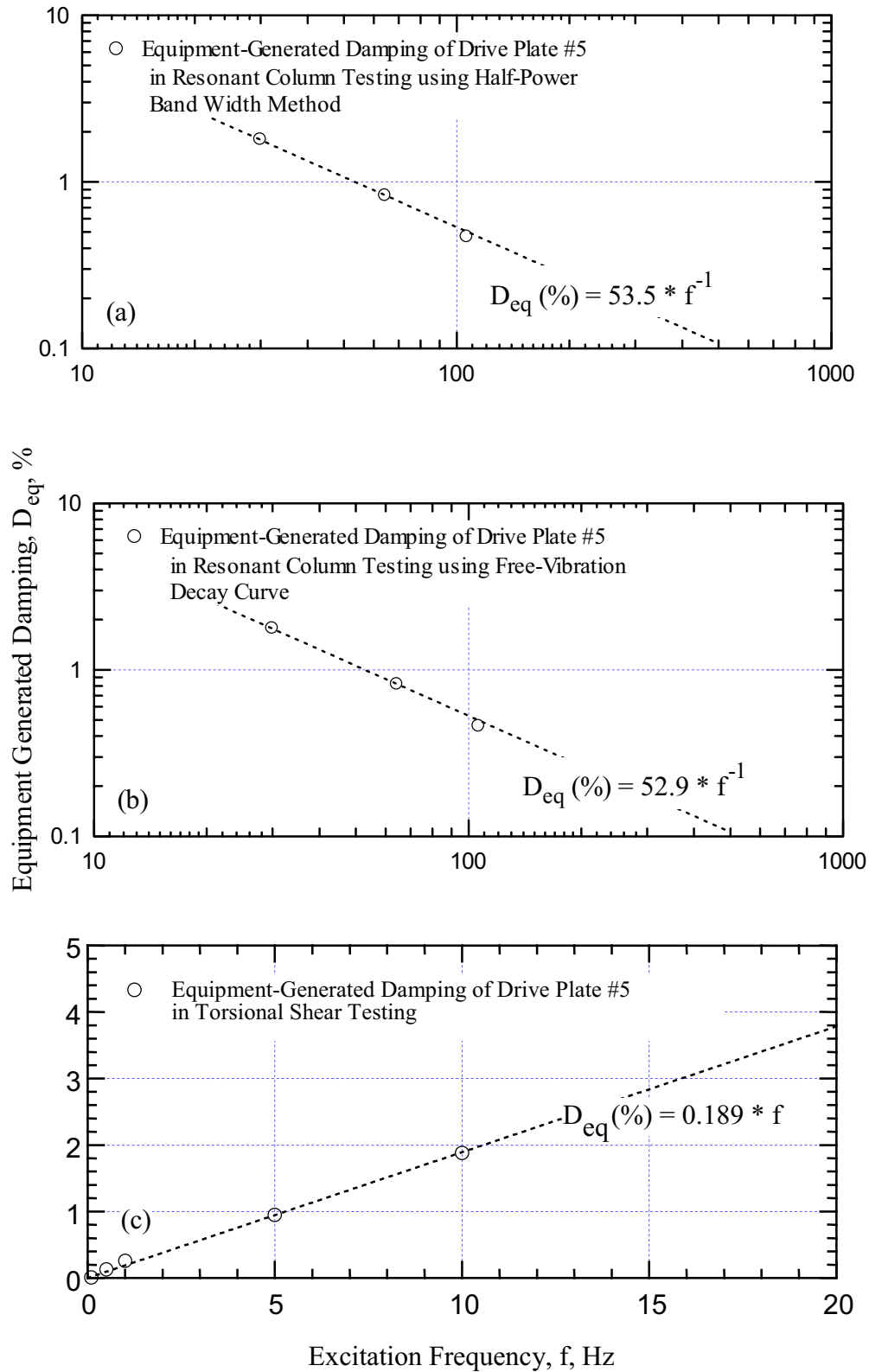
where D is the material damping ratio. If the damping in the system is zero, ω_n and ω_r are equal.

A typical damping ratio encountered in the resonant column test is less than 20 percent, which corresponds to a difference of less than 5 percent between ω_r and ω_n . In this study, the damping measured in the resonant column test was usually less than 10 percent, and ω_r can be used instead of ω_n with less than a two-percent error.



Source: Wong (2002e, Appendix 42, p. 25)

Figure 106. Calibration Curves of Equipment-Generated Damping for Drive Plate #4



(Wong 2002e, Appendix 42, p. 26)

Figure 107. Calibration Curves of Equipment-Generated Damping for Drive Plate #5

Once the shear-wave velocity is determined, shear modulus is calculated from the relationship (PBRCTS-1 Rev 4, page 13):

$$G = \rho V_s^2 \quad (\text{Eq. 13})$$

where ρ is the total mass density of the specimen (total unit weight divided by gravity).

Shearing Strain

The shearing strain varies radially within the specimen and may be expressed as a function of the distance from the longitudinal axis as illustrated on Figure 108. The equivalent shearing strain, γ_{eq} or γ , is represented by (PBRCTS-1 Rev 4, page 13):

$$\gamma = r_{\text{eq}} \theta_{\text{max}} / \ell \quad (\text{Eq. 14})$$

where r_{eq} = equivalent radius,

θ_{max} = angle of twist at the top of the specimen, and

ℓ = length of the specimen.

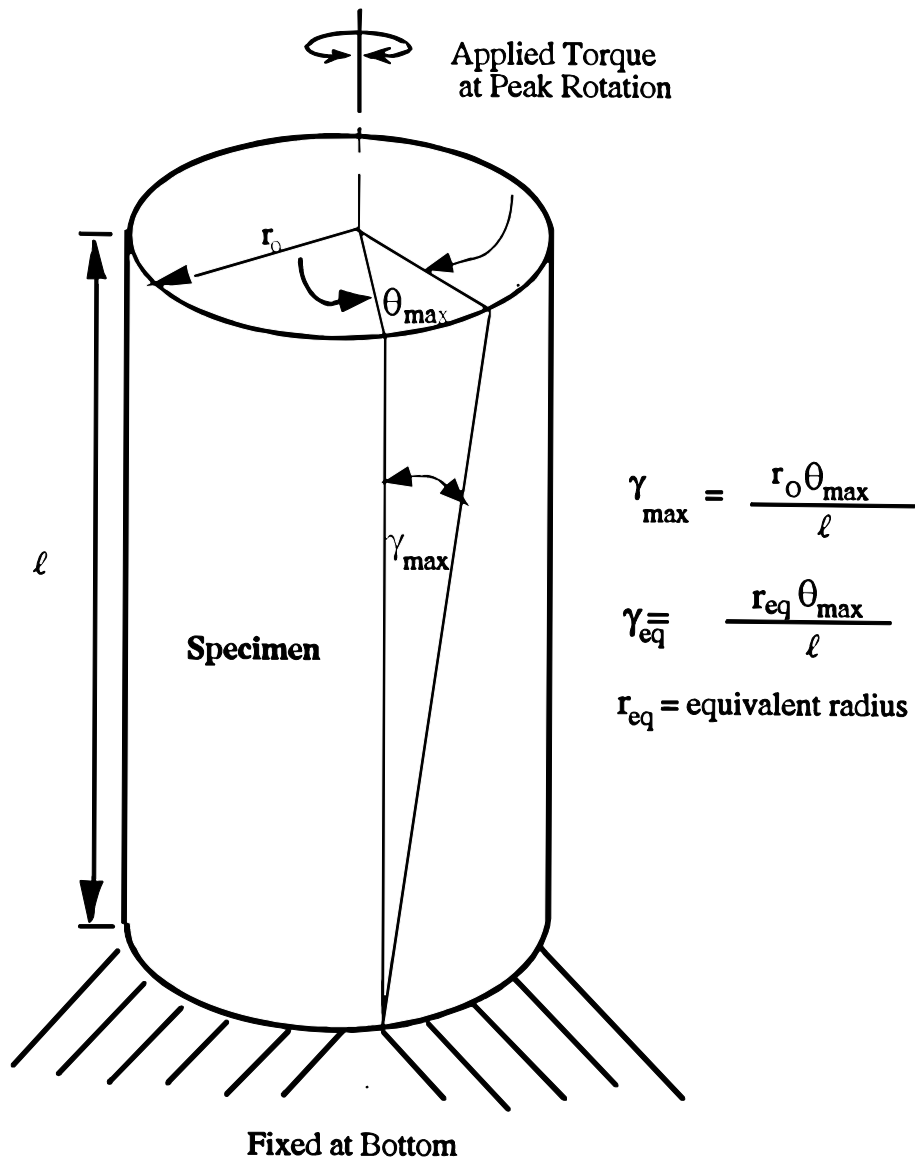
Chen and Stokoe (1979) studied the radial distribution in shearing strain to find a value of r_{eq} for the specimen tested in the RCTS equipment to evaluate an effective strain. They found that the value of r_{eq} for a solid specimen varied from $0.82r_0$ for a peak shearing strain amplitude below 0.001% (Chen and Stokoe 1979, page 41) to $0.79r_0$ for a peak shearing strain of 0.1% (Chen and Stokoe 1979, page 21), where r_0 is the initial specimen radius. These values of r_{eq} have been adopted in this study.

In the resonant column test, the resonant period (T_r , seconds), and output voltage of accelerometer (A_c , volts (RMS)) at resonance are measured. Accelerometer output is changed to displacement by using the accelerometer calibration factor (CF, volts (RMS)/in/sec²) and using the principles of harmonic motion. The accelerometer displacement is divided by the distance (D_{ac} , inches) between the location of accelerometer and the axis of the specimen to calculate the angle of twist at the top of the specimen (θ_{max}). The shearing strain is then calculated by Eq. 15 (PBRCTS-1 Rev 4, page 13):

$$\gamma = r_{\text{eq}} \frac{A_c T_r^2}{4\pi^2 CF} \frac{1}{D_{\text{ac}}} \frac{1}{\ell} \quad (\text{Eq. 15})$$

Material Damping

In the resonant column test, the material damping ratio can be evaluated from either the free-vibration decay method or from the half-power bandwidth method (PBRCTS-1 Rev 4, pages 13-17). Each of these methods is discussed below. It is important to note that, in these measurements, the damping measurement includes material damping in the specimen plus any damping in the equipment.



Source: PBRCTS-1 Rev 4 (page 14)

Figure 108. Shearing Strain in RCTS Specimen Column

Free-Vibration Decay Method – Material damping in soil and rock specimens can be quite complex to define. However, the theory for a single-degree-of-freedom system with viscous damping is an appropriate framework for describing the effect of damping that occurs in soil (Richart et al. 1970, page 15). The decay of free vibrations of a single-degree-of-freedom system with viscous damping is described by the logarithmic decrement, δ , which is the ratio of the natural logarithm of two successive amplitudes of motion (PBRCTS-1 Rev 4, page 15):

$$\delta = \ln\left(\frac{Z_1}{Z_2}\right) = \frac{2\pi D}{\sqrt{1-D^2}} \quad (\text{Eq. 16})$$

where Z_1 and Z_2 = two successive strain amplitudes of motion, and
 D = material damping ratio.

The free-vibration decay curve is recorded using an oscilloscope by shutting off the driving force while the specimen is vibrating at the resonant frequency. The amplitude of each cycle is measured from the decay curve, and the logarithmic decrement is then calculated using Eq. 16. The material damping ratio is calculated from the logarithmic decrement according to:

$$D = \sqrt{\frac{\delta^2}{4\pi^2 + \delta^2}} \quad (\text{Eq. 17})$$

A typical damping measurement from a free-vibration decay curve (from a metal calibration specimen) is shown on Figure 109.

In this method, the selection of which strain amplitude is a representative strain for the damping ratio calculated by Eq. 17 is uncertain because strain amplitude decreases during free-vibration decay. In this study, a representative strain amplitude was selected as the peak strain amplitude during steady-state vibration for shearing strains below 0.001%. However, at larger strains, the representative strain is smaller than the peak strain, and the average strain determined for the first three cycles of free vibration was selected as the representative strain amplitude.

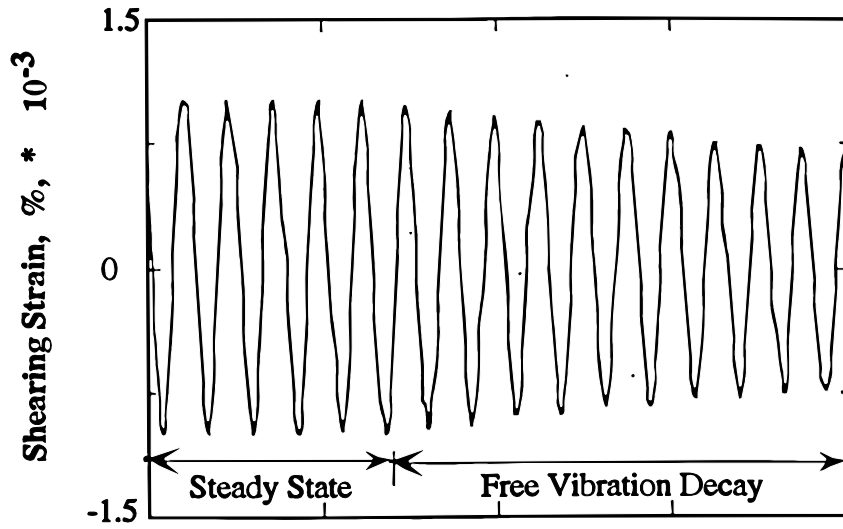
Half-Power Bandwidth Method – Another method of measuring damping in the resonant column test is the half-power bandwidth method, which is based on measurement of the width of the frequency response curve near resonance. From the frequency response curve, the logarithmic decrement can be calculated from (PBRCTS-1 Rev 4, page 15):

$$\delta = \frac{\pi}{2} \frac{f_2^2 - f_1^2}{f_r^2} \sqrt{\frac{A^2}{A_{\max}^2 - A^2} \frac{\sqrt{1 - 2D^2}}{1 - D^2}} \quad (\text{Eq. 18})$$

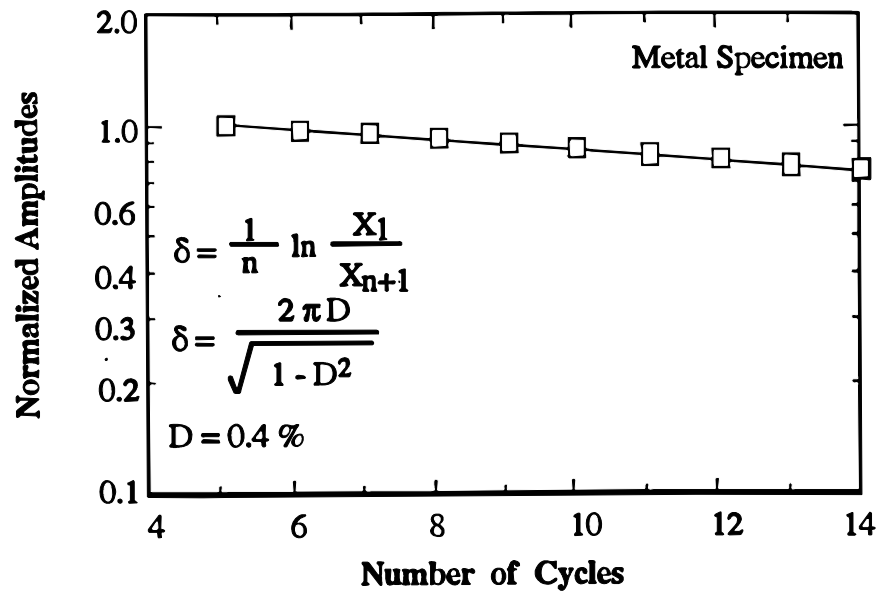
where A_{\max} = maximum strain amplitude or strain amplitude at resonance,
 f_1 = frequency below the resonance where the strain amplitude is A ,
 f_2 = frequency above the resonance where the strain amplitude is A ,
 f_r = resonant frequency, and
 D = material damping ratio.

If the damping ratio is small and A is chosen as $\sqrt{2} A_{\max}/2$, which is called the half-power point, Eq. 18 can be simplified as:

$$\delta \cong \pi \frac{f_2 - f_1}{f_r} \quad (\text{Eq. 19})$$



a) Free-Vibration Decay Curve



b) Analysis of Free-Vibration Decay Curve

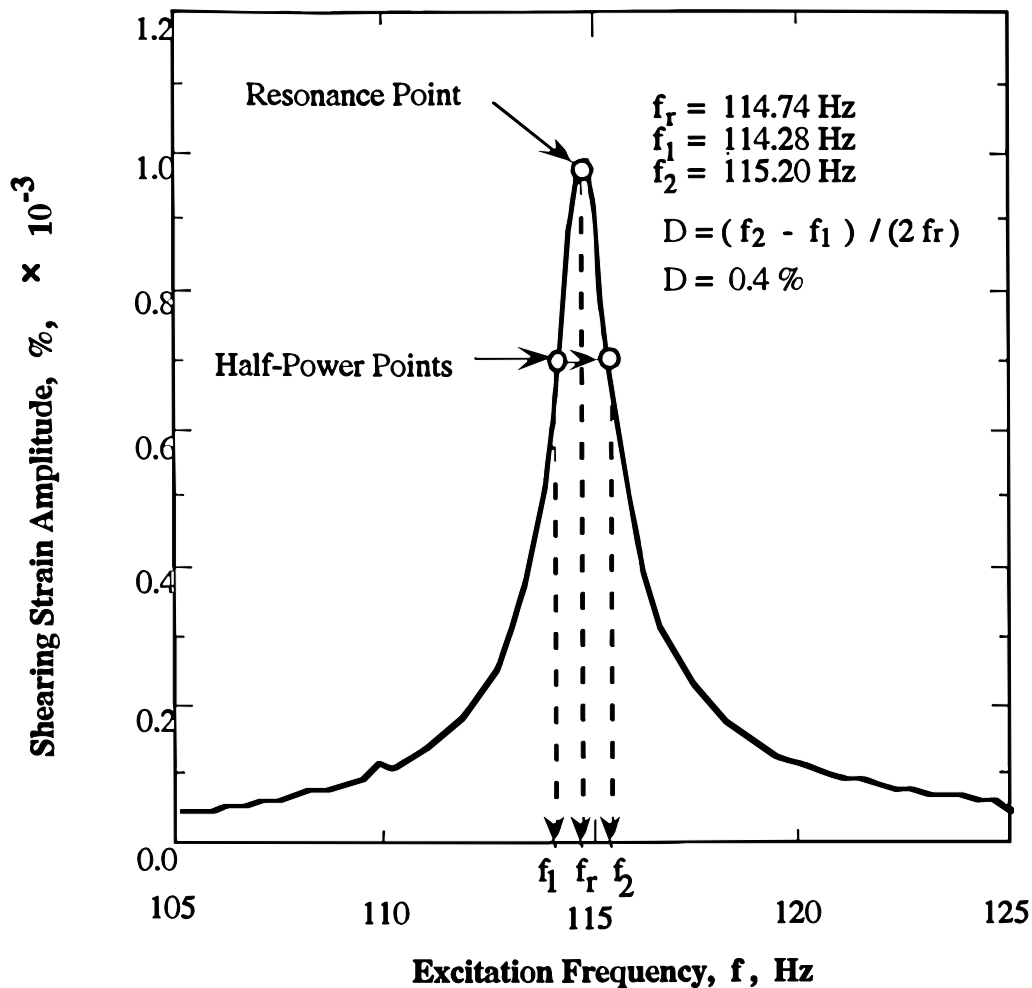
Source: PBRCTS-1 Rev 4 (page 16)

Figure 109. Determination of Material Damping Ratio from the Free-Vibration Decay Curve Using Metal Specimen

Therefore, the damping ratio can be expressed as:

$$D \cong \frac{f_2 - f_1}{2f_r} \quad (\text{Eq. 20})$$

A typical damping measurement by the half-power bandwidth method (for a metal calibration specimen) is shown on Figure 110.



Source: PBRCTS-1 Rev 4 (page 18)

Figure 110. Determination of Material Damping from the Half-Power Bandwidth Method Using a Metal Specimen

Background noise can be a problem in measuring material damping using the free-vibration decay method at strains less than about 0.001%. On the other hand, background noise generally has a smaller effect on the frequency response curve at strains below 0.001%. Therefore, the half-power bandwidth method is preferred to the free-vibration decay method for making small-strain damping measurements. However, at large strains, symmetry in the frequency response curve is no longer maintained, and a serious error can be introduced in the half-power

bandwidth method. In this study, both types of damping measurements were made at small strains in an attempt to obtain good data sets, while only the free-vibration decay method was used at larger strains (above 0.001%).

Method of Analysis in the Torsional Shear Test

The torsional shear test is another method of determining the deformational characteristics (modulus and damping) of soil or rock specimens using the same RCTS device (PBRCTS-1 Rev 4, pages 17-20). Rather than measuring the dynamic response of the specimen, the actual stress-strain hysteresis loop is determined by means of measuring the torque-twist curve. Shear modulus is calculated from the slope of the hysteresis loop, and the hysteretic damping ratio is calculated using the area of the hysteresis loop.

Shear Modulus

Because shear modulus is calculated from the stress-strain hysteresis loop, shearing stress and shearing strain in the torsional shear test need to be defined.

Shearing Stress – Determination of shearing stress in the torsional shear test is based on the theory of elasticity for circular or tubular rods in pure torsion. For the case where pure torque, T , is applied to the top of the specimen, the torque can be calculated from:

$$T = \int_{r_i}^{r_o} \tau_r (2\pi r) r dr \quad (\text{Eq. 21})$$

where τ_r is the shearing stress at a distance r from the axis of specimen and, r_o and r_i are outside and inside radii, respectively. For a shearing stress that varies linearly across the radius:

$$\tau_r = \tau_m (r/r_o) \quad (\text{Eq. 22})$$

where τ_m is the maximum shearing stress at $r = r_o$.

Substituting Eq. 22 into Eq. 21 and integrating yields:

$$T = \frac{\tau_m}{r_o} \frac{\pi}{2} (r_o^4 - r_i^4) = \frac{\tau_m}{r_o} J_p \quad (\text{Eq. 23})$$

where J_p is the area polar moment of inertia. From Eq. 23, one can write:

$$\tau_m = r_o \frac{T}{J_p} \quad (\text{Eq. 24})$$

For the shearing stress varying linearly across the radius, the average torsional shearing stress is defined as:

$$\tau_{\text{avg}} = r_{\text{eq}} \frac{T}{J_p} \quad (\text{Eq. 25})$$

The value of r_{eq} is the same value as used in the resonant column analysis for calculation of shearing strain.

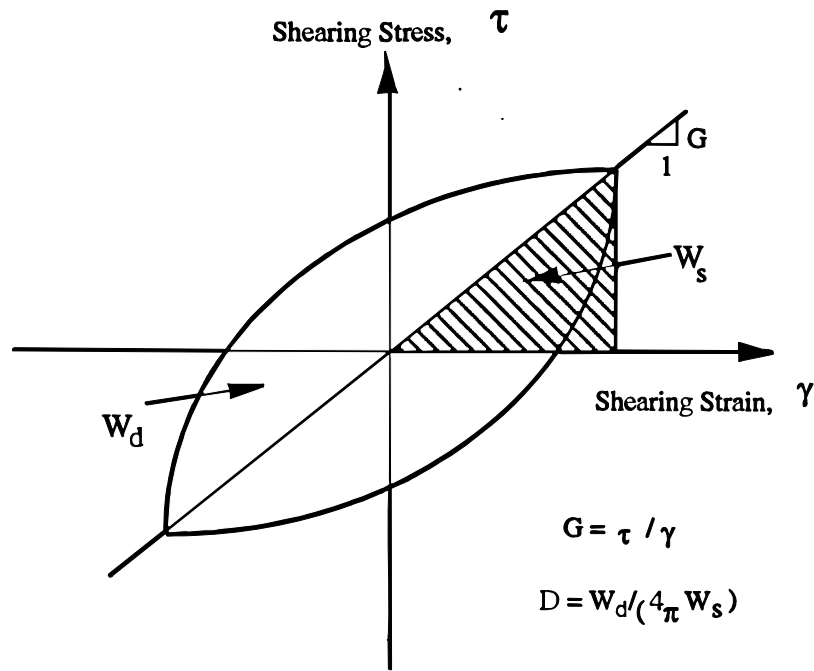
The value of applied torque, T , is calculated from the input voltage applied to the drive system, V_T (volts), and the torque calibration factor, K_T (torque/volts). Thus, average shearing stress is:

$$\tau_{avg} = r_{eq} K_T V_T / J_p \quad (\text{Eq. 26})$$

Shearing Strain – Calculation of shearing strain in the torsional shear test follows the same procedure used in the resonant column test. The proximator system directly measures the displacement (instead of the acceleration measured in the resonant column test). Hence, the angle of twist (θ) is calculated from the proximator output voltage V_p (volts), and the proximator calibration factor, K_p (rad/volt). Shearing strain, γ , is then calculated from:

$$\gamma = r_{eq} \sum K_p V_p / \ell \quad (\text{Eq. 27})$$

Shear Modulus – Once the stress-strain hysteresis loop is measured, the shear modulus, G , is calculated from the slope of a line through the end points of the hysteresis loop, as shown on Figure 111.



Source: PBRCTS-1 Rev 4 (page 20)

Figure 111. Determination of Shear Modulus and Damping Ratio in the Torsional Shear Test

Thus, the shear modulus is calculated from:

$$G = \tau / \gamma \quad (\text{Eq. 28})$$

where τ is peak shearing stress and γ is peak shearing strain.

Hysteretic Damping Ratio

Hysteretic damping ratio in the torsional shear test is measured using the amount of energy dissipated in one complete cycle of loading and the peak strain energy stored in the specimen during the cycle.

In the torsional shear test, the dissipated energy is measured from the area of the stress-strain hysteresis loop. The energy per cycle, W_d , due to a viscous damping force, F_d , is:

$$W_d = \int_0^T F_d \dot{x} dt \quad (\text{Eq. 29})$$

where \dot{x} is a velocity and T is a period. For simple harmonic motion with frequency ω , i.e., $x = A \cos(\omega t - \phi)$, W_d becomes:

$$W_d = \pi C \omega A^2 \quad (\text{Eq. 30})$$

where the constant of integration, C , is referred to as the viscous damping coefficient. From the Eq. 30, the viscous damping coefficient can be expressed as:

$$C = W_d / (\pi \omega A^2) \quad (\text{Eq. 31})$$

The peak strain energy, W_s , stored by the spring is equal to the area under the secant modulus line on Figure 109 and can be written as:

$$W_s = k A^2 / 2 \quad (\text{Eq. 32})$$

The critical damping coefficient, C_c , is:

$$C_c = 2\sqrt{km} = 2k / \omega_n \quad (\text{Eq. 33})$$

where k is an elastic spring constant, m is a mass, and ω_n is a natural frequency of a system. Solving Eq. 32 for k and substituting the resulting expression into Eq. 33 yields:

$$C_c = \frac{4 W_s}{\omega_n A^2} \quad (\text{Eq. 34})$$

Therefore, the damping ratio, D , can be expressed as:

$$D \equiv \frac{C}{C_c} = \frac{W_d}{4\pi W_s} \frac{\omega_n}{\omega} \quad (\text{Eq. 35})$$

For soil or rock materials, damping is commonly taken as being frequency-independent. Therefore, ω_n/ω is ignored and hysteretic damping is written as:

$$D = \frac{W_d}{4\pi W_s} \quad (\text{Eq. 36})$$

where W_d is the area of the hysteresis loop and W_s is the area of the triangle, as shown on Figure 109.

6.2.10.2 Measurements

Rock specimens were selected to represent the range of tuff types present. However, core samples had to be of sufficient size and quality to be tested. Individual intact core samples could not contain fractures, xenocrysts, or lithophysae larger than 0.5 centimeters in diameter, which would cause the specimen to fail prematurely during testing. Also, several attempts were made to obtain intact alluvial specimens without success. The material failed during the sampling process. Only one alluvial sample (not intact) was collected. Additional alluvial samples were not collected because reconstituted alluvial specimens are not as representative of in-situ conditions and previous reconstituted alluvial samples had been tested (CRWMS M&O 1999b, Appendix Q; DTN: MO9905LABDYNRS.000). All specimens were shipped as core samples from the Sample Management Facility (SMF) to the Geotechnical Engineering Center at the University of Texas at Austin. All core samples were contained in cardboard shipping containers, with each core individually wrapped in plastic and surrounded by packing material.

Of the 19 specimens, 18 were intact tuff specimens and one was a alluvial specimen. Fourteen of the tuff specimens were derived by carefully wet-coring specimens with a nominal diameter of 3.97 cm (1.56 inches) from each larger-diameter core sample. The ends of the cylindrical specimens were trimmed with a rock saw so that the specimens had the shape of a right circular cylinder. The remaining 4 tuff specimens were wet cored from 4 of the above 14 tested specimens. In this case, the re-tested, smaller tuff specimens had a nominal diameter of 2.11 cm (0.83 inches). The one alluvial specimen was reconstituted in the laboratory because this material was disturbed upon sampling in the field and could not be tested intact. The alluvial specimen was reconstituted using the standard under-compaction method by Ladd (1978).

The initial properties of the 18 intact tuff specimens are presented in Tables 14 to 16. Photographs of the specimens are presented on Figures 112 to 114. As shown in Tables 14 to 16, the 14 tuff specimens with a nominal diameter of 3.97 cm (1.56 inches) have heights that ranged from about 2 to 2.5 times the diameter. The 4 tuff specimens with a nominal diameter of 2.11 cm (0.83 inches) have heights that ranged from about 2.2 to 4.8 times the diameter. These 18 tuff specimens are divided into three groups based on their dry unit weight, γ_d : Group 1: γ_d from 133 pcf to 147 pcf; Group 2: γ_d from 117 pcf to 132 pcf; and Group 3: γ_d from 78 pcf to 94 pcf. This grouping was chosen because of the relationship between V_s and dry unit weight (see further discussion in this section).

INTENTIONALLY LEFT BLANK

Table 14. Initial Properties of Intact Tuff Specimens with a Dry Unit Weight Between 133 pcf and 147 pcf from WHB Boreholes (Group 1)

UTACED ^a Designation	SMF Designation	Borehole	Depth (ft)	Stratigraphic Unit	Height ^c (cm)	Diameter ^c (cm)	Mass ^c (g)	Water Content ^c (%)	Dry Unit Weight (pcf)	Total Unit Weight ^c (pcf)
UTA-23-C	01012518	RF#14	361.0	Tpcpul	11.38	3.98	305.1	0.65	133.5	134.4
UTA-23-D	01012519	RF#14	397.0	Tpcpmn	11.26	3.97	329.1	1.00	146.0	147.5
UTA-23-G	01012525	RF#15	192.5	Tpcpul	11.12	3.95	317.9	0.43	144.9	145.5
UTA-23-T ^b	01012525	RF#15	192.5	Tpcpul	10.30	2.15	87.0	0.43	144.5	145.1
UTA-23-H	01012527	RF#15	322.0	Tpcpln	11.53	3.96	332.9	0.53	145.4	146.2
UTA-23-J	01012538	RF#17	575.6	Tpcpul	10.98	3.96	304.8	0.27	140.2	140.6

Sources: DTN: MO0203DHRSSWHB.001, ^cWong (2002e, Appendix 42, page 12)

Notes: ^a UTACED means University of Texas at Austin, Civil Engineering Department

^b UTA-23-T was cored from UTA-23-G after RCTS testing was completed

Table 15. Initial Properties of Intact Tuff Specimens with a Dry Unit Weight between 117 pcf and 132 pcf from WHB Boreholes (Group 2)

UTACED ^a Designation	SMF Designation	Borehole	Depth (ft)	Stratigraphic Unit	Height ^d (cm)	Diameter ^d (cm)	Mass ^d (g)	Water Content ^d (%)	Dry Unit Weight (pcf)	Total Unit Weight ^d (pcf)
UTA-20-B	01012372	RF#16	189.5	Tpcrn	11.46	3.97	275.1	0.38	120.9	121.4
UTA-20-C	01012373	RF#16	235.5	Tpcpul	10.22	3.96	258.4	2.30	125.3	128.1
UTA-23-B	01012516	RF#14	241.5	Tpcrn	11.18	3.96	278.6	1.54	124.5	126.4
UTA-23-R ^b	01012516	RF#14	241.5	Tpcrn	5.75	2.11	38.7	1.50	118.2	120.0
UTA-23-E	01012520	RF#15	27.3	Tpcrn	11.70	3.96	273.6	1.02	117.2	118.4
UTA-23-F	01012522	RF#15	88.7	Tpcpul	11.45	3.98	302.7	0.68	131.5	132.4
UTA-23-S ^c	01012522	RF#15	88.7	Tpcpul	10.66	2.03	73.8	4.55	127.4	133.2

Sources: DTN: MO0203DHRSSWHB.001, ^dWong (2002e, Appendix 42, page 13)

Notes: ^a UTACED means University of Texas at Austin, Civil Engineering Department

^b UTA-23-R was cored from UTA-23-B after RCTS testing was completed

^c UTA-23-S was cored from UTA-23-F after RCTS testing was completed

Table 16. Initial Properties of Intact Tuff Specimens with a Dry Unit Weight between 78 pcf and 94 pcf from WHB Boreholes (Group 3)

UTACED ^a Designation	SMF Designation	Borehole	Depth (ft)	Stratigraphic Unit	Height ^c (cm)	Diameter ^c (cm)	Mass ^c (g)	Water Content ^c (%)	Dry Unit Weight (pcf)	Total Unit Weight ^c (pcf)
UTA-20-A	01012371	RF#16	126.8	Tpki	11.56	3.96	201.2	9.28	80.8	88.3
UTA-23-Q ^b	01012371	RF#16	126.8	Tpki	4.73	2.10	21.7	5.10	78.8	82.8
UTA-20-D	01012370	RF#16	80.5	Tpki	11.47	3.97	225.4	8.30	91.5	99.1
UTA-23-A	01012512	RF#14	104.5	Tpki	10.95	3.94	209.4	4.82	93.5	98.0
UTA-23-I	01012535	RF#17	400.2	Tpcrn	10.67	3.96	181.4	0.32	86.0	86.2

Sources: DTN: MO0203DHRSSWHB.001, ^cWong (2002e, Appendix 42, page 14)

Notes: ^a UTACED means University of Texas at Austin, Civil Engineering Department

^b UTA-23-Q was cored from UTA-23-A after RCTS testing was completed



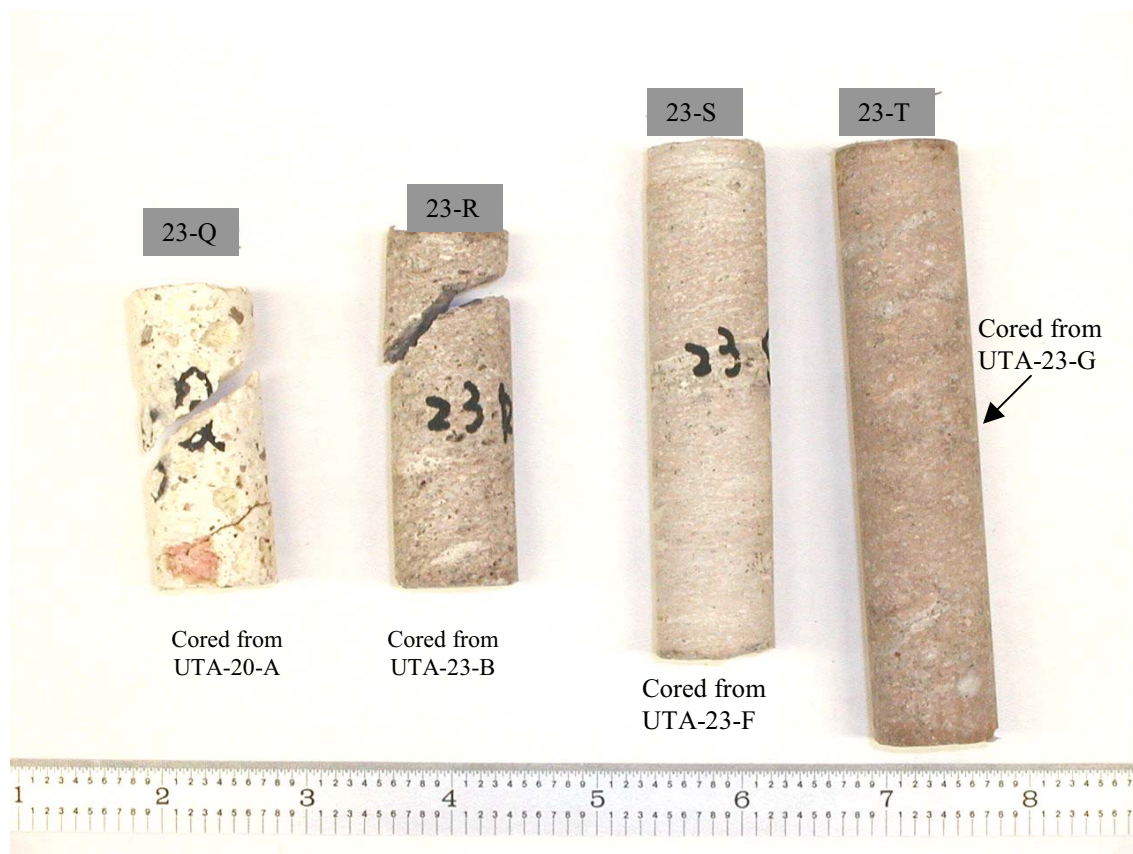
Source: Modified from Wong (2002e, Appendix 42, page 60)

Figure 112. Specimens UTA-23-A to 23-J



Source: Modified from Wong (2002e, Appendix 42, page 61)

Figure 113. UTA-20 Group: Specimens 20-A, 20-B, 20-C, and 20-D are from the WHB Boreholes. Specimens 20-F, 20-G, 20-I, 20-J, and 20-L are from the ESF (Section 6.3.3)



Source: Modified from Wong (2002e, Appendix 42, page 62)

Figure 114. Specimens UTA-23-Q, UTA-23-R, UTA-23-S, and UTA-23-T, which were Cored from Larger Test Specimens

The initial properties of the reconstituted alluvial specimen are presented in Table 17. The alluvial specimen had a diameter of 6.96 cm and a height just slightly larger than 2 times the diameter. The 19 specimens were generally observed to contain some moisture and the water contents measured in the laboratory ranged from 0.27 to 9.28 % for the tuff specimens and 18.04% for the alluvial specimen (Tables 14 to 17). The water contents of the specimens are not representative of in-situ conditions due to the use of drilling mud in the borehole drilling.

RCTS testing was performed on each specimen. All testing was conducted in accordance with either Nevada Work Instruction NWI-SPO-004Q, *Laboratory Dynamic Rock/Soil Testing*, or Line Procedure LP-GEO-002Q-BSC, *Laboratory Dynamic Rock/Soil Testing*. LP-GEO-002Q-BSC superseded NWI-SPO-004Q during the testing program. The equipment, software, data collection procedures and data reduction procedures are given in PBRCTS-1, Rev. 4, which is contained in Appendix 1 of Scientific Notebook SN-M&O-SCI-033-V1 (Wong 2002e). The resonant column testing was conducted with software RCTEST Version 2.1. The torsional shear testing was conducted with software TSTEST Version 3.1. Table 18 lists the test pressures and types of tests performed on the specimens.

Table 17. Initial Properties of Reconstituted Alluvial Specimen

UTACED Designation	SMF Designation	Borehole	Depth (ft)	Stratigraphic Unit	Height ^a (cm)	Diameter ^a (cm)	Mass ^a (g)	Water Content ^a (%)	Dry Unit Weight (pcf)	Total Unit Weight ^a (pcf)
UTA-23-X	01012646	RF#17	59.0	Qal	14.10	6.96	924.3	18.04	91.1	107.5

Sources: DTN: MO0203DHRSSWHB.001, ^aWong (2002e, Appendix 42, page 15)

Table 18. Confining Pressures at Which RCTS Tests were Performed on Intact Tuff and Reconstituted Qal Specimens from WHB Boreholes

UTACED Designation	SMF Designation	Borehole	Depth (ft)	Stratigraphic Unit	Estimated Mean Total Stress (psi)	Low-Amplitude RC Test Pressures (psi)	High-Amplitude RC Test Pressures (psi)	Low- and High-Amplitude TS Test Pressures (psi)
UTA-23-C	01012518	RF#14	361.0	Tpcpul	280	0, 70, 140, 280, 450	280, 450	280, 450
UTA-23-D	01012519	RF#14	397.0	Tpcpmn	340	0, 70, 170, 340, 450	340, 450	340, 450
UTA-23-G	01012525	RF#15	192.5	Tpcpul	120	0, 30, 60, 120, 240, 450	120, 450	120, 450
UTA-23-T	01012525	RF#15	192.5	Tpcpul	120	0, 30, 60, 120, 240, 450	120, 450	120, 450
UTA-23-H	01012527	RF#15	322.0	Tpcpln	200	0, 50, 100, 200, 400, 450	200, 450	200, 450
UTA-23-J	01012538	RF#17	575.6	Tpcpul	360	0, 90, 180, 360, 450	360, 450	360, 450
UTA-20-B	01012372	RF#16	189.5	Tpcrn	115	0, 29, 58, 115, 230, 460	115, 460	115, 460
UTA-20-C	01012373	RF#16	235.5	Tpcpul	150	0, 38, 75, 150, 300, 450	150, 450	150, 450
UTA-23-B	01012516	RF#14	241.5	Tpcrn	176	0, 44, 88, 176, 352, 450	176, 450	176, 450
UTA-23-R	01012516	RF#14	241.5	Tpcrn	176	0, 44, 88, 176	176	176
UTA-23-E	01012520	RF#15	27.3	Tpcrn	18	0, 5, 9, 18, 36, 72	18, 72	18, 72
UTA-23-F	01012522	RF#15	88.7	Tpcpul	68	0, 17, 34, 68, 136, 272	68, 272	68, 272
UTA-23-S	01012522	RF#15	88.7	Tpcpul	68	0, 17, 34, 68, 136, 272	68, 272	68, 272
UTA-20-A	01012371	RF#16	126.8	Tpki	70	0, 18, 35, 70, 140, 280	70, 280	70, 280
UTA-23-Q	01012371	RF#16	126.8	Tpki	70	0, 18, 35, 70	70	70
UTA-20-D	01012370	RF#16	80.5	Tpki	56	0, 14, 28, 56, 110, 220	56, 220	56, 220
UTA-23-A	01012512	RF#14	104.5	Tpki	66	0, 16, 33, 66, 132, 264	66, 264	66, 264
UTA-23-I	01012535	RF#17	400.2	Tpcrn	250	0, 62, 125, 250, 450	250, 450	250, 450
UTA-23-X	01012646	RF#17	59.0	Qal	32	8, 16, 32	32	32

Sources: Wong (2002e, Appendix 42, page 18)

The RCTS equipment is described in detail in PBRCTS-1 Rev. 4, including a listing of the equipment model names and serial numbers and a discussion of the testing and analysis methodologies. The measured dynamic properties were shear-wave velocity, shear modulus (G), and the material damping ratio in shear (D). These parameters were evaluated to determine the effect of the following variables:

- 1) Magnitude of isotropic state of stress (isotropic confining pressure), σ_0 . Four to five isotropic pressures that ranged from below to above the estimated in-situ mean total stress were generally used, where the in-situ mean total stress was estimated using an earth pressure coefficient (σ_h/σ_v) of either 0.5 or 0.75, as discussed in Scientific Notebook SN-M&O-SCI-033-V1 (Wong 2002e, page 139).
- 2) Time of confinement at each isotropic state of stress, t . Times at each pressure ranged from 1 hour to 1 day or more.
- 3) Shearing strain amplitude, γ . Shearing strains ranged from the small-strain range, less than 0.0003% for the tuff specimens and 0.001% for the reconstituted specimen, to medium strain amplitudes, ranging from 0.003% to about 0.1%.
- 4) Numbers of cycles of loading, N. Ten cycles of loading were used in the torsional shear test followed by about 1000 cycles in the resonant column test.
- 5) Excitation frequencies (f) ranging from 0.1 to about 10 Hz were used in the torsional shear test, while the frequency associated with resonance in the resonant column test varied with stiffness of the specimen and ranged from 21 to 458 Hz.

A summary of the tests performed on the specimens is given in Tables 19 to 22 (note that ksf means kips per square foot). Results from individual tests are plotted on Figures XII-1 to XII-19.

It should also be noted that all material damping values reported herein have been corrected to remove equipment-generated damping, as discussed in PBRCTS-1, Rev. 4. This correction involves subtracting equipment-generated damping, which was determined in the initial calibration phase of this work. The values of equipment-generated damping are shown on Figures 106 and 107 for drive plates #4 and #5, respectively.

Table 19. Fixed-Free, Small-Strain RCTS Test Results of Group 1 Intact Tuff Specimens at Estimated In-Situ Stress State

UTACED Designation	Stratigraphic Unit	Resonant Column			Torsional Shear ^a	
		Vs (ft/s)	Gmax (ksf)	Dmin (%)	Gmax (ksf)	Dmin (%)
UTA-23-C	Tpcpul	7632	276820	1.27	251000	1.36
UTA-23-D	Tpcpmn	7263	243190	0.63	229000	0.44
UTA-23-G	Tpcpul	7426	249540	0.53	232900	0.43
UTA-23-T	Tpcpul	8763	345320	0.21	282900	0.43
UTA-23-H	Tpcpln	7271	240740	1.07	189900	1.11
UTA-23-J	Tpcpul	6987	208720	1.14	185000	1.16

DTN: MO0203DHRSSWHB.001

Note: ^a from tenth loading cycle

Table 20. Fixed-Free, Small-Strain RCTS Test Results of Group 2 Intact Tuff Specimens at Estimated In-Situ Stress State

UTACED Designation	Stratigraphic Unit	Resonant Column			Torsional Shear ^a	
		Vs (ft/s)	Gmax (ksf)	Dmin (%)	Gmax (ksf)	Dmin (%)
UTA-20-B	Tpcrn	5539	115670	0.64	107000	0.66
UTA-20-C	Tpcpul	5251	109810	0.43	100800	0.45
UTA-23-B	Tpcrn	6174	150100	1.30	127600	1.55
UTA-23-R	Tpcrn	6235	145370	0.27	124800	0.27
UTA-23-E	Tpcrn	5024	92275	0.44	80900	0.32
UTA-23-F	Tpcpul	6405	168870	0.34	147500	0.27
UTA-23-S	Tpcpul	7136	210880	0.34	199999	0.24

DTN: MO0203DHRSSWHB.001

Note: ^a from tenth loading cycle

Table 21. Fixed-Free, Small-Strain RCTS Test Results of Group 3 Intact Tuff Specimens at Estimated In-Situ Stress State

UTACED Designation	Stratigraphic Unit	Resonant Column			Torsional Shear ^a	
		Vs (ft/s)	Gmax (ksf)	Dmin (%)	Gmax (ksf)	Dmin (%)
UTA-20-A	Tpki	3419	32094	0.72	30210	0.57
UTA-23-Q	Tpki	3753	36283	1.00	34210	1.00
UTA-20-D	Tpki	4072	51035	0.52	46200	0.52
UTA-23-A	Tpki	4645	65697	0.89	54700	0.91
UTA-23-I	Tpcrn	4560	55766	0.21	53450	0.19

DTN: MO0203DHRSSWHB.001

Note: ^a from tenth loading cycle

Table 22. Fixed-Free, Small-Strain RCTS Test Results of Reconstituted Quaternary Alluvial Specimen

UTACED Designation	Stratigraphic Unit	Resonant Column			Torsional Shear ^a	
		Vs (ft/s)	Gmax (ksf)	Dmin (%)	Gmax (ksf)	Dmin (%)
UTA-23-X	Qal	923	2854	1.04	2499	0.98

DTN: MO0203DHRSSWHB.001

Note: ^a from tenth loading cycle

6.2.10.3 Results

The shear-wave velocities, shear moduli, and material damping values from the RCTS tests are presented in tabular and graphical forms in Attachment XII. In this section, the principal results from these measurements are presented in summary tables and graphs and are briefly discussed.

Small-Strain Behavior of Intact Tuff Specimens

The values of shear-wave velocity (V_s), shear modulus (G_{max}), and material damping ratio (D_{min}) measured at small shearing strains (strains less than 0.0003%) are summarized in Tables 19 to 21 for intact tuff specimens from Groups 1, 2 and 3, respectively. The values presented were measured at the estimated in-situ mean total stress ($\sigma_{in-situ}$). The in-situ mean total stress was

estimated using an earth pressure coefficient (σ_h/σ_v) of either 0.5 or 0.75, as discussed in Scientific Notebook SN-M&O-SCI-033-V1 (Wong 2002e, page 139). D_{\min} and G_{\max} in Tables 19-22 are determined by fitting a curve through the data. Four to five isotropic pressures that ranged from below to above the estimated in-situ mean total stress were generally used, where the in-situ mean total stress was estimated using an earth pressure coefficient of either 0.5 or 0.75.

The variations in small-strain shear modulus, G_{\max} , with confining pressure, σ , that were measured by resonant column testing are presented in a normalized form (G_{\max} at $\sigma_{\text{cell}} / G_{\max}$ at $\sigma_{\text{in-situ}}$ versus $\sigma_{\text{cell}} / \sigma_{\text{in-situ}}$) on Figures 115 to 117 for the three groups of tuff specimens. As shown, all intact tuff specimens, except one (UTA-23-C; Figure 115), exhibit only small increases in G_{\max} as confining pressure ranges from 0.25 to 4 times $\sigma_{\text{cell}} / \sigma_{\text{in-situ}}$. In fact, the small increases in G_{\max} with increasing σ occur mainly at confining pressures less than $\sigma_{\text{in-situ}}$. This behavior is interpreted as the closing of micro-cracks in the specimens in this pressure range.

The variation in V_S measured at $\sigma_{\text{in-situ}}$ with dry unit weight, γ_{dry} , of the tuff specimens is shown on Figure 118. As shown, there is a general trend of increasing V_S with increasing γ_{dry} . This general relationship formed the basis for subdividing the intact tuff specimens into three groups based on dry unit weight. The following general relationships are observed:

Group 1: 8,800 ft/s > V_S > 6,900 ft/s

Group 2: 6,500 ft/s > V_S > 5,000 ft/s

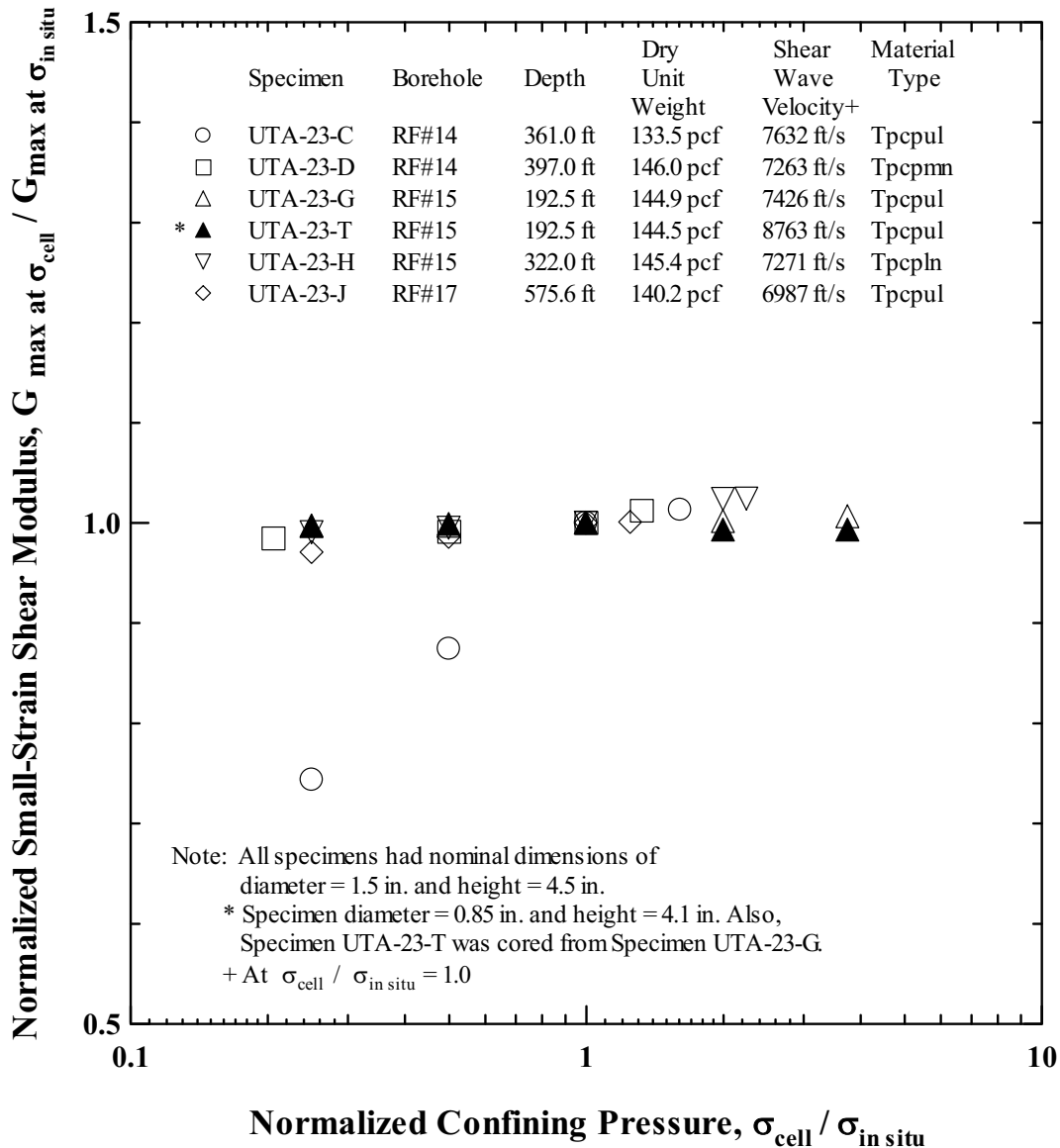
Group 3: 4,700 ft/s > V_S > 3,400 ft/s

The one exception is specimen UTA-23-S in Group 2, which has $\gamma_d = 127.4$ pcf and $V_S = 7,136$ ft/s. This specimen was cored from specimen UTA-23-F and exhibits a shear-wave velocity about 10% greater than the parent specimen. In fact, all four specimens that were cored from larger specimens show slightly higher velocities than the parent specimens (UTA-23-T, UTA-23-R, UTA-23-S, and UTA-23-Q). This difference might be attributed to an increase in micro-cracking (possibly caused by the field sampling process) that increases with radial distance from the center of the original core sample.

The general relationship shown on Figure 118 between dry unit weight and shear-wave velocity is also found between total unit weight and shear-wave velocity, as shown on Figure 119.

The variations in small-strain material damping ratio, D_{\min} , with normalized confining pressure ($\sigma_{\text{cell}} / \sigma_{\text{in-situ}}$) that were measured by resonant column testing are shown on Figures 120 to 122 for Groups 1, 2 and 3, respectively. As with G_{\max} , D_{\min} shows little effect of σ . The values of D_{\min} range from about 0.2 to 2.0% at $\sigma_{\text{in-situ}}$ and are not correlated with γ_d as was found with shear-wave velocity (and hence G_{\max}).

The effects on G_{\max} and D_{\min} of the intact tuff specimens of two other parameters were also studied. These parameters are time of confinement at a constant isotropic stress state, t , and excitation frequency, f . The effect of t on G_{\max} and D_{\min} was inconsequential in these tests (less than a 1% change over the testing time). The effect of f was investigated in two ways.



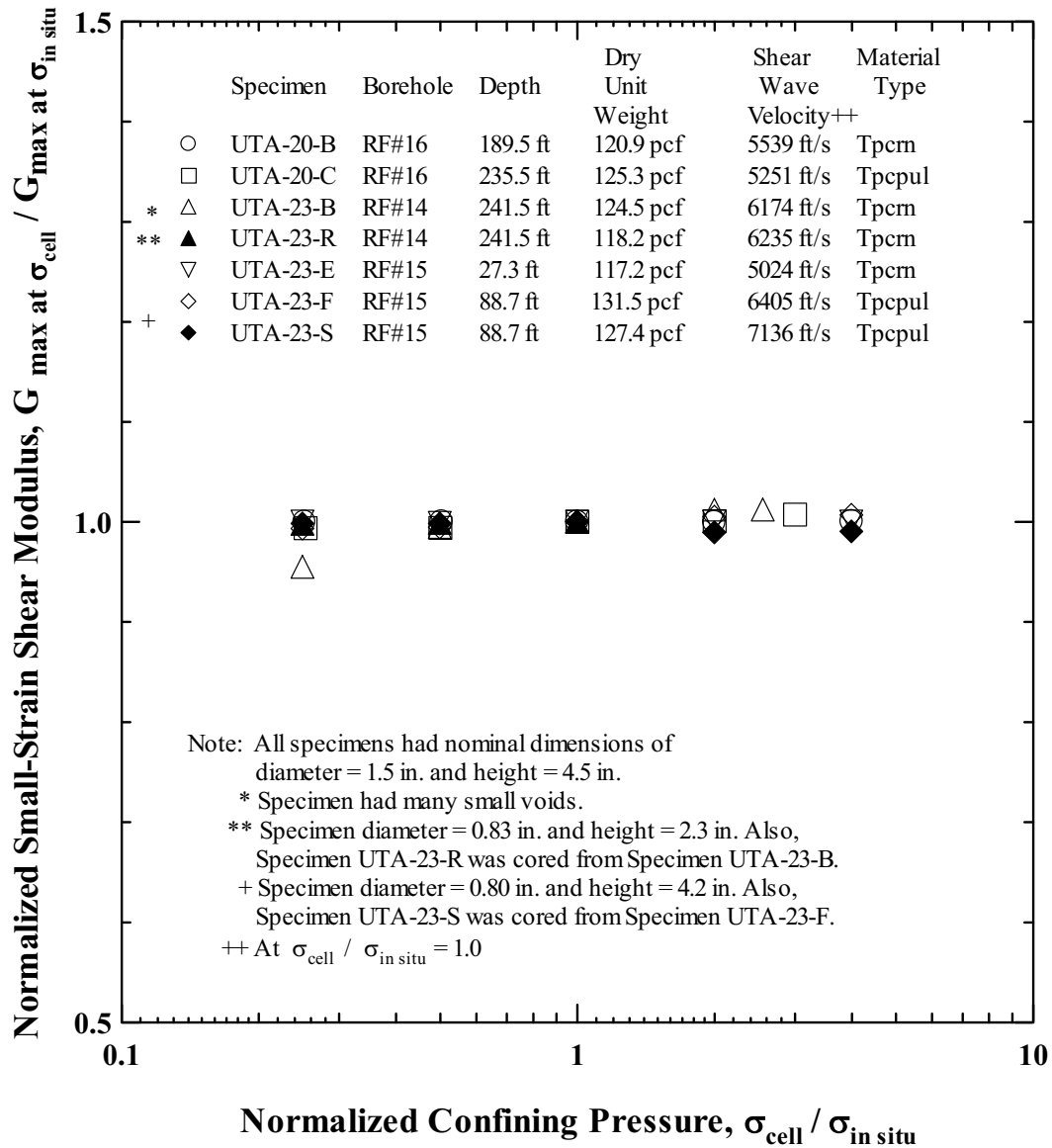
Source: Wong (2002e, Appendix 42, page 27)

Figure 115. Variation in Normalized Small-Strain Shear Modulus with Normalized Confining Pressure of Group 1 Intact Tuff Specimens

First, in torsional shear testing at the estimated $\sigma_{in-situ}$, G_{max} and D_{min} were measured over a frequency range of 0.1 to about 10 Hz. The effect of frequency on G_{max} over this range was very small, less than 2%.

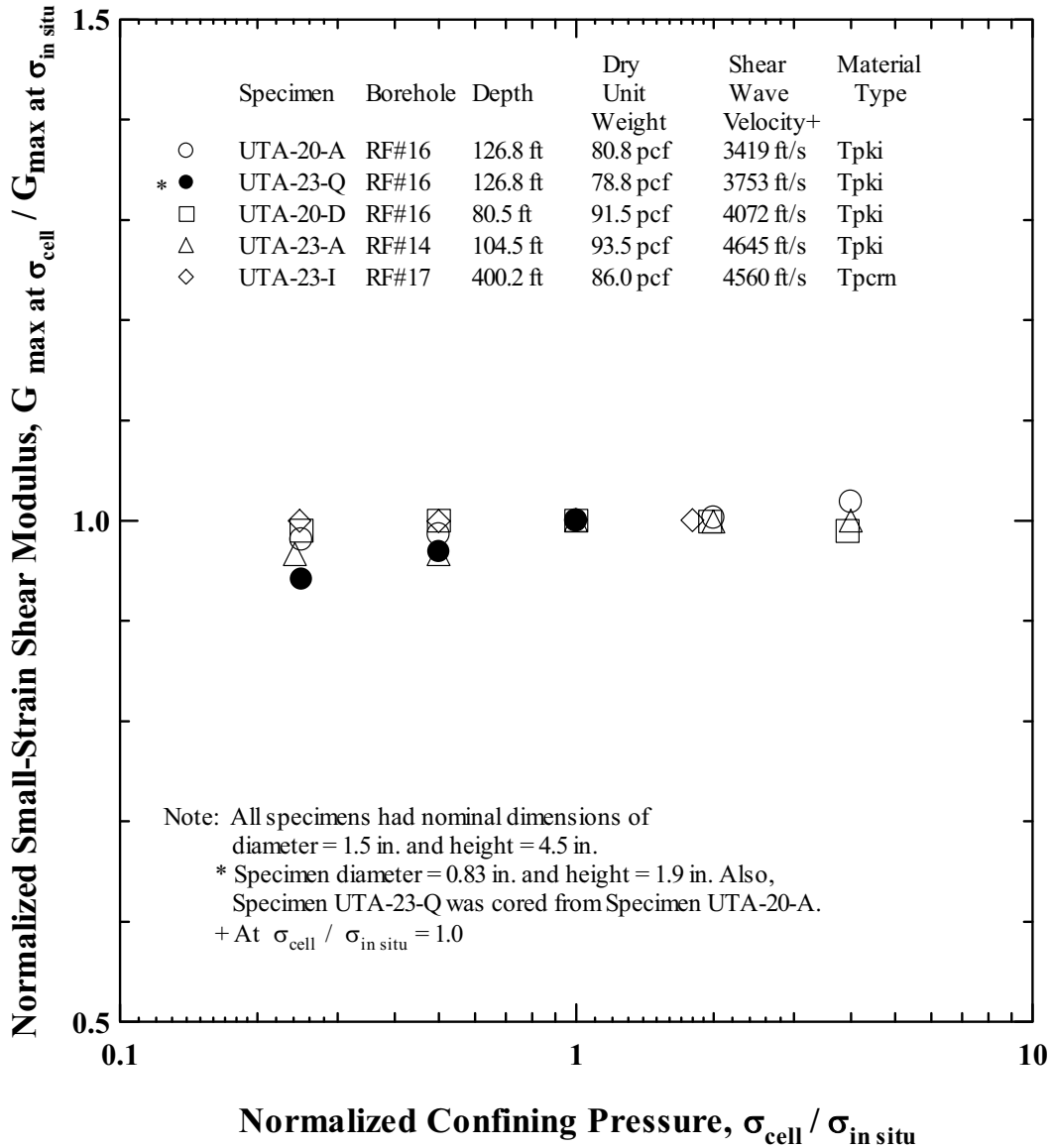
Second, the effect of changing the excitation frequency from 1 Hz in the torsional shear test to the range of several 100 Hz in the resonant column test was evaluated. In this case, G_{max} increased about 11% (ranging from 1 to 27%) for the 18 intact tuff specimens, as can be seen in Tables 19 to 21. (All results over the complete frequency range are shown on Figures XII-20 to XII-25.) G_{max} increased 14% for the reconstituted alluvium specimen (Table 22). This increase can be attributed to both excitation frequency and limitations in each testing technique, as

discussed in Section 6.2.10.4. An average increase in G_{\max} of 11% is approximately equivalent to a 5.4% increase in shear-wave velocity over this frequency range. This variation in values is considered small and within the range of typical variability to be expected in such measurements.



Source: Modified from Wong (2002e, Appendix 42, page 28)

Figure 116. Variation in Normalized Small-Strain Shear Modulus with Normalized Confining Pressure of Group 2 Intact Tuff Specimens

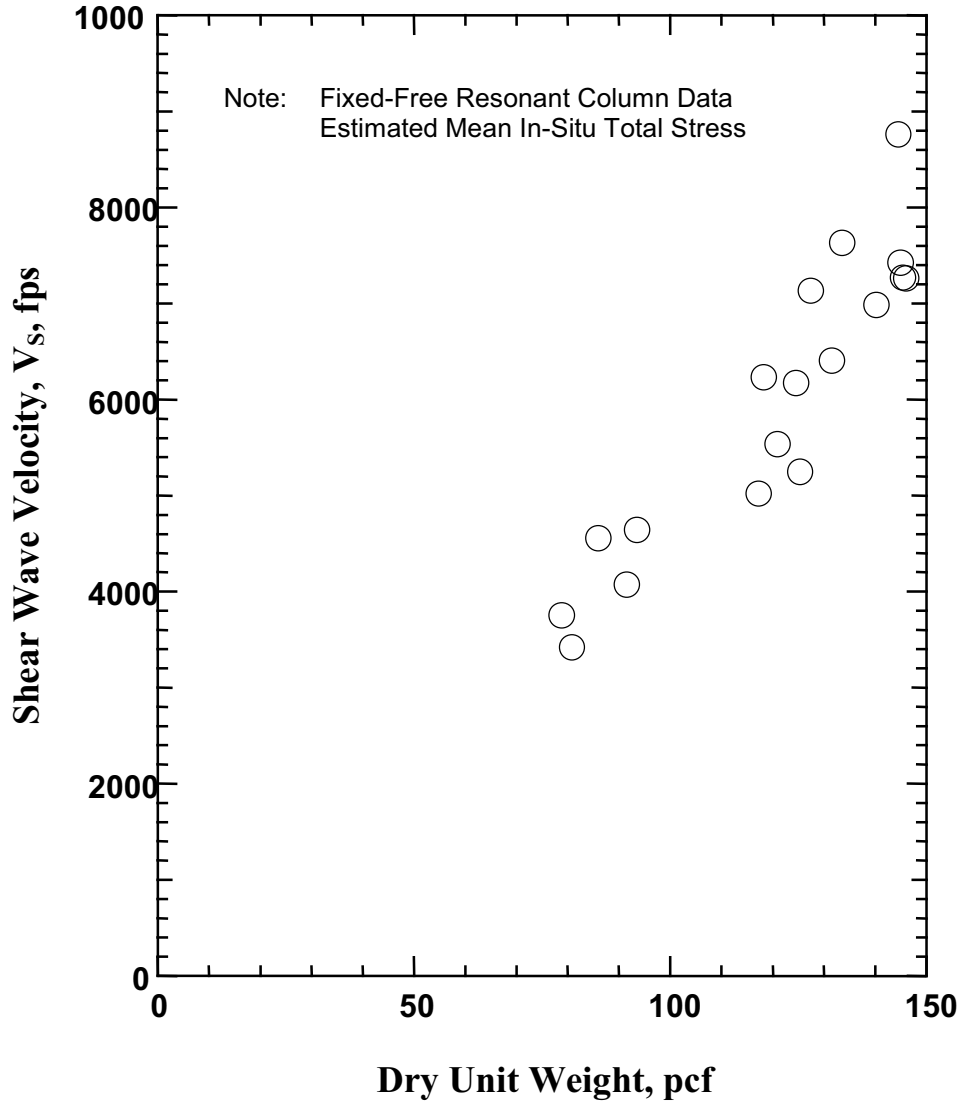


Source: Modified from Wong (2002e, Appendix 42, page 29)

Figure 117. Variation in Normalized Small-Strain Shear Modulus with Normalized Confining Pressure of Group 3 Intact Tuff Specimens

Nonlinear Behavior of Intact Tuff Specimens

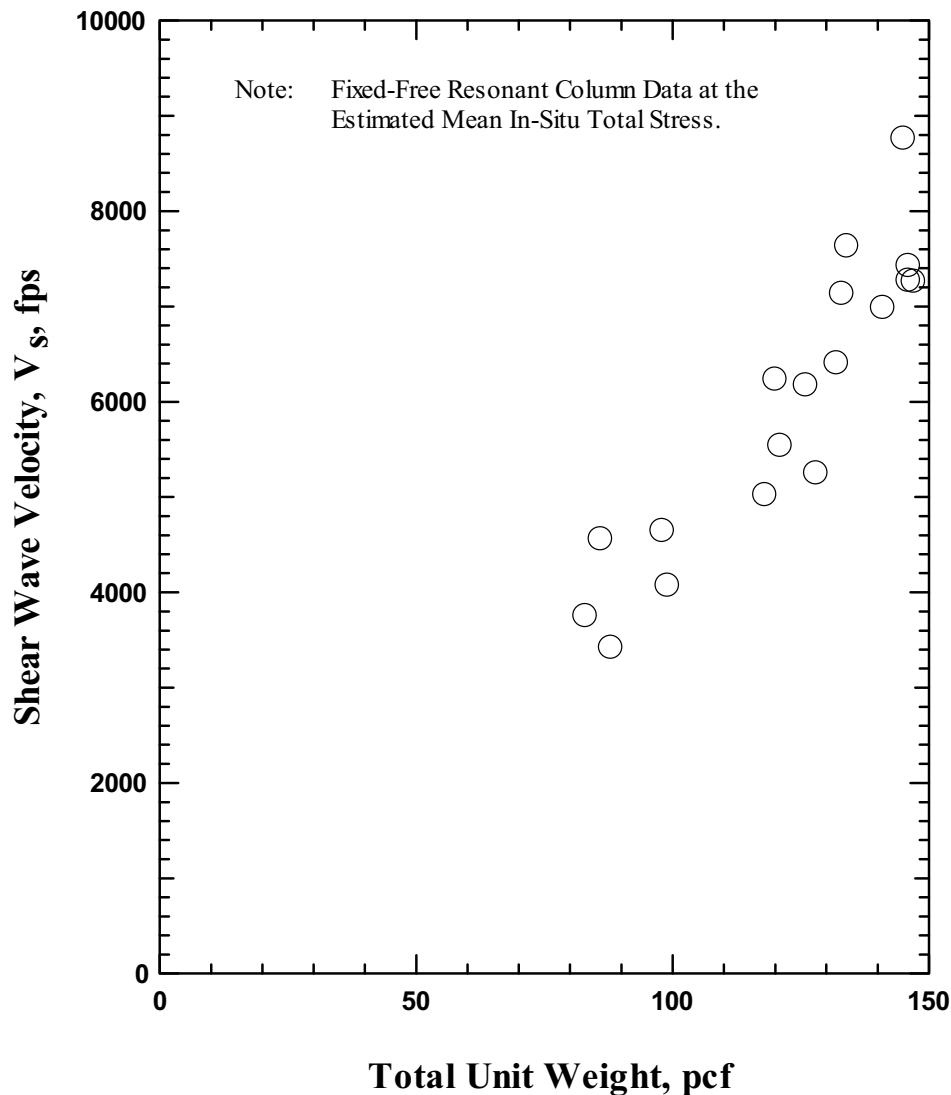
The influence of shearing strain, γ , on G as measured by resonant column testing is shown on Figures 123 to 125 for the intact tuff specimens in Groups 1, 2 and 3, respectively. The influence of γ on normalized shear modulus, G/G_{max} is presented for the same groups on Figures 126 to 128, respectively. Typical nonlinear curves proposed for sands by Seed et al. (1986, Figure 2) are also shown on Figures 126 to 128 for comparison purposes. As shown, the intact tuff specimens exhibited only a small amount of nonlinearity at $\gamma = 0.01\%$, with G/G_{max} generally greater than 0.9. However, two of the small-diameter specimens (UTA-23-R and UTA-23-Q) failed at γ around 0.1%.



DTN: MO0203DHRSSWHB.001

Figure 118. Variation of Shear-Wave Velocity Measured in the Laboratory at In-Situ Mean Total Stress with Dry Unit Weight of Intact Tuff Specimens

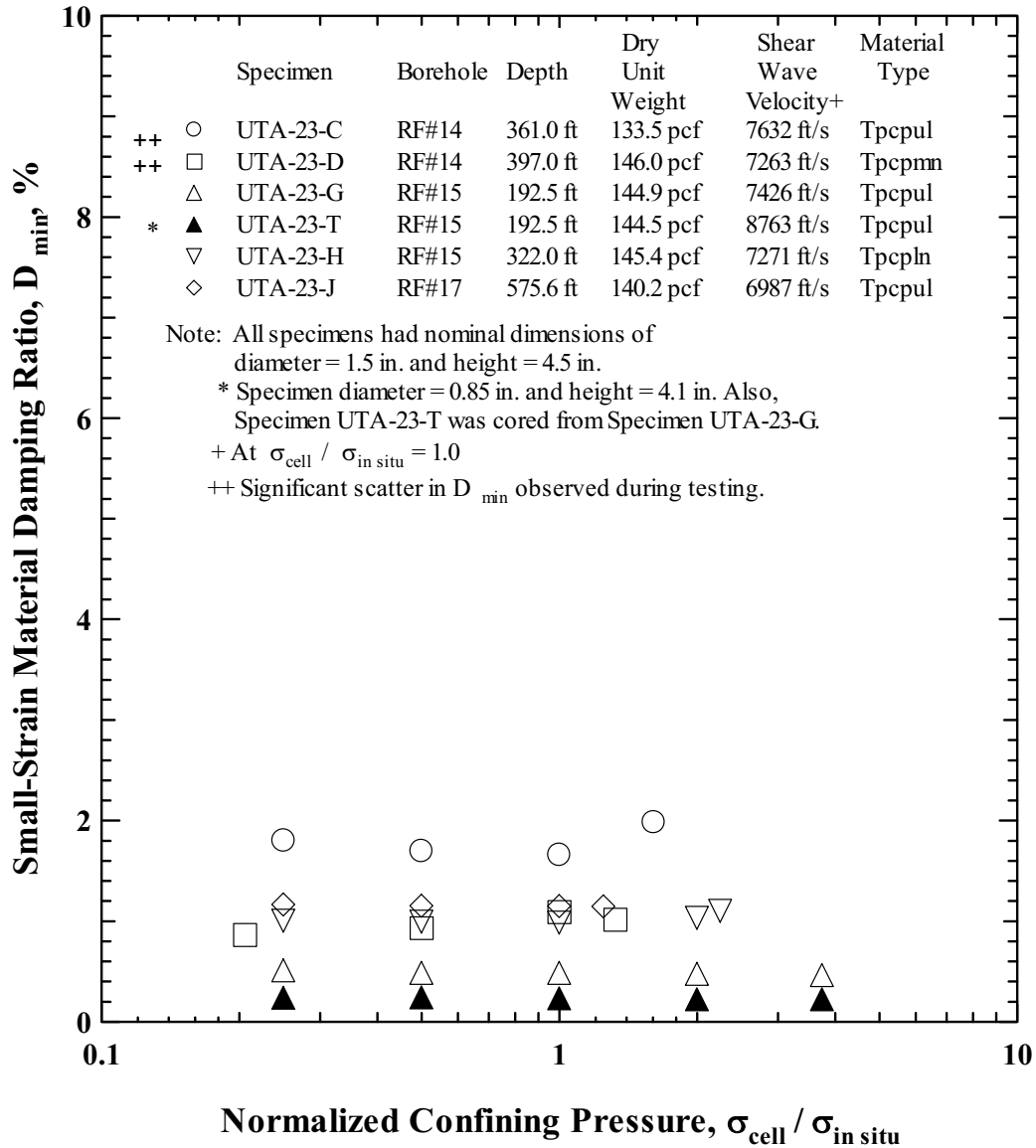
The influence of shearing strain on D as measured by resonant column testing is shown on Figures 129 to 131 for the tuff specimens in Groups 1, 2 and 3, respectively. In general, the intact tuff specimens exhibit a rather linear response, with D at $\gamma = 0.01\%$ generally less than $2D_{\min}$. This response is more linear than typically exhibited by sands, as seen by comparing the results with the D -log γ curves proposed by Seed et al. (1986, Figure 6) for sands. There are, however, three obvious exceptions, UTA-23-C (Figure 129), UTA-23-B (Figure 130), and UTA-23-A (Figure 131). These specimens exhibited significant increases in D as γ increases above 10^{-4} percent.



DTN: MO0203DHRSSWHB.001

Figure 119. Variation of Shear-Wave Velocity Measured in the Laboratory at In-Situ Mean Total Stress with Total Unit Weight of Intact Tuff Specimens

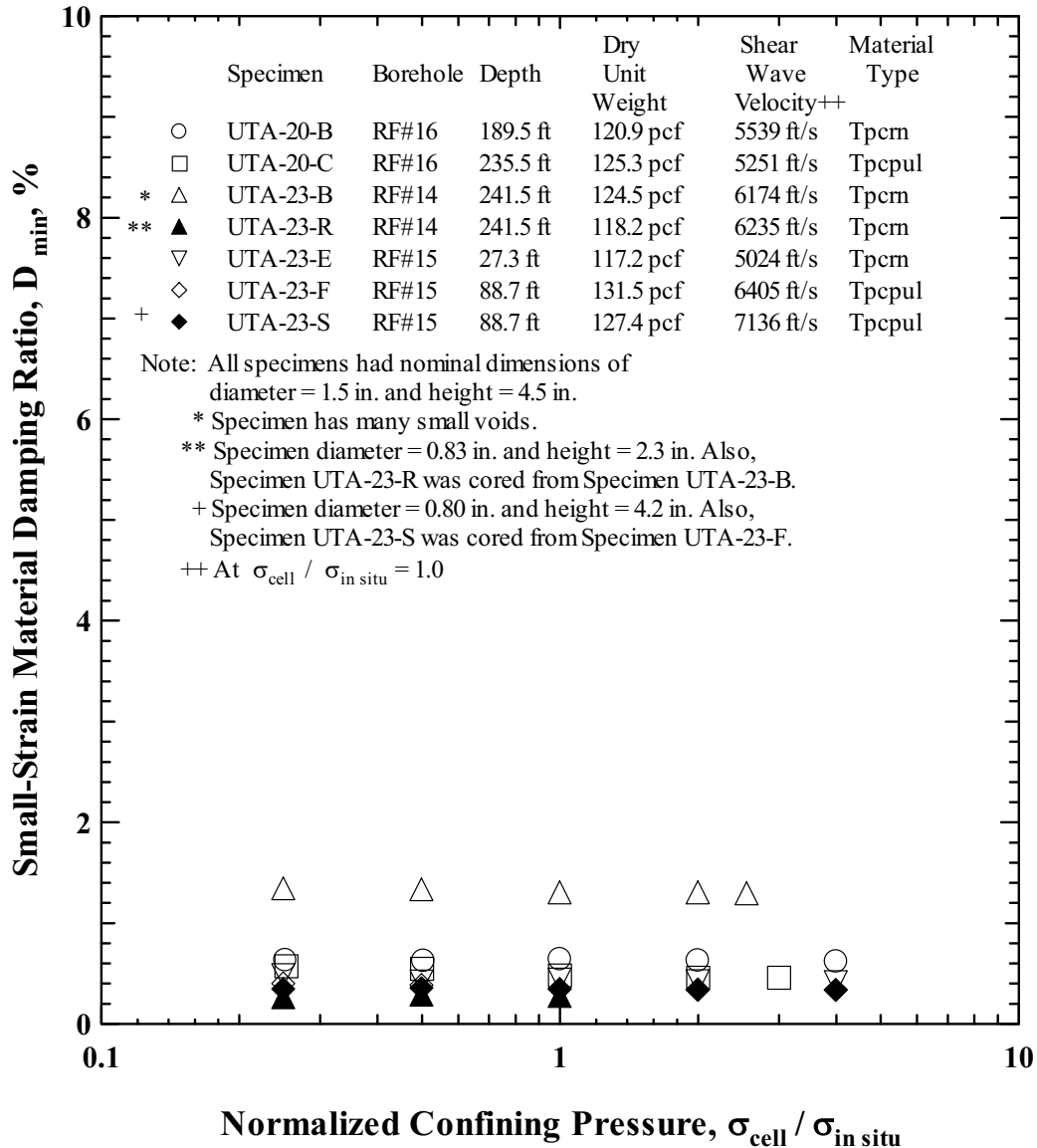
In addition to grouping the samples by unit dry weight, the specimens were grouped by lithostratigraphic unit: Tpcpmn, Tpcpln, Tpcpul, Tpcrn, and Tпки (see Section 6.6.2 for a review of lithostratigraphic units). The influence of shearing strain on normalized G and damping ratio for the five types of tuff are shown on Figures 132 to 136. As shown, the units of Tiva Canyon Tuff exhibit only a small amount of nonlinearity in normalized G except for UTA-23-B. The discordant behavior of the same specimens noted earlier (e.g., UTA-23-A on Figure 136) are also apparent in the plots of D versus shearing strain (Figures 129 to 131).



Source: Wong (2002e, Appendix 42, page 32)

Figure 120. Variation in Small-Strain Material Damping Ratio with Normalized Confining Pressure of Group 1 Intact Tuff Specimens

On Figures 137 and 138, T_{pki} is separated out from the Tiva Canyon Tuff units (T_{pcpmn}, T_{pcpul}, and T_{pcrn}) and the effects of shearing stress on normalized G and D are shown. The results from the 1999 testing (DTN: MO9905LABDYNRS.000) are also shown on Figures 137 and 138. In general, the 2000 tests of the T_{pcrn} show more nonlinear behavior in terms of normalized G and D at higher strains than was observed for the welded Tiva Canyon Tuff results in 1999 (Figure 137). The 2000 T_{pki} test results are consistent with the 1999 results in the behavior of normalized G. However, the 2000 test results show significant nonlinear behavior in material damping at strains of only 0.001% for one specimen (Figure 138).

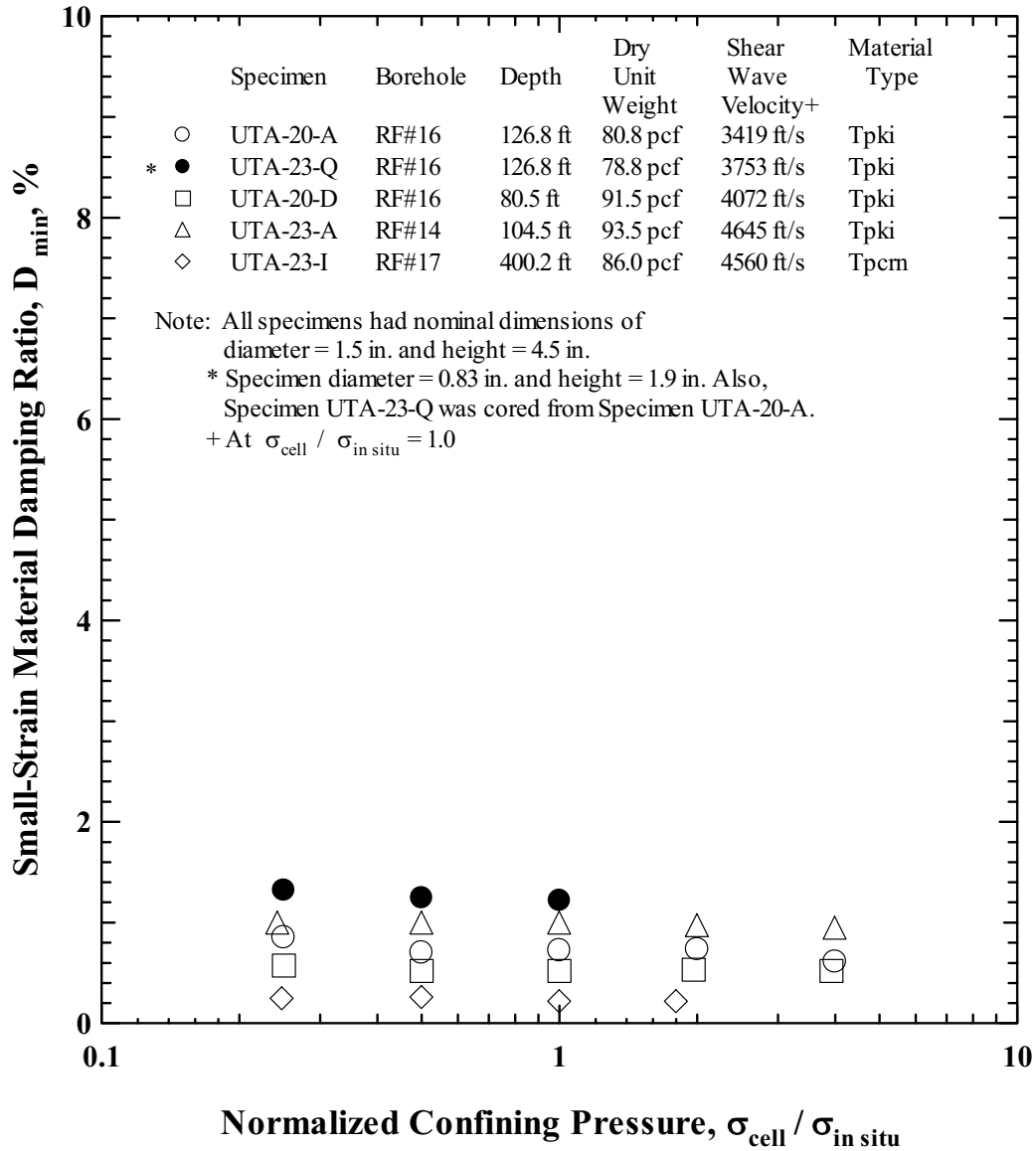


Source: Modified from Wong (2002e, Appendix 42, page 33)

Figure 121. Variation in Small-Strain Material Damping Ratio with Normalized Confining Pressure of Group 2 Intact Tuff Specimens

Small- and Large-Strain Behavior of Reconstituted Alluvial Specimens

The effects of σ on G_{max} and D_{min} of the reconstituted specimen of Quaternary alluvium are shown on Figures 139 and 140, respectively. This reconstituted material is behaving like a granular soil, as expected. The effects of f on G_{max} and D_{min} are small (Figures XII-26 and XII-27). The effects of γ on G , G/G_{max} and D are shown on Figures 141 to 143, respectively. Again, the material is behaving like a sandy soil, as shown by the comparisons with the curve for sand in Seed et al. (1986, Figures 2 and 6) on Figures 142 and 143.



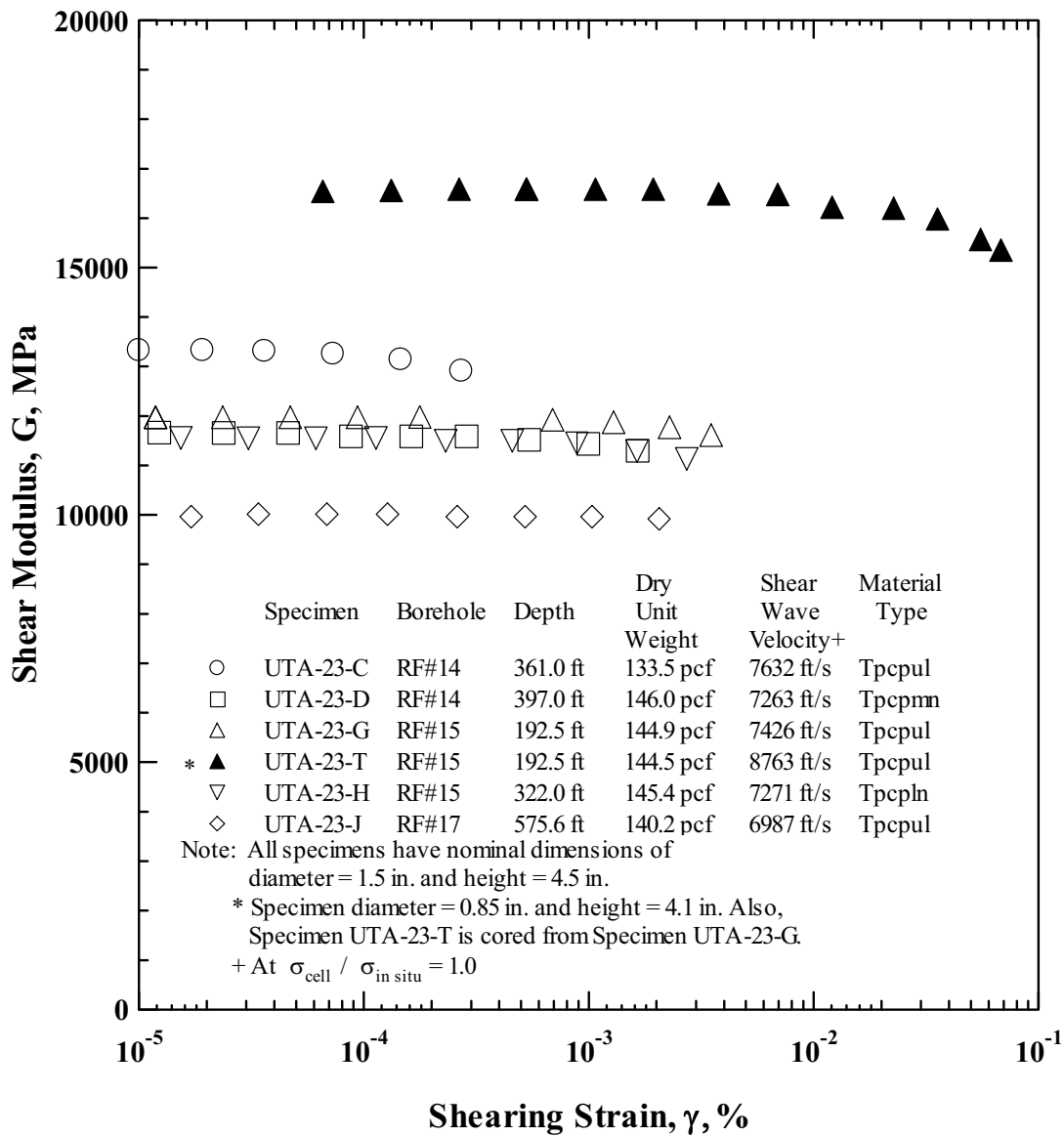
Source: Modified from Wong (2002e, Appendix 42, page 34)

Figure 122. Variation in Small-Strain Material Damping Ratio with Normalized Confining Pressure of Group 3 Intact Tuff Specimens

6.2.10.4 Limitations of Test Equipment

The RCTS equipment has several limitations, which are apparent from the test results. The limitations include the confining pressure range over which testing can be performed and the shearing strain range that can be excited in the test specimens.

The maximum test pressure of the confinement chamber is around 500 psi (3.4 MPa). Therefore, a slightly lower pressure of 460 psi (3.1 MPa) was the maximum pressure used to confine the tuff specimens from the greatest depths, which would have in-situ mean stresses greater than or equal to 460 psi.



DTN: MO0203DHRSSWHB.001

Figure 123. Variation in Shear Modulus with Shearing Strain of Group 1 Intact Tuff Specimens

The maximum shearing strain of about 0.1% was generated in the granular fill specimens because these were the least stiff specimens (discussed in Section 6.5.3). The maximum strain was generated in resonance, not in torsional shear, because of the dynamic amplification associated with resonating a specimen.

It is important to note that the limitation on torque generated by this equipment in the torsional shear testing combined with the large stiffness of the tuff specimens resulted in very small strains being generated in the tests. Sometimes the strains were below $5 \times 10^{-4}\%$, which is around the threshold resolution level in torsional shear testing with this equipment (Kim and Stokoe 1994,

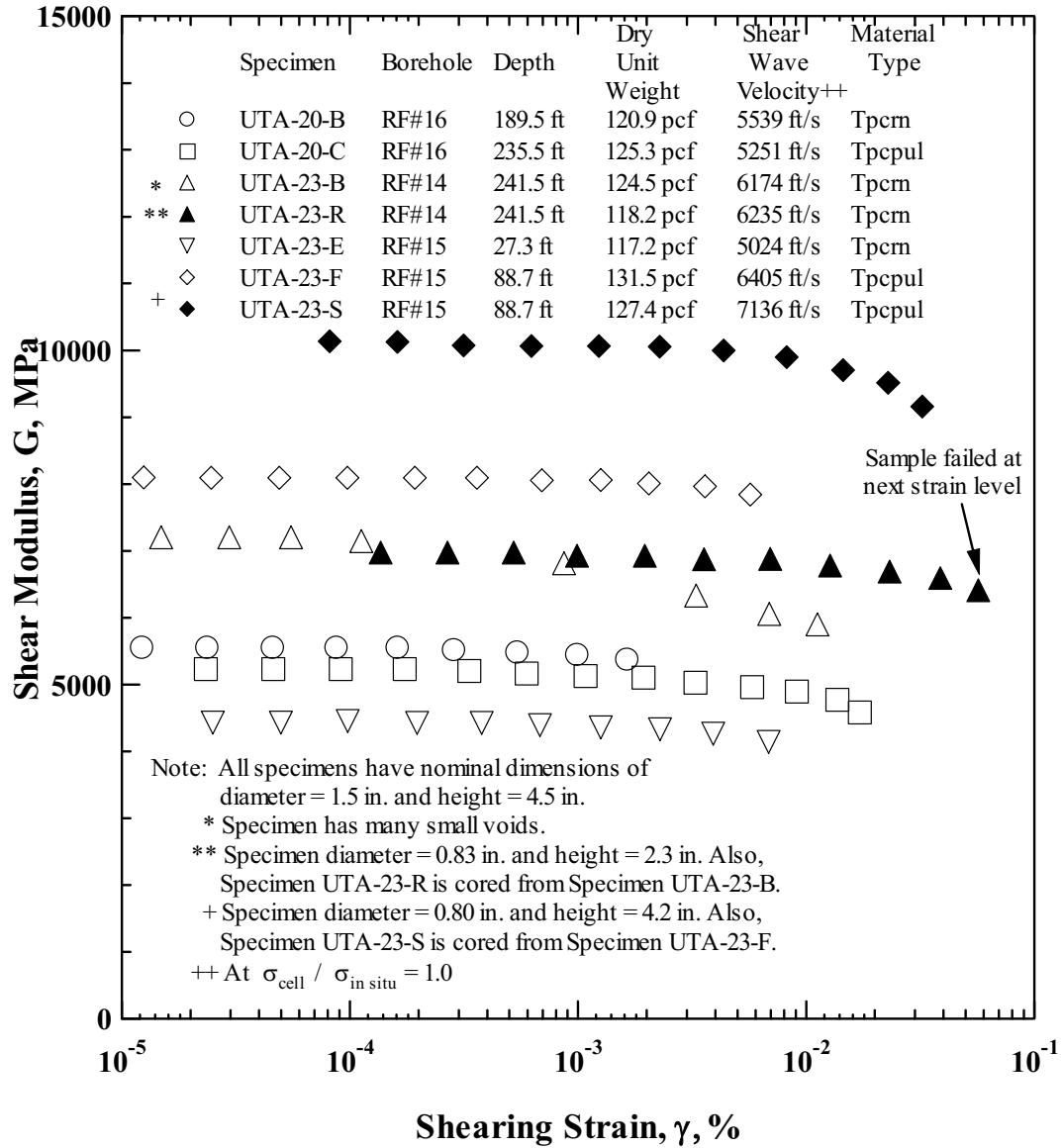


Figure 124. Variation in Shear Modulus with Shearing Strain of Group 2 Intact Tuff Specimens

page 25, Figure 10). Therefore, considerable scatter occurred in the very small strain measurements, especially in evaluations of D_{min} .

Two other limitations that could have potentially impacted the results are: 1) the highly nonlinear behavior in resonant column testing that occurs at strains greater than about 0.5% in specimens, and 2) extremely stiff specimens, which result in straining or movement in the base pedestal and top cap. The first limitation did not occur in these tests, as determined by all strain measurements which were less than 0.2%. The second limitation was checked by independent testing. This was done by testing several tuff specimens with free-free resonant column equipment (Wong 2002e, Appendix 42, page 11). The general free-free test set-up is described in Stokoe, Hwang et al. (1994). In these tests there are no end plates and both ends of the

specimen are free to move. Although these tests are unqualified (i.e., were not conducted in accordance with the YMP quality assurance procedures), the same calibrated waveform analyzer as used to verify the RCTS equipment was used to perform the free-free tests. Comparison of the results in terms of shear-wave velocities measured in each type of resonant column test is shown on Figure XII-28. As shown, the shear-wave velocities measured in the fixed-free test are generally equal to or slightly greater than the velocities measured in the free-free resonant column test, verifying the proper functioning of the RCTS equipment (fixed-free resonant column) and showing that base fixity was not a limitation in these results.

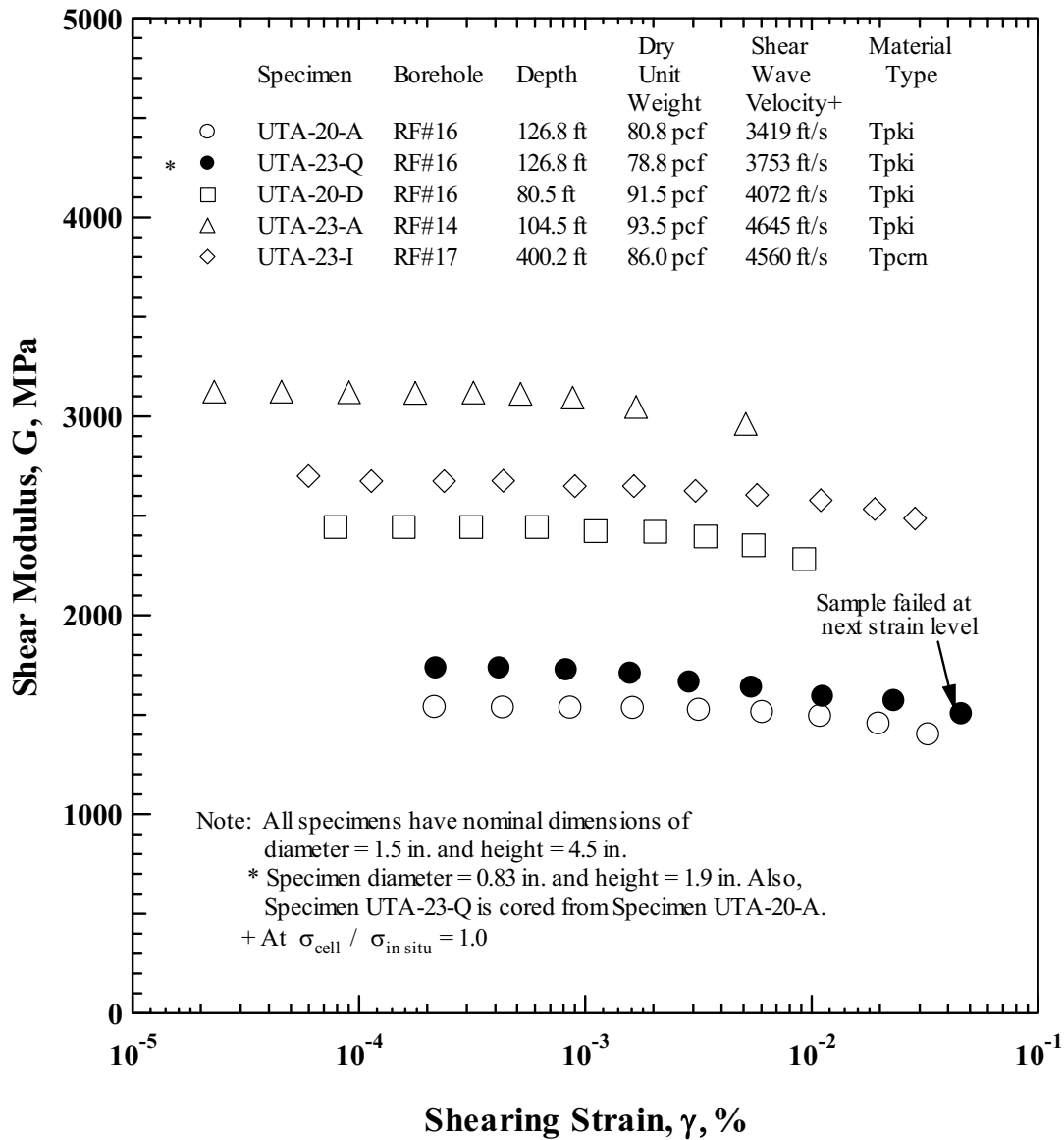
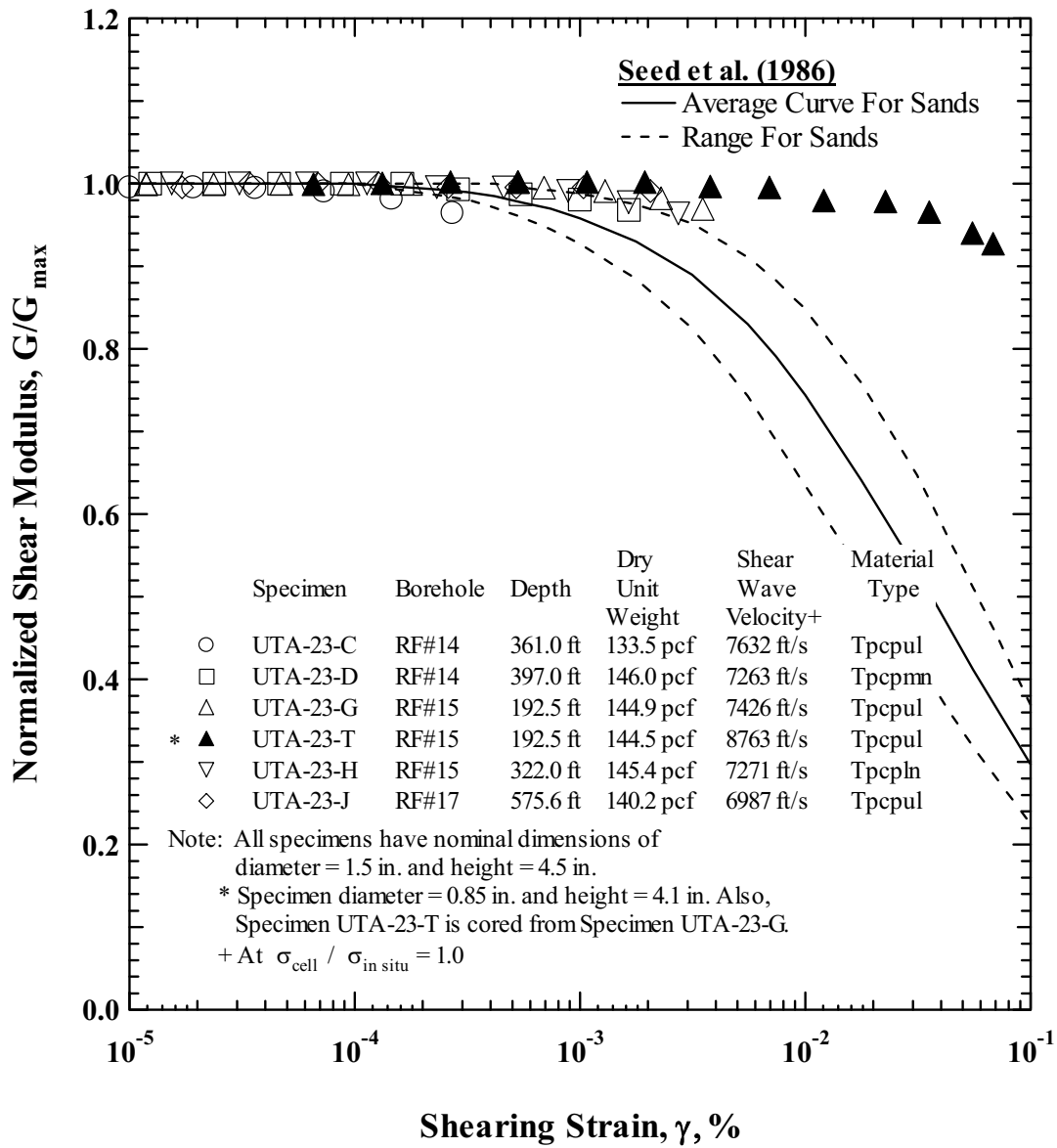
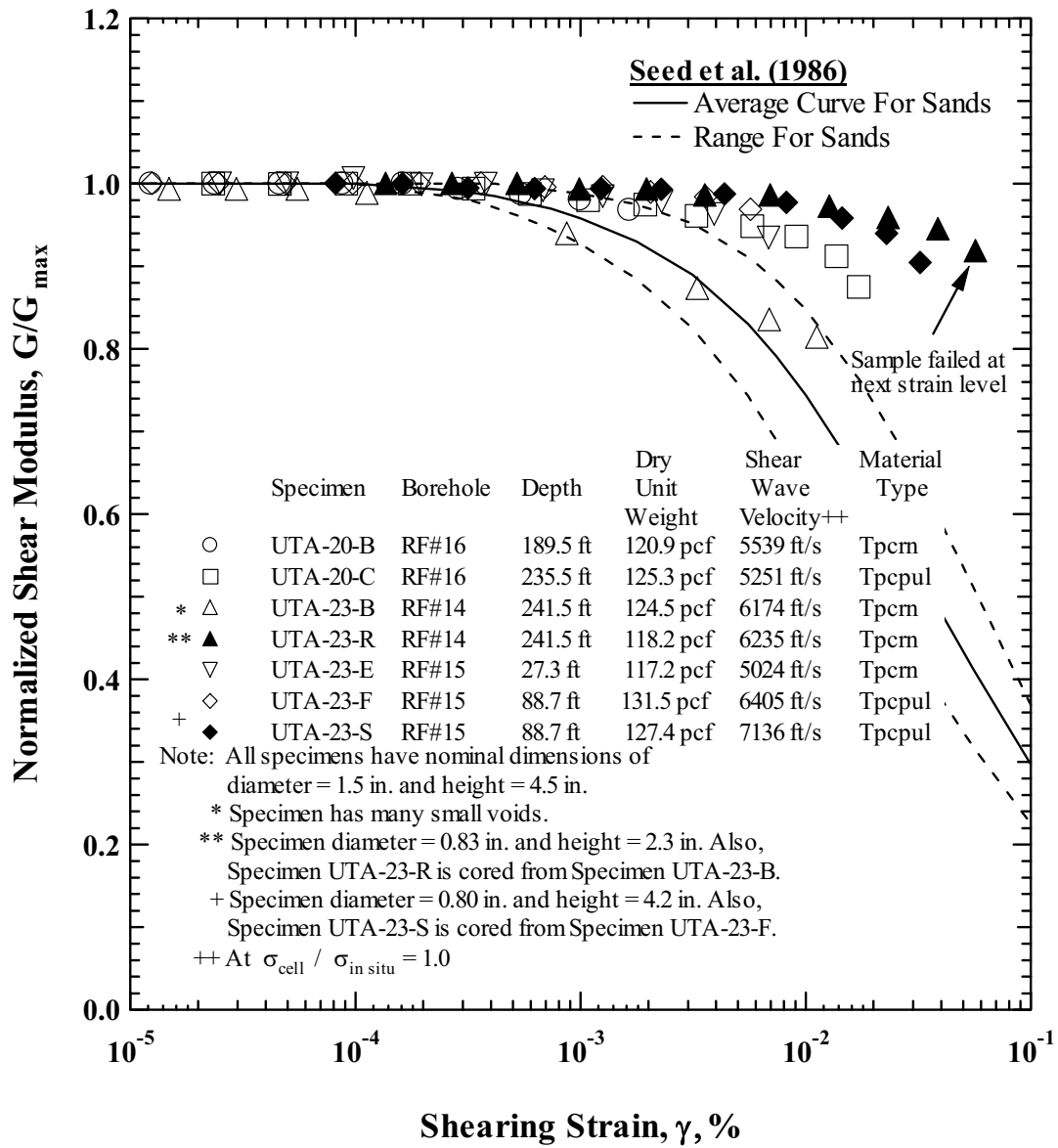


Figure 125. Variation in Shear Modulus with Shearing Strain of Group 3 Intact Tuff Specimens



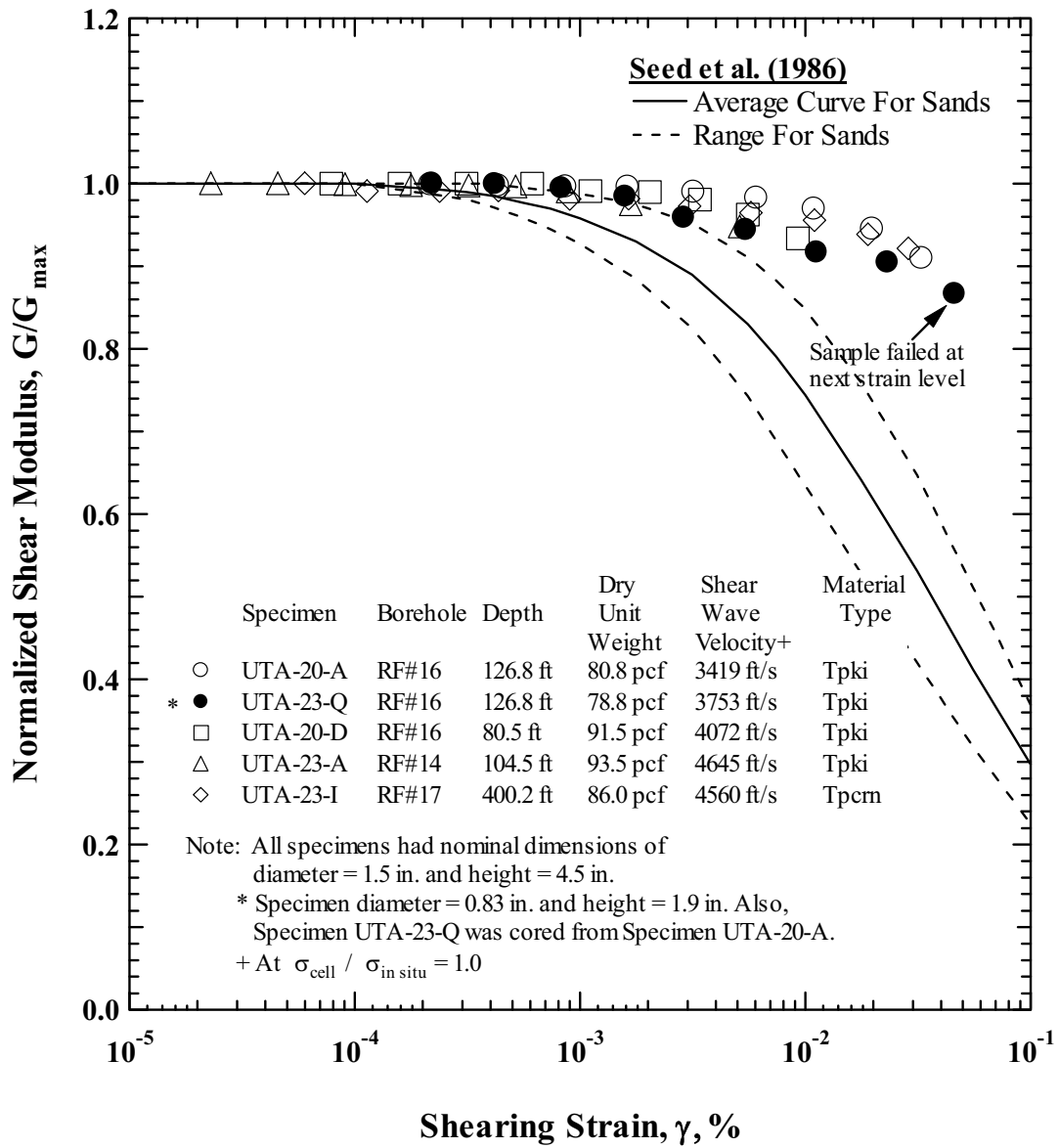
DTN: MO0203DHRSSWHB.001

Figure 126. Variation in Normalized Shear Modulus with Shearing Strain of Group 1 Intact Tuff Specimens



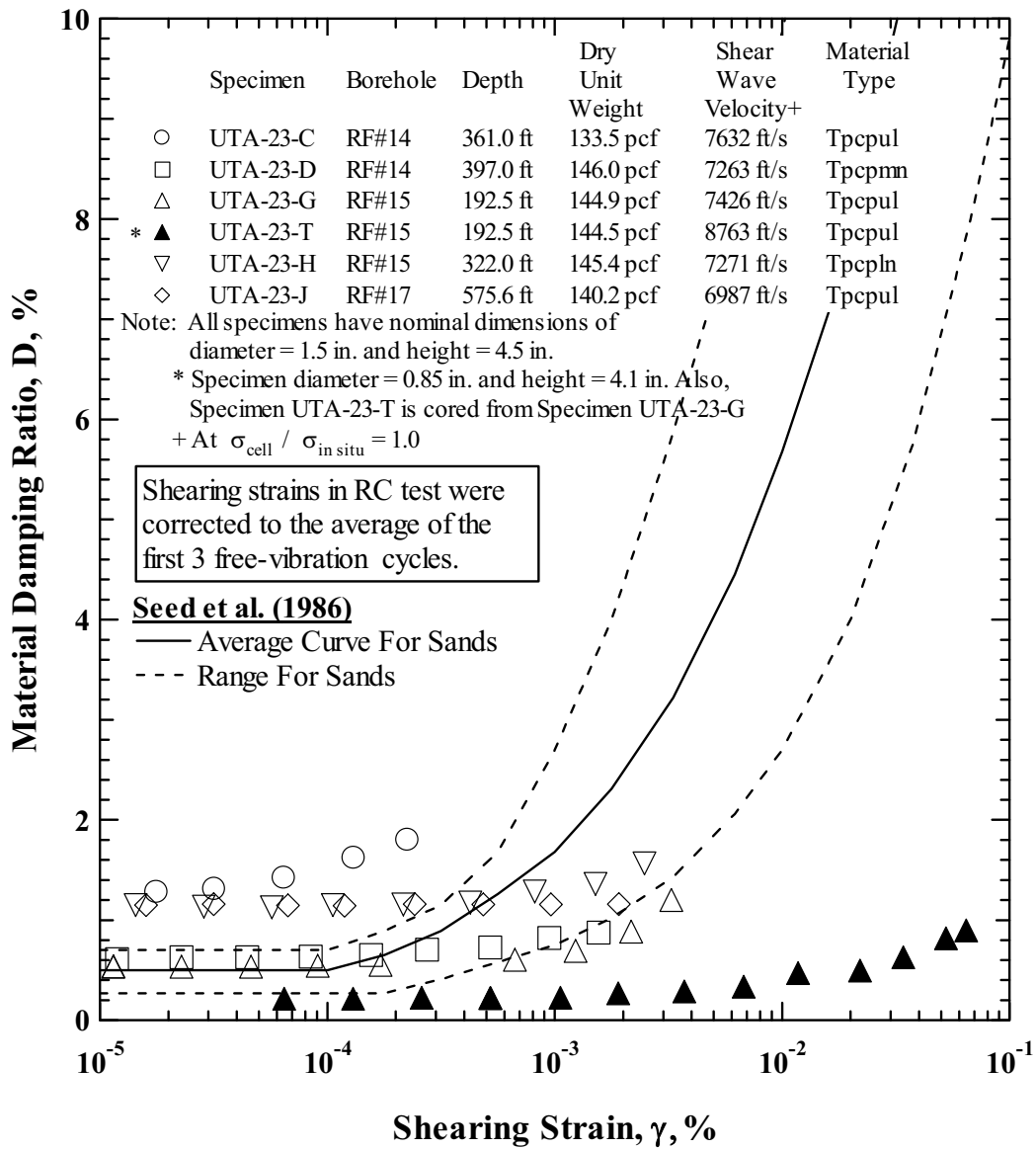
DTN: MO0203DHRSSWHB.001

Figure 127. Variation in Normalized Shear Modulus with Shearing Strain of Group 2 Intact Tuff Specimens



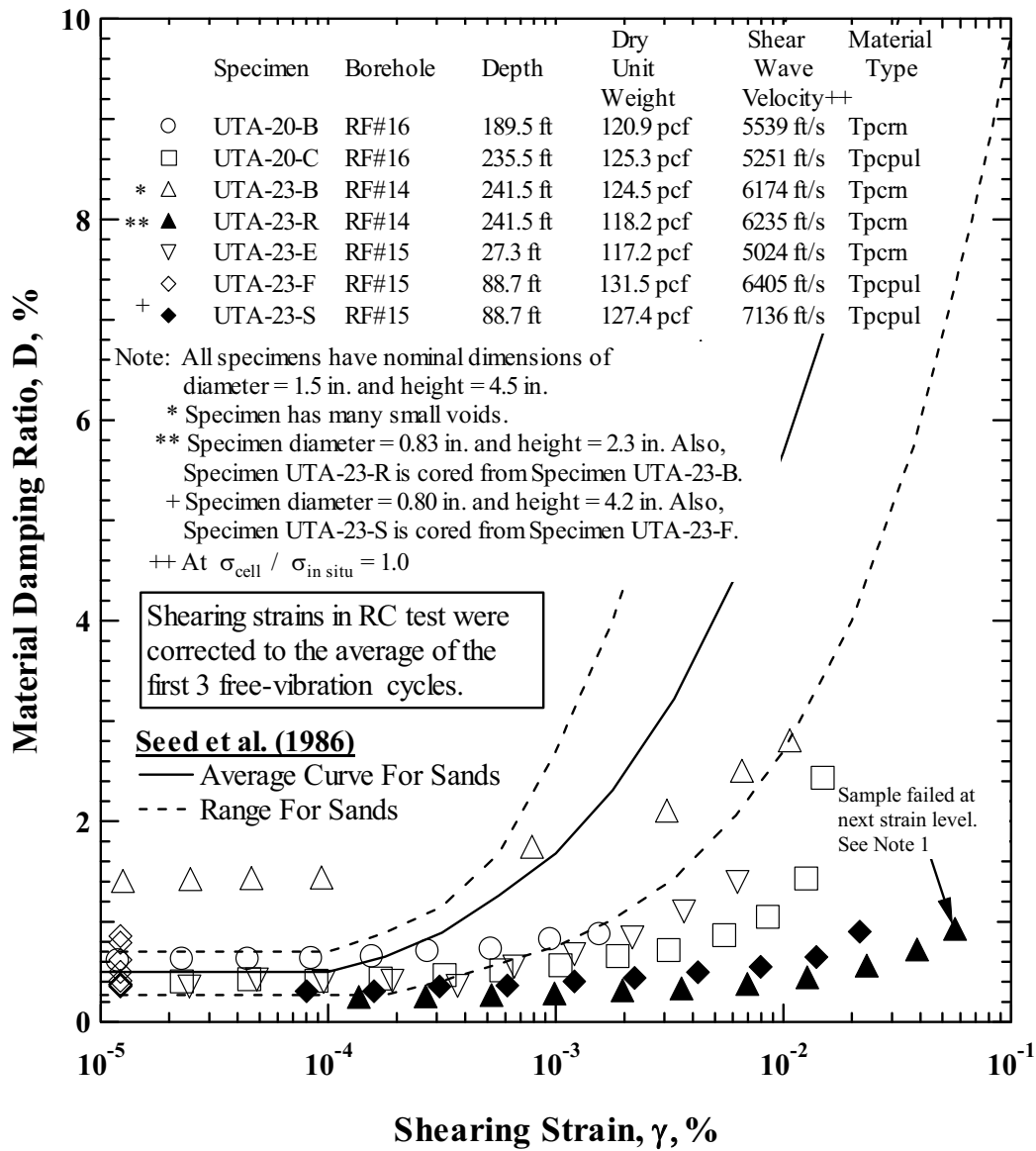
DTN: MO0203DHRSSWHB.001

Figure 128. Variation in Normalized Shear Modulus with Shearing Strain of Group 3 Intact Tuff Specimens



DTN: MO0203DHRSSWHB.001

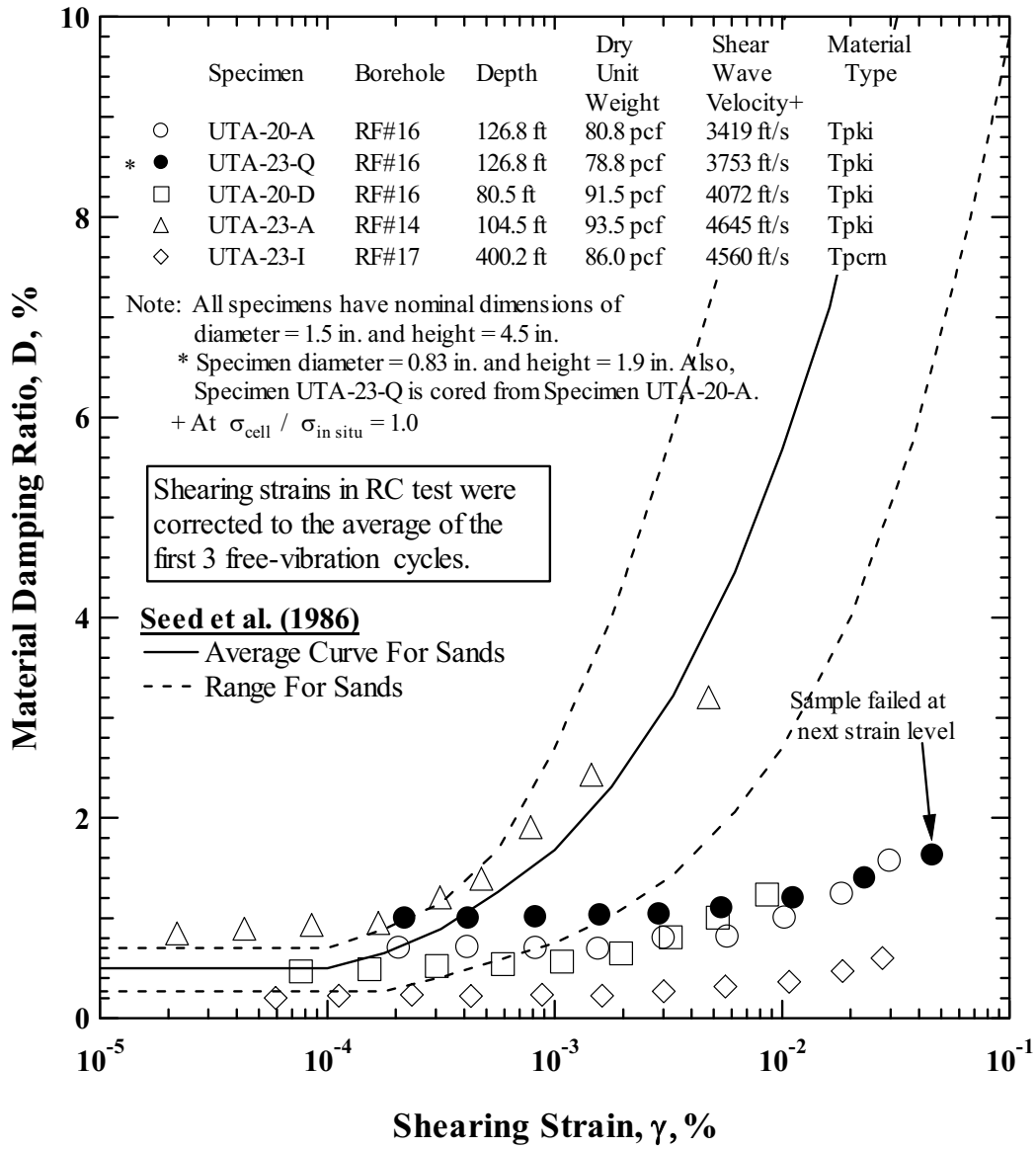
Figure 129. Variation in Material Damping Ratio with Shearing Strain of Group 1 Intact Tuff Specimens



DTN: MO0203DHRSSWHB.001

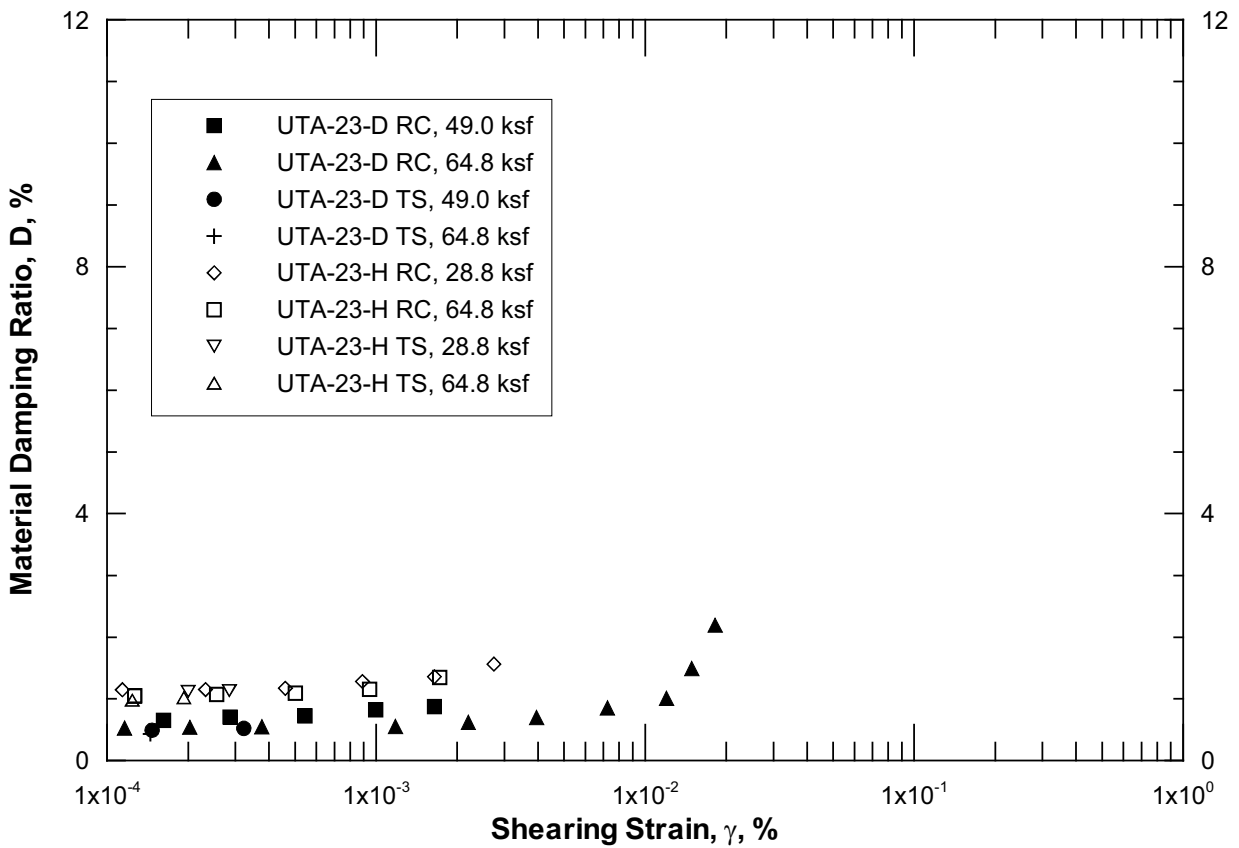
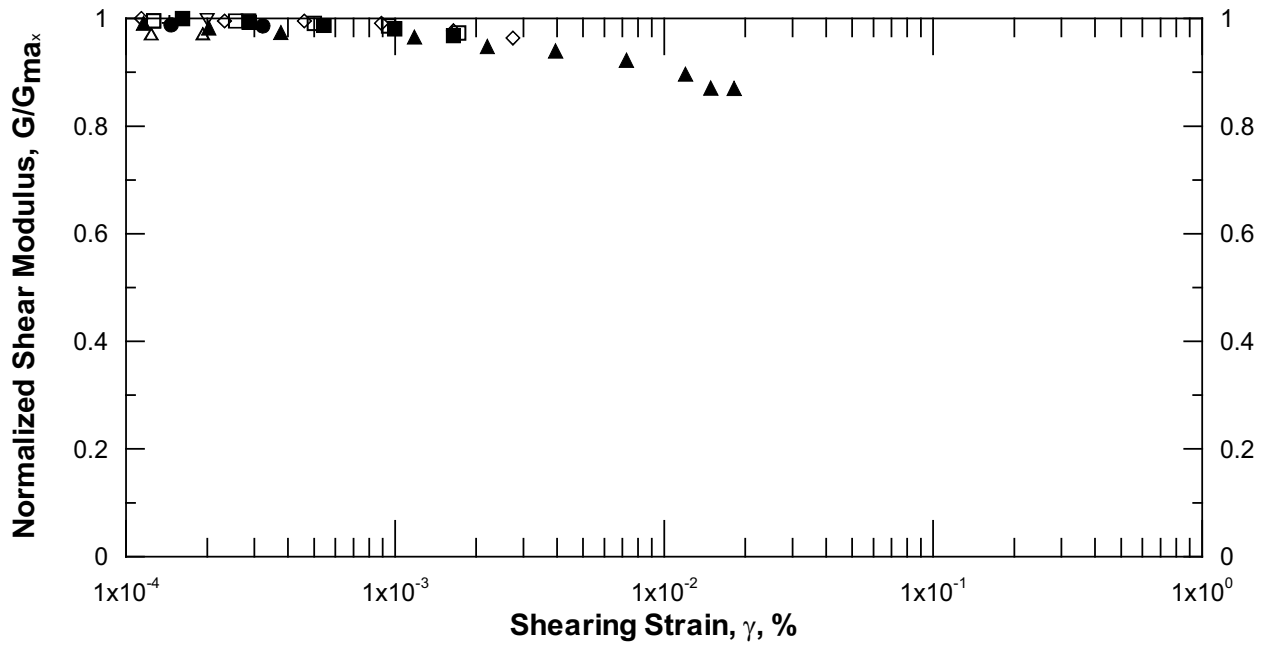
Note: (1) Wong (2002e, Appendix 42, page 42)

Figure 130. Variation in Material Damping Ratio with Shearing Strain of Group 2 Intact Tuff Specimens



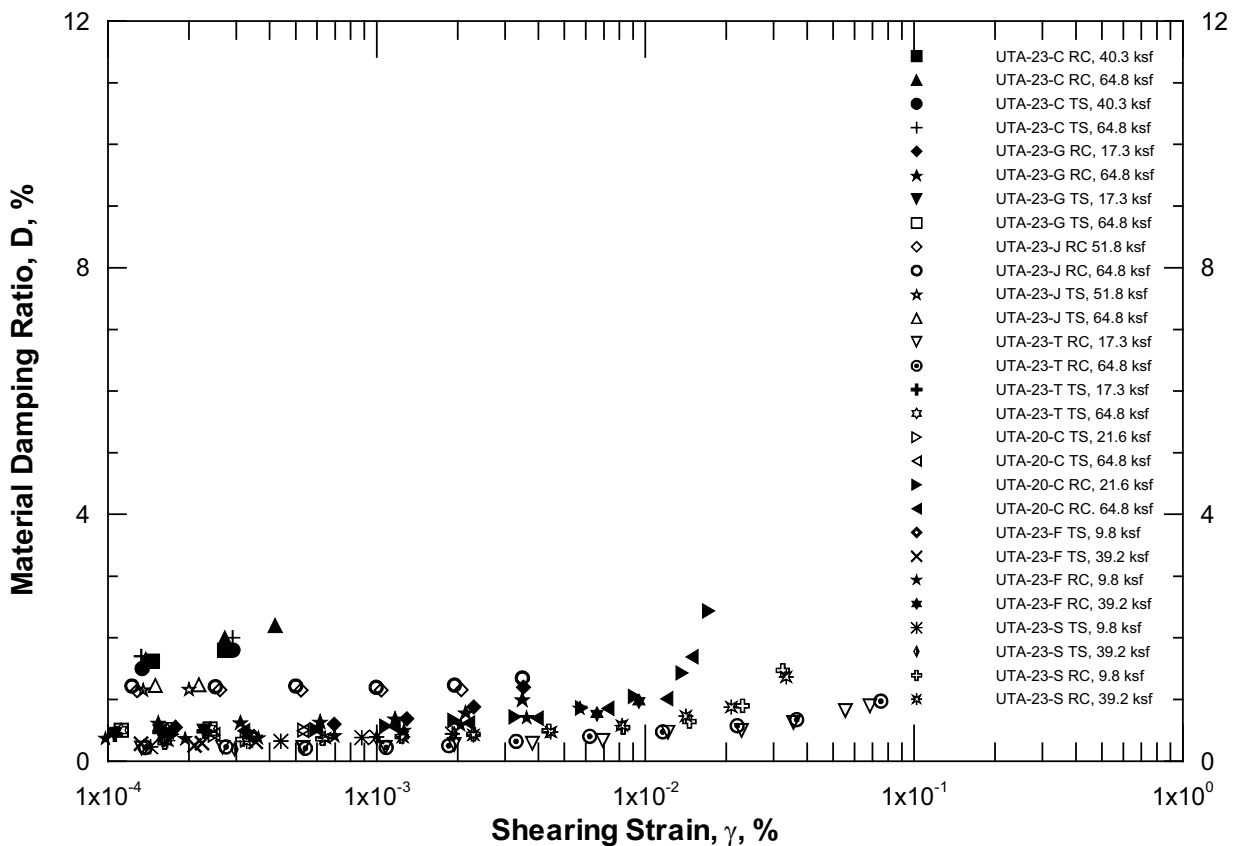
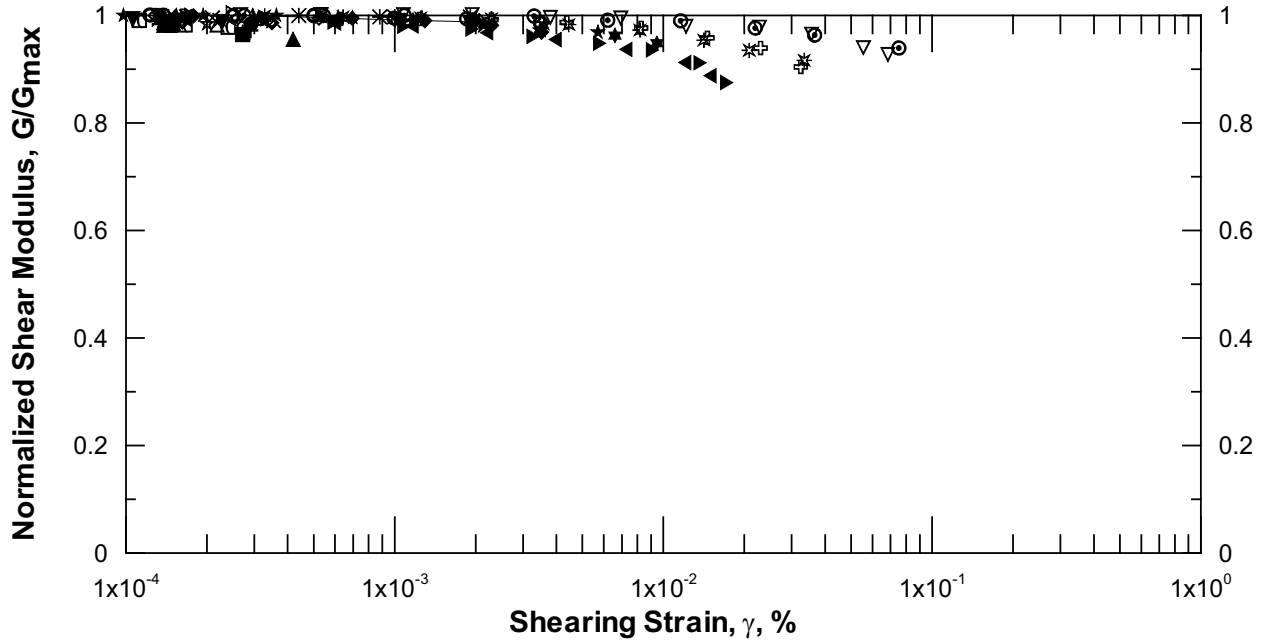
DTN: MO0203DHRSSWHB.001

Figure 131. Variation in Material Damping Ratio with Shearing Strain of Group 3 Intact Tuff Specimens



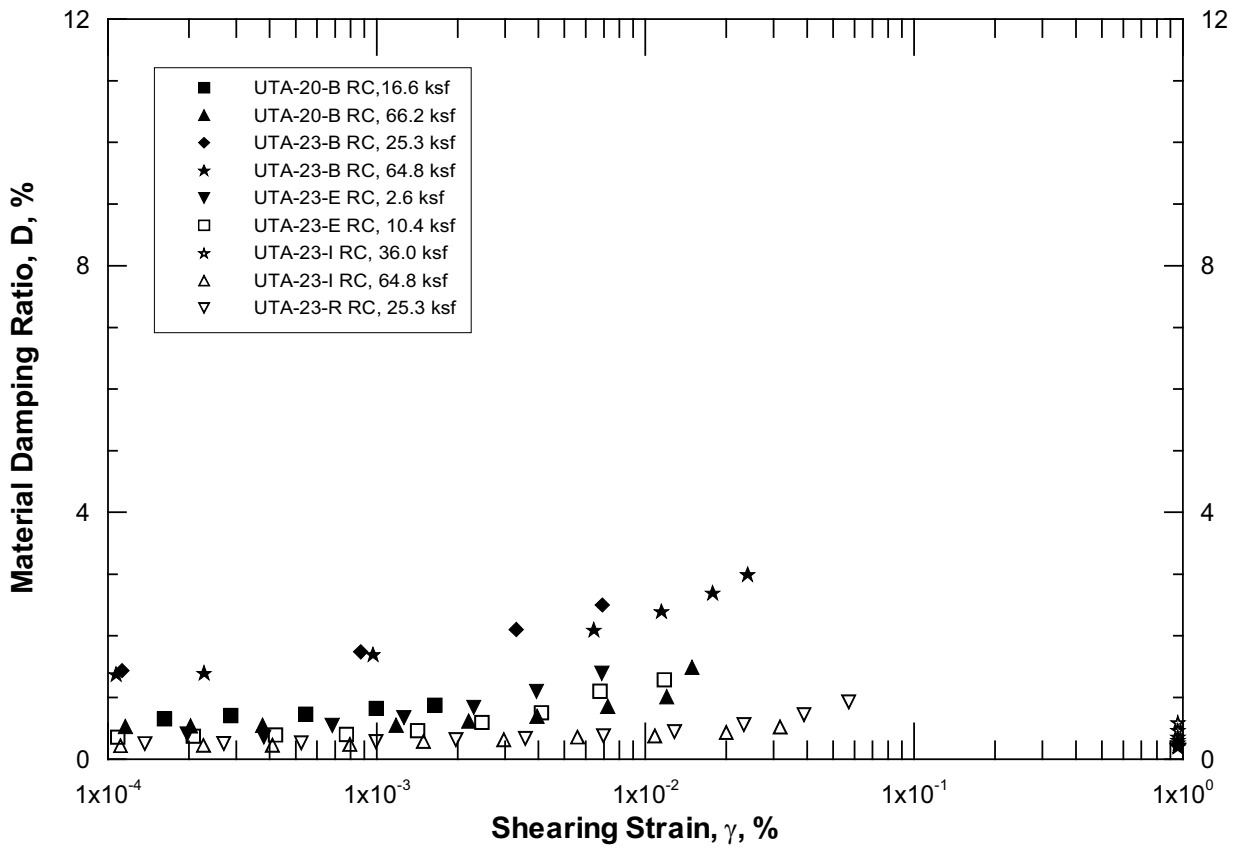
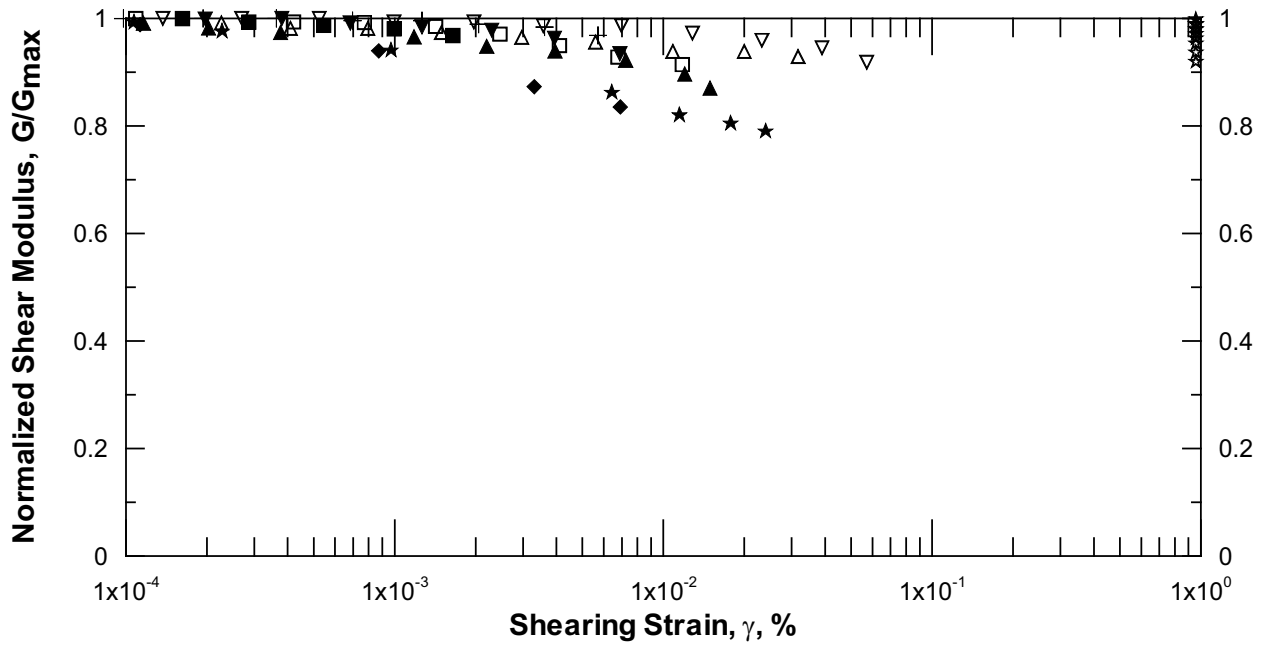
DTN: MO0203DHRSSWHB.001

Figure 132. Resonant Column and Torsional Shear Results for Tpcpmn and Tpcpln



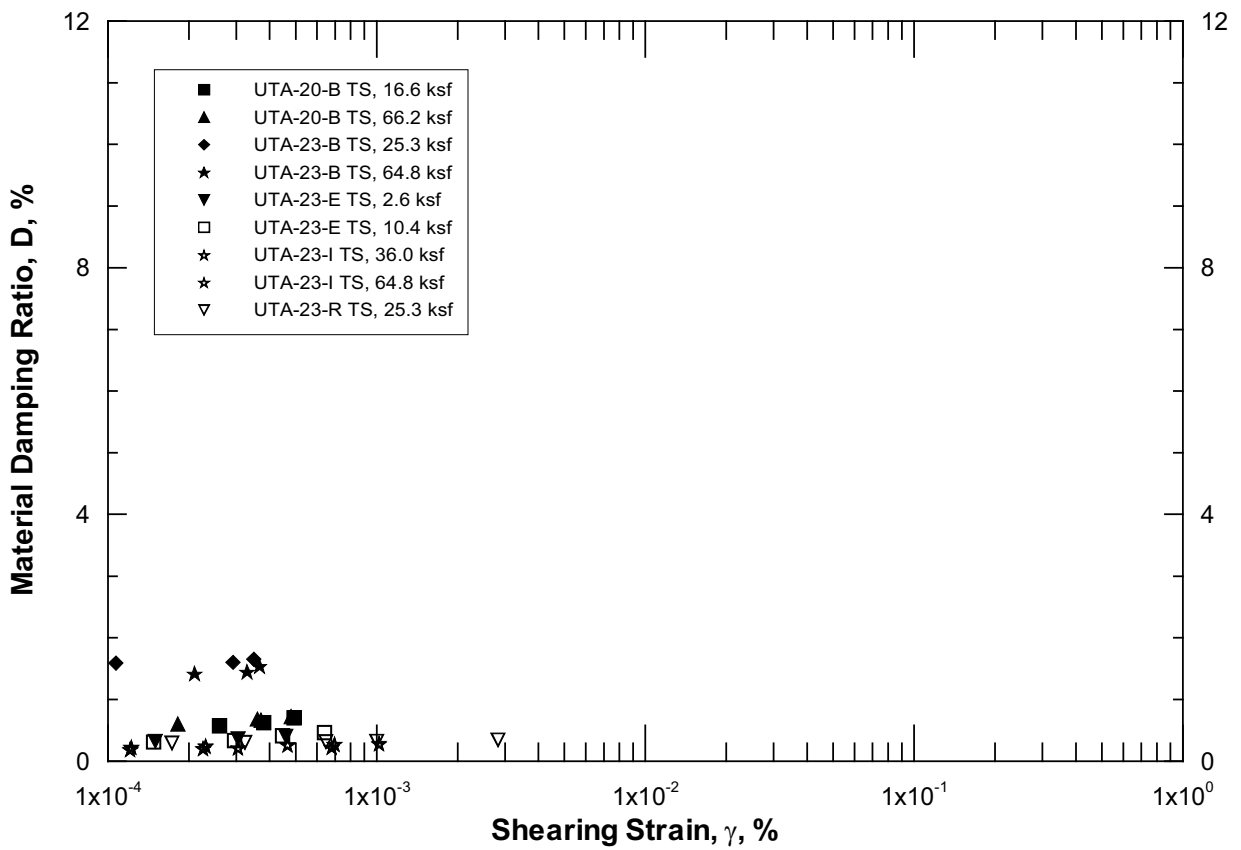
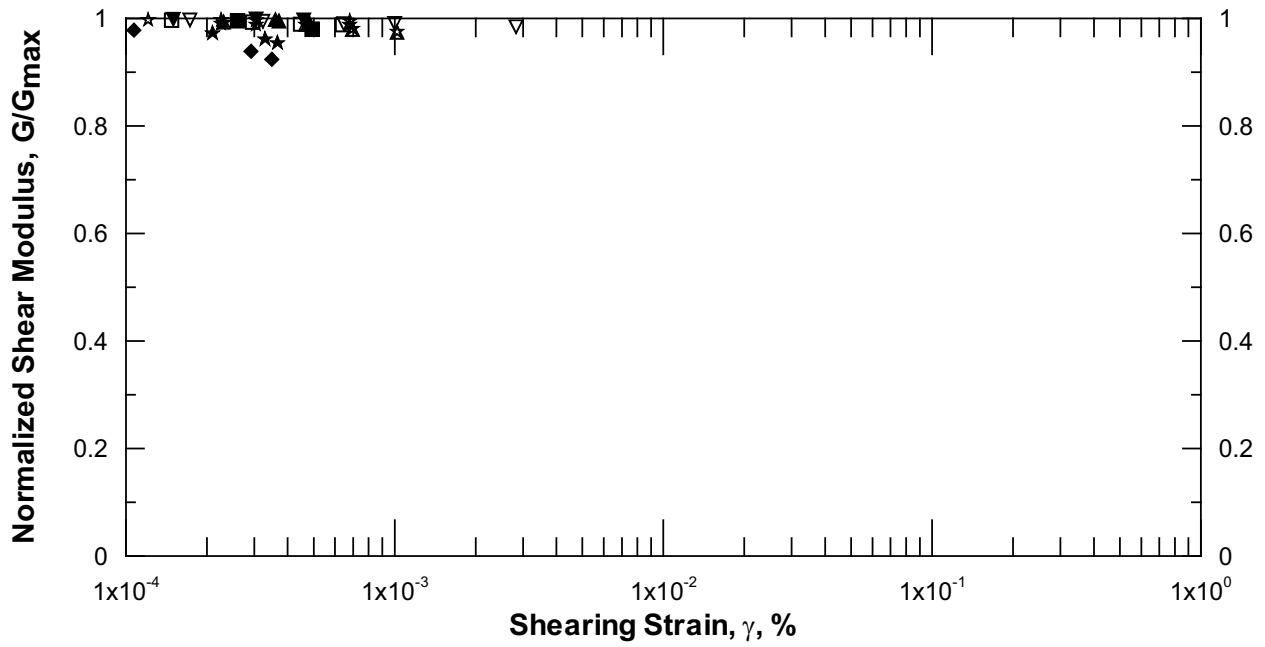
DTN: MO0203DHRSSWHB.001

Figure 133. Resonant Column and Torsional Shear Results for Tpcpul



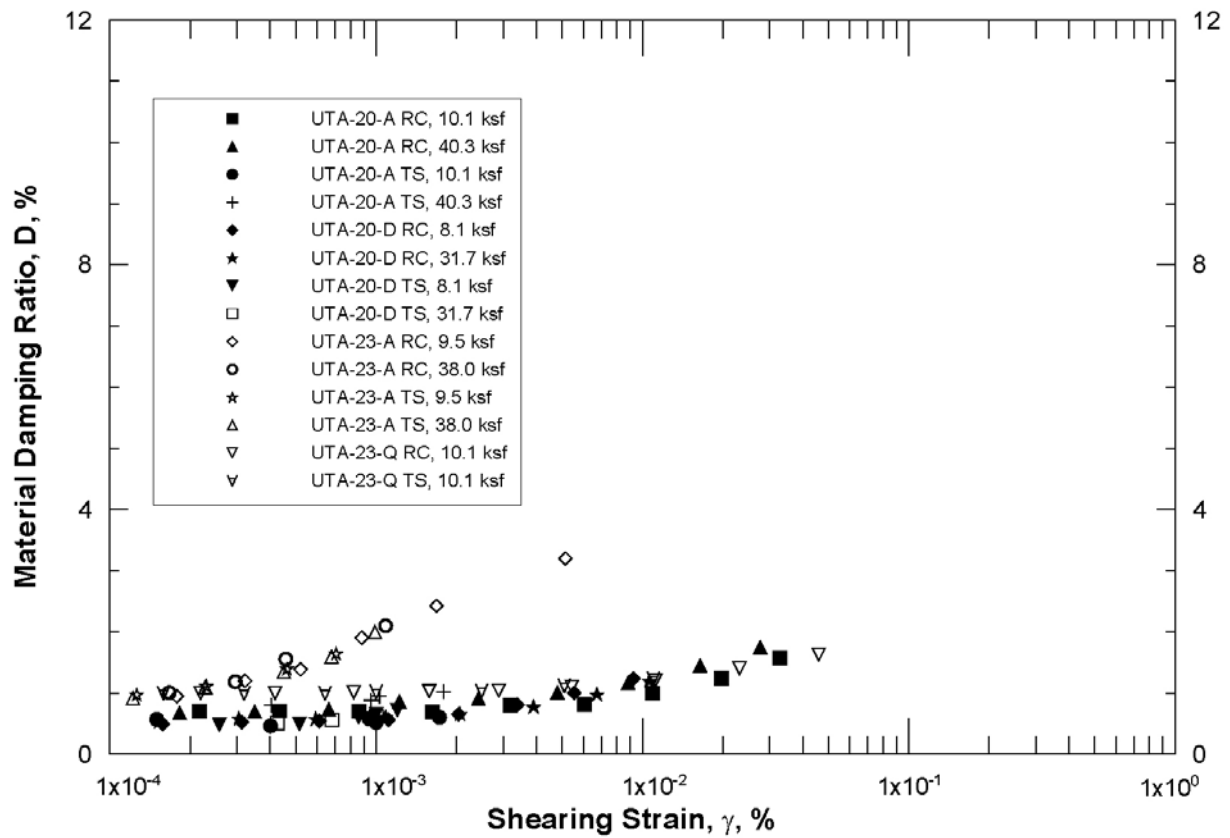
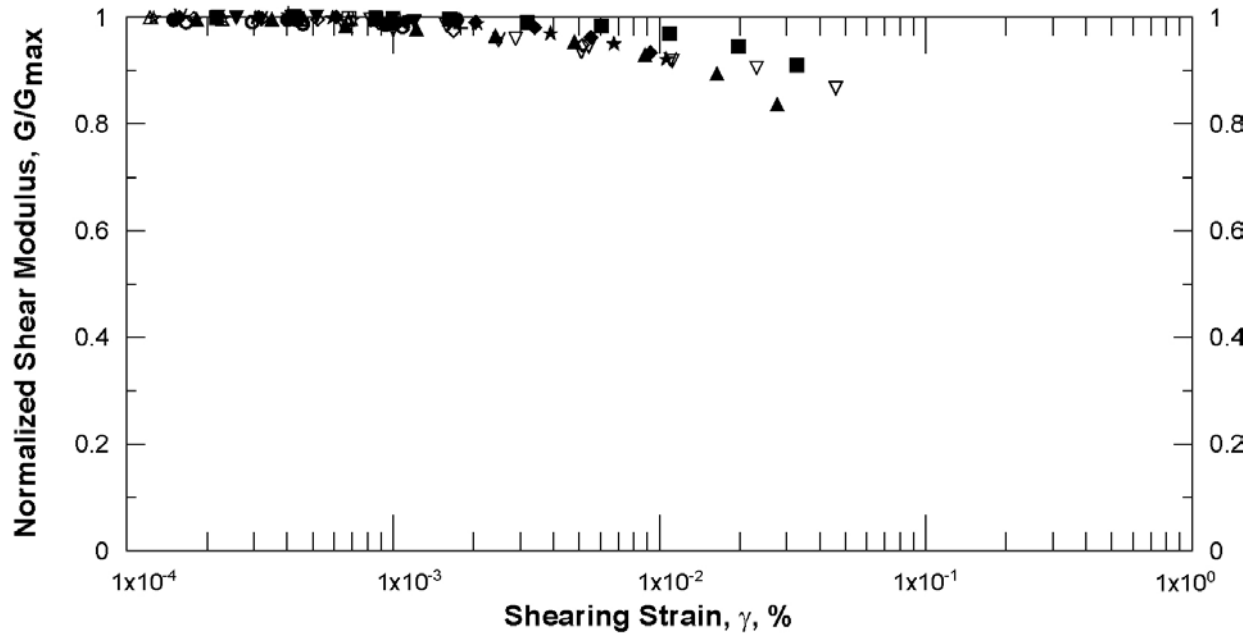
DTN: MO0203DHRSSWHB.001

Figure 134. Resonant Column Shear Results for Tpcrn



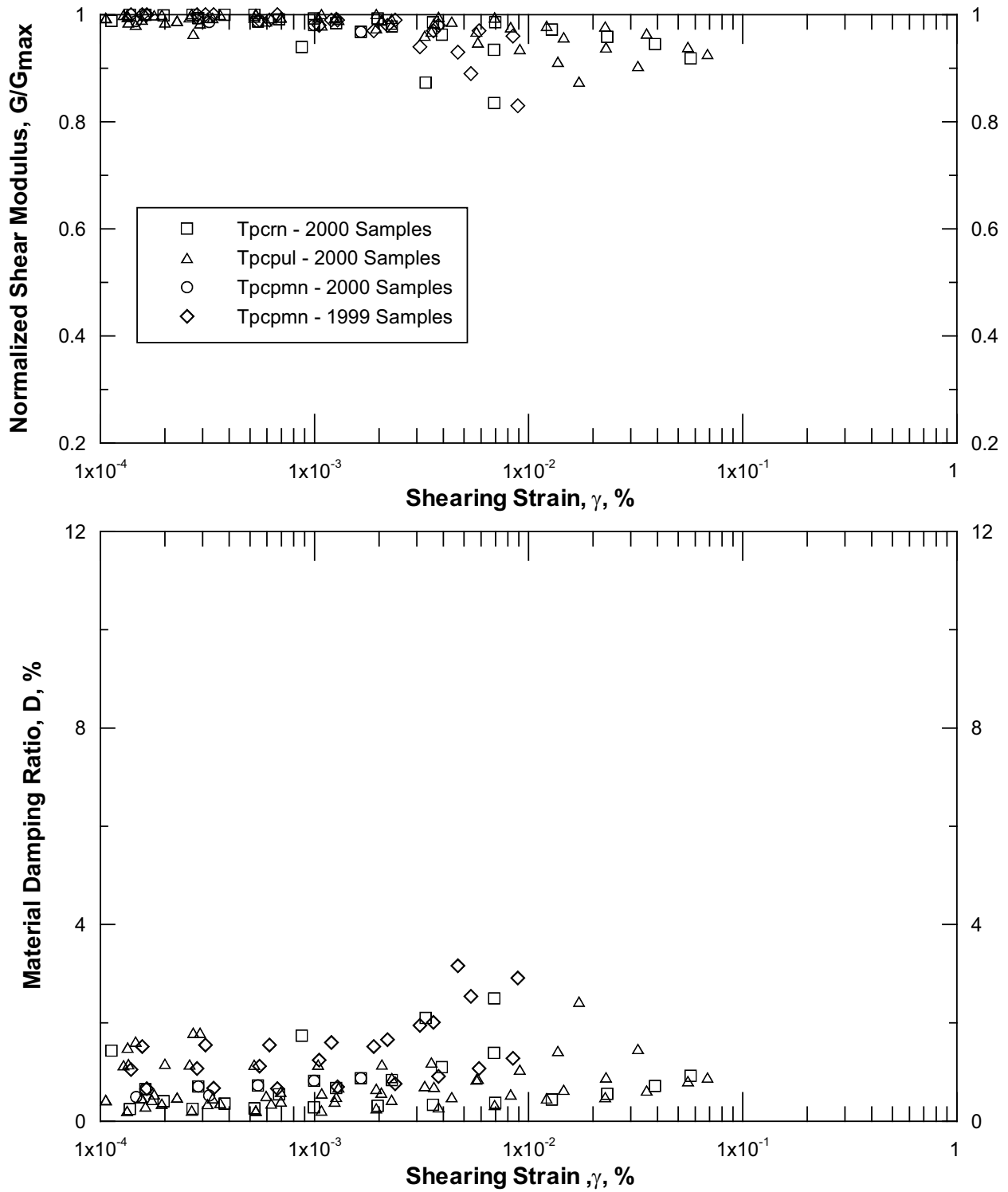
DTN: MO0203DHRSSWHB.001

Figure 135. Torsional Shear Results for Tpcrn



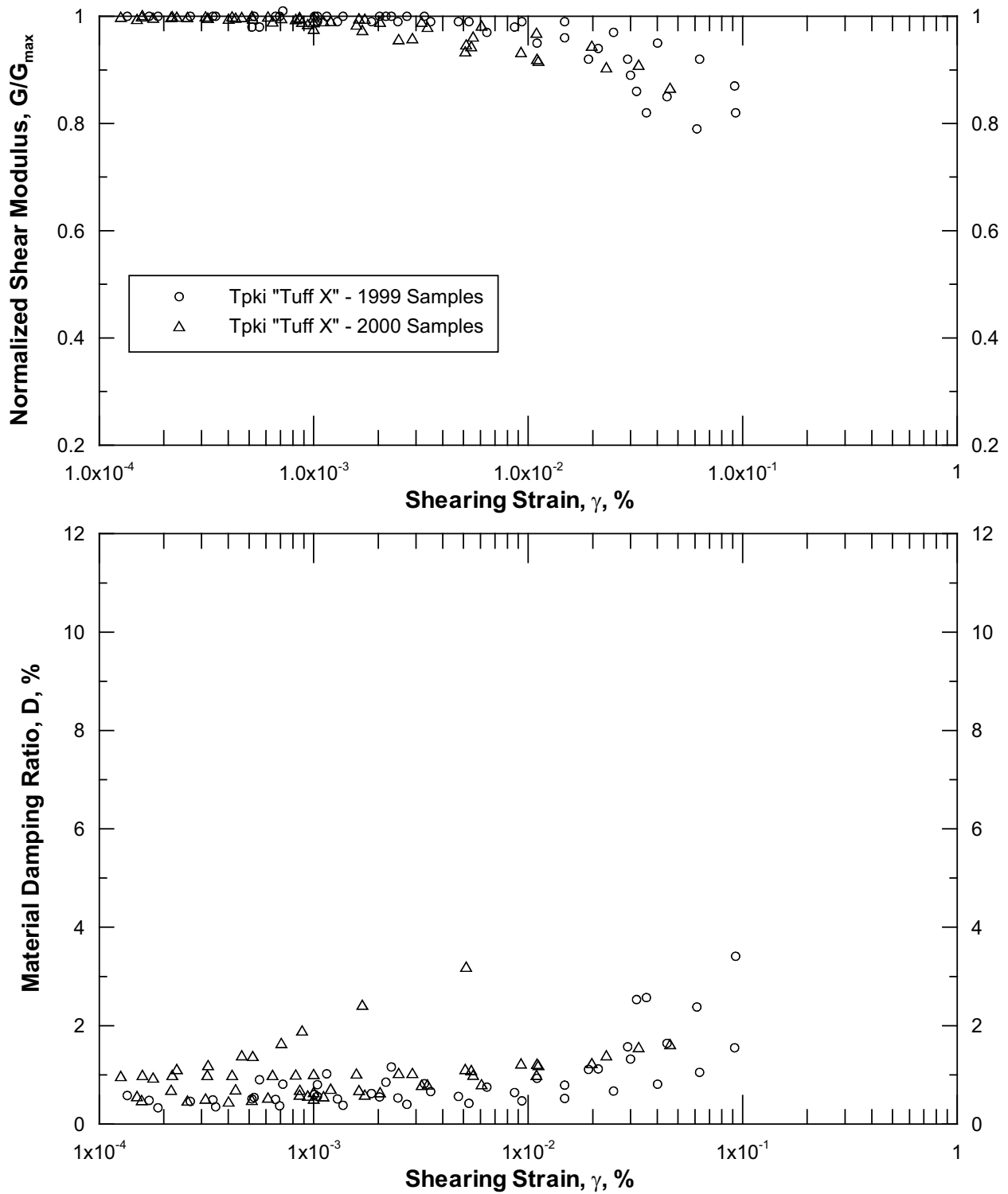
DTN: MO0203DHRSSWHB.001

Figure 136. Resonant Column and Torsional Shear Results for Tpk1



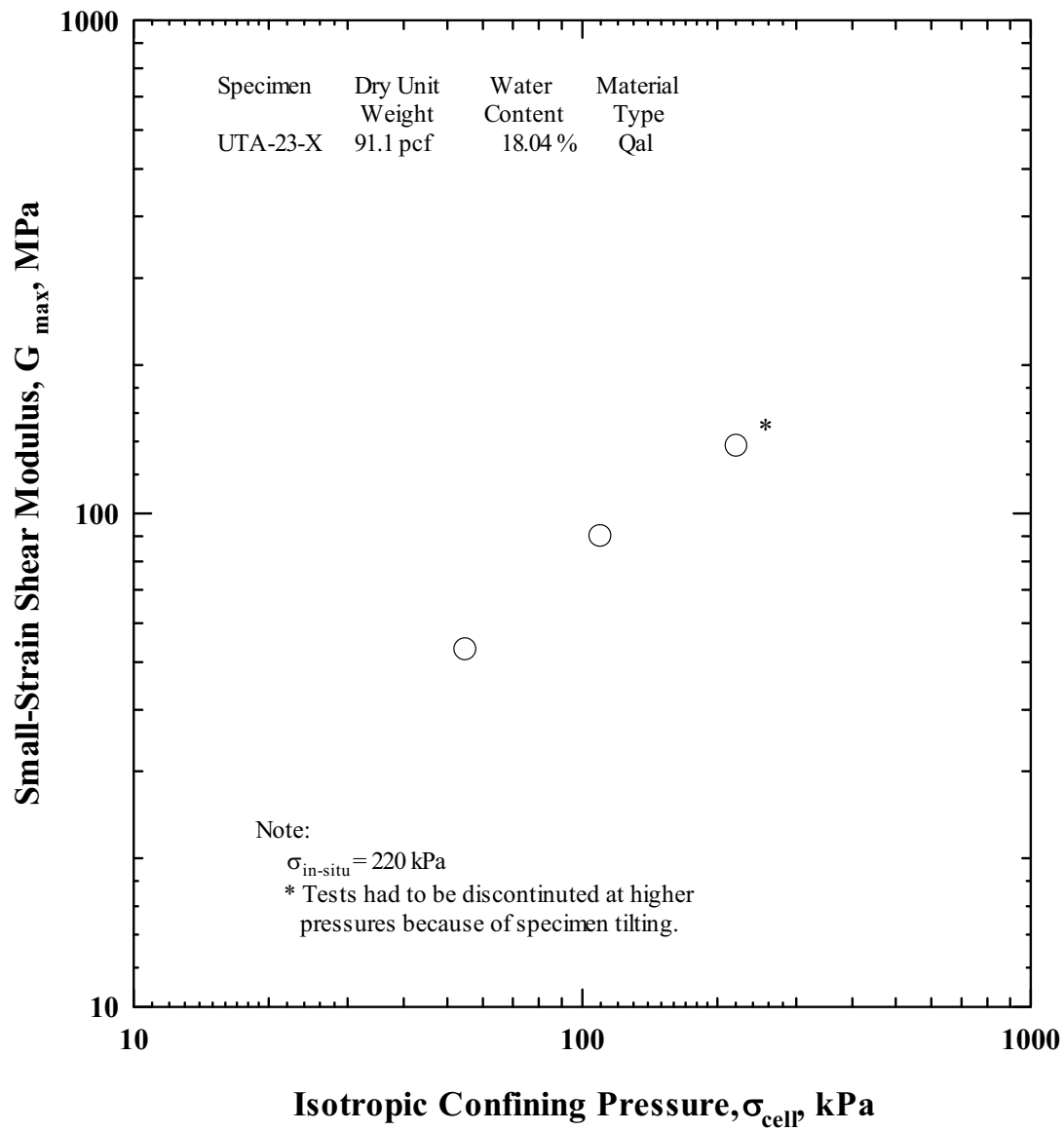
DTNS: MO0203DHRSSWHB.001, MO9905LABDYNRS.000

Figure 137. Resonant Column and Torsional Shear Results for Tiva Canyon Tuff from 1999 Study and This Study



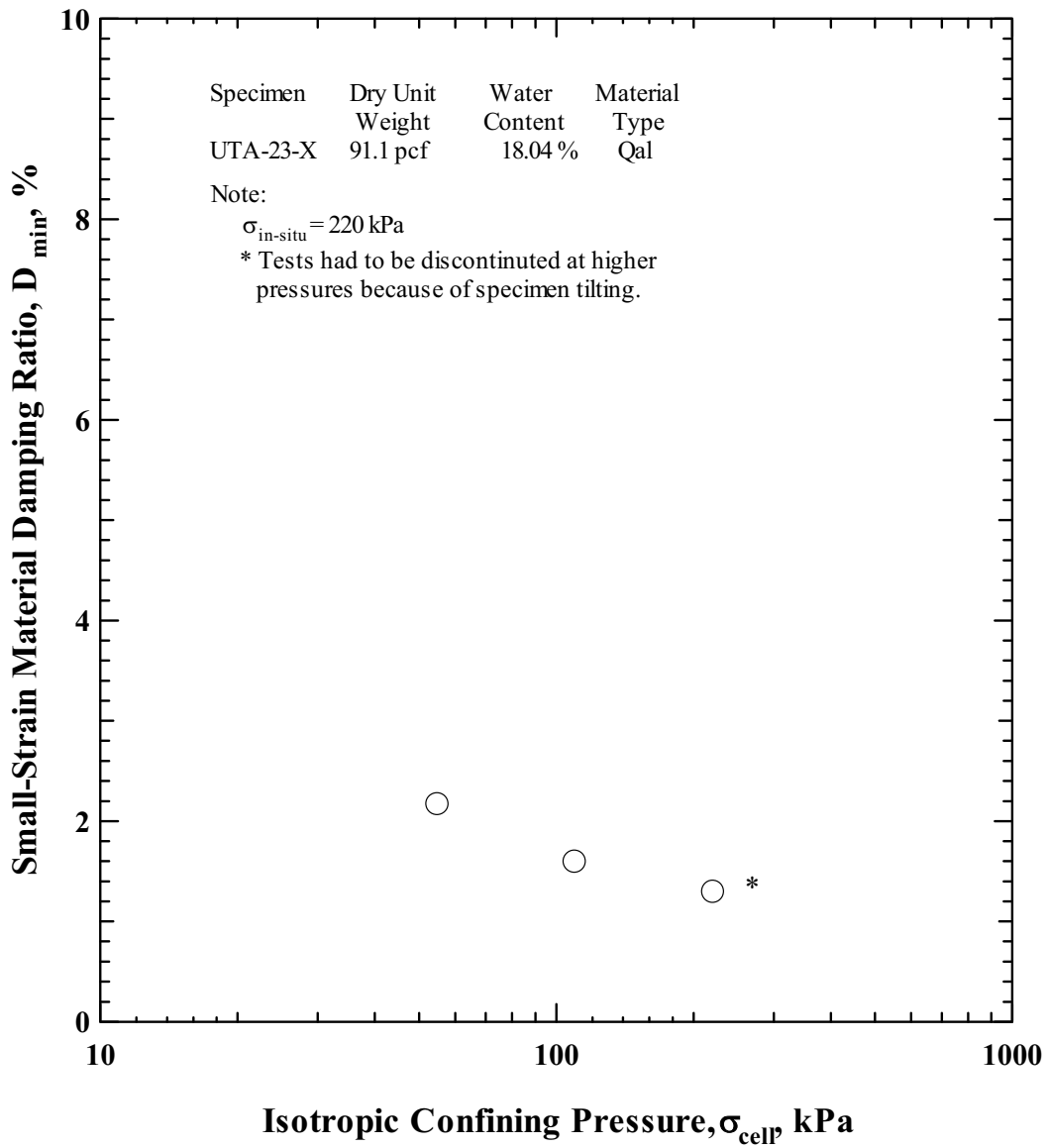
DTNS: MO0203DHRSSWHB.001, MO9905LABDYNRS.000

Figure 138. Resonant Column and Torsional Shear Results for Tpk1 from 1999 Study and This Study



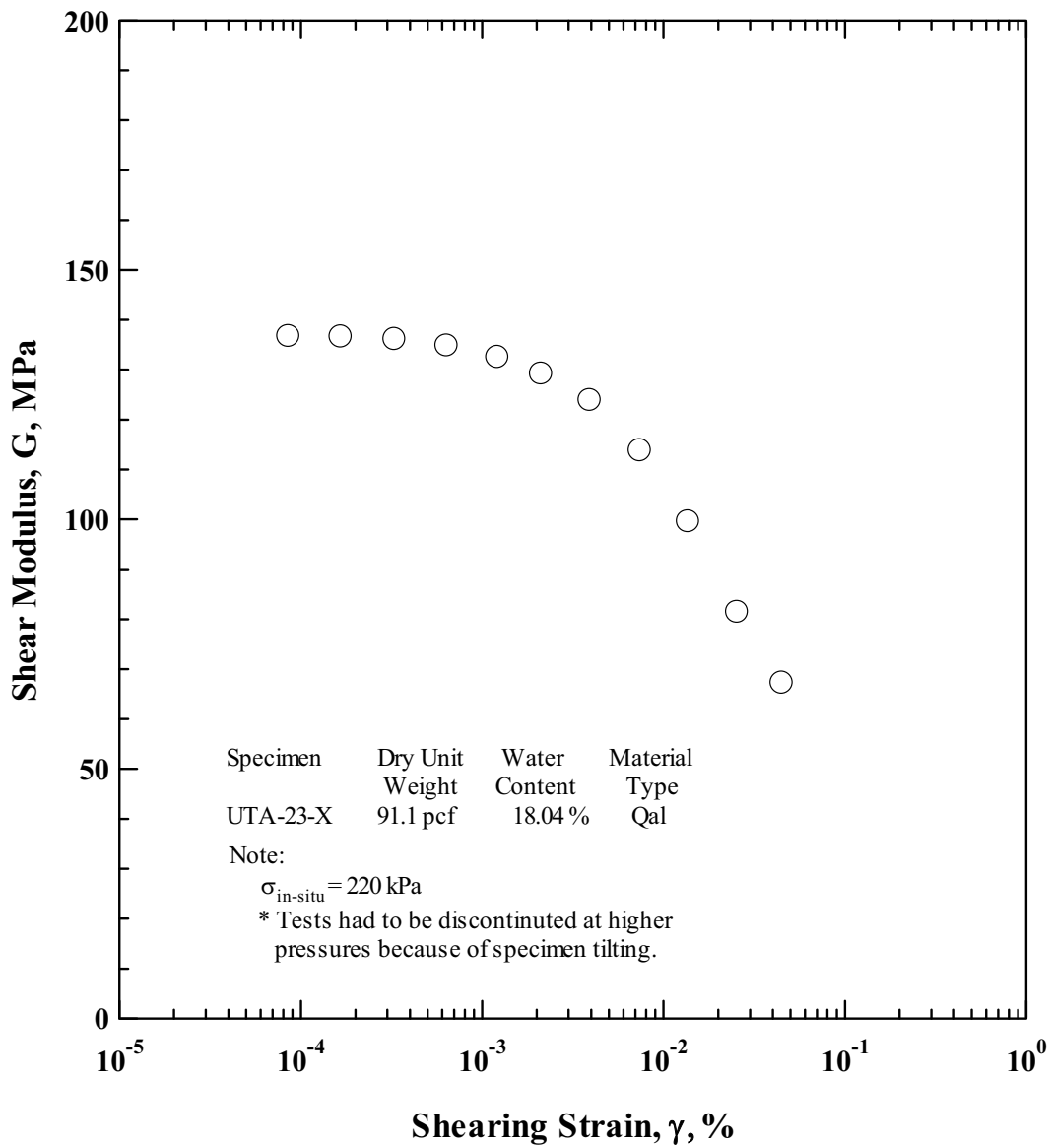
DTN: MO0203DHRSSWHB.001

Figure 139. Variation in Small-Strain Shear Modulus with Isotropic Confining Pressure of Reconstituted Quaternary Alluvium Specimen



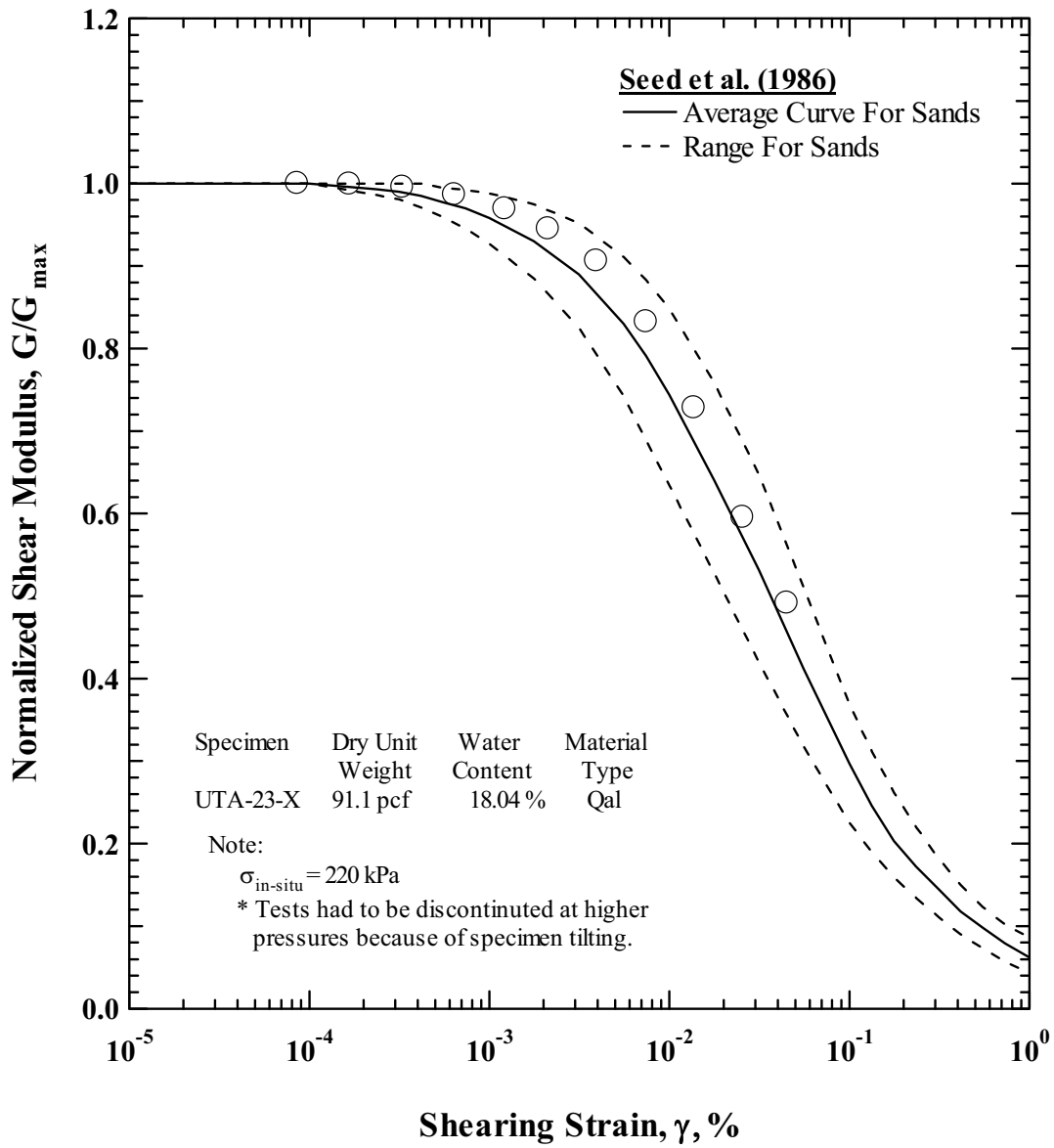
DTN: MO0203DHRSSWHB.001

Figure 140. Variation in Small-Strain Material Damping Ratio with Isotropic Confining Pressure of Reconstituted Quaternary Alluvium Specimen



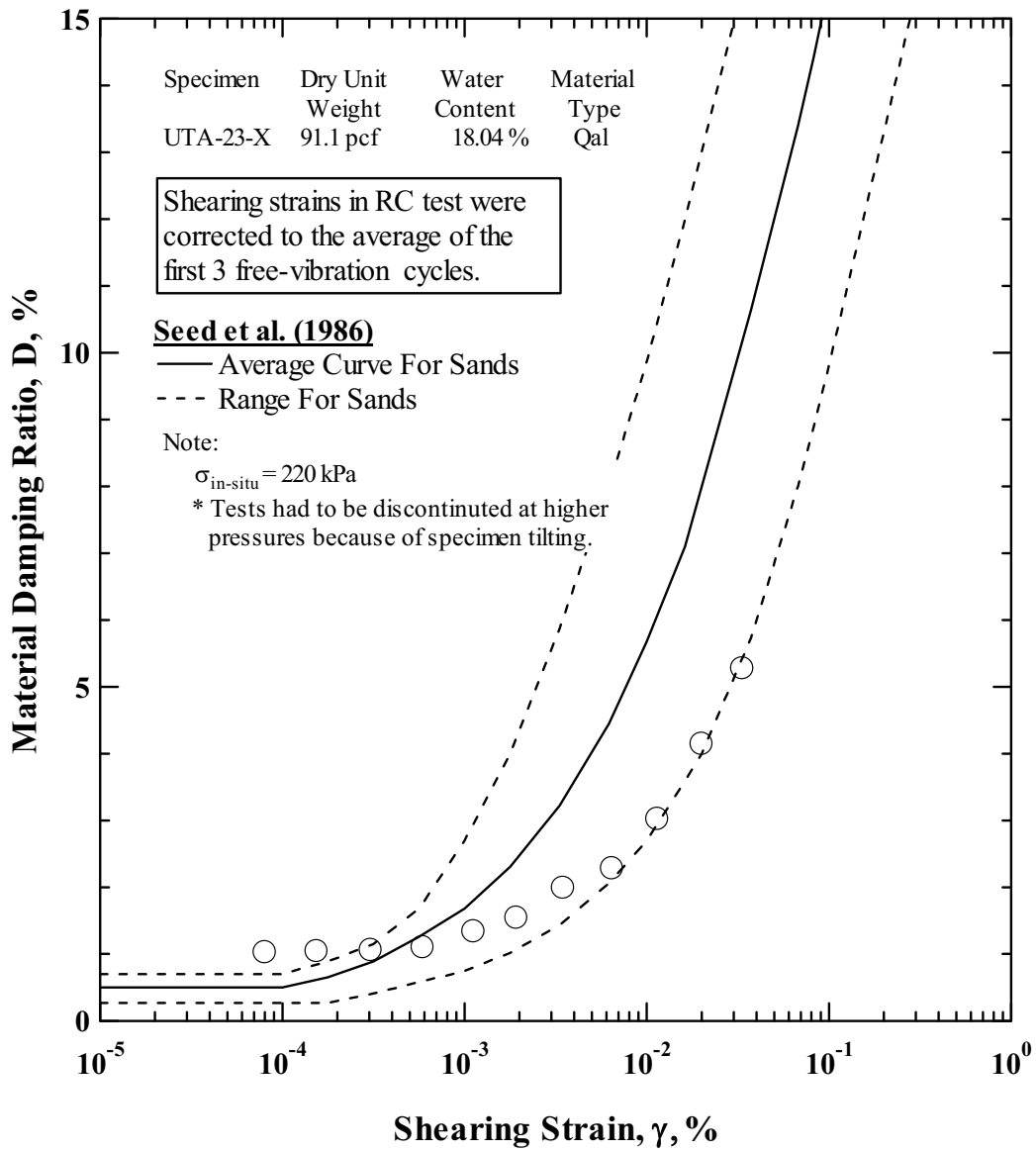
DTN: MO0203DHRSSWHB.001

Figure 141. Variation in Shear Modulus with Shearing Strain of Reconstituted Quaternary Alluvium Specimen



DTN: MO0203DHRSSWHB.001

Figure 142. Variation in Normalized Shear Modulus with Shearing Strain of Reconstituted Quaternary Alluvium Specimen



DTN: MO0203DHRSSWHB.001

Figure 143. Variation in Material Damping Ratio with Shearing Strain of Reconstituted Quaternary Alluvium Specimen

6.3 DATA ACQUIRED IN THE ESF MAIN DRIFT

6.3.1 Overview

SASW surveys were performed in the ESF main drift tunnel and are discussed in Section 6.3.2. Samples were taken by coring into the tunnel wall; the results of laboratory RCTS tests on these samples are discussed in Section 6.3.3.

6.3.2 SASW Surveys

SASW surveys were performed in the ESF in July 2001 by UTA. A total of five surveys were performed along the north-south drift in the ESF (Figure 144). The purpose of these measurements was to provide information on the shear-wave velocity structure between the potential emplacement area and the crest of Yucca Mountain. As described later in Sections 6.4.2 and 6.4.3, SASW and downhole velocity surveys were performed on top of Yucca Mountain. However, data were only obtained to depths of about 700 ft and thus shear-wave velocity information was lacking for the depth range of 700 to 1,000 ft immediately above the emplacement area. To help constrain the deeper portion of the shear-wave velocity model, surveys were performed in the ESF.

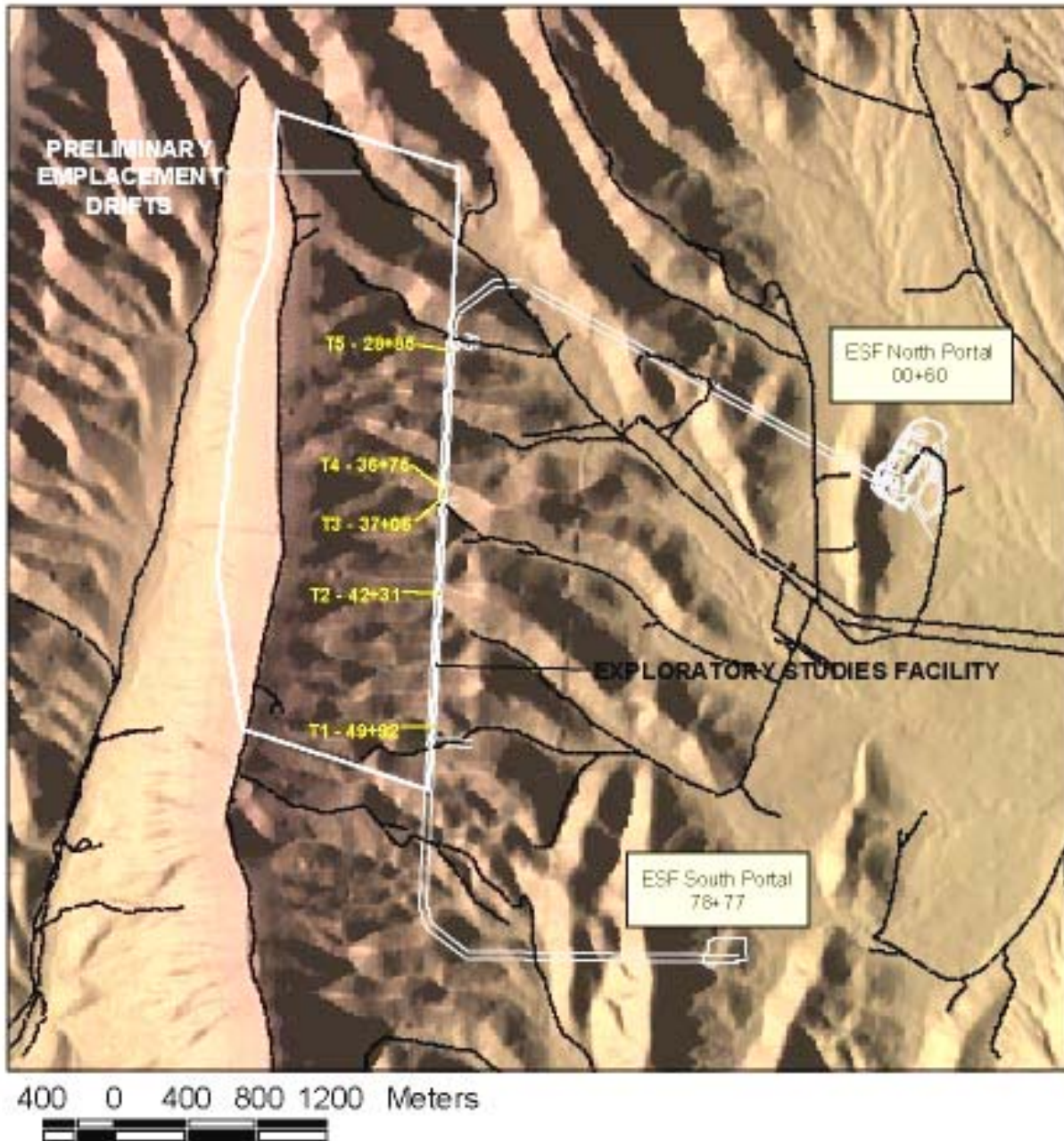
6.3.2.1 Approach

Descriptions of the approach used in the SASW surveys are presented in Section 6.2.7.2 and in Section 6.4.2.1 and only differences from that approach are described below. Details of the investigations are described in Scientific Notebook SN-M&O-SCI-040-V1 (Wong 2002a).

Five locations along the main drift of the exploratory tunnel wall (rib) were surveyed using the SASW method. The five locations, denoted as T-1 through T-5, are shown on Figure 144. All surveys were performed on the west rib at a height of about 4 to 5 ft above the tunnel invert.

The sites were selected to represent a range in materials exposed along the main drift. T-1 and T-3 had highly fractured tuff at the surface. In addition, at T-1, the rock sounded “hollow” at many places along the rib. T-2, T-4, and T-5 exhibited much less fracturing, with T-2 showing only a few fractures over the maximum receiver spacing of 32 ft. It should be noted that there were locations where the rock was more fractured than at T-1 and T-3, but these sites were not surveyed due to time constraints and the increased difficulty in making measurements on fractured tuff. No area was surveyed where metal ground support was installed. Visually, such sites along the tunnel exhibited considerably more fracturing than any of the five SASW sites, which is consistent with the need for support.

Wilcoxon Model 736 accelerometers were used for receivers. They were coupled to the rock surface with magnets applied to nails inserted into drilled holes. Common receivers-midpoint geometry (Section 6.2.7.2) was used in the ESF. Receiver spacings of 6 inches and 1, 2, 4, 8, 16, and 32 ft were generally used. Various impact hammers ranging from a 4 oz. hammer to a 6 lb. sledgehammer were used to excite the surface wave energy along the tunnel wall.



Source: Wong (2002a, Appendix 38, Figure 6)

Figure 144. Locations of SASW Surveys in the ESF

6.3.2.2 Results

The shear-wave velocity profiles are shown on Figures 145 to 149. The dispersion curves are included in Attachment XIII. T-2 and T-5 show the highest shear-wave velocities (ranging from 6,000 to 7,000 ft/s) and these values begin within 0.5 ft of the exposed surface (Figures 146 and 149). T-3 and T-4 show a transitioning of shear-wave velocities from around 2,000 ft/s at the tunnel wall to values ranging from 5,100 to 6,250 ft/s at distances of 3 ft and greater into the tunnel wall (Figures 147 and 148). For T-3, T-4, and T-5, the low velocities at the shallow depths into the tunnel wall are probably due to the effects of fracturing from the tunneling process.

T-1 shows the most scatter in the dispersion curve, which is attributed to severe fracturing. As a result of the scattering, three dispersion curves (an upper-bound, a lower-bound, and an approximate mean curve) were fit to the data; hence the reason for the three profiles on Figure 145. The shear-wave velocity profiles at T-1 have the lowest velocities at distances of 3 ft and greater into the tunnel wall. Based on the test data, the fractured tuff at T-1 extends to at least 20 ft into the tunnel wall and has an average velocity of 3,500 ft/s (Figure 145).

Figure 150 shows all the shear-wave velocity profiles obtained in the ESF surveys and Figure 151 shows the mean, median, 16th and 84th percentile profiles for just T-2 to T-5. The SASW results in the tunnel demonstrate that the intact rock with few fractures exhibit shear-wave velocity values in the range of 6,000 to 7,000 ft/s. When the tuff is fractured near the tunnel walls, these values fall into the general range of 3,000 to 4,000 ft/s. Unfortunately, with the limited number of surveys, it is unlikely that the velocities of either the softest (highly fractured) tuff or the stiffest (unfractured) tuff were measured.

6.3.3 Geotechnical Laboratory Dynamic Testing

The dynamic properties of 5 tuff specimens from the North Portal area of the ESF were evaluated in the laboratory at the Geotechnical Engineering Center at the University of Texas at Austin using RCTS equipment. The procedures are described in Section 6.2.10.1. A detailed description of the testing is contained in Scientific Notebook SN-M&O-SCI-033-V1 (Wong 2002e). The results from the dynamic testing specimens are presented in this section. The specimens were taken from stratigraphic units that are also present beneath the WHB site (Table 23). Logistical constraints limited the collection sites to within 300 meters of the North Portal of the ESF.

6.3.3.1 Measurements

Five intact tuff specimens from the ESF (Figure 113) were dynamically tested. These specimens were constructed by carefully wet-coring specimens with a nominal diameter of either 1.56 in. (3.97 cm) or 2.48 in. (6.30 cm) from larger-diameter core samples. The same procedure was used to construct the intact tuff specimens from the WHB was used with these specimens (Section 6.2.10.2). The resulting height-to-diameter ratios ranged from about 2 to 3. The initial specimen properties are listed in Table 23. The test pressures and types of tests performed on the specimens are listed in Table 24.

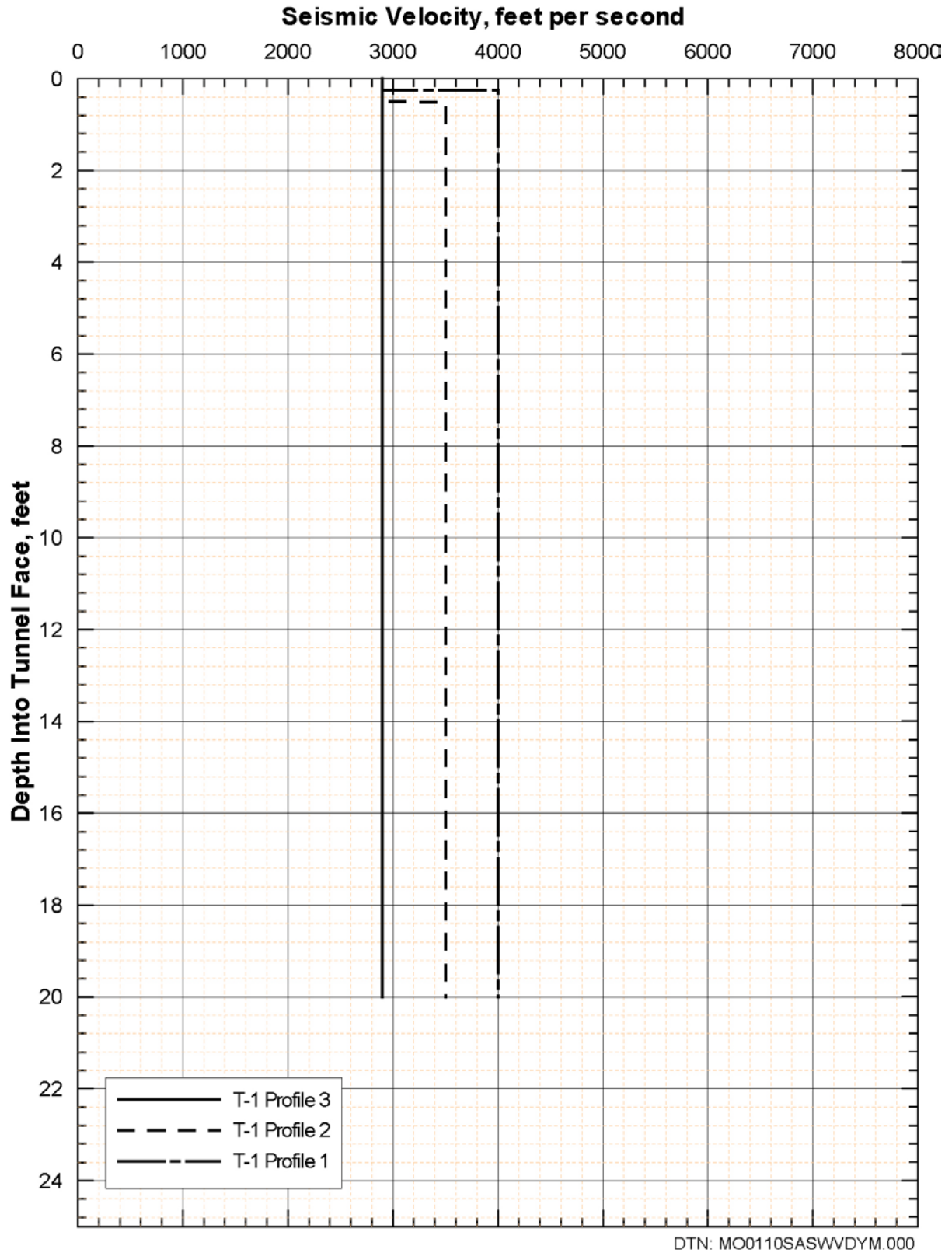


Figure 145. Shear-Wave Velocity Profiles from SASW T-1

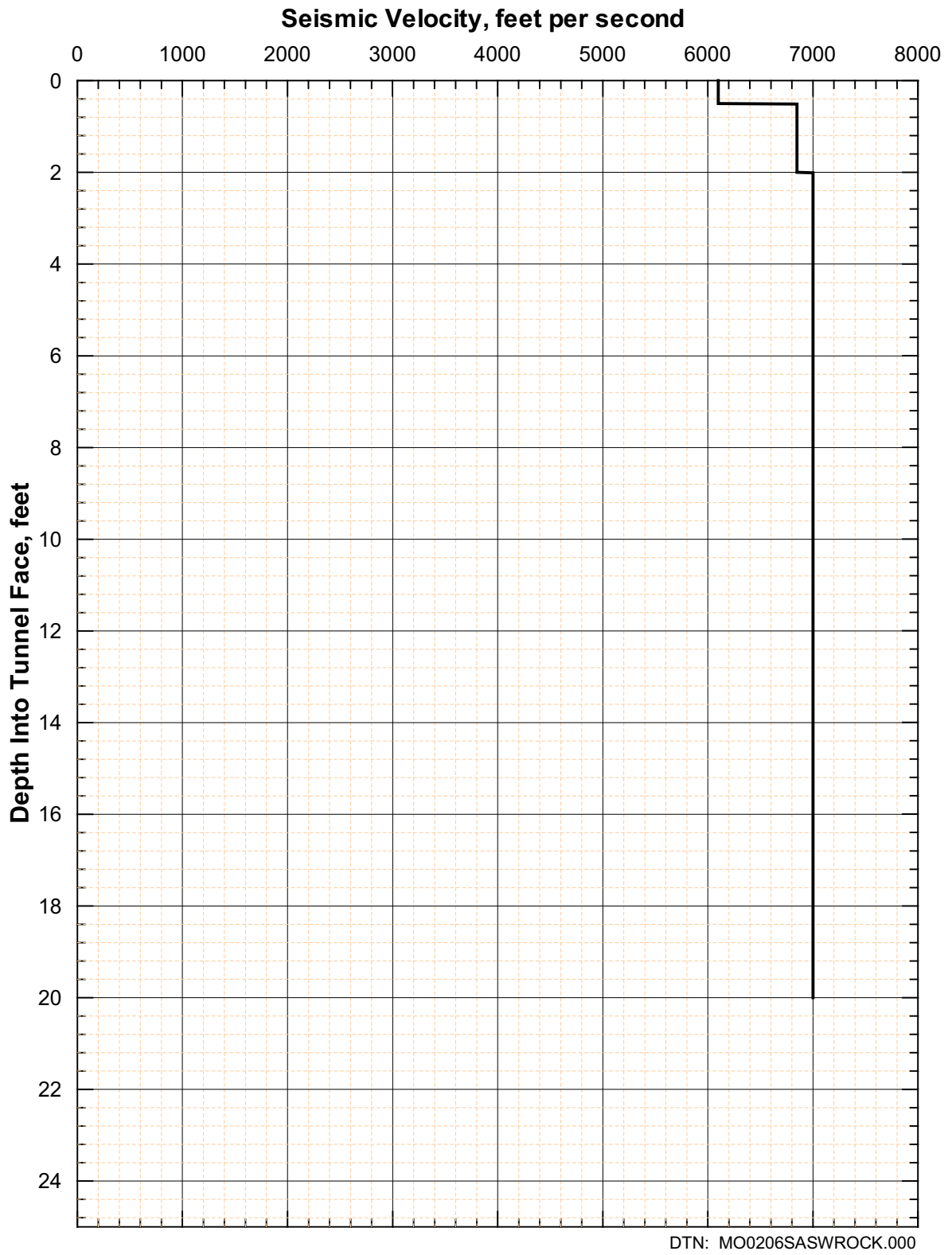


Figure 146. Shear-Wave Velocity Profile from SASW T-2

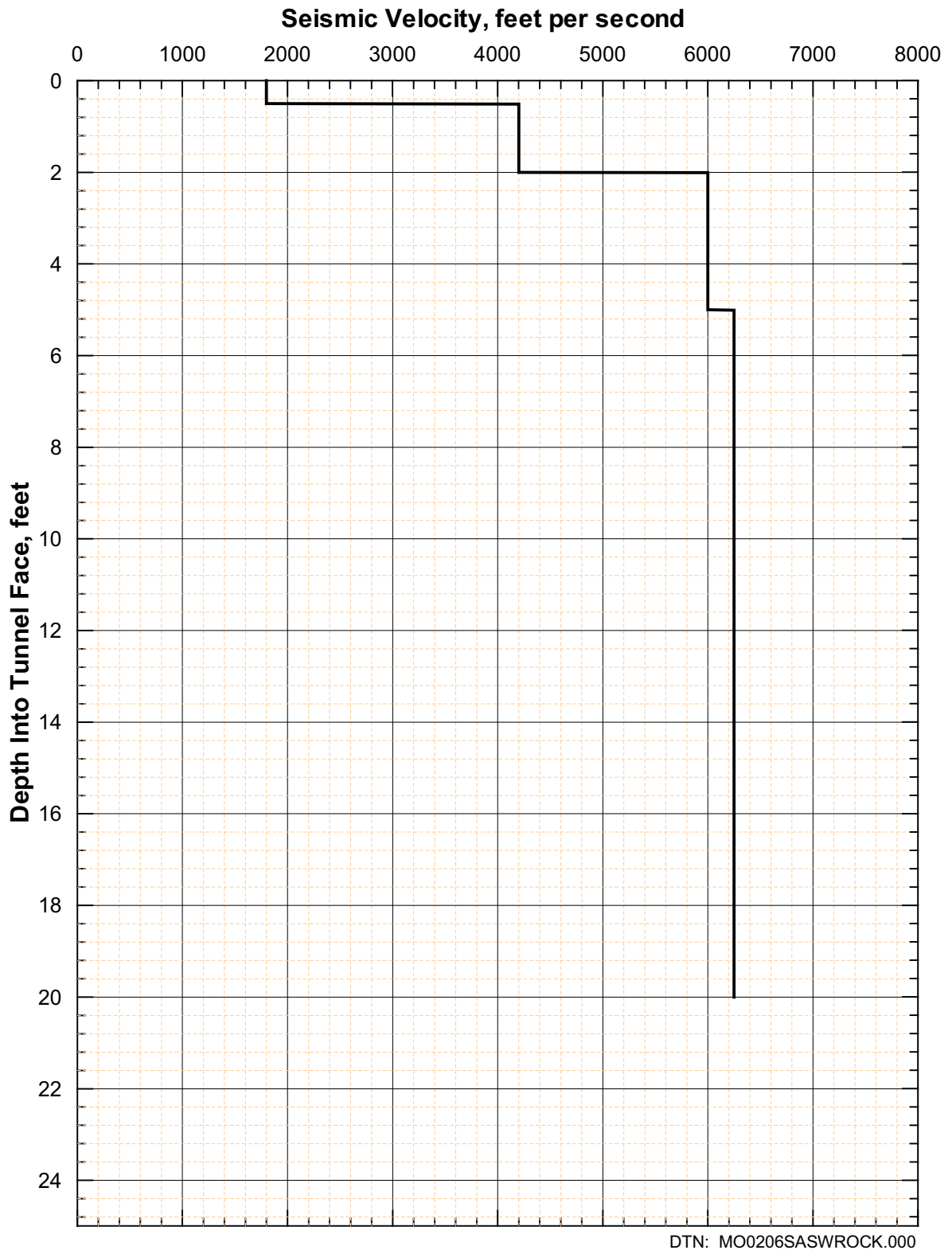


Figure 147. Shear-Wave Velocity Profile from SASW T-3

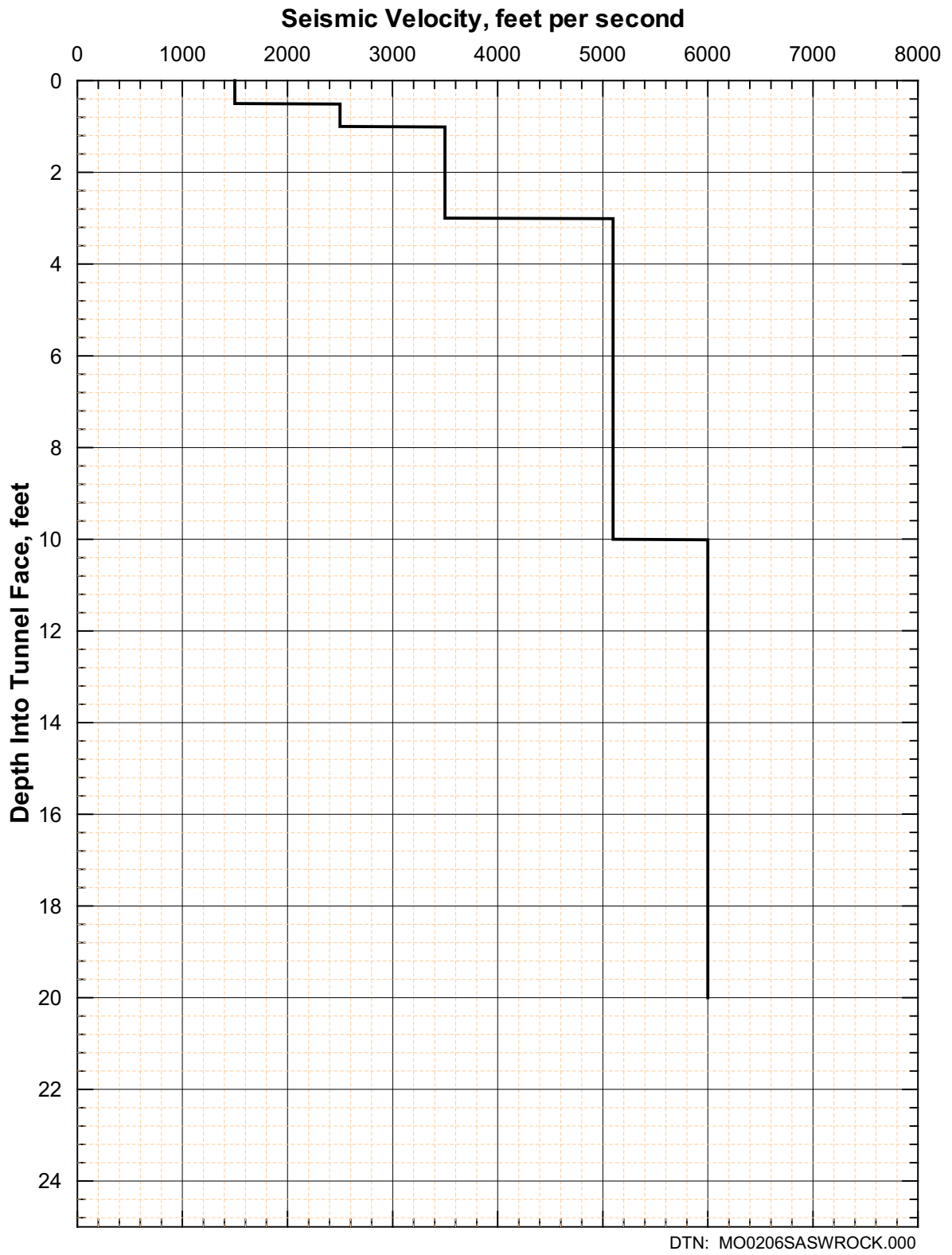


Figure 148. Shear-Wave Velocity Profile from SASW T-4

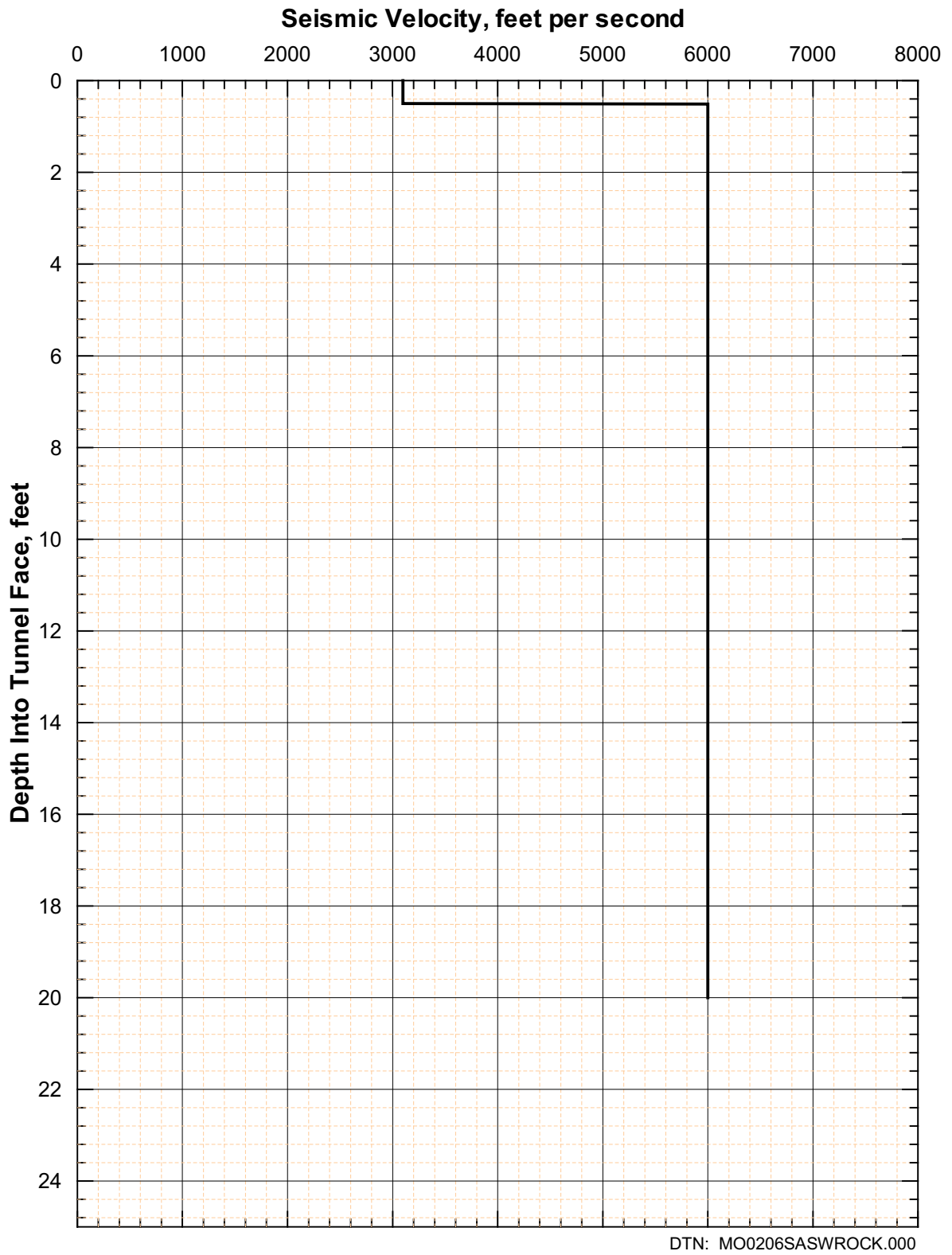


Figure 149. Shear-Wave Velocity Profile from SASW T-5

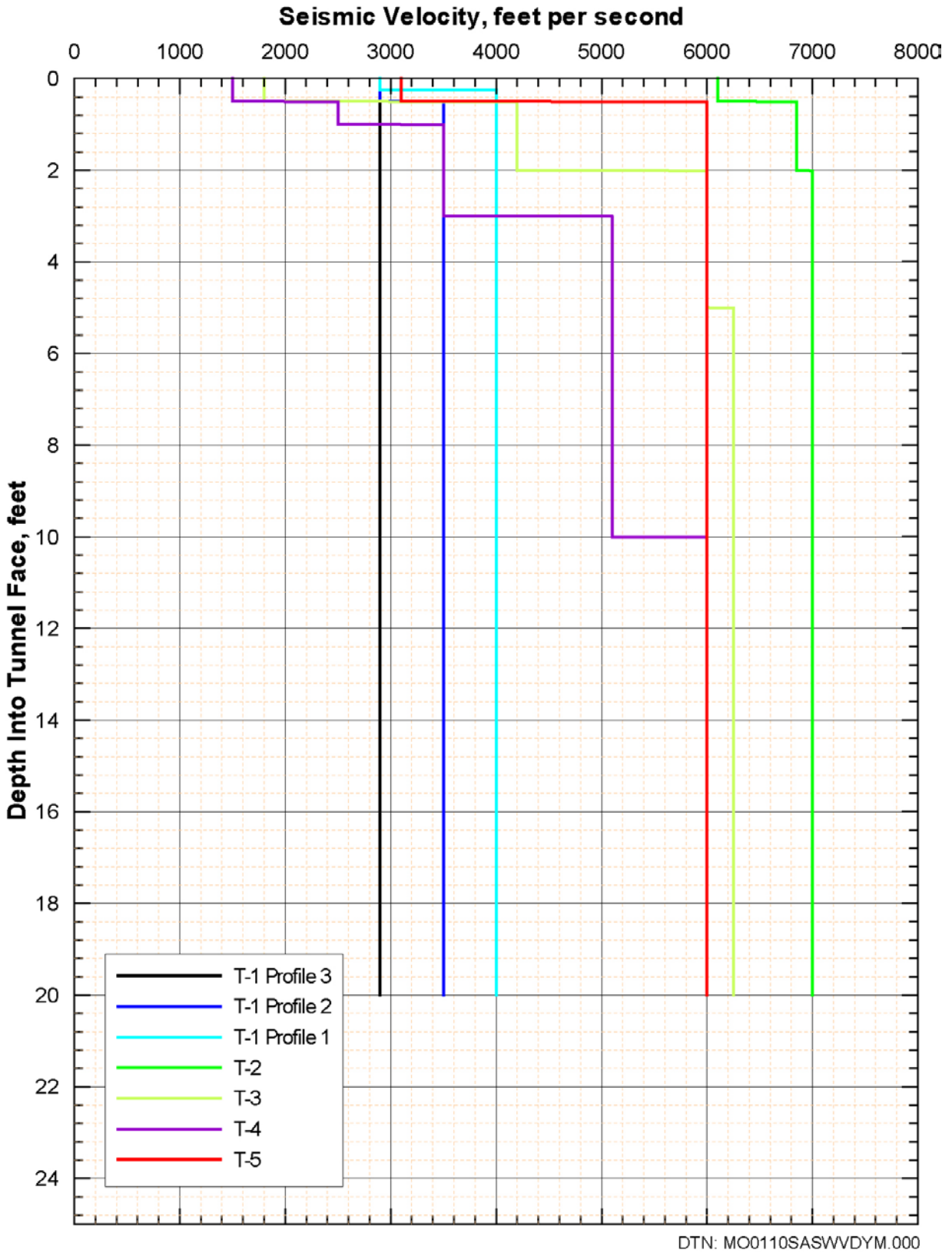
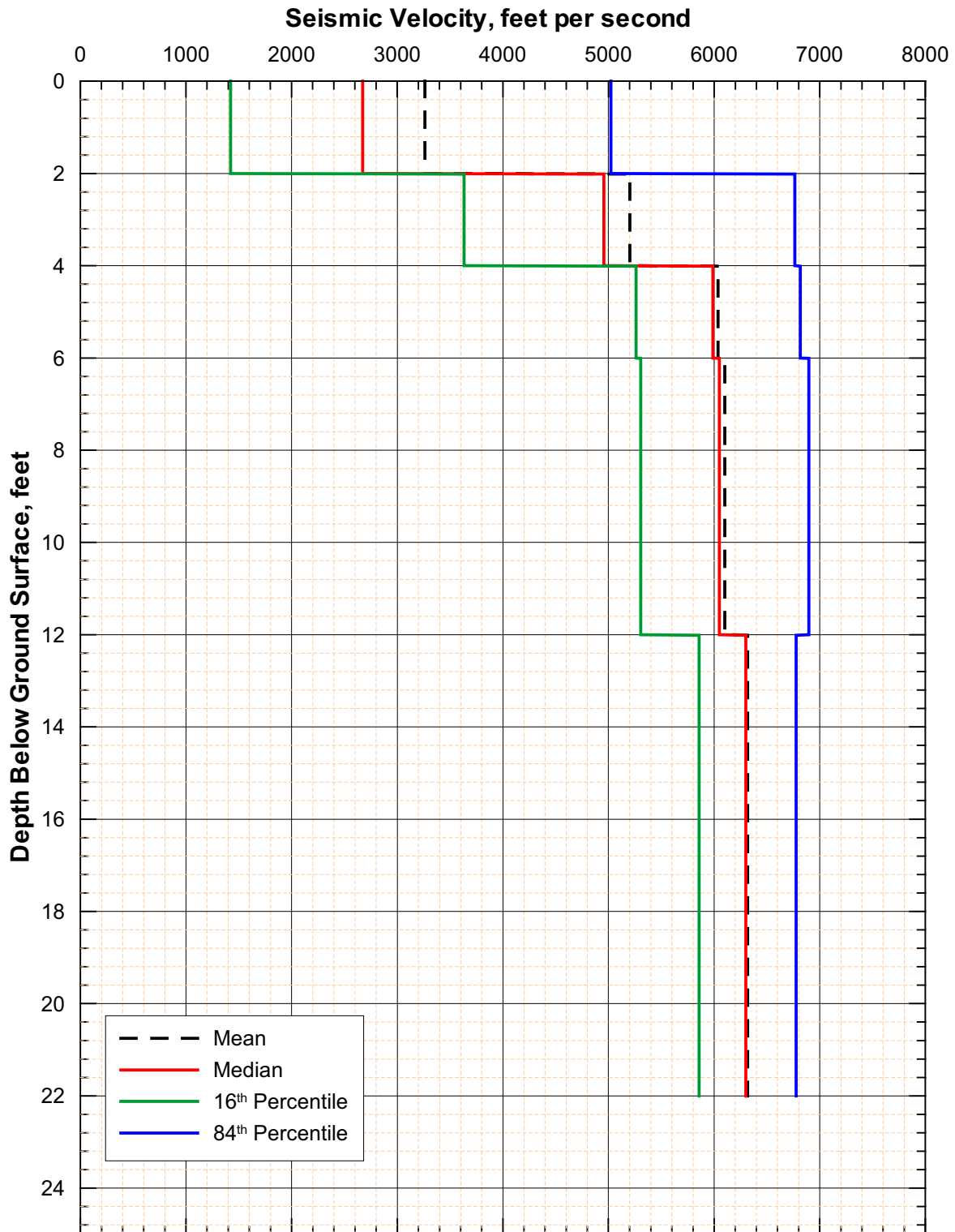


Figure 150. Shear-Wave Velocity Profiles from SASW Measurements in ESF



Note: These statistics have been calculated for illustrative purposes only. Final statistics calculated for use in the forthcoming scientific analysis entitled *Development of Seismic Design Input Ground Motions for a Geologic Repository at Yucca Mountain* will be submitted to the TDMS.

Figure 151. Statistical Analyses of Shear-Wave Velocity Profiles from SASW Measurements in ESF

Table 23. Initial Properties of Intact Tuff Specimens from the ESF

UTACED Designation	SMF Designation	Location	Depth (ft)	Lithostratigraphic Unit	Height ^a (cm)	Diameter ^a (cm)	Total Mass ^a (g)	Water Content ^a (%)	Dry Unit Weight (pcf)	Total Unit Weight ^a (pcf)
UTA-20-F	01011666	ESF-Geotek#3	4.5	Tpki	11.55	3.95	170.3	6.69	70.4	75.1
UTA-20-G	01011668	ESF-Geotek#3	6.5	Tpki	11.50	3.96	182.1	13.90	70.5	80.3
UTA-20-I	00564008	SPC-564008	0.5	Tpcrv	11.58	3.96	290.6	0.96	125.8	127.0
UTA-20-J	00564000	SPC-564000	0.5	Tmbt1	11.43	3.95	248.6	4.36	106.2	110.8
UTA-20-L	00564005	SPC-564005	0.5	Tpki	12.75	6.30	499.4	1.64	77.1	78.4

Sources DTN: MO0203DHRSSWHB.001, ^a Wong (2002e, Appendix 42, page 17)

Table 24. Confining Pressures at which RCTS Tests Were Performed on the Intact Tuff Specimens from the ESF

UTACED Designation	SMF Designation	Depth (ft)	Lithostratigraphic Unit	Estimated Mean Total Stress (psi)	Low-Amplitude RC Test Pressures (psi)	High-Amplitude RC Test Pressures (psi)	Low- and High-Amplitude TS Test Pressures (psi)
UTA-20-F	01011666	4.5	Tpki	2.4	0, 0.6, 1.2, 2.4	2.4	2.4
UTA-20-G	01011668	6.5	Tpki	4	0, 1, 2, 4	4	4
UTA-20-I	00564008	0.5	Tpcrv	10	0, 3, 5, 10, 20, 40, 80	10, 40	10, 40
UTA-20-J	00564000	0.5	Tmbt1	10	0, 3, 5, 10, 20, 40, 80, 160	10, 40	10, 40
UTA-20-L	00564005	0.5	Tpki	10	0, 3, 5, 10, 20, 40, 80, 160	10, 40	10, 40

Source: Wong (2002e, Appendix 42, page 20)

6.3.3.2 Results

The effects of normalized confining pressure on G_{\max} and D_{\min} of the 5 ESF specimens are presented in Figures 152 and 153, respectively. In general, the small-strain behavior of the tuff is quite similar to that of the tuff from the WHB area. The effects of f on G_{\max} and D_{\min} are small (Figures XIV-6 and XIV-7).

The effects of γ on G , G/G_{\max} and D are shown in Figures 154 to 156, respectively. The main differences between the ESF tuffs and those from the WHB site are that two ESF specimens show more nonlinearity in their G/G_{\max} versus $\log \gamma$ relationship (UTA-20-I and UTA-20-L in Figure 155) and one specimen (UTA-20-I) shows relatively large values of D at $\gamma > 10^{-3}\%$ (Figure 156). These differences are thought to likely be attributed to the very shallow depths behind the tunnel wall from which the specimens in the ESF were taken where disturbance from the tunnel boring process is likely to be significant and the likelihood of micro-cracking in the specimens.

6.4 DATA ACQUIRED AT THE CREST OF YUCCA MOUNTAIN

6.4.1 Overview

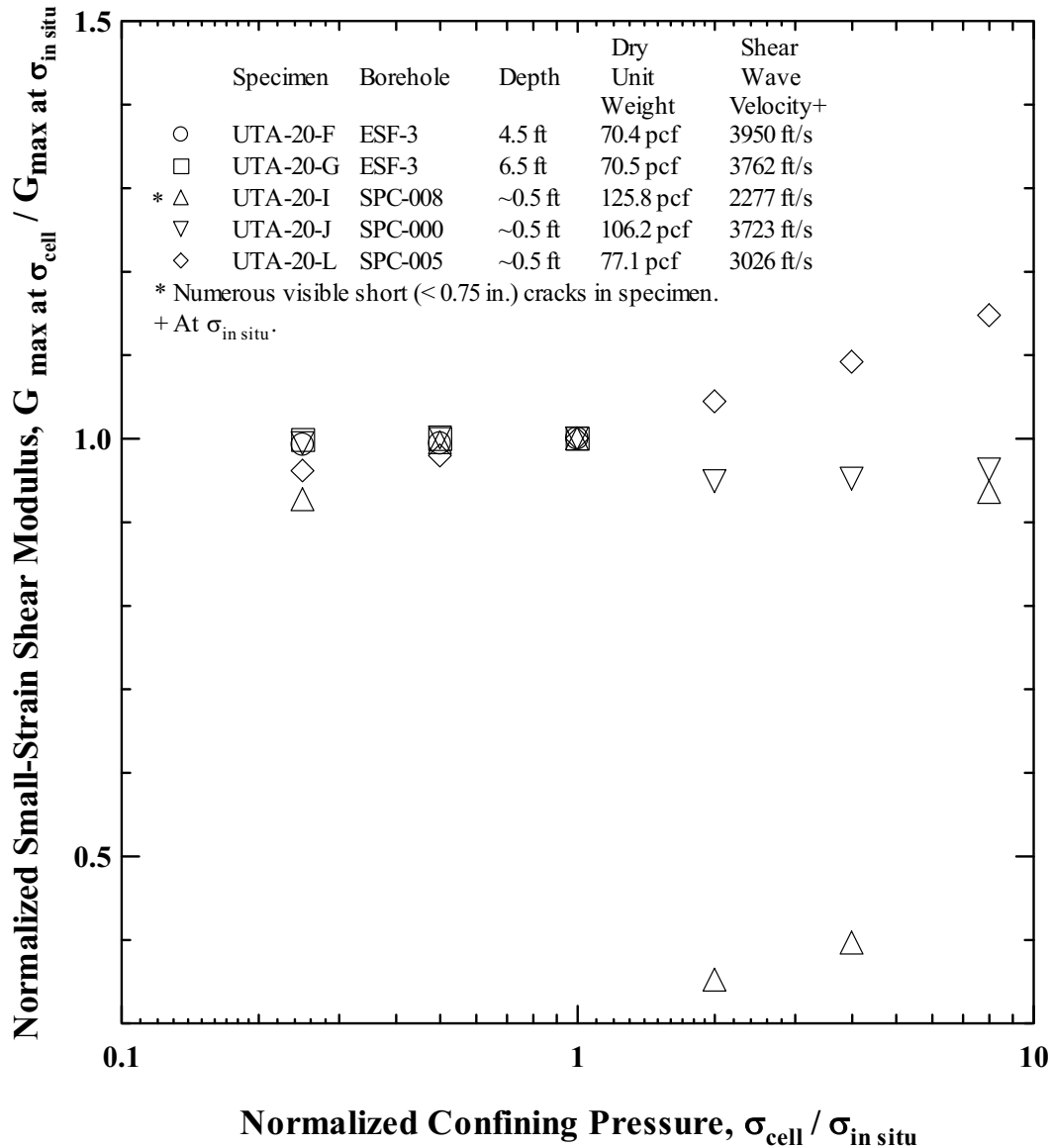
In the computation of preliminary seismic design ground motions, best-estimate, lower- and upper-bound velocity profiles were estimated based on Vertical Seismic Profiling (VSP) surveys performed at six boreholes (Daley et al. 1994). Only one borehole, SD-12, was within the surface projection of the potential emplacement area as defined in July 2001 (Figure 157). This borehole was located at the eastern boundary of the emplacement block. Thus, an adequate characterization of the seismic velocities of the block and their variability was not available. To obtain velocity information, a program of shallow downhole velocity measurements and SASW surveys along the Yucca Mountain crest and downslope (east) were undertaken in the summers of 2000 and 2001. The following describes the approaches and results of those surveys.

6.4.2 SASW Surveys

SASW surveys were performed on the top of Yucca Mountain generally above the potential emplacement area in the summers of 2000 and 2001 by UTA. In the first phase, SASW surveys were performed from 12 to 15 September 2000. The goal of these measurements was to determine the shear-wave velocity structure to depths of approximately 500 to 700 ft at several locations beneath the crest of Yucca Mountain. In total, 7 SASW surveys were carried out along the crest and these are designated with a "C" (e.g., C-1) (these lines were also referred to at one time as "CYM", including in some of the data sets).

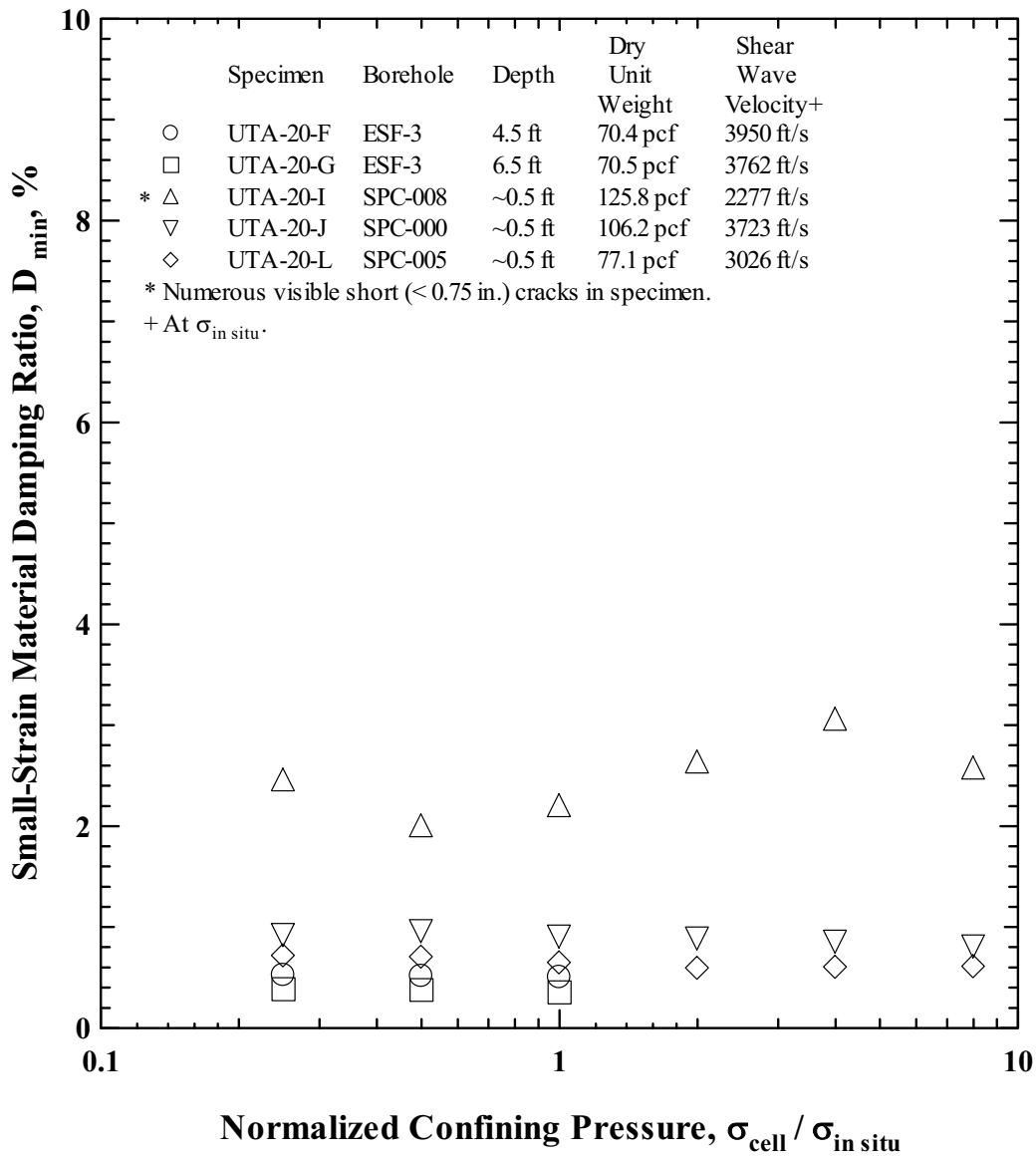
In June and July 2001, additional SASW measurements were made at 26 locations along the crest of Yucca Mountain as well as downslope to the east of the crest. Twelve of these surveys were performed to obtain shear-wave velocity profiles to depths of 150 to 200 ft. These SASW tests are designated in this report with an "S" to represent relatively shallow profiling depths (S-1 to S-12). Eleven surveys were performed to obtain profiles to depths of 400 ft or greater, where spatial access was not limited. These surveys are designated with the letter "D" (D-1 to D-11) to represent relatively deep profiling depths (survey D-12 is discussed in Section 6.2.7).

In addition to the C, S, and the D surveys, 3 sets of SASW measurements were performed on the surface of exposed rock at the crest. These tests are designated with the letter “R” for rock and are referred to as R-1, R-2, and R-3 herein. This section describes the SASW measurements, analysis procedures, and the results of the SASW surveys at the top of Yucca Mountain.



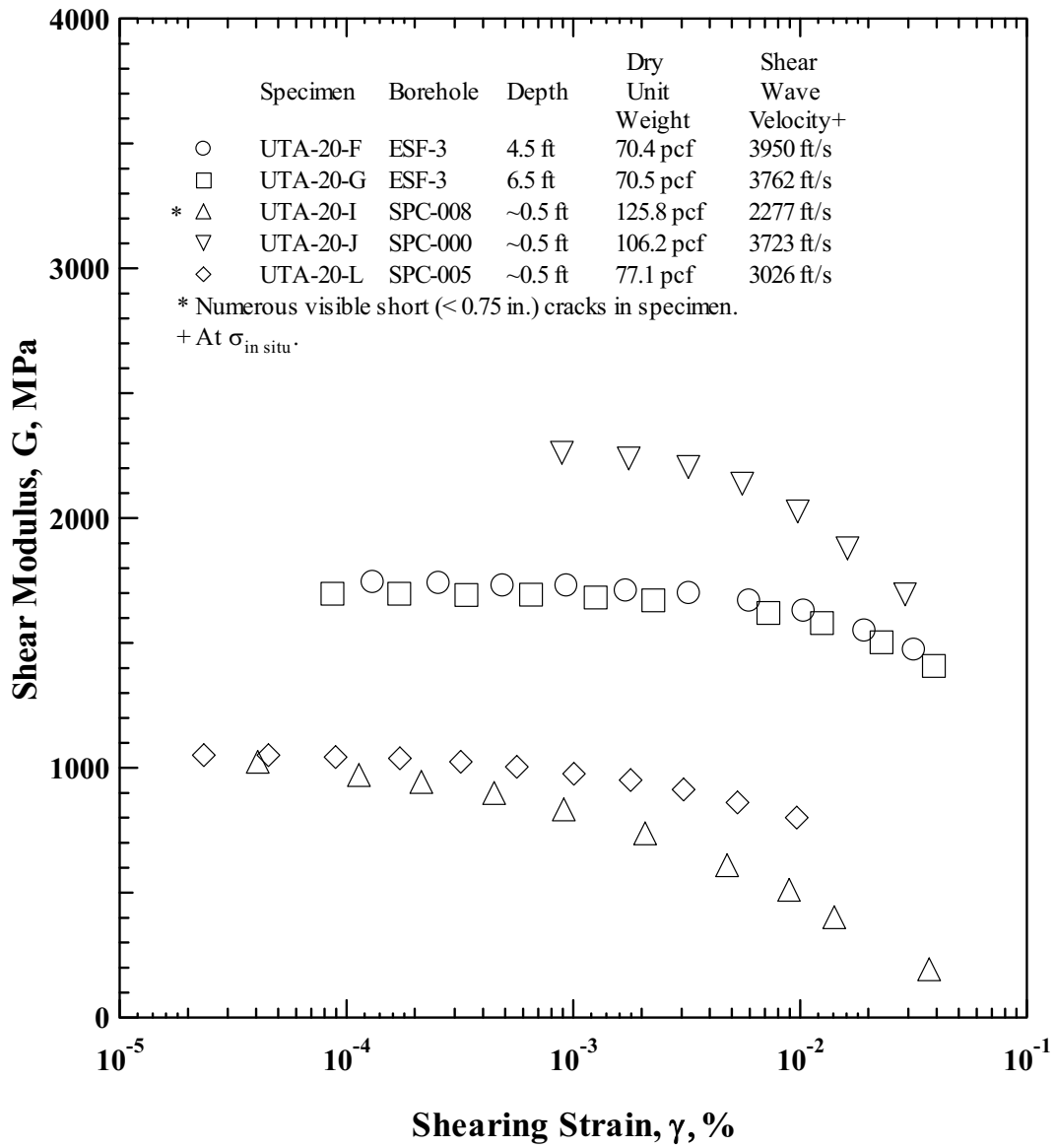
Source: Wong (2002e, Appendix 42, page 54)

Figure 152. Variation in Normalized Small-Strain Shear Modulus with Normalized Confining Pressure of Intact Tuff Specimens from the ESF



Source: Wong (2002e, Appendix 42, page 55)

Figure 153. Variation in Small-Strain Material Damping Ratio with Normalized Confining Pressure of Intact Tuff Specimens from the ESF



DTN: MO0203DHRSSWHB.001

Figure 154. Variation in Shear Modulus with Shearing Strain of Intact Tuff Specimens from the ESF

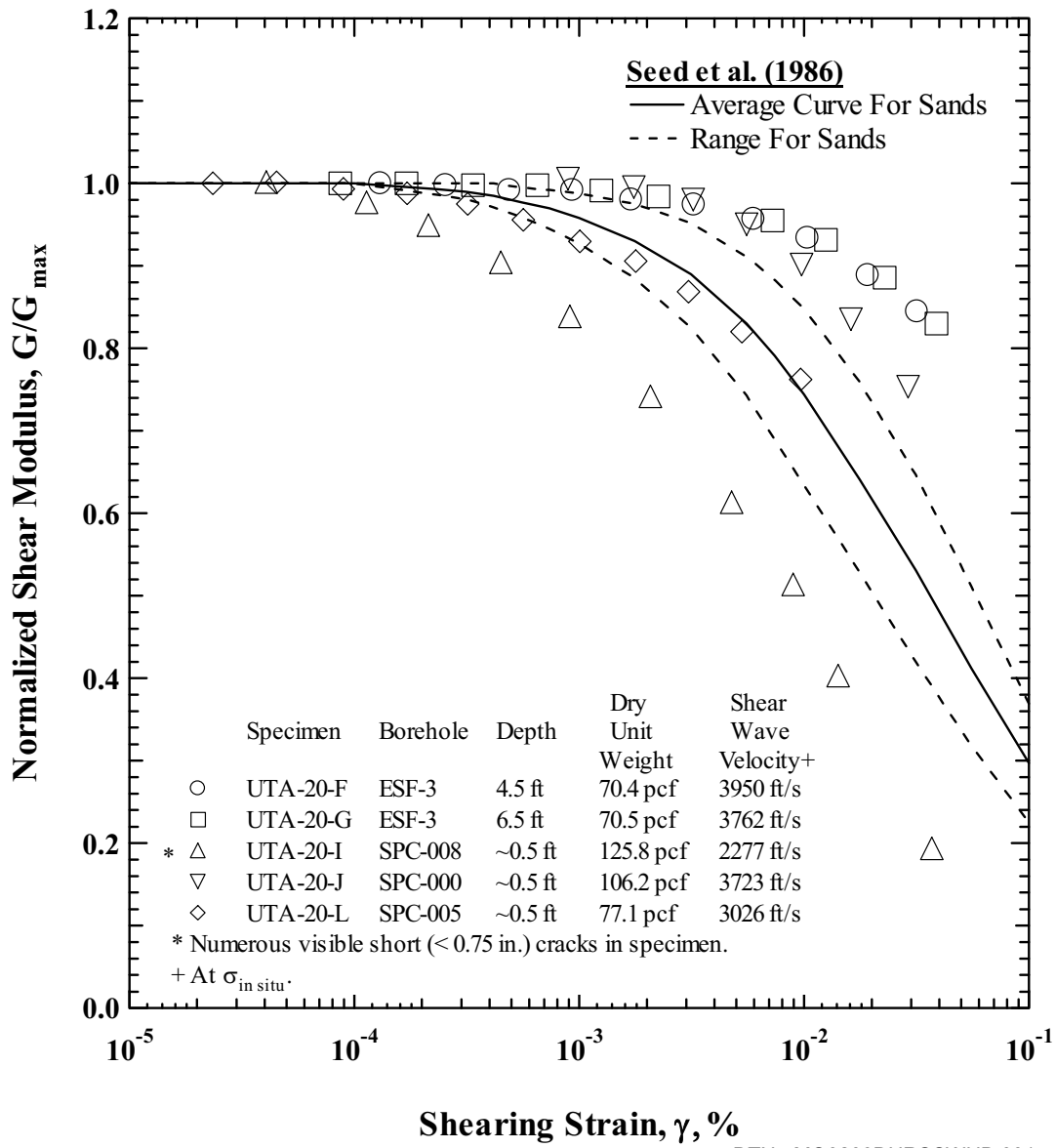
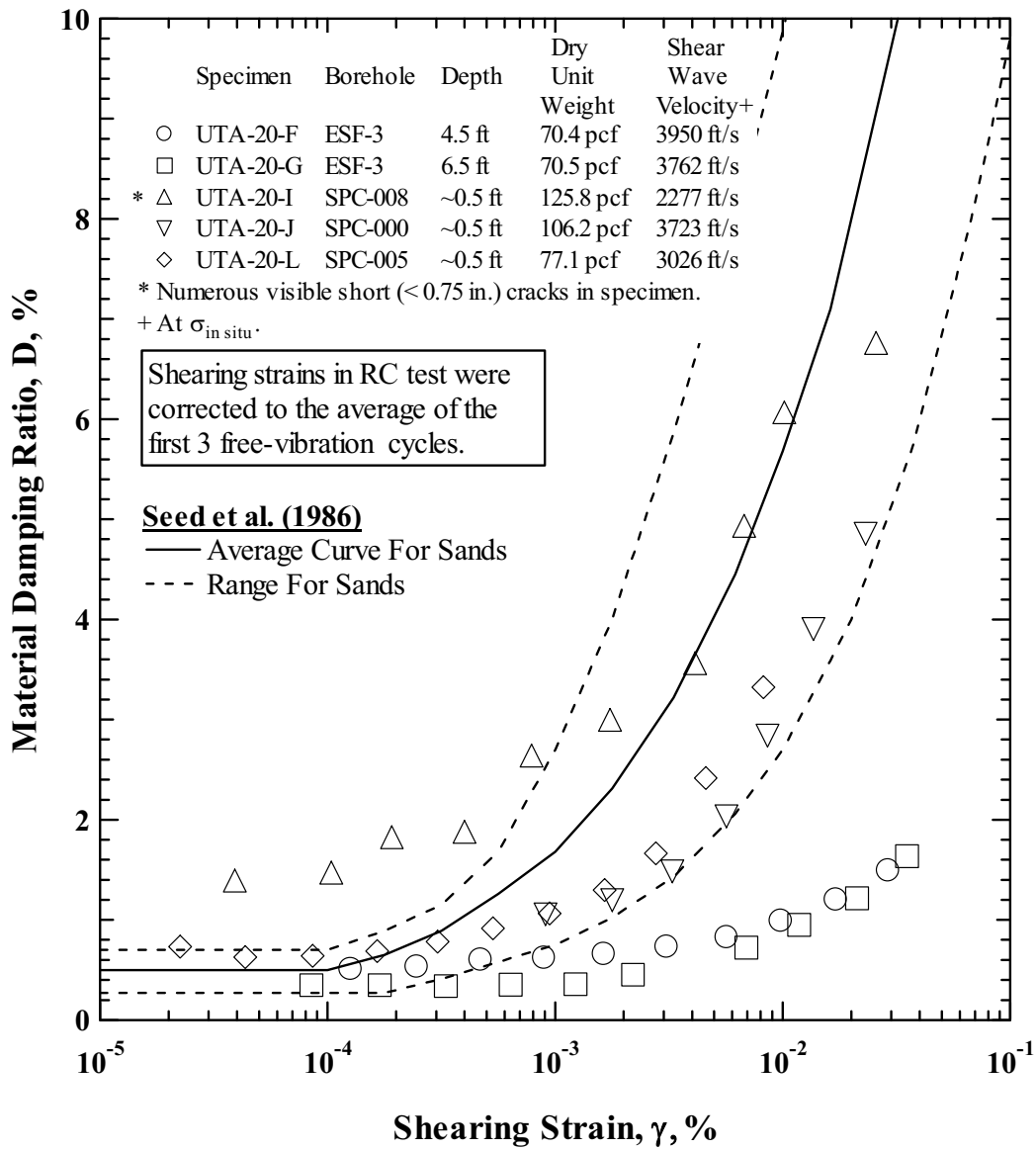


Figure 155. Variation in Normalized Shear Modulus with Shearing Strain of Intact Tuff Specimens from the ESF



DTN: MO0203DHRSSWHB.001

Figure 156. Variation in Material Damping Ratio with Shearing Strain of Intact Tuff Specimens from the ESF

6.4.2.1 Approach

A total of 33 SASW surveys were performed on top of Yucca Mountain generally above the potential emplacement area. The locations of these surveys are shown on Figure 157. The lengths of the lines as shown on Figure 157 are approximately equal to the maximum receiver spacing along the survey. The locations of these surveys referenced to other landmarks are presented in Scientific Notebooks SN-M&O-SCI-023-V1 (Wong 2002d) and SN-M&O-SCI-040-V1 (Wong 2002a). A general description of the approach used in the SASW surveys is contained in Section 6.2.7.2 and only differences in that approach are described below.

To cover the broad range in frequencies required for the SASW measurements over the wide range of sites, three different sources were utilized. Impact hammers were used to generate higher-frequency surface waves. At the shortest receiver spacings (typically 3 ft), a small, hand-held geology hammer was used to impact the ground. At larger receiver spacings (typically 6, 12, and 25 ft), a sledgehammer was employed. At the R sites, a small ball-peen hammer was used to excite the surface wave energy.

For receiver spacings equal to and greater than 25 ft at the S sites, a bulldozer was used to excite surface wave energy. Similarly at the D sites, a Vibroseis truck was used to excite the necessary frequencies (Figure 158). Figure 159 shows the Vibroseis truck performing a SASW survey with the receivers (shown in foreground) running downslope of the Yucca Mountain crest. The Vibroseis truck can excite energy at frequencies below those excited by a bulldozer source and can, therefore, be used to obtain profiles to greater depths.

A common receivers-midpoint geometry was employed whenever it was possible (Section 6.2.7.2). In some cases (e.g., SASW D-10), space and access limitations did not allow for a common receivers-midpoint geometry to be used at all spacings. These cases are noted in the scientific notebooks. Additionally, at each spacing, SASW measurements are ideally performed with the source located first on one end of the survey and then repeated with the source moved to the opposite end of the survey (termed forward and reverse directions). If good quality data are recorded in both directions, the cross-power spectra can be combined to eliminate any differences in receiver phase shifts or receiver coupling. At most locations, surveys were performed in only one direction at spacings greater than 25 ft due to the space and time limitations of moving the low-frequency source (bulldozer or Vibroseis truck) back and forth around the receiver alignment. Moving and replacing the receivers to allow the source to pass from one end of the survey to the other would change the coupling and defeat the purpose of performing forward and reverse tests. At the shorter spacings (< 25 ft) where impact hammers were used as the source, the test was performed in both the forward and reverse directions.

The SASW surveys oriented downslope of the crest could not be performed in both directions due to the restrictions on moving the Vibroseis truck into undisturbed areas. Performing the survey in only one direction had an insignificant impact on the results in these cases because the receivers had already been shown to be well matched, and any differences in receiver-to-ground coupling were insignificant.



Figure 158. Photograph of Vibroseis Truck in Operation on the Crest of Yucca Mountain



Figure 159. Photograph of SASW Survey Going Downslope with the Vibroseis Truck Being Readied for Use as the Source

SASW measurements were performed using a sequence of increasing spacings. Distances between receivers of 3, 6, 12, 25, 50, 100, and 200 ft were typically used. At the C and D sites, additional receiver spacings of 400, 600, and 800 ft were used when space considerations allowed. This number and progression of receiver spacings resulted in extensive overlapping of individual dispersion curves used to develop the composite field curve, which enhanced the measurement reliability. At the R sites, only two receiver spacings of typically 6 inches and 1 ft were used. The exact receiver spacings used at all of the SASW sites can be found on the data sheets presented in the Supplemental Records to Scientific Notebooks SN-M&O-SCI-023-V1 (Wong 2002d) and SN-M&O-SCI-040-V1 (Wong 2002a).

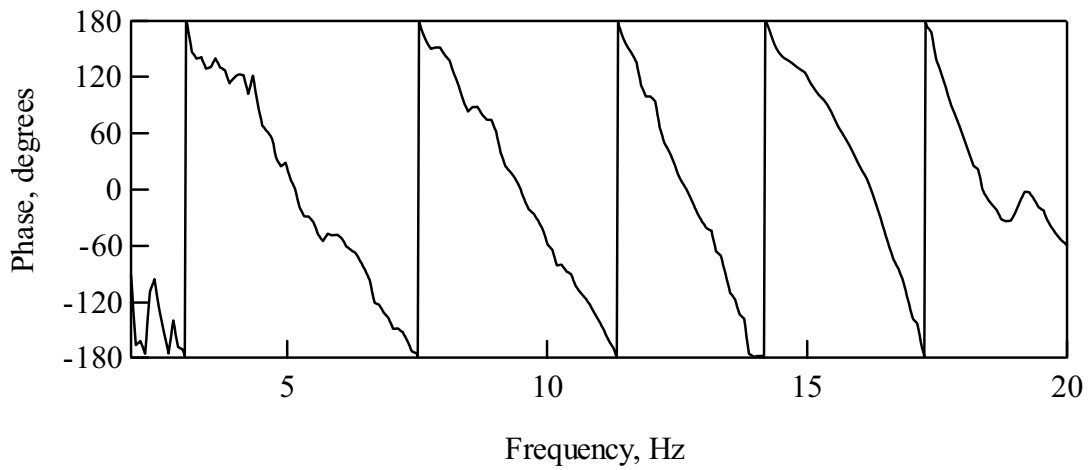
The SASW surveys with the Vibroseis truck were performed in a swept-sine mode where the source signal was swept over the frequencies of interest, and the relative phase and coherence were determined at each frequency. The source output of the Hewlett-Packard Dynamic Signal Analyzer was used to control the vibration frequency and amplitude of the Vibroseis truck. This process also allowed the operator to subjectively evaluate the data being collected in the field to assure consistency with the expected Rayleigh wave propagation in a layered halfspace.

For the surveys performed with impact hammers and the bulldozer, several time records were collected and averaged in the frequency domain to compute the phase and coherence functions. Typically, 3 to 5 measurements were averaged for the hammer measurements, and 10 to 20 measurements were averaged for the bulldozer surveys. For the measurements performed with the Vibroseis truck, the spectral functions were determined one frequency at a time in a swept-sine fashion. The number of averages and integration time was adjusted in the field to control how long the source remained at each frequency. Typically, 3 to 5 averages were used at each frequency in the determination of the spectral functions when the Vibroseis was used. All of the phase plots that were used in the interpretation of the data are presented in the Supplemental Records to Scientific Notebooks SN-M&O-SCI-023-V1 (Wong 2002d) and SN-M&O-SCI-040-V1 (Wong 2002a). The wrapped phase spectrum and coherence function from one receiver spacing are shown on Figure 160 as an example. These data were collected from the 400-ft receiver spacing recorded at D-2.

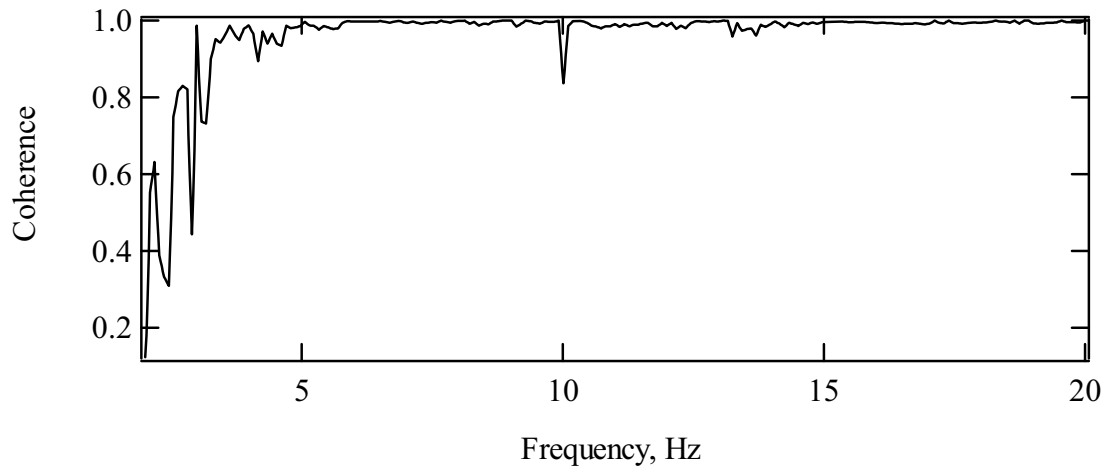
6.4.2.2 Results

All shear-wave velocity profiles are shown on Figures 161 through 191 and values are listed in Attachment XV. Of the 33 SASW surveys performed on Yucca Mountain, 22 were on or very near the crest of Yucca Mountain (Figure 157). Surveys C-2, C-6, D-6, and D-11 resulted in dispersion curves that indicated significant lateral variability. Thus at these sites, multiple shear-wave velocity profiles were estimated to reflect the variability over the distance of the survey. A total of 38 profiles are shown in composite on Figure 192 (R surveys not shown). The median, mean, and 16th and 84th percentile profiles are shown on Figure 193. Also shown is the base case tuff velocity model developed in 1999 (DTN: MO98PRECLOSURE.000).

Examination of the individual shear-wave velocity profiles suggests that unlike the typical increase in velocity with depth observed in most geologic settings, many of the profiles indicate low-velocity zones beneath higher velocity rock, which are often observed in volcanic terrain (Wong et al. 1995, pages 6-15 to 6-20). The limited shallow downhole shear-wave velocity data are consistent with the presence of these zones (Section 6.4.3).



a. Cross-Power Spectrum



b. Coherence Function

Source: Wong (2002a, Appendix 37)

Figure 160. Cross-Power Spectrum and Coherence Function Measured at Site D-2 from the 400-ft Receiver Spacing

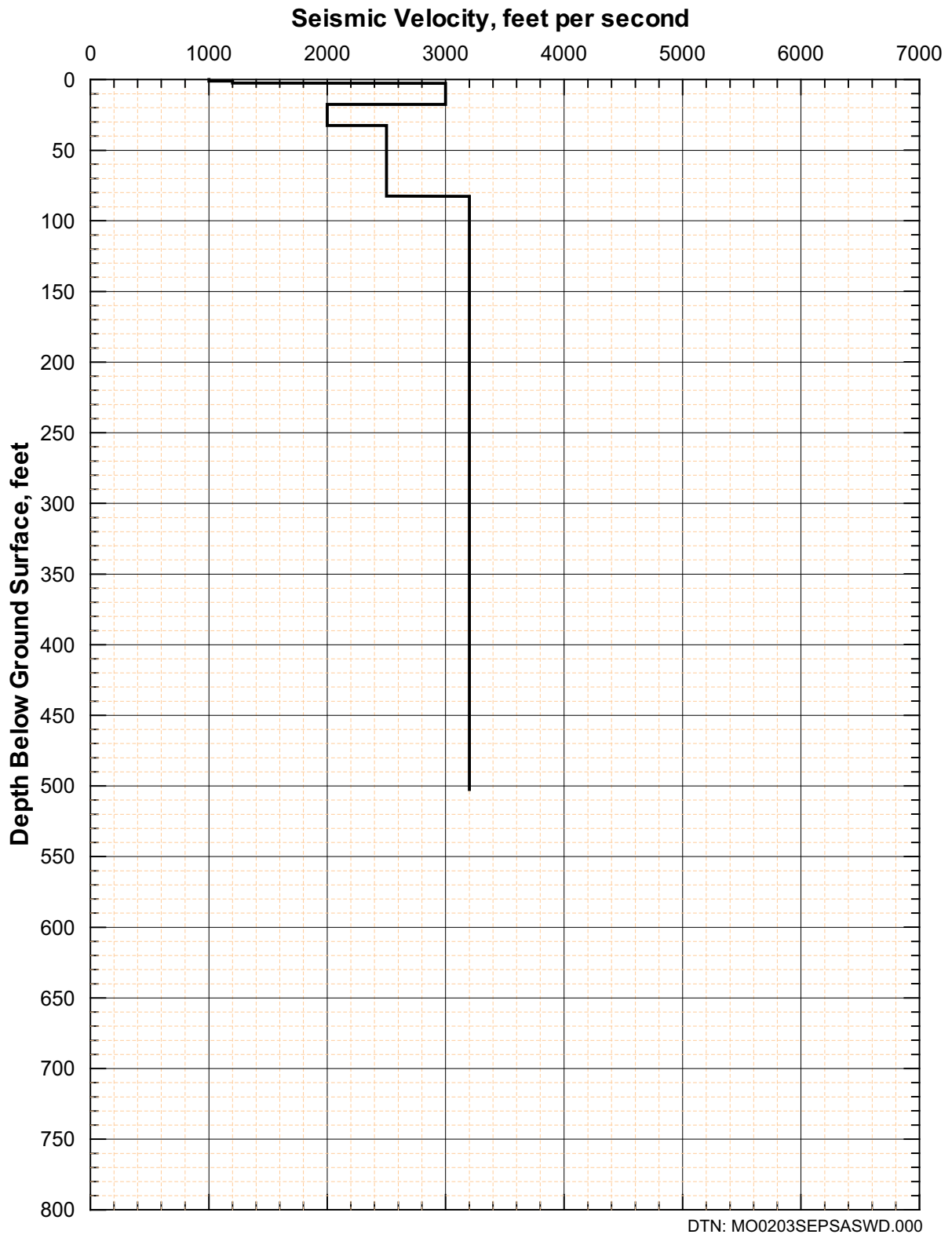


Figure 161. Shear-Wave Velocity Profile from SASW C-1

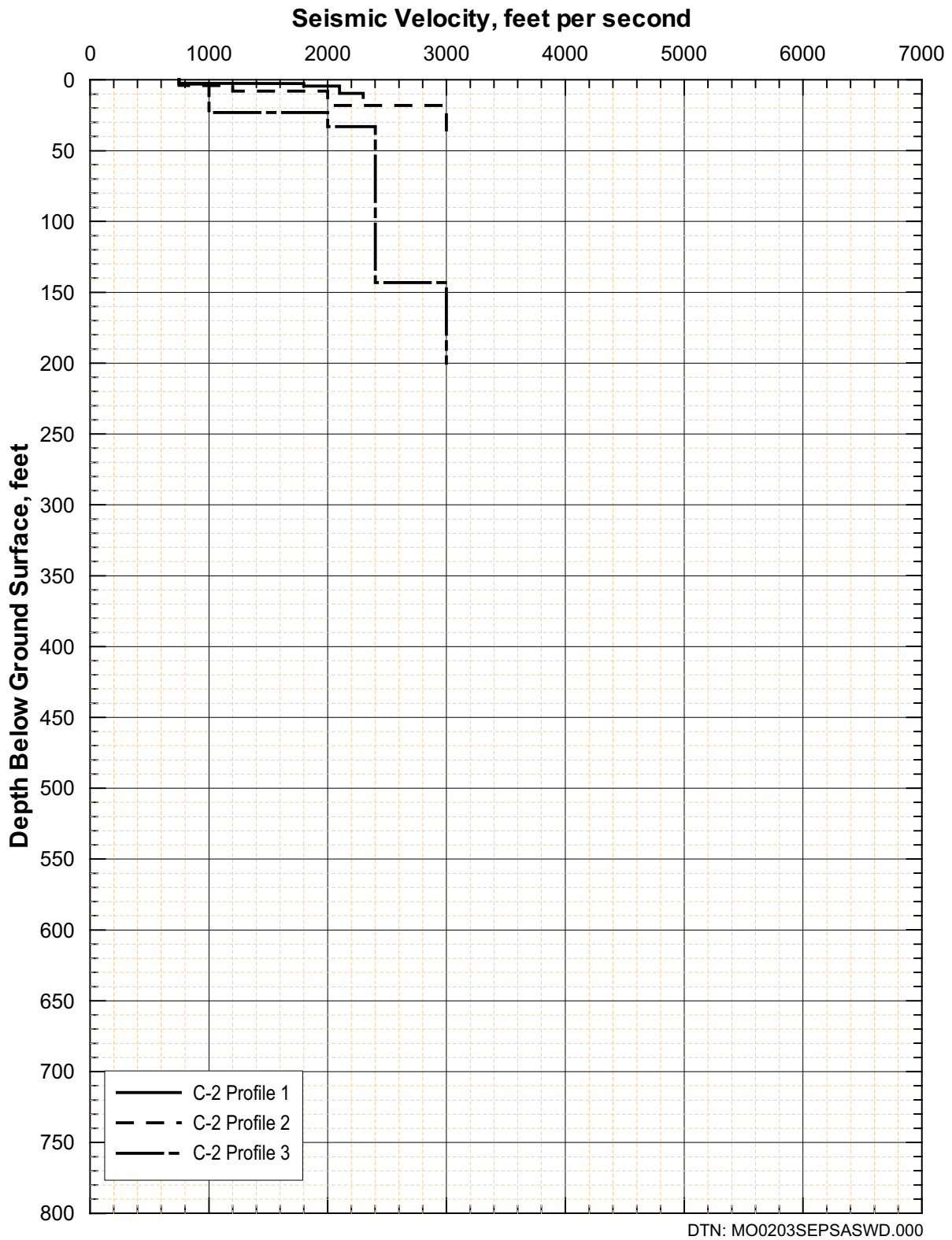


Figure 162. Shear-Wave Velocity Profiles from SASW C-2

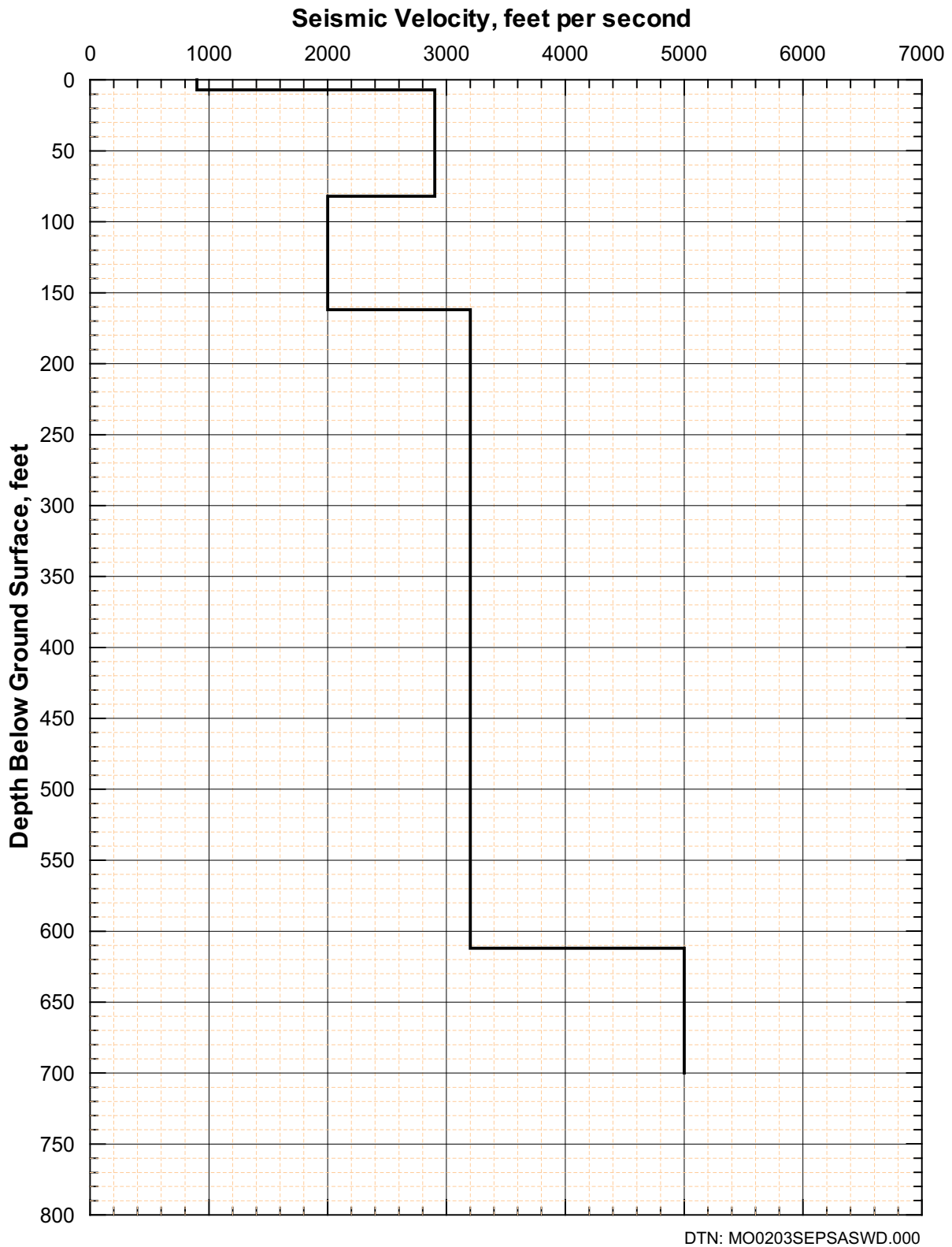


Figure 163. Shear-Wave Velocity Profile from SASW C-3

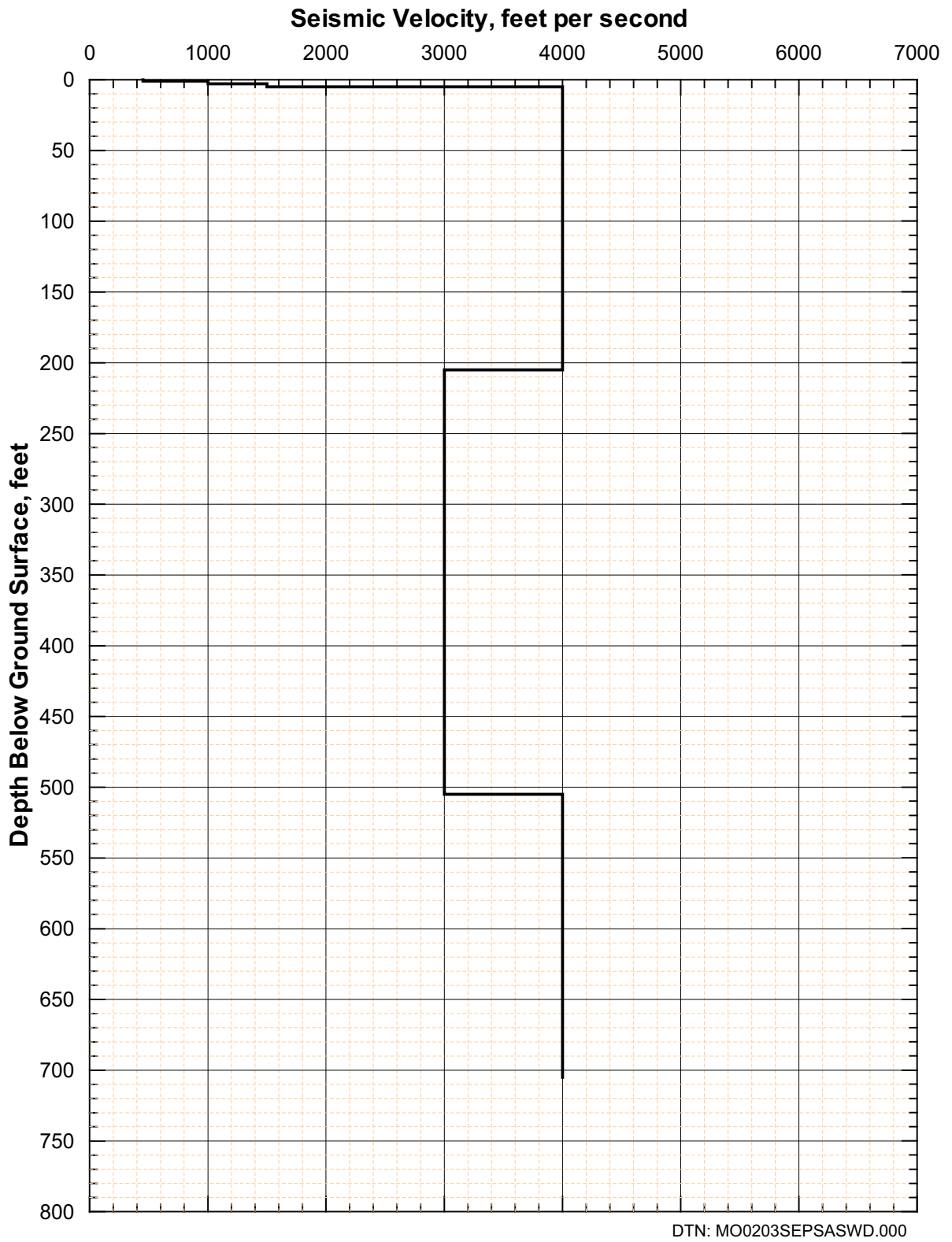


Figure 164. Shear-Wave Velocity Profile from SASW C-4

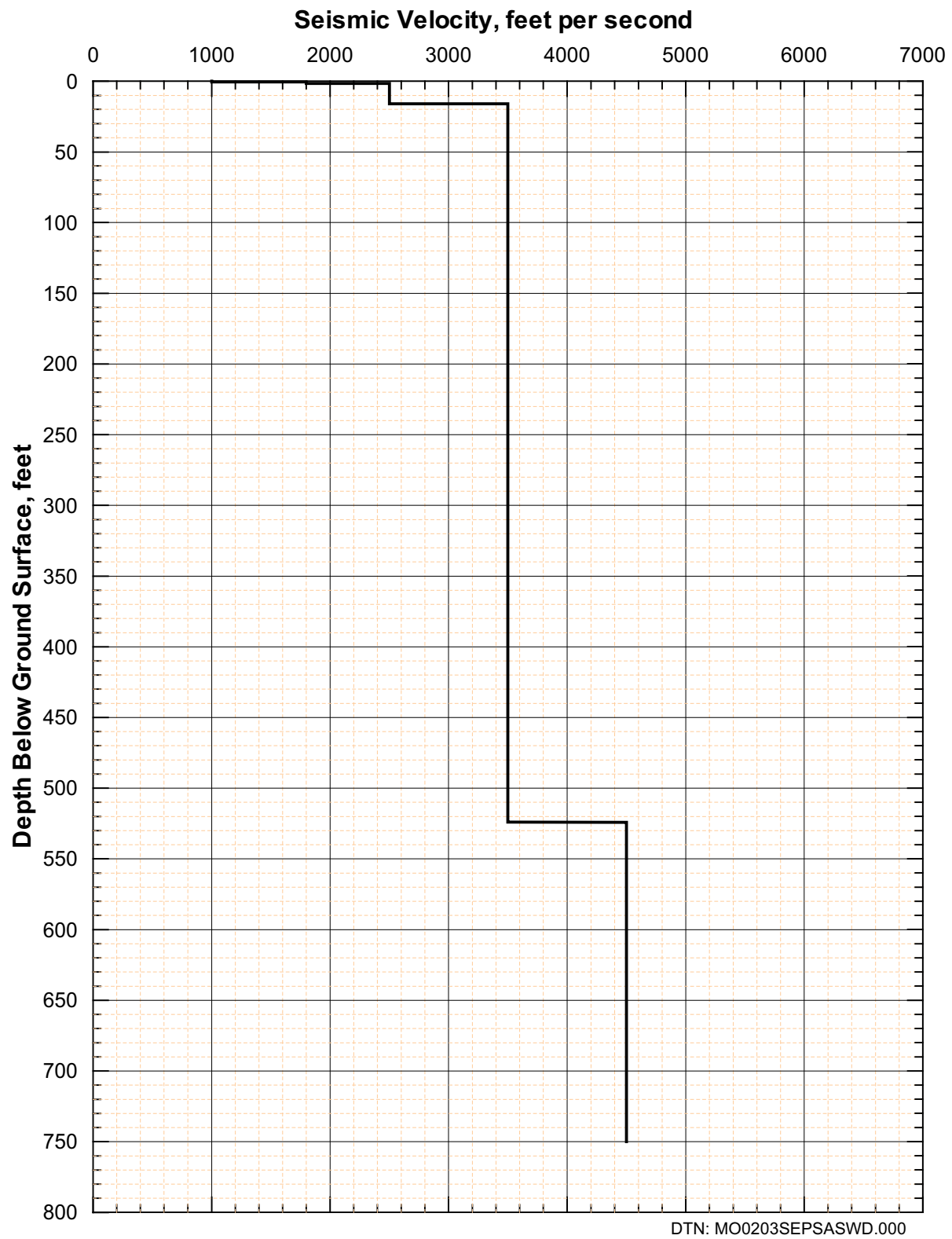


Figure 165. Shear-Wave Velocity Profile from SASW C-5

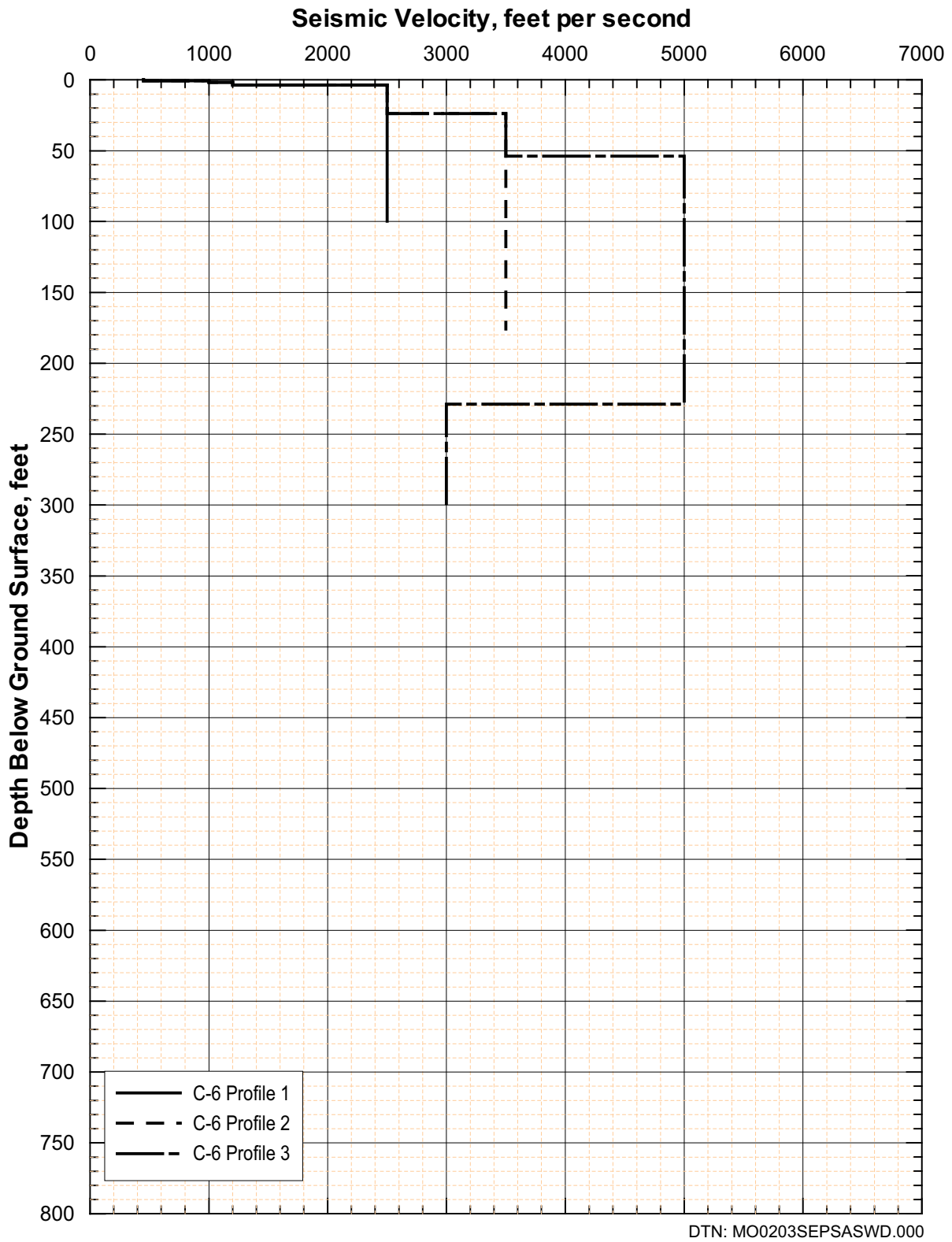


Figure 166. Shear-Wave Velocity Profiles from SASW C-6

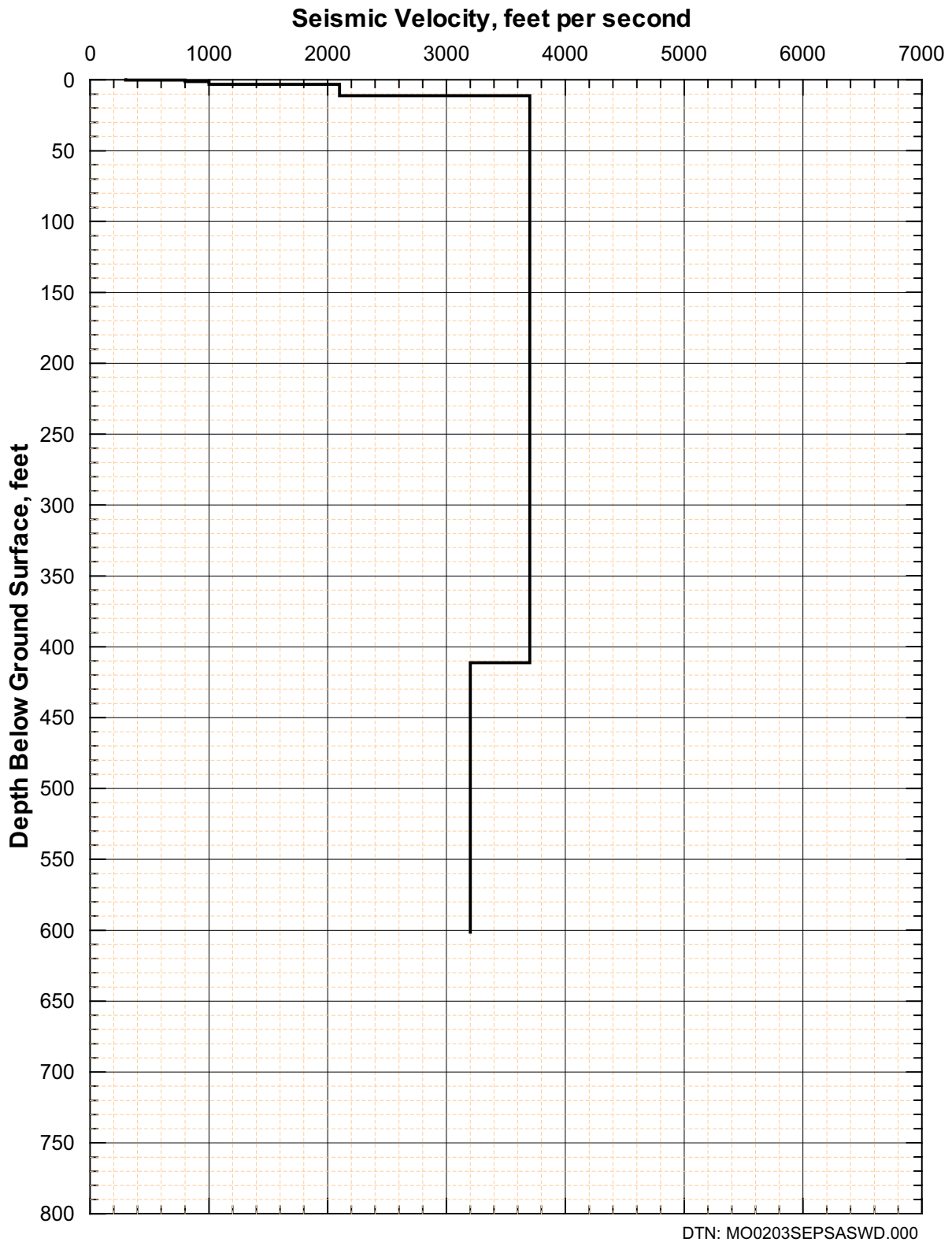


Figure 167. Shear-Wave Velocity Profile from SASW C-7

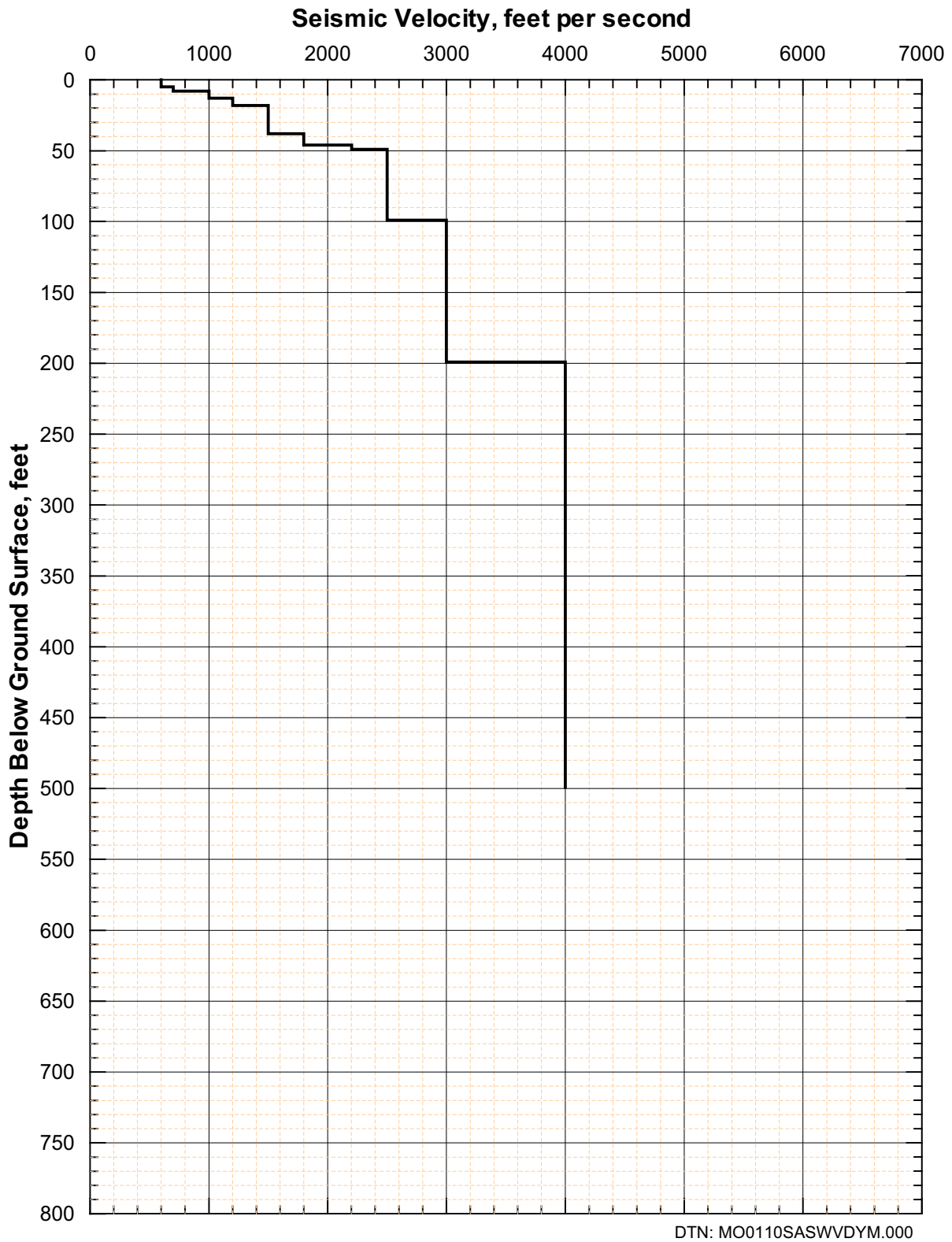


Figure 168. Shear-Wave Velocity Profile from SASW D-1

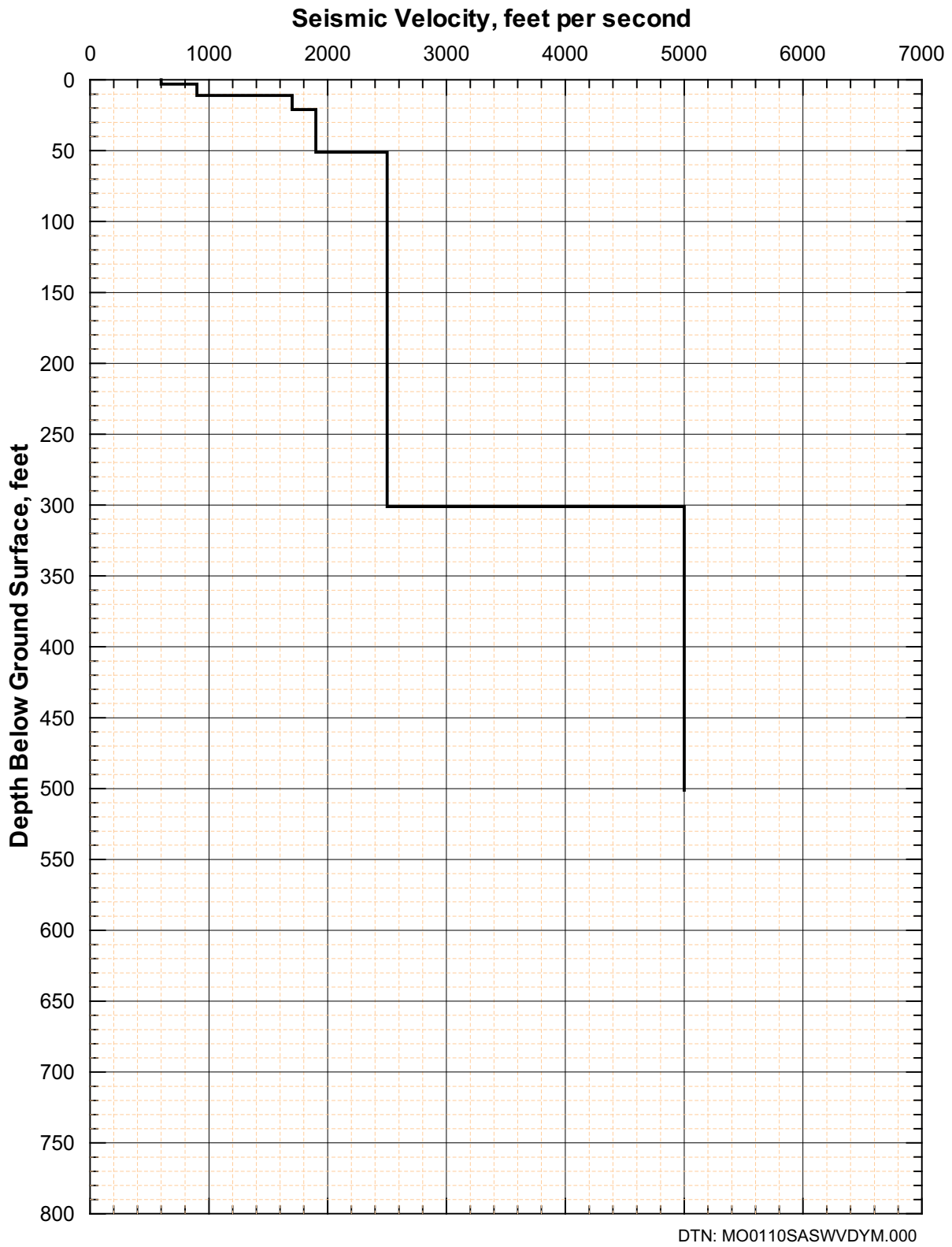
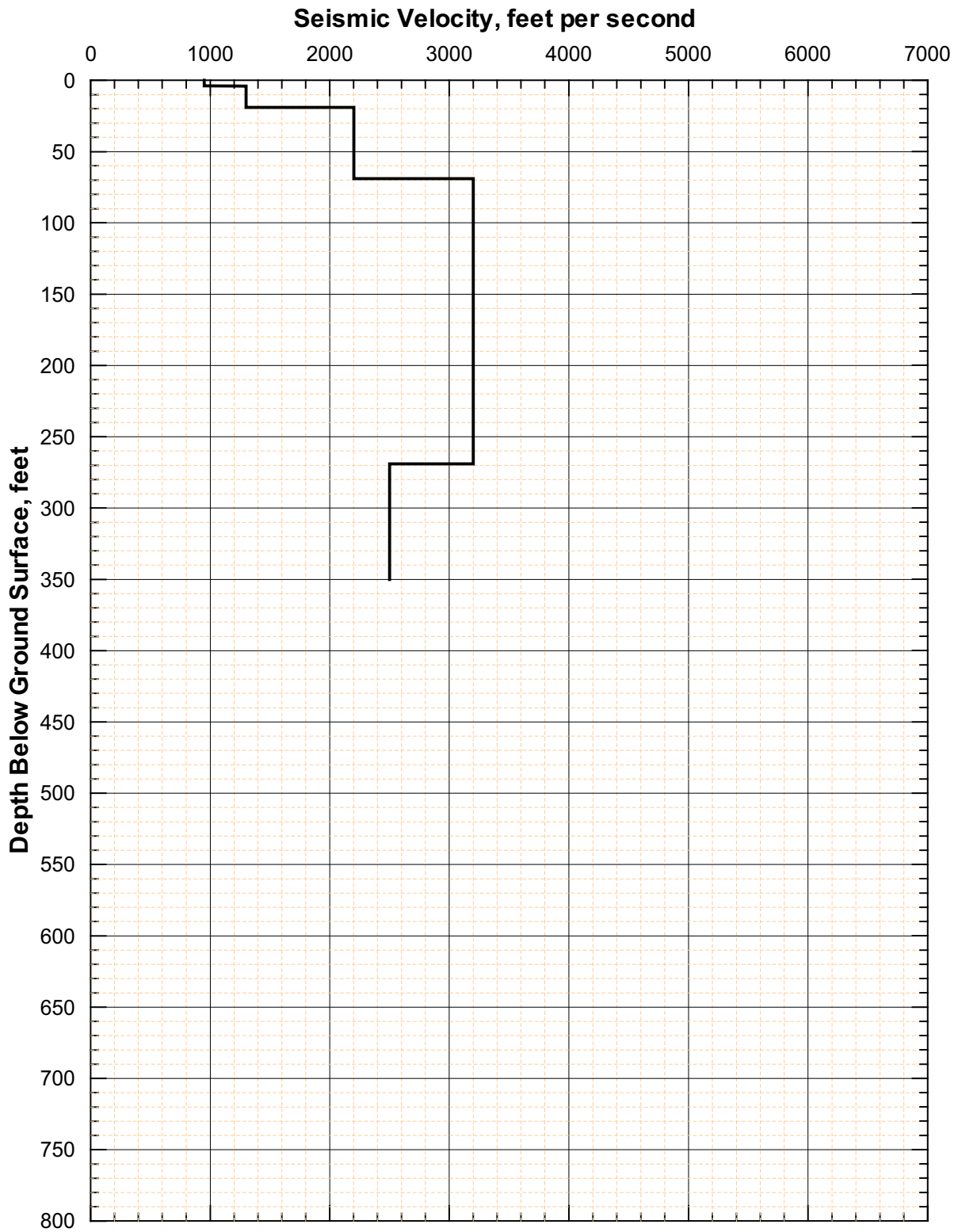


Figure 169. Shear-Wave Velocity Profile from SASW D-2



DTN: MO0110SASWVDYM.000

Figure 170. Shear-Wave Velocity Profile from SASW D-3

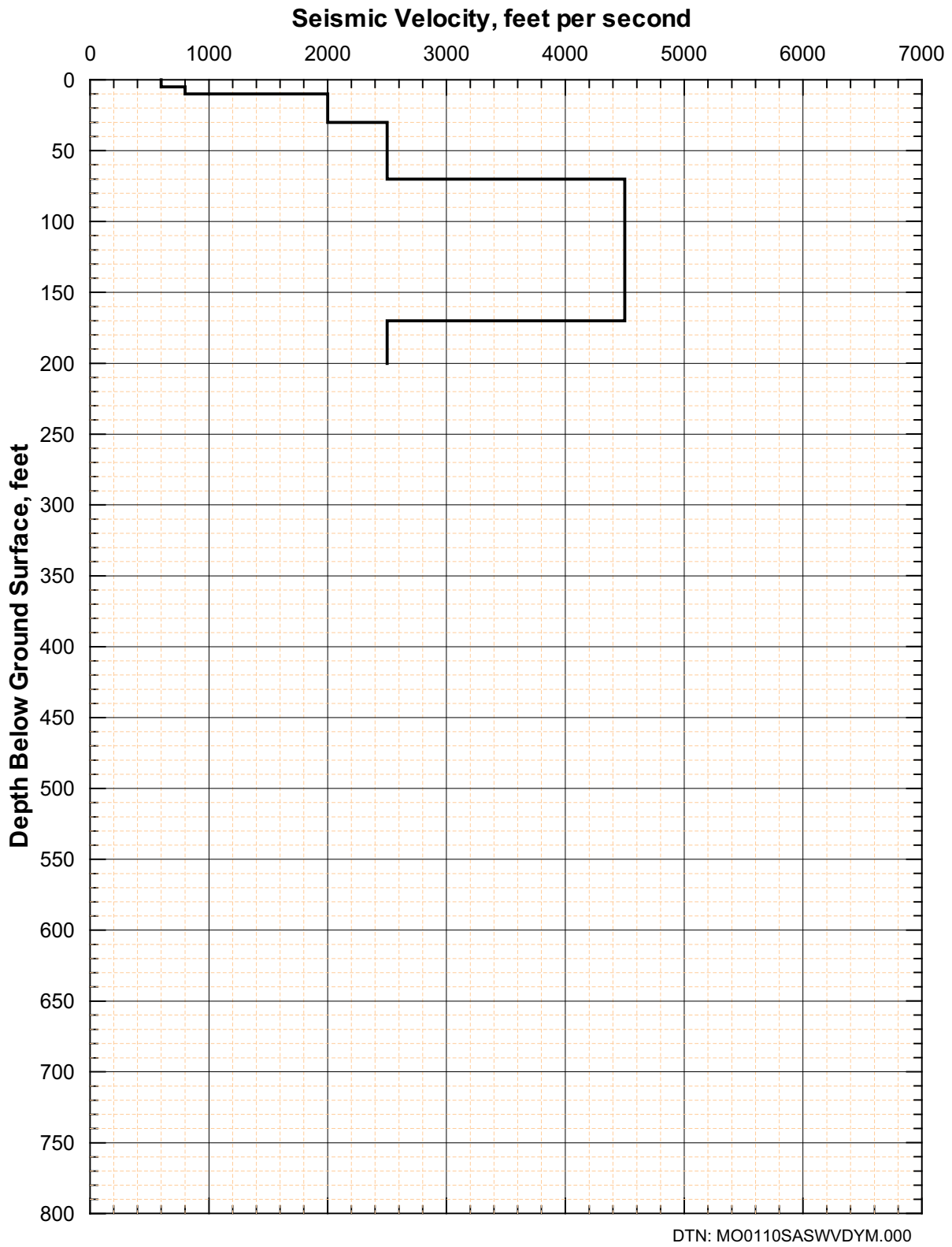


Figure 171. Shear-Wave Velocity Profile from SASW D-4

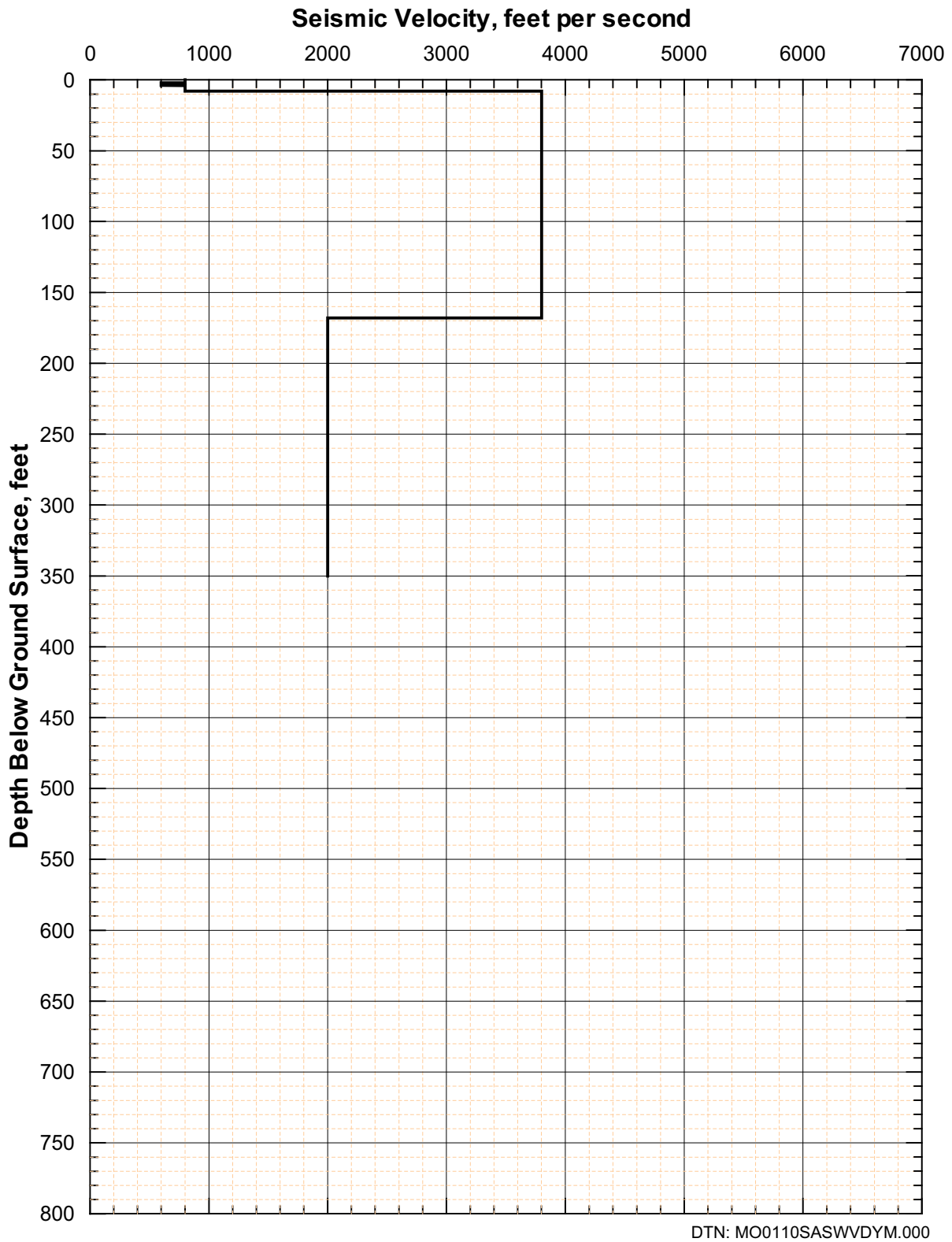


Figure 172. Shear-Wave Velocity Profile from SASW D-5

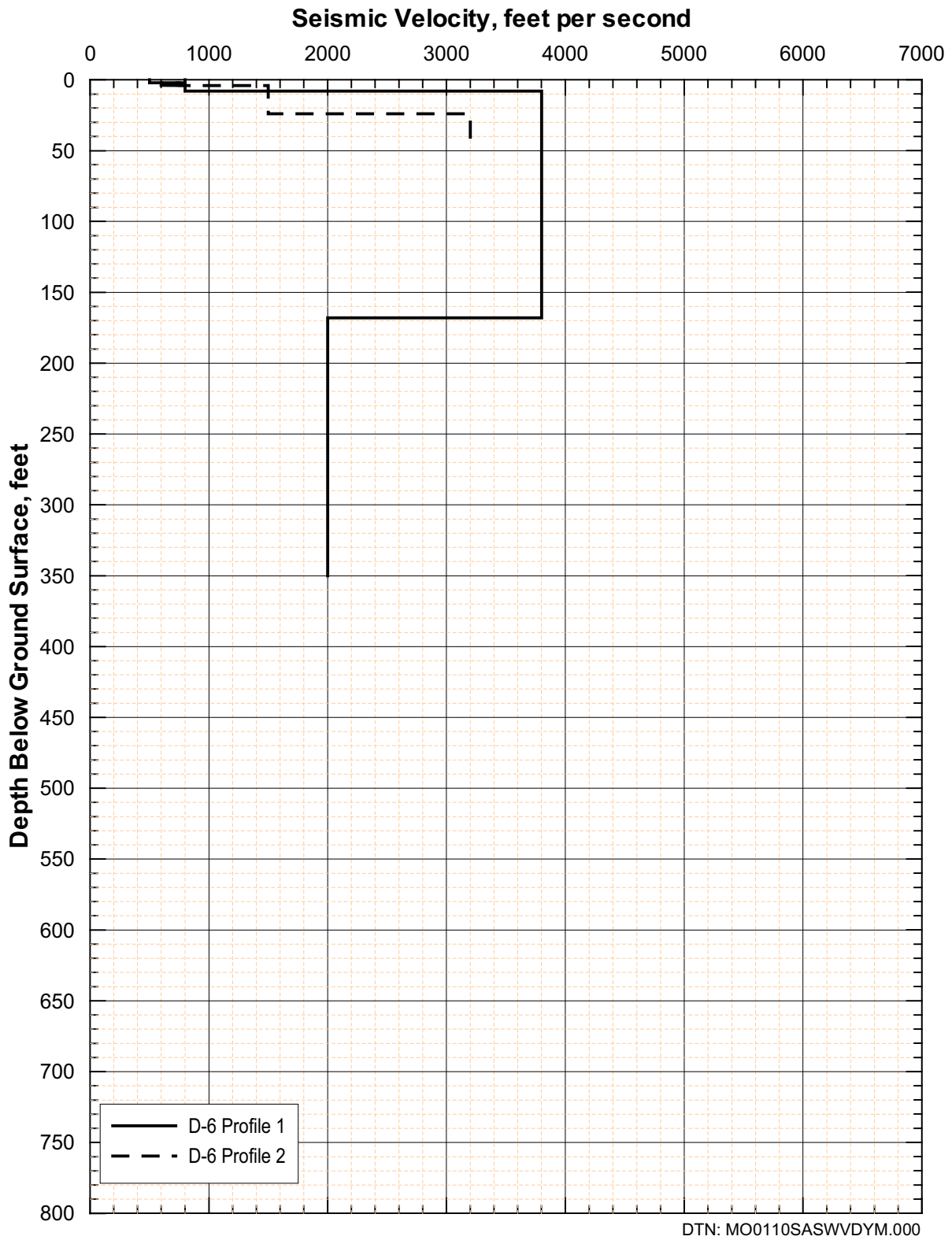
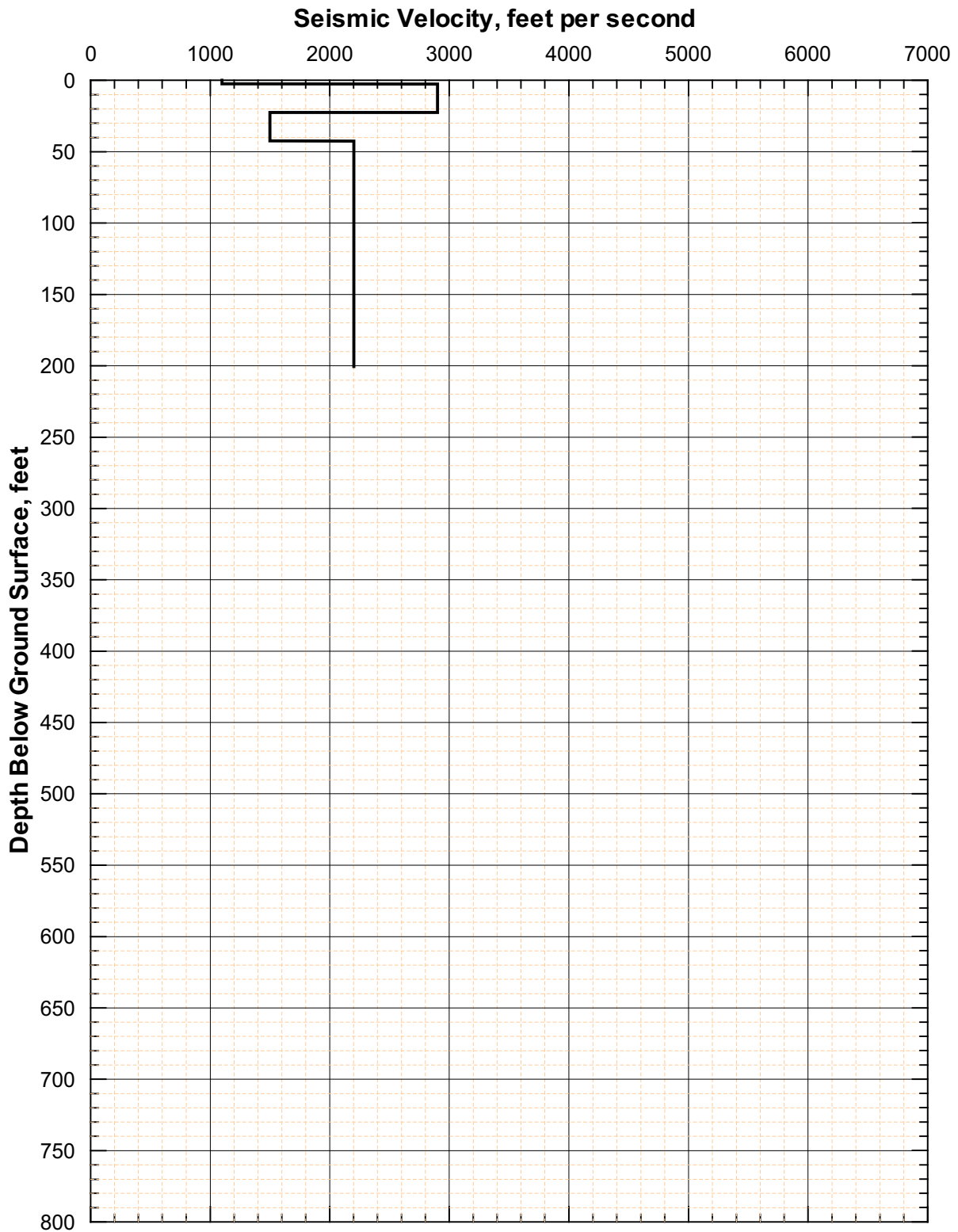


Figure 173. Shear-Wave Velocity Profiles from SASW D-6



DTN: MO0110SASWVDYM.000

Figure 174. Shear-Wave Velocity Profile from SASW D-7

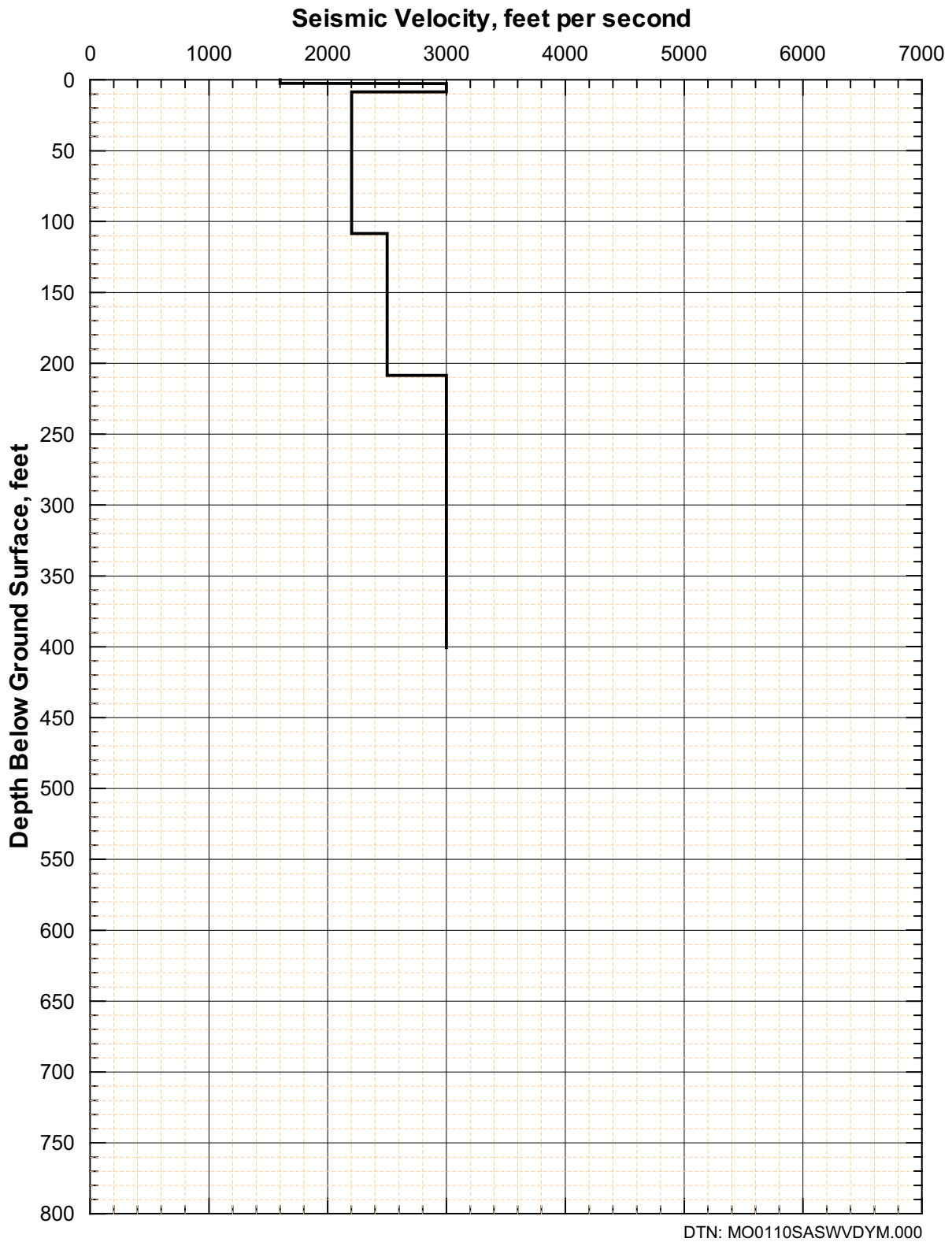


Figure 175. Shear-Wave Velocity Profile from SASW D-8

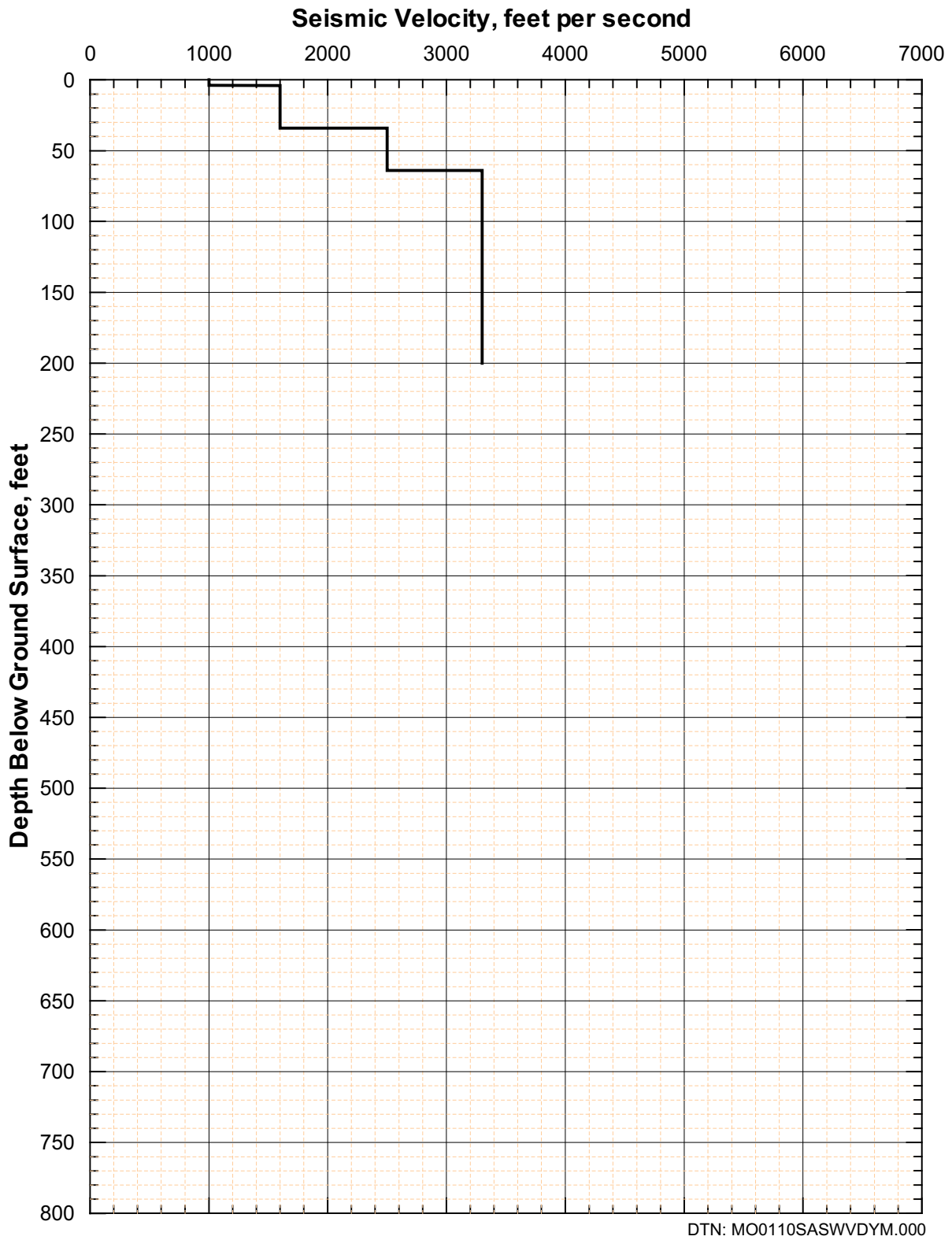


Figure 176. Shear-Wave Velocity Profile from SASW D-9

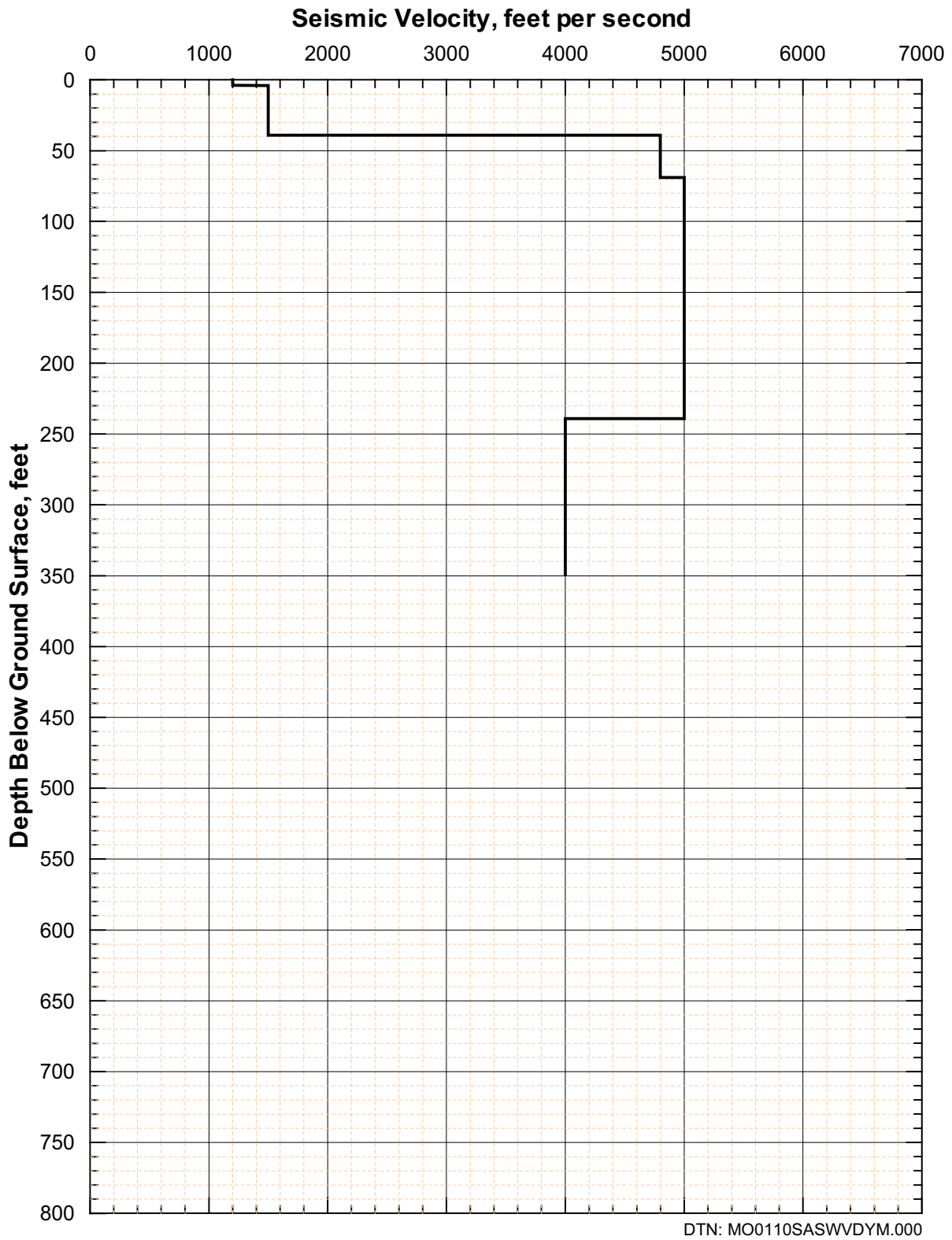


Figure 177. Shear-Wave Velocity Profile from SASW D-10

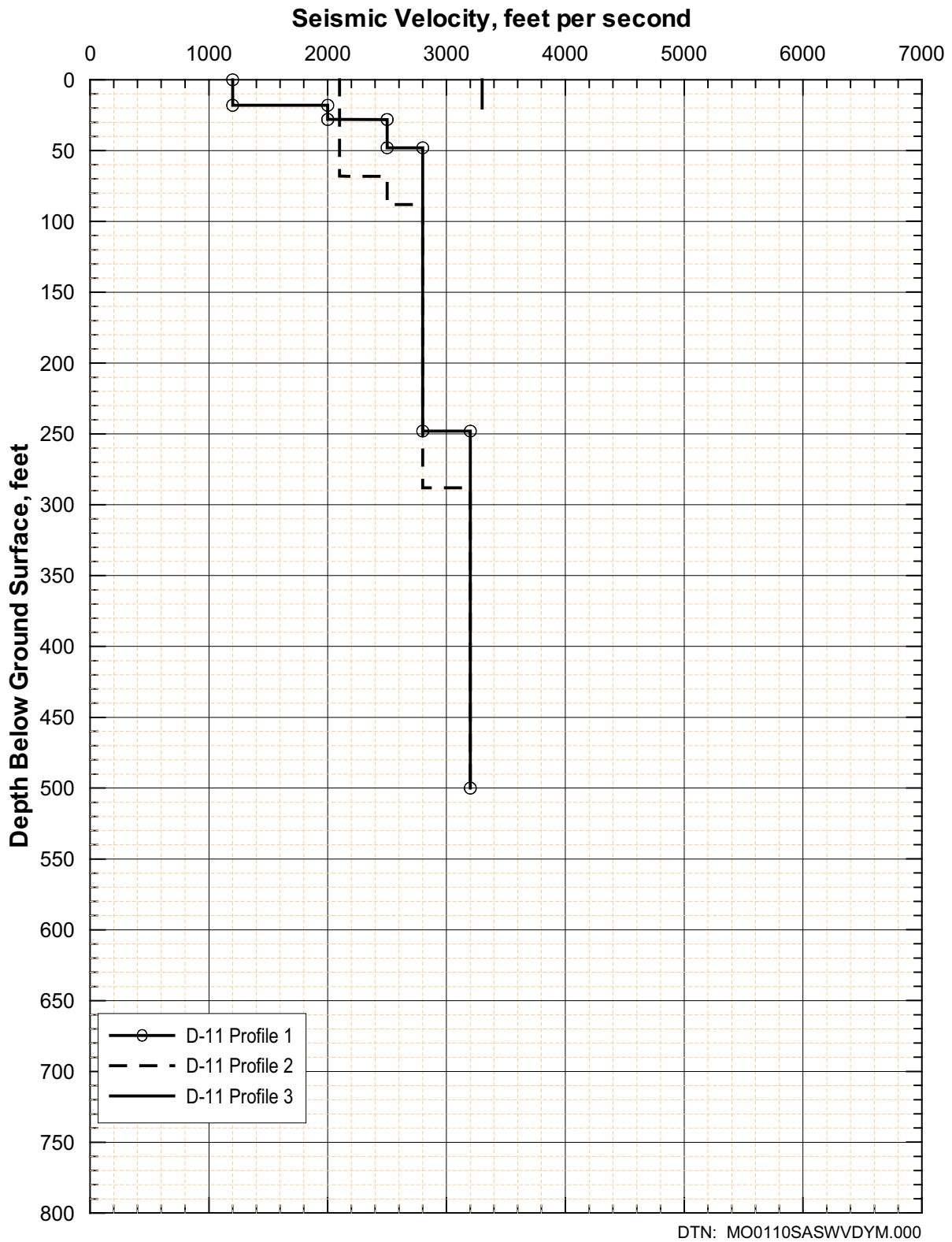


Figure 178. Shear-Wave Velocity Profiles from SASW D-11

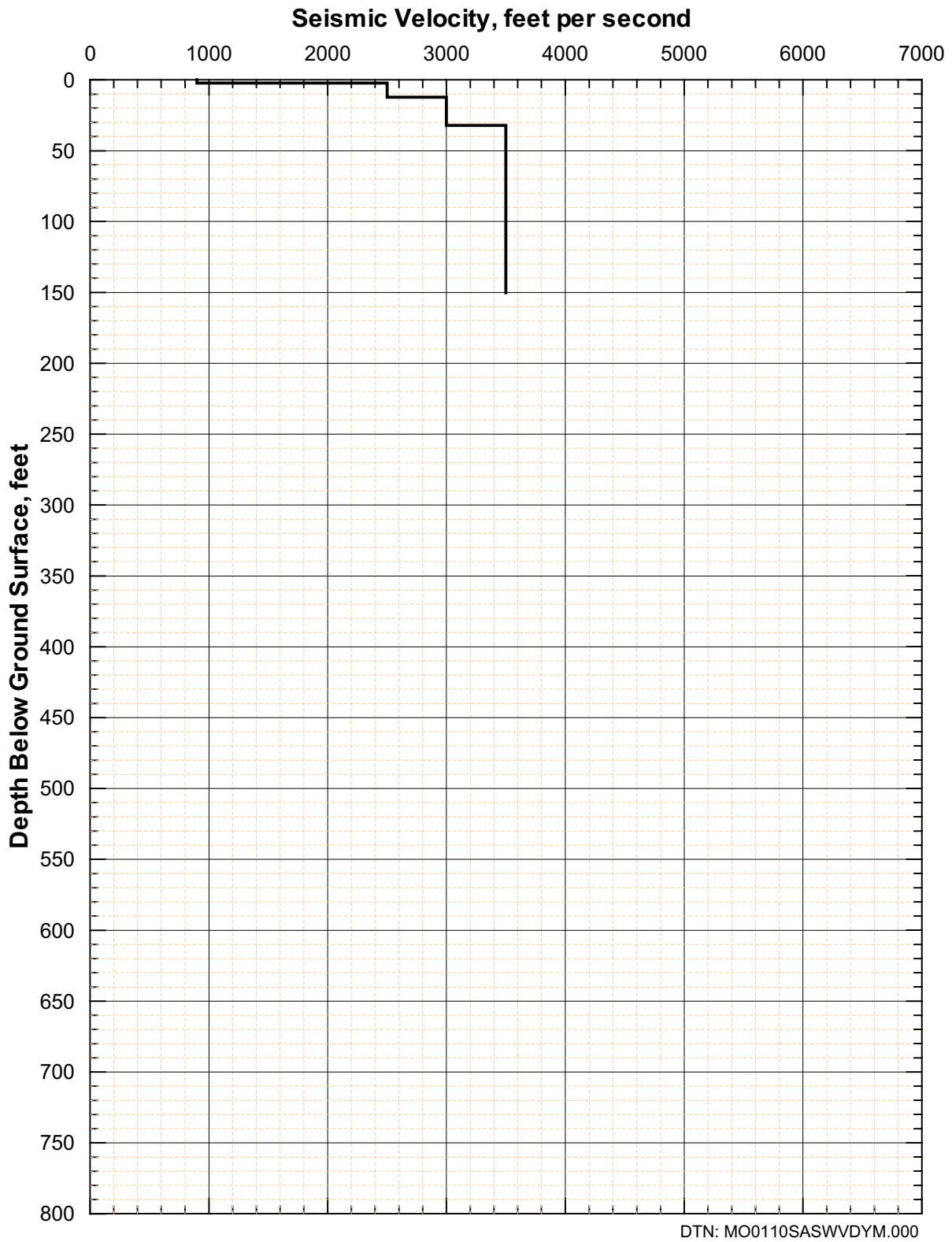


Figure 179. Shear-Wave Velocity Profile from SASW S-1

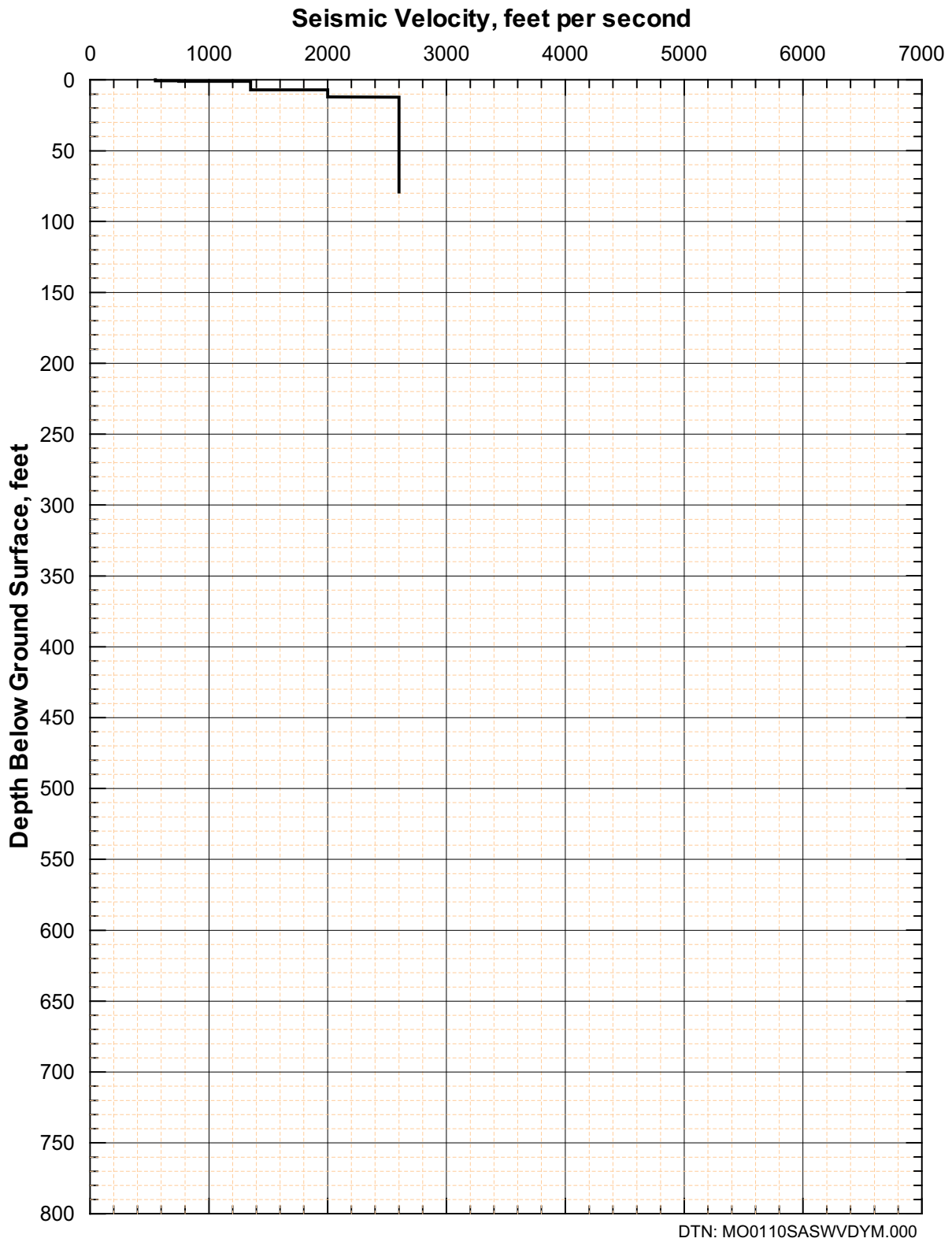


Figure 180. Shear-Wave Velocity Profile from SASW S-2

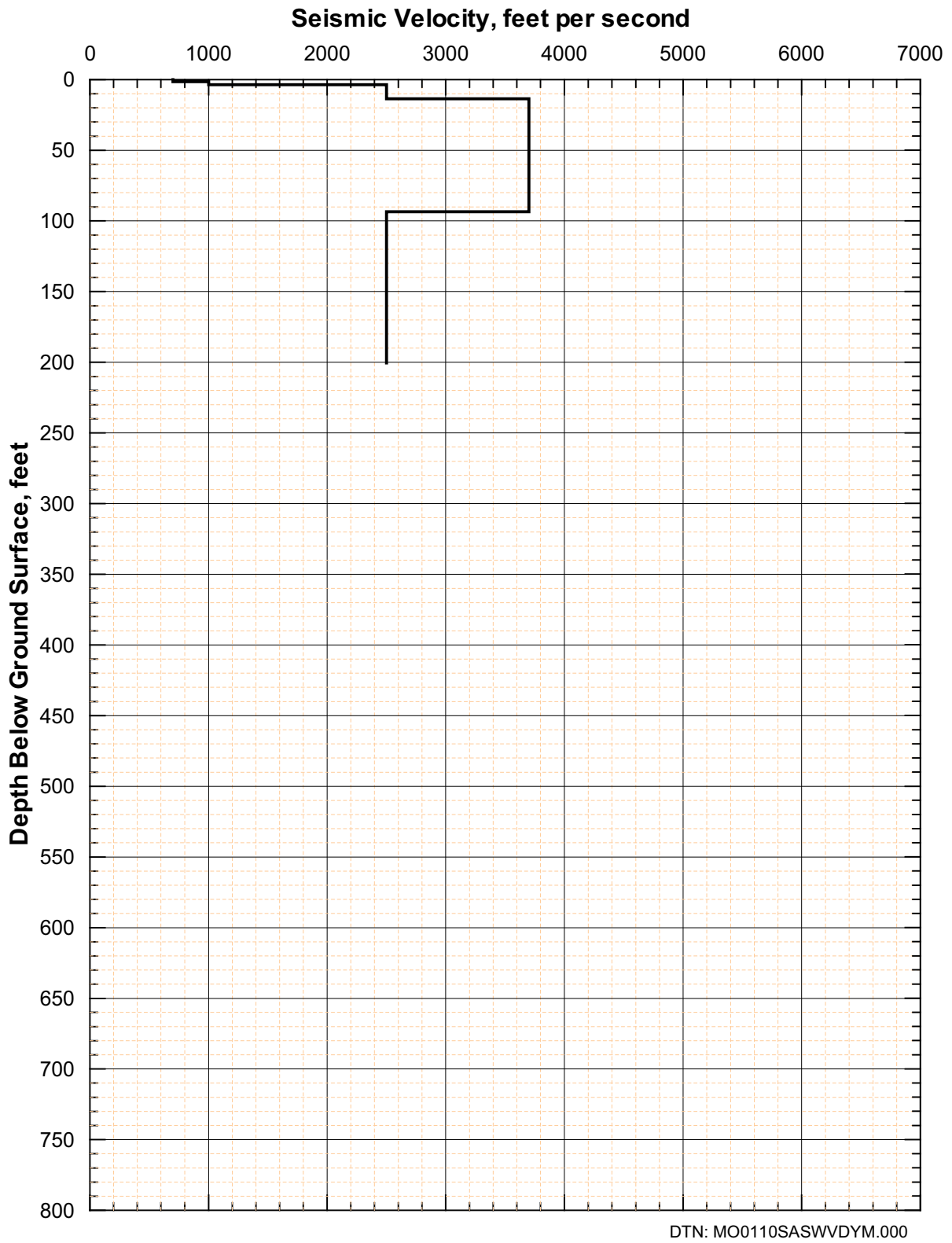


Figure 181. Shear-Wave Velocity Profile from SASW S-3

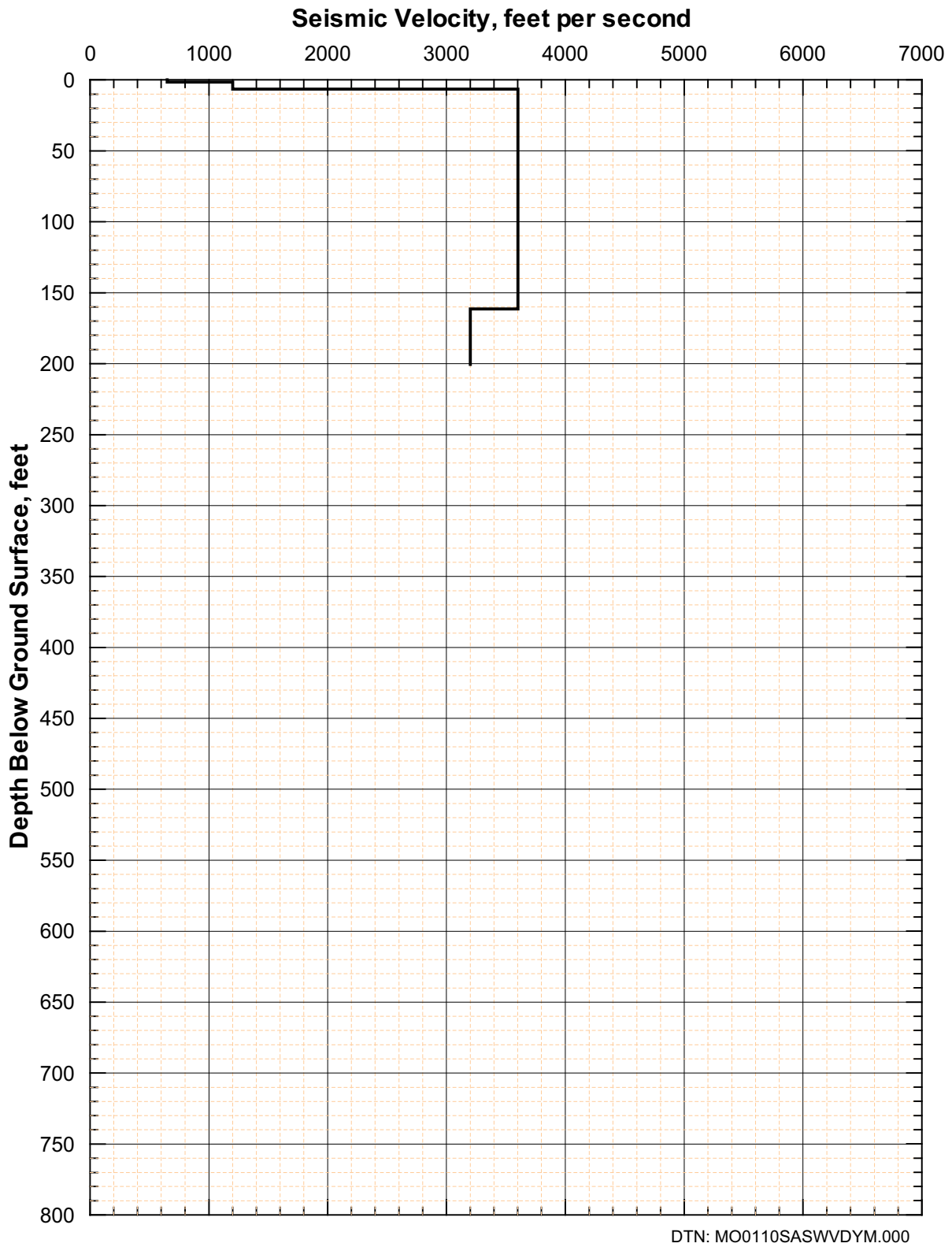


Figure 182. Shear-Wave Velocity Profile from SASW S-4

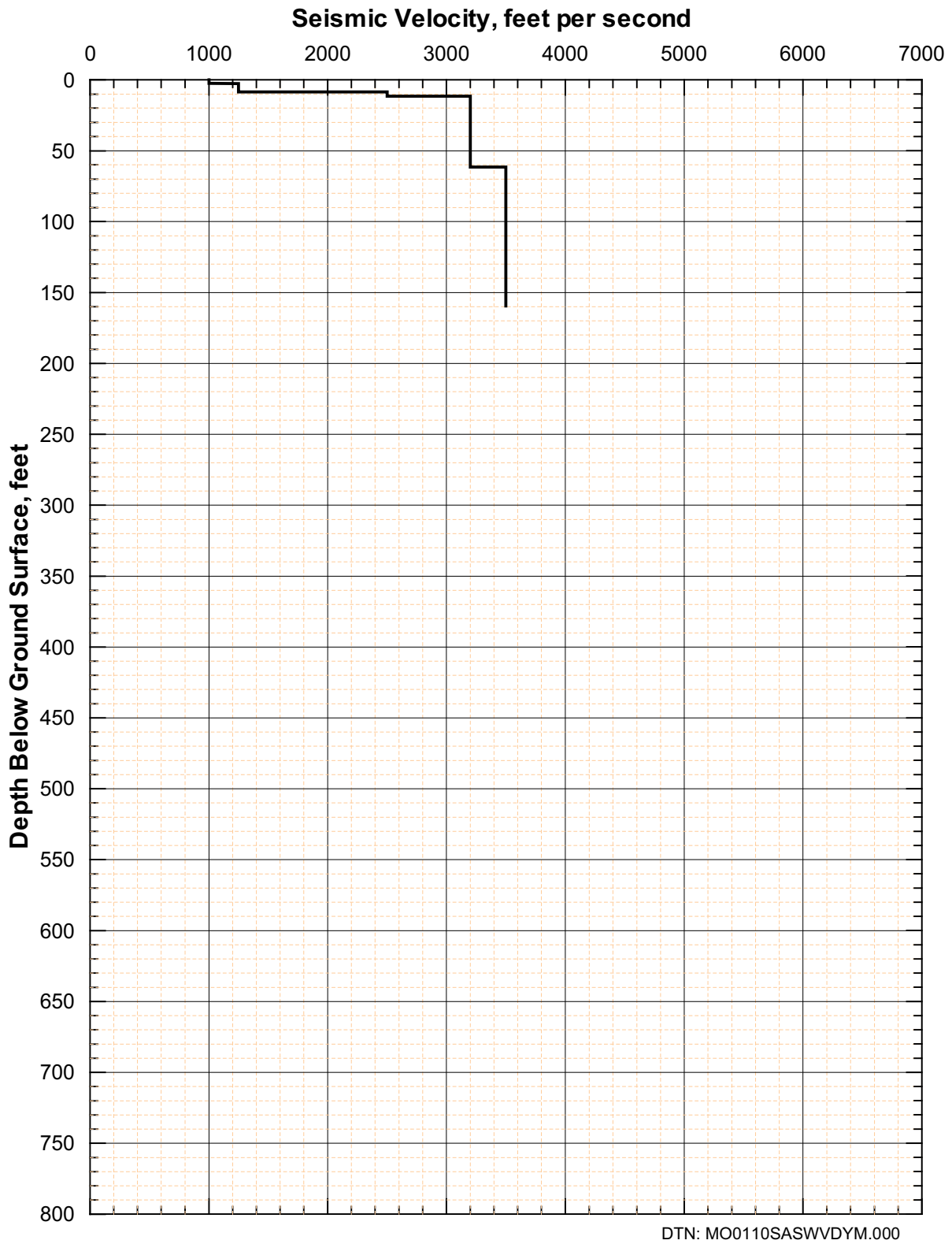


Figure 183. Shear-Wave Velocity Profile from SASW S-5

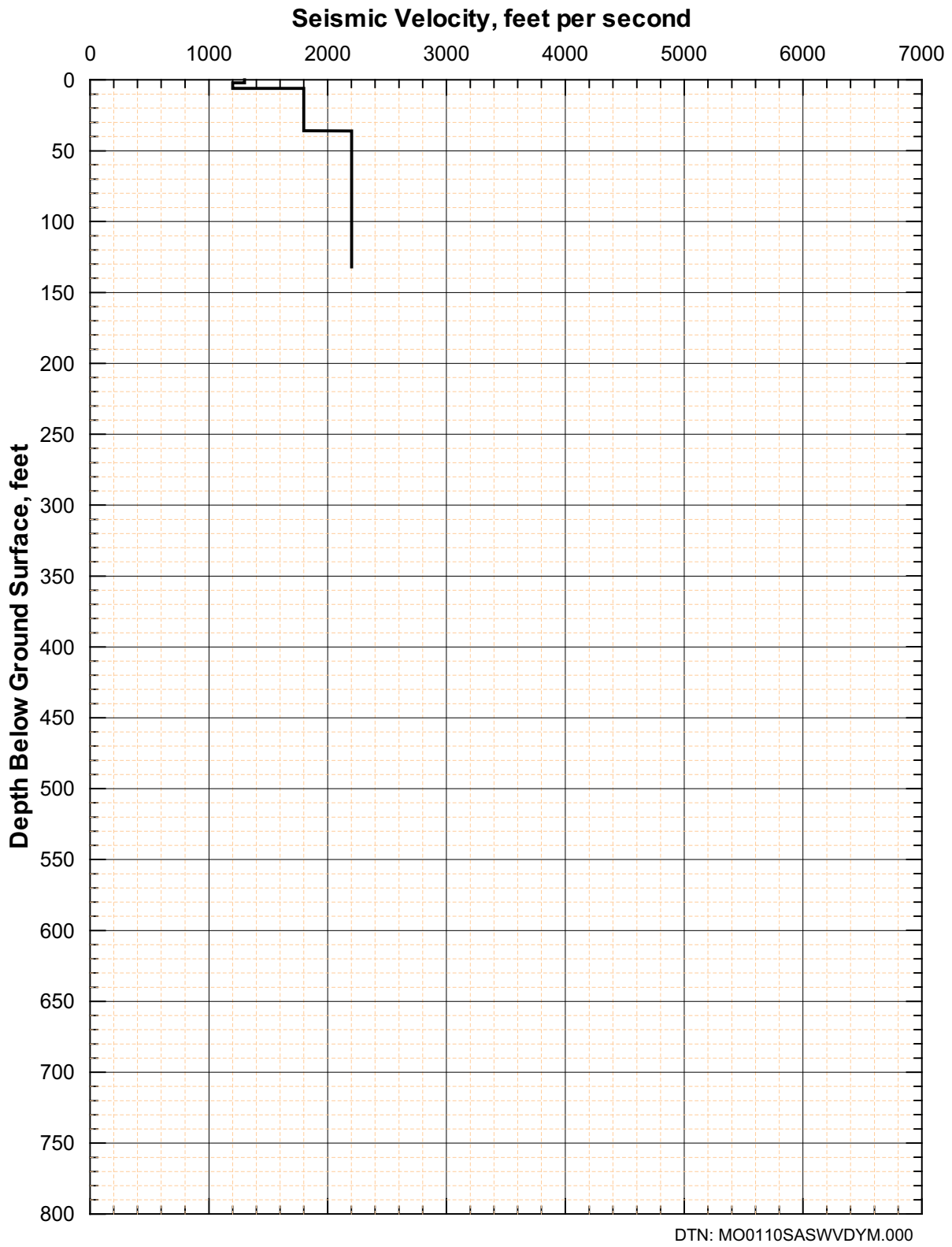


Figure 184. Shear-Wave Velocity Profile from SASW S-6

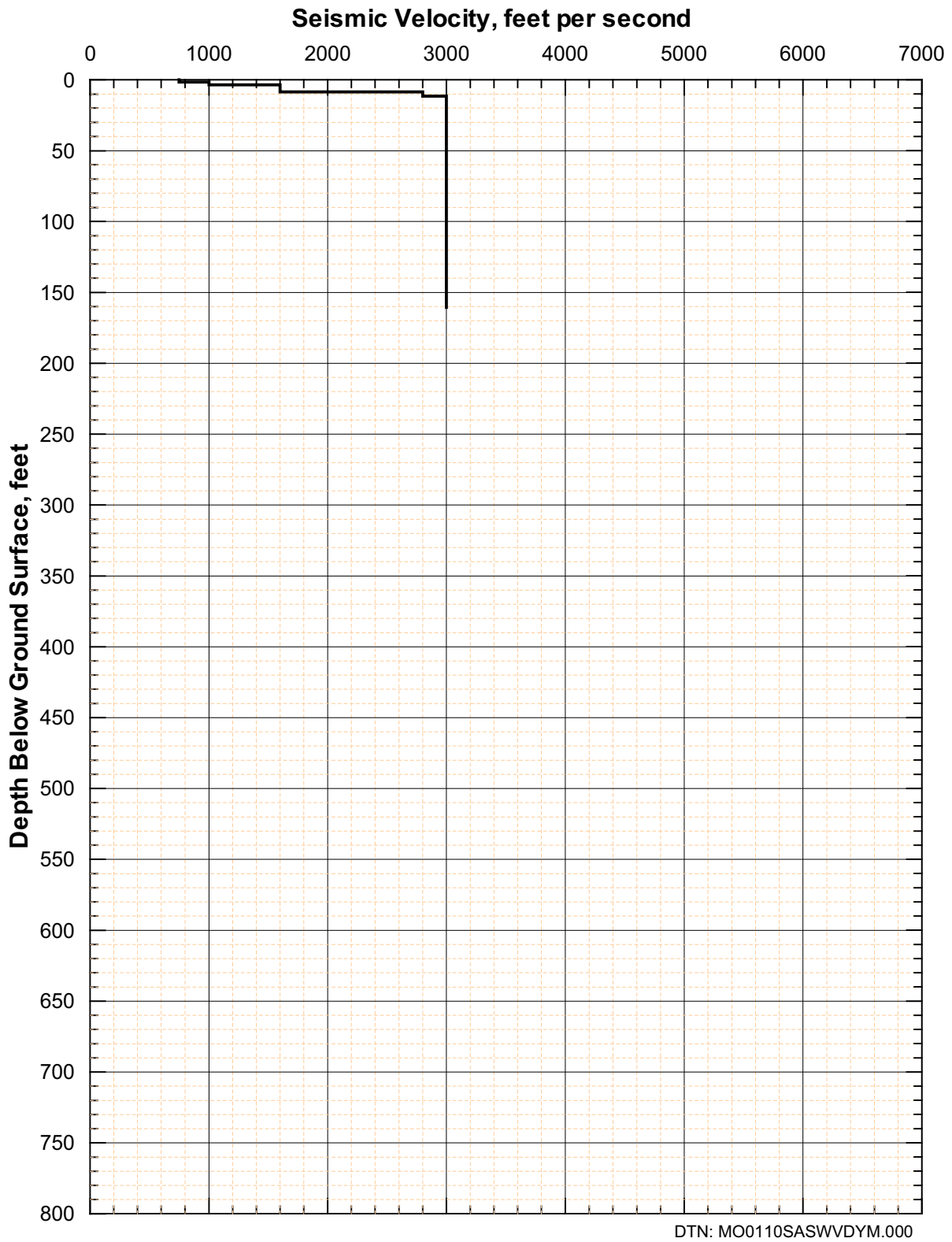


Figure 185. Shear-Wave Velocity Profile from SASW S-7

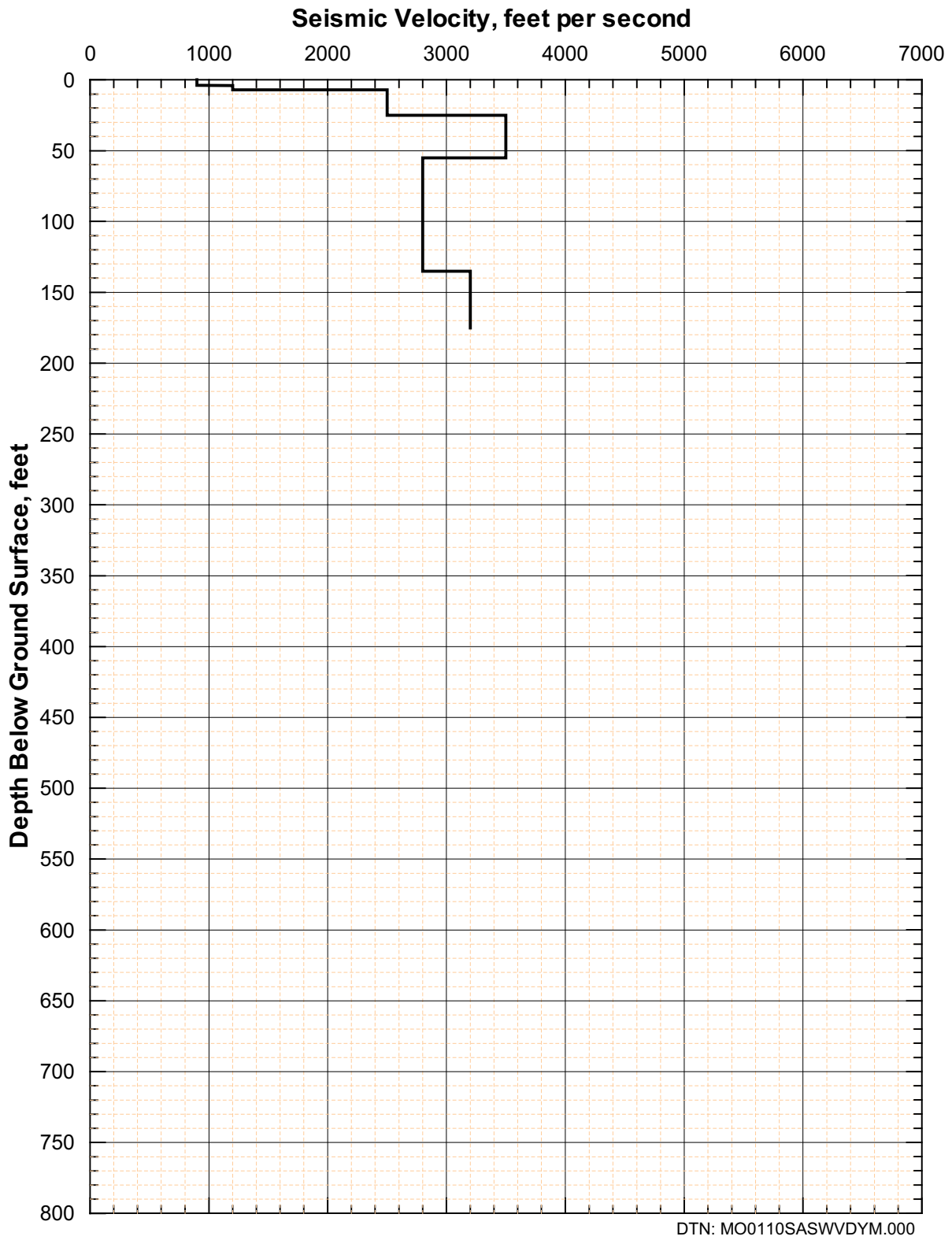


Figure 186. Shear-Wave Velocity Profile from SASW S-8

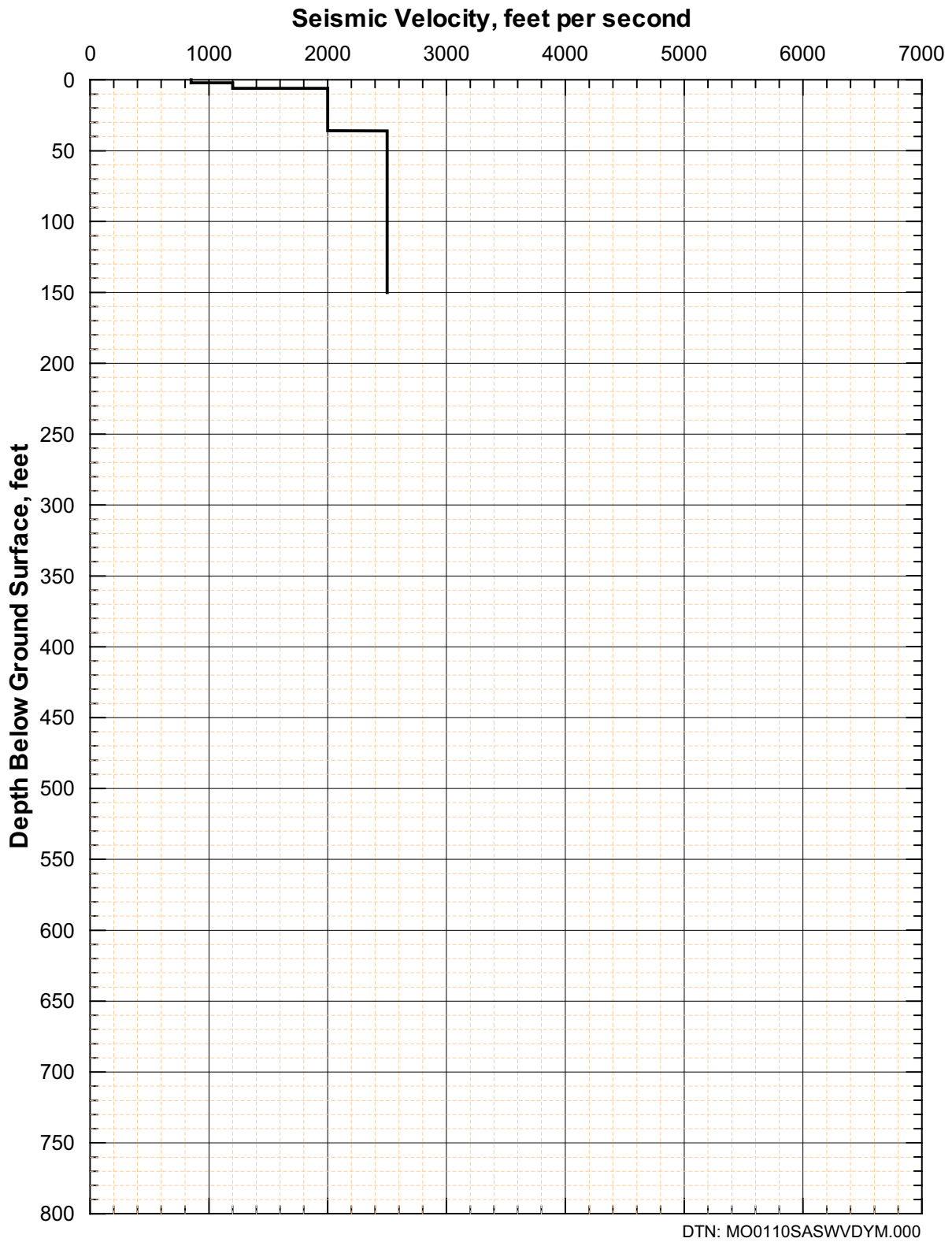


Figure 187. Shear-Wave Velocity Profile from SASW S-9

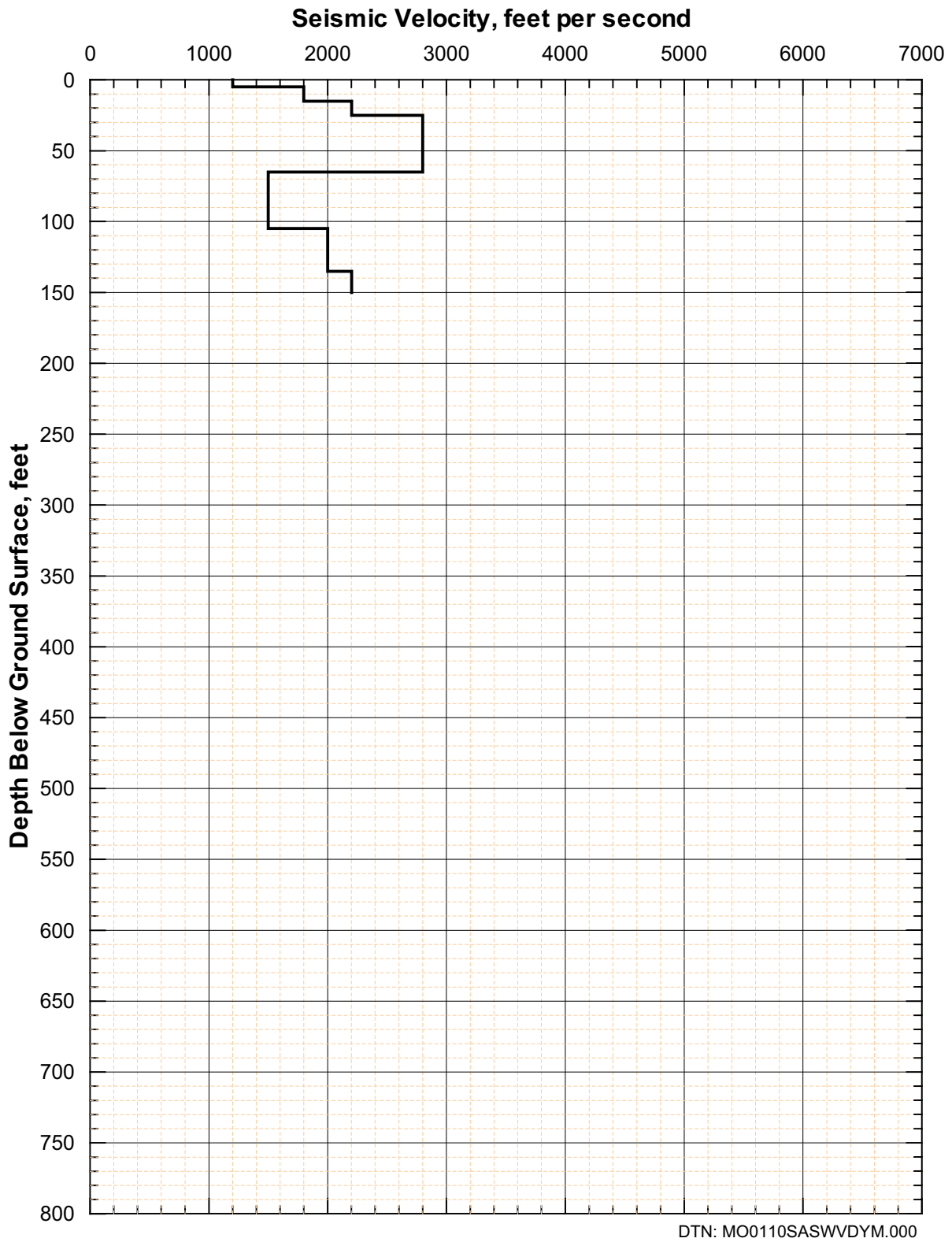


Figure 188. Shear-Wave Velocity Profile from SASW S-10

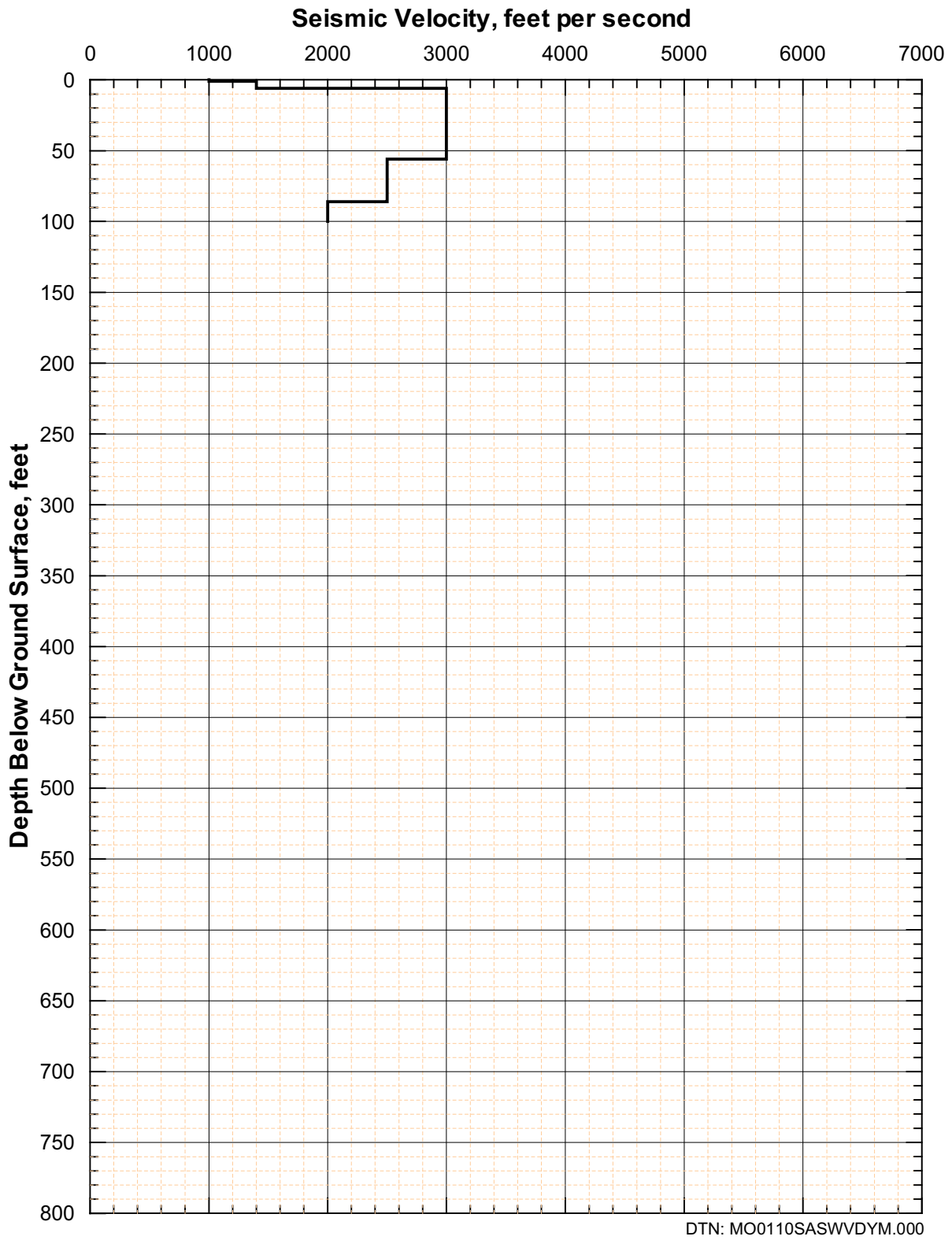


Figure 189. Shear-Wave Velocity Profile from SASW S-11

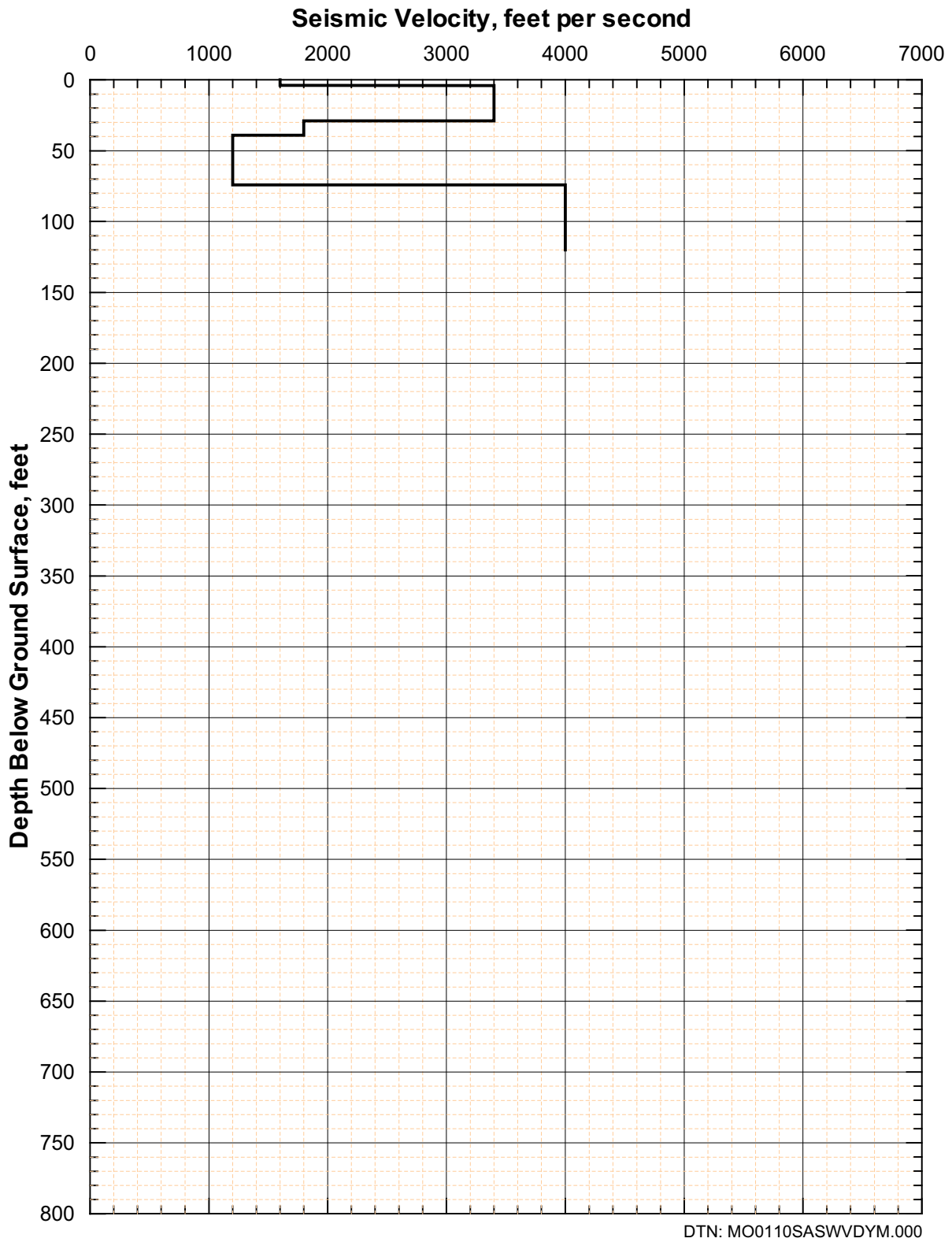


Figure 190. Shear-Wave Velocity Profile from SASW S-12

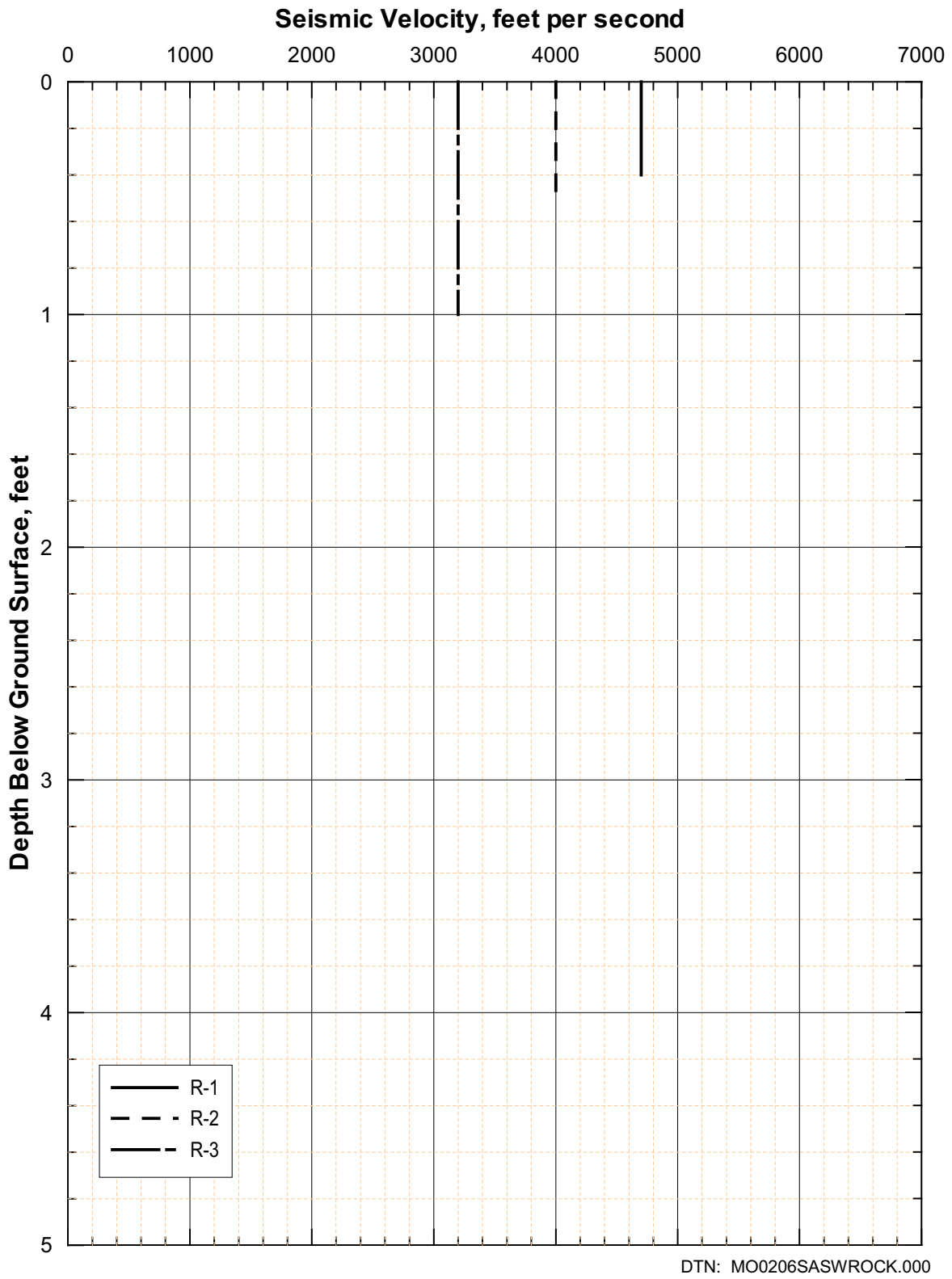


Figure 191. Shear-Wave Velocity Profiles from SASW R Measurements

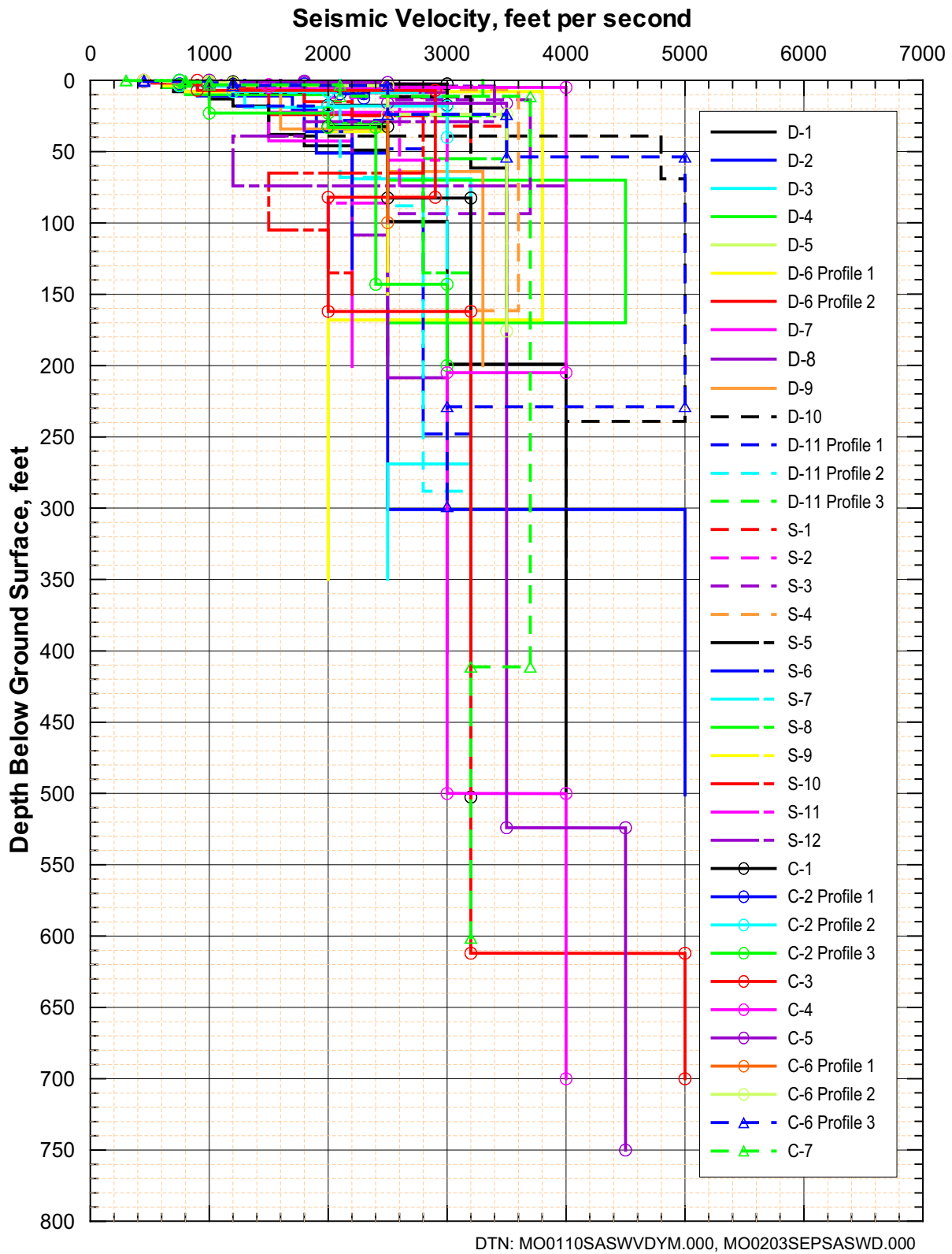
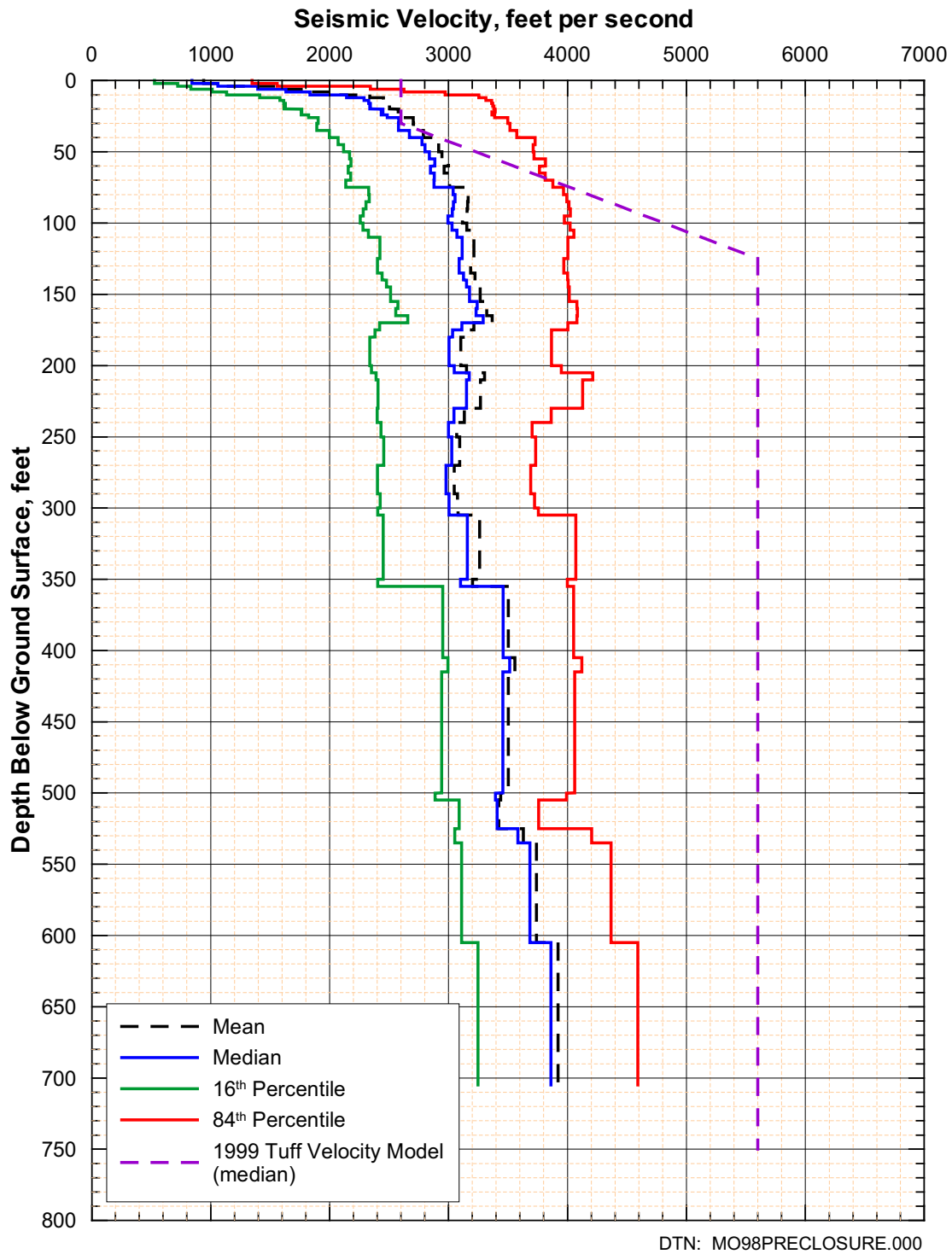


Figure 192. Shear-Wave Velocity Profiles from SASW Measurements on Top of Yucca Mountain



Note: These statistics have been calculated for illustrative purposes only. Final statistics calculated for use in the forthcoming scientific analysis entitled *Development of Seismic Design Input Ground Motions for a Geological Repository at Yucca Mountain* will be submitted to the TDMS.

Figure 193. Statistical Analyses of Shear-Wave Velocity Profiles from SASW Measurements on Top of Yucca Mountain

Of the 22 surveys performed along or near the crest, 13 surveys (C-1, C-3, C-4, C-5, C-7, S-1, S-3, S-4, S-5, S-7, S-8, D-10, and D-11) were oriented approximately parallel to the crest of Yucca Mountain (Figure 157). The profiles determined from these 13 surveys are shown on Figure 194. Nine surveys (C-2, C-6, S-2, S-6, S-9, S-10, S-11, D-8, and D-9) were oriented approximately perpendicular to the crest and generally downslope of the crest (some are on the road leading to the top of Yucca Mountain). The shear-wave velocity profiles from these 9 surveys are presented on Figure 195. On Figure 194, profile D-10 has much higher shear-wave velocities than the other profiles. Likewise, in Figure 195, C-6 yielded profiles that were significantly greater than the others. Interestingly, C-6 and D-10 are located relatively near each other on the mountain (Figure 157), and may reflect an area of locally higher velocity, although the intervening S-5 profile is not anomalously higher than the other profiles.

A comparison between the mean shear-wave velocity profile oriented parallel to the crest and the mean profile from surveys oriented perpendicular to the crest indicates a difference of up to about 600 ft/s in the top 150 ft (Figure 196). This difference may be related to anisotropy due to fracturing in the near-surface volcanic units of Yucca Mountain. Fractures were observed to be generally oriented parallel to the crest and thus velocity measurements perpendicular to the crest are being made across open(?) fractures, possibly resulting in lower velocities. At this time, this hypothesis is speculative. Below a depth of 150 ft, there are few deep profiles perpendicular to the crest to make a valid comparison. Only two profiles extend to depths greater than 200 ft (Figure 195). This lack of deep penetration was due to access limitations down the side of Yucca Mountain.

Eight SASW surveys (D-1, D-2, D-3, D-4, D-5, D-6, D-7, and S-12) were located at some distance on several roads east of the crest of the mountain (Figure 157). In several cases, surveys were conducted along roads situated in drainages where low-velocity alluvial sediments have accumulated. These shear-wave velocity profiles are examined separately. There is considerable variability in the velocities (Figure 197). Figure 198 presents the shear-wave velocity profiles from D-1, D-2, and D-3, which were located towards the north end of the potential (as of July 2000) repository footprint (Figure 157). These three profiles generally show similar trends in shear-wave velocity in the top 200 ft. Below 200 ft, the profiles differ significantly. Figure 199 shows the shear-wave velocity profiles from D-4, D-5, and D-6 located near the central region of the potential (as of July 2000) emplacement area (Figure 157). They are also fairly consistent, and appear to generally have higher velocities in the top 150 ft than profiles D-1, D-2, and D-3. Lastly, Figure 200 presents the shear-wave velocity profiles from D-7 and S-12 located near the south end (Figure 157). As indicated by their shallow velocities, both surveys were located on a ridge and thus on rock rather than alluvium. Both of these profiles exhibit significant velocity inversions. However, the shear-wave velocity below the low-velocity zone is not well resolved with the SASW method. Therefore, the difference in velocities at depth may not be as great as is indicated on Figure 200.

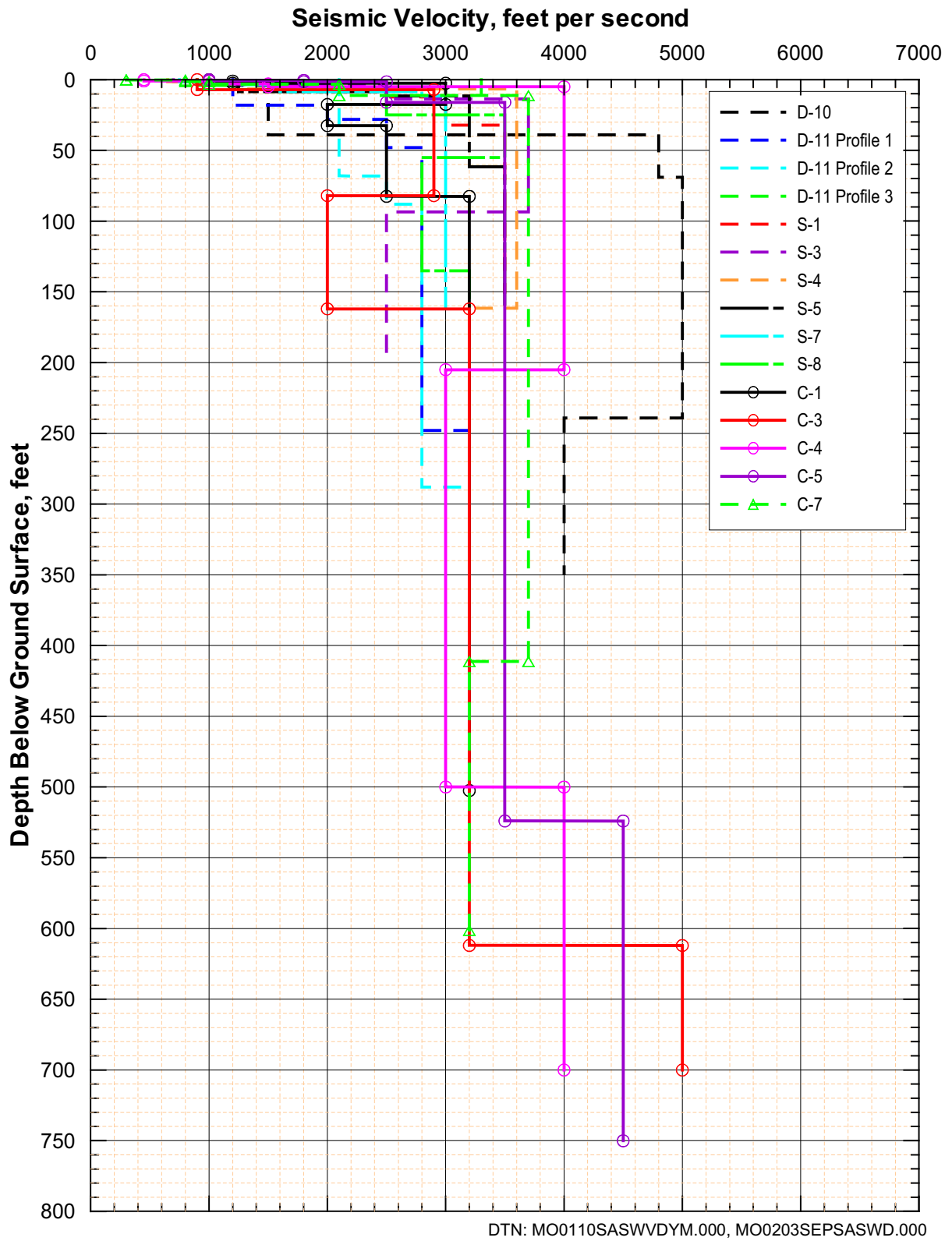


Figure 194. Shear-Wave Velocity Profiles from SASW Measurements Parallel to the Crest of Yucca Mountain

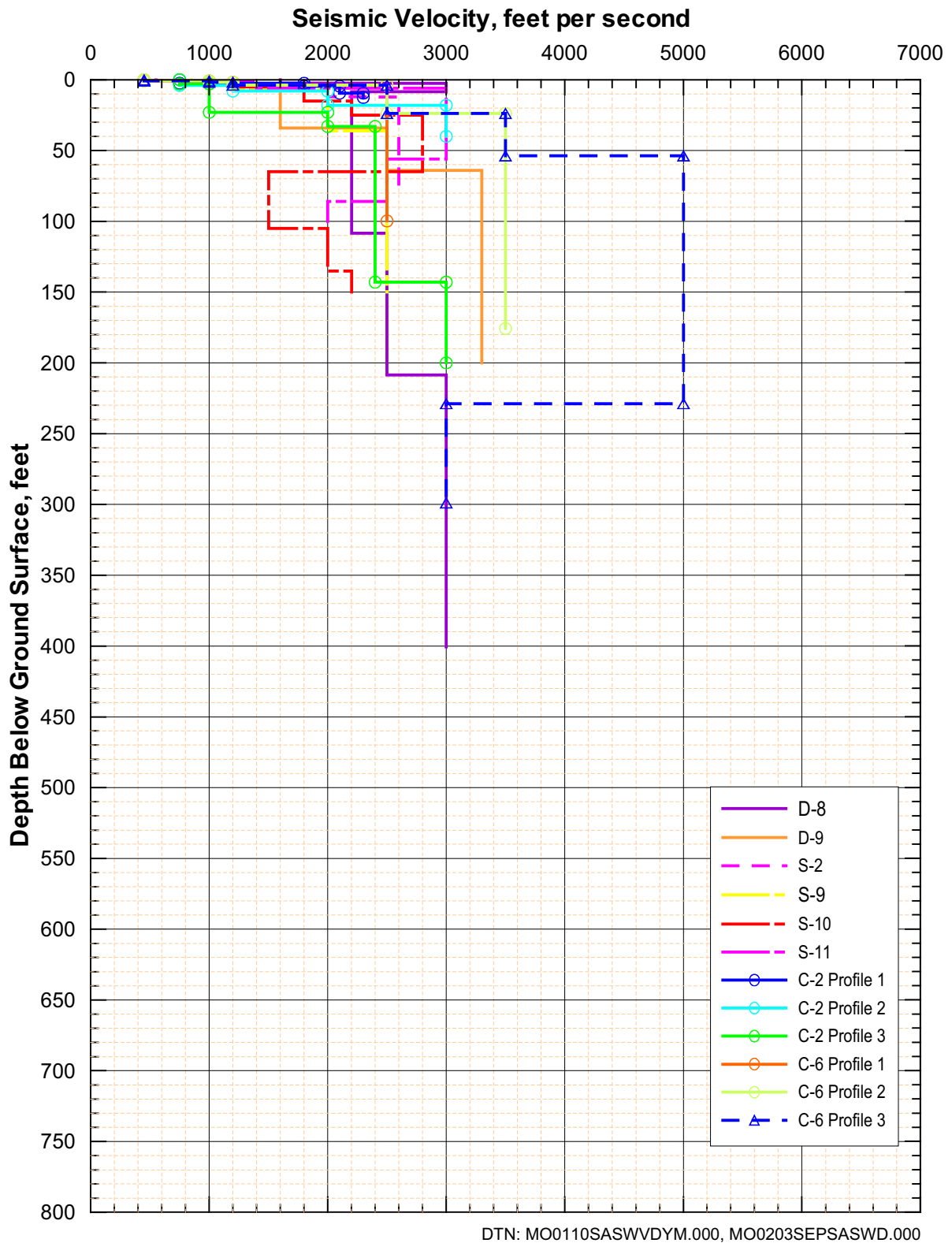
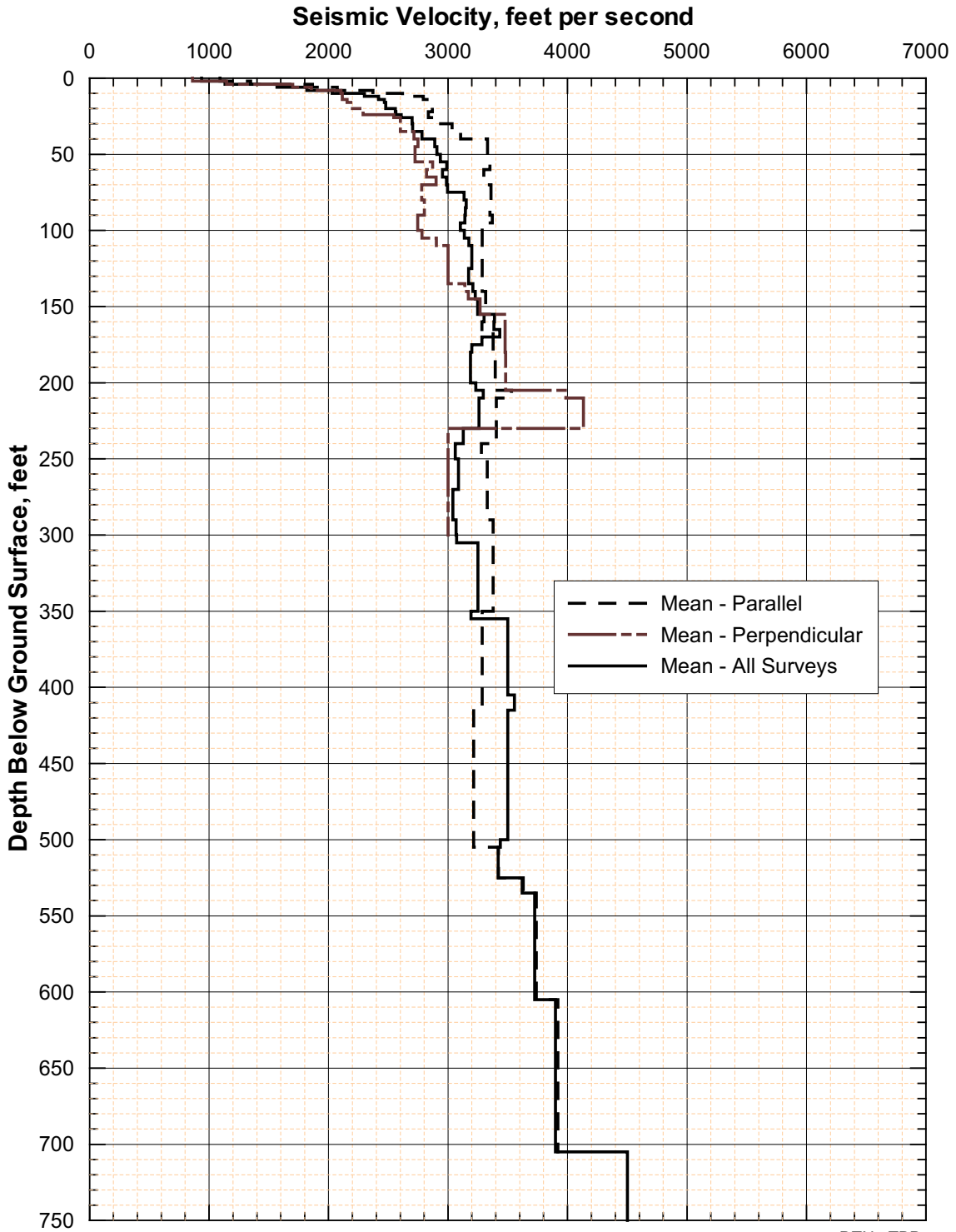


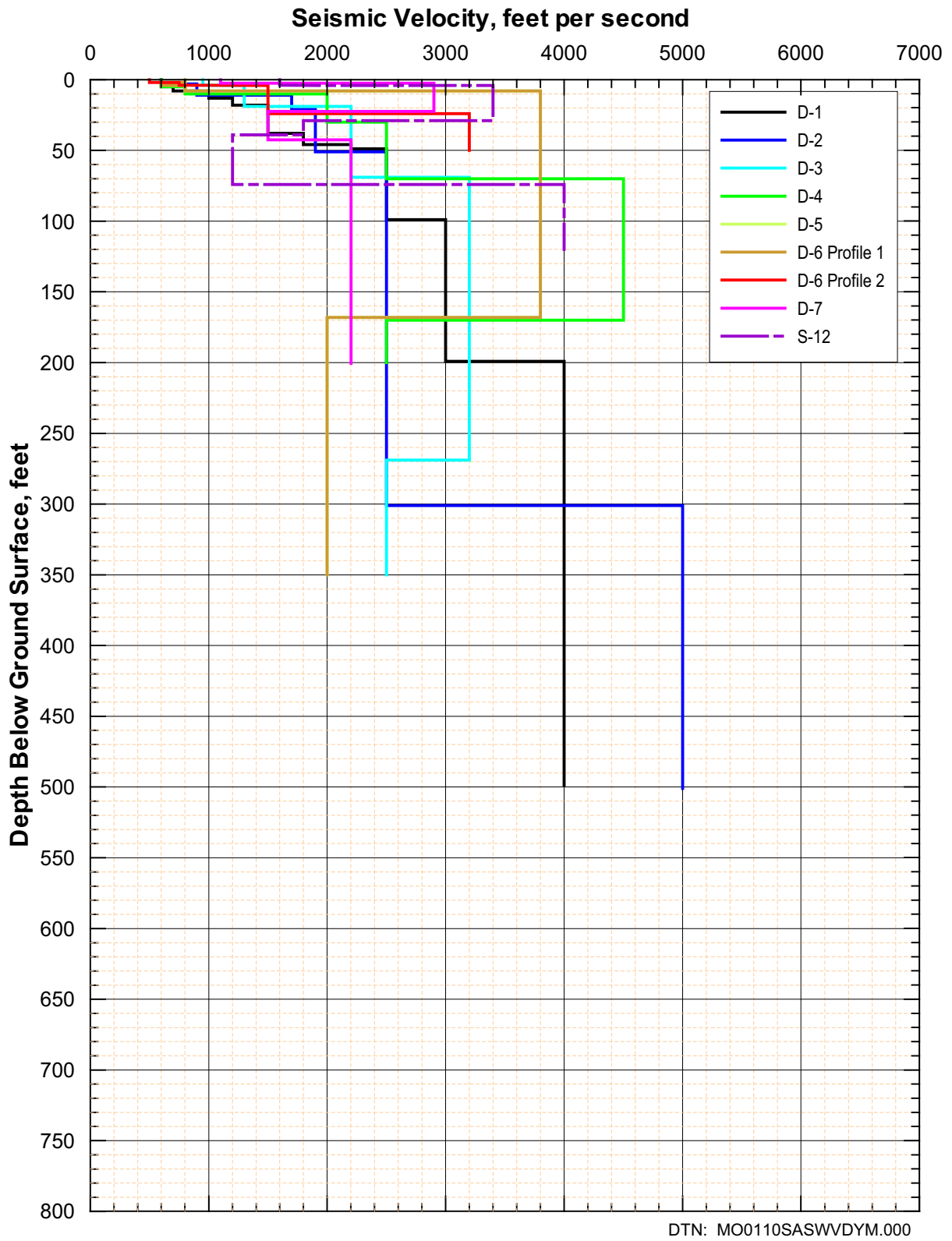
Figure 195. Shear-Wave Velocity Profiles from SASW Measurements Perpendicular to the Crest of Yucca Mountain



DTN TBD

Note: These statistics have been calculated for illustrative purposes only. Final statistics calculated for use in the forthcoming scientific analysis entitled *Development of Seismic Design Input Ground Motions for a Geologic Repository at Yucca Mountain* will be submitted to the TDMS.

Figure 196. Comparison of Mean Shear-Wave Velocity Profiles from SASW Measurements Relative to the Orientation to the Crest of Yucca Mountain



Note: D-5 and D-6, Profile 1, have identical profiles (line for D-5 is hidden by line for D-6, Profile 1).

Figure 197. Shear-Wave Velocity Profiles Off the Crest of Yucca Mountain

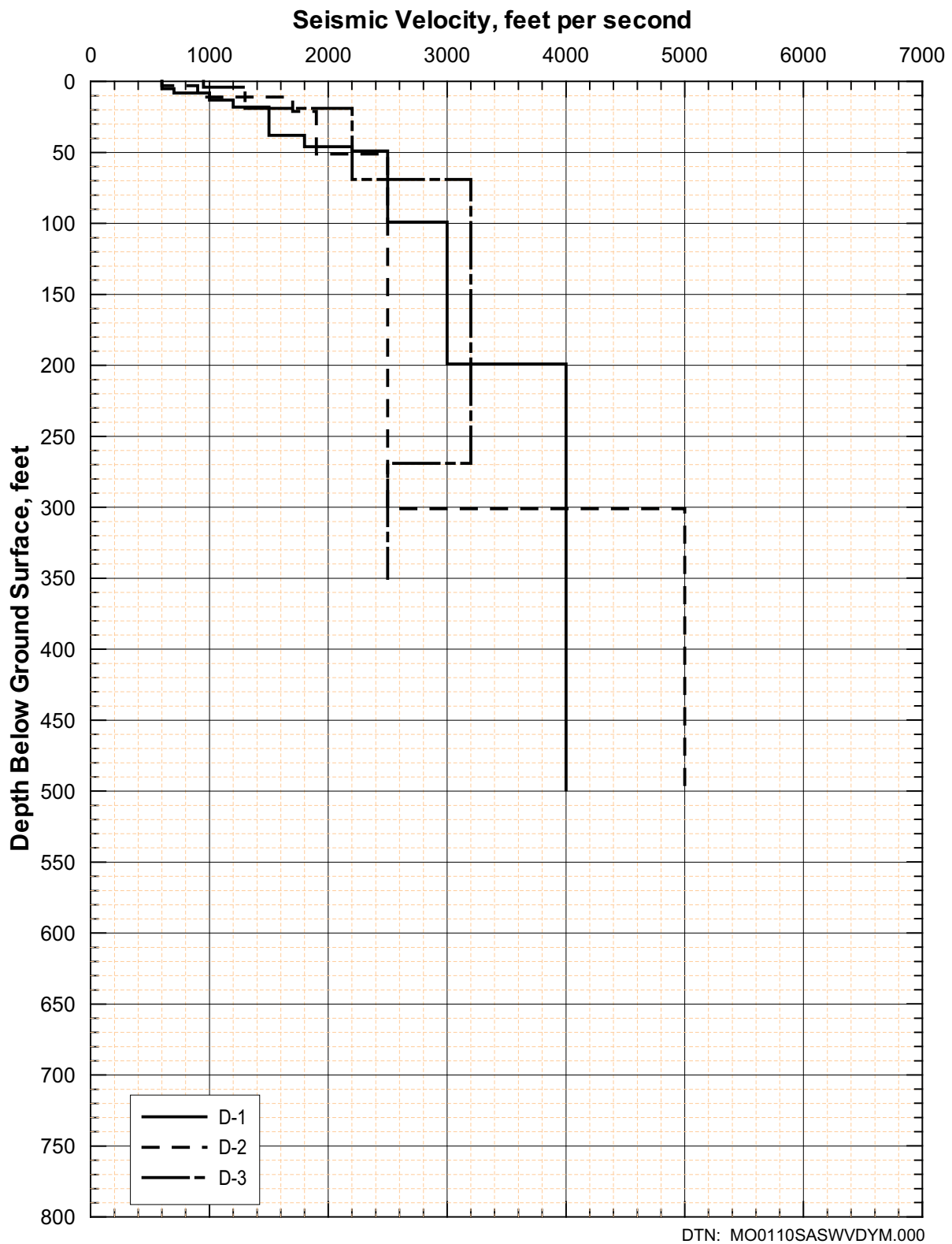


Figure 198. Shear-Wave Velocity Profiles from SASW D-1, D-2, and D-3

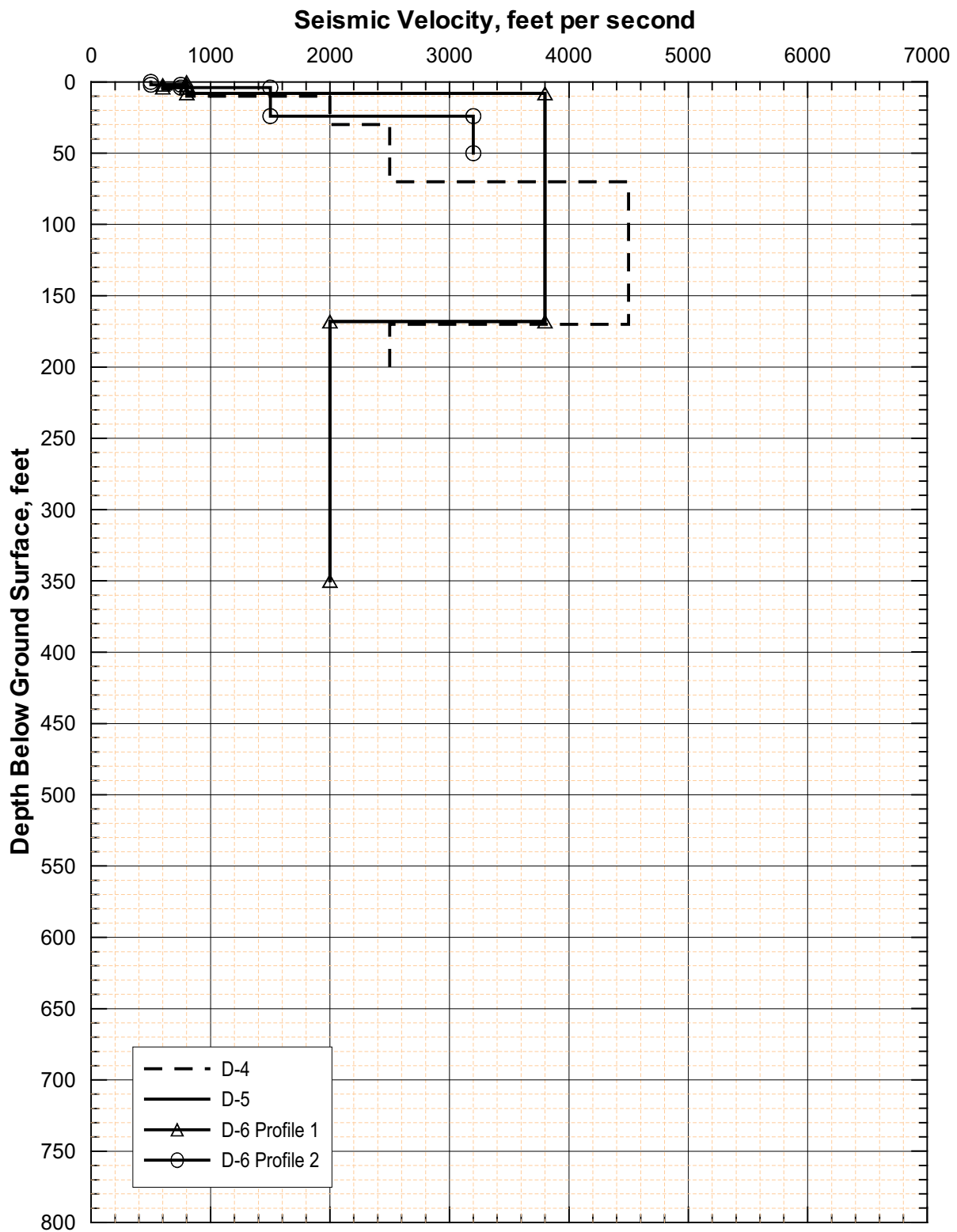


Figure 199. Shear-Wave Velocity Profiles from SASW D-4, D-5, and D-6

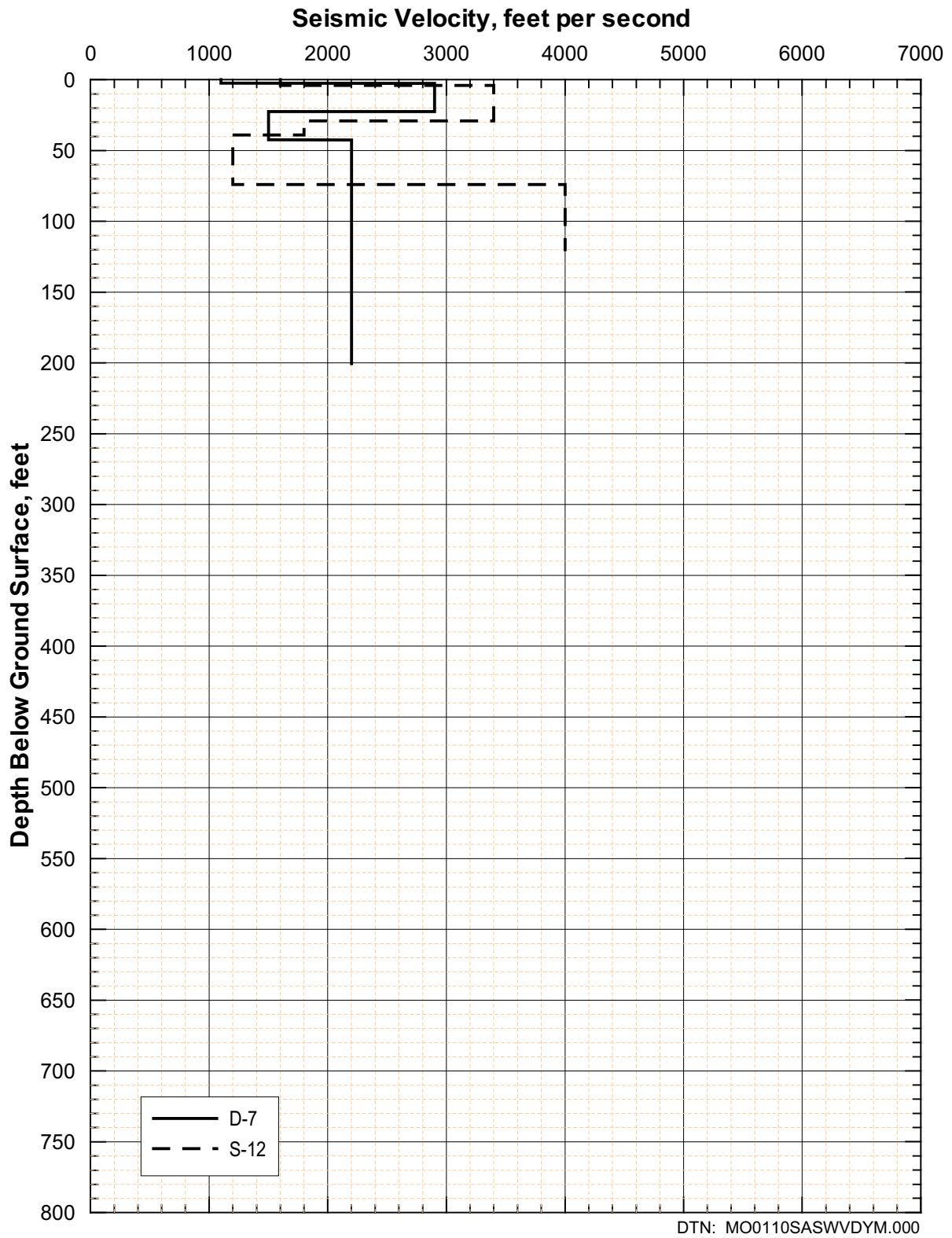
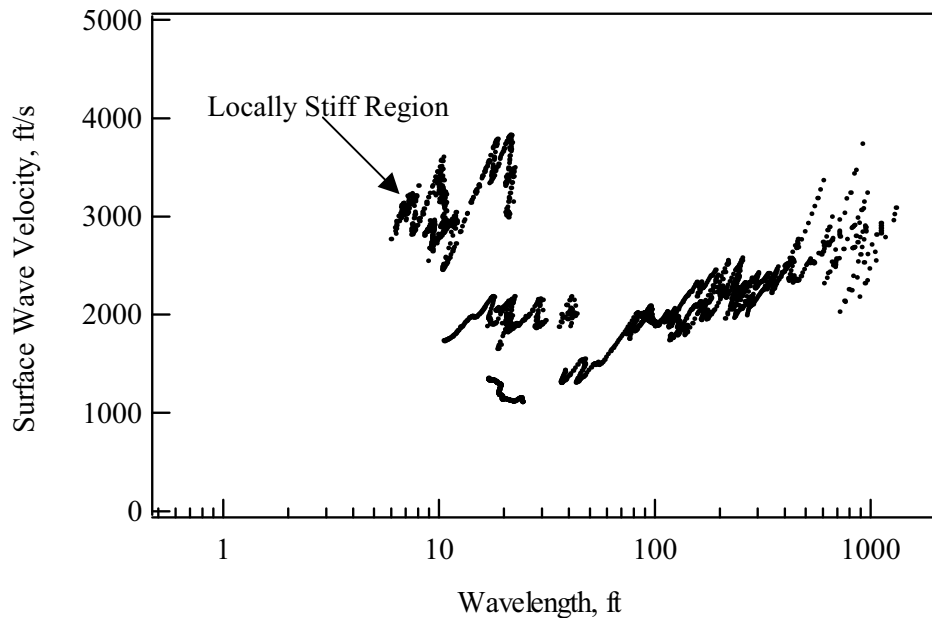


Figure 200. Shear-Wave Velocity Profiles from SASW D-7 and S-12

Three SASW surveys (R-1 to R-3) were performed to measure the shear-wave velocity of the exposed, visually intact (although weathered) rock (Figure 157). The rock outcrop size allowed only very close receiver spacings (0.5 ft to 1 ft) to be used. Figure 191 presents the three shear-wave velocity profiles estimated from these sites. The velocities range from 3,200 to 4,700 ft/s.

It is interesting to note that the shear-wave velocities from the exposed rock are much higher than the velocities recorded for wavelengths ranging from approximately 5 to 20 ft from the other surveys. For example, at C-1 adjacent to R-1 (Figure 157), the shear-wave velocities near the surface (top 5 ft) are on the order of 1,100 ft/s, much less than the 4,700 ft/s recorded at R-1. Likewise at C-3, the velocity in the top 7 ft is 900 ft/s compared with 4,000 ft/s at R-2. At D-10, the quality of the near-surface dispersion curve is poor and shows some variability; however, the same trend of lower velocities as compared with the rock site is observed. These results illustrate the difference between local and global measurements of surface-wave velocity at a discontinuous rock/soil site with lateral variability. Although there are localized regions of intact higher velocity rock, the SASW method at longer spacings measures the velocity of a larger area consisting of the matrix of rock, damaged rock, and infill material.

The results from D-11 indicate that, in some cases, these locally stiff regions may be detected by SASW measurements. Figure 201 shows the dispersion curve recorded from D-11. At shorter wavelengths (shallow penetration, close receiver spacings, and small lateral extent), it can be seen that three different shear-wave velocities are measured over similar wavelength ranges. These multiple dispersion curves indicate local regions of different stiffness that are detected by the SASW method. As the receivers are spread out and a larger volume of the ground is sampled, the global velocity is measured. The stiffest region measured at D-11 had a shear-wave velocity of 3,300 ft/s, which is within the range of velocities measured at the intact rock sites. The three profiles determined at D-11 are presented on Figure 178.



Source: Wong (2002a, Appendix 37)

Figure 201. Experimental Dispersion Curve Recorded at D-11 showing the Variability in Surface Wave Velocity at Shallow Depths

6.4.3 Downhole Seismic Surveys

The results of SASW (C) surveys conducted on the crest in the summer 2000 indicated that a high shear-wave velocity gradient may exist in the near-surface rock (Section 6.4.2). It was considered important to acquire near-surface velocity information using an independent approach. Thus, shear- and compression-wave velocities were measured in 8 boreholes along or near the crest of Yucca Mountain by Redpath Geophysics (Figure 202). These downhole velocity surveys were performed in the few open holes above the emplacement area on Yucca Mountain. The procedures, equipment, and analysis techniques of this standard downhole method are described in Section 6.2.5.

Unfortunately, the number of surveyed holes was small and they consisted of neutron-logging holes that are shallow, generally less than 100 ft deep. They also contained a 5-inch ID hanging steel casing that was ungrouted for the entire depth of the borehole. Thus the contact between the casing and the walls of boreholes was unknown and the steel casing prevented the use of the fluxgate compass in the sensor package (Section 6.2.5).

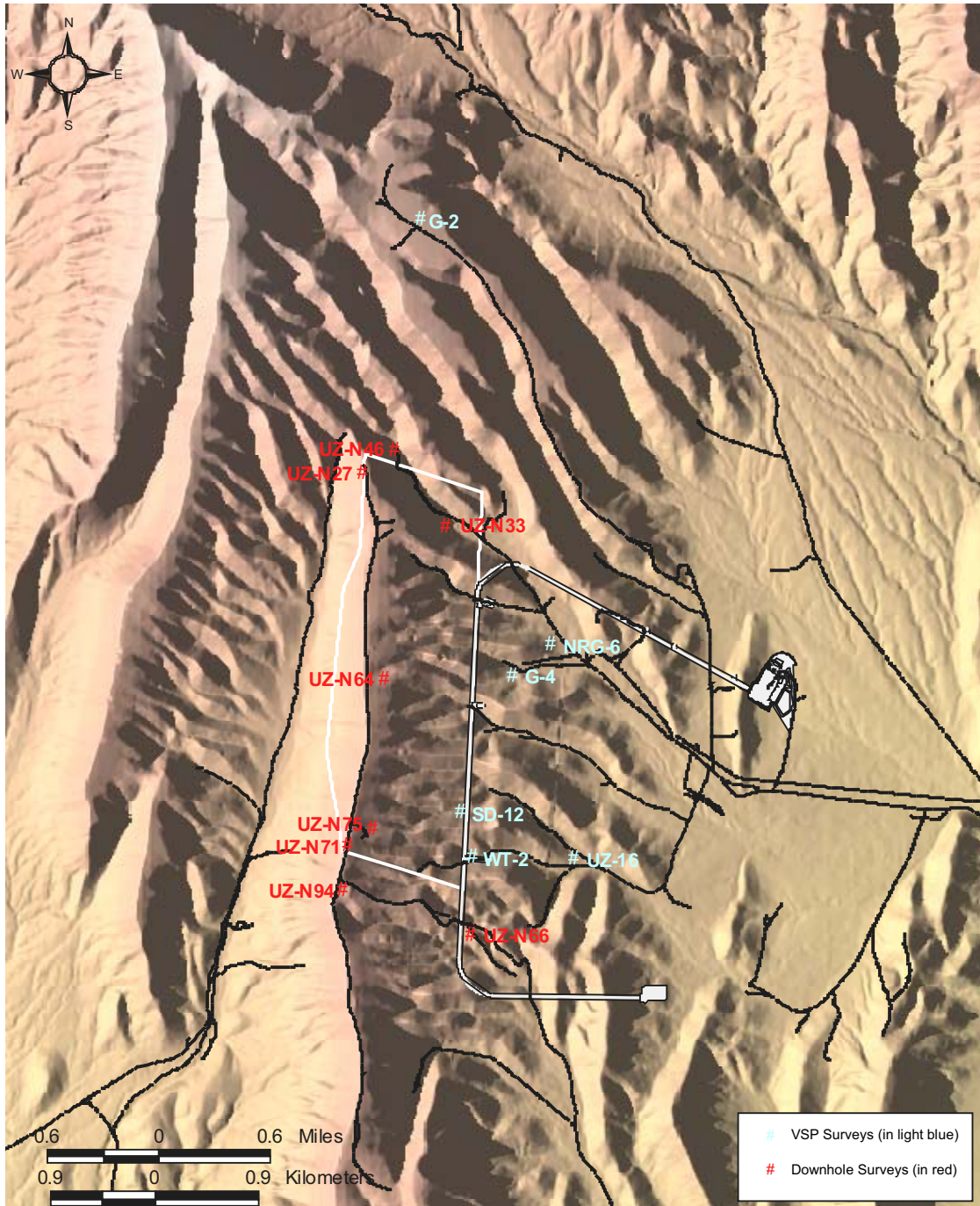
Shear-wave refraction was also attempted. The initial attempt near hole UZ-N27 was not successful, primarily because of a velocity inversion immediately below the surface. Thus, no other refraction surveys were attempted.

Despite the seeming unsuitability of the neutron-logging holes for velocity surveys, the initial results were promising and 8 holes were surveyed. (The results of the downhole and SASW surveys showed that velocity inversions were not unusual in the vicinity of the crest and that further attempts to acquire seismic refraction data were not warranted.) All procedures and relevant calibration information for the downhole measurements at the top of Yucca Mountain are documented in Scientific Notebook SN-M&O-SCI-039-V1 (Redpath 2002). The field work for these investigations was performed from 18 to 23 June 2001. Table 25 lists the neutron-logging holes that were surveyed and their locations are shown on Figure 202.

Table 25. Boreholes Used for Downhole Surveys at Crest of Yucca Mountain

Borehole Number	Elevation Above MSL (ft)	Depth of Survey (ft)
UZ-N27	4857	179
UZ-N33	4329	71
UZ-N46	4501	95
UZ-N64	4789	54
UZ-N66	4358	48
UZ-N71	4925	48
UZ-N75	4799	28
UZ-N94	4926	25

DTN: MO0202DVDWHBSC.002, MO0101COV00396.000



Note: The potential emplacement area as of July 2000 is shown.

Figure 202. Boreholes on or Near the Crest of Yucca Mountain Where Downhole Velocity and VSP Measurements Were Performed

6.4.3.1 Procedures, Equipment, and Analysis

The analysis procedures have been previously described in Section 6.2.5.2. In 7 of the 8 holes, the BHG-2 sensor package was oriented so that one of the horizontal geophones was roughly

aligned with the shear-wave beam. This alignment was done manually since the fluxgate compass in the sensor package could not be used. A half-inch-square piece of reflective tape was attached to the top of the geophone housing. By looking down the borehole with the aid of a flashlight and twisting the connecting cable, the BHG-2 could generally be rotated to an acceptable and known alignment simply by observing the position of the reflected spot of light. Because the lock-in spring is extended at the bottom of the hole and the transducer is dragged up the hole as the survey progresses, the sensor package tended to maintain its initial orientation all the way up the hole. Frequent checks of the orientation were made by looking down the hole and, if necessary, the spring could be released to re-orient the BHG-2. This simple technique was effective even to a depth of 100 ft. UZ-N27 was too deep to use this method so, not knowing the orientation of the BHG-2, the output of both horizontal geophones was recorded.

Travel times were measured from the bottom up at 1-m (3.3 ft) intervals to the surface. An exception to this procedure was made at UZ-N27, in which measurements were made at 2-m (6.6 ft) intervals from 55 to 9 m (180.5 to 29.5 ft) bgs, and then at 1-m (3.3 ft) intervals above that. Although a downhole cable with metric depth markings was used, all results are reported in ft and ft/s.

6.4.3.2 Results

Plots of corrected shear-and compression-wave times *vs.* depth are shown in Attachment XVI. These plots also show the least-squares values of shear-wave velocities, rounded to the nearest 5-ft/s, and the depths to the interfaces.

Very little of the compression-wave data acquired in these surveys is usable. In almost every instance, a relatively strong signal propagated down the steel casing (labeled as a ‘casing wave’ on the time *vs.* depth plots in Attachment XVI) and obscured the compression wave traveling through the rock. A good example of this phenomenon can be seen in the compression-wave records for UZ-N27 (Redpath 2002, Attachment A). A casing wave is dominant down to about 15 m (~ 50 ft), but below this depth, the true compression wave can be seen. The offset of the compression source from the hole collar was increased in an effort to enhance the actual compression wave, but this was not effective. In general, only data points for the shallowest and for the very deepest measurement points are considered valid. An exception is hole UZ-N46, for which the compression-wave velocity seems plausible for the entire depth of the hole.

The question as to why the shear-wave data are considered valid and most of the compression signals are considered to be unreliable can only be answered intuitively. The contact between the steel casing and the surrounding rock is probably not continuous and frictional rather than a solid, uniform, cemented bond as would be the case had it been grouted. A compression wave propagating down through the rock must excite the casing along its axis, *i.e.*, in its stiff direction, in order to be detected by the vertically-sensitive geophone locked inside the casing. It is suspected that it is difficult for a compression wave with sufficient amplitude to be transmitted across the friction contact between the rock and steel pipe. Conversely, a downward traveling shear wave excites the casing in its radial or flexible direction, and any slippage along the length of the casing at the boundary would not be an issue.

The final values of shear-wave velocities are listed in Table 26 and shown in Figures 203 to 210. Also shown is the generalized lithology based on an examination and re-evaluation of the borehole logs. The re-evaluation of these mainly pre-1989 boreholes was required largely because of a change in lithostratigraphic nomenclature. The nomenclature used in this report is based on Buesch et al. (1996). In general, there is only a weak correlation between the velocity layers and the lithology (e.g., UZ-N46). All profiles are shown in Figure 211, illustrating the large variability in shear-wave velocities. Note that there are considerable differences in elevation of the ground surface at these boreholes (maximum of 597 ft; Table 25). The median and plus and minus one standard deviation profiles for the 8 profiles are shown in Figure 212. Compression-wave velocities are not tabulated because of the spotty and questionable results due to interference from the casing wave.

In general, the overall quality of the shear-wave arrival times is surprisingly good considering the uncertainty regarding the contacts between the casing and borehole wall. There is little scatter of the data points about their respective trend lines (Attachment XVI). The scatter is most probably attributable to the absence of grout and the intermittent contact between the steel casing and the rock. The scatter is not due to insufficient signal amplitudes, to noise from extraneous sources such as nearby machinery, nor to some systemic flaw in the recording instrumentation or procedures.

The most questionable data were acquired in UZ-N71, and two attempts were required to obtain plausible shear signals. The shear waves collected in the first attempt were judged to be non-identifiable, and the source was moved to another location for the second try, which resulted in marginally acceptable signals.

The near-surface velocity inversion at UZ-N27, noted earlier as an impediment to a refraction survey, is shown on the plot of travel times against depth for that hole (Figure XVI-1). The inversion exists immediately below a thin (~ 5 ft), relatively fast ($v_s \sim 2200$ ft/s) layer of rock present right at the surface. In an attempt to collect shear-wave refraction data at UZ-N27, usable signals would not propagate beyond about 100 ft, despite many blows to the shear-wave beam, and only the velocity of the thin layer at the surface was evident on the time vs. distance plot.

As previously mentioned, there is always some judgement involved when assigning travel-time data points to a layer. Often the change of slope of the data points is not especially pronounced when crossing the boundary between one velocity zone and the one immediately below, and the exact depth of the boundary becomes somewhat uncertain due to the inherent scatter in the data. Nevertheless, least-squares calculations of slopes were used to determine shear-wave velocities in each hole.

An examination of Figure 211, which shows all the velocity profiles, indicates considerable variability in the top 50 ft. A significant velocity contrast is observed in UZ-N46 and UZ-N71. A significant high-velocity spike (?) is observed in UZ-N64. This variability is reflected in the mean, median, and plus and minus one standard deviation profiles shown in Figure 212. The wide range in the values of shear-wave velocities and the apparent lack of stratigraphic correlation between holes (Figures 203 to 210) demonstrate the heterogeneous nature of the volcanic deposits that comprise the Yucca Mountain site.

Table 26. Downhole Shear-Wave Velocities at Crest of Yucca Mountain

UZ-N27	Depth Range (ft)	Velocity (ft/s)
	1.5 - 5	2,200
	5 - 28	1,265
	28 - 88	1,860
	88 - 127	3,365
	127 - 179	2,535
UZ-N33	Depth Range (ft)	Velocity (ft/s)
	1.5 - 9	1,245
	9 - 71	2,790
UZ-N46	Depth Range (ft)	Velocity (ft/s)
	2 - 31	1,275
	31 - 81	1,580
	81 - 95	5,500 ±
UZ-N64	Depth Range (ft)	Velocity (ft/s)
	2 - 8	1,735
	8 - 31	2,140
	31 - 41	3,995
	41 - 54	2,190
UZ-N66	Depth Range (ft)	Velocity (ft/s)
	2 - 5	1,525
	5 - 31	2,650
	31 - 48	1,280
UZ-N71	Depth Range (ft)	Velocity (ft/s)
	2 - 22	1,735
	22 - 48	5,000 ±
UZ-N75	Depth Range (ft)	Velocity (ft/s)
	1.5 - 10	2,065
	10 - 28	2,680
UZ-N94	Depth Range (ft)	Velocity (ft/s)
	1.5 - 25	2,835

DTN: MO0202DVDWHBSC.002

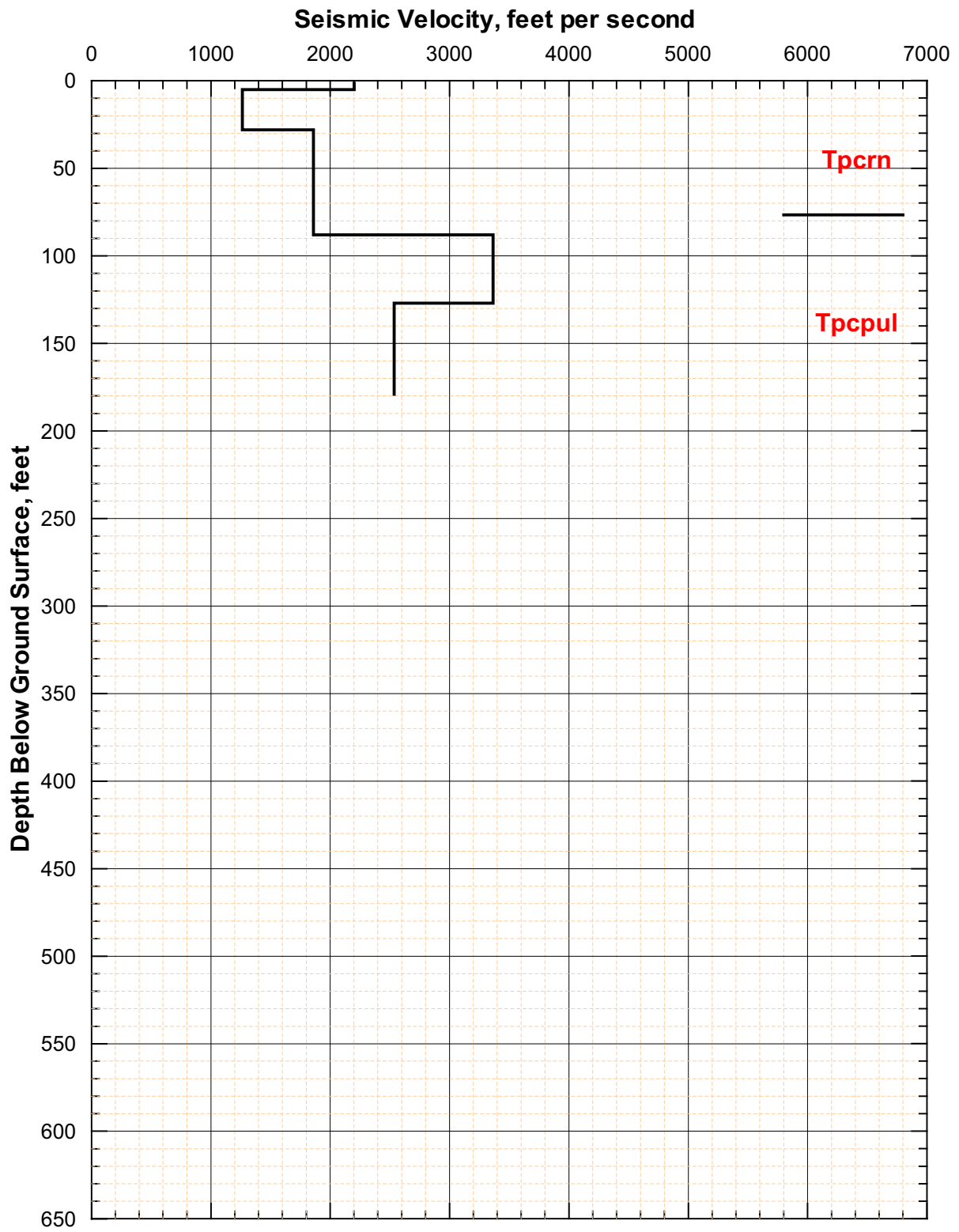
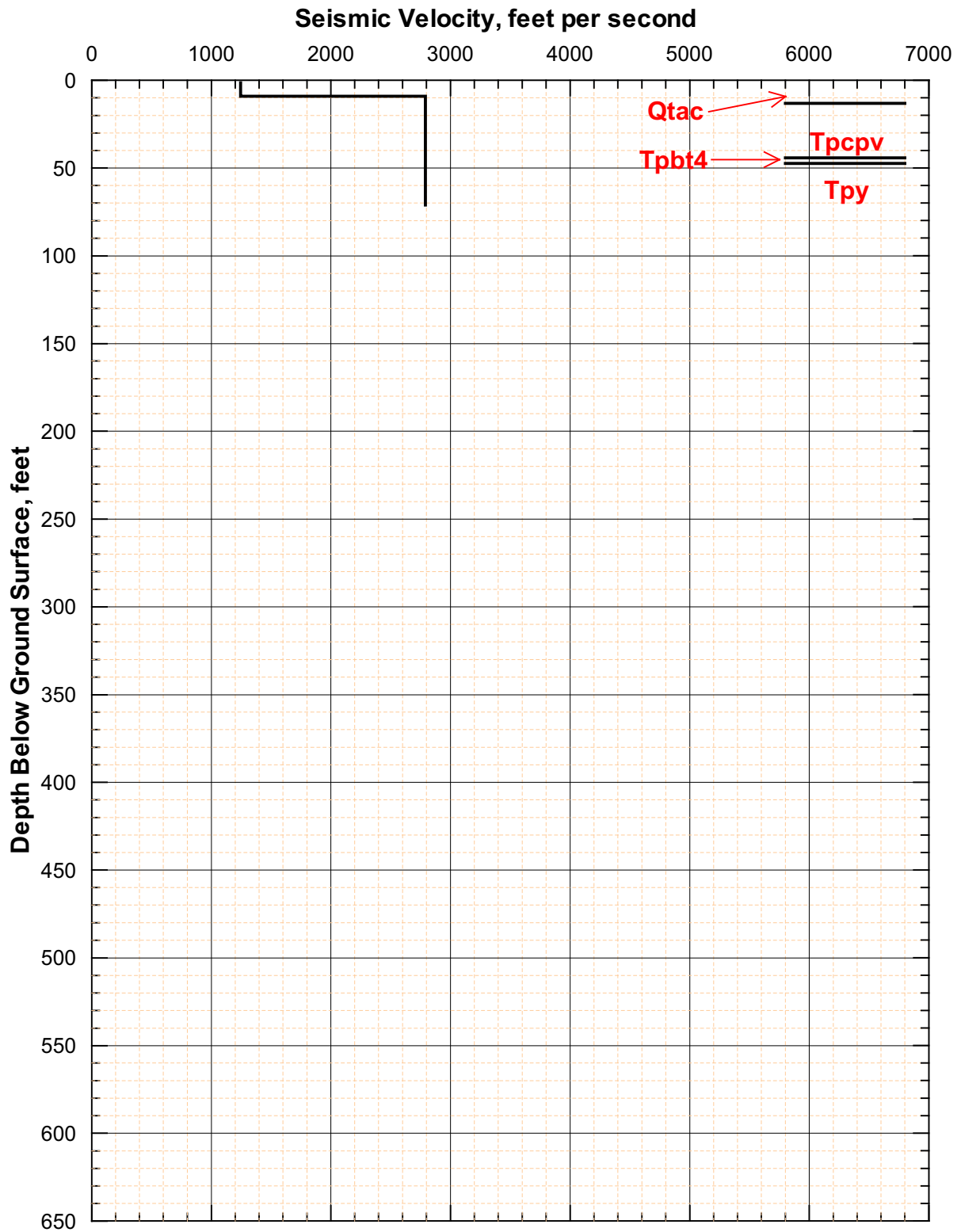
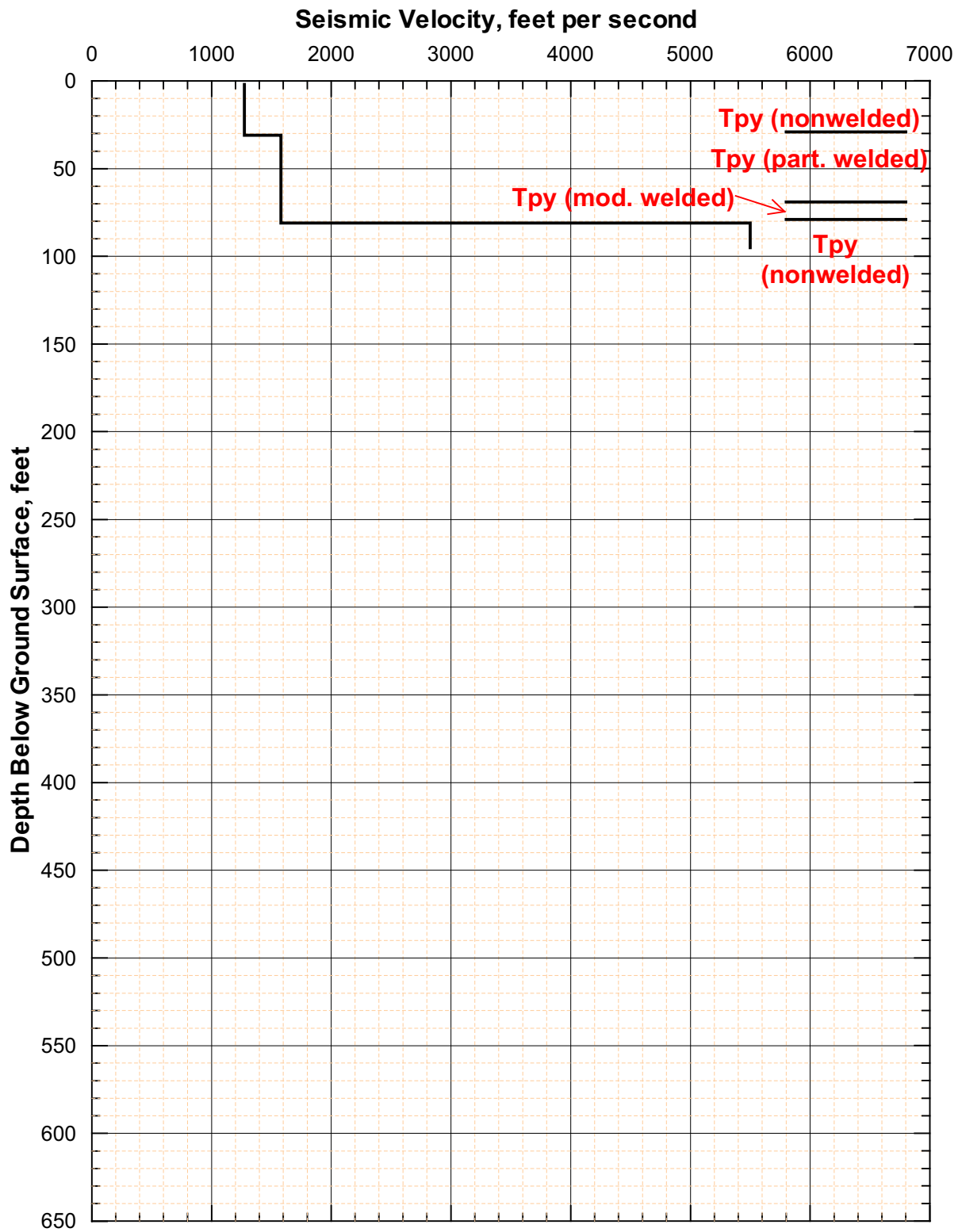


Figure 203. UZ-N27 Shear-Wave Velocities from Downhole Measurements and Generalized Lithology



DTNs: MO0202DVDWHBSC.002, GS940208314211.006

Figure 204. UZ-N33 Shear-Wave Velocities from Downhole Measurements and Generalized Lithology



Sources: DTN: MO0202DVDWHBSC.002, Blout et al. (1994, page 51)

Figure 205. UZ-N46 Shear-Wave Velocities from Downhole Measurements and Generalized Lithology

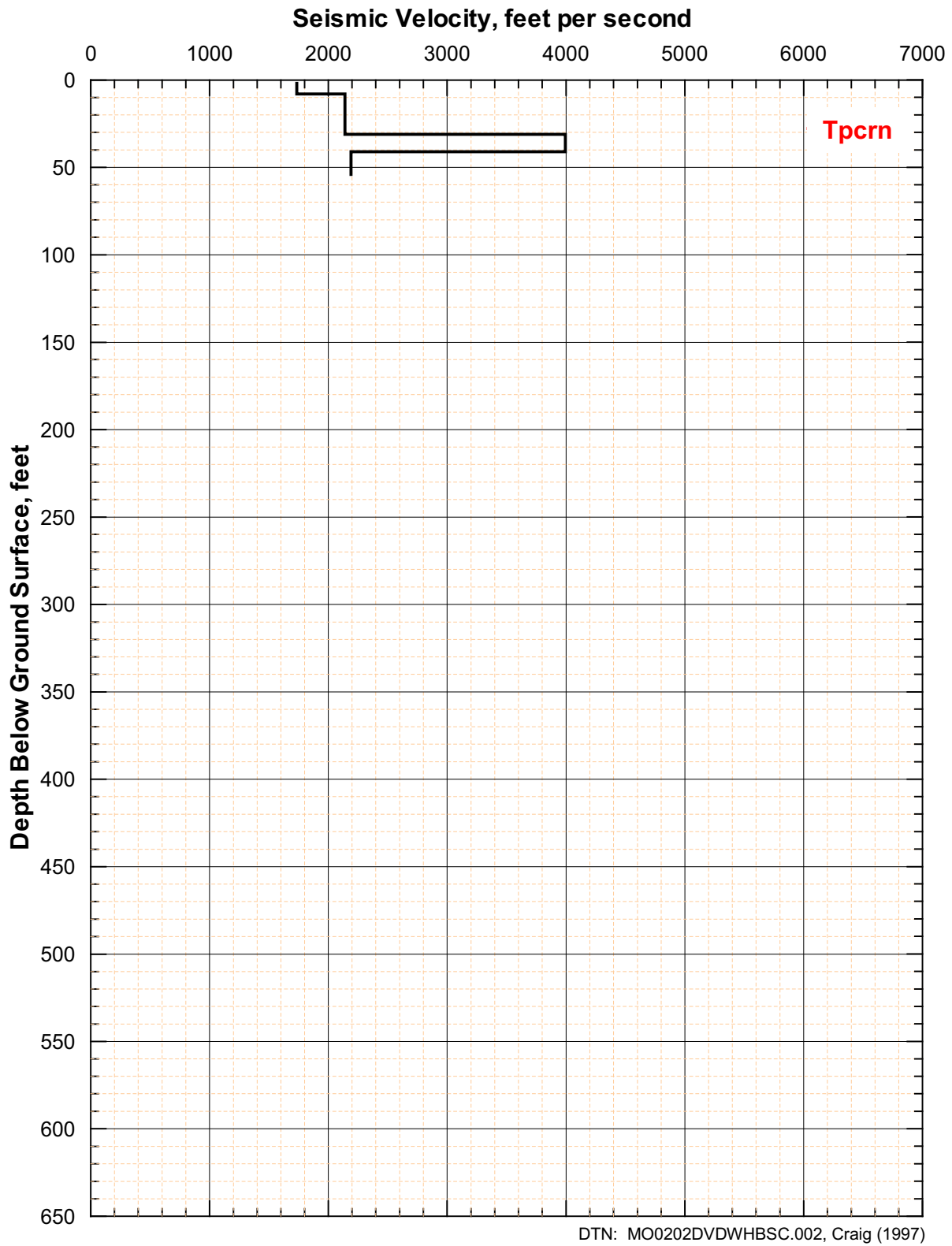
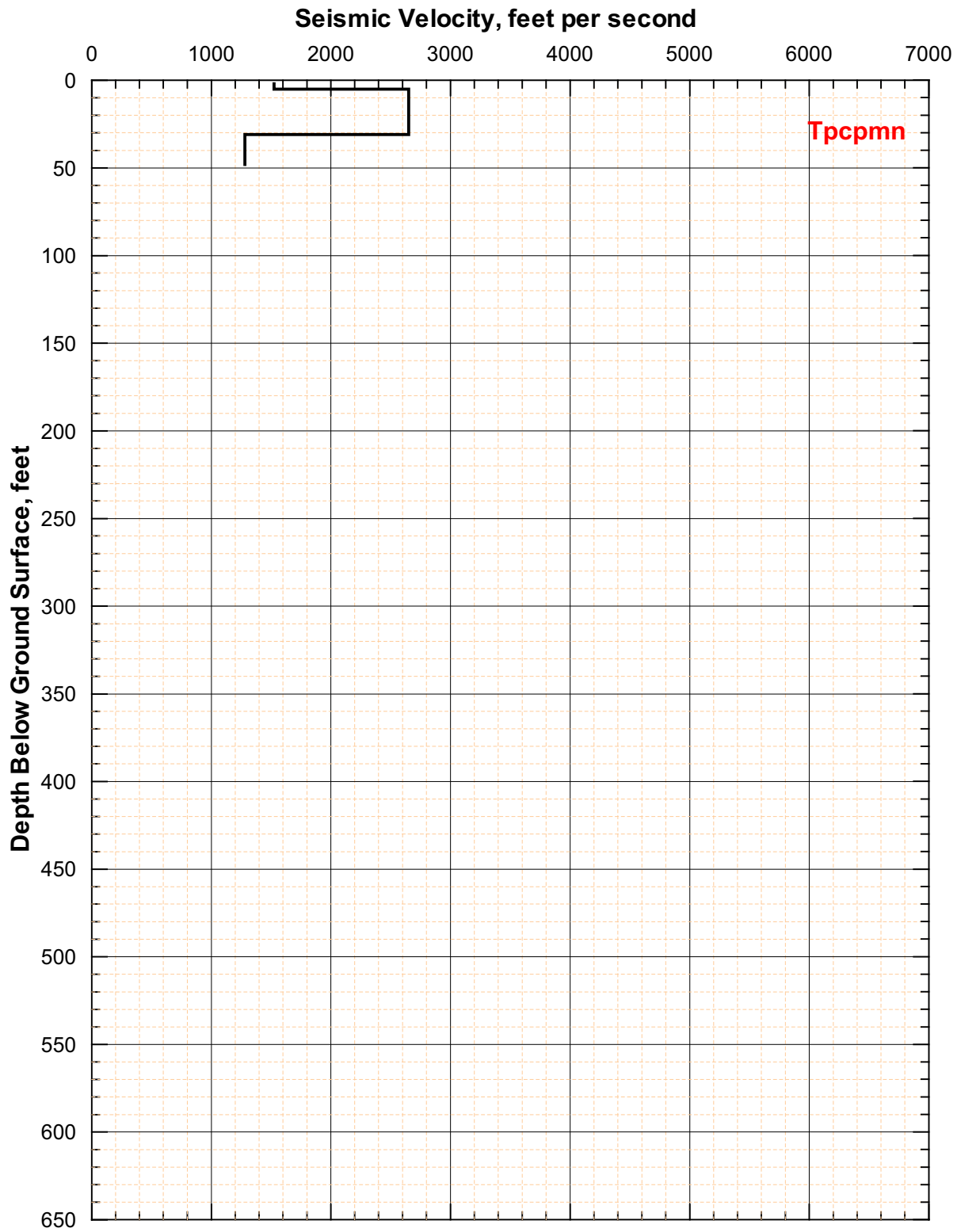
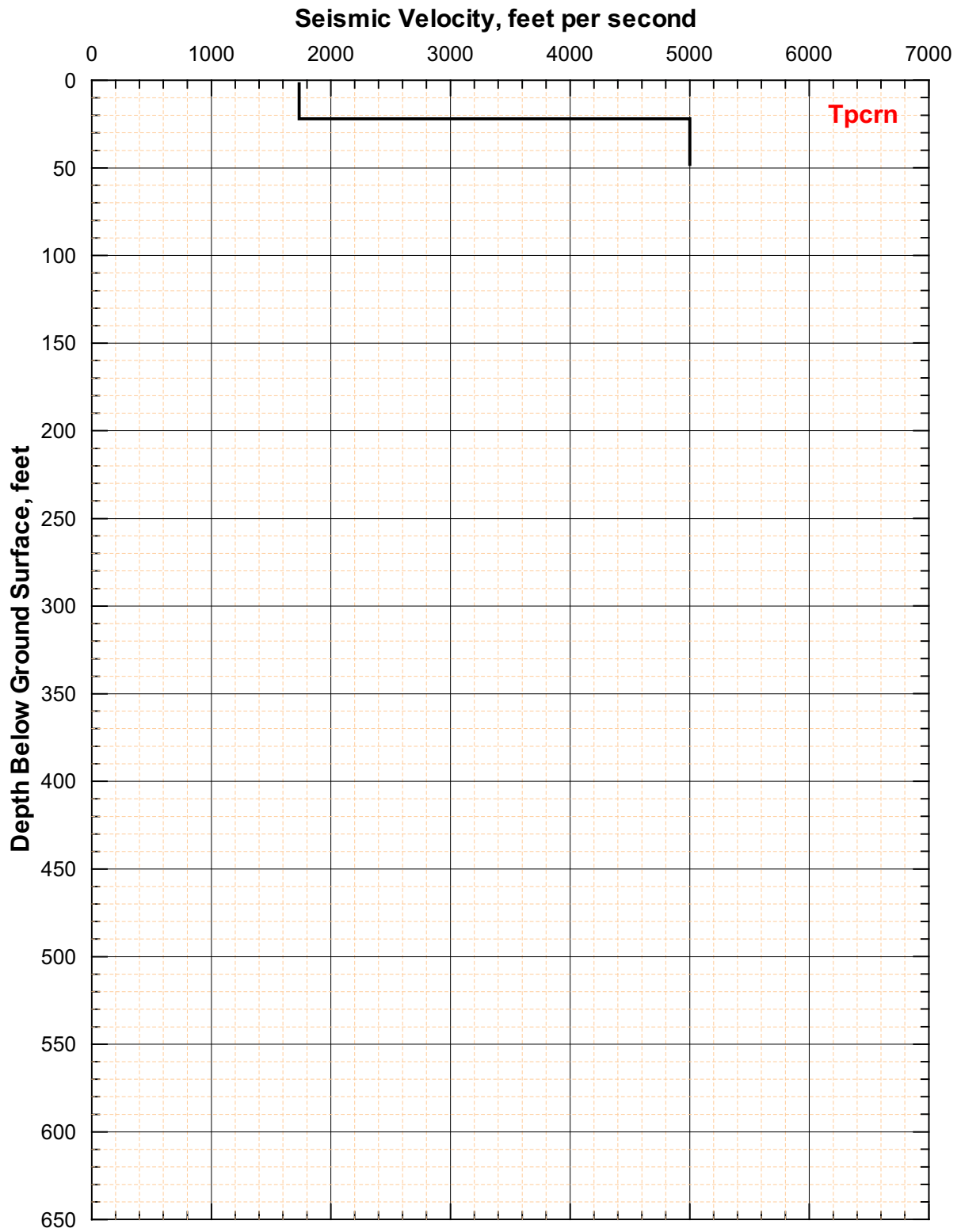


Figure 206. UZ-N64 Shear-Wave Velocities from Downhole Measurements and Generalized Lithology



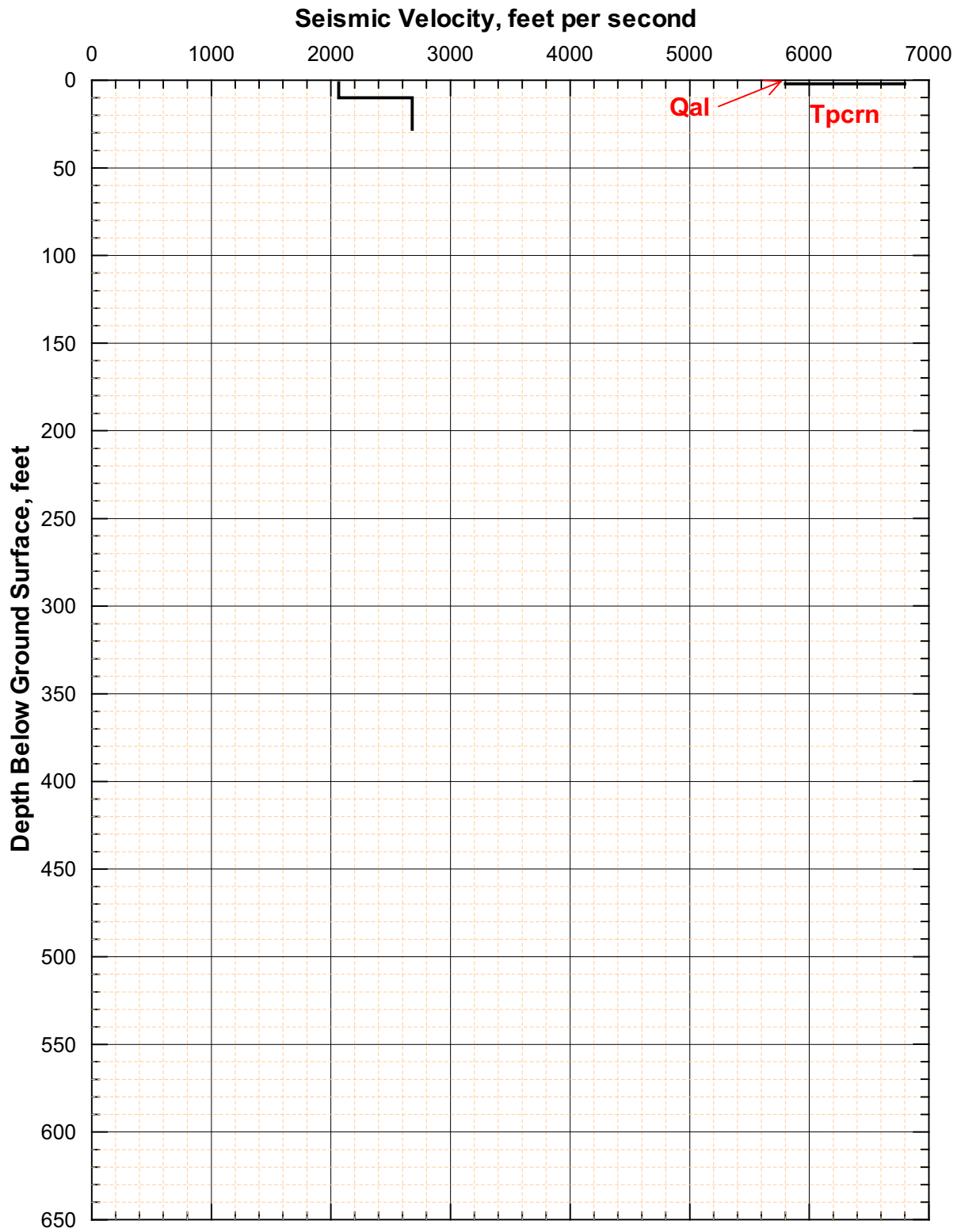
Sources: DTN: MO0202DVDWHBSC.002, Blout et al. (1994, page 54)

Figure 207. UZ-N66 Shear-Wave Velocities from Downhole Measurements and Generalized Lithology



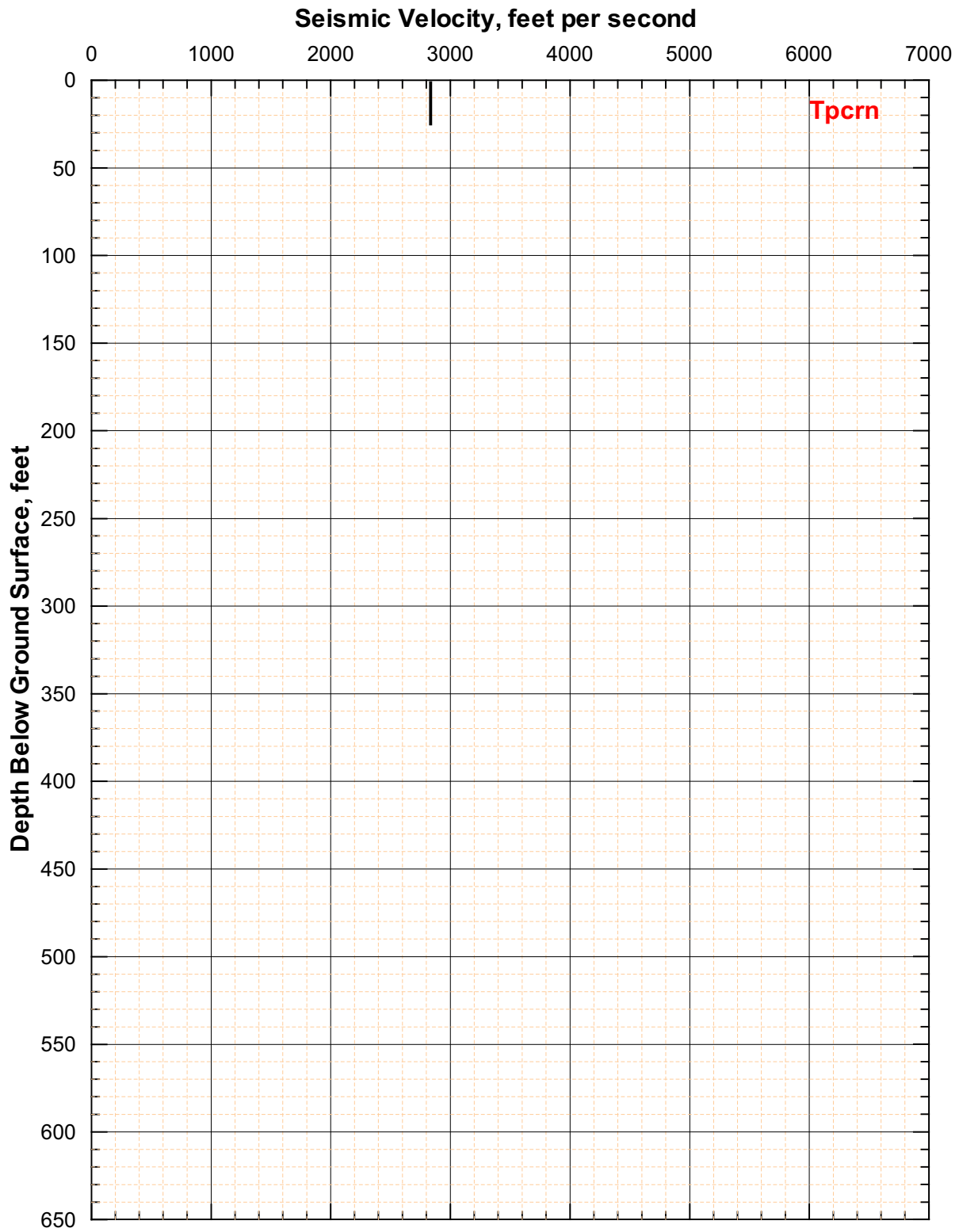
Sources: DTN: MO0202DVDWHBSC.002, Blout et al. (1994, page 55)

Figure 208. UZ-N71 Shear-Wave Velocities from Downhole Measurements and Generalized Lithology



Sources: DTN: MO0202DVDWHBSC.002, Blout et al. (1994, page 56)

Figure 209. UZ-N75 Shear-Wave Velocities from Downhole Measurements and Generalized Lithology



Sources: DTN: MO0202DVDWHBSC.002, Blout et al. (1994, page 63)

Figure 210. UZ-N94 Shear-Wave Velocities from Downhole Measurements and Generalized Lithology

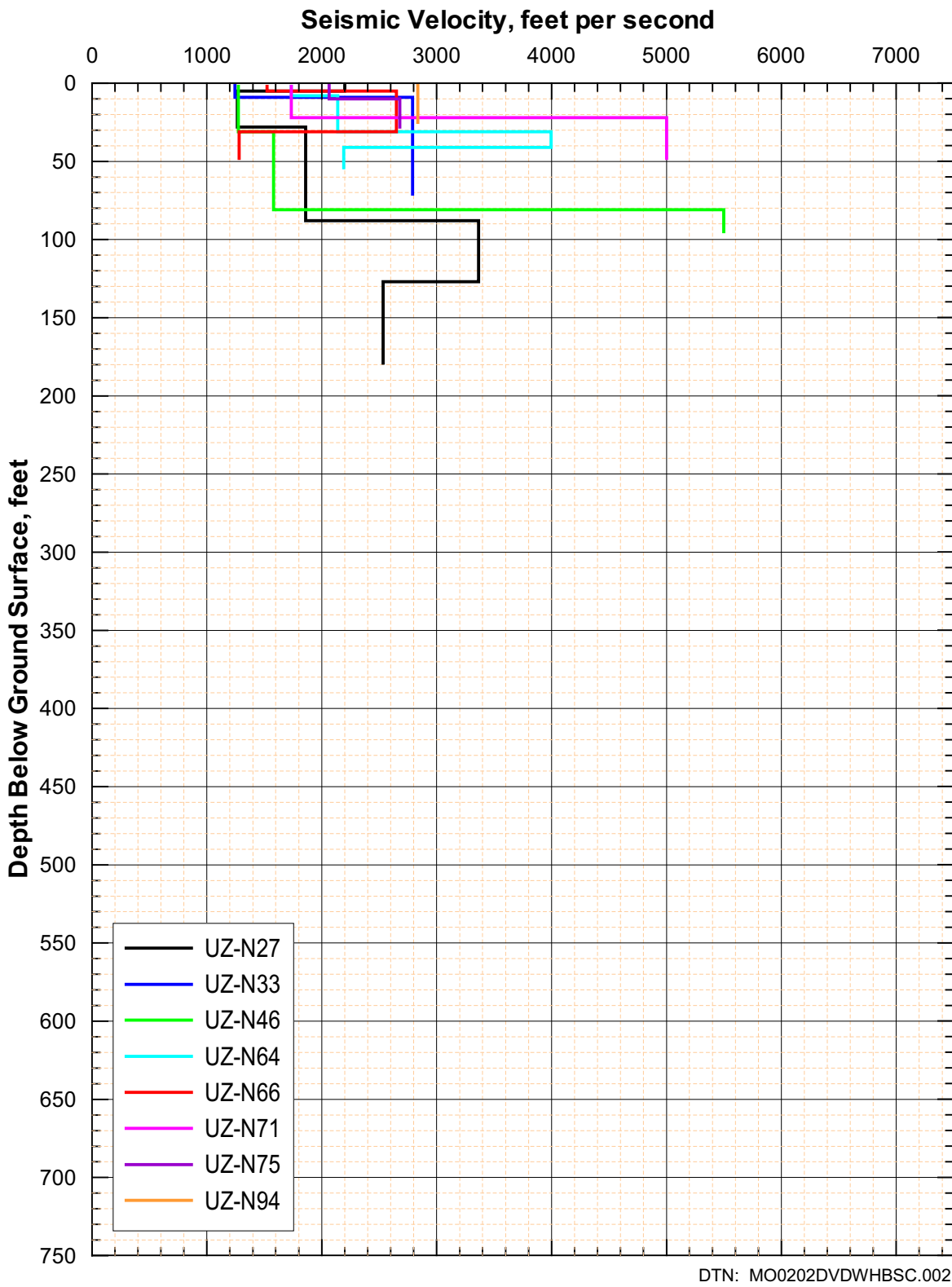
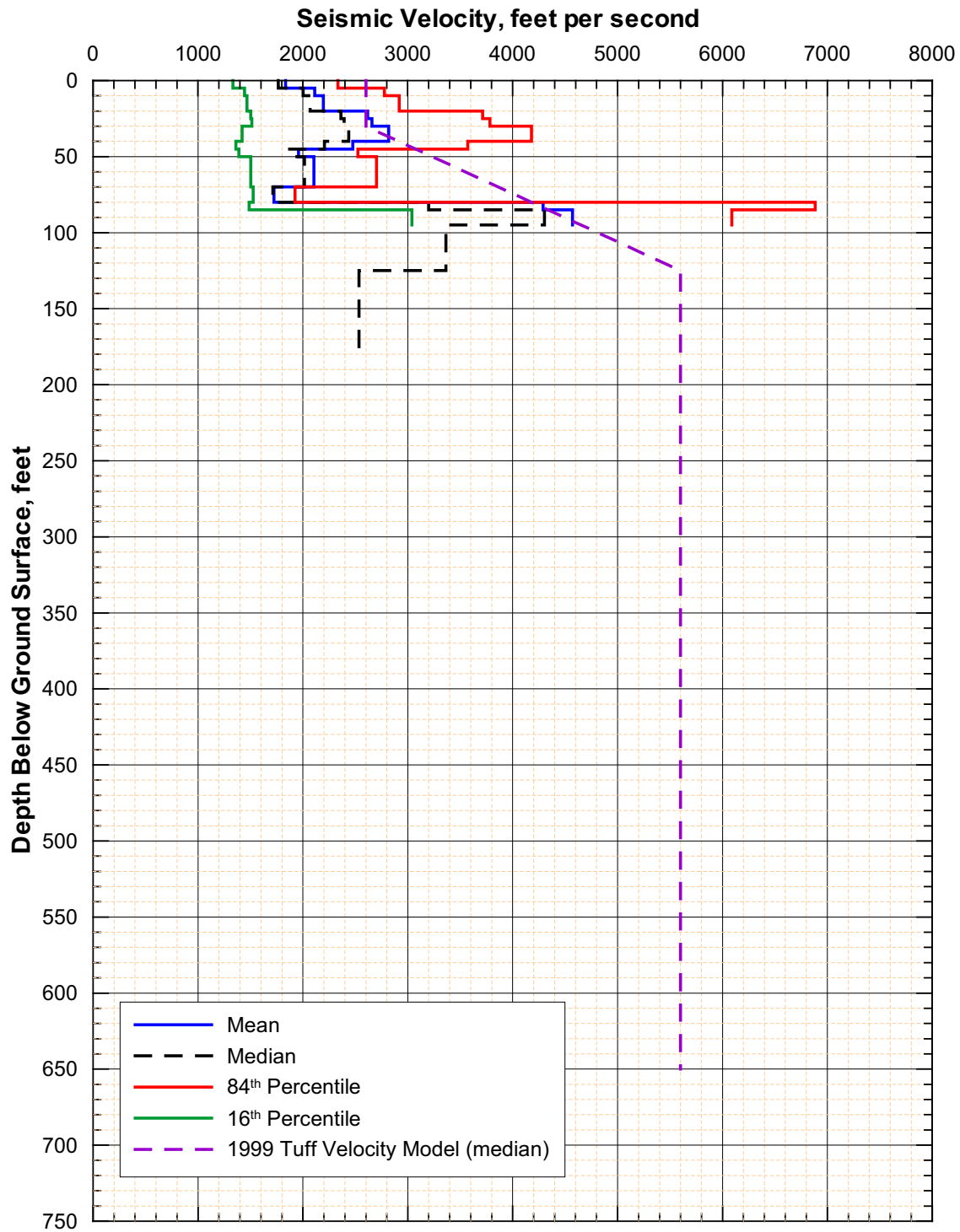


Figure 211. Shear-Wave Velocities from Downhole Measurements at Crest of Yucca Mountain



DTN: MO98PRECLOSURE.000

Note: These statistics have been calculated for illustrative purposes only. Final statistics calculated for use in the forthcoming scientific analysis entitled *Development of Seismic Design Input Ground Motions for a Geologic Repository at Yucca Mountain* will be submitted to the TDMS.

Figure 212. Statistical Analyses of Shear-Wave Velocities from Downhole Measurements at Crest of Yucca Mountain

6.5 DATA ACQUIRED FOR BORROW MATERIAL

6.5.1 Overview

Four samples of potential borrow material from an existing borrow area called Fran Ridge Borrow Area, whose general outlines as of November 2001 are shown on Figure 213. The objective was to evaluate the borrow area as a potential source for the engineered fill for the future North Portal surface facilities. The four samples were taken at the widely spaced locations shown on Figure 213. The samples were collected with a shovel; four sacks were taken at each of the four locations.

6.5.2 Geotechnical Laboratory Static Testing

Testing in Denver, CO - The four samples of potential borrow material from the Fran Ridge Borrow Area were combined following USBR 5205-89, *Procedure for Preparing Soil Samples by Splitting or Quartering*. The Denver, CO, laboratory performed some tests on the material, including a gradation analysis test and maximum/minimum density tests. These test results are summarized in Table 27. The sample classifies as a poorly graded sand (SP) according to the USCS; however, with 48.8% sand-size particles and 48.3% gravel-size particles, the material is nearly a poorly graded gravel (GP) and could be assigned a borderline classification of SP/GP.

The particles retained on a 19.0 mm ($\frac{3}{4}$ -inch) sieve were then removed from the material and the remaining material was split in accordance with USBR 5205-89 at the Denver, CO geotechnical laboratory and a part of the sample was sent to a geotechnical laboratory in Santa Ana, CA. A second part was sent to a geotechnical laboratory in Austin, Texas. The testing performed in Austin, Texas is discussed in Section 6.5.3, while the testing performed by the Santa Ana, CA and the Denver, CO laboratories is discussed in this section. The Denver, CO geotechnical laboratory also performed specific gravity tests on the sand fraction (the part of the sample passing the No. 4 sieve), and specific gravity and absorption tests on the fine gravel (fraction passing the $\frac{3}{4}$ -inch sieve and retained on the No. 4 sieve) and coarse gravel (fraction passing the 3-inch sieve and retained on the $\frac{3}{4}$ -inch sieve). Liquid limit and plastic limit tests were performed and the sample found to be non-plastic (Table 27). Note that the value of the specific gravity of the minus No. 4 sieve fraction in Table 27, 2.52, is the same as the average of the values in Table 13 for the samples from the test pits in the WHB Area. This is not a surprising result, given that the materials from both locations are alluvium derived from similar source material.

Testing in Santa Ana, CA - Testing in Santa Ana, California was performed in accordance with YMP Line Procedure LP-GEO-001Q-M&O, *Laboratory Geotechnical Testing of Soil, Rock and Aggregate Samples*. Testing consisted of particle-size distribution tests, a compaction characteristics test using modified effort and triaxial compression tests, performed in accordance with Sections 5.5.5, 5.5.7, and 5.5.12, respectively, of LP-GEO-001Q-M&O.

Particle-size distribution tests were performed on the sample in three conditions: (1) as received (including materials greater than $\frac{1}{2}$ -inch in size); (2) after scalping on the $\frac{1}{2}$ -inch sieve and prior to compaction, and (3) after the compaction test on the $\frac{1}{2}$ -inch minus material. Note that

Section 5.5.5 of LP-GEO-001Q-M&O allows the choice of two different test methods to measure

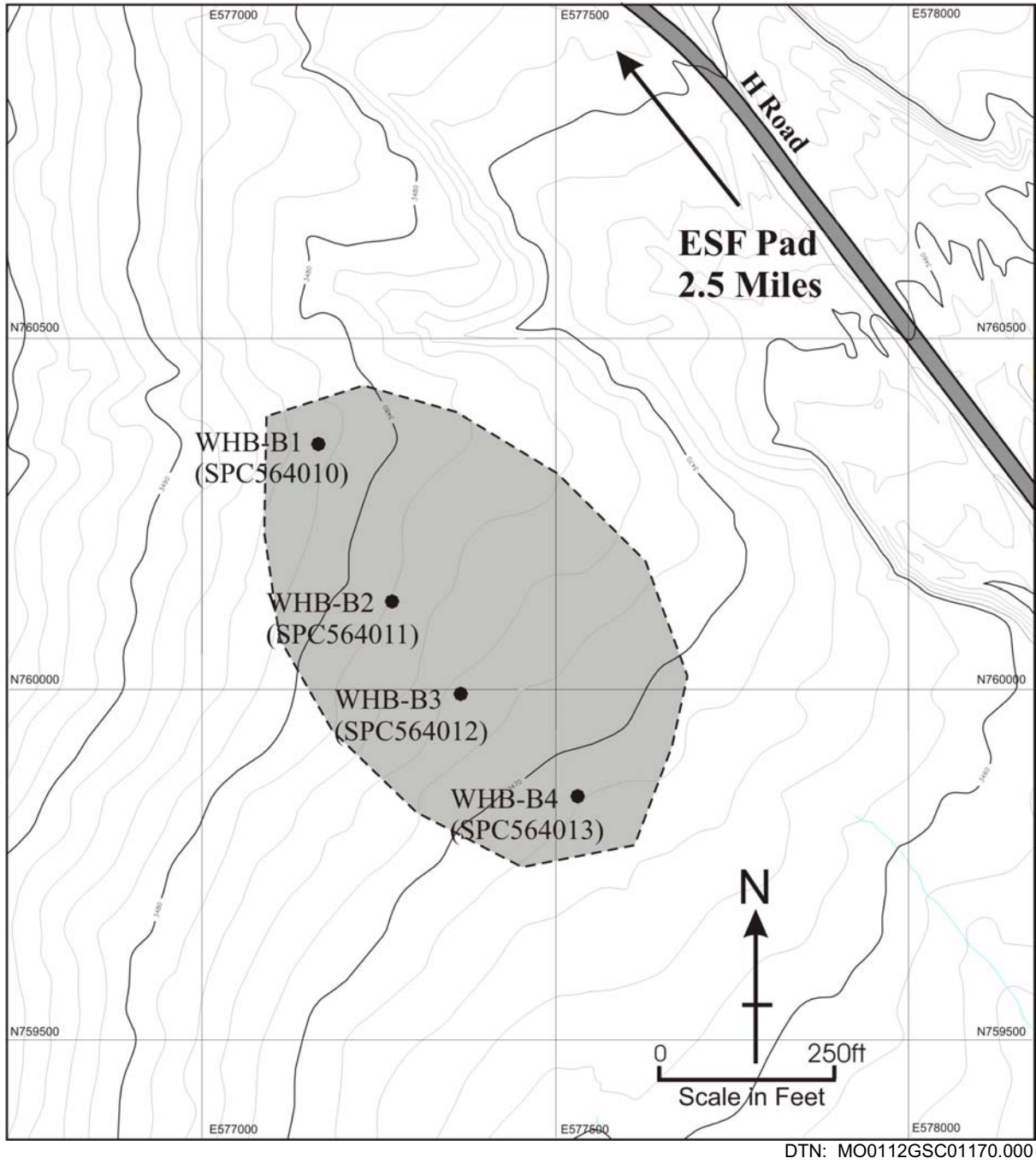


Figure 213. Location of Fran Ridge Borrow Samples

Table 27. Tests Performed in Denver, CO, on a Composite Sample of Fran Ridge Materials

Test	Result
Particle-size distribution per USBR 5325-89 and 5335-89	100% passing 3" sieve; 95.2% passing 1½" sieve; 86.5% passing ¾" sieve; 68.8% passing 3/8" sieve; 51.7% passing No. 4 sieve; 42.1% passing No. 8 sieve; 33.2% passing No. 16 sieve; 27.4% passing No. 30 sieve; 18.8% passing No. 50 sieve; 8.5% passing No. 100 sieve; 2.9% passing No. 200 sieve
Maximum and minimum index unit weights of the particles passing the 3-inch sieve per USBR 5525-89 and 5530-89	Maximum 112.4 pcf (dry method) Minimum 94.0 pcf
Specific gravity and absorption of the particles retained on the ¾-inch sieve and passing the 3-inch sieve per USBR 5320-89 (volume method)	2.39 apparent 2.24 bulk (saturated surface dry) 2.13 bulk (oven dry) 5.3% absorption
Specific gravity and absorption of the particles retained on the 4.75 mm (No. 4) sieve and passing the 19.0 mm (¾-inch) sieve per USBR 5320-89 (suspension method)	2.45 apparent 2.24 bulk (saturated surface dry) 2.10 bulk (oven dry) 6.9% absorption
Specific gravity of the particles passing the 4.75 mm (No. 4) sieve per USBR 5320-89 (volume method)	2.52
Liquid and plastic limits per USBR 5350-89	Nonplastic
Unified Soil Classification System per USBR 5000-86	SP

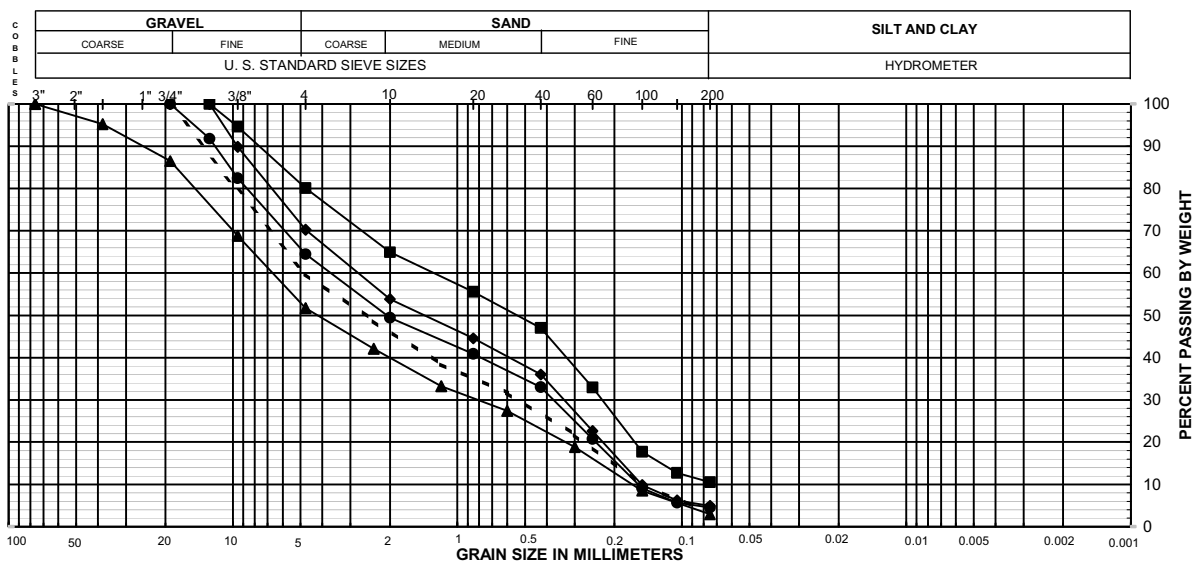
DTN: MO0206EBSFRBLT.018

particle-size distribution; for these tests, ASTM C 136-96a, *Standard Test Method for Sieve Analysis of Fine and Coarse Aggregates*, was used.

The results of the particle-size distribution tests are presented on Figure 214 and on the bottom half of Figure 215. Note that the percent of particles passing the No. 200 sieve increased from 4.9 percent before the compaction test to 10.5 percent after the compaction test, which causes the USCS group name/symbol to change from poorly graded sand with gravel (SP) to poorly graded sand with silt and gravel (SP-SM). Figure 214 also shows the particle-size distribution curve for the test at the geotechnical laboratory in Denver, CO on the sample before scalping and splitting and the theoretical particle-size distribution curve (dashed line) representing perfect scalping and splitting of the sample before processing.

The compaction characteristics were measured in accordance with ASTM D 1557-91 (1998), *Standard Test Method for Laboratory Compaction Characteristics of Soil Using Modified Effort (56,000 ft-lbf/ft³ (2,700 kN-m/m³))*. The compaction characteristics test was performed on the material after it had been scalped on the one-half inch sieve. The one-half inch size corresponds to the maximum particle size that was to be included in the triaxial test specimens tested by the Santa Ana geotechnical laboratory and the resonant column and torsion shear tests conducted in Austin, Texas on a portion of composite sample No. 65A-X613. The results of the compaction test are summarized on the top half of Figure 215 and indicate a maximum dry unit weight of 114.5 pounds-force per cubic foot (pcf or lbf/ft³) and an optimum water content of 11 percent.

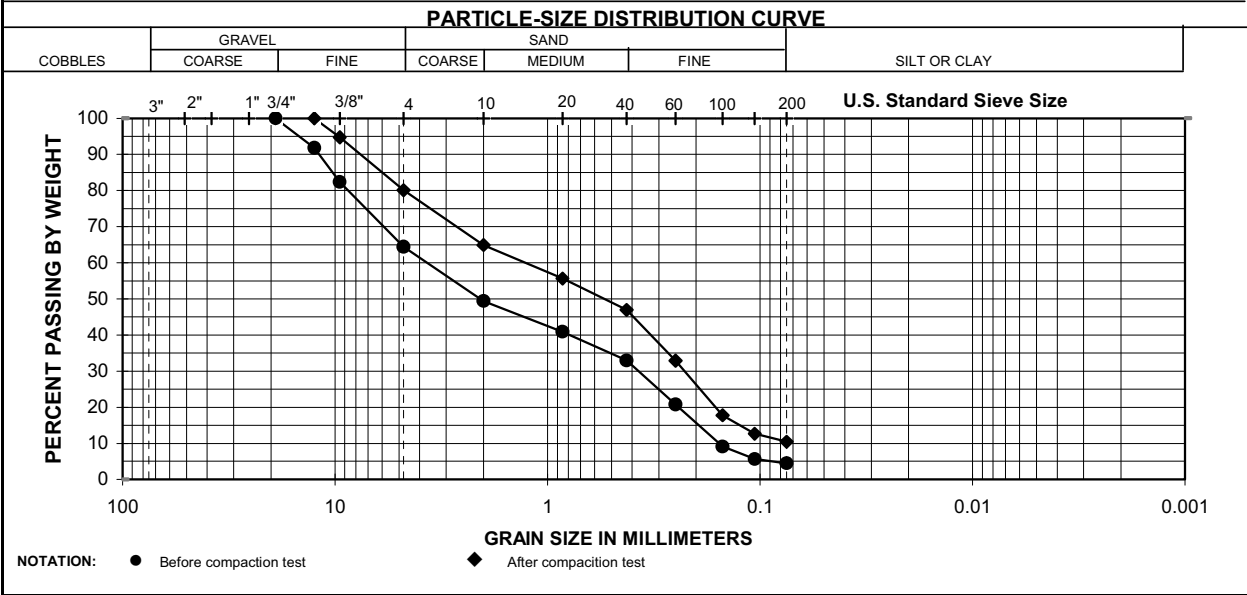
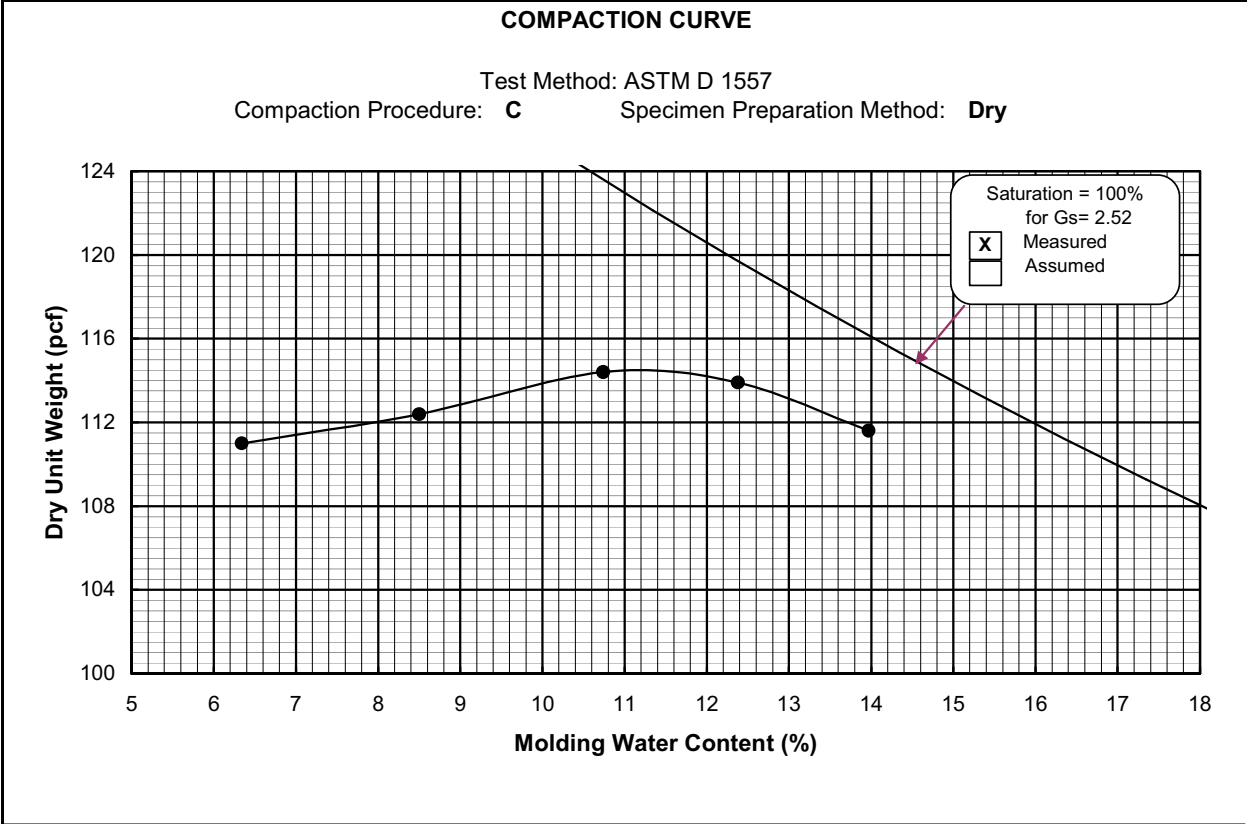
UNIFIED SOIL CLASSIFICATION



Sample No.	SYMBOL	LL	PI	CF	Description and Classification	D ₆₀	D ₃₀	D ₁₀	Cu	Cc
65A-X613 (test by USBR before splitting)	☐	NP	NP		Poorly graded Sand with gravel (SP)	6.9	0.82	0.17	40.6	0.6
65A-X613 (as-received by URS)	●				Poorly graded Sand with gravel (SP)	3.8	0.37	0.16	23.8	0.2
65A-X613 (-1/2 inch, before compaction)	◆				Poorly graded Sand with gravel (SP)	2.8	0.34	0.16	17.5	0.3
65A-X613 (-1/2 inch, after compaction)	■				Poorly graded Sand with silt and gravel (SP-SM)	1.3	0.23	0.07	18.6	0.6
Theoretical curve for 65A-X613 (test by USBR before splitting) scalped on 3/4-inch sieve	---	NP	NP		Poorly graded Sand with gravel (SP)	4.9	0.53	0.16	30.6	0.4

DTN: MO0203EBSCTCTS.016

Figure 214. Particle-Size Distributions – Fran Ridge Borrow Area Composite Sample



Sample No.	Depth (ft)	Opt. Water Content (%)	Max. Dry Unit Weight (pcf)	Description and/or Classification
65A-X613	NA	11.0	114.5	Brown poorly graded Sand with gravel (SP) (before test)

DTN: MO0203EBSCTCTS.016

Figure 215. Compaction Test Results – Fran Ridge Borrow Area Composite Sample

The triaxial tests were performed under isotropically consolidated, drained conditions at confining stresses ranging from 1.18 kips per square foot (ksf) to 8.70 ksf. The initial conditions and results are summarized in Table 28. Plots of axial strain versus deviator stress, change in volume and obliquity (i.e., ratio of major to minor principal stress, σ'_1/σ'_3) are presented on Figure 216. Mohr circles based on the peak deviator stress for each of the confining stresses are shown on Figure 217. Two strength envelopes have been fitted to the data as shown on Figure 217. One of these envelopes is the traditional straight line Mohr-Coulomb failure envelope:

$$\tau_{ff} = c' + \sigma_{ff} \tan \phi' = 1790 \text{psf} + 0.7587 \sigma_{ff} \quad (\text{Eq. 37})$$

where: τ_{ff} is the shear stress acting on the failure plane at failure, i.e., the effective shear strength
 c' is the effective cohesion intercept
 ϕ' is the effective friction angle
 σ_{ff} is the normal stress acting on the failure plane at failure.

The other is a curved failure envelope (with zero cohesion at zero confining pressure) that reflects the important influence of confining pressure on shear strength:

$$\tau_{ff} = \sigma_{ff} \tan(\phi'(\sigma_{ff})) \quad (\text{Eq. 38})$$

where: τ_{ff} and σ_{ff} are as defined previously
 $\phi'(\sigma_{ff})$ is a function defined by Eq. 39.

$$\phi'(\sigma_{ff}) = \phi_1 - \Delta\phi \log\left(\frac{\sigma_{ff}}{p_a}\right) = 54.2^\circ - 16.0^\circ \log\left(\frac{\sigma_{ff}}{p_a}\right) \quad (\text{Eq. 39})$$

where: ϕ_1' is the effective friction angle for $\sigma_{ff} = 1$ atmosphere
 $\Delta\phi'$ is the decrease in ϕ' per log cycle change in σ_{ff}
 p_a is 1 atmosphere (approximately 2,116.22 lbs/ft²).

Either failure envelope may be selected for use in design calculations. However, if the Mohr-Coulomb failure envelope approach is used, the geotechnical engineer may need to modify the values of c' and ϕ' to fit the specific range of confining pressures involved in a particular analysis.

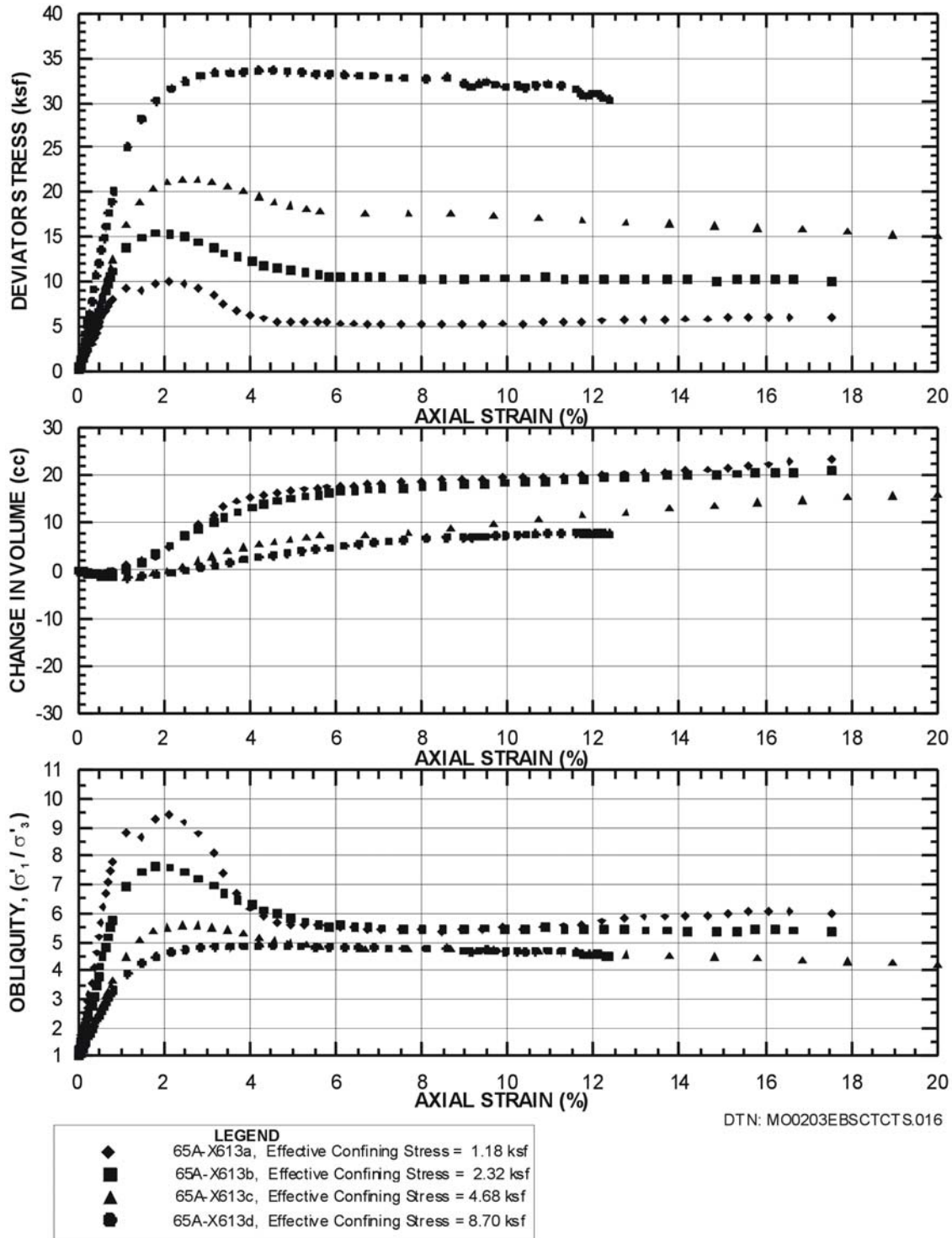
Note that some particle breakage occurred during the compaction characteristics test (Figure 214), which employs a 10-pound-force steel rammer falling 18 inches. The triaxial specimens are compacted in a three-inch diameter mold with a small steel tamper that is manipulated by the laboratory technician. Typically, less particle breakage occurs during triaxial specimen preparation relative to the compaction characteristics test, though some breakage may occur. Thus, it is possible that the material tested (after compaction and consolidation, but before shear) was a poorly graded sand with silt and gravel (SP-SM).

Table 28. Summary of Isotropically Consolidated, Drained Triaxial Compression Tests Performed on Laboratory-Compacted Specimens of the Fran Ridge Borrow Area Composite Sample

Specimen No.	USCS Group Symbol	Compaction Characteristics ⁽⁴⁾		Initial Molding Conditions		W _o	γ _{do}	σ' _{pm}	OCR	ε _{ac}	B factor (%)	at Maximum Deviator Stress at Maximum Obliquity								
		γ _{d,max} (pcf)	w _{opt} (%)	% Comp.	w-w _{opt} (%)							ε _a (%)	$\frac{\sigma_1 - \sigma_3}{2}$ (ksf)	$\frac{\sigma'_1 + \sigma'_3}{2}$ (ksf)	$\frac{\sigma'_1}{\sigma'_3}$	A factor	φ ⁽²⁾ for c=0			
65A-X613	SP																			
a	2.52	114.5	11.0	95.4	1.4	12.4	109.2	---	---	0.41	96.1	2.127	4.999	6.180	9.467	0.500	54.0			
65A-X613	SP																			
b	2.52	114.5	11.0	96.4	1.3	12.3	110.4	---	---	0.43	96.2	1.802	7.687	10.006	7.632	0.221	50.2			
65A-X613	SP																			
c	2.52	114.5	11.0	95.7	1.7	12.7	109.6	---	---	1.30	96	2.439	10.719	15.399	5.581	0.051	44.1			
65A-X613	SP																			
d	2.52	114.5	11.0	95.9	1.7	12.7	109.8	---	---	0.42	98.1	4.201	16.807	25.505	4.865	0.083	41.2			
						17.0	110.1	8.70	1.0	-0.29	1.74	---	---	---	---	---	---			

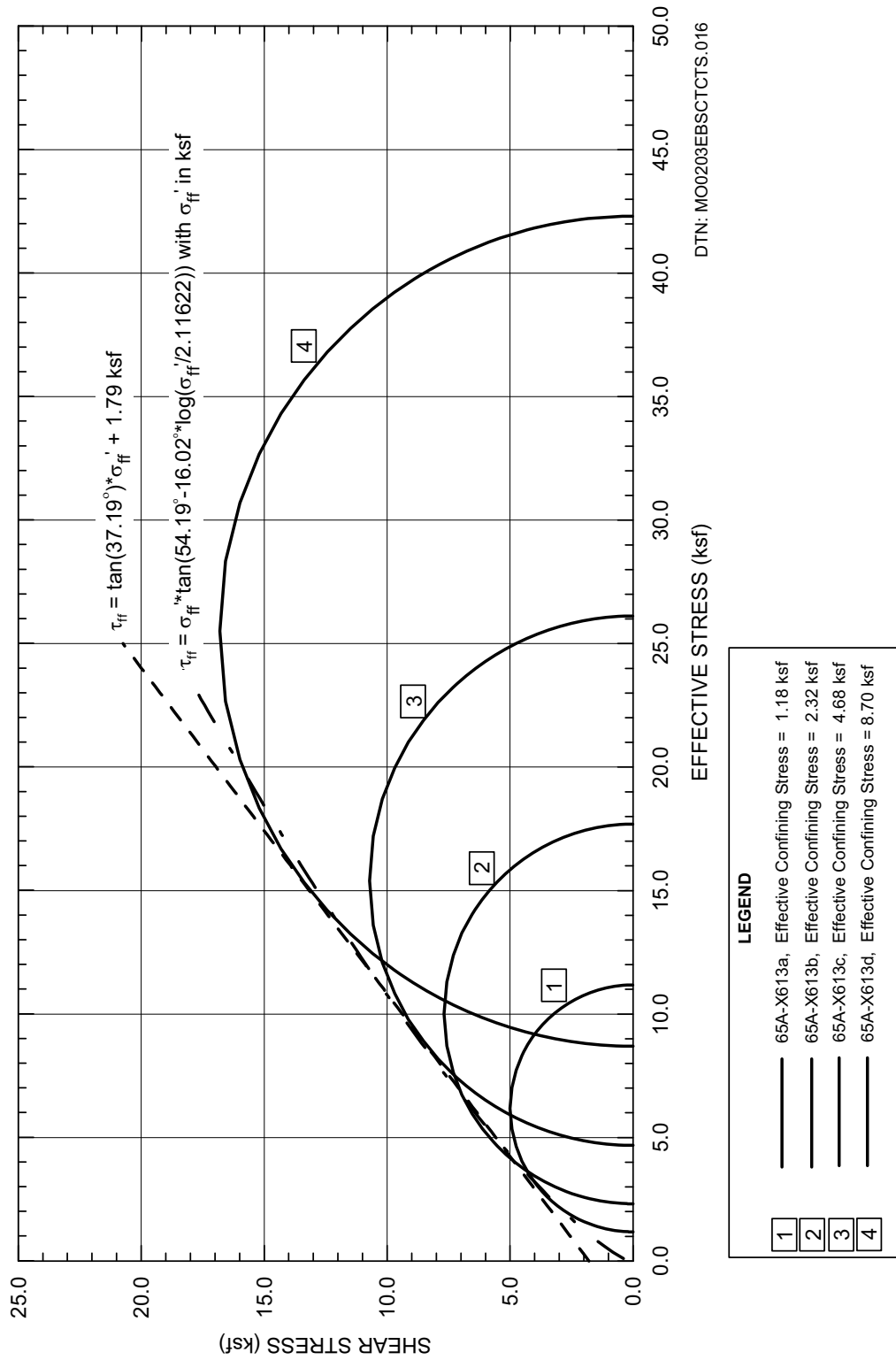
DTN: MO0203EBSCTCTS.016

- NOTES: ⁽¹⁾ Description of the material before compacting the specimens: Brown poorly graded Sand with gravel (SP).
⁽²⁾ The value of specific gravity is for the particles passing the No. 4 sieve and was provided by the Denver CO, laboratory (see Table 27).
⁽³⁾ The value of φ is based on the Mohr-Coulomb failure criterion with c=0 and is calculated at peak deviator stress (σ₁-σ₃), which is the same as peak obliquity for a drained test.
⁽⁴⁾ Per ASTM D 1557-91 (1998)



Note: The material used to prepare triaxial specimens was scalped on the 1/2 inch sieve.

Figure 216. Results of Isotropically Consolidated Drained Triaxial Compression Tests - Fran Ridge Borrow Area Composite Sample



NOTE: The material used to prepare triaxial specimens was scalped on the 1/2 inch sieve.

Figure 217. Mohr Circles at Peak Deviator Stress for Isotropically Consolidated Drained Triaxial Compression Tests - Fran Ridge Borrow Area Composite Sample

6.5.3 Geotechnical Laboratory Dynamic Testing

The dynamic properties of 10 specimens of the proposed engineered fill material for the WHB foundation were evaluated in the laboratory at the Geotechnical Engineering Center at the University of Texas at Austin using RCTS equipment. The specimens were collected from the Fran Ridge Borrow Area. The procedures used in this testing are described in Section 6.2.10.1. A detailed description of this evaluation is contained in Scientific Notebook SN-M&O-SCI-033-V1 (Wong 2002e, pages 1050-1601). The results from the dynamic testing of the 10 fill specimens are presented in the following section.

6.5.3.1 Measurements

Ten reconstituted specimens of the Fran Ridge borrow material were tested dynamically. These specimens were constructed from samples sent to UTACED by the USBR Laboratory (see Section 6.5.2). Each specimen was compacted using tamping. The initial properties of the specimens are presented in Table 29. The nominal specimen diameters were either 2.78 in (7.05 cm) or 1.38 in (3.51 cm) and the heights were about 2.0 to 2.3 times the diameters. The specimens were compacted to dry densities that ranged from 90 to 97% of the modified Proctor maximum dry density. The value of the modified Proctor maximum dry density is 114.5 pcf and the optimum water content is 11% (Section 6.5.2). Also, the specimens were compacted with “scalped” material such that the maximum particle size was no larger than 17% (1/6) of the specimen diameter.

Four of the specimens were tested in two stages. In stage 1, the specimens were dynamically tested at their molding water contents to evaluate the small- and large-strain properties. These four specimens are denoted as UTA-23-K ($w = 2.63\%$), UTA-23-L ($w = 2.77\%$), UTA-23-U ($w = 10.92\%$) and UTA-23-W ($w = 11.15\%$). Upon completion of stage 1 testing, the confining chamber and drive system were removed, and water was percolated through each specimen for one day using a vacuum assist of about 0.1 atmospheres on the downstream side of the specimen. Each specimen was then re-tested dynamically in this state of increased water content (stage 2), to investigate the impact on the dynamic properties of increasing the water content of the granular fill after placement. The specimens were renamed in stage 2 as UTA-23-M ($w = 13.47\%$), UTA-23-N ($w = 15.78\%$), UTA-23-V ($w = 13.50\%$) and UTA-23-Y ($w = 13.53\%$), respectively. Unfortunately, the heights and total unit weights of the four specimens were not measured in stage 2; hence, the dry unit weight from stage 1 was used for the dry unit weight in stage 2. The test pressures and types of tests performed on the Fran Ridge specimens are shown on Table 30.

6.5.3.2 Results

The variation of G_{\max} with σ_{cell} for the 10 Fran Ridge specimens is shown in Figure 218. The $\log G_{\max} - \log \sigma$ relationship can be approximated by a linear relationship on a semilog plot, as expected (Hardin and Drnevich 1972, page 622). The value of G_{\max} generally increases with increasing dry unit weight and, for the denser specimens, decreases with increasing water content.

Table 29. Initial Properties of Reconstituted Specimens of the Fran Ridge Borrow Material

UTACED Designation	SMF Designation	Depth (ft)	SMF Classification	Height ^a (cm)	Diameter ^a (cm)	Total Mass ^a (grams)	Water Content ^a (%)	Dry Unit Weight (pcf)	Total Unit Weight ^a (pcf)	% of Modified Proctor ^{a,b}
UTA-23-K	65A-X613	N.A.	Granular Fill	14.26	7.05	944.1	2.63	103.1	105.8	90
UTA-23-M	65A-X613	N.A.	Granular Fill	14.26 ^c	7.05	-- ^c	13.47	103.1 ^c	117.0	90
UTA-23-L	65A-X613	N.A.	Granular Fill	7.20	3.48	116.5	2.77	103.1	105.9	90
UTA-23-N	65A-X613	N.A.	Granular Fill	7.20 ^c	3.48	-- ^c	15.78	103.1 ^c	119.3	90
UTA-23-O	65A-X613	N.A.	Granular Fill	14.13	7.04	962.1	4.72	104.2	109.1	91
UTA-23-P	65A-X613	N.A.	Granular Fill	7.15	3.50	119.4	4.55	103.5	108.2	90
UTA-23-U	65A-X613	N.A.	Granular Fill	7.70	3.80	172.8	10.92	111.1	123.3	97
UTA-23-V	65A-X613	N.A.	Granular Fill	7.70 ^c	3.80	-- ^c	13.50	111.1 ^c	126.2	97
UTA-23-W	65A-X613	N.A.	Granular Fill	16.00	7.12	1244.0	11.15	109.7	121.9	96
UTA-23-Y	65A-X613	N.A.	Granular Fill	16.00 ^c	7.12	-- ^c	13.53	109.7 ^c	124.5	96

Sources: DTN: MO0203DHRSSWHB.001, ^a Wong (2002e, Appendix 42, page 16)

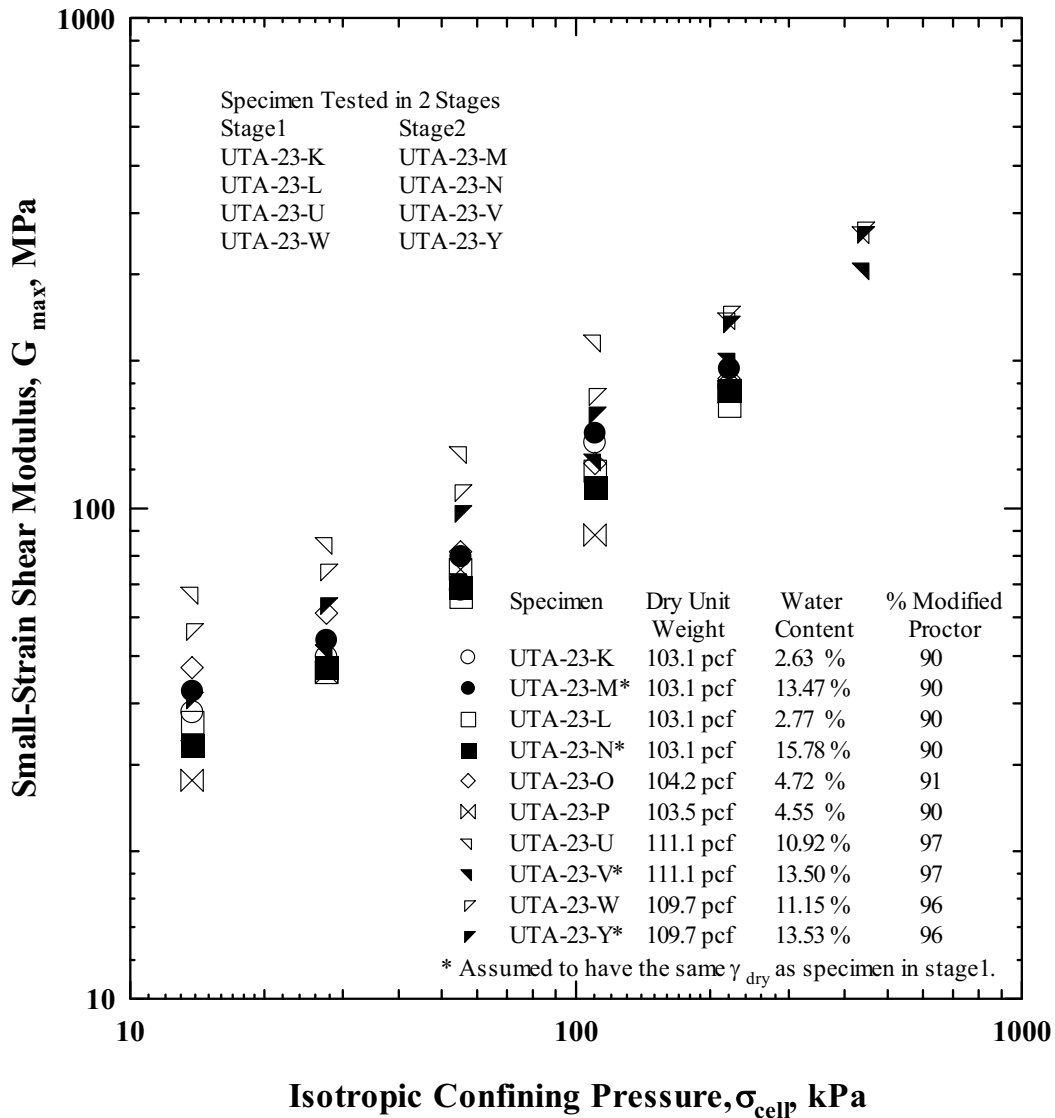
^b Based on Modified Proctor (ASTM D 1557) results (Figure 215).

^c Initial height and total unit weight of these specimens were inadvertently not measured in stage 2. The dry unit weight from stage 1 was used for the dry unit weight in stage 2.

Table 30. Confining Pressures at which RCTS Tests Were Performed on the Fran Ridge Borrow Material

UTACED Designation	SMF Designation	Depth (ft)	SMF Classification	Estimated Mean Total Stress (psi)	Low-Amplitude RC Test Pressures (psi)	High-Amplitude RC Test Pressures (psi)	Low- and High-Amplitude TS Test Pressures (psi)
UTA-23-K	65A-X613	N.A.	Granular Fill	8	2, 4, 8, 16, 32	8, 32	8, 32
UTA-23-L	65A-X613	N.A.	Granular Fill	8	2, 4, 8, 16, 32	8, 32	8, 32
UTA-23-M	65A-X613	N.A.	Granular Fill	8	2, 4, 8, 16, 32	8, 32	8, 32
UTA-23-N	65A-X613	N.A.	Granular Fill	8	2, 4, 8, 16, 32	8, 32	8, 32
UTA-23-O	65A-X613	N.A.	Granular Fill	8	2, 4, 8, 16, 32	8, 32	8, 32
UTA-23-P	65A-X613	N.A.	Granular Fill	8	2, 4, 8, 16, 32	8, 32	8, 32
UTA-23-U	65A-X613	N.A.	Granular Fill	8	2, 4, 8, 16, 32, 64	8, 32	8, 32
UTA-23-V	65A-X613	N.A.	Granular Fill	8	2, 4, 8, 16, 32, 64	8, 64	8, 64
UTA-23-W	65A-X613	N.A.	Granular Fill	8	2, 4, 8, 16, 32, 64	8, 32	8, 32
UTA-23-Y	65A-X613	N.A.	Granular Fill	8	2, 4, 8, 16, 32, 64	8, 32	8, 32

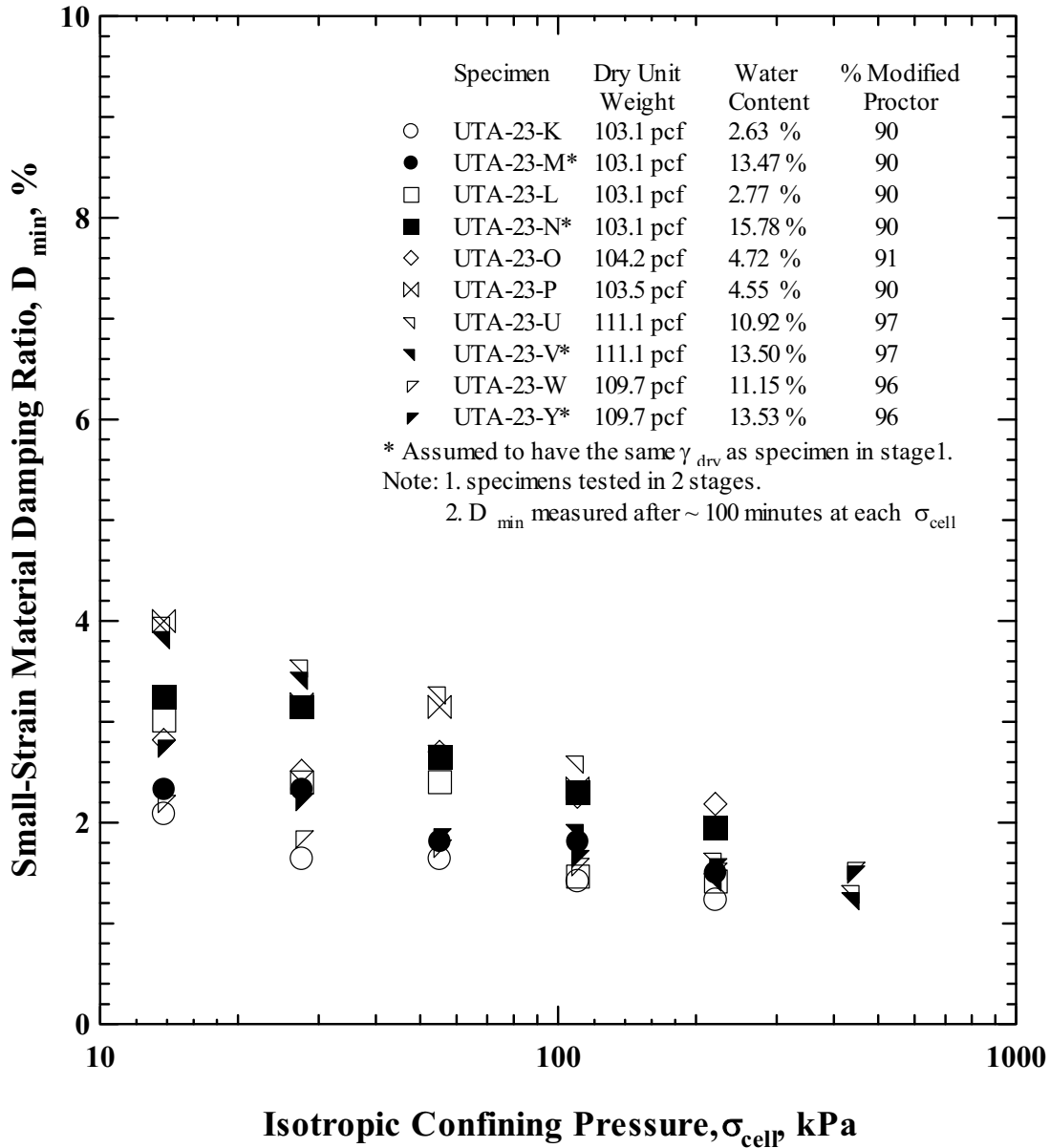
Source: Wong (2002e, Appendix 42, page 19)



Source: Wong (2002e, Appendix 42, page 49)

Figure 218. Variation in Small-Strain Shear Modulus with Isotropic Confining Pressure of Reconstituted Specimens from the Fran Ridge Borrow Area

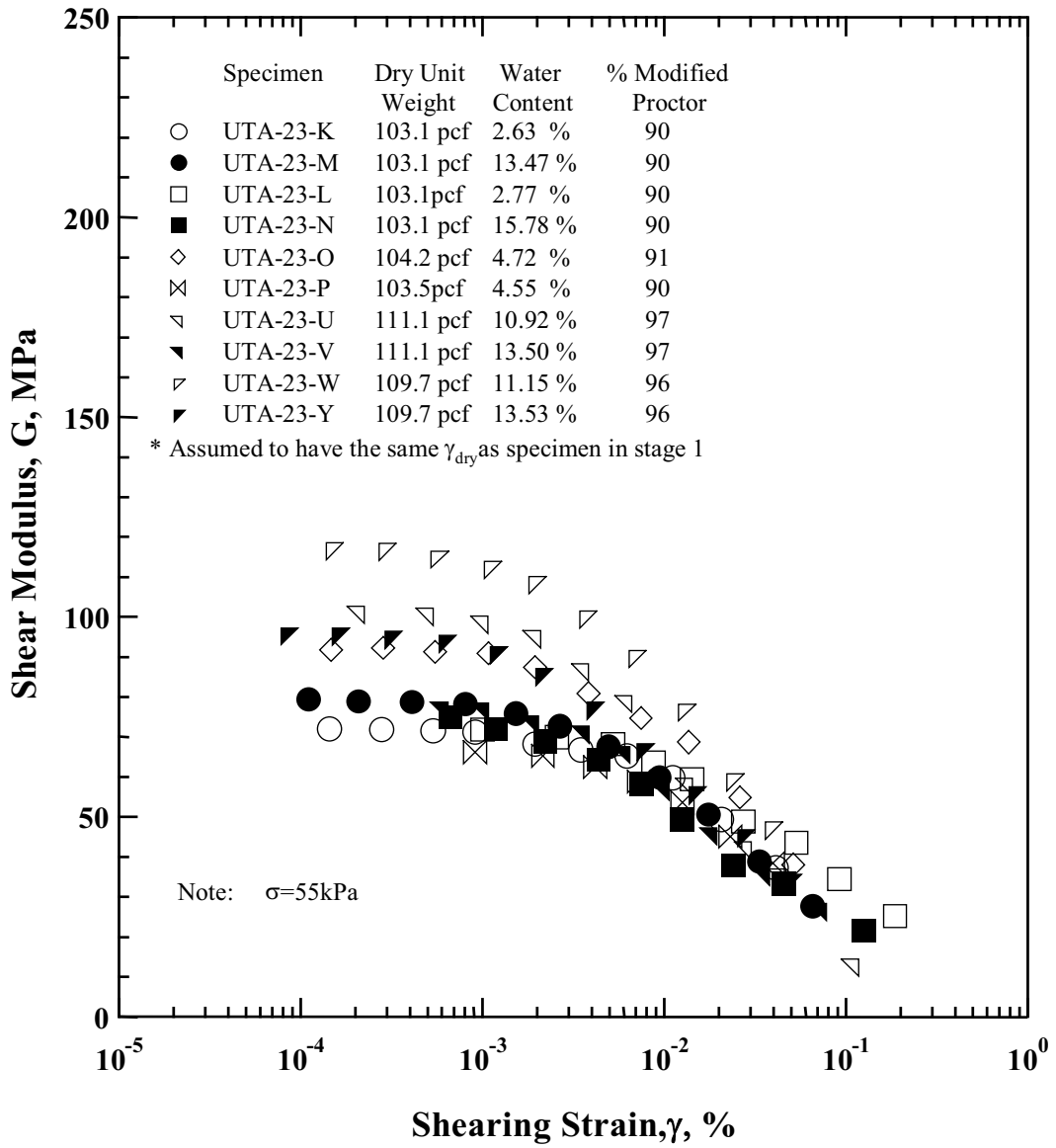
The variation of D_{min} with σ_{cell} for the ten specimens is shown in Figure 219. The value of D_{min} decreases as σ_{cell} increases as expected (Hardin and Drnevich 1972, page 622). The values of D_{min} at 1 atmosphere are above those predicted for sands by Seed et al. (1986, Figure 6) as seen by looking at the small-strain values shown in Figure 143. The effects of f on G_{max} and D_{min} are small and are shown in Figures XVII-11 and XVII-12, respectively.



Source: Wong (2002e, Appendix 42, page 50)

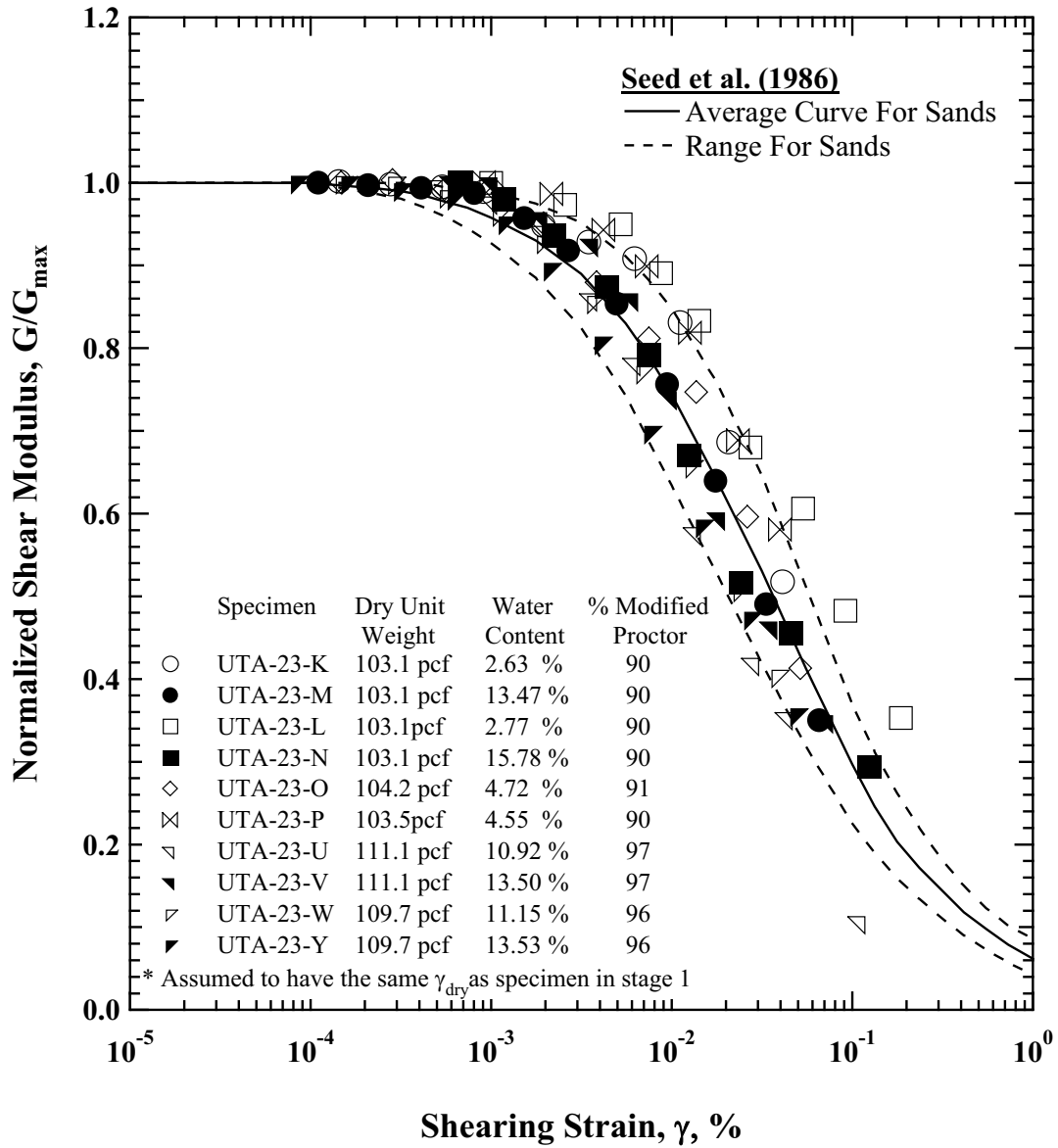
Figure 219. Variation in Small-Strain Material Damping Ratio with Isotropic Confining Pressure of Reconstituted Specimens from the Fran Ridge Borrow Area

The influence of γ on G , G/G_{max} , and D is shown in Figures 220 to 222, respectively. The specimens are behaving very much like a sandy soil, as seen by the comparisons in Figures 221 and 222 with the Seed et al. (1986, Figures 2 and 6) curves. The main difference is the higher values of D_{min} measured in the specimens.



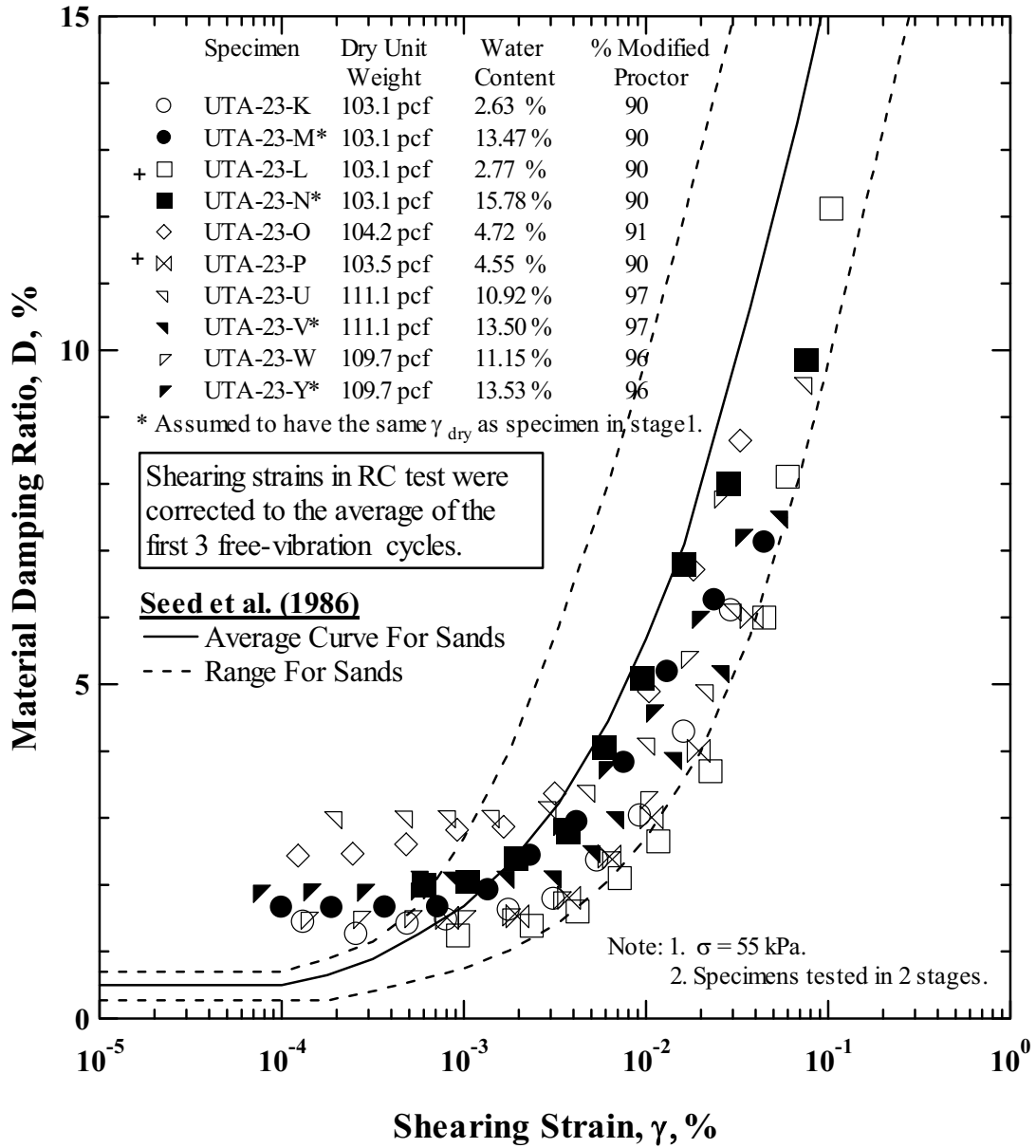
DTN: MO0203DHRSSWHB.001

Figure 220. Variation in Shear Modulus with Shearing Strain of Reconstituted Specimens from the Fran Ridge Borrow Area



DTN: MO0203DHRSSWHB.001

Figure 221. Variation in Normalized Shear Modulus with Shearing Strain of Reconstituted Specimens from the Fran Ridge Borrow Area



DTN: MO0203DHRSSWHB.001

Figure 222. Variation in Material Damping Ratio with Shearing Strain of Reconstituted Specimens from the Fran Ridge Borrow Area

6.6 GEOLOGIC CONDITIONS

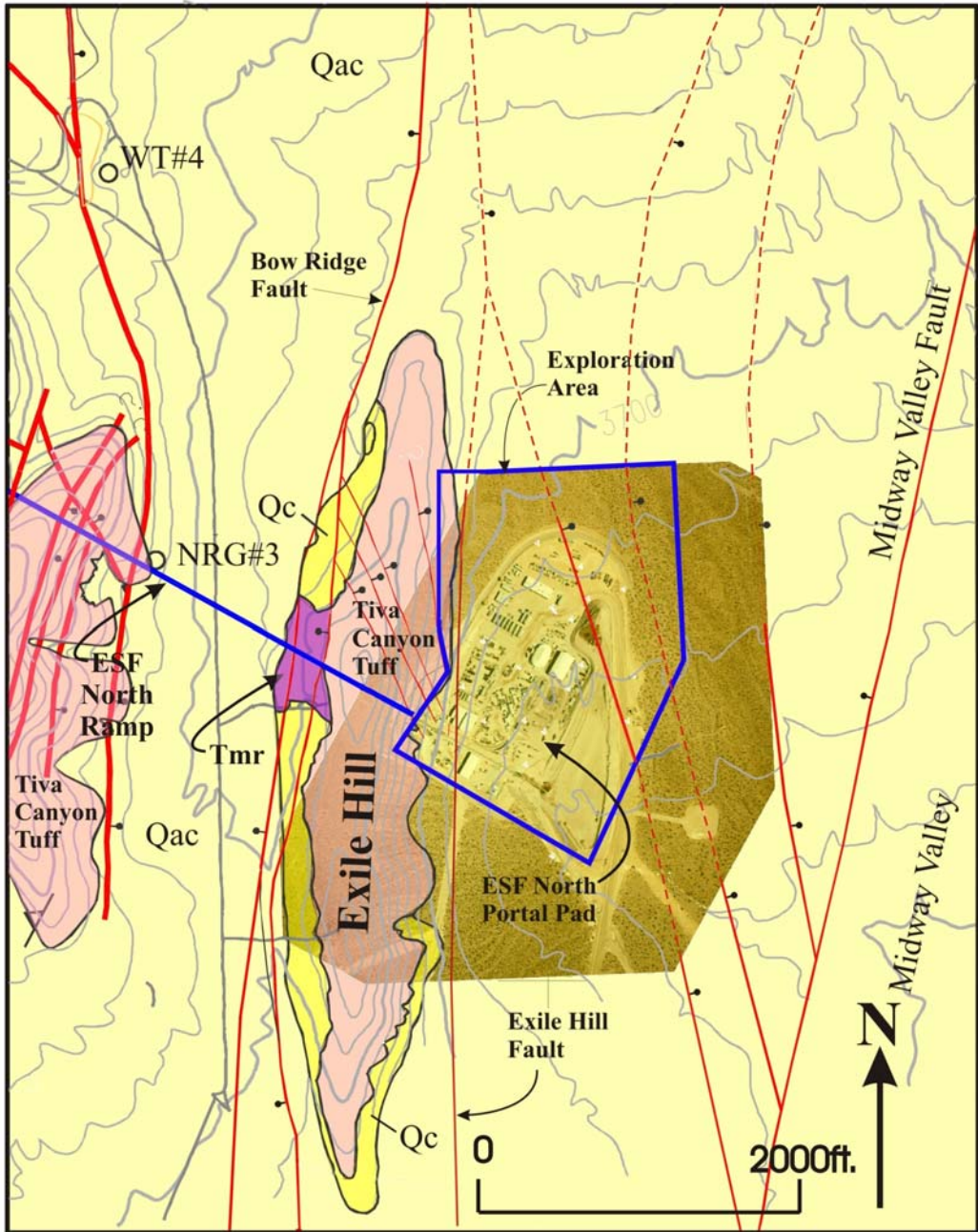
6.6.1 Regional Geologic and Topographic Conditions

Yucca Mountain and the WHB Area (Figure 1) lie within the central southern part of Nevada within the Great Basin, which is part of the Basin and Range structural/physiographic province. Pre-Tertiary rocks, consisting of a thick sequence of Proterozoic and Paleozoic sedimentary rocks, underlie approximately 1,000 to 3,000 meters of Miocene volcanic rock in the Yucca Mountain area (Gibson et al. 1990, page 3).

Units of the Paintbrush and Timber Mountain groups are included in the Miocene volcanic sequence exposed at Yucca Mountain (Sawyer et al. 1994, page 1314). The Claim Canyon caldera and environs, located approximately 6 km north of the study area, is the source of the 12.7 to 12.8 million-year old pyroclastic rock and lava comprising the Paintbrush Group (Byers et al. 1976, page 24; Sawyer et al. 1994, pages 1312-1314). Four formations of pyroclastic-flow and pyroclastic-fall deposits with interbedded lavas, dipping 5 to 10° to the east, form a homoclinal sequence included in the Paintbrush Group (Byers et al. 1976, page 24; Christiansen et al. 1977, page 951). Two of these formations, the Topopah Spring Tuff and Tiva Canyon Tuff, are voluminous, densely welded ignimbrites, grading upward from rhyolite to quartz latite composition (Lipman et al. 1966, page F7; Byers et al. 1976, page 25; Schuraytz et al. 1989, page 5925).

As shown on Figure 223, the WHB Area (Figure 1) is situated mainly in Midway Valley along the east side of Exile Hill, though a small part of the WHB Area laps onto Exile Hill. Exile Hill is a horst, bounded on its west side by the Bow Ridge fault and on its east side by the Exile Hill fault. Exile Hill consists of Tiva Canyon Tuff that is surrounded and partially covered by Quaternary alluvium/colluvium. The upper Tertiary and Quaternary sediments (identified by the symbol Qac) that fill Midway Valley consist mostly of alluvial deposits (fluvial and colluvial sediments) and some thin eolian deposits. Over most of the WHB Area the alluvium is covered by an artificial fill known as the North Portal pad or by the adjacent muck piles. The North Portal pad is a man-made fill constructed on the Midway Valley alluvium to support tunneling of the ESF.

Elevation of the ground surface in the region of the WHB Area ranges from about 3,000 feet southeast of the site, in the lower reaches of Forty Mile Wash, to over 6,000 feet about 4 miles to the north, in the area of the Timber Mountain caldera. The crest of Yucca Mountain, located about 2 miles to the west, is at an average elevation of about 4,900 feet. Near the site of the proposed WHB, relief is approximately 250 feet, ranging from about elevation 3,850 feet at the crest of Exile Hill, to the west, to about elevation 3,600 feet at the center of Midway Valley, to the east.



Modified from DTN: GS980608314221.002

Figure 223. Generalized Geologic Map of the WHB Area, including Exile Hill

6.6.2 Subsurface Geologic Conditions

Based on the drilling data discussed in Sections 6.2.2 and 6.2.3, an interpretation of subsurface geologic conditions has been developed for the WHB Area (Figure 224).⁸ The interpretation presumes that the thicknesses of lithostratigraphic units remain relatively constant across the WHB Area (Assumption 2), and that a northeast-striking, southeast-dipping volcanic sequence has been structurally disrupted by several northerly-trending, high-angle, primarily normal, faults.⁹ These faults are depicted as cutting the entire volcanic bedrock sequence, but not disrupting the overlying alluvium. The top of rock profile developed from drilling indicates a relatively even bedrock/alluvium contact. Therefore, the results of this program do not provide any evidence of structural displacement at the base of the alluvium. This is consistent with the findings of Swan et. al. (2001), who found no evidence of Quaternary faulting in trenches excavated in the area of the WHB.

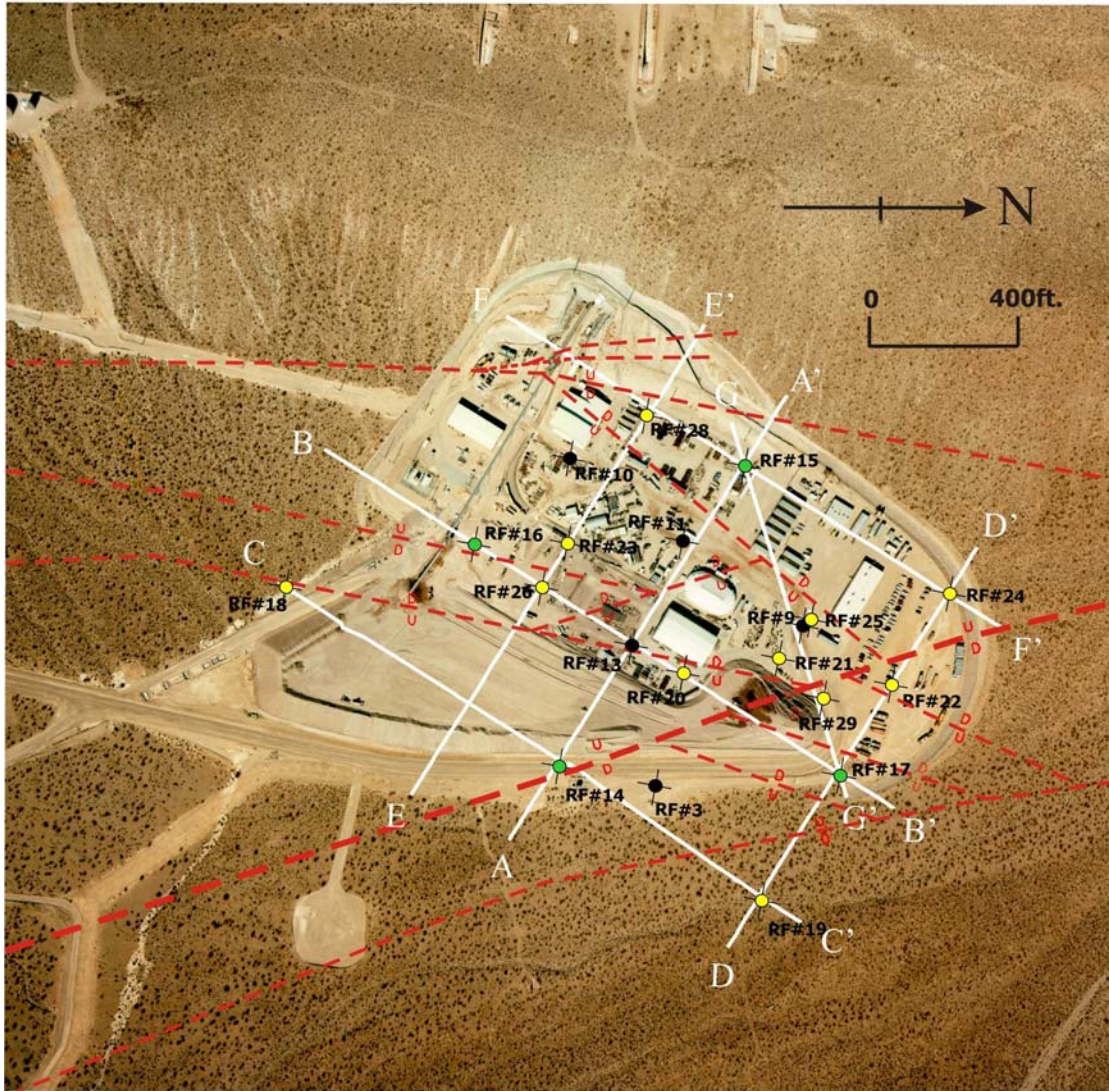
The subsurface depictions represent an interpretation of general geologic conditions beneath the WHB Area that is consistent with the available subsurface data. It is recognized, however, that the number and locations of faults are possibly different than shown, and other interpretations of the data are possible. In fact, most of the faults have been observed in only a single borehole or not at all. Faults shown on the cross sections are represented with a single line; however, elevation changes in contacts between boreholes could be the result of displacement along several parallel or imbricate faults.

Figure 224 is a plan view map showing the location of boreholes, interpreted geologic structures (faults), and cross sections. Seven cross sections, designated A-A' through G-G', are presented on Figures 225 through 231 and illustrate the subsurface geologic interpretation developed for the site. Sections A-A', D-D' and E-E' are cut approximately parallel to the dip of the volcanic stratigraphy. Sections B-B', C-C' and F-F' are cut approximately parallel to the strike of the volcanic stratigraphy. Section G-G' is cut normal to the strike of a normal fault that cuts across the northeast corner of the WHB Area, which will be referred to herein as the "Exile Hill fault splay." Figure 232 presents a map of interpreted contours of top-of-bedrock developed from the borehole data and bedrock outcrops on Exile Hill. The following paragraphs discuss the interpretive geologic features shown on the sections. Note that borehole RF#21 was not used in creating Figure 232.

In most of the WHB Area, the alluvium is covered by a man-made fill constructed on the Midway Valley alluvium to support tunneling of the ESF. The North Portal pad fill was constructed of colluvium and bedrock from shallow excavations at the toe of Exile Hill and for the north portal of the ESF, alluvium from distant borrow pits, and tunnel muck. The North Portal pad is about 800 to 1,200 feet by 600 to 700 feet in size and slopes roughly 2 percent to the east, from approximately elevation 3,683 at the base of Exile Hill to 3,670 feet.

⁸ This interpretation concerns the part of the WHB Area lying east of the Exile Hill fault. Different stratigraphic units and a different bedding strike and dip pertain west of the Exile Hill fault.

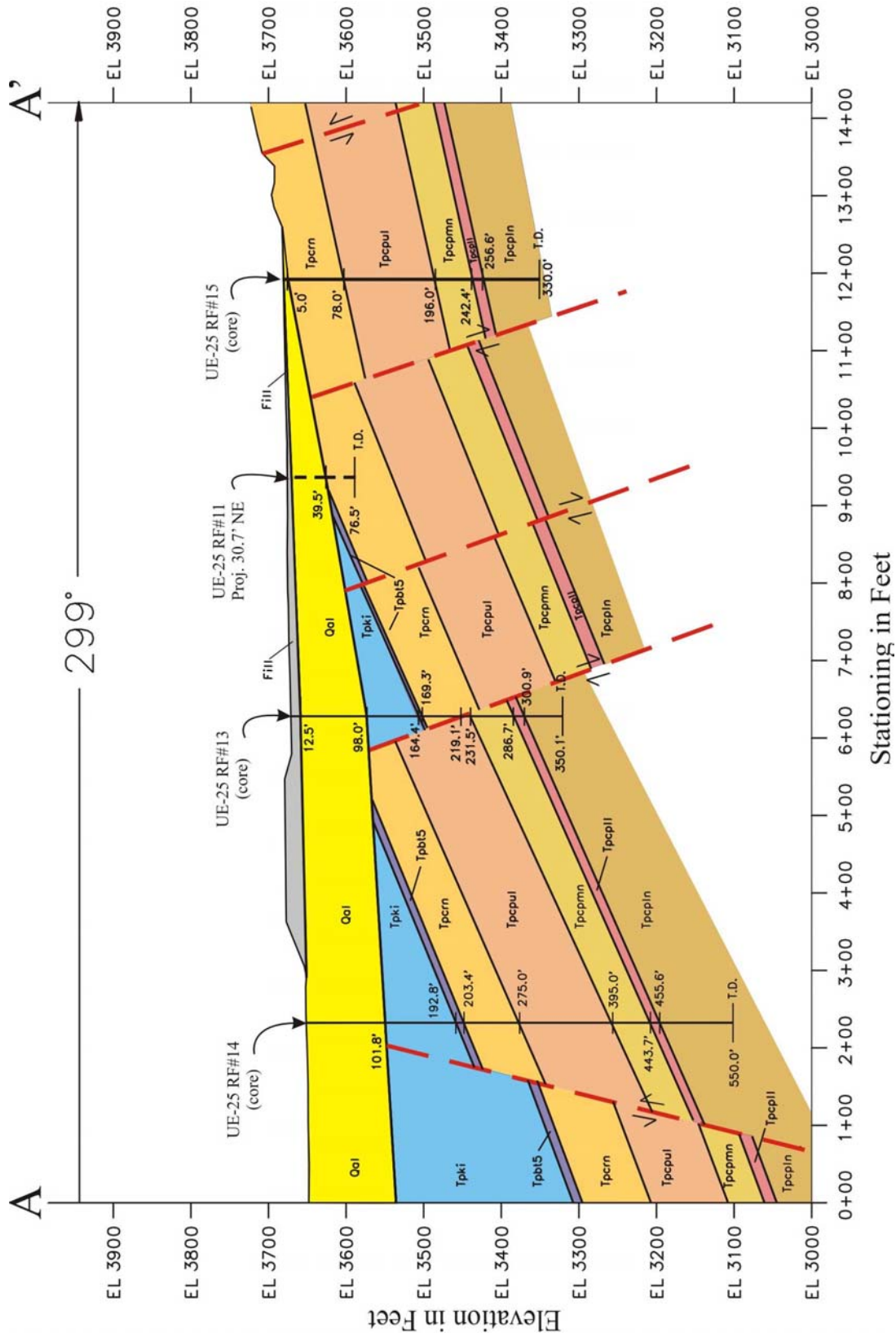
⁹ The welded and nonwelded tuffs encountered in the drilling program are deposited in various thicknesses over an unknown paleo-topography. Developing a geologic interpretation that takes paleo-topography into account is beyond the scope of this investigation; and any insight into this factor is limited by the use of mud rotary drilling techniques and widely spaced core holes. Surficial processes, such as erosion by wind and rain, could have easily developed highs and lows along the surface of bedrock units before subsequent deposition occurred.



DTNs: GS020383114233.003, MO0008GSC00286.000,
Assumption 6; YMP Photograph Number - BN 8811-50

Note: Boreholes in black are pre-existing holes, boreholes in yellow are mud rotary holes, and boreholes in green are core holes. Faults are projected from top-of-bedrock and are dashed where approximate.

Figure 224. Locations of Cross Sections and Interpreted Faults through the WHB Area



DTNs: GS020383114233.003, MO0008GSC00286.000
and Assumption 6

Figure 225. WHB Area Geologic Cross Section A-A', Looking South

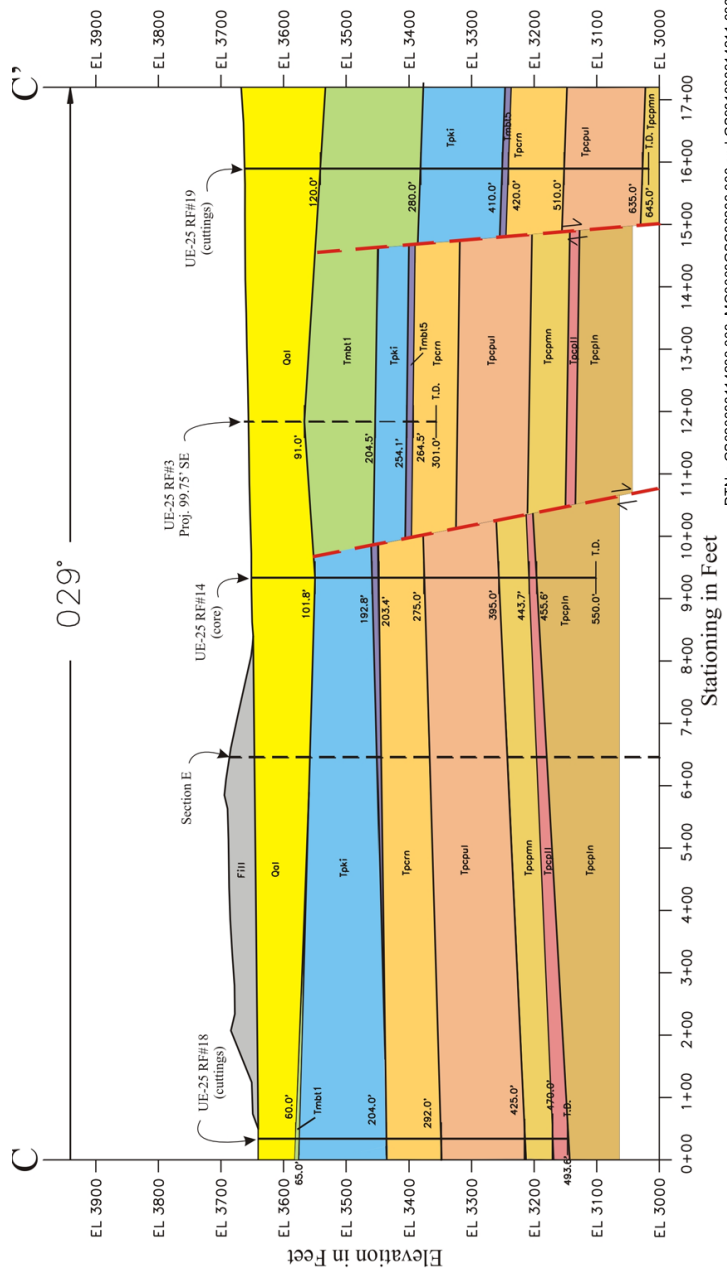


Figure 227. WHB Area Geologic Cross Section C-C', Looking West

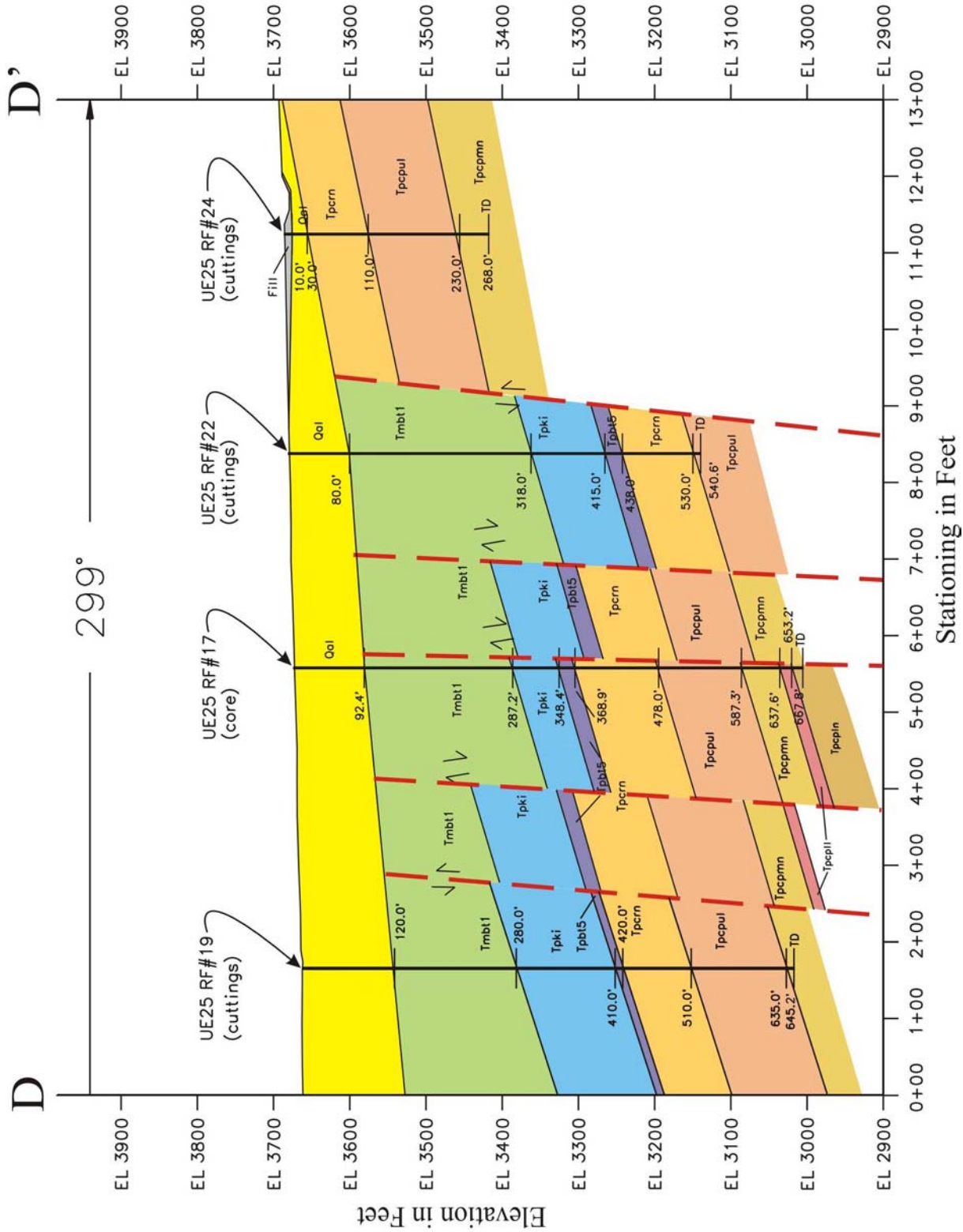
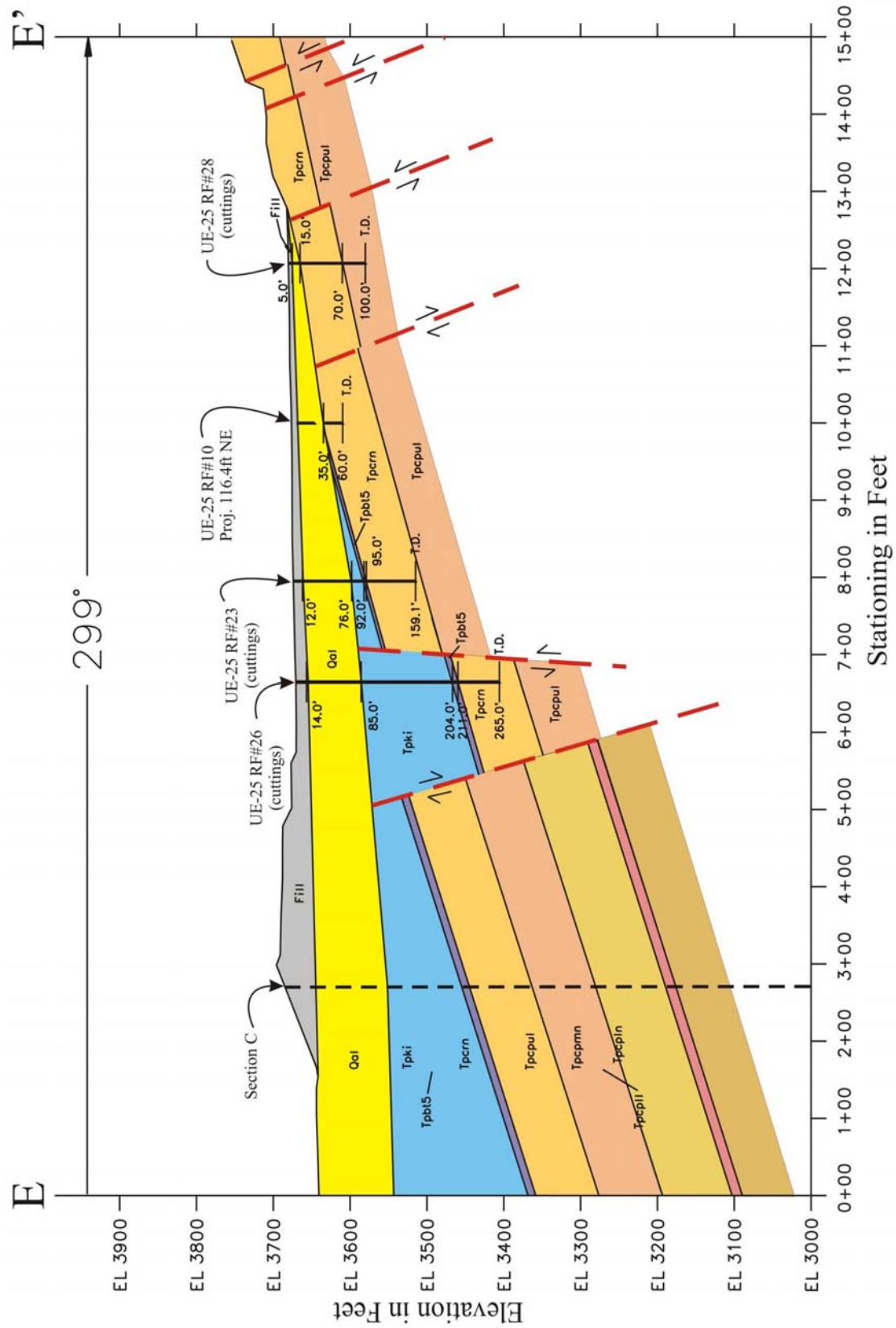
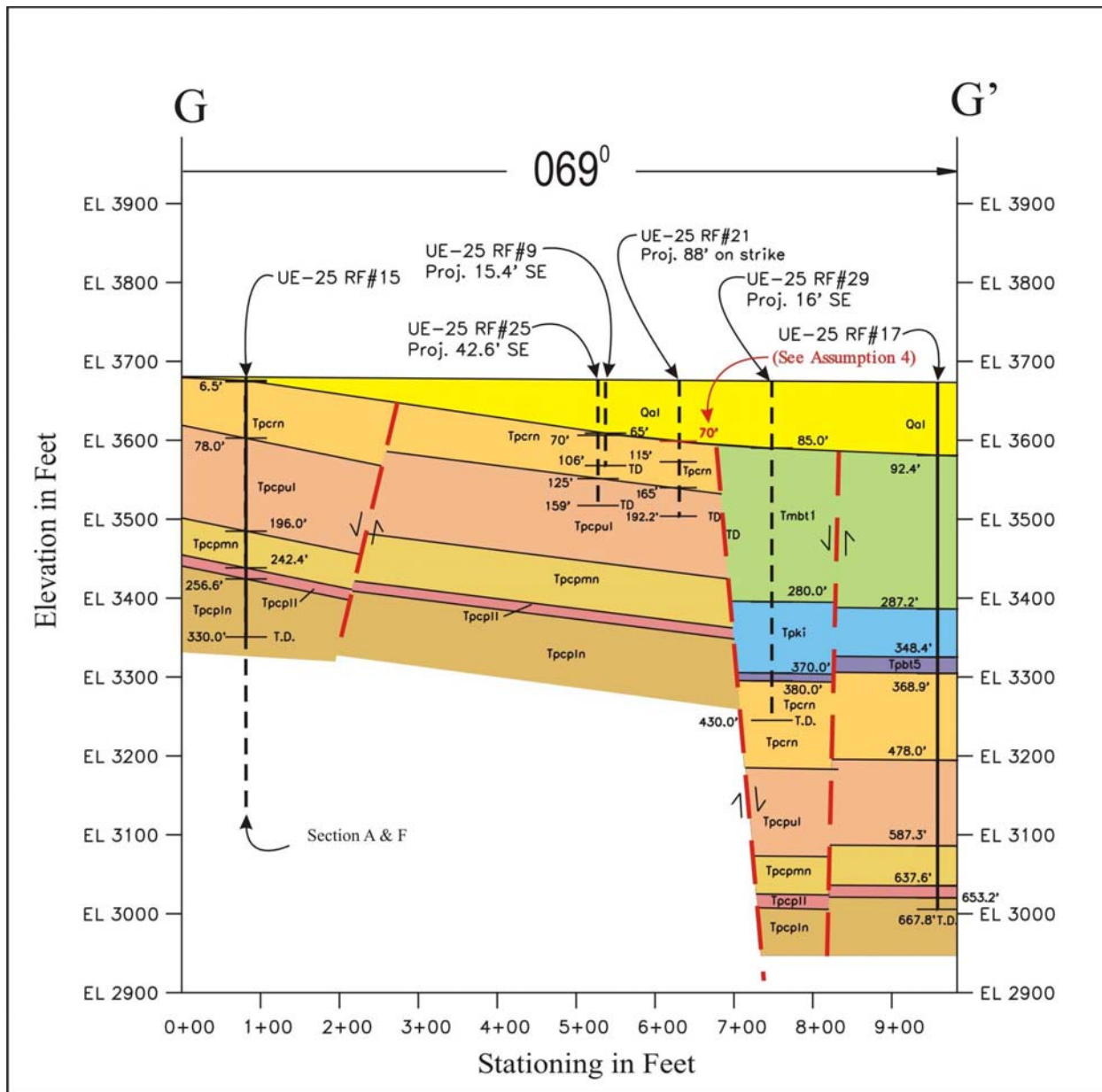


Figure 228. WHB Area Geologic Cross Section D-D', Looking South



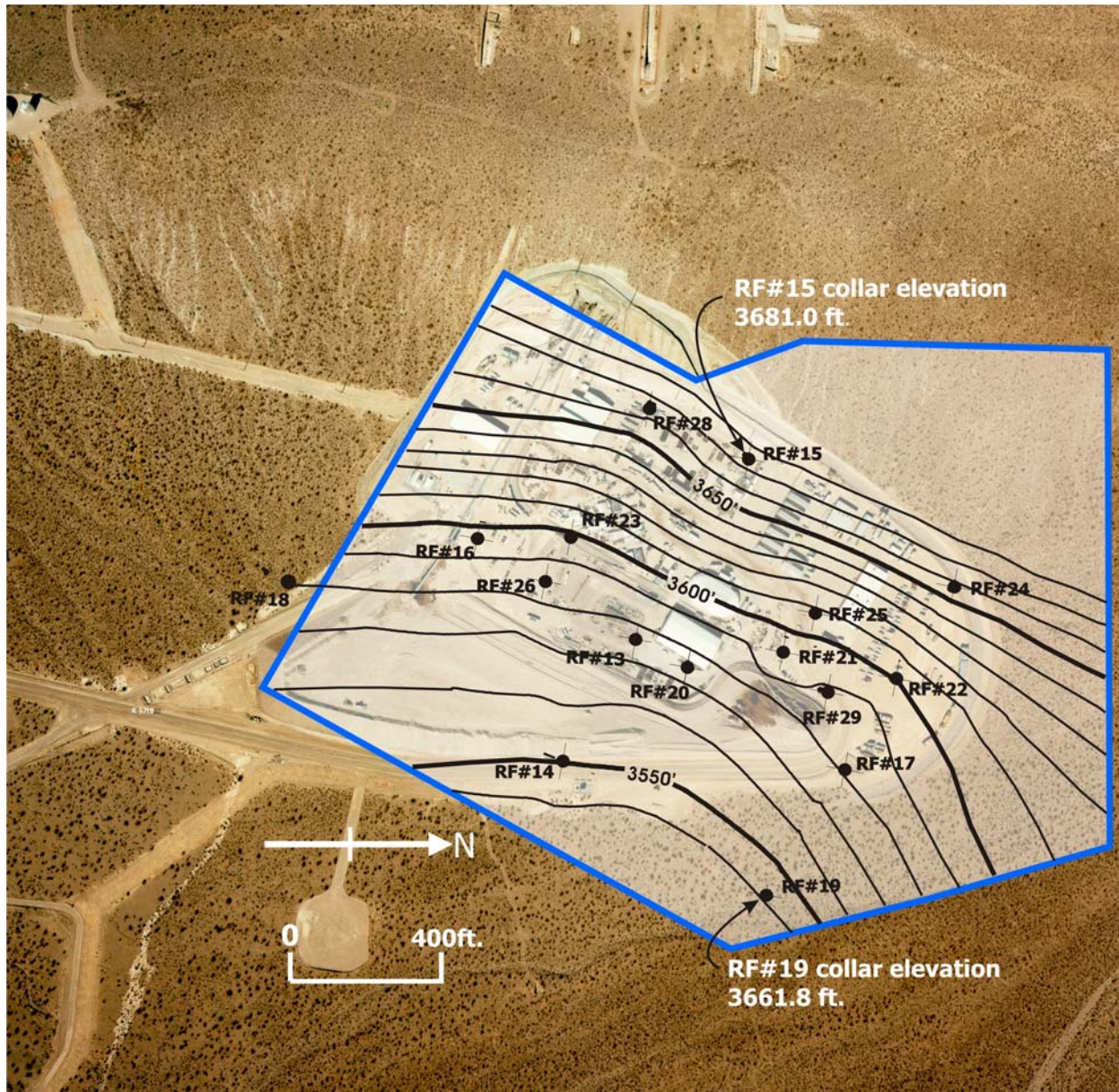
DTNs: GS020383114233.003, MO0008GSC00286.000
and Assumption 6

Figure 229. WHB Area Geologic Cross Section E-E', Looking South



DTN: GS020383114233.003 and Assumption 6

Figure 231. WHB Area Geologic Cross Section G-G', Looking Northwest



DTN: GS020383114233.003

Note: Contours are of top-of-bedrock, including welded and nonwelded units (10-foot contour interval). In accordance with Assumption 4 (Section 5), data from borehole RF#21 was not used in creating these contours.

Figure 232. Elevation Contours for Top-of-Bedrock Encountered in Boreholes

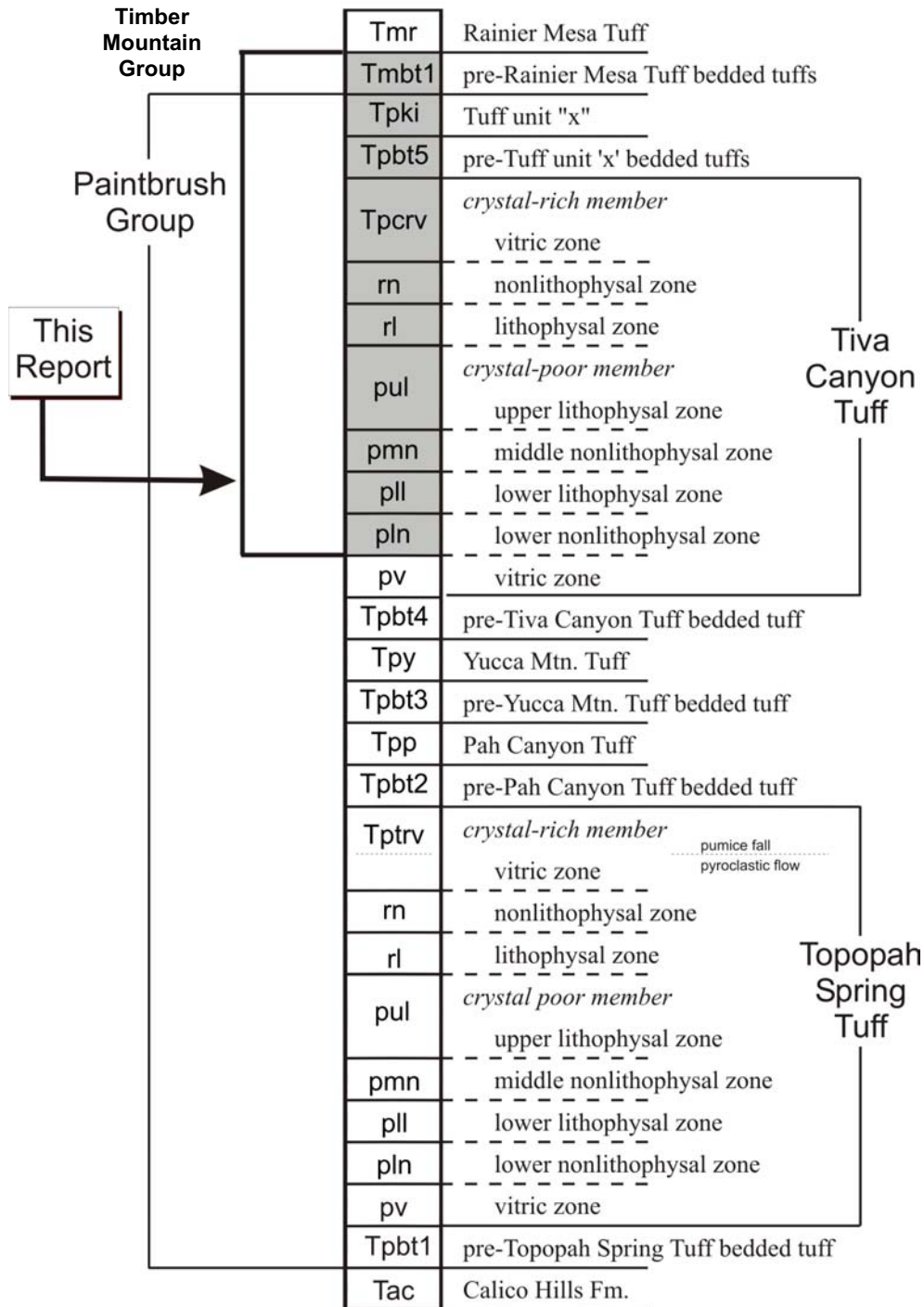
The alluvium varies in thickness from zero on the western edge of the WHB Area along the base of Exile Hill to over 100 feet in the part of the WHB Area located east of the muck pile. Alluvial materials in the WHB area consist of interbedded caliche-cemented and non-cemented, poorly sorted gravel with some fines, cobbles and boulders. For detailed descriptions of the alluvial material, refer to Section 6.2.4.

Under the alluvium are welded and nonwelded volcanic rock units of the Timber Mountain and Paintbrush groups. Figure 233 provides a lithostratigraphic column for relevant units of these groups. Nonwelded units beneath the site include the pre-Rainier Mesa Tuff bedded tuffs (Tmbt1) of the Timber Mountain Group, and the Tuff unit "x" (Tpki) and pre-Tuff unit "x" bedded tuffs (Tpbt5) of the Paintbrush Group. Beneath these nonwelded units is the Tiva Canyon Tuff, which is generally densely welded. The Tiva Canyon Tuff has been divided into two members; the younger crystal-rich member (Tpcr) and the older crystal-poor member (Tpcp). These members are further divided into zones, for example, the Tiva Canyon Tuff crystal-rich nonlithophysal zone (Tpcrn) (Buesch et al. 1996, pp. 22, 33-38). Detailed geologic descriptions of the various zones of Tiva Canyon Tuff encountered in the boreholes are presented in Attachments I and II. To simplify the distinction between the welded and nonwelded Tiva Canyon Tuff and the post-Tiva Canyon Tuff bedded tuffs, the vitric and lithophysal zones (Tpcrv and Tpcrl) of the crystal-rich member of the Tiva Canyon Tuff have been included with the crystal-rich nonlithophysal zone (Tpcrn) in this report. For the purposes of this report, subzones are not identified on the logs of boreholes RF#14 to RF#29.

The general orientation of bedding beneath the WHB Area is northeast-striking and southeast-dipping, which is slightly different than the orientation of bedding mapped on nearby Exile Hill. The *Plan View Geologic Map of the Drainage Channel and North Portal* (DTN: GS940408314224.004) shows the strike and dip of five contact observations in the North Portal cut, located west of the Exile Hill fault. Four of the contacts are in the upper lithophysal zone of the crystal-poor member of the Tiva Canyon Tuff (Tpcpul); their strikes ranged from N36°W to N8°W and their dips ranged from 14 to 22 degrees to the northeast. The remaining contact was in an intensely fractured zone in the lithophysal zone of the crystal-rich member of the Tiva Canyon Tuff (Tpcrl); its strike and dip were N40°E and 20°SE. Therefore, the bedding on Exile Hill is, in general, north-northwest-striking and east-northeast-dipping.

The following three-point problems were solved to interpret strike and dip of the bedrock stratigraphy beneath the WHB Area, based on the drilling data (Figure 224). These results are based on limited information from fault-bounded blocks within the WHB area. The elevations of the top of the Tpcpul in boreholes RF#18, RF#14, and RF#20 suggest that the bedding in this area is oriented N33°E, 23°SE. The elevations of the top of the Tpcpul in boreholes RF#13 (Tpcpul projected to 249ft.), RF#25, and RF#21 yield an orientation of N43°E and 18°SE.

General Lithostratigraphic Column at Yucca Mountain, Nevada



Source: Modified from Mongano et. al. (1999, Page 13).

Note: Gray-shaded areas indicate the units that are referred to in this report.

Figure 233. Generalized Lithostratigraphic Column Showing the Stratigraphic Interval Considered in this Scientific Analysis

However, given that boreholes RF#18, RF#20, RF#21, and RF#25 were mud rotary holes, the exact elevations of Tpcpul contacts are not known precisely. Therefore, the strikes and dips from these three-point problems are considered approximate. For example, if the top of the Tpcpul in borehole RF#21 is actually five feet¹⁰ higher, then the orientation derived from the elevations of the top of the Tpcpul in boreholes RF#13, RF#25, and RF#21 becomes N51°E, 17°SE.

For the purposes of this report, the strike and dip of the volcanic stratigraphy beneath the WHB Area are interpreted to be about N16°E and 25°SE. Various representations of the orientation of bedding in the WHB Area are shown on Figures 225 through 231. Regional mapping efforts (DTN: GS980608314221.002) demonstrate a large degree of variability in strike and dip of the Tiva Canyon Tuff, N16°E, 25°SE is within this variability and can be considered a reasonable representation of subsurface conditions.

The most prominent structural feature encountered during this exploration is a north-northwest-trending, east-northeast-dipping normal fault that cuts across the WHB Area, near boreholes RF#14 and RF#29. This fault, informally referred to in this report as the “Exile Hill fault splay,” is shown as the bolder (wider) fault trace on Figure 224. A regional geologic map (DTN: GS980608314221.002) shows a down-to-the-east fault east of Exile Hill that terminates at the Midway Valley fault south of the WHB Area. The fault mapped in DTN: GS980608314221.002 can be represented by the Exile Hill fault splay by having the splay terminate into the Midway Valley fault further to the north than previously mapped. This relationship between the regional mapping and the Exile Hill fault splay is shown on a modified portion of the regional geologic map (Figure 223).

The largest displacement associated with the Exile Hill fault splay is on the northern edge of the WHB Area. Between boreholes RF#22 and RF#24 there is approximately 300 feet of down-to-the-northeast separation, dropping the nonwelded pre-Rainier Mesa Tuff bedded tuffs (Tmbt1) on the northeast against the densely welded Tiva Canyon Tuff on the southwest. This relatively substantial vertical displacement along the Exile Hill fault splay has, in effect, subdivided the WHB Area into two distinct domains. Southwest of this fault, the top of the welded Tiva Canyon Tuff is relatively near the surface, ranging from zero to a maximum of about 190 feet below natural grade. In contrast, on the northeast side of the Exile Hill fault splay, the top of the Tiva Canyon Tuff ranges from about 250 to 480 feet below natural grade. A substantially greater thickness of the post-Tiva Canyon Tuff nonwelded bedded tuffs (Tptb5, Tпки, Tmbt1) occurs beneath the alluvium on the northeast side of the Exile Hill fault splay relative to the southwest side. The offset diminishes to the southeast along the strike of the fault, with 65 feet of down-to-the-east separation near borehole RF#14.

In addition to the Exile Hill fault splay, the interpretation of subsurface conditions includes several other faults that cut the volcanic bedrock within the WHB Area. These other faults are shown on Figure 224 as the thinner fault traces on either side of the Exile Hill fault splay. As

¹⁰ The estimated accuracy of the contacts is plus or minus 5 feet for mud rotary boreholes and plus or minus 1 foot for core, relative to the designated contact depth. If some of the rock that is cored is not recovered, this introduces additional uncertainty. The contacts within the Tiva are also gradational, as the units are based on considerations such as differences in phenocryst content and percentage of lithophysae voids.

shown on Figure 224, most, but not all, of these faults strike north-northeasterly and exhibit down-to-the-east normal displacement. Thickening and thinning of units across the cross sections could be the result of strike slip movement along faults, however, given the dynamic environment of deposition and the limitations of the data set, no attempt has been made to demonstrate lateral movement on faults. Further discussion of these faults and the subsurface geology, with specific reference to each of the seven sections, is provided in the following paragraphs.

Section A-A' (Figure 225) cuts approximately parallel to the dip of bedding across the central part of the WHB Area. It shows an easterly dipping, homoclinal volcanic sequence consisting of Tiva Canyon Tuff (Tpc), pre-Tuff unit "x" bedded tuffs (Tptb5), and Tuff unit "x" (Tpki) that is unconformably overlain by an easterly thickening sequence of Quaternary alluvium and by North Portal pad fill/muck. The crystal-rich member of the Tiva Canyon Tuff (Tpcrn) outcrops along the west side of the section, on the east slope of Exile Hill and the alluvium thickens to the east, from zero near borehole RF#15 to about 120 feet near borehole RF#14.

The Exile Hill fault splay, which is east of borehole RF#14, shows about 75 feet of down-to-the-east separation. The fault intersected by borehole RF#13 is a northeast-trending, northwest-dipping normal fault that exhibits approximately 100 feet of down-to-the-west separation. The fault between boreholes RF#13 and RF#11 is a northwest-trending, northeast-dipping reverse fault that exhibits about 25 feet of up-to-the-west separation. The fault between boreholes RF#11 and RF#15 is a northeast-trending, northwest-dipping normal fault that shows about 25 feet of down-to-the-west separation. The Exile Hill fault, located west of borehole RF#15, has about 5 feet of up-to-the-west separation.

Section D-D' (Figure 228) cuts approximately parallel to the dip of bedding across the northern part of the WHB Area. It shows an easterly dipping volcanic sequence consisting of Tiva Canyon Tuff (Tpc), pre-Tuff unit "x" bedded tuffs (Tptb5), Tuff unit "x" (Tpki), and pre-Rainier Mesa Tuff bedded tuffs (Tmbt1), unconformably overlain by an easterly thickening sequence of Quaternary alluvium and by North Portal pad fill/muck. At the western edge of the section the alluvium is only a few feet thick, deepening to over 120 feet to the east of RF#19. Between boreholes RF#24 and RF#22 is the Exile Hill fault splay, with approximately 360 feet of down-to-the-northeast separation along this section. East of the Exile Hill fault splay, three northeast-trending, northwest-dipping normal faults drop the volcanic stratigraphy approximately 220 feet down to the northwest. The southeasternmost fault on Section D-D' is a northwest-trending, southwest-dipping reverse fault that has produced about 5 feet of up-to-the southwest separation along this section.

Section E-E' (Figure 229) cuts approximately parallel to the dip of bedding across the southern part of the WHB Area. It shows a southeasterly dipping volcanic sequence consisting of Tiva Canyon Tuff (Tpc), pre-Tuff unit "x" bedded tuffs (Tptb5), and Tuff unit "x" (Tpki), that is unconformably overlain by an easterly thickening sequence of Quaternary alluvium and by North Portal pad fill/muck. From west to east this section shows the alluvium thickening from zero near the base of Exile Hill to approximately 100 feet on the eastern edge of the section. It also shows the presence of a down-dropped block that accounts for the relatively thick section of Tuff unit "x" encountered in borehole RF#26, compared to that encountered in borehole RF#23. The fault along the eastern side of this down-dropped block is a northeast-trending, northwest-

dipping normal fault that has produced about 120 feet of down-to-the-west separation. The fault along the western side of this block is a northeast-trending, southeast-dipping normal fault that has produced about 90 feet of down-to-the-east separation. The fault between boreholes RF#28 and RF#10 is a northeast-trending, northwest-dipping normal fault that has produced minor down-to-the-west separation. The Exile Hill fault just west of borehole RF#28 has approximately 10 to 15 feet of up-to-the-west separation. The other faults west of borehole RF#28 are north- to northwest-trending, west-dipping reverse faults that have produced minor up-to-the-west separations.

Section B-B' (Figure 226) cuts approximately parallel to the strike of bedding across the central part of the WHB Area. It shows a volcanic sequence consisting of Tiva Canyon Tuff (Tpc), pre-Tuff unit "x" bedded tuffs (Tptb5), Tuff unit "x" (Tpki), and pre-Rainier Mesa Tuff bedded tuffs (Tmbt1) that is unconformably overlain by Quaternary alluvium. The alluvium is overlain in some areas by North Portal pad fill or muck.

The volcanic stratigraphy exhibits a slight (approximately 3°) northeasterly apparent dip and is disrupted by five normal faults. North of borehole RF#16, a graben brackets borehole RF#26. The northeast-trending, northwest-dipping normal fault along the south side of this graben has dropped the top of the Tiva Canyon Tuff about 70 feet. An uplifted block, or horst, centered on borehole RF#20 is bounded on the southwest by the fault encountered by borehole RF#13 and on the northeast by the Exile Hill fault splay. The northeast-trending, northwest-dipping normal fault encountered in borehole RF#13 exhibits about 120 feet of down-to-the-northwest separation, and the Exile Hill fault splay exhibits about 330 feet of down-to-the-northeast separation. Between the graben and the horst is an intermediate block that is bounded on the south by the fault shown immediately to the north of borehole RF#26. This northwest-trending, southwest-dipping normal fault exhibits about 50 feet of down-to-the-south separation between the graben and the intermediate block. The northernmost fault on this section is a northeast-trending, northwest-dipping normal fault that terminates at the Exile Hill fault splay. This fault exhibits about 90 feet of down-to-the-west separation.

Section C-C' (Figure 227) cuts approximately parallel to the strike of bedding across the southeastern edge of the WHB Area. It shows a volcanic sequence consisting of Tiva Canyon Tuff (Tpc), pre-Tuff unit "x" bedded tuffs (Tptb5), Tuff unit "x" (Tpki), and pre-Rainier Mesa Tuff bedded tuffs (Tmbt1) that is unconformably overlain by a northeasterly thickening sequence of Quaternary alluvium. Alluvium thickens to the north edge of the section to over 120 feet. The alluvium is overlain in some areas by muck. The Exile Hill fault splay exhibits about 50 feet of down-to-the-northeast separation just north of borehole RF#14. The fault immediately south of borehole RF#19 is a northwest trending, southwest-dipping normal fault that exhibits about 160 feet of up-to-the-south separation.

Section F-F' (Figure 230) cuts approximately parallel to the strike of bedding across the northwestern edge of the WHB Area, near the base of Exile Hill. This section shows the Tiva Canyon Tuff unconformably overlain by a thin veneer of alluvium and North Portal pad fill in some areas and cropping out on Exile Hill. The alluvium thickens to about 30 feet on the northern edge of the section. Three north- to northwest-trending, southwest-dipping reverse faults exhibit minor separation to the south of borehole RF#28.

Section G-G' (Figure 231) cuts normal to the strike of the Exile Hill fault splay across the northern portion of the WHB Area. It shows a volcanic sequence consisting of Tiva Canyon Tuff (Tpc), pre-Tuff unit "x" bedded tuffs (Tptb5), Tuff unit "x" (Tpki), and pre-Rainier Mesa Tuff bedded tuffs (Tmbt1) that is unconformably overlain by a northeasterly thickening sequence of Quaternary alluvium and North Portal pad fill (a surface profile of this section was not developed, therefore, the pad fill is not represented). The alluvium thickens to the northeast from zero at the southwest end to about 75 feet thick at the east-northeast end of the section. Along this section, the Exile Hill fault splay shows approximately 320 feet of down-to-the-northwest separation. The fault between RF#15 and RF#25 is a northeast-trending, northwest-dipping normal fault that shows about 75 feet of down-to-the-west separation. The fault to the southwest of RF#17 is a northeast-trending, northwest-dipping fault.

In summary, the WHB Area can be characterized as underlain by densely welded, rhyolitic, pyroclastic flows of the Tiva Canyon Tuff, nonwelded bedded tuffs of the post-Tiva Canyon Tuff and the pre-Rainier Mesa Tuff bedded tuffs and by Quaternary alluvium. The Quaternary alluvium thickens towards the east from zero along Exile Hill to over 120 feet thick on the eastern side of the area. Structurally, the area is crisscrossed with mostly high-angle normal faults of various displacements. A northwest-trending normal fault, cutting across the northeastern edge of the WHB site, informally referred to in this report as the Exile Hill fault splay, has produced significant down-to-the-northeast displacement of the volcanic stratigraphy. As a result, the area to the northeast of the Exile Hill fault splay is characterized by a significantly thicker sequence of nonwelded bedded tuffs overlying the Tiva Canyon Tuff, and the area to the southwest of the Exile Hill fault splay is typically characterized by no or a relatively thin sequence of nonwelded tuffs overlying the Tiva Canyon Tuff. The westernmost extent of the nonwelded bedded tuffs occurs midway across the WHB area. From this line, the nonwelded bedded tuffs generally thicken to the east. The exception to this trend is the result of an elongate graben that trends to the southeast beginning just north of borehole RF#26.

6.6.3 Groundwater Conditions

The WHB Area is located in a part of the Yucca Mountain area with about a 1270-foot thick unsaturated zone, where the water table slopes to the east-southeast (USGS 2001, Figure 6-1). There are no boreholes within the WHB Area that penetrate the water table and thus the depth to the water table is approximated based on nearby boreholes (see below). The water table elevation map developed for the Yucca Mountain Saturated Zone Site-Scale Flow and Transport Model (USGS 2001, Figure 6-1) indicates an area typically referred to as the large hydraulic gradient to the north of the WHB Area, but this feature is at least 8,500 feet north. USGS (2001, Table I-1, DTN: GS000508312332.001) list all borehole information in metric units; for this report, these metric values have been converted to feet.

The approximation of depth to and gradient of the water table beneath the center of the WHB Area is based on several boreholes (DTN: GS000508312332.001). The water table in borehole UE-25 WT#4 (Figure 223), which is 5,000 feet to the northwest of the WHB Area, is at an elevation of 2397.6 feet. There are four additional boreholes within about 8,500 feet of the WHB Area (UE-25 WT#18, UE-25 a#1, UE-25 b#1, and UE-25 WT#14,) that penetrate the water table at 2397.6, 2398.3, 2397.0, and 2394.0 feet, respectively. With respect to the WHB Area, borehole UE-25 WT#18 is located northwest, UE-25 a#1 and UE-25 b#1 are to the

west-southwest, and UE-25 WT#14 is to the southeast. The location of the boreholes and the elevation of the water table indicate an extremely small gradient that slopes to the east-southeast beneath the WHB Area. A typical elevation of the water table under the WHB Area is about 2400 feet, and the typical ground (fill pad) elevation for the WHB Area is about 3670 feet; therefore, the typical depth to the water table is about 1270 feet. Because both the water table and the ground elevation have little gradient in the WHB Area, a depth to the water table of 1270 feet is a reasonable value for the entire WHB Area. The elevations of the UE-25 RF# series of boreholes used in this investigation have elevations that vary from 3640.3 to 3680.8 feet and depths that vary from 100.0 to 667.8 feet (Table 3). These relations of ground elevation, total depth of the boreholes, and the elevation of the water table indicate that the water table is about twice as deep as the deepest borehole in the WHB Area; therefore, all boreholes are within the unsaturated zone.

6.7 EVALUATION OF SEISMIC VELOCITY DATA FROM WHB AREA

Section 6.7 compares the results obtained using various seismic methods. First, Section 6.7.1 reviews some comparison studies that have been published that substantiate that agreement can be obtained by the methods used: downhole seismic, suspension seismic and SASW. Section 6.7.2 then examines the data obtained at the WHB Area using these three methods.

6.7.1 Shear-Wave Velocities Determined by Various Seismic Methods at Other Sites

In-situ seismic methods (downhole, suspension, SASW) have been used to measure low-strain v_s and v_p , and laboratory test methods (resonant column, torsional shear) have been used to measure low-strain shear modulus. According to the theory of elasticity, low-strain shear modulus, G_{max} , is the product of the total density, ρ , and the square of the low-strain shear-wave velocity, v_s , so the values of G_{max} can be converted to v_s and vice versa by Eq. 14 (Section 6.2.5).

It is reasonable to ask if these different techniques can be expected to provide the same values of v_s or, equivalently, G_{max} . This section reviews some of the studies of this subject that have been published, while Section 6.7.2 focuses on comparing the data acquired and developed for the WHB. Although some attention is given to compression-wave velocities, the primary focus is on shear-wave velocity and G_{max} as being more important analysis parameters.

In the in-situ tests, it is very difficult to apply dynamic stresses that induce various strain levels, but the measurement of P and S wave velocity at low strain levels is quite easy. On the other hand, it is difficult in laboratory tests to measure v_s and v_p under actual stress conditions (which are often not known) and the test specimens are always disturbed to some degree. However, it is easier to carry out a laboratory test with various levels of strain under controlled stress conditions.

Geophysical methods have the advantage of testing a large volume of the geologic formation, including discontinuities and imperfections that typically are not represented in laboratory test specimens. The volume tested varies with the technique and the arrangement of source and receiver(s). The distances involved are relatively small in the typical suspension seismic setup, while in the downhole seismic and SASW technique, larger volumes of the formation are involved when the receiver(s) are placed farther from the source. Laboratory tests involve

relatively small specimens, and in some cases the sample tested may have been selected because it could be trimmed into a stable cylindrical specimen, that is, the material was not so weak that it would be damaged by the coring or other sampling procedure and it did not contain joints, shears or other types of discontinuities that would cause the specimen to separate into fragments during handling. In the case of granular soil, such as the alluvium at the site, the material is recompacted to the estimated in-situ density and water content, but the original soil fabric and other features (cementation, aging) cannot be reestablished.

Downhole seismic and SASW surveys are useful for evaluating the average seismic velocity of a layer with a relatively uniform seismic velocity. However, downhole seismic and SASW surveys are not generally relied upon to detect the presence of relatively thin¹¹ layers of high or low seismic velocity, although interval velocities between successive depths can be calculated from downhole seismic results.¹² Suspension seismic surveys, on the other hand, are useful for identifying the seismic velocity over relatively short intervals (typically 3.3 feet). In addition, the seismic energy in a downhole survey tends to lessen with depth due to material damping, leading to difficulties in interpreting the records from greater depths. Material damping does not affect the suspension seismic survey at deeper depths because the source and receivers that are lowered down the borehole are connected by tubes that maintain them at a constant spacing. Rather, suspension seismic measurements are affected by local material conditions that can result in unusually high signal attenuation.

Table 31 summarizes some of the main characteristics of the downhole seismic, suspension seismic, and SASW methods.

Several published studies compare the shear-wave velocities obtained by various seismic methods. EPRI (1993) contains shear-wave velocity comparisons for three sites with distinctly different subsurface conditions. The seismic methods used are summarized in Table 32.

EPRI (1993, Section 8) compared the seismic surveys performed at each of the sites and concluded “that velocities vary significantly with local geologic conditions, but that with a reasonable level of care in the interpretation of data, very similar values of velocity are obtained by the different investigators.” However, it should be noted that the variability in the results obtained, when plotted as a function of depth, was sometimes wide, and sometimes exceeded 100 percent. Because the boreholes used were sometimes different, as well as the logger/interpreter and the seismic method being different, it is generally difficult to assess how much of the variability is due to subsurface conditions, method, logger technique, and interpreter decisions.

The crosshole data presented is particularly indicative of the variability that can result from subsurface conditions. For example, at Gilroy 2, compression-wave velocity was measured by the crosshole method using four boreholes drilled on a line at 15-foot spacings. The variability in interpreted velocity was as much as 70 percent at certain depths, although the method, logger

¹¹ Relatively thin, i.e., a few feet or less

¹² When it is desirable to obtain interval velocities with the downhole method, it is preferred to use multiple geophones in the borehole and compute the interval velocities from measurements made with a single source excitation.

technique and interpreter were all apparently constant, suggesting that variation of this magnitude can occur over short distances due to geologic variability.

Table 31. Comparison of Downhole Seismic, Suspension Seismic and SASW Methods

Characteristic	Suspension Seismic	Downhole Seismic	SASW
Energy source	Built-in solenoid hammer	Hammer on plank	Hammer at close source-receiver spacings; sledgehammer, dropped weight, bulldozer or vibroseis at longer spacings
Type of wave generated	P and S	P and S	Rayleigh or other surface wave
Ability to reverse polarity	Yes	Yes	No
Primary direction of wave motion	Upward, vertical	Downward, near vertical but becoming more inclined at shallow depth	Horizontal
Wave frequency, Hz	S wave 500 - 1,000 P wave 1,000 – 3,000	S wave 20 - 40 P wave 50 – 200	5 – 500 or more
Boreholes required	One	One	None
Borehole requirements	Liquid-filled; uncased generally preferred; plastic casing is acceptable	Dry preferred; casing optional	Not applicable
Maximum effective depth, ft	1,600	300 to 700	Up to 500
Resolution	Resolution constant with depth	Resolution decreasing with depth	Resolution decreasing with depth
Borehole drift survey	Not required	Not required	Not applicable
Space limitations	Can be performed wherever a borehole can be drilled	Can be performed wherever a borehole can be drilled	Line length is about 2 times the depth surveyed, so on-site and off-site constraints may limit survey depth
Type of wave interpreted	P and S _H	P and S _H	R, converted to S using theory and assumed Poisson's ratio
Interval velocity	Yes	Only with geophones at multiple depths	No
Average velocity	Yes, by accumulation of individual travel times	Yes	Yes

Table 32. Seismic Methods Used at EPRI Comparison Sites

Site	Seismic Surveys
Gilroy 2	P-S downhole; P-S suspension; P-S crosshole and damping; P-S crosshole and damping
Treasure Island	P-S downhole; P-S crosshole and damping; seismic cone
Lotung	P-S uphole and P-S crosshole; v_s refraction

Source: EPRI (1993, Tables 8-2, 8-4 and 8-6)

Ohya (1986) compared suspension seismic and downhole seismic measurements made in the same boreholes at five sites. Based on 144 measurement pairs, the v_s (suspension) to v_s (downhole) ratio averaged 1.028, indicating that the suspension values averaged 2.8 percent higher than the downhole values.

For the compression-wave velocities, even better agreement was obtained. Based on 137 measurement pairs, the v_p (suspension) to v_p (downhole) ratio averaged 1.014, indicating that the suspension values averaged 1.4 percent higher than the downhole values. The observed range of v_s (suspension)/ v_s (downhole) was from approximately 0.79 to 1.20, and v_p (suspension)/ v_p (downhole) from approximately 0.90 to 1.49. Given that the suspension method yields an interval velocity, while the downhole method yields an average velocity, the agreement is very good.

Ohya (1986, page 1229) also compared suspension seismic and crosshole seismic measurements made at three sites. For this comparison, different boreholes are necessarily used, since the suspension method uses a sole borehole while the crosshole uses three or more boreholes. Based on 36 measurement pairs, v_s (suspension)/ v_s (crosshole) averaged 1.133 and v_p (suspension)/ v_p (crosshole) averaged 1.06. Because the subsurface conditions at these sites were not uniform, many factors may be responsible for the divergences. In addition, the shear wave measured by suspension is a upwardly propagating wave with particle motion in the horizontal plane, while cross hole measures a horizontally propagating wave with particle motion in the vertical plane.

Ohya (1986, page 1234) concluded that:

- If subsurface conditions are uniform, the suspension, downhole and crosshole methods will produce the same values of P and S wave velocity.
- If subsurface conditions are not uniform, the three methods will produce the different values of P and S wave velocity as follows:
 - ▶ the downhole method will produce an average velocity for the layers
 - ▶ the suspension method will provide more detailed, accurate velocity information, reflecting the changes in velocity from layer to layer
 - ▶ the crosshole method may produce false velocity measurements.

- Deformation or failure of the ground may be significantly influenced by the properties of a weak layer. To this end, it is important to obtain velocity information for a weak layer accurately, even if the weak layer is thin. Suspension logging is suited to this application.

Brown (1998) conducted SASW measurements at nine strong-motion station sites where borehole seismic measurements were previously conducted. The team performing the SASW measurements collected their data and made their interpretations without recourse to the available borehole logs or borehole seismic profiles. Brown (1998) presents detailed results for the nine sites. In addition to the traditional comparison of v_s versus depth, quarter-wavelength amplification ratios and predicted dispersion curves from the downhole profiles were calculated.

Based on his interpretation of the SASW data and subsequent comparison with the other available data (downhole seismic at all sites and suspension seismic at some sites), Brown concluded that:

At five of the nine sites, agreement between the SASW and borehole v_s profiles was very good; at four of the nine sites the SASW and borehole v_s profiles had significant differences.

Some of the differences between the SASW and borehole v_s profiles are due to lateral variability and the difference between the “point” borehole measurements and the global SASW measurements.

The lateral variability in the subsurface, as measured by differences in surface-wave dispersion curves and SASW v_s profiles, were generally low at the test sites with multiple arrays. The differences were greatest near the ground surface and decreased with depth. This trend is due in part to the larger volume of material that is sampled as the sampling depth increases, so that the velocities at depths of several hundred feet represent the average properties over lateral distances of several hundred feet.

Because so much dispersion data is collected in the near-surface and there is little ambiguity in interpreting shorter wavelength data, the accuracy of the SASW method is considered greater near the ground surface than at depth. The SASW models have low resolution at depth.

At several sites the largest relative difference between the downhole and SASW v_s profiles occurred in the upper 10 feet, with the SASW v_s typically being lower than the downhole v_s . At two sites this was likely due to the borehole having been advanced through well-compacted fill while the SASW profile was located in softer surficial ground conditions beyond the fill. At several sites, however, the SASW profile appeared to be in visually similar material and a discrepancy was still observed. In these cases, different moisture conditions (and hence different effective stress conditions) may have contributed to a change in v_s values.

The discrepancies between SASW and downhole profiles near the surface may also be because the downhole velocities are averaged over greater depths and are therefore higher. The downhole method also samples a smaller volume of material than the SASW method and may

not be representative of average or global properties at the site.¹³ If the subsurface is non-uniform, the downhole shear-wave travel path may not follow the straight line path used in the interpretation. In the downhole method, identification of the shear wave arrivals is difficult because the compression wave is usually still present at the onset of the shear wave, obscuring the shear wave.¹⁴

The SASW interpretations were made with one exception using an adopted value of Poisson's ratio of 0.25. However, based on the borehole seismic measurements and groundwater level, a higher value of Poisson's ratio would have been appropriate. At most of the sites the groundwater table is situated between 20 and 50 feet bgs, and Poisson's ratio is in the range of 0.4 to 0.49 below the water table. If the SASW interpreter had had knowledge of the depth to groundwater, he would have chosen a higher value of Poisson's ratio and would have achieved better agreement with the borehole seismic results. This indicates the value of considering all available data when making SASW interpretations relative to "blind" interpretations.

At sites where v_s increases gradually with depth, the v_s increase may be difficult to interpret, making the profile less reliable. Depending on the profiles should be accurate. In this case, layer boundaries are somewhat arbitrary, but the trend of increasing v_s with depth is well defined. The v_s profile is fairly well resolved to a depth of one-half to one-third or the maximum wavelength in the dispersion curve.

SASW measurements from sites with a sudden large v_s increase may be difficult to interpret, making the profile less reliable. Depending on the velocity contrast, the profile may only be resolved to one-fifth the maximum wavelength in the dispersion curve or less.

Brown et al. (2000) present further discussion of the studies presented by Brown (1998) and focus primarily on the results obtained at one site, the Rinaldi Receiving Station, as a typical and uncomplicated example of the nine study sites .

Based on their interpretation of the SASW data and subsequent comparison with the other available data (downhole seismic and suspension seismic at Rinaldi), the authors concluded that:

- The shear-wave velocity profiles from the downhole seismic and SASW methods compare well in general.
- In many situations the SASW can provide profiles suitable for site response predictions.
- SASW measurements are inherently different than borehole measurements as they involve a much larger volume of material. Lateral variations and non-homogeneities in

¹³ Note: However, when collecting the near-surface SASW data, the source and receivers are closer together and therefore sample a smaller volume of material. Thus, the SASW data at shallow depths may not be representative of the average or global properties of the site, so data for shallow depths should be collected at several locations.

¹⁴ The potential for refraction along a nonlinear travel path would be particularly great near the surface where the geophone depth is less than the source offset from the borehole, as well as at sites with non-horizontal velocity layering, as could result from faults with vertical offset and dipping beds.

the materials may cause differences in the shear-wave velocity profiles interpreted from the two methods.

In summary, the various seismic geophysical methods appear to provide good agreement in many cases. However, even when practiced at the same location, each method is measuring properties of a different volume of soil and in a different manner. Thus, the resulting velocity profiles may be different, but it is not evident that one of these profiles may be “correct” while the others are “incorrect”.

Laboratory tests are generally used to obtain the modulus reduction and damping ratio curves, but the low-strain shear modulus is taken from in-situ measurements. In cases where the in-situ material is a fill that has not yet been constructed, in-situ measurements are not possible and the results of laboratory tests on laboratory-compacted samples must be used. However, v_s and G_{max} are affected very significantly by factors such as aging, which may not be properly represented in laboratory-compacted samples.

6.7.2 Comparison of Shear-Wave Velocities from Borehole Seismic Methods

The traditional method of comparing several shear-wave velocity profiles (v_s as a function of depth) is to plot the profiles on a common graph and make a visual comparison. For this purpose, the downhole and SASW profiles are the interpreted average layer velocities, and for suspension, the interpreted interval velocities. This type of comparison between downhole and suspension shear-wave velocities is made on Figures VII-1 to VII-16. This comparison method may be appropriate if the absolute values of velocity over a particular range of depth are important. The drawback to this method is that the comparison is often subjective and qualitative. Where velocity is high, absolute differences in velocity may stand out, while larger relative differences in lower velocity layers near the surface may not stand out. Further, the suspension velocity measured over a short interval may be highly variable and difficult to visually compare with averaged velocities from downhole or SASW surveys.

In terms of site response to ground motion, travel time is a more fundamental parameter than is velocity. Travel time can be calculated by (Brown 1998, equation 3.1 on page 39):

$$tt_s(z) = \sum_1^j \frac{h_i}{v_{s,i}} \quad (\text{Eq. 40})$$

where $tt_s(z)$ is the shear-wave travel time to depth z below ground surface; h_i is the thickness of the i^{th} layer, where layers range from 1 at the surface to j at depth z ; and $v_{s,i}$ is the shear-wave velocity of the i^{th} layer (for the bottom layer, layer j , only the part of the layer above depth z is considered in determining h_j). For SASW velocity profiles, the above equation is used. For suspension, the travel times from individual measurements must be accumulated with depth. In addition, the travel time from the ground surface to the shallowest measurement must be assigned arbitrarily. For downhole surveys, travel times have been interpreted from the measured data and subsequently further interpreted to yield a velocity profile. Either the interpreted travel times or the interpreted velocity profiles could be used: in this report, the interpreted velocity profile is used as the basis for comparisons because these are the

interpretations that would actually be used in ground motion analyses. Plots of accumulated shear-wave travel time versus depth are shown on Figures VIII-1 to VIII-16.

A plot of \bar{v}_s , the average shear-wave velocity from the ground surface to a given depth z , also emphasizes differences in travel times between two profiles. Equation 41 (Brown 1998, equation 3.2 on page 40) can be used to calculate \bar{v}_s :

$$\bar{v}_s = \frac{z}{tt_s(z)} \quad (\text{Eq. 41})$$

where $tt_s(z)$ is as defined by Eq. 40. The information contained in the travel time versus depth and \bar{v}_s versus depth plots is similar. Plots of \bar{v}_s versus depth for the deeper profiles are presented on Figures VIII-17a through VIII-23a.

Although the \bar{v}_s versus depth comparison provides a better understanding of the potential effect of alternative profiles on a ground motion analysis, its interpretation is still subjective. A better understanding can be achieved by the quarter-wavelength amplification ratio (Boore and Brown 1998). This technique derives from the quarter-wavelength amplification approximation introduced by Joyner et al. (1981, pages 1346-1347). The quarter-wavelength amplification approximation states that, for a particular frequency, the amplification, A , of shear waves propagating vertically towards the surface can be approximated by the square root of the ratio of the seismic impedance (product of shear-wave velocity and density) averaged over a depth corresponding to a quarter wavelength and the seismic impedance at the depth of the source. The approximation is relatively insensitive to discontinuities in seismic velocity and does not produce the peaks and valleys resulting from the interference of reflected waves. Thus, a smoothed amplification function is obtained. Then, the quarter-wavelength amplification ratio, A_2/A_{dh} , is the ratio of the quarter-wavelength amplifications for two different velocity profiles, and is calculated by Eq. 42 (Brown 1998, equation 3.6 on page 42):

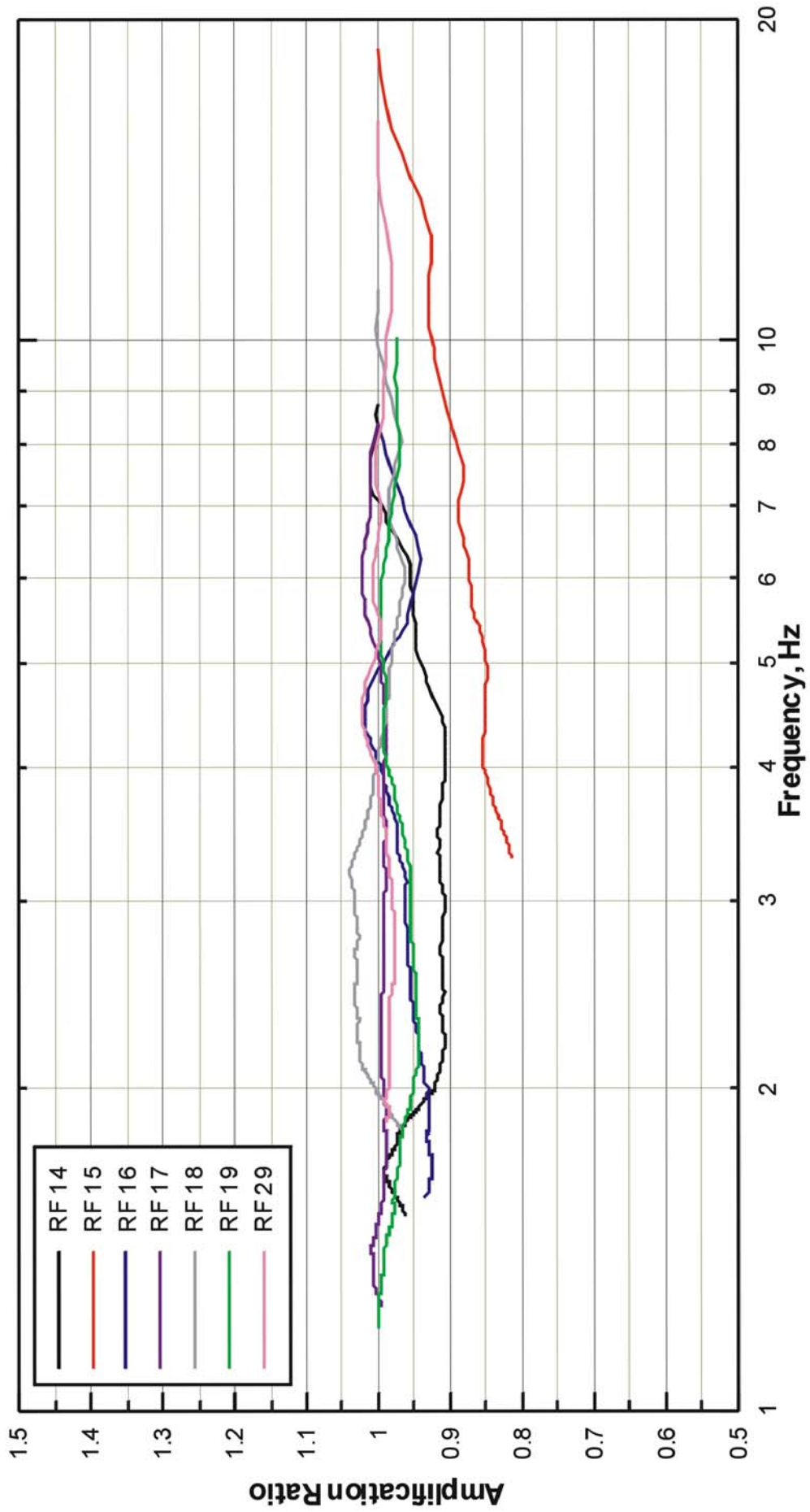
$$\frac{A_2}{A_{dh}} = \sqrt{\frac{\bar{v}_{s,dh}}{\bar{v}_{s,2}}} \quad (\text{Eq. 42})$$

where the subscript 2 represents an alternative velocity profile and the subscript dh represents the reference profile, which, in this report, is always taken as the downhole velocity profile. As implied by earlier discussion, calculation of the quarter-wavelength amplification ratio for suspension results requires making an assumption (Assumption 5 in Section 5) about the part of the profile above the shallowest data. In this report, the suspension profile is assumed to be the same as the downhole profile at shallow depths where there are no suspension data. This assumption causes the ratio to equal unity at the highest frequency (shallowest depth). Plots of amplification ratio versus depth for the deeper profiles are presented on Figures VIII-17b through VIII-23b. Figure 234 presents all the suspension to downhole profile comparisons on a single figure. The remainder of this section provides some comments about these various comparative figures.

Velocity is used frequently in this section, and abbreviations are adopted as follows:

- v_s is shear-wave velocity
- v_p is compression-wave velocity
- V_{sdh} , V_{pdh} are downhole seismic shear-wave velocity and compression-wave velocity
- V_{sRR} , V_{pRR} are suspension seismic (based on receiver-to-receiver data) shear-wave velocity and compression-wave velocity
- V_{sSR} , V_{pSR} are suspension seismic (based on source-to-receiver data) shear-wave velocity and compression-wave velocity

Borehole RF#13 was advanced in 1998 using compressed air as the drilling fluid to lift drill cuttings from the borehole. Observations of borehole wall conditions made in that borehole led to the decision to advance boreholes RF#14 to RF#29 using other methods (rotary wash and diamond core barrel). These same conditions may have had some impact on the suspension seismic measurements and so are summarized here.



DTN: MO0205SWDQRTWF.000

NOTE: Method based on Quarter-Wavelength Amplification Ratio (Joyner, et. al. 1981, pp. 1346-1347, Brown 1998, pp. 41-42)

Figure 234. Amplification Ratio Comparing Shear-Wave Velocity from Downhole and Suspension Logging Surveys

A downhole video camera was used to record borehole conditions after the borehole had been advanced to a depth of approximately 185 feet bgs (YMP 1998). The recording made in the portion of the boring below the surface casing (i.e., from 95 to 185 feet bgs) showed an enlarged hole immediately below the surface casing (from approximately 95 to 97 feet bgs) of as much as three to four times the 6¼-inch nominal drill bit diameter and is consistent with an observed abnormally high grout volume used in that interval to backfill the annular space between the casing and borehole wall. Additional zones of erosion were observed from 118 to 121, 134 to 159, 166 to 173, and 184 to 185 feet bgs. Much of the borehole wall did not appear to have a smooth surface; rather, coarse particles (gravel?) could be observed protruding out of the borehole wall. These observations were key to the decision to advance later boreholes using water as the drilling fluid.

As mentioned above, the video log was made when the borehole had been advanced to a depth of approximately 185 feet bgs. After the video log was made, the borehole was advanced to a total depth of 350 feet bgs. In view of the nature of materials and operation, it is likely that additional erosion of the borehole walls occurred in the interval that was video-logged after the video logging had been completed. Erosion may also have occurred below a depth of 185 feet bgs, but there is no video log of this deeper interval.

Because of the enlargement of the borehole due to erosion by compressed air, when the PVC casing was grouted in place for use in taking downhole seismic and suspension seismic measurements, either a larger annulus of grout was created or voids were left between the casing and the surrounding tuff, or both. Either of these possible conditions can affect the suspension seismic measurements at the borehole, but should have little effect on the downhole seismic or SASW measurements.

The suspension seismic method measures the waves that travel from the source through the material in close proximity to the borehole wall to the two closely spaced receivers (Figure 29). Under normal conditions, the grout annulus surrounding the casing is too thin to act as a wave carrier that affects the velocities. However, if the grout annulus is sufficiently large, the waves may be transmitted through grout, which may have a higher or lower shear-wave velocity than the native bedrock, in which case the observed arrival time would not be correct. The grout used to fill the annulus around the casing likely had a higher shear-wave velocity than the material at the borehole site above about 245 feet bgs.

A suspension seismic measurement is more affected than a downhole seismic measurement by the thickness of the grout-filled annulus between the casing and the borehole wall. Because of the close spacing of suspension receivers, the measured shear wave necessarily travels parallel to and relatively close to the boring. Depending on the wavelength, a thin grouted zone should be transparent to the shear waves. However, thicker grout zones could act as wave-guides, resulting in the measurement of the shear-wave velocity of the grout rather than that of the rock. Downhole measurements are not as affected by the thicker grout zones because most of the waves' travelpaths before arriving at the receiver is within the in-situ subsurface material.

Figure VII-1 indicates that the suspension shear-wave velocity profile in borehole RF#13 generally agrees with the downhole shear-wave velocity profile, except for the interval between about 100 feet and 140 feet bgs, approximately corresponding to the tuff unit "x" (Tpki). The

difference at this interval is likely due to the effects of erosion of the borehole walls (by the compressed air used to lift drill cuttings from the borehole) on the suspension seismic measurements.

As expected, the suspension shear-wave interval velocities plotted on Figure VII-1 indicate considerably more variation than does the downhole profile due to the shorter suspension sampling length (1 meter). For the purposes of ground motion analysis, these localized variations from the trend value do not appear to be significant. Based on the average suspension velocities derived from the accumulated time curve and shown on Figure VII-1, the suspension average velocities are about 10 to 15 percent greater than the downhole velocities to about 250 feet bgs. However, the suspension shear-wave interval velocities are clearly higher than the downhole average velocity between about 100 and 140 feet, where the downhole seismic is judged to better reflect the shear-wave velocity of the rock materials. Below about 250 feet bgs the receiver-to-receiver average shear-wave velocity (v_{SRR}) agrees well with the shear-wave velocity profiles from the 1998 and 2000-1 downhole surveys, while the shear-wave velocity from the 2000-2 downhole survey is about 10 percent higher than the v_{SRR} . The SASW-1 profile agrees well with the downhole seismic surveys and the suspension seismic survey at shallow depths, but yields a much higher velocity below 69 feet bgs.

Figure VIII-1 shows that the downhole shear-wave travel times from the 2000-1 survey are unchanged from 265 to 275 feet and increase at an abnormally low rate from 275 to 290 feet. The downhole travel times appear to indicate that the travel path in the downhole survey is not a simple straight line path from source to receiver; thus, the suspension and downhole methods may be measuring the velocities of different rock, which could explain why the velocities are somewhat different. Figure VIII-1 indicates remarkable agreement between the three downhole v_p surveys, both in general and in detail. Of the three v_s surveys, the 1998 and 2000-1 surveys agree well except between 265 and 315 feet, where the 2000-1 data show some unusual travel times, which differ from the 1998 survey. The 2000-2 v_s survey shows faster travel times than the 1998 and 2000-1 v_s surveys, but agrees very well with the suspension v_s survey down to about 215 feet. At that depth, the 2000-2 downhole v_s survey shows an unusual decrease in travel time and, below that depth, shows a value of v_s that is almost identical to the velocity interpreted below 246 feet in the 1998 survey.

At borehole RF#14 (Figure VII-2), the suspension v_s are somewhat higher than the v_{sdh} to a depth of about 305 feet. Below that depth, a single average value of v_{sdh} was interpreted, while the suspension survey indicates the existence of four source-to-receiver and five receiver-to-receiver intervals of vastly different v_s . As shown on Figure VIII-2, the downhole shear-wave travel times are unusual from about 335 to 340 feet bgs. Two values of travel time were interpreted at depths of 335 and 340 feet, and a gap of 13 ms separates the record above and below 335/340 feet (Section 6.2.5). Because this gap was ignored in developing the downhole v_s profile, the suspension profile agrees better with the downhole profile than with the actual downhole data.

Figure VIII-17a shows that the average v_s from the downhole and suspension methods does not agree very well above 380 feet bgs in borehole RF#14, but the two methods agree well below 380 feet. This figure also shows that the average v_s from the downhole profile agrees well with

the actual downhole travel times down to 335 feet, but poorly below that depth. This finding was expected due to the unusual offset in the travel times discussed above.

Figure VIII-17b shows that the amplification expected at borehole RF#14 from the suspension profile is less than or approximately the same as the amplification expected from the downhole profile. Also, the amplification expected from the actual downhole travel times is greater than the amplification expected from the downhole profile at low frequencies.

Figure VII-18 shows that the v_{pRR} , v_{pSR} at borehole RF#14 are higher than v_{pdh} from about 50 to 220 feet and from about 440 to 520 feet, and are somewhat lower from about 220 to 330 feet and from 380 to 420 feet. However, a major difference in the v_{pSR} and the v_{pdh} values occurs between about 332 and 381 feet, where the suspension data indicates a major reduction in the v_{pSR} in the Tiva Canyon Tuff crystal-poor upper lithophysal zone (Tpcpul) unit. Sheet 3 of the log of borehole RF#14 (Attachment I) indicates that there are zones of nonwelded fracture fill from 334 to 359 feet and from 369 to 395 feet; these zones are described as reworked and variously bedded clay/silt sized tuffaceous material. Based on this description, the material traversed by the borehole is more of a soil than a rock; consequently, it is expected that the velocity would be lower compared to depth intervals where competent Tpcpul was encountered. However, this does not imply that the downhole data needs to be reinterpreted because the seismic waves undoubtedly reached the geophone emplacement by traveling a nonlinear path through solid rock over most of their path and only briefly crossing through the fracture fill. The suspension seismic waves, on the other hand, travel a relatively short distance from source to receivers and have less potential for “straying” from the material immediately adjacent to the borehole walls.

At borehole RF#15 (Figure VII-3), the suspension v_s are somewhat higher than the v_{sdh} . Figure VIII-18a shows that the average v_s from the suspension survey is greater than that from the downhole profile at all depths, while the average v_s from nearby SASW survey 10+37 is greater than that from the downhole profile at depths greater than about 45 feet, but less at shallower depths. As a result, the amplification expected from the SASW profile is greater than that expected from the downhole profile at frequencies greater than about 11 Hz, and less at smaller frequencies (Figure VIII-18b).

Figure VII-19 shows that the v_{pRR} and v_{pSR} at borehole RF#15 are higher than the v_{pdh} to a depth of about 133 feet and are somewhat lower below that depth.

At borehole RF#16 (Figure VII-4), the suspension v_s are somewhat higher than the v_{sdh} to a depth of about 376 feet. Below that depth, the downhole travel times exhibit a marked increase in slope (Figure VIII-4), indicating a higher shear-wave velocity, whereas the suspension travel times show little change in trend. The trend of compression-wave travel times below 376 feet is about the same as above 376 feet for both suspension and downhole surveys (Figure VIII-4). The v_p/v_s ratio from the downhole interpretation implies that Poisson's ratio is near zero. Below 376 feet, the suspension interpretation appears more credible than the downhole interpretation. The suspension v_p are somewhat higher than the v_{pdh} .

Figure VIII-19a shows that the average v_s from the suspension survey in borehole RF#16 is greater than that from the downhole profile at depths greater than about 110 feet. The

amplification expected from the suspension profile is somewhat less than that expected from the downhole profile (Figure VIII-19b).

Figure VII-20 shows that the v_{pRR} and v_{pSR} at borehole RF#16 are higher than the v_{pdh} from about 30 to 280 feet bgs, are nearly identical from about 280 to 376 feet bgs and are significantly lower below about 376 feet bgs. As shown on Figure VII-36, the Poisson's ratio from the downhole interpretation is only about 0.02 below a depth of about 376 feet, while the Poisson's ratio values from the suspension survey have values of about 0.25 to 0.28, which are more typical for the rock at the site.

At borehole RF#17 (Figure VII-5), the suspension and downhole v_s agree well at all depths. Figure VIII-20a shows that the average v_s values from the suspension survey are nearly identical to those from the downhole profile and, as a result, the amplification ratio is nearly equal to one (Figure VIII-20b). The average v_s values from nearby SASW survey 34+36 are quite different from the downhole and suspension profiles at all depths. As a result, the amplification expected from the SASW profile is less than that expected from the downhole profile at frequencies above approximately 4.7 Hz and greater at lower frequencies (Figure VIII-19b).

Figure VII-21 shows that v_{pSR} at borehole RF#17 are higher than v_{pdh} from about 55 to 400 feet bgs, though only slightly so from about 100 to 280 feet bgs. The v_{pSR} and v_{pdh} are nearly identical from about 400 to 500 feet bgs. From about 500 to 620 feet bgs, v_{pdh} are higher than v_{pSR} , though only slightly so below about 560 feet.

At borehole RF#18 (Figure VII-6), the suspension and downhole v_s agree well except from 170 to 220 feet and below 350 feet. In the interval from 170 to 220 feet the layer of lower v_s rock detected in the suspension survey was not interpreted from the downhole data. Below 350 feet the suspension interval v_s (Figure VII-6) is highly variable, as are the downhole travel times (Figure VIII-6). The shear-wave travel times on Figure VIII-6 indicate better agreement between the downhole and suspension than does Figure VII-6. The average v_s shown on Figure VIII-21a indicates excellent agreement above about 170 feet bgs, and fair agreement below that. The amplification ratio (Figure VIII-21b) is close to unity. If Figure VIII-21b were based on the actual downhole travel times rather than the downhole profile, the agreement would likely be even better. At this borehole, the basic data agrees very well, but the profiles have been developed somewhat differently, and accentuate differences.

As for the compression wave data in borehole RF#18, Figure VIII-6 indicates that the compression-wave travel time in the downhole survey becomes progressively greater than that in the suspension survey. This is reflected on Figure VII-22 by v_{pSR} that are significantly higher than v_{pdh} .

At borehole RF#19 (Figure VII-7), the suspension and downhole v_s agree well at all depths. The downhole v_s is somewhat less than the suspension v_s from about 105 to 282 feet, but is somewhat greater from about 282 to 550 feet. This leads to the divergence in the average v_s curves on Figure VIII-22a between about 130 and 575 feet. However, the amplification ratio is close to unity.

The average v_s values from nearby SASW survey 34+36 are quite different from the downhole profile at borehole RF#19 at depths above about 210 feet, though they agree well below that depth. As a result, the amplification expected from the SASW profile is less than that expected from the downhole profile at frequencies above approximately 3 Hz and is about the same at lower frequencies (Figure VIII-22b).

As for the compression wave data at borehole RF#19, Figure VIII-7 indicates that the compression-wave travel time in the downhole survey becomes progressively greater than that in the suspension survey. This is reflected on Figure VII-23 by v_{pSR} that are somewhat to significantly higher than v_{pdh} at all depths below about 95 feet.

At borehole RF#20 (Figure VII-8), the suspension v_s are about 10 to 20 percent higher than the v_{sdh} .

As for the compression wave data at borehole RF#20, Figure VIII-8 indicates that the compression-wave travel time in the downhole survey becomes progressively greater than that in the suspension survey. This is reflected on Figure VII-24 by v_{pSR} that are somewhat higher than v_{pdh} at all depths.

At borehole RF#21 (Figure VII-9), the suspension and downhole v_s agree well at all depths except from about 84 to 118 feet. Between 90 and 110 feet, the downhole shear-wave travel times (Figure VIII-9) form an unusual pattern that make the downhole difficult to interpret. The same pattern does not repeat itself in the downhole compression-wave travel times. Thus, in the interval from 84 to 118 feet, the suspension interpretation appears more credible than the downhole interpretation.

Figure VII-25 shows that v_{pSR} at borehole RF#21 are higher than v_{pdh} from about 20 to 91 feet. The v_{pSR} and v_{pdh} are nearly identical from about 91 to 116 feet bgs and from about 120 to 183 feet bgs.

At borehole RF#22 (Figure VII-10), the suspension and downhole v_s agree well at all depths where data are available for both methods. Figures VIII-10 and VII-26 indicate that the v_{pSR} at borehole RF#21 are somewhat higher than v_{pdh} .

At borehole RF#23 (Figure VII-11), the suspension v_s are about 30 percent lower than the v_{sdh} from 20 to about 54 feet bgs, and about 20 higher from 120 to 150 feet. The methods agree well from 9 to 21 feet and from 70 to 110 feet bgs. Some of the discrepancy between the methods can be explained by the differences in layer interface depths that the investigators selected as part of their interpretation.

Figure VIII-11 indicates that the suspension and downhole compression-wave travel times at borehole RF#23 are fairly similar down to about 120 feet and below 120 feet the suspension travel times are faster than the downhole travel times. However, an unusual time offset occurs in the downhole record between 12 and 15 feet bgs. Figure VII-27 does not appear to reflect the similarities in travel times above about 70 feet bgs, probably due to differences in where the velocity layers were picked by the different investigators. This is probably also due in part to the time jump in the downhole travel times that occurs between the measurements at 12 and 15 feet bgs.

At borehole RF#24 (Figure VII-12), the suspension v_s are generally higher than (often near double) the v_{sdh} at all depths where suspension data is available. The suspension interval velocities indicate that v_s is highly variable from 25 feet to 260 feet, while the downhole travel times on Figure VIII-12 indicate that v_s is relatively uniform in this interval, though there is significant scatter about the trendline. The downhole and suspension shear-wave travel times on Figure VIII-12 diverge markedly while the compression wave travel times agree rather well.

Figure VIII-12 indicates that the suspension and downhole compression wave travel times at borehole RF#24 are fairly similar overall, but that the suspension times exhibit more variation from a constant slope (constant velocity). Figure VII-28 reflects this situation in that a single downhole velocity has been assigned to the rock below about 30 feet bgs, while several layer velocities have been assigned to the suspension results.

At borehole RF#25 (Figure VII-13), the suspension and downhole v_s agree well at all depths where data is available for both methods. Figures VIII-13 and VII-29 indicate that the v_{pdh} are generally higher than the v_{pSR} and v_{pRR} .

At borehole RF#26 (Figure VII-14), the suspension and downhole v_s agree well at all depths where data is available for both methods, though there is some variation in selection of the number of velocity layers and thus in layer interface depths.

Figure VIII-14 indicates that the suspension and downhole compression-wave travel times at borehole RF#26 are fairly similar overall. Figure VII-30 reflects this situation in that the v_{pdh} are sometimes higher and sometimes lower than the v_{pSR} and v_{pRR} .

At borehole RF#28 (Figure VII-15), the suspension and downhole v_s are difficult to compare due to differences in layer interface depths. The shear-wave travel times on Figure VIII-15 suggest that the two sets of data agree well. As for the v_p , a meaningful comparison on Figure VII-31 is hampered by the differences in velocity-layer boundaries. The small divergence in the compression-wave travel times on Figure VIII-15 indicates that the v_{pSR} and v_{pRR} are slightly higher than the v_{pdh} .

At borehole RF#29 (Figure VII-16), the suspension and downhole v_s agree well except from about 120 to 138 feet bgs, although v_{sSR} and v_{sRR} are about 10 percent higher than the v_{sdh} from about 138 to 230 feet bgs. The downhole shear-wave travel times shown on Figure VIII-16 are somewhat nonlinear from about 105 to 130 feet, making it possible to make alternative interpretations, which might yield better agreement between the downhole and the suspension v_s in the interval from 120 to 138 feet. The downhole shear-wave travel times on Figure VIII-16 show some unusual travel time changes from about 340 feet to the measurement at 405 feet, which coincide with a “cycle” of extreme variation of the suspension seismic shear-wave interval velocities over the same depth interval, as shown on Figure VII-16.

Figure VIII-16 indicates that the shear-wave travel times for the downhole and suspension surveys agree well, while Figure VIII-23a indicates that the average v_s for both methods are fairly close at all depths. As a result, the amplification ratio is close to unity (Figure VIII-23b).

The steady and significant divergence in the compression-wave travel times on Figure VIII-16 indicates that the v_{pSR} are higher than the v_{pdh} at borehole RF#29. This is reflected on

Figure VII-32 by higher v_{pSR} than v_{pDH} at all depths except from about 75 to 127 feet bgs, where the difference is only slight.

The agreement between downhole and suspension results at individual boreholes is sometimes very good and sometimes only fair. The reasons for this variable agreement can probably be attributed to geologic conditions, although a detailed analysis of the correlation of velocity to geologic conditions has not been undertaken. Some of the geologic factors that may be influential include:

- As discussed in Section 6.2.2, several zones of “fracture fill material” were identified in some of the cored boreholes. These fractures are believed to be vertical and have been infilled with detrital volcanic material consisting primarily of clay and fine-grained sediment. Due to the short measurement interval and the limited potential for refraction, in the suspension method, the typically low density, non-cemented clayey fill could result in spurious suspension velocity values in what is otherwise high-velocity rock. The velocities from the downhole and SASW methods, which involve much longer travel paths and have much greater potential for refraction, would not be greatly affected by the fractures.
- As discussed in Section 6.2.2, the densely welded pyroclastic flows of Yucca Mountain contain zones within the flows that are characterized by having an abundance of lithophysae. Lithophysal zones occur where vapor concentrates in the densely welded part of ignimbrites to form lithophysal cavities. The WHB drilling encountered the upper and lower lithophysal zone of the Tiva Canyon Tuff (Tpcpul and Tpcpll respectively). As noted, grout can fill in these voids during casing installation. The grout may have greater or lesser velocity than the surrounding rock. Due to the short measurement interval and the limited potential for refraction, in the suspension method, the grout-filled voids could result in spurious suspension velocity values. The velocities from the downhole and SASW methods, which involve much longer travel paths and have much greater potential for refraction, would not be greatly affected by the grout-filled voids located only adjacent to the borehole.

It can also be observed that some of the differences in velocities obtained from the different methods could be reduced by considering alternative interpretations, that is, selecting different layer boundaries than have been reported here in recognition of what information can be obtained by considering information external to that furnished by the individual seismic method alone.

6.8 PREVIOUS DATA

6.8.1 Overview

In addition to previously acquired data discussed above (mainly related to borehole RF#13 and general geologic data), there are additional geotechnical data that may be useful to the current objectives. These include the results of qualified geotechnical laboratory tests performed on core specimens from boreholes UE-25 NRG#2, UE-25 NRG#2a, UE-25 NRG#2b, UE-25 NRG#3,

USW NRG-6, USW NRG-7/7a, USW SD-9 and USW SD-12¹⁵ (discussed in Section 6.8.2) and a few in-place and laboratory measurements of the density of alluvium (discussed in Section 6.8.3).

6.8.2 Previous Geotechnical Testing on Core Samples

CRWMS M&O (1997, Section 5.1) presented a statistical summary of physical and mechanical properties of bedrock for the YMP. A similar analysis was performed for this scientific analysis because (1) some of the lithostratigraphic contacts changed since the previous analysis was performed, (2) the previous statistical summary had no data tracking number associated with it, and (3) the details of statistical analysis could not be traced to source information.

Table 33 summarizes the depth at which the tops of the lithostratigraphic zones or subzones of interest were encountered in boreholes NRG#2, NRG#2a, NRG#2b, NRG#3, NRG-6, NRG-7a, SD-9 and SD-12. Only Tpbt4 and younger units have been considered because the older units are located at depths beyond those investigated for this report.

Table 34 summarizes statistical values of dry density, saturated density, particle density and porosity derived from the laboratory data in DTNs: SNL01A05059301.005 and SNL02030193001.001 through SNL02030193001.027, excluding SNL02030193001.025 (superseded). The total densities and water contents of the specimens were not measured and are unknown. The porosity values represent the total porosity, n , defined by:

$$n = \frac{\rho_s - \rho_d}{\rho_s} \quad (\text{Eq. 43})$$

where: ρ_s = grain density (i.e., the density of the solid particles in the soil or rock mass)
 ρ_d = dry density.

Table 35 shows values of porosity, void ratio, and saturation water content that were calculated from the mean values of specific gravity and dry density values in Table 34. Void ratio equals the ratio of the porosity to the quantity one minus the porosity. Saturation water content is the water content when the rock is saturated, which equals the ratio of the void ratio to the specific gravity. Note that the values of porosity computed from the mean values are slightly different than the mean of the reported porosity values given in Table 34. This may be due to not having a particle density value for every dry density value.

The magnitude of the saturation water content, as well as the difference between the values of dry density and saturated density, indicates that a wide range of values of total density is possible for tuff unit “x” (Tpki), the bedded tuffs (Tmbt1 and Tpbt4), and the nonwelded to partially welded Tpcpv1 subzone. The smaller values of saturation water content for the welded zones of the Tiva Canyon Tuff bedrock limit the range of possible values for water content and total density.

¹⁵ These boreholes will be referred to herein by the abbreviated designations NRG#2, NRG#2a, NRG#2b, NRG#3, NRG-6, NRG-7, SD-9 and SD-12.

DTN: MO9905LABDYNRS.000 reports water content measurements on three specimens of unwelded tuff (Tpki) acquired in borehole RF#13 between 138.3- and 142.0-foot depth; the values range from 3.0 to 3.2 percent (Table 36). Water content measurements on three specimens of welded tuff (Tpcpmn) acquired in borehole RF#13 between 254.6- and 257.3-foot depth

Table 33. Depths in Feet to Tops of Selected Lithostratigraphic Units by Borehole

Lithostratigraphic unit ⁽¹⁾	Symbol	UE-25 NRG#2	UE-25 NRG#2a	UE-25 NRG#2b	UE-25 NRG#3	USW NRG-6	USW NRG-7a	USW SD-9	USW SD-12
Not described	--						0.0	0.0	0.0
alluvium/ colluvium	Qal		0.0	0.0					
Rainier Mesa Tuff	Tmr	0.0		2.2					
pre-Rainier Mesa Tuff bedded tuff	Tmbt1	138.6		119.4					
Tuff unit "x"	Tpki	⁽²⁾	80.6	157.3					
Post-Tiva Canyon Tuff bedded tuff	Tpbt5		151.0	⁽³⁾					
Tiva Canyon Tuff crystal rich, vitric, non to partially welded	Tpcrv3		165.9						
Tiva Canyon Tuff crystal rich vitric, moderately welded subzone	Tpcrv2		168.0						
Tiva Canyon Tuff crystal rich, vitric, vitrophyre subzone	Tpcrv1		170.2						
Tiva Canyon Tuff crystal rich, nonlithophysal	Tpcrn		172.0		0.0				
Tiva Canyon Tuff crystal poor upper lithophysal	Tpcpul		261.5		100.0				
Tiva Canyon Tuff crystal poor middle nonlithophysal	Tpcpmn				206.7				5.3
Tiva Canyon Tuff crystal poor lower lithophysal	Tpcpll				268.2	0.0			93.4
Tiva Canyon Tuff crystal poor lower nonlithophysal	Tpcpln	169.8				55.0	17.0	53.6	129.5
Tiva Canyon Tuff, crystal-poor vitric densely welded subzone	Tpcpv3								
Tiva Canyon Tuff crystal-poor vitric moderately welded subzone	Tpcpv2	276.3				135.3	69.7	57.2	239.5
Tiva Canyon Tuff crystal-poor vitric nonwelded to partially welded subzone	Tpcpv1	282.8				151.8	79.2	76.5	256.0
pre-Tiva Canyon Tuff bedded tuff	Tpbt4			265.2		158.6	102.0	91.5	263.7
Total depth of borehole, if borehole terminated above the top of Tpbt4		294	265.7		330.0				

DTNs: GS941108314211.052 for SD-9, GS940908314211.045 for SD-12, GS940708314211.032 for NRG-7a, and GS940308314211.009 for the other boreholes

Notes:

- (1) Units older than Tpbt4 are not shown.
- (2) Bow Ridge Fault Zone penetrated from 164.6-169.8 ft in NRG#2.
- (3) Bow Ridge Fault Zone penetrated from 232.3-265.2 (?) ft in NRG#2b. No Tiva Canyon Tuff below 232.3 ft.
- (4) Shading in cells indicates that the zone was not encountered.

INTENTIONALLY LEFT BLANK

Table 34. Statistics by Lithostratigraphic Unit

Properties	Statistic	Lithostratigraphic Unit													
		Tmr	Tmbt1	Tpki	Tpb15	Tpcrv3	Tpcrn	Tpcpul	Tpcpmm	Tpcpl1	Tpcplh	Tpcpv2	Tpcpv1	Tpb14	
Saturated Density (lbm/ft ³)	Count	NRG#2													
		NRG#2a			13		19								
		NRG#2b	8												
		NRG#3					14	9	18	4					
		NRG#6								19	11	4	1		
		NRG#7									14	5	5	2	
		SD-9											1		
		SD-12										9	1	2	
		All	8		13		33	9	22	23	150.1	51	10	7	4
		NRG#2													
		NRG#2a			103.5		131.4								
		NRG#2b	109.0							144.8	146.2	118.8	110.5		
		NRG#3					134.3	139.5	147.4	149.8	146.0	122.7	112.0	95.5	
NRG#6											111.7				
NRG#7															
SD-9															
SD-12															
All	109.0		103.5		132.6	139.5	147.3	149.0	148.2	121.6	111.7	103.6			
Coefficient of Variation	Coefficient of Variation	NRG#2													
		NRG#2a			3.25		5.69								
		NRG#2b	3.58												
		NRG#3					4.74	2.76	1.67	3.71	1.71	6.13			
		NRG#6								0.95	2.87	3.05	2.29		
		NRG#7									0.62	0.62	6.05		
		SD-9											1.93		
		SD-12												9.96	
		All	3.58		3.25		5.33	2.76	1.52	2.06	2.18	4.62	1.93	9.96	
		NRG#2													
		NRG#2a		3											
		NRG#2b	10		13		19								
		NRG#3					14	9	18	4					
NRG#6								19	12	4	2	4			
NRG#7									14	6	6	2			
All	10		13		33	9	18	23	43	10	8	6			
NRG#2															
NRG#2a		104.9													
NRG#2b	83.3		76.3		115.8										
NRG#3					120.6	131.1	142.3	139.2							
NRG#6								146.5	140.9	101.1	82.7	80.5			
NRG#7									140.0	105.7	86.6	62.9			
All	83.3	104.9	76.3		117.8	131.1	142.3	145.2	142.7	103.8	85.6	74.7			
NRG#2		3.36							0.62						
NRG#2a			5.80		11.67										
NRG#2b	7.88														
NRG#3					9.01	3.69	2.62	4.25							
NRG#6								1.36	2.84	14.18	1.60	18.40			
NRG#7									4.82	5.33	3.54	0.42			
All	7.88	3.36	5.80		10.61	3.69	2.62	2.76	3.61	9.22	3.73	19.65			

Table 35. Porosity, Void Ratio, and Saturation Water Content by Lithostratigraphic Unit

Lithostratigraphic Unit	Saturated Density, lbs/ft ³	Dry Density, lbs/ft ³	Particle Density, lbs/ft ³	Porosity %	Porosity *	Void Ratio *	Saturation Water Content *, %
Tmr	109.0	83.3	145.9	42.9	42.9	75.2	51.5
Tmbt1	-	104.9	152.5	31.3	31.2	45.4	29.8
Tpki	103.5	76.3	145.6	47.4	47.6	90.8	62.4
Tpbt5	-	-	149.3	45.6	-	-	-
Tpcrv3	-	-	149.4	30.8	-	-	-
Tpcrn	132.6	117.8	159.8	26.2	26.3	35.6	22.3
Tpcpul	139.5	131.1	157.2	16.5	16.6	19.9	12.6
Tpcpmn	147.3	142.3	155.5	9.2	8.5	9.2	5.9
Tpcpll	149.0	145.2	156.1	6.9	7.0	7.5	4.8
Tpcpln	148.2	142.7	156.7	9.1	8.9	9.8	6.3
Tpcpv2	121.6	103.8	152.3	31.8	31.8	46.7	30.6
Tpcpv1	111.7	85.6	146.9	39.8	41.7	71.5	48.7
Tpbt4	103.6	74.7	150.4	49.0	50.4	101.5	67.5

DTN: MO0204SEPSOILP.000

* Porosity, n, in percent may be calculated using $n = 100(1 - \gamma_d / \gamma_s)$, where γ_d and γ_s are the mean values of dry density and particle density in Table 34, respectively. Void ratio, e, in percent may be calculated using $e = 100(\gamma_s / \gamma_d - 1)$. Saturation water content, w_{sat} , may be calculated as $w_{sat} = (e / G)$, where G is the specific gravity. Specific gravity equals the particle density divided by the density of water (62.427961 lbm/ft³, density of water under standard conditions was used).

Table 36. Moist and Dry Density Results for Borehole RF#13

Depth feet	Lithostratigraphic Unit	Total Density		Water Content, %	Dry Density	
		lbs/ft ³	g/cm ³		lbs/ft ³	g/cm ³
138.3	tuff unit "x" (Tpki)	80.1	1.28	3.0	77.8	1.25
141.5		79.9	1.28	3.2	77.4	1.24
142.0		79.9	1.28	3.0	77.6	1.24
254.6	middle nonlithophysal zone of the crystal-poor member of the Tiva Canyon Tuff (Tpcpmn)	144.6	2.316	0.5	143.9	2.305
255.5		148.1	2.372	0.4	147.5	2.363
257.3		147.8	2.368	0.5	147.1	2.356

DTN: MO9905LABDYNRS.000. Values given in source in *Système International* units were converted to American units using $1 \text{ g/cm}^3 = 62.428 \text{ lbm/ft}^3$.

ranged from 0.4 to 0.5 percent (Table 36) (DTN: MO9905LABDYNRS.000). Unfortunately, the core samples were not stored using specific measures to maintain the field water content. Thus, these values of water content are likely less than the actual values, and the same would be true of the total density values. The same is true for the water content values in Tables 14 through 16.

Figure 235 compares the mean values of total density from the gamma-gamma surveys (Table 12) with those from the RCTS tests (Tables 14, 15, 16 and 36) and from previous laboratory measurements on NRG and SD borehole samples (Table 34). Although the RCTS samples may have lost some moisture, their mean total density exceeds that from the gamma-gamma measurements in the Tiva Canyon Tuff, but is less in the nonwelded tuff unit "x". The differences in the mean values are large in the Tpk1 and Tpcpul. However, the number of RCTS results (the "count" shown on Figure 235) is too low to provide a reliable mean value. The values of dry and saturated density from the previous NRG and SD boreholes are not directly comparable with the total density for the gamma-gamma or RCTS measurements. However, the total density of a material must be between its dry density and saturated density, so these values should bracket the total density values. However, this relationship seems to hold only for units Tpk1 and Tpcpmn. It does not seem to be the case for Tpcpl1 and Tpcpln, and the situation is marginal for Tpcrn and Tpcpul.

At this time, it is reasonable to use the standard deviation values for the dry density measurements in bedrock in Table 33 as an approximation of the variability of the bedrock units.

6.8.3 Alluvium

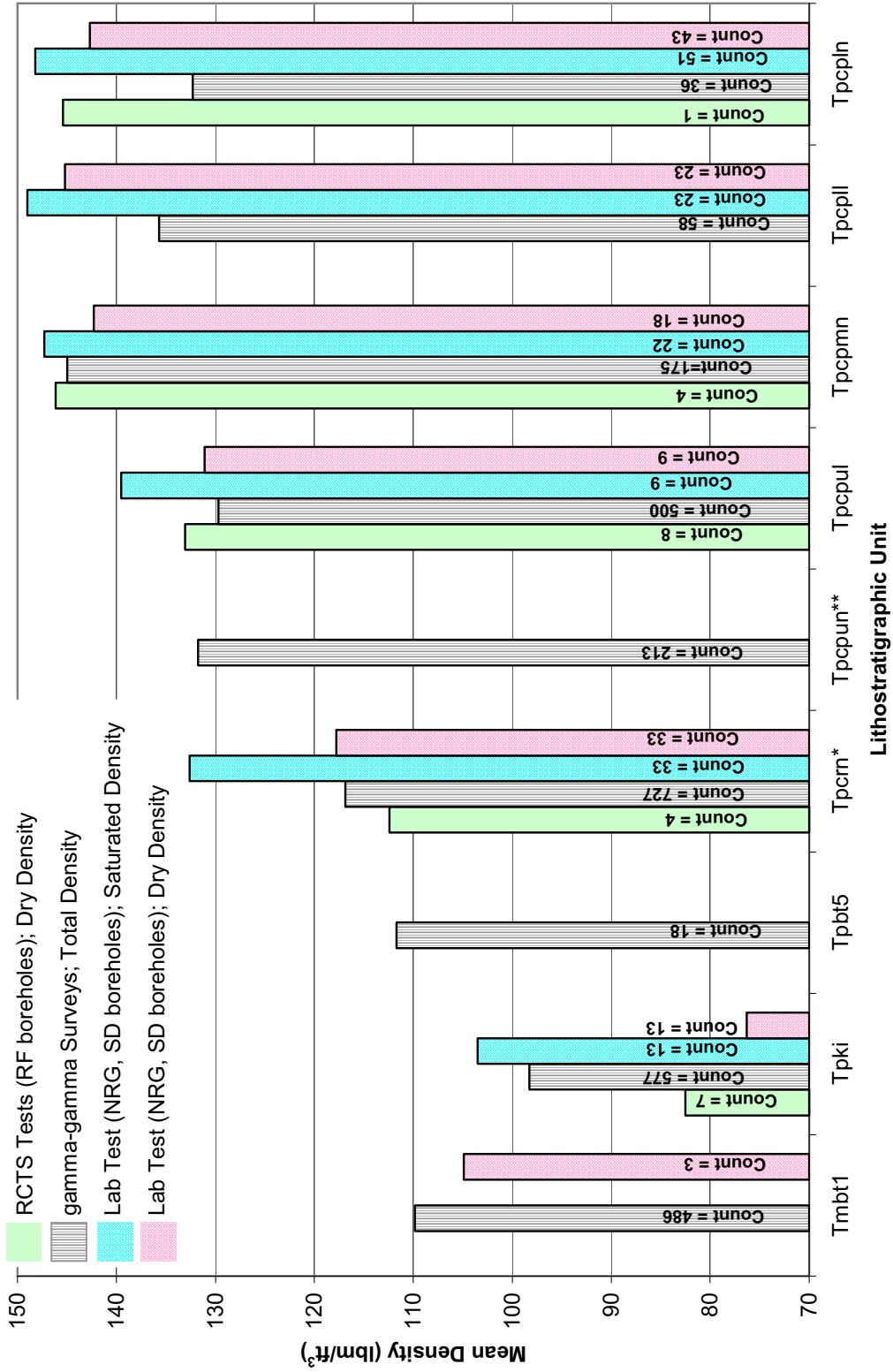
In addition to the in-place density tests performed in alluvium in test pits TP-WHB-1 through -4 (Section 6.2.4), a few other measurements of alluvium density have been made in-situ or in the laboratory by previous investigators. Density of the alluvium/colluvium in the WHB Area was measured by:

- Water replacement tests in alluvium/colluvium (QTac) encountered in some of the NRSF-TP series (also known as the NRG-TP series) of test pits (DTN: GS920983114220.001).
- Laboratory tests on drive-tube samples¹⁶ of alluvium/ colluvium (QTac) from borehole UE-25 RF#3b (DTN: SNSAND85081500.000, Table 3).¹⁷
- Sand-cone and nuclear tests¹⁸ in alluvium encountered in test pit SFS-3 (Ho et al. 1986, pp. 6, 7, 14, 22, and 54).

¹⁶ DTN: SNSAND85081500.000 does not state the dimensions of the drive tube sampler and other details.

¹⁷ One problem with the data should be noted. For the sample from a depth of 22.0 feet, the various values reported in Table 3 of DTN: SNSAND85081500.000 are inconsistent. Based on a review of the data, it appears that the reported values of total density and water content are correct, and the reported value of dry density is incorrect and should be 1.460 g/cm³ or 92.2 lbs/ft³. The reported porosity is also incorrect and should be 41.8 percent.

¹⁸ Ho et al. (1986) do not state the dimensions of the sand cone or the source penetration for the nuclear gage tests.



Note: * Tpcrn includes Tpcrv, Tpcrl and Tpcrm.
 ** Tpcpun is logged as a subunit in DTN: MO0101SEPBLOG.000

DTNs: MO0204DENBROCK.000,
 MO0202GEOSOLP.000, MO0204SEPGAMD.000

Figure 235. Comparison of Density from gamma-gamma Surveys, RCTS tests and Previous Laboratory Data

The test pit SFS-3 data reported by Ho et al. (1986) is ambiguous. Dry density and water content results are reported in three places (Ho et al. 1986, pages 14, 22 and 54). The measured total density is never reported. Unfortunately, the dry density is not measured directly, but is calculated using the total density and water content. The values of water content reported on page 22 differ from those reported on pages 14 and 54, although the values of dry density are the same in all cases, which would seem impossible because it implies that the total density (a measured quantity) changes depending on a quantity that is calculated from it. Two possible explanations are: (1) transcription errors were made at some time, or (2) the water content was measured by two different methods. Assuming the latter as the more likely case, it is not known which of the two values was used to compute the dry density, which makes it impossible to know how to compute the total density, which, as mentioned above, is not reported in Ho et al. (1986). For this report, the values on page 14 were arbitrarily used to calculate total density.

Figure 236 shows this previous data and, for comparison, the data presented in Sections 6.2.4 and 6.2.8.

The densities reported for the drive tube samples (DTN: SNSAND85081500.000, Table 3) appear to be significantly lower than the in-situ densities measured at similar depths. It is a common observation that the density of a dense granular material decreases significantly because of sampling, so the discrepancy between laboratory and in-situ densities is in line with expectations (see, for example, Marcuson 1978, p. 338). At best, the laboratory density values can be used as a guide to the trend of densities at depths greater than those at which in-situ tests were performed. Given the coarse nature of the alluvial/colluvial material, the water replacement tests should provide more reliable estimates of density than the sand-cone and nuclear tests because the former involves a much larger volume of material. In addition, the personnel performing the sand-cone and nuclear tests avoided testing coarser soil because of limitations in the methods they used (Ho et al. 1986, p. 6).

It should be emphasized that the number of density values is small, and the data quality is questionable in some cases (preferential sampling of finer-grained materials, driven samples). Consequently, significant variations from the recommended values are possible.

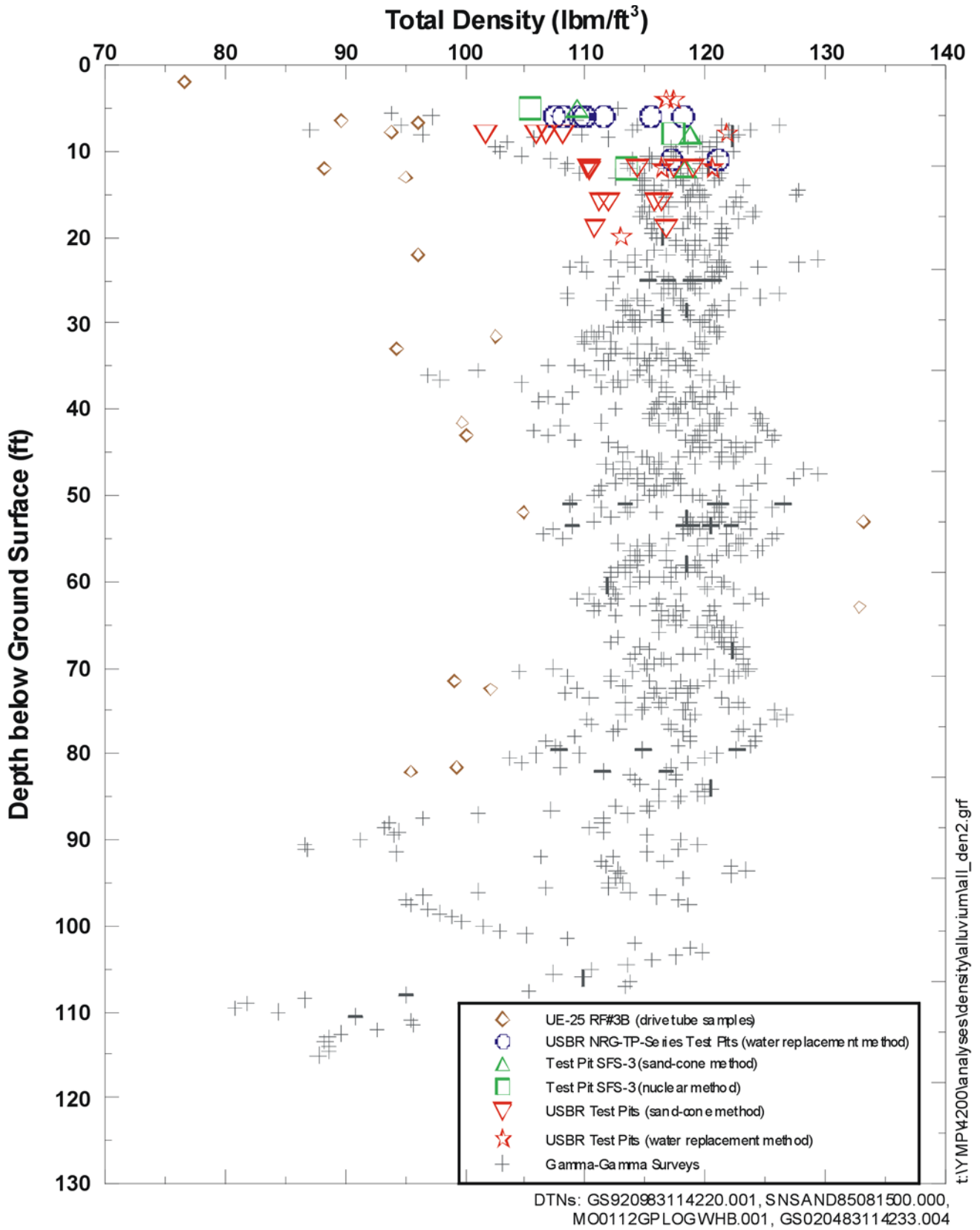


Figure 236. Total Density of Alluvium

7. CONCLUSION

This scientific analysis presents data that were acquired for use in preliminary geotechnical analyses for the WHB foundations and in the development of seismic design input ground motions for the WHB and the repository. The types of data considered herein are shear-wave velocity profile, compression-wave velocity profile, low-strain Poisson's ratio, low-strain shear modulus, modulus reduction, damping ratio, and total density. In addition, basic geotechnical data were acquired for borrow material that could potentially be used to construct an engineered fill pad at the WHB. The interpretations, findings, and recommendations in this scientific analysis supersede any conflicting interpretations, findings, and recommendations presented in CRWMS M&O (1999b).

7.1 SUMMARY

Field and geotechnical laboratory data are presented for three distinct geographic areas:

- The WHB Area
- The North Ramp and Main Drift of the ESF
- The crest of Yucca Mountain.

In addition, geotechnical laboratory data are presented for a composite sample of material from the Fran Ridge Borrow Area.

Data Acquired at the WHB Area

Section 6.2 summarizes the results of the explorations and tests performed in 2000 and 2001 in the WHB Area for the WHB and laboratory tests performed on samples from these explorations. The type of exploration or test and the scientific analysis section where the results are presented are as follows:

- 6.2.2 - Boreholes RF#14 through RF#29
- 6.2.3 - Revision of RF#13 borehole log
- 6.2.4 - Test pits TP-WHB-1 through TP-WHB-4
- 6.2.5 - Downhole seismic surveys in boreholes RF#13 through RF#29
- 6.2.6 - Suspension seismic surveys in boreholes RF#13 through RF#29
- 6.2.7 - SASW surveys SASW-1 through SASW-37 and D-12
- 6.2.8 - Borehole caliper and gamma-gamma in boreholes RF#16, RF#18, RF#20, RF#21, RF#22, RF#24, and RF#28
- 6.2.9 - Geotechnical laboratory static testing
- 6.2.10 - Geotechnical laboratory dynamic testing.

Data Acquired at the North Ramp and Main Drift of the ESF

Section 6.3 summarizes the results of geophysical surveys performed in 2001 along the Main Drift of the ESF and of laboratory tests performed on samples taken along the North Ramp. The type of exploration or test and the scientific analysis section where the results are presented are as follows:

- 6.3.2 - Shear-wave velocity profiles from SASW surveys T-1 to T-5.
- 6.3.3 - RCTS test results for samples of bedrock taken in the ESF North Ramp.

Data Acquired at the Crest of Yucca Mountain

Section 6.4 summarizes the results of the explorations and tests performed in 2000 and 2001 at or near the crest of Yucca Mountain. The type of exploration or test and the scientific analysis section where the results are presented are as follows:

- 6.4.2 - SASW surveys C-1 to C-7, S-1 to S-12, D-1 to D-11, and R-1 to R-3.
- 6.4.3 - Downhole seismic surveys using eight existing boreholes.

Data Acquired for Material from the Fran Ridge Borrow Area

Section 6.5 summarizes the results of geotechnical laboratory tests that were performed in 2000 and 2001 on a composite sample from the Fran Ridge Borrow Area. The type of tests and the scientific analysis section where the results are presented are as follows:

- 6.5.2 – Static tests.
- 6.5.3 – Dynamic tests.

The remainder of Section 6 presents analysis and discussions of the data as follows:

- 6.6 - Interpreted geologic conditions (stratigraphy, structure and groundwater) at the WHB Area.
- 6.7 - Evaluation of seismic velocity data for the WHB Area.
- 6.8 - Comparison with previous data.

7.2 RESTRICTIONS

The data in this report are valid for the specific sites investigated, i.e., the WHB Area shown on Figure 1, the emplacement area shown on Figure 157, and the Fran Ridge Borrow Area shown on Figure 213. The data in this report should be used only for the intended purposes, which were discussed in Section 1, and may not be adequate for other purposes.

7.3 UNCERTAINTIES AND LIMITATIONS

7.3.1 Sufficiency of Geotechnical Data for Fran Ridge Borrow Area

Currently, only four surface samples from the Fran Ridge Borrow Area have been taken, and only the composite of these four samples has been subjected to limited static and dynamic testing. Consequently, there is significant, high uncertainty concerning the materials in this borrow area and their geotechnical properties.

7.3.2 Sufficiency of Seismic Data for Emplacement Area

At the time that the data collection activities in this study were planned and conducted, the proposed emplacement area represented the base case repository layout that was evaluated as

part of site recommendation analyses (DOE 2001, Section 2.3.1.1). More recently, concepts regarding the repository layout have evolved, with the objectives of reducing uncertainties in a License Application and supporting a flexible design with respect to waste types and receipt. The current layout includes additional area to the east and north of the base case layout (Board et al. 2002, Figure 3-1). Thus, the velocity data collected to date does not sample some of these areas. Also, velocity surveys were limited in their depth penetration beneath the crest of Yucca Mountain. Measurements are lacking in the depth range from about 700 to 1000 feet bgs.

7.3.3 Sufficiency of Seismic Data in the WHB Area

With regards to the development of seismic design input ground motions, there are areas within the WHB Area where no velocity measurements have been made. In particular, there are areas outside of the existing pad in the northern part of the WHB Area where no surveys were performed based on environmental restrictions and the likelihood that all structures would be sited in the current pad/muck pile area. The lack of sampling can be adequately accounted for by incorporating a greater degree of variability in the velocity profiles used in the ground motion calculations. This would, however, result in more conservative design ground motions.

7.3.4 Accuracy of Contacts

Each of the lithostratigraphic units in the WHB area has distinctive characteristics that enable identification of the unit and the bounding contacts; therefore, there is very small uncertainty in the identification of lithostratigraphic units. The contacts are formed from depositional, welding, or crystallization processes and can be sharp or gradational. For gradational contacts, even though the features are gradational across 3 to 10 ft, the criteria for identification of the contact typically permits identification within a few feet. In boreholes with core, the accuracy of the contact is typically plus or minus 1 foot; however, where recovery of core is poor, the accuracy of contact identification is increased. In mud rotary boreholes, the accuracy is dependent on the sampling interval and the drilling and sampling techniques. In the WHB mud-rotary boreholes, the sampling interval is 5 ft and the minimum accuracy plus or minus 5 ft. Borehole geophysical logs and the trends in lithostratigraphic thickness can be used in many of the boreholes to help resolve the depth to lithostratigraphic contacts and minimize the uncertainty of the contact to the estimated accuracy of plus or minus 5 ft.

7.3.5 Strike and Dip of Bedding

The strike and dip of the stratigraphic beds were not directly measured in any of the qualified explorations in the WHB Area, but were calculated based on lithostratigraphic contact elevations in various boreholes in areas where it is thought that no fault disrupts the bedding (Section 6.6.2). Based on this approach, the bedding beneath the WHB Area appears to be northeast-striking and southeast-dipping, which is different than the orientation of bedding mapped on Exile Hill near the North Portal, where it tends to strike from N36°W to N8°W and dip from 14 to 22 degrees to the northeast. Therefore, the bedding on Exile Hill is, in general, north to northwest-striking and east to northeast-dipping. Because of the limited number of data sets that could be used to calculate the strike and dip, there is significant, high uncertainty concerning the distribution of strike and dip across the WHB Area. The absence of direct measurements of strike and dip and the discordance with measurements on nearby Exile Hill

introduce uncertainty in the structural interpretation (locations of faults) and the geologic cross sections.

7.3.6 Fault Locations

When the tops of stratigraphic units are connected between boreholes, there were often apparent discrepancies between calculated bedding dip and the dip anticipated on the basis of the assumed strike and dip of bedding. To account for this discrepancy, several faults have been interpreted as crisscrossing the WHB Area. In some cases, a point on the interpreted fault plane and the fault dip are known because the fault was observed in the borehole core; this helps constrain the potential location of the fault. In other cases, the fault was not directly observed, but is only inferred as being somewhere between boreholes. In addition, whenever faulting was invoked to explain an apparent stratigraphic offset, a single fault was introduced – however, multiple faults with lesser separation could also explain these situations. Thus, there is a moderate degree of uncertainty regarding the fault locations.

7.3.7 Dynamic Properties at High Shear Strain

The dynamic laboratory measurements of material properties were limited to strains of about 0.1% in this study because the emphasis was placed on the preclosure seismic design (hazard levels defined at annual exceedance probabilities of 10^{-3} and 10^{-4}). Consequently, data are lacking at higher strain levels, and the behavior at higher strain levels must be based on results published in the literature for other sites. Thus, there is a high degree of uncertainty regarding the dynamic material properties at high strain levels.

7.3.8 Uncertainty Concerning Borrow Area

At the time that this investigation was planned, exploration had been approved at only one potential borrow area for engineered fill material. Other potential borrow areas exist closer to the North Portal. If other borrow areas are considered, the data in this report for the Fran Ridge borrow area will not be pertinent.

8. INPUTS AND REFERENCES

8.1 DOCUMENTS CITED

Barr, D.L.; Moyer, T.C.; Singleton, W.L.; Albin, A.L.; Lung, R.C.; Lee, A.C.; Beason, S.C.; and Eatman, G.L.W. 1996. *Geology of the North Ramp — Stations 4+00 to 28+00, Exploratory Studies Facility, Yucca Mountain Project, Yucca Mountain, Nevada*. Denver, Colorado: U.S. Geological Survey. ACC: MOL.19970106.0496.

Beason, S.C.; Turlington, G.A.; Lung, R.C.; Eatman, G.L.W.; Ryter, D.; and Barr, D.L. 1996. *Geology of the North Ramp - Station 0+60 to 4+00, Exploratory Studies Facility, Yucca Mountain Project, Yucca Mountain, Nevada*. Denver, Colorado: U.S. Geological Survey. ACC: MOL.19970106.0449.

Blout, D.O.; Hammermeister, D.P.; Loskot, C.L.; and Chornack, M.P. 1994. *Geohydrologic Data Collected from Shallow Neutron-Access Boreholes and Resultant-Preliminary Geohydrologic Evaluations, Yucca Mountain Area, Nye County, Nevada*. Open-File Report 92-657. Denver, Colorado: U.S. Geologic Survey. ACC: NNA.19940228.0027.

Board, M.; Linden, A.; and Zhu, M. 2002. *Design Evolution Study-Underground Layout*. TDR-MGR-MG-000003 REV 00. Las Vegas, Nevada: Bechtel SAIC Company. ACC: MOL.20020429.0023.

Boore, D.M. and Brown, L.T. 1998. "Comparing Shear-Wave Velocity Profiles from Inversion of Surface-Wave Phase Velocities with Downhole Measurements: Systematic Differences Between the CXW Method and Downhole Measurements at Six USC Strong-Motion Sites." *Seismological Research Letters*, 69 (3), 222-229. El Cerrito, California: Seismological Society of America. TIC: 251417.

Brown, L.T. 1998. *Comparison of Vs Profiles from SASW and Borehole Measurements at Strong Motion Sites in Southern California*. Master's thesis. Austin, Texas: University of Texas, Austin. TIC: 251296.

Brown, L.T.; Boore, D.M.; and Stokoe, K.H., II. 2000. "Comparison of Shear-Wave Velocity Profiles from SASW and Downhole Seismic Tests at a Strong-Motion Site." Paper 2202 of *12WCEE 2000, 12th World Conference on Earthquake Engineering, Auckland, New Zealand, Sunday 30 January - Friday 4 February 2000*. Upper Hut, New Zealand: New Zealand Society for Earthquake Engineering. TIC: 251263.

BSC (Bechtel SAIC Company) 2001. *Technical Work Plan for: Testing and Monitoring*. TWP-MGR-MD-000018 REV 00. Las Vegas, Nevada: Bechtel SAIC Company. ACC: MOL.20011015.0022.

Buesch, D.C.; Dickerson, R.P.; Drake, R.M.; and Spengler, R.W. 1994. "Integrated Geology and Preliminary Cross Section Along the North Ramp of the Exploratory Studies Facility, Yucca Mountain." *High Level Radioactive Waste Management, Proceedings of the Fifth Annual International Conference, Las Vegas, Nevada, May 22-26, 1994*. 2, 1055-1065. La Grange Park, Illinois: American Nuclear Society. TIC: 210984.

- Buesch, D.C.; Spengler, R.W.; Moyer, T.C.; and Geslin, J.K. 1996. *Proposed Stratigraphic Nomenclature and Macroscopic Identification of Lithostratigraphic Units of the Paintbrush Group Exposed at Yucca Mountain, Nevada*. Open File Report 94-469. Denver, Colorado: U.S. Geological Survey. ACC: MOL.19970205.0061.
- Byers, F.M. Jr.; Carr, W.J.; Orkild, P.P.; Quinlivan, W.D.; and Sargent, K.A. 1976. *Volcanic Suites and Related Cauldrons of Timber Mountain-Oasis Valley Caldera Complex, Southern Nevada*. Professional Paper 919. Washington, D.C.: U.S. Geological Survey. TIC: 201146.
- Chen, A.T.F. and Stokoe, K.H., II. 1979. *Interpretation of Strain-Dependent Modulus and Damping from Torsional Soil Tests*. USGS-GD-79-002. Menlo Park, California: U.S. Geological Survey. TIC: 251943.
- Christiansen, R.L.; Lipman, P.W.; Carr, W.J.; Byers, F.M., Jr.; Orkild, P.P.; and Sargent, K.A. 1977. "The Timber Mountain-Oasis Valley Caldera Complex of Southern Nevada." *Geological Society of America Bulletin*, 88 (7), 943-959. [Boulder, Colorado]: Geological Society of America. TIC: 201802.
- Craig, R. 1997. "Completion of Milestone SPG391M4, Re-Evaluation of Subsurface Lithostratigraphic Contacts." E-mail from R. Craig to M. Tynan, October 1, 1997, with an attachment. ACC: MOL.19980513.0181; MOL.19980513.0182.
- CRWMS M&O 1997. *Yucca Mountain Site Geotechnical Report*. B00000000-01717-5705-00043 REV 01. Las Vegas, Nevada: CRWMS M&O. ACC: MOL.19980212.0354.
- CRWMS M&O 1999a. *Monitored Geologic Repository Site Layout System Description Document*. BCB000000-01717-1705-00007 REV 00. Two volumes. Las Vegas, Nevada: CRWMS M&O. ACC: MOL.19990512.0159.
- CRWMS M&O 1999b. *Preliminary Geotechnical Investigation for Waste Handling Building, Yucca Mountain Site Characterization Project*. BCB000000-01717-5705-00016 REV 00. Las Vegas, Nevada: CRWMS M&O. ACC: MOL.19990625.0182.
- Daley, T.M., Majer, E.L., and Karageorgi, E. 1994. *Combined Analysis of Surface Reflection Imaging and Vertical Seismic Profiling at Yucca Mountain, Nevada*. LBL-36467. Berkeley, California: Lawrence Berkeley National Laboratory. TIC: 247870.
- Day, W.C.; Potter, C.J.; Sweetkind, D.S.; Dickerson, R.P.; and San Juan, C.A. 1998. *Bedrock Geologic Map of the Central Block Area, Yucca Mountain, Nye County, Nevada*. Miscellaneous Investigations Series Map I-2601. [Washington, D.C.]: U.S. Geological Survey. ACC: MOL.19980611.0339.
- DOE (U.S. Department of Energy) 2001. *Yucca Mountain Science and Engineering Report*. DOE/RW-0539. [Washington, D.C.]: U.S. Department of Energy, Office of Civilian Radioactive Waste Management. ACC: MOL.20010524.0272.

EPRI (Electric Power Research Institute) 1993. *Method and Guidelines for Estimating Earthquake Ground Motion*. Volume 1 of *Guidelines for Determining Design Basis Ground Motions in Eastern North America*. EPRI TR-102293. Palo Alto, California: Electric Power Research Institute. TIC: 226495.

Foinquinos Mera, R. 1991. *Analytical Study and Inversion for the Spectral Analysis of Surface Waves Method*. Master's thesis. Austin, Texas: University of Texas, Austin. TIC: 252162.

Geslin, J.K.; Moyer, T.C.; and Buesch, D.C. 1995. *Summary of Lithologic Logging of New and Existing Boreholes at Yucca Mountain, Nevada, August 1993 to February 1994*. Open-File Report 94-342. Denver, Colorado: U.S. Geological Survey. ACC: MOL.19940810.0011.

Gibson, J.D.; Shephard, L.E.; Swan, F.H.; Wesling, J.R.; and Kerl, F.A. 1990. "Synthesis of Studies for the Potential of Fault Rupture at the Proposed Surface Facilities, Yucca Mountain, Nevada." *High Level Radioactive Waste Management, Proceedings of the International Topical Meeting, Las Vegas, Nevada, April 8-12, 1990, 1*, 109-116. La Grange Park, Illinois: American Nuclear Society. TIC: 202058.

Hardin, B.O. and Drnevich, V.P. 1972. "Shear Modulus and Damping in Soils: Measurement and Parameter Effects." *Journal of The Soil Mechanics and Foundations Division*, 98, (SM6), 603-624. New York, New York: American Society of Civil Engineers. TIC: 251418.

Ho, D.M.; Sayre, R.L.; and Wu, C.L. 1986. *Suitability of Natural Soils for Foundations for Surface Facilities at the Prospective Yucca Mountain Nuclear Waste Repository*. SAND85-7107. Albuquerque, New Mexico: Sandia National Laboratories. ACC: NNA.19890327.0053.

Joh, S.-H. 1996. *Advances in the Data Interpretation Technique for Spectral-Analysis-of-Surface-Waves (SASW) Measurements*. Ph.D. dissertation. Austin, Texas: University of Texas at Austin. TIC: 252117.

Joyner, W.B.; Warrick, R.E.; and Fumal, T.E. 1981. "The Effect of Quaternary Alluvium on Strong Ground Motion in the Coyote Lake, California, Earthquake of 1979." *Bulletin of the Seismological Society of America*, 71 (4), 1333-1349. Berkeley, California: Seismological Society of America. TIC: 251490.

Kausel, E. and Roesset, J.M. 1981. "Stiffness Matrices for Layered Soils." *Bulletin of the Seismological Society of America*, 71 (6), 1743-1761. Berkeley, California: Seismological Society of America. TIC: 251419.

Kim, D.-S. 1991. *Deformational Characteristics of Soils at Small to Intermediate Strains from Cyclic Tests*. Ph.D. dissertation. Austin, Texas: University of Texas at Austin. TIC: 252163.

Kim, D.-S. and Stokoe, K.H., II 1994. "Torsional Motion Monitoring System for Small-Strain (10^{-5} to $10^{-3}\%$) Soil Testing" *Geotechnical Testing Journal*, 17, (1), 17-26. Philadelphia, Pennsylvania: American Society for Testing and Materials. TIC: 251420.

Ladd, R.S. 1978. "Preparing Test Specimens Using Undercompaction." *Geotechnical Testing Journal*, 1 (1), 16-23. New York, New York: American Society for Testing and Materials. TIC: 243278.

Lipman, P.W.; Christiansen, R.L.; and O'Connor, J.T. 1966. *A Compositionally Zoned Ash-Flow Sheet in Southern Nevada*. Professional Paper 524-F. Washington, D.C.: U.S. Geological Survey. TIC: 219972.

Lodde, P.F. 1982. *Dynamic Response of San Francisco Bay Mud*. Ph.D. dissertation. Austin, Texas: University of Texas at Austin, Civil Engineering Department. TIC: 252236.

Luebbers M.J. 2000. Waste Handling Building - Revised Shear Wave Velocity Model. Scientific Notebook SN-M&O-SCI-015-V1. ACC: MOL.20000718.0213.

Luebbers, M.J. 2002a. Borehole Suspension Seismic Component of Geotechnical Investigation for a Potential Waste Handling Building. Scientific Notebook SN-M&O-SCI-024-V1. ACC: MOL.20020509.0127, MOL.20020509.0129, MOL.20020509.0130, MOL.20020509.0132.

Luebbers, M.J. 2002b. Borehole Suspension Seismic Component of Geotechnical Investigation for a Potential Waste Handling Building. Scientific Notebook SN-M&O-SCI-024-V2. ACC: MOL.20020509.0128, MOL.20020509.0130, MOL.20020509.0131, MOL.20020509.0132, MOL.20020509.0133.

Luebbers, M.J. 2002c. Downhole Seismic Component of Geotechnical Investigation for a Potential Waste Handling Building. Scientific Notebook SN-M&O-SCI-025-V1. ACC: MOL.20020228.0297.

Marcuson, W.F., III. 1978. "Determination of In Situ Density of Sands." *Dynamic Geotechnical Testing, A Symposium Sponsored by ASTM Committee D-18 on Soil and Rock for Engineering Purposes, American Society for Testing and Materials, Denver, Colorado, 28 June 1977*. ASTM STP 654. Pages 318-340. Philadelphia, Pennsylvania: American Society for Testing and Materials. TIC: 210237.

Mongano, G.S.; Singleton, W.L.; Moyer, T.C.; Beason, S.C.; Eatman, G.L.W.; Albin, A.L.; and Lung, R.C. 1999. *Geology of the ECRB Cross Drift – Exploratory Studies Facility, Yucca Mountain Project, Yucca Mountain, Nevada*. [Deliverable SPG42GM3]. Denver, Colorado: U.S. Geological Survey, ACC: MOL.20000324.0614.

Ohya, S. 1986. "In Situ P and S Wave Velocity Measurement." *Use of In Situ Tests in Geotechnical Engineering, Proceedings of In Situ '86, a Specialty Conference Sponsored by the Geotechnical Engineering Division of the American Society of Civil Engineers, Blacksburg, Virginia, June 23-25, 1986*. Geotechnical Special Publication No. 6. Clemence, S.P., ed. Pages 1218-1235. New York, New York: American Society of Civil Engineers. TIC: 250977.

Redpath, B. 2002. Downhole Seismic Logging at Yucca Mountain Crest. Scientific Notebook SN-M&O-SCI-039-V1. ACC: MOL.20020429.0150, MOL.20020429.0151, MOL.20020429.0152, MOL.20020429.0154.

Richart, F.E., Jr.; Woods, R.D.; and Hall, J.R., Jr. 1970. *Vibrations of Soils and Foundations*. Englewood Cliffs, New Jersey: Prentice Hall. TIC: 240470.

Roesset, J.M.; Chang D.-W.; and Stokoe, K.H., II. 1991. "Comparison of 2-D and 3-D Models for Analysis of Surface Wave Tests." *Soil Dynamics and Earthquake Engineering V, Fifth International Conference on Soil Dynamics and Earthquake Engineering, SDEE 91, Karlsruhe, Germany, September 23-26, 1991*. Pages 111-126. Boston, [Massachusetts]: Computational Mechanics Publications. TIC: 251643.

Ross, C.S. and Smith, R.L. 1961. *Ash Flow Tuffs: Their Origin, Geologic Relations, and Identification*. Professional Paper 366. Reston, Virginia: U.S. Geological Survey. TIC: 216668.

Sawyer, D.A.; Fleck, R.J.; Lanphere, M.A.; Warren, R.G.; Broxton, D.E.; and Hudson, M.R. 1994. "Episodic Caldera Volcanism in the Miocene Southwestern Nevada Volcanic Field: Revised Stratigraphic Framework, 40Ar/39Ar Geochronology, and Implications for Magmatism and Extension." *Geological Society of America Bulletin*, 106, (10), 1304-1318. Boulder, Colorado: Geological Society of America. TIC: 222523.

Schlumberger Educational Services 1987. *Log Interpretation Principles/Applications*. Houston, Texas: Schlumberger Educational Services. TIC: 236275.

Schuraytz, B.C.; Vogel, T.A.; and Younker, L.W. 1989. "Evidence for Dynamic Withdrawal from a Layered Magma Body: The Topopah Spring Tuff, Southwestern Nevada." *Journal of Geophysical Research*, 94, (B5), 5925-5942. Washington, D.C.: American Geophysical Union. TIC: 225936.

Seed, H.B.; Wong, R.T.; Idriss, I.M.; and Tokimatsu, K. 1986. "Moduli and Damping Factors for Dynamic Analyses of Cohesionless Soils." *Journal of Geotechnical Engineering*, 112 (11), 1016-1033. New York, New York: American Society of Civil Engineers. TIC: 243355.

Stokoe, K.H., II; Hwang, S.-K.; Roesset, J.M.; and Sun, C.W. 1994. "Laboratory Measurement of Small-Strain Material Damping of Soil Using a Free-Free Resonant Column." *Earthquake Resistant Construction and Design, Proceedings of the Second International Conference on Earthquake Resistant Construction and Design, Berlin, 15-17 June 1994*. Savidis, S.A., ed. Pages 195-202. Rotterdam, The Netherlands: A.A. Balkema. TIC: 251641.

Stokoe, K.H., II; Wright, S.G.; Bay, J.A.; and Roesset, J.M. 1994. "Characterization of Geotechnical Sites by SASW Method." *Volume Prepared by ISSMFE Technical Committee #10 for XIII ICSMFE, 1994, New Delhi, India*. Woods, R.D., ed. New York, New York: International Science Publisher. TIC: 251421.

USGS (U.S. Geological Survey) 2001. *Water-Level Data Analysis for the Saturated Zone Site-Scale Flow and Transport Model*. ANL-NBS-HS-000034 REV 01. Denver, Colorado: U.S. Geological Survey. ACC: MOL.20020209.0058.

Wahl, J.S.; Tittman, J.; Johnstone, C.W.; and Alger, R.P. 1964. "The Dual Spacing Formation Density Log." *Journal of Petroleum Technology*, [16], ([12]), 1411-1416. Dallas, Texas: Society of Petroleum Engineers of AIME. TIC: 250964.

Wilson, R.C.; Warrick, R.E.; and Bennett, M.J. [1978]. "Seismic Velocities of San Francisco Bayshore Sediments." [*Earthquake Engineering and Soil Dynamics, Proceeding of the ASCE Geotechnical Engineering Division Specialty Conference, June 19-21, 1978, Pasadena, CA.*] [3], 1007-1023. [New York, New York: American Society of Civil Engineers]. TIC: 252168.

Wong, I.G. 2001. Crosshole Seismic Velocity Measurements in the North Ramp of the Exploratory Studies Facility [Initial Entry - Notebook Cancelled]. Scientific Notebook SN-M&O-SCI-020-V1. ACC: MOL.20010827.0034.

Wong, I.G. 2002a. SASW Measurements Near the Top of Yucca Mountain and in the Potential Repository Block. Scientific Notebook SN-M&O-SCI-040-V1. ACC: MOL.20020619.0461, MOL.20020619.0462.

Wong, I.G. 2002b. Downhole Seismic Measurements at the Potential Waste Handling Building Site. Scientific Notebook SN-M&O-SCI-030-V1. ACC: MOL.20020227.0168.

Wong, I.G. 2002c. SASW Measurements at Waste Handling Building Site. Scientific Notebook SN-M&O-SCI-022-V1. ACC: MOL.20020520.0222; MOL.20020520.0223; MOL.20020520.0225; MOL.20020520.0226.

Wong, I.G. 2002d. SASW Measurements at the Top of Yucca Mountain. Scientific Notebook SN-M&O-SCI-023-V1. ACC: MOL.20020607.0198, MOL.20020607.0201, MOL.20020607.0202.

Wong, I.G. 2002e. Laboratory Dynamic Testing of Rock and Soil Specimens for the Potential Waste Handling Building Site. Scientific Notebook SN-M&O-SCI-033-V1. ACC: MOL.20020508.0336; MOL.20020508.0392; MOL.20020508.0337; MOL.20020508.0394.

Wong, I.; Kelson, K.; Olig, S.; Kolbe, T.; Hemphill-Haley, M.; Bott, J.; Green, R.; Kanakari, H.; Sawyer, J.; Silva, W.; Stark, C.; Haraden, C.; Fenton, C.; Unruh, J.; Gardner, J.; Reneau, S.; and House, L. 1995. *Seismic Hazards Evaluation of the Los Alamos National Laboratory*. Volume 1. Oakland, California: Woodward-Clyde Federal Services. TIC: 247191.

YMP (Yucca Mountain Site Characterization Project) 1998. Borehole Video for Geotechnical Hole UE-25 RF#13. LA-EES-7-LV-NBK-98-001, 41V. [Las Vegas, Nevada: Yucca Mountain Site Characterization Office]. ACC: MOL.19990914.0122.

YMP (Yucca Mountain Site Characterization Project) 2001. *Q-List*. YMP/90-55Q, Rev. 7. Las Vegas, Nevada: Yucca Mountain Site Characterization Office. ACC: MOL.20010409.0366.

8.2 STANDARDS AND PROCEDURES

10 CFR 63. 2002. *Energy: Disposal of High-Level Radioactive Wastes in a Geologic Repository at Yucca Mountain, Nevada*. Readily available.

AP-2.21Q, Rev. 1, BSCN 1. *Quality Determinations and Planning for Scientific, Engineering, and Regulatory Compliance Activities*. Las Vegas, Nevada: CRWMS M&O. ACC: MOL.20010212.0018.

AP-2.22Q, Rev. 0. *Classification Criteria and Maintenance of the Monitored Geologic Repository Q-List*. Las Vegas, Nevada: CRWMS M&O. ACC: MOL.20020314.0046.

AP-SI.1Q, Rev. 3, ICN 4. *Software Management*. Las Vegas, Nevada: CRWMS M&O. ACC: MOL.20020520.0283.

AP-SIII.5, Rev. 0. *Yucca Mountain Site Characterization Project Field Verification of Geophysical Operations*. Las Vegas, Nevada: CRWMS M&O. ACC: MOL.20010604.0219.

AP-SIII.6Q, Rev. 0. *Geophysical Logging Programs for Surface-Based Testing Program Boreholes*. Las Vegas, Nevada: CRWMS M&O. ACC: MOL.20010604.0045.

AP-SV.1Q, Rev 0, ICN 2. *Control of the Electronic Management of Information*. Las Vegas, Nevada: CRWMS M&O. MOL.20000831.0065.

ASTM C 136-96a. 1996. *Standard Test Method for Sieve Analysis of Fine and Coarse Aggregates*. West Conshohocken, Pennsylvania: American Society for Testing and Materials. TIC: 241447.

ASTM D 653-97. 1997. *Standard Terminology Relating to Soil, Rock, and Contained Fluids*. West Conshohocken, Pennsylvania: American Society for Testing and Materials. TIC: 248967.

ASTM D 1557-91. 1998. *Standard Test Method for Laboratory Compaction Characteristics of Soil Using Modified Effort (56,000 ft-lbf/ft³ (2,700 kN-m/m³))*. West Conshohocken, Pennsylvania: American Society for Testing and Materials. TIC: 242992.

LP-GEO-001Q-M&O, Rev. 0, ICN 0. *Laboratory Geotechnical Testing of Soil, Rock and Aggregate Samples*. Washington, D.C.: U.S. Department of Energy, Office of Civilian Radioactive Waste Management. ACC: MOL.20001215.0254.

LP-GEO-002Q-BSC, Rev. 0, ICN 1. *Laboratory Dynamic Rock/Soil Testing*. Washington, D.C.: U.S. Department of Energy, Office of Civilian Radioactive Waste Management. ACC: MOL.20010406.0165.

NWI-SPO-004Q, Rev. 0. *Laboratory Dynamic Rock/Soil Testing*. Las Vegas, Nevada: CRWMS M&O. ACC: MOL.19990317.0325.

PBRCTS-1, Rev. 4. *Technical Procedures for Resonant Column and Torsional Shear (RCTS) Testing of Soil and Rock Samples*. Austin, Texas: Geotechnical Engineering Center, University of Texas, Austin. TIC: 252682.

USBR 5000-86. *Procedure for Determining Unified Soil Classification (Laboratory Method)*. Denver, Colorado: U.S. Department of the Interior, Bureau of Reclamation. TIC: 232041.

USBR 5005-86. *Procedure for Determining Unified Soil Classification (Visual Method)*. Denver, Colorado: U.S. Department of the Interior, Bureau of Reclamation. TIC: 232041.

USBR 5205-89. *Procedure for Preparing Soil Samples by Splitting or Quartering*. Denver, Colorado: U.S. Department of the Interior, Bureau of Reclamation. TIC: 232041.

USBR 5300-89. *Procedure for Determining Moisture Content of Soil and Rock by the Oven Method*. Denver, Colorado: U.S. Department of the Interior, Bureau of Reclamation. TIC: 232041.

USBR 5320-89. *Procedure for Determining Specific Gravity of Soils*. Denver, Colorado: U.S. Department of the Interior, Bureau of Reclamation. TIC: 232041.

USBR 5325-89. *Procedure for Performing Gradation Analysis of Gravel Size Fraction of Soils*. Denver, Colorado: U.S. Department of the Interior, Bureau of Reclamation. TIC: 232041.

USBR 5330-89. *Procedure for Performing Gradation Analysis of Fines and Sand Size Fraction of Soils, Including Hydrometer Analysis*. Denver, Colorado: U.S. Department of the Interior, Bureau of Reclamation. TIC: 232041.

USBR 5335-89. *Procedure for Performing Gradation Analysis of Soils Without Hydrometer – Wet Sieve*. Denver, Colorado: U.S. Department of the Interior, Bureau of Reclamation. TIC: 232041.

USBR 5350-89. *Procedure for Determining the Liquid Limit of Soils by the One-Point Method*. Denver, Colorado: U.S. Department of the Interior, Bureau of Reclamation. TIC: 232041.

USBR 5360-89. *Procedure for Determining the Plastic Limit and Plasticity Index of Soils*. Denver, Colorado: U.S. Department of the Interior, Bureau of Reclamation. TIC: 232041.

USBR 5525-89. *Procedure for Determining the Minimum Index Unit Weight of Cohesionless Soils*. Denver, Colorado: U.S. Department of the Interior, Bureau of Reclamation. TIC: 232041.

USBR 5530-89. *Procedure for Determining the Maximum Index Unit Weight of Cohesionless Soils*. Denver, Colorado: U.S. Department of the Interior, Bureau of Reclamation. TIC: 232041.

USBR 7205-89. *Procedure for Determining Unit Weight of Soils In-Place by the Sand-Cone Method*. Denver, Colorado: U.S. Department of the Interior, Bureau of Reclamation. TIC: 232041.

USBR 7221-89. *Procedure for Determining Unit Weight of Soils In-Place by the Water Replacement Method in a Test Pit*. Denver, Colorado: U.S. Department of the Interior, Bureau of Reclamation. TIC: 232041.

8.3 SOURCE DATA, LISTED BY DATA TRACKING NUMBER (DTN)

GS000508312332.001. Water-Level Data Analysis for the Saturated Zone Site-Scale Flow and Transport Model. Submittal date: 06/01/2000.

GS020383114233.001. Waste Handling Building Test Pit Logs With Photomosaic Test Pit Maps. TDIF: 312887. Submittal date: 03/28/2002.

GS020383114233.003. Geotechnical Borehole Logs for the Waste Handling Building, Yucca Mountain Project, Nevada Test Site, Nevada. Submittal date: 03/28/2002.

GS020483114233.004. Geotechnical Field and Laboratory Test Results from Waste Handling Building Foundation Investigation. Submittal date: 04/15/2002.

GS020783114233.005. Gradation Analysis Test Results and Graphical Plots from Tests Performed on Materials Excavated from In-Situ Density Test Locations in Test Pits from the Waste Handling Building Foundation Investigations. Submittal date: 07/23/2002.

GS920983114220.001. Log of Test Pit or Auger Hole, Physical Properties Summary, Gradation Test, and Summary of Physical Properties Test Results for Hole Numbers NRSF-TP-11, TP-19, TP-21, TP-25, TP-28, TP-29, and TP-30. Submittal date: 09/03/1992.

GS931008314211.036. Graphical Lithologic Log of Borehole RF-3 (UE-25 RF#3), Version 1.0. Submittal date: 10/07/1993.

GS940208314211.004. Table of Contacts in Borehole USW UZ-N27. Submittal date: 02/10/1994.

GS940208314211.006. Table of Contacts in Boreholes USW UZ-N33 AND USW UZ-N34. Submittal date: 02/10/1994.

GS940308314211.009. Summary of Lithologic Logging of New and Existing Boreholes at Yucca Mountain, Nevada: August 1993 to February 1994. Submittal date: 03/01/1994.

GS940408314224.004. Plan View Geologic Map of the Drainage Channel and North Portal. Submittal date: 04/20/1994.

GS940708314211.032. Summary of Lithologic Logging of New and Existing Boreholes at Yucca Mountain, Nevada, March 1994 to June 1994. Submittal date: 07/08/1994.

GS940908314211.045. Graphical Lithologic Log of the Paintbrush Group for Borehole USW SD-12. Submittal date: 09/12/94.

GS941108314211.052. Graphical Lithologic Log of Borehole USW SD-9 from the Base of the Paintbrush Group to Total Depth. Submittal date: 11/03/1994.

GS980608314221.002. Revised Bedrock Geologic Map of the Yucca Mountain Area, Nye County, Nevada. Submittal date: 06/09/1998.

MO0001SEPRADSD.000. Downhole Seismic Data. Submittal date: 01/11/2000.

MO0008GSC00286.000. Exploratory Studies Facility (ESF) North Portal Pad, Waste Handling Building (WHB) Profile Sections #3, #4, #5, #6, #7, and #8. Submittal date: 08/17/2000.

MO0012GSC00405.000. Waste Handling Building (WHB) Site Investigations, As-Built Surveys for Test Pit #1 through #4. Submittal date: 12/22/2000.

MO0101COV00396.000. Coverage: Bores 3. Submittal date: 01/05/2001.

MO0101SEPBGLOG.000. Sample Management & Drilling Department Records Package for Borehole Records (Geologic Logs) from the "Geotechnical Field Investigation for the Waste Handling Building" FWP-SB-00-003. Submittal date: 01/10/2001.

MO0110DVDBOREH.000. Downhole Velocity Data from Boreholes RF-13 and RF-17. Submittal date: 10/17/2001.

MO0110SASWVDYM.000. SASW Velocity Data from the Top of Yucca Mountain. Submittal date: 10/02/2001.

MO0110SASWWHBS.000. SASW Velocity Data from the Waste Handling Building Site Characterization Area. Submittal date: 10/02/2001.

MO0111DVDWHBSC.001. Downhole Velocity Data at the Waste Handling Building Site Characterization Area. Submittal date: 11/08/2001.

MO0112GPLOGWHB.001. Developed Geophysical Log Data from Forensic Evaluation of Geophysical Log Data Collected in Support of the Waste Handling Building. Submittal date: 12/03/2001.

MO0112GSC01170.000. Borrow Pit #1 (Fran Ridge), USBR Sample Locations, for WHB Investigations. Submittal date: 12/04/2001.

MO0202DVDWHBSC.002. Downhole Velocity Data from the Top of Yucca Mountain. Submittal date: 02/11/2002.

MO0202DWAVEATD.000. Downhole S-Wave and P-Wave Interpreted Arrival Time Data from Boreholes RF#13 and RF#17. Submittal date: 02/13/2002.

MO0202GEOSOILP.000. Statistical Summary of Geotechnical Soil Properties by Lithostratigraphical Units. Submittal date: 02/19/2002.

MO0202WHBTMPKS.000. Time Picks for Downhole Seismic Surveys.
Submittal date: 02/13/2002.

MO0203DHRSSWHB.001. Dynamic Laboratory Test Data for Rock and Soil Samples from the Waste Handling Building Site Characterization Area. Submittal date: 03/19/2002.

MO0203EBSCTCTS.016. Compaction and Triaxial Compression Tests of Soil Sample.
Submittal date: 04/01/2002.

MO0203SEPSASWD.000. SASW Velocity Data from the Top of Yucca Mountain. Submittal date: 03/28/2002.

MO02045FTDSUSP.001. Statistics for Shear-Wave Velocity, Compression-Wave Velocity, and Poisson's Ratio by 1.5-Meter Depth Intervals from Suspension Seismic Measurements.
Submittal date: 04/23/2002.

MO020498DNHOLE.000. Shear-Wave and Compression-Wave Velocity Profiles from 1998 Downhole Survey at Borehole UE-25 RF#13. Submittal date: 04/08/2002.

MO0204DENBROCK.000. Statistics for Bulk Density Values by Lithostratigraphic Unit.
Submittal date: 04/23/2002.

MO0204SEISDWHB.001. Suspension Seismic Data for Borehole UE-25 RF#13 at the Waste Handling Building Site Characterization Area. Submittal date: 04/08/2002.

MO0204SEPBSWHB.001. Borehole Suspension Data for Waste Handling Building Site Characterization Area. Submittal date: 04/10/2002.

MO0204SEPFDSSS.000. Profiles of Average Shear-Wave Velocity, Compression-Wave Velocity and Poisson's Ratio from Accumulated Travel Times from Suspension Seismic Surveys at Boreholes UE-25 RF#14 to #26 and RF#28 and RF#29. Submittal date: 04/22/2002.

MO0204SEPGAMDM.000. Statistical Analysis of Gamma-Gamma Density Measurements by Lithostratigraphic Unit. Submittal date: 04/22/2002.

MO0204SEP_SOILP.000. Mean Values of Soil Properties by Lithostratigraphic Unit.
Submittal date: 04/02/2002.

MO0204SEPSWSSS.000. Profile of Average Shear-Wave Velocities from Accumulated Travel Times from a Suspension Seismic Survey at Borehole UE-25 RF#13.
Submittal date: 04/22/2002.

MO0204SUSPSEIS.001. Statistics for Shear-Wave Velocity, Compression-Wave Velocity, and Poisson's Ratio by Lithostratigraphic Unit from Suspension Seismic Measurements. Submittal Date 04/23/2002.

MO0205SEPPRDSV.000. Profiles of Poisson's Ratio from Downhole Seismic Velocity Profiles at Boreholes UE-25 RF#13 to #26 and RF#28 and RF#29. Submittal date: 05/28/2002.

MO0205SWDQRTWF.000. Plots of Average Shear-Wave Velocity Versus Depth and Quarter-Wavelength Amplification Ratio Versus Frequency at Boreholes UE-25 RF#14 to UE-25 RF#19 and UE-25 RF#29. Submittal date: 05/01/2002.

MO0206EBSFRBLT.018. Fran Ridge Borrow Lab Testing. Submittal date: 06/10/2002.

MO0206SASWROCK.000. SASW Velocity Data from Rock Sites on the Crest of Yucca Mountain and in the ESF. Submittal date: 06/19/2002.

MO98PRECLOSURE.000. Design Event Spectra Based on the Results of the Probabilistic Seismic Hazard Analyses for Yucca Mountain and a Velocity Profile for the Repository Block to Support Development of Ground Motion Design Inputs. Submittal date: 02/20/1998.

MO9905LABDYNRS.000. Laboratory Dynamic Rock/Soil Testing for UE-25 RF#13. Submittal date: 05/06/1999.

SNL01A05059301.005. Laboratory Thermal Conductivity Data for Boreholes UE25 NRG-4, NRG-5; USW NRG-6 and NRG-7/7A. Submittal date: 02/07/1996.

SNL02030193001.001. Mechanical Properties for Drill Hole USW NRG-6 Samples from Depth 22.2 ft. to 328.7 ft. Submittal date: 05/17/1993.

SNL02030193001.002. Mechanical Properties Data for Drill Hole USW NRG-6 Samples from Depth 22.2 ft. to 427.0 ft. Submittal date: 06/25/1993.

SNL02030193001.003. Mechanical Properties Data for Drill Hole UE-25 NRG#2 Samples from Depth 170.4 ft. to 200.0 ft. Submittal date: 07/07/1993.

SNL02030193001.004. Mechanical Properties Data for Drill Hole USW NRG-6 Samples from Depth 462.3 ft. to 1085.0 ft. Submittal date: 08/05/1993.

SNL02030193001.005. Mechanical Properties Data for Drill Hole UE-25 NRG#3 Samples from Depth 15.4 ft. to 297.1 ft. Submittal date: 09/23/1993.

SNL02030193001.006. Mechanical Properties Data for Drill Hole UE-25 NRG#2A Samples from Depth 90.0 ft. to 254.5 ft. Submittal date: 10/13/1993.

SNL02030193001.007. Mechanical Properties Data for Drill Hole UE25 NRG#3 Samples from Depth 263.3 ft. to 265.7 ft. Submittal date: 10/20/1993.

SNL02030193001.008. Mechanical Properties Data for Drill Hole USW NRG-6 Sample at Depth of 416.0 ft. Submittal date: 10/20/1993.

SNL02030193001.009. Mechanical Properties Data for Drill Hole UE-25 NRG-5 Samples from Depth 781.0 ft. to 991.9 ft. Submittal date: 11/18/1993.

SNL02030193001.010. Mechanical Properties Data for Drill Hole UE25 NRG-2B Samples from Depth 2.7 ft. to 87.6 ft. Submittal date: 11/18/1993.

SNL02030193001.011. Mechanical Properties Data for Drill Hole UE25 NRG-2A Samples from Depth 135.3 ft. to 166.5 ft. Submittal date: 11/18/1993.

SNL02030193001.012. Mechanical Properties for Drill Hole UE25 NRG-5 Samples from Depth 847.2 ft. to 896.5 ft. Submittal date: 12/02/1993.

SNL02030193001.013. Mechanical Properties Data for Drill Hole UE25 NRG-2B Samples from Depth 2.7 ft. to 87.6 ft. Submittal date: 12/02/1993.

SNL02030193001.014. Mechanical Properties Data for Drill Hole UE25 NRG-4 Samples from Depth 378.1 ft. to 695.8 ft. Submittal date: 01/31/1994.

SNL02030193001.015. Mechanical Properties Data for Drill Hole UE25 NRG-4 Samples from Depth 527.0 ft. Submittal date: 02/16/1994.

SNL02030193001.016. Mechanical Properties Data for Drill Hole USW NRG-7/7A Samples from Depth 18.0 ft. to 472.9 ft. Submittal date: 03/16/1994.

SNL02030193001.017. Mechanical Properties Data for Drill Hole USW NRG-7/7A Samples from Depth 18.0 ft. to 495.0 ft. Submittal date: 03/21/1994.

SNL02030193001.018. Mechanical Properties Data for Drill Hole USW NRG-7/7A Samples from Depth 344.4 ft. Submittal date: 04/11/1994.

SNL02030193001.019. Mechanical Properties Data for Drill Hole USW NRG-7/7A Samples from Depth 507.4 ft. to 881.0 ft. Submittal date: 06/29/1994.

SNL02030193001.020. Mechanical Properties Data for Drill Hole USW NRG-7/7A Samples from Depth 554.7 ft. to 1450.1 ft. Submittal date: 07/25/1994.

SNL02030193001.021. Mechanical Properties Data (Ultrasonic Velocities, Static Elastic Properties, Triaxial Strength, Dry Bulk Density & Porosity) for Drill Hole USW NRG-7/7A Samples from Depth 345.0 ft. to 1408.6 ft. Submittal date: 02/16/1995.

SNL02030193001.022. Mechanical Properties Data for Drill Hole USW NRG-6 Samples from Depth 5.7 ft. to 1092.3 ft. Submittal date: 02/27/1995.

SNL02030193001.023. Mechanical Properties Data (Ultrasonic Velocities, Static Elastic Properties, Unconfined Strength, Triaxial Strength, Dry Bulk Density & Porosity) for Drill Hole USW SD-12 Samples from depth 16.1 ft. to 1300.3 ft. Submittal date: 08/02/1995.

SNL02030193001.024. Elevated Temperature Confined Compression Tests (Ultrasonic Velocities, Static Elastic Properties, Unconfined Strength, Triaxial Strength, Dry Bulk Density & Porosity) for Drill Hole USW SD-9 Samples from 52.6 ft. to 2222.9 ft. Submittal date: 09/05/1995.

SNL02030193001.026. Mechanical Properties Data (Ultrasonic Velocities, Elastic Moduli and Fracture Strength) for Borehole USW SD-9. Submittal date: 02/22/1996.

SNL02030193001.027. Summary Of Bulk Property Measurements Including Saturated Bulk Density For NRG-2, NRG-2A, NRG-2B, NRG-3, NRG-4, NRG-5, NRG-6, NRG-7/7A, SD-9, and SD-12. Submittal date: 08/14/1996.

SNSAND85081500.000. Preliminary Validation of Geology at Site for Repository Surface Facilities, Yucca Mountain, Nevada. Submittal date: 11/01/1986.

SNSAND90249100.000. Summary and Evaluation of Existing Geological and Geophysical Data Near Prospective Surface Facilities in Midway Valley, Yucca Mountain Project, Nye County, Nevada. Submittal date: 01/01/1992.

8.4 SOFTWARE CODES

University of Texas 2002. *Software Code: WinSASW*. V1.23. 10588-1.23-00.

9. ATTACHMENTS

Attachment	Title
I	Logs of Boreholes RF#14 to RF#29
II	Revised Logs of Borehole RF#13
III	Logs of Test Pits TP-WHB-1 to TP-WHB-4
IV	Photomosaic Maps of Test Pits TP-WHB-1 to TP-WHB-4
V	Downhole Seismic Velocity Plots (Redpath) – WHB Area
VI	Downhole Seismic Velocity Plots (GEOVision) – WHB Area
VII	Suspension Seismic Interval Velocity Results
VIII	Suspension Seismic Accumulated Velocity Results
IX	SASW Velocity Plots – WHB Area
X	Borehole Geophysical Surveys
XI	Geotechnical Laboratory Static Testing – WHB Area
XII	Geotechnical Laboratory Dynamic Testing – WHB Area
XIII	SASW Velocity Plots – ESF
XIV	Geotechnical Laboratory Dynamic Testing – ESF
XV	SASW Velocity Plots – Yucca Mountain Crest
XVI	Downhole Seismic Velocity Plots– Yucca Mountain Crest
XVII	Geotechnical Laboratory Dynamic Testing – Fran Ridge
XVIII	Glossary